

# Low-Dimensional Carbon Nanomaterials: Synthesis, Properties, and Applications

Guest Editors: Sulin Zhang, Teng Li, Jianyu Huang, and Vivek Shenoy





---

# **Low-Dimensional Carbon Nanomaterials: Synthesis, Properties, and Applications**

## **Low-Dimensional Carbon Nanomaterials: Synthesis, Properties, and Applications**

Guest Editors: Sulin Zhang, Teng Li, Jianyu Huang,  
and Vivek Shenoy



---

Copyright © 2011 Hindawi Publishing Corporation. All rights reserved.

This is a special issue published in volume 2011 of “Journal of Nanomaterials.” All articles are open access articles distributed under the Creative Commons Attribution License, which permits unrestricted use, distribution, and reproduction in any medium, provided the original work is properly cited.

## Editorial Board

- Katerina Aifantis, Greece  
Nageh K. Allam, USA  
Margarida Amaral, Portugal  
Xuedong Bai, China  
Enrico Bergamaschi, Italy  
Theodorian Borca-Tasciuc, USA  
C. Jeffrey Brinker, USA  
Christian Brosseau, France  
Xuebo Cao, China  
Sang-Hee Cho, Republic of Korea  
Shafiul Chowdhury, USA  
Cui ChunXiang, China  
Miguel A. Correa-Duarte, Spain  
Shadi A. Dayeh, USA  
Ali Eftekhari, USA  
Claude Estournes, France  
Alan Fuchs, USA  
Lian Gao, China  
Russell E. Gorga, USA  
Hongchen Chen Gu, China  
Mustafa O. Guler, Turkey  
John Zhanhu Guo, USA  
Smrati Gupta, Germany  
Michael Harris, USA  
Zhongkui Hong, USA  
Michael Z. Hu, USA  
David Hui, USA  
Y.-K. Jeong, Republic of Korea  
Sheng-Rui Jian, Taiwan  
Wanqin Jin, China  
Rakesh K. Joshi, India  
Zhenhui Kang, China
- Fathallah Karimzadeh, Iran  
Do Kyung Kim, Republic of Korea  
Kin Tak Lau, Australia  
Burtrand Lee, USA  
Benxia Li, China  
Jun Li, Singapore  
Shijun Liao, China  
Gong Ru Lin, Taiwan  
J.-Y. Liu, USA  
Jun Liu, USA  
Tianxi Liu, China  
Songwei Lu, USA  
Daniel Lu, China  
Jue Lu, USA  
Ed Ma, USA  
Gaurav Mago, USA  
Sanjay R. Mathur, Germany  
Nobuhiro Matsushita, Japan  
A. McCormick, USA  
Vikas Mittal, UAE  
Weihai Ni, Germany  
Sherine Obare, USA  
Edward Andrew Payzant, USA  
Kui-Qing Peng, China  
Anukorn Phuruangrat, Thailand  
Ugur Serincan, Turkey  
Huaiyu Shao, Japan  
Donglu Shi, USA  
Suprakas Sinha Ray, South Africa  
Vladimir Sivakov, Germany  
Marinella Striccoli, Italy  
Bohua Sun, South Africa
- Saikat Talapatra, USA  
Nairong Tao, China  
Titipun Thongtem, Thailand  
Somchai Thongtem, Thailand  
Valeri P. Tolstoy, Russia  
Tsung-Yen Tsai, Taiwan  
Takuya Tsuzuki, Australia  
Raquel Verdejo, Spain  
Mat U. Wahit, Malaysia  
Shiren Wang, USA  
Yong Wang, USA  
Cheng Wang, China  
Zhenbo Wang, China  
Jinquan Wei, China  
Ching Ping Wong, USA  
Xingcai Wu, China  
Guodong Xia, Hong Kong  
Zhi Li Xiao, USA  
Ping Xiao, UK  
Shuangxi Xing, China  
Yangchuan Xing, USA  
N. Xu, China  
Doron Yadlovker, Israel  
Ying-Kui Yang, China  
Khaled Youssef, USA  
Kui Yu, Canada  
Haibo Zeng, China  
Tianyou Zhai, Japan  
Renyun Zhang, Sweden  
Yanbao Zhao, China  
Lianxi Zheng, Singapore  
Chunyi Zhi, Japan

# Contents

**Low-Dimensional Carbon Nanomaterials: Synthesis, Properties, and Applications**, Sulin Zhang, Teng Li, Jianyu Huang, and Vivek Shenoy  
Volume 2011, Article ID 518189, 2 pages

**Synthesis, Properties, and Applications of Low-Dimensional Carbon-Related Nanomaterials**, Ali Mostofizadeh, Yanwei Li, Bo Song, and Yudong Huang  
Volume 2011, Article ID 685081, 21 pages

**Structural and Electronic Properties of Low-Dimensional C-Nanoassemblies and Possible Analogues for Si (and Ge)**, N. H. March and A. Rubio  
Volume 2011, Article ID 932350, 9 pages

**Synthesis and Characterization of Glassy Carbon Nanowires**, C. M. Lentz, B. A. Samuel, H. C. Foley, and M. A. Haque  
Volume 2011, Article ID 129298, 8 pages

**Fracture Toughness of Carbon Nanotube-Reinforced Metal- and Ceramic-Matrix Composites**, Y. L. Chen, B. Liu, Y. Huang, and K. C. Hwang  
Volume 2011, Article ID 746029, 9 pages

**Size Dependence of the Nonlinear Elastic Softening of Nanoscale Graphene Monolayers under Plane-Strain Bulge Tests: A Molecular Dynamics Study**, Sukky Jun, Tenzin Tashi, and Harold S. Park  
Volume 2011, Article ID 380286, 6 pages

**Localized Quantitative Characterization of Chemical Functionalization Effects on Adhesion Properties of SWNT**, Hao Lu, Jiangnan Zhang, and Jun Lou  
Volume 2011, Article ID 145148, 5 pages

**A Molecular Mechanics Study of Morphologic Interaction between Graphene and Si Nanowires on a SiO<sub>2</sub> Substrate**, Zhao Zhang and Teng Li  
Volume 2011, Article ID 374018, 7 pages

**Preparation, Characterization, and Modeling of Carbon Nanofiber/Epoxy Nanocomposites**, Lan-Hui Sun, Zoubeida Ounaies, Xin-Lin Gao, Casey A. Whalen, and Zhen-Guo Yang  
Volume 2011, Article ID 307589, 8 pages

**Effect of Source, Surfactant, and Deposition Process on Electronic Properties of Nanotube Arrays**, Dheeraj Jain, Nima Rouhi, Christopher Rutherglen, Crystal G. Densmore, Stephen K. Doorn, and Peter J. Burke  
Volume 2011, Article ID 174268, 7 pages

**Fabrication and Electrical Characterization of Multiwalled Carbon Nanotube-Based Circuit at Room Temperature**, Yitian Peng, Yuanzhong Hu, and Weibing Lu  
Volume 2011, Article ID 297534, 5 pages

**Purity and Defect Characterization of Single-Wall Carbon Nanotubes Using Raman Spectroscopy**, Yasumitsu Miyata, Kohei Mizuno, and Hiromichi Kataura  
Volume 2011, Article ID 786763, 7 pages

**Field Emission Properties of the Dendritic Carbon Nanotubes Film Embedded with ZnO Quantum Dots**, Shu Zuo, Xin Li, Weihua Liu, Yongning He, Zhihao Xiao, and Changchun Zhu  
Volume 2011, Article ID 382068, 5 pages

**Large Deflections Mechanical Analysis of a Suspended Single-Wall Carbon Nanotube under Thermoelectrical Loading**, Assaf Ya'akovovitz, Slava Krylov, and Yael Hanein  
Volume 2011, Article ID 190360, 8 pages

**Ferromagnetic Property and Synthesis of Onion-Like Fullerenes by Chemical Vapor Deposition Using Fe and Co Catalysts Supported on NaCl**, Yongzhen Yang, Xuguang Liu, Yanxing Han, Wenfang Ren, and Bingshe Xu  
Volume 2011, Article ID 720937, 6 pages

**Diameter Tuning of Single-Walled Carbon Nanotubes by Diffusion Plasma CVD**, Toshiaki Kato, Shunsuke Kuroda, and Rikizo Hatakeyama  
Volume 2011, Article ID 490529, 7 pages

**Homogeneous Carbon Nanotube/Carbon Composites Prepared by Catalyzed Carbonization Approach at Low Temperature**, Hongjiang Li, Changhong Liu, and Shoushan Fan  
Volume 2011, Article ID 281490, 5 pages

**Humidity Sensor Based on Multi-Walled Carbon Nanotube Thin Films**, C. L. Cao, C. G. Hu, L. Fang, S. X. Wang, Y. S. Tian, and C. Y. Pan  
Volume 2011, Article ID 707303, 5 pages

**Single Nucleotide Polymorphism Detection Using Au-Decorated Single-Walled Carbon Nanotube Field Effect Transistors**, Keum-Ju Lee, Hye-Mi So, Byoung-Kye Kim, Do Won Kim, Jee-Hwan Jang, Ki-Jeong Kong, Hyunju Chang, and Jeong-O Lee  
Volume 2011, Article ID 105138, 8 pages

**Study of Mg Powder as Catalyst Carrier for the Carbon Nanotube Growth by CVD**, Jianli Kang, Jiajun Li, Naiqin Zhao, Philip Nash, Chunsheng Shi, and Ronglu Sun  
Volume 2011, Article ID 938493, 6 pages

**The Microstructure of Ni Layer on Single-Walled Carbon Nanotubes Prepared by an Electroless Coating Process**, Weixue Li, Hui Jin, Yuan Hao, Tijun Chen, Jianfeng Dai, and Qing Wang  
Volume 2011, Article ID 348958, 5 pages

**Pore-Width-Dependent Preferential Interaction of  $sp^2$  Carbon Atoms in Cyclohexene with Graphitic Slit Pores by GCMC Simulation**, Natsuko Kojima, Tomonori Ohba, Yasuhiko Urabe, Hirofumi Kanoh, and Katsumi Kaneko  
Volume 2011, Article ID 853989, 7 pages

**Synthesis of  $Fe_3O_4$ /Pt Nanoparticles Decorated Carbon Nanotubes and Their Use as Magnetically Recyclable Catalysts**, Hongkun He and Chao Gao  
Volume 2011, Article ID 193510, 10 pages

## Editorial

# Low-Dimensional Carbon Nanomaterials: Synthesis, Properties, and Applications

**Sulin Zhang,<sup>1</sup> Teng Li,<sup>2</sup> Jianyu Huang,<sup>3</sup> and Vivek Shenoy<sup>4</sup>**

<sup>1</sup>Department of Engineering Science and Mechanics, The Pennsylvania State University, University Park, PA 16802, USA

<sup>2</sup>Department of Mechanical Engineering, University of Maryland, College Park, MD 20742, USA

<sup>3</sup>Center for Integrated Nanotechnologies, Sandia National Laboratories, Albuquerque, NM 87185, USA

<sup>4</sup>Division of Engineering, Brown University, Providence, RI 02912, USA

Correspondence should be addressed to Sulin Zhang, suz10@psu.edu

Received 11 April 2011; Accepted 11 April 2011

Copyright © 2011 Sulin Zhang et al. This is an open access article distributed under the Creative Commons Attribution License, which permits unrestricted use, distribution, and reproduction in any medium, provided the original work is properly cited.

Carbon has long been known to exist in three forms: amorphous carbon, graphite, and diamond. However, the discovery of buckyballs in 1985 has created an entirely new branch of carbon chemistry. The subsequent discovery of carbon nanotubes (CNTs) in 1991 has opened up a new era in materials science and nanotechnology. The wonder of the carbon world remains with the successful isolation of monolayer graphene from graphite simply using adhesive tape in 2004. Over the last decades, carbon nanotechnology has been evolved into a truly interdisciplinary field, encompassing chemistry, physics, materials science, and mechanics. The research excitement was largely driven by the unique properties and diverse applications of these low-dimensional carbon nanomaterials. For example, they are promising candidates for nanofillers to strengthen polymeric composites because of their high strength and stiffness; CNTs can be functionalized to serve as nanoscale probes and can be used as a drug delivery system because of their hollow center; nanodiamond has recently found applications in nanomedicine; due to its exceptional electrical properties, graphene may replace silicon as the next-generation electronic materials.

This special issue features research and review articles that cover a wide range of recent progress on the studies of low-dimensional carbon nanomaterials. These studies span from theoretical/computational to experimental efforts, from pristine to defected low-dimensional carbon nanomaterials, from their mechanical and thermal to their electrical properties, and from their synthesis to their patterning and

applications of various kinds. Highlighted below are several important contributions from this special issue.

Mechanical properties of low-dimensional carbon nanomaterials continue to be one of the important research topics. Using atomistic simulations, Jun et al. rationalized the underlying physics of the nonlinear elastic softening of monolayer graphene under high pressure. They also predicted that the elastic softening is size dependent. Combining the shear-lag model and fracture mechanics, Liu et al. carried out a hierarchical failure analysis on CNT-reinforced composites with hard matrix. Their analyses predicted an optimal interfacial bond density for enhanced fracture toughness. They further predicted that the interface length plays a key role in determining the fracture toughness of the CNT-reinforced composites. This study is particularly useful to the rational design CNT-based composites. Zhang and Li addressed the morphologic interaction between graphene and Si nanowires on a SiO<sub>2</sub> substrate using molecular mechanics simulations. Their predictive results provide valuable guidance in patterning of graphene sheets on substrates with nanoscale scaffolds. Lu et al. quantified adhesive interactions of small functionalized single-walled CNT (SWCNT) bundles using an atomic force microscopy-based adhesive force mapping technique combined with a statistical analysis method. This measurement turns out to be important in the design and fabrication of SWCNT-reinforced nanocomposites. Ya'akovovitz et al. developed a geometrically nonlinear string model to analyze the mechanical behavior of SWCNTs under thermoelectrical loading.

Several articles addressed new synthesis approaches of low-dimensional carbon nanomaterials. Peng et al. fabricated multiwalled carbon nanotube-(MWCNT-)-based circuits and characterized their electrical properties. Yang et al. synthesized onion-like fullerenes by chemical vapor deposition and characterized their ferromagnetic properties. Li et al. developed a catalyzed carbonization approach with which homogeneous CNT/carbon composites are fabricated. Lentz et al. synthesized and characterized glassy carbon nanowires. He and Gao developed a novel method to synthesize  $\text{Fe}_3\text{O}_4/\text{Pt}$  nanoparticles-decorated CNTs. These synthesis approaches add new capabilities to the community on making carbon nanomaterials of unique properties.

Novel applications of low-dimensional carbon nanomaterials have been proposed in this special issue. Cao et al. demonstrated the promise of MWCNT-based humidity sensor. Lee et al. proposed that Au-decorated single-walled carbon nanotube field effect transistors can be used as single nucleotide polymorphism detector. He and Gao pointed out that  $\text{Fe}_3\text{O}_4/\text{Pt}$  nanoparticles-decorated CNTs can be used as magnetically recyclable catalysts.

Finally, Mostofizadeh et al. thoroughly reviewed the synthesis, properties, and applications of low-dimensional carbon nanomaterials, ranging and 0-dimensional fullerenes, carbon-encapsulated metal nanoparticles, nanodiamonds, 1-dimensional carbon nanofibers, CNTs, and 2-dimensional graphene sheets. The review article provided the latest update of the progress in the low-dimensional carbon nanomaterials research and would serve as a convenient resource for the researchers in the field.

We would like to thank the authors across the world for their valuable contributions to this special issue as well as the reviewers for their constructive comments to the manuscripts. We envision that low-dimensional carbon will continue to be one of the promising research fields in the years to come, manifested by the active responses of researchers in the course of this special issue. We are happy to be informed that, owing to the great success of this special issue, Journal of Nanomaterials has decided, for the first time since its launch, to establish an annual/special issue on low-dimensional carbon nanomaterials. We encourage and appreciate your further support for this annual/special issue series.

*Sulin Zhang  
Teng Li  
Jianyu Huang  
Vivek Shenoy*

## Review Article

# Synthesis, Properties, and Applications of Low-Dimensional Carbon-Related Nanomaterials

Ali Mostofizadeh,<sup>1,2</sup> Yanwei Li,<sup>1</sup> Bo Song,<sup>1</sup> and Yudong Huang<sup>1</sup>

<sup>1</sup>Department of Polymer Science and Engineering, School of Chemical Engineering and Technology, Harbin Institute of Technology, Harbin 150001, China

<sup>2</sup>Nuclear Science and Technology Research Institute (NSTRI), P.O. Box 11365-8486, Tehran, Iran

Correspondence should be addressed to Yudong Huang, ydhuang.hit1@yahoo.com.cn

Received 15 June 2010; Accepted 1 November 2010

Academic Editor: Sulin Zhang

Copyright © 2011 Ali Mostofizadeh et al. This is an open access article distributed under the Creative Commons Attribution License, which permits unrestricted use, distribution, and reproduction in any medium, provided the original work is properly cited.

In recent years, many theoretical and experimental studies have been carried out to develop one of the most interesting aspects of the science and nanotechnology which is called carbon-related nanomaterials. The goal of this paper is to provide a review of some of the most exciting and important developments in the synthesis, properties, and applications of low-dimensional carbon nanomaterials. Carbon nanomaterials are formed in various structural features using several different processing methods. The synthesis techniques used to produce specific kinds of low-dimensional carbon nanomaterials such as zero-dimensional carbon nanomaterials (including fullerene, carbon-encapsulated metal nanoparticles, nanodiamond, and onion-like carbons), one-dimensional carbon nanomaterials (including carbon nanofibers and carbon nanotubes), and two-dimensional carbon nanomaterials (including graphene and carbon nanowalls) are discussed in this paper. Subsequently, the paper deals with an overview of the properties of the mainly important products as well as some important applications and the future outlooks of these advanced nanomaterials.

## 1. Introduction

Carbon (from the Latin language, Carbo means coal) as a non-metal element can be found in every living organism; therefore, it can be bravely confirmed that the basis of one aspect of life is carbon. Carbon, as the original component presented in millions of various compounds, is capable to be very hard such as diamond or very soft as graphite. The use of this unique chemical element is almost unlimited from the hardest diamond for drilling to the softest form, graphite, for using as a lubricant in skin health and beauty. This nontoxic element is used as a filter to reduce other toxins. It has the highest melting point among all the known elements and occurs free in nature. On the other hand, carbon nanomaterials are known as the chemical fruits of the mother tree of carbon and most importantly carbon 60 molecules. Since a series of exciting carbon nanomaterials are arising, they have attracted tremendous attention and have been intensively studied on numerous carbon-based nanomaterials because of their unique structure, electronic, mechanical,

optical, and chemical characteristics. Low-dimensional carbon nanomaterials can be divided into categories of different dimensionality ranging from zero-dimensional (0-D) to one-dimensional (1-D) and two-dimensional (2-D) depending on their nanoscale range (<100 nm) in different spatial directions. The representatives in family of low-dimensional carbon nanomaterials focus on fullerene, onion-like carbon, carbon-encapsulated metal nanoparticles, nanodiamond (0-D), carbon nanofibers, carbon nanotubes (1-D), graphene, and carbon nanowall (2-D).

As a brief history, it is worth to remember that in 1952 Radushkevich and Lukyanovich introduced the hollow graphitic carbon fibers with 50 nm in diameter in the Soviet Journal of Physical Chemistry mentioned in [1]. In 1960, Bollmann and Spreadborough [2] showed the structure of multiwall carbon nanotubes (MWNTs) using an electron microscope. They investigated the friction properties of carbon due to rolling sheets of graphene in "Nature" [2]. In 1976, Oberlin et al. [3] showed the CVD growth of nanometer-scale carbon fibers. In 1985, the revolutionary

discovery in this area occurred, which was the discovery of fullerenes by Kroto et al. [4]. The discovery of fullerene seems to be very important because it might be the first new allotrope of carbon to be discovered in the 20th century [5]. The nickname for fullerene comes from Richard Buckminster “Bucky” Fuller (July 12, 1895–July 1, 1983), an American architect, author, designer, inventor, and futurist who used geodesic spheres structures in his work. Other important well-known carbon nanomaterials are carbon nanotubes (CNTs) which will be introduced with the full features and aspects in this paper. As a pictorial introduction, we have summarized the main structures of various low-dimensional carbon nanomaterials in Figure 1 [6–11].

In the past decade, by using nanotechnology and carbon-based nanomaterials, the world might be able to see an industrial revolution surpassing any one before. This new technology could end the world’s hunger, make affordable goods, have massive implications for medical breakthroughs, and unfortunately also be used in military applications. In this paper, we will discuss the synthesis, properties, and applications of these characteristic examples as well as the latest research results and developments, that hopefully more researchers can address the area and look forward to more research results.

## 2. Carbon Nanomaterials Synthesis

In this paper, our purpose is to summarize the well-known methods and to provide recent progress synthesizes of the entire nanostructure class of carbon nanomaterials. Where appropriate, we also provide a short historical background and the structure description of carbon nanomaterials.

### 2.1. Zero-Dimensional Carbon Nanomaterials (0-DCNs)

**2.1.1. Fullerene.** Fullerenes are spherical, caged molecules with carbon atoms located at the corner of a polyhedral structure consisting of pentagons and hexagons. A spherical fullerene looks like a soccer ball and is often called “buckyball.” Fullerenes were named after Richard Buckminster Fuller, an architect known for the design of geodesic domes which resemble spherical fullerenes in appearance. In fact, fullerenes were discovered as an unexpected surprise during laser spectroscopy experiments in 1985, by researchers at Rice University. As mentioned in the Nobel Prize records at [12], the 1996 Nobel Prize in chemistry was awarded jointly to Robert F. Curl, Jr., Richard E. Smalley, and Sir Harold W. Kroto “for their discovery of fullerenes” [12]. The first method of production of fullerenes shown in Figure 2 by Kroto et al. in 1985 [4] used laser vaporization of carbon in an inert atmosphere in which microscopic amounts of fullerenes were produced. However, for the first time in 1990, the physicists Krätschmer et al. [13] produced isolable quantities of C60 by using an arc to vaporize graphite. The way was thus open for studying an entirely new branch of chemistry. Alekseyev and Dyuzhev [14] systemically discussed fullerene formation in an arc discharge and all the aspects of the problem from arc

discharge calculations to the immediate fullerene molecule assembly.

Fullerene chemistry has become a very hot research field in the last two decades. A variety of fullerene derivatives with unique properties were produced, and several techniques for producing them in greater volumes have been suggested. In 1991 and 1992, Howard et al. [15, 16] observed fullerenes C60 and C70 from benzene/oxygen flames and developed a method of synthesis of fullerenes in combustion. On the other hand, Xie et al. [17] synthesized fullerenes C60 and C70 via microwave plasma from chloroform at low-pressure argon atmosphere. The microwave plasma synthesis from chloroform opened a new way to large quantity and low-cost production of fullerenes, various perchlorinated intermediates of fullerenes, and the perchlorinated carbon clusters. Taylor et al. [18] introduced a synthesis of C60 and C70 by pyrolysis of naphthalene at 1,000°C. The advantages involve a continuous process that does not require rod replacement, and closed fullerene cages can be prepared from well-defined aromatic fragments. Koshio et al. [19] also used a method of fullerene by pyrolysis ragged single-wall carbon nanotubes treated by ultrasonication with an organic solvent followed by heating in oxygen gas. As a new event in 2009, Chen and Lou [20] reported that C60 can also be synthesized from the reduction CO<sub>2</sub> via metallic lithium or MgCO<sub>3</sub> at 700°C, ca. 100 MPa. Although the yield via the above method was low, this method could resolve the biggest contamination problem in the previous synthesis methods and could provide some new insights for the formation of C60.

Koprinarov et al. [21] reported fullerene structures (FSs), and FSs with incorporated iron atoms were obtained via DC arc discharge between carbon electrodes in Ar and ferrocene gas mixture ambient. The method supplied the electrode deposit growth with carbon from the ferrocene, which made fullerene creation easier and increased the product quantity. Richter et al. [22] made a detailed research on the process of fullerene formation in acetylene/oxygen/argon flat flames with adding chlorine and burning at low pressure. Recently, many chemical syntheses of fullerenes also have been reported in [23].

**2.1.2. Carbon-Encapsulated Metal Nanoparticles (CEMNPs).** Carbon-encapsulated metal (magnetic) nanoparticles (CEMNPs) represent a new class of Zero-dimensional carbon-metal composite nanomaterials. It is the shape of core-shell structure on the nanoscale. The polyhedral metallic core is entirely encapsulated by the multilayer-graphitized carbon shell. So, the carbon layers isolate the particles magnetically from external environment and protect them against corrosion and magnetic coupling between individual particles.

Since the first report on LaC<sub>2</sub> encapsulated within nanoscale polyhedral carbon particles in a carbon arc synthesized by Ruoff et al. [24] and Tomita [25] in 1993, carbon-encapsulated metal nanoparticles have received considerable attention because of their novel structures and obvious technological promise. Several groups have succeeded in encapsulating various materials into a hollow graphitic

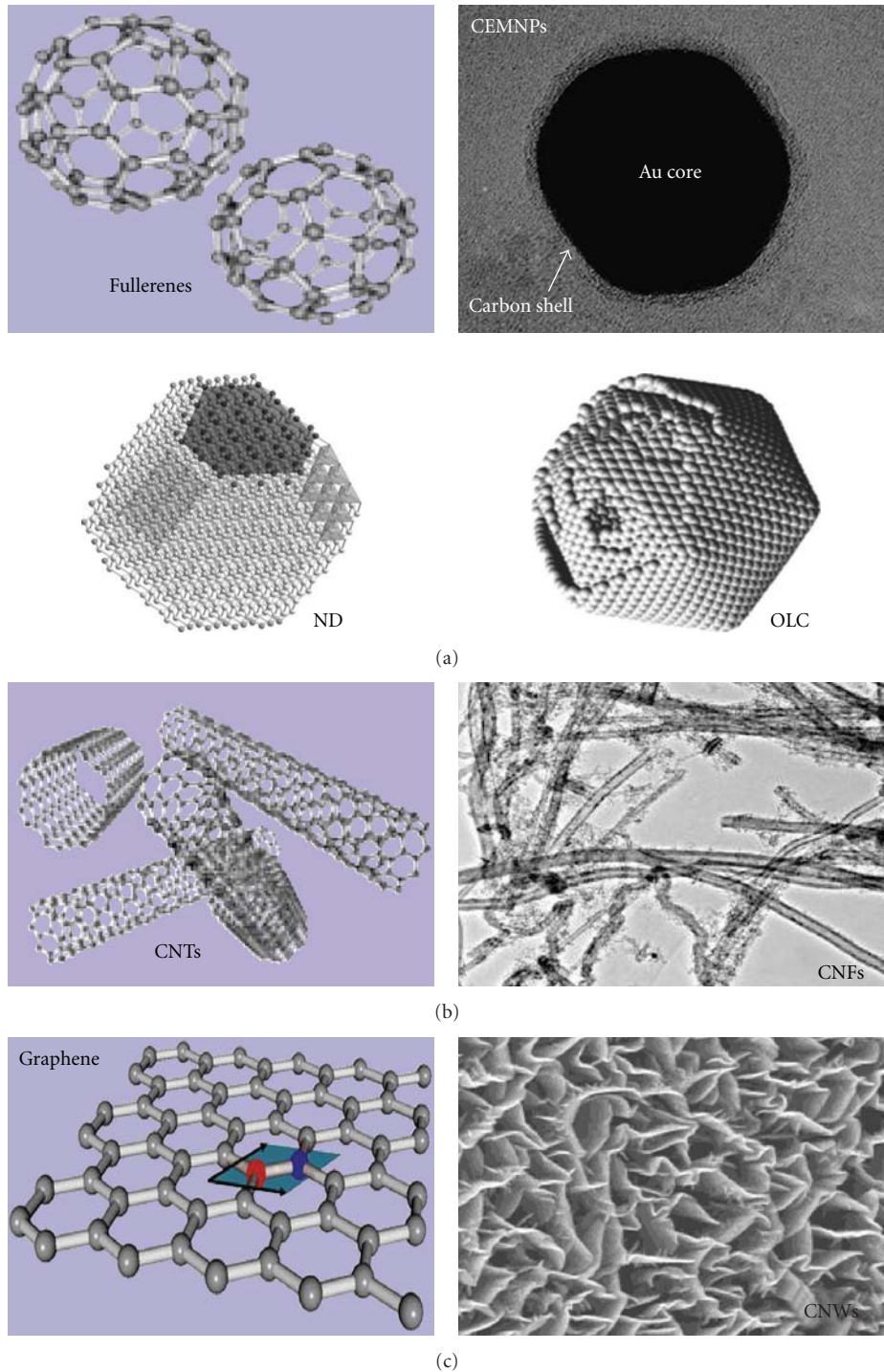


FIGURE 1: Crystal structures of the different low-dimensional nanocarbon. From left to right: (a) Fullerene, Carbon-encapsulated metal nanoparticles, Nanodiamond, and Onion-like carbon, (0-D); (b) carbon nanotube and carbon nanofibers, (1-D); (c) graphene and carbon nanowalls, (2-D) [6–11].

cage by arc discharge method. Saito [26] reported that 13 rare earth metals and iron-group metals were wrapped in graphitic carbon in 1995. Dravid et al. [27] solved the major problem about the production of large amounts of unwanted carbonaceous debris in the standard arc method with the synthesis of graphite-encapsulated nanocrystals.

They used tungsten arc technique which lowers the amount of carbonaceous debris produced by lowering the carbon content of the arc. Host et al. [28] also reported the structure and magnetic studies of carbon-coated nanocrystals of nickel and cobalt synthesized in a special low carbon to metal ratio arc chamber using tungsten arc techniques. Host et

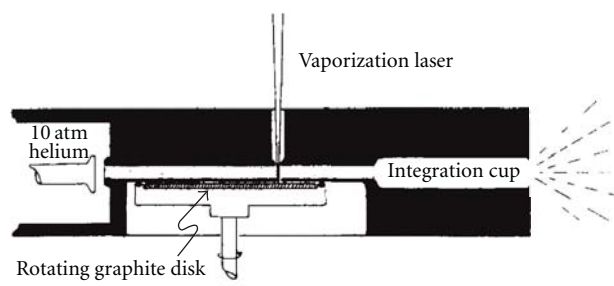


FIGURE 2: The schematic diagram of fullerene fabrication system using laser vaporization [4].

al. in 1998 [28] and Jiao et al. in 1996 and 1998 [29, 30] reported that a set of carbon encapsulated Ni, Co, Cu, and Ti particles were prepared by an arc discharge process modified in the geometry of the anode and the flow pattern of helium gas. However, the traditional method requires an expensive vacuum system to generate the arc plasma, and the carbon-encapsulated nanoparticles are only found in the soot deposited on the cathode. In 2004, Qiu and Tsang [31] reported the preparation of carbon-coated nickel metal nanoparticles using the arcing coal-based carbon rods submerged in deionized water. The coal-based carbon rods were prepared from a mixture of coal and nickel powders, and the arc discharge was carried out in water instead of in inert gases. The mentioned method resolved a variety of the previous problems.

In 1998, Harris and Tsang [32] described a new technique for carrying out the high-temperature heat treatments on microporous carbons used to encapsulate molybdenum, uranium, and cobalt. The method based on their researches solved the difficulties with the scaleup of low yield. In 2002, Flahaut et al. [33] reported cobalt nanoparticles encapsulated in graphitized carbon shells synthesized using catalytic chemical vapor deposition (CCVD) in high yield involving the reduction by an  $H_2/CH_4$  mixture of an  $Mg_{1-x}Co_xO$  solid solution prepared by the combustion method. In 2003, during the researches made by Wang et al. [34], carbon-coated cobalt nanocapsules were synthesized by the chemical vapor-condensation process with cobalt carbonyl ( $Co(CO)$ ) used as a precursor and carbon monoxide ( $CO$ ) as a carrier gas. Tsai et al. [35] reported that a method using microwave plasma enhanced chemical vapor deposition (MPECVD) system to synthesize pure carbon-encapsulated metal nanoparticles on silicon wafer without the existence of other carbon nanostructures.

Liu et al. demonstrated in their paper [36] that carbon-encapsulated cobalt nanoparticles were synthesized via the modified catalytic pyrolysis, the mechanical milling derived  $Co/NaCl$  as catalyst, and the productivity was almost 100%. This method is superior to early catalytic methods in high productivity and is fully separated from the supporting materials by simple washing process, especially the by-products carbon nanotubes (CNTs) [37].

In 2005, Lu et al. [38] reported the synthesis of carbon-encapsulated Fe nanoparticles via a picric acid-detonation-induced pyrolysis of ferrocene. Their technique was a

self-heating and extremely fast process. Wu et al. [39] reported a novel method for the synthesis of amorphous carbon-encapsulated  $Fe_7C_3$  nanocrystals via the explosion of a hybrid xerogel containing oxidized pitch and iron nitrate. Wang et al. [40] reported a continuous synthesis of high purity, high coercive force and good ferromagnetism CEMNPs based on the spray pyrolysis of a mixture of iron carbonyl and alcohol at  $500\text{--}900^\circ\text{C}$ . The technique based on spray pyrolysis offers a large-scale production, the simplicity of the apparatus, and good productivity. Song et al. [41] proposed that the similar carbon-encapsulated  $Fe_3C$  nanoparticles can be synthesized on a large scale via the cocarbonization of 1, 2, 4, 5-tetramethylbenzene and ferrocene under autogenous pressure. Huo et al. [42] synthesized Carbon-encapsulated iron nanoparticles with uniform diameters by cocarbonization of an aromatic heavy oil and ferrocene at  $480^\circ\text{C}$  under autogenous pressure. This preparation method of CEMNs is characterized by simplicity, low cost, controllability, and high yields. Bystrzejewski et al. [43] synthesized Fe,  $Fe_3C$ , and  $NdC_2$  carbon-encapsulated magnetic nanoparticles using thermal radio frequency (RF) plasma torch technique. In that paper, authors found the nonlinear transmission behavior in CEMNPs material with the smallest saturation.

In 2008, Park et al. [44] reported a method (pulsed laser irradiation synthesis, PLIS) to synthesize CEMNPs such as Fe-C, Ni-C, and Co-C by irradiating nanosecond laser pulses into a metallocene-xylene solution under room temperature and atmospheric pressure. There will be more CEMNP synthesis arising, because the PLIS method is simple and can be operated under ambient conditions. In 2006, Nishijo et al. [45] synthesized the carbon-encapsulated nanoparticles via thermal decomposition of metal acetylide at a low temperature. Using this method, nanoparticles of low-melting point Sn and metastable carbide phases of Pd, Ni, and Co were successfully encapsulated in amorphous carbon shells owing to the low synthesis temperature. Recently, Maya et al. [46] have produced and characterized encapsulated silver nanoparticles provided by high-current pulsed electric arcs system in an argon atmosphere. The main advantage of this method is that the metal nanoparticles are encapsulated in amorphous carbon from the beginning, and this layer acts as an efficient chemical barrier.

In summary, as briefed in Table 1, CEMNPs can be synthesized by a variety of techniques such as arc discharge method, tungsten arc techniques, high-temperature heat treatments, the mechanical milling, cocarbonization, pulsed laser irradiation, and high-current pulsed electric arcs system.

**2.1.3. Nanodiamond (ND).** As we all know, diamond is one of the carbon allotropes as graphite. Graphite is the most stable form of carbon at ambient pressure. Spherical and truncated octahedron diamond with predominant  $sp^3$ -bonded carbon is one of the hardest materials known to date and is often regarded as the king of all gemstone and top-drawer materials because of its excellent scientific qualities in hardness, chemical corrosiveness, thermal expansion and conductivity, electrical insulation, and biocompatibility. On

the other hand, nanodiamond (ND) is a cubic structural diamond. It possesses diamond structure and diamond properties. The average size is mere 5 nm in diameter. In the wide sense of the word, “nanodiamond” contains a variety of diamond-based materials at the nanoscale (the length scale of approximately 1–100 nm) including pure-phase diamond films, diamond particles, and their structural assemblies. Several synthesis methods have been developed to synthesize laboratory-produced nanodiamonds. There are two main methods for fabrication of nanodiamond: transformation of graphite under high temperature and high pressure and detonation of the carbon explosive materials.

In 1955, Bundy et al. [47] realized the 30-year dream of many scientists in which diamond can be transformed from graphite. Under the title “Man-made diamonds” in Nature [47], Bundy and his coworkers successfully reported the synthesis of diamond using a high-temperature and high-pressure process. However, the synthesis of diamond by the detonation of explosives with a negative oxygen balance in a steel container under vacuum condition was reported in the 1980s [48, 49]. There are also some related literatures in recent reports shown two mentioned methods [50–55]. Explosive detonation is still widely used; however, the process of the detonator explosion is extremely fast and very complex. Moreover, there are some disadvantages observed in detonation method. In fact, the fraction of surface to bulk atom and oxygen, hydrogen, and nitrogen content in the nanodiamond resulting from after-purification process are difficult to remove.

As an interesting matter, most previous researches on detonation synthesis have been done at military or commercial plants; thus several reports are available for the scientific community. Therefore, the best method is to develop new techniques to the synthesis of well-dispersed and pure nanodiamonds. Recently, more researches also about the aspects of low energy, low cost, easily controlled, few byproducts, controlled-sized, and large scale have been reported in related literatures, such as microwave plasma chemical vapor deposition [56–58], hot filament chemical vapor deposition [59], pulse laser ablation [60–62], electron irradiation [63], and high-energy X-ray diffraction [64].

**2.1.4. Onion-Like Carbons (OLCs).** Ugarte [65] in 1992 reported that carbon soot particles and tubular graphitic structures were radiated by intense electron-beam and reorganized into quasispherical particles. Subsequently, Harris and Tsang [66] in 1997 studied the structure of two typical nongraphitizing carbons by heat treatment. They observed the fullerene-like structure close to carbon nanoparticles. Then, a new model for nongraphitizing carbons was proposed which was different with the other representatives of the carbon family graphite, fullerenes, and nanotubes. The onion-like carbons (OLCs) have the three to eight closed graphitic shell structures with the hollow core. The outer diameters are in the range of 20–100 nm. The polyhedral nanoparticles exhibited a well aligned concentric and high degree of symmetry structure. Quasispherical shape, nanometer size, and surface specificity of OLCs have attracted enormous attention. Several routes were developed

from synthesis of carbon onions including arc discharge [67, 68], high-electron irradiation [69], chemical vapor deposition [70], radio frequency plasma [71] and high-dose carbon ion implantation into metals [72], and [73, 74] thermal annealing of diamond nanoparticles [75].

The current researches on OLCs are limited because of unmanageable reaction, many byproducts, complex equipments, and high cost. Extensive research has been devoted to search the optimal synthetic route. At present, the most OLCs were synthesized using vacuum annealing of nanodiamond particles at fixed temperatures [75]. For instance, in 2007, Bulusheva et al. [76] produced quasispherical and polyhedral OLCs using vacuum annealing of nanodiamond (ND) particles, and the first researched quantum chemistry characterization and the electronic structure of OLCs by X-ray absorption spectroscopy. Recently, in 2010, Bystrzejewski et al. [77] described a simple, facile, and low-cost process of the synthesis of OLCs by a catalyst-free ( $\text{NaN}_3\text{-C}_6\text{Cl}_6$  mixture) thermolysis route, and meanwhile, this method solved the problem of separation.

Zhao et al. [78] reported a large quantities synthesis of OLCs using carbonization of the solid-state catalyst of PF resin as the carbon resource and ferric nitrate as the precursor at 1000°C. Liu et al. [79] also synthesized OLCs using  $\text{Fe/Al}_2\text{O}_3$  as catalyst by chemical vapor deposition (CVD) at a relatively low temperature (400°C) and efficiently avoided the growth of CNTs. Du et al. [80] synthesized high-purity OLCs in high yields from coal by radio frequency plasma economically.

## 2.2. One-Dimensional Carbon Nanomaterials (1-DCNs)

**2.2.1. Carbon Nanofibers.** Carbon nanofibers (CNFs) are composed of stacked and curved graphene layers from a quasi-one-dimensional (1D) filament. CNFs have cylindrical or conical nanostructures. Their diameters vary from a few to hundred nanometers, while lengths range from less than a micrometer to millimeters. As shown in Figure 3, according to the angle between graphene layers and fiber axis, the morphological structure is often divided into plate CNFs, ribbon-like CNFs, herringbone CNFs [81].

CNFs known as filamentous carbon have been known for a long time [82]. However, the synthesis of filamentous carbons did not evoke great interest of scientists in those early years until the discovery of carbon nanotubes by Iijima in 1991 [83]. Generally, CNFs can be synthesized through the traditional vapor growth method [84–86], cocatalyst deoxidization process [84], catalytic combustion technique [85], plasma-enhanced chemical vapor deposition [87, 88], hot filament-assisted sputtering [89], ultrasonic spray pyrolysis [90], and ion beam irradiation [91].

The large-scale production of CNFs has usually been carried out by using PECVD in which CNFs are grown by catalytic decomposition of hydrocarbon under high temperature. Catalytic PECVD provides a means for the controlled synthesis of CNTs and CNFs and grows individual nanostructures with deterministic characteristics by changing the starting materials or plasma conditions during growth. This review will focus on the catalytic PECVD

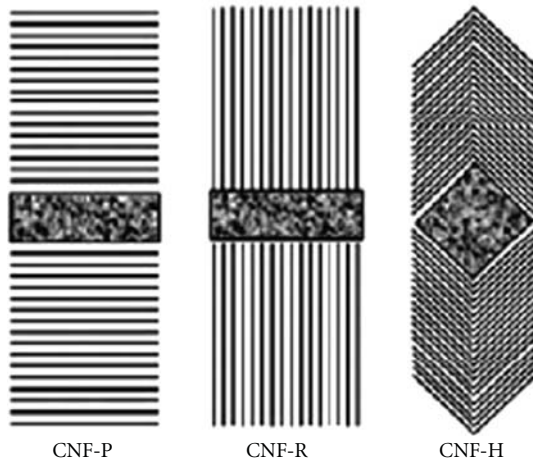


FIGURE 3: The schematic diagram of three different CNFs: platet CNFs and ribbon-like CNFs, herringbone CNFs [81].

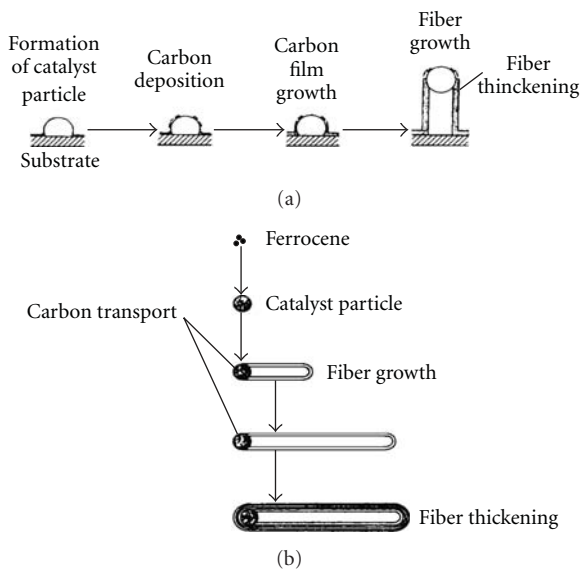


FIGURE 4: Two methods of synthesizing VACNFs: (a), “seeded catalyst on a flat plate” and (b), “floating catalyst” [92].

growth process used to produce vapor grown carbon fibers (VGCFs) as depicted. As shown in Figure 4, there are two methods to synthesize VACNFs. First, the method based on “seeded catalyst on a flat plate” and second, the “floating catalyst method”. The first technique uses the catalysts seeded on a substrate within the reactor, while in another method, the catalyst is deposited on a selected substrate as a film by sputtering or evaporation techniques.

Firstly, the commonest way used thin films of Ni, Fe, or Co metallic catalyst [93, 94] or their alloys [95], Cu–Ni composition [96], nickel-copper-aluminum takovite [97], mixture of  $\text{Ni}(\text{OH})_2$ – $\text{Mg}(\text{OH})_2$  [98], ferrocene [99], copper titrate [100], and cobaltocene [101] as catalyst precursors. Moreover, a buffer-layer such as Ti was often used as a barrier to diffuse and promote particle formation. Secondly, it is a “pretreatment step”; Carrier gas such as ammonia ( $\text{NH}_3$ )

or hydrogen ( $\text{H}_2$ ) is introduced as the chamber to a few Torr, and the sample is heated to the desired temperature, usually 500–700°C. Plasma is then initiated for several seconds to minutes. Lastly, there is the carbon source gas (such as  $\text{C}_2\text{H}_6$  [102],  $\text{C}_2\text{H}_5\text{OC}_2\text{H}_5$  [103],  $\text{C}_2\text{H}_2$  [104],  $\text{C}_{60}$  [105]) in the plasma, which immediately initiates CNF growth. The later way uses the catalysts and the carbon source gas floating in the reactor space at the same time.

This paper focuses mainly on the PECVD technique from the aspects of metal catalyst, carbon source, processing method, and other techniques by virtue of the classical examples and the recent reports. Pham-Huu et al. [102] showed that large-scale and uniform carbon nanofibers with a diameter of about 50 nm can be synthesized using the catalytic decomposition of a mixture of ethane and hydrogen over a nickel catalyst decorating carbon nanotubes at 550–650°C. The attained CNFs need not subsequent purification, due to the use of carbon nanotubes as support, the high nanofiber yields, and the purity reached. Zou et al. [103] reported that CNFs were prepared by cocatalyst Zn and Fe powders deoxidation process using  $\text{C}_2\text{H}_5\text{OC}_2\text{H}_5$  as starting material at 650°C. The obtained nanofibers possessed diameters about 80 nm, lengths ranging from several micrometers to tens of micrometers, low graphitic crystalline, and good electrochemical properties. The cocatalyst synergetic effect is valuable in controlling the resultant nanofiber diameter for synthesis and the study of other carbonous materials. Yu et al. [104] synthesized carbon nanofibers using the thermal decomposition of acetylene by a copper nanocatalyst derived from cupric nitrate trihydrate at a low temperature of 260°C. The copper nanoparticle size has a considerable effect on the morphology of carbon nanofibers. Helical carbon nanofibers and straight carbon nanofibers laid on catalyst copper nanoparticles with a grain size less than 50 nm or within 50–200 nm. The present study further assumes that it is possible to control the diameter of CNFs by controlling the size of the catalyst particle. Zhang et al. [105] successfully prepared carbon nanofibers with a diameter of about 100 ~ 500 nm using  $\text{C}_{60}$ , graphite-carbon, and boron powders via the ultrasonic spray pyrolysis method of ethanol without using metal catalysts. The experiment indicates that the clusters composed of carbon- and boron-related materials act as nucleating sites for CNFs formation. Kimura et al. [106] synthesized CNFs (lengths of 1–20  $\mu\text{m}$ , uniform diameters of 20–100 nm) with high electrical conductivity by ion beam irradiation of decacyclene whiskers at ambient temperature. This novel method of preparation without catalyst is advantageous for aligning the fibers as desired. The mechanisms of CNFs formation were shown in detail and found that CNFs were not grown from the film but were generated by the conversion of pre-existing whiskers of decacyclene on the film. Matsumoto et al. [107] described that carbon nanofibers were obtained using a hot filament-assisted sputtering system with pure argon gas as the sputtering gas, with a tungsten hot filament as the thermal electron emission source. Guláš et al. [108] observed that CNFs and related structures with outer diameters 20–60 nm were prepared by combination of aerosol synthesis and plasma-enhanced catalytic chemical vapor deposition with

alcohol as carbon precursor catalytic CVD (PE CCVD).  $\text{Al}_2\text{O}_3$  and Si coated Fe and Ni were deposited as catalysts. Ethanol and isopropyl alcohol vapors were used as a carbon source. HCGD is used as a gas activation process without any specific heating of the substrate that plays an important role in gas decomposition and activation for CNFs growth. On the other hand, Ren et al. [109] reported a simple synthesis method of carbon nanofibers using combustion of ethyl alcohol. Copper plate was employed as substrate, iron nitrate, and iron chloride as catalyst precursor and ethanol as carbon source. Carbon nanofibers with diameters of 10–100 nm were produced in bulk by the floating catalyst method by Ci et al. [110]. Several experiments showed the growth of carbon fibers depending on the reactor conditions and experimental parameters, so it was easily controlled to synthesize the large scale of carbon nanofibers. Mori and Suzuki [111] demonstrated that vertically aligned free-standing CNFs can be synthesized at low temperature as low as  $90^\circ\text{C}$  by plasma-enhanced chemical vapor deposition at low temperature CO/Ar DC plasma. The low-temperature synthesis of carbon nanofibers was demonstrated that the addition of a small amount of  $\text{O}_2$  was favorable for the synthesis of CNFs, because it suppresses the deposition of amorphous carbon.

**2.2.2. Carbon Nanotubes.** Carbon nanotubes are rolled up into tubular structures by  $\text{sp}^2$ -bonded graphite sheets with nanometer diameter and large length ratio. The nanotubes may consist of two different types of carbon nanotubes. Namely, singlewall nanotubes (SWNTs) made of single layers of graphene cylinders with typical diameter of the order of 1.4 nm and the multiwall nanotubes (MWNTs) made of 4–24 concentric cylinders of graphene layers with adjacent shells separation of 0.34 nm and a diameter typically of the order 10–20 nm. Nowadays, carbon nanotubes are still mainly synthesized by the arc-discharge, laser-ablation (vaporization), and chemical vapor decomposition (CVD) method.

The MWNTs were first observed which deposited on the negative electrode during the direct current arc-discharge of two graphite electrodes for preparation of fullerenes in an argon-filled vessel by Iijima in 1991 [112]. Large-scale and high-quality MWNTs were achieved by arc-discharge technique first by Ebbesen and Ajayan in 1992 [113]. In 1993, singlewall carbon nanotubes (SWNTs) are almost simultaneously obtained by arc-discharge and catalyst-assisted arc-discharge by Iijima and Ichihashi [114] and Bethune et al. [115]. Iijima and Ichihashi [114] used arc-discharge chamber that installed two vertical thin electrodes with a small piece of iron filled with a gas mixture of methane and argon. On the other hand, Bethune et al. [115] reported that SWNTs can be obtained by arc-discharge of anode thin electrodes with bored holes powdered metal catalysts (Fe, Ni or Co) incorporated into anode. As the arc method, metal catalysts were needed for the growth of SWNTs in contrary to MWNTs. Journet et al. [116] obtained large quantities of SWNTs by arc-discharge using a carbon anode with yttrium and nickel as catalysts. In 1996, high-yield SWNTs were produced using laser-ablation method of graphite with Ni and Co catalysts at

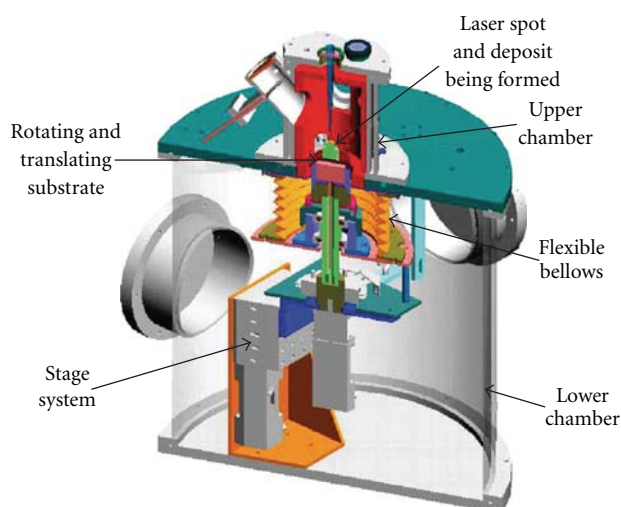


FIGURE 5: The schematic diagram of CNTs fabrication using the laser CVD reactor [129].

$1200^\circ\text{C}$  by Thess et al. [117]. The techniques based on arc-discharge and laser-ablation both have the advantage of high yield but also face the problem of high temperature needed and impurity. The chemical vapor deposition has been used successfully for producing carbon fiber and filament since the 1960s. Yacaman et al. [118] first produced the MWNTs by chemical vapor decomposition method in 1993. Flahaut et al. [119] made bulk amounts of SWNTs using CVD of methane catalyzed on mixed oxide spinels. When using CVD for synthesized CNTs, catalysts brought high yield because the increased metal-supporting interactions were propitious to the growth of carbon nanotube, which also caused impurity and aggregation of the metal nanoparticles. A diagram of CNTs fabrication by the method of CVD is schematically shown in Figure 5. Vast amount of reviews on carbon nanotubes have been discussed in the recent literature in detail, including the synthesis and growth mechanisms of CNT [120–129]; therefore, we described only three main productions in brief.

### 2.3. Two-Dimensional Carbon Nanomaterials (2-DCNs)

**2.3.1. Graphene.** Graphene, one-atom-thick planar sheet of  $\text{sp}^2$ -bonded carbon atoms, is arranged densely in a two-dimensional hexagonal honeycomb crystal lattice. There are three extremely strong  $\sigma$  bonds in-plane result in the mechanical stability of the carbon sheet,  $\pi$  orbitals perpendicular to the plane interactions between graphene and a substrate or between graphene layers are responsible for the electron conduction. It is the basic building block of (0-D) fullerenes, (1-D) carbon nanotubes, and (3-D) graphite.

In a large scientific community, more allotropes of carbon have been reported in succession. Diamond and graphite have been known for centuries, and the recently discovered fullerenes and nanotubes also have been studied in the last two decades. For a long time, graphene was

only considered as theoretical concept. Until 2004, [130] a physicists group led by Andre Geim and Kostya Novoselov from Manchester University, UK used mechanical exfoliation approach to obtain graphene. The discovery of isolated graphene monolayer has attracted wide attention to investigate the properties of this new yet ancient two-dimensional carbon nanomaterial due to its exceptional electronic and mechanical properties. More and more simple methods were searched for the growth of graphene. Several typical methods have been developed and reviewed as follows.

*Mechanical Exfoliation.* As mentioned above, [130] graphene flakes were first produced by continuously cleaving a bulk graphite crystal with a common adhesive tape and then transferred the thinned down graphite onto a cleaned oxidized silicon wafer substrate with visible color. The technique started with three-dimensional graphite and extracted a single sheet (a monolayer of atoms) called mechanical exfoliation or micromechanical cleavage.

Until now, mechanical exfoliation of graphite is still the best method to provide a small amount of high-quality samples for the study of a variety of graphene properties. Furthermore, the venerable technique has been used easily to obtain large size (up to  $100\ \mu\text{m}$ ), high-quality, two-dimensional graphene crystallites, which immediately brought enormous experimental researches [131–134]. Meanwhile, modified techniques are needed to provide a high yield of graphene for industrial production.

*Epitaxial Growth.* Recently, graphene was obtained by the epitaxial growth of graphene layers on metal carbides using thermal desorption of metal atoms from the carbides surface, or directly on metal surfaces by chemical vapor deposition (CVD). The typical carbide is SiC; silicon carbide heated to very high temperatures leads to evaporation of Si and the reformation of graphite; the control of sublimation results in a very thin graphene coatings over the entire surface of SiC wafers, which initially showed more performances than devices made from exfoliated graphene. So far, all of known synthesis approaches, however, are required in specialized laboratories for graphene sheets whose electronic properties are often altered by interactions with substrate materials. The development of graphene required an economical fabrication method compatible with mass production. The latest modified method was demonstrated by Aristov et al. [135]. Based on their work, for the first time, graphene was synthesized commercially on available cubic  $\beta$ -SiC/Si substrates, which was a simple and cheap procedure to obtain industrial mass production graphene, which meets the need of technological application. Moreover, many other types of carbide have been exploited to produce supported graphene, such as TiC (111), TiC (410), and TaC (111). It is well proved that metal surfaces can efficiently catalyze decomposition of hydrocarbons into graphitic materials to support growth of graphene on metallic surfaces by CVD. The advantage of epitaxial growth is large-scale area, but it is difficult to control morphology, adsorption energy, and high-temperature process.

*Chemical Exfoliation.* The theory of chemical exfoliation is to insert reactants in the interlayer space for weakening the van der Waals cohesion. At first, the graphite flakes are forced upon oxidative intercalation of potassium chlorate in concentrated sulphuric and nitric acid, received carbon sheets with hydroxyl and carboxyl moieties. The suspension is known as graphite oxide (GO). The GO is highly dispersible in water, and it can be easily deposited onto SiO<sub>2</sub> substrates. The precipitate of GO is sonicated to form separated graphene oxide sheet, then another reduction, and finally graphene sheet is formed. When KClO<sub>3</sub> is used, it generates a lot of chlorine dioxide gas and emits a great deal of heat, so the mixture is highly hazardous [136]. In 1958, Hummers and Offeman [136] reported a modified method which was much faster and safer. Based on the technique introduced by them, graphite is dispersed into a mixture of concentrated sulfuric acid, sodium nitrate, and potassium permanganate in contrast to KClO<sub>3</sub> [137]. Meanwhile, it must use H<sub>2</sub>O<sub>2</sub> to eliminate the MnO<sub>2</sub> generated from KMnO<sub>4</sub> time after time. This process faced a similar situation when it used m-CPBA [138] as an oxidant. Chandra et al. [139] also reported a novel synthetic route using oxidation acidified dichromate, to get high quality and stable aqueous dispersed graphene sheets. After GOs were deposited, chemical reduction of GO was accompanied by the elimination of epoxy and carboxyl groups using different reductants such as hydrazine [140], dimethylhydrazine [141], hydroquinone [142], and NaBH<sub>4</sub> [143], under alkaline conditions [144] or with thermal methods [145]. Because the reductants are usually hazardous, there are lots of interests on green routes to speed deoxygenation of graphene oxide. Wakeland et al. [146] introduced an approach to synthesize graphene from GO using urea as expansion reducing agent heated in an inert gas environment (N<sub>2</sub>) for a very short time to a moderate temperature (600°C). Chen et al. [147] successfully achieved thermal reduction of graphene oxide (GO) to graphene with the assistance of microwaves in a mixed solution of N, N-dimethylacetamide, and water (DMAc/H<sub>2</sub>O). The reduction of GO can be accomplished rapidly and mildly. This method is rapid, not requiring any solvents or stabilizers, inexpensive, and easy to scale up.

2.3.2. *Carbon Nanowalls.* Carbon nanowalls (CNWs) consist of vertical aligned graphene sheets standing on the substrates, form two-dimensional wall structure with large surface areas and sharp edges. The thickness of CNWs ranges from a few nm to a few tens nm. So far, research groups have explored different synthesis methods of CNWs based on plasma-enhanced chemical vapor deposition techniques. The main approaches are as follows.

- (1) Microwave plasma-enhanced chemical vapor deposition (MWPECVD).
- (2) Radio-frequency plasma-enhanced chemical vapor deposition (RFPECVD) (RF inductively coupled plasma (ICP) and RF capacitively coupled plasma (CCP)).
- (3) Hot-wire chemical vapor deposition (HWCVD).

- (4) Electron beam excited plasma-enhanced chemical vapor deposition (EBEPECVD).

For the first time, carbon nanowalls were accidentally discovered during the growth of carbon nanotubes by Wu et al. [148] using MWPECVD. In the experiment, the NiFe-catalyzed substrate (Si, SiO<sub>2</sub>/Si, sapphire) was preheated to about 650–700°C in hydrogen plasma; the mixtures of CH<sub>4</sub> and H<sub>2</sub> were utilized as flow gases. The nanowalls were monitored using SEM in different growth stages. The well-controlled MWPECVD synthesis process induced further studies to search more flexible control of the growth of CNWs, which aided to understand the mechanisms of CNWs growth and solving unwanted byproduct owing to the use of metal catalyst particles.

Recently, some groups have prepared CNWs without catalysts, using RFPECVD, assisted by a hydrogen atom injection. Shiji et al. [149, 150] synthesized carbon nanowalls on a Si substrate without catalysts using capacitively coupled RFPECVD by H atom injection. The grown samples employed fluorocarbon/hydrogen mixtures, used C<sub>2</sub>F<sub>6</sub>, CF<sub>4</sub>, CH<sub>4</sub>, and CHF<sub>3</sub> as the carbon source gas, and heated a substrate temperature of 500°C. The SEM images monitored the grow of carbon nanowalls using different system and the vacuum ultraviolet absorption spectroscopy (VUVAS) measured H atom density in the plasma in order to discuss the growth mechanism of carbon nanowalls. The experiment demonstrated that the structure and growth rate of carbon nanowalls depended on the types of carbon source gases and H atoms and played an important role for the formation of carbon nanowalls.

Considering the practical applications of carbon nanowalls, large scales of CNWs using MWPECVD and RFPECVD are difficult to provide. A promising method such as HWCVD enables to access the large scales easily compared with the above two methods. Moreover, HWCVD/CAT-CVD have the additional advantage of a high-hydrogen radical density.

Itoh et al. [151] reported that CNW films have been successfully prepared using only CH<sub>4</sub> by HWCVD. In the growth of CNWs, a substrate heated over 500°C would be needed. The hydrogen H<sub>2</sub> pressure is of 133 Pa by radical treatment. The structure of the CNWs has been studied by scanning electron microscope (SEM) and Raman spectroscopy. There are two reports about CNWs synthesis using CH<sub>4</sub> with different hydrogen dilution [152] and without hydrogen dilution [151] by HWCVD. Furthermore, Mori et al. [153] studied fabrication of vertically aligned and definite CNWs by an EBEPECVD employing a mixture of CH<sub>4</sub> and H<sub>2</sub> at relatively low temperature of 570°C. Figure 6 shows a schematic diagram of CNWs fabrication using EBEPECVD. An EBEP is a high-density plasma directly obtained by a high-current and low-energy electron beam. CNWs were characterized using SEM, TEM, and MRS [153].

According to the recent progress report [154], carbon nanowalls with large-surface areas and sharp edges were obtained on nickel-coated oxidized silicon substrates by PECVD in a radiofrequency Ar plasma beam injected with acetylene at temperature of 600°C. The formation of carbon

nanowalls was proved by SEM, TEM, ED, and Raman spectra. The mentioned study showed that the shape, surface distribution, and size of the nanostructures depended on the nature of the active gas and on the gas mass flow ratio in the Ar/H<sub>2</sub>/C<sub>2</sub>H<sub>2</sub> mixture.

Different from previous reports, various growth mechanisms and deposition parameters (catalyst, the effect of localized plasma) of CNWs were explored on a flat substrate, where existed a different growth mechanism. Non-surface-bound (freestanding) growth of CNWs by the method of MWPECVD without using the metal catalyst under a gas mixture of C<sub>2</sub>H<sub>2</sub> and NH<sub>3</sub> was developed by Chuang et al. [155]. A growth stage was used to facilitate energy-intensive, localized plasma for the growth of carbon nanowalls. Owing to the freestanding nature of their growth and the absence of catalyst, the synthesis process easily obtains a large scale of carbon nanowalls without impurity by metal catalyst particles and processed for various applications. There is a similar report [156] of freestanding graphite sheets with thickness less than 1 nm, in which “carbon nanosheets” were synthesized on a variety of substrates by RFPECVD without any catalyst or special substrate treatment. Further studies will be required to understand the formation of non-surface-bound (freestanding) carbon nanowall materials.

Sato et al. [157] investigated the density peak in argon plasma and found that the helicon wave was effectively excited and produced the plasma antenna. For the first time, the helicon-wave discharge was demonstrated to be used as PECVD source for the growth of CNWs. Using the helicon-wave reactive plasma as a precursor source for plasma-enhanced chemical vapor deposition, well-aligned carbon nanowalls are found to be formed even in a very low gas pressure of 0.7 Pa. Table 1 briefs the main synthesis methods of different low-dimensional carbon nanomaterials as described in this section. Further development in this field is expected on their rich physics and potential applications.

### 3. Properties and Applications

There are several various allotropes of carbon such as graphite, diamond, and amorphous carbon. Therefore, the physical and mechanical properties of carbon strongly depended on the allotropic forms of carbon. As an example for the mechanical property of hardness, diamond is known as one of the hardest materials, while graphite is soft enough to be used for making pencils. About the property of color, diamond is considered transparent while graphite is an opaque material and black. As another example, while graphite is a good conductor, diamond just demonstrates a low electrical conductivity. On the other hand, diamond is normally known as a highly thermal conductive, while graphite is considered as the most thermodynamically stable material.

**3.1. Fullerene.** As described in Section 2.1.1, fullerene belongs to zero-dimensional carbon nanomaterials. Applications of fullerene include the applications in medicine such as their aid to produce the specific antibiotics and drugs for

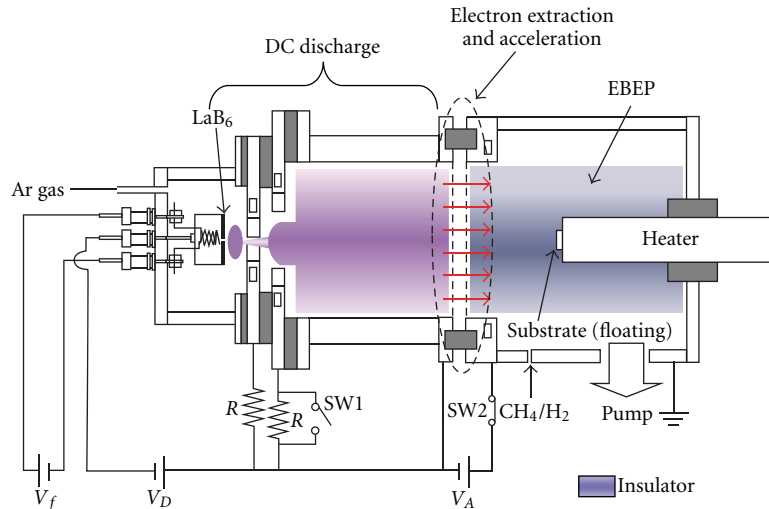


FIGURE 6: The schematic diagram of CNWs fabrication using EBEPECVD [153].

TABLE 1: Comparison of the main synthesis methods of different low-dimensional carbon nanomaterials.

LDC-nanomaterial	Synthesis methods
Fullerene	Laser vaporization, Arc discharge, Combustion, Microwave plasma Pyrolysis, Flat flames
CEMNPs	Arc-discharge, high-temperature heat treatment, mechanical milling, Co-carbonization, Pulse-laser irradiation
ND	MPCVD, Hot-filament, CVD, Pulse laser ablation, Electro irradiation, High-energy X-ray diffraction
OLCs	Arc-discharge, High-electron irradiation, CVD, RFP Thermal annealing of diamond nano-particle
CNFs	Traditional vapor growth, Catalytic combustion, PECVD, Hot filament-assisted sputtering, Ultrasonic spray pyrolysis, Ion beam
CNTs	Arc-discharge, Laser-ablation, CVD, Other methods
Graphene	Mechanical exfoliation, Epitaxial growth, Chemical exfoliation
CNWs	MWPECVD, RFPECVD, HWCVD, EBEPECVD

certain cancers particularly melanoma. On the other hand, due to their specific properties, fullerenes have had great applications in the field of superconductivity.

In 1991, Haddon et al. [158] reported the preparation of alkali-metal-doped films of C<sub>60</sub> and C<sub>70</sub> which have electrical conductivities at room temperature that are comparable to those attained by n-type-doped polyacetylene. They observed the highest conductivities in the doped films equal to 4 Scm<sup>-1</sup> (Cs/C<sub>60</sub>), 100 (Rb/C<sub>60</sub>), 500 (K/C<sub>60</sub>), 20 (Na/C<sub>60</sub>), 10 (Li/C<sub>60</sub>), and 2 (K/C<sub>70</sub>) [152]. In the same year, Hebard et al. [159] reported that potassium-doped C<sub>60</sub> becomes superconducting at 18 K [159]. As the researchers stated in their paper [159], the observed superconductivity at 18 K was the highest yet observed for a molecular superconductor. Furthermore, the superconductivity in fullerene doped with various other alkali metals was reported by some other researchers [160, 161]. Subsequently, Zhou et al. in 1992 [162] and Brown et al. in 1999 [163] showed that the superconducting transition temperature in alkaline-metal-doped fullerene was elevated while the unit-cell volume *V* was increased. In 2008, Ganin et al. [164] reported the bulk superconductivity at 38 K in a molecular system. The system introduced by the researchers was bulk Cs<sub>3</sub>C<sub>60</sub> as a key material in this family [164], and as the authors explained,

cesium-doped fullerene is an important material in the same family [164].

On the other hand, fullerenes are almost stable chemically, however, not completely uncreative. In the view of the solubility, apart from some fullerene structures which are not soluble due to the presence of a small band gap in their structure between the ground and excited states, they are generally soluble in various solvents. In fact, fullerenes are the only carbon allotropes which can be dissolved in common solvents at room temperature. The mentioned common solvents can be aromatics such as toluene and carbon disulfide.

**3.2. Nanodiamond Properties.** The physical properties of nanodiamonds (NDs) are briefed in Table 2 [165]. Due to the unique structure of nanodiamonds, they are known as the nanomaterials with significant properties. In fact, 30 percent of nanodiamond atoms are located on the surface of their structure. The maximum size of the single grains of nanodiamonds is 10 nm, while the average particle size is obtained between 4 and 6 nm [50, 166].

In 2000, Iakoubovskii et al. [50] applied the method of X-ray diffraction (XRD) to study the characterization of the structure and defects in detonation synthesis and

TABLE 2: Physical properties of nanodiamond [165].

Structure	Cubic ( $a = 0.3573$ nm)
Particle size	4.5 nm
Number of C atoms	ca. 10,000
Molar mass	120,000 g
Specific surface area	300 m <sup>2</sup> /g
Graphitization temperature	1100°C
Zeta potential	-78.44 mV
Refractive index	2.55

ultradisperse diamond (UDD). In 2008, Iakoubovskii et al. have applied the method based on high-resolution transmission electron microscopy (HRTEM) [166]. They have showed that the surface area of nanodiamond is relatively large, and the size of diamond grains is distributed around 5 nm. According to a FTIR study of the adsorption of water on ultradispersed diamond powder surface by Ji et al. [167], the surface of detonation nanodiamonds can naturally adsorb the water and hydrocarbon molecules from the environment atmosphere [167]. As the result of the research work by Iakoubovskii et al. using HRTEM, although the detonation nanodiamond grains were mostly cubic lattice, yet they were not perfect structures. According to the results of HRTEM, the main defects are shown as the multiple twins [166].

Applications of nanodiamonds cover a wide range, mainly including the commercial products such as the polishing products, additives to engine oils, reinforcing fillers for plastics and rubbers, dry lubricants for metal industry, and their applications in galvanic electrolytes. On the other hand, the recent researches on application of nanodiamonds in medical science particularly in chemotherapy drugs production are being performed.

**3.3. Carbon Nanotubes.** Due to the amazing structure and properties of CNTs, these materials have found great applications in very wide areas of science and technology including nanotechnology, electronics, optics, materials science, and architecture. In the view of the structural applications of CNTs, these applications cover a wide ranges of industrials such as clothes, sports equipment such as stronger and lighter tennis rackets, bike, various kinds of balls, combat jacket like combat jackets, concrete as the increase of the tensile strength, polyethylene, the possibility of the space elevator, synthetic muscles in medical science and sports, high tensile strength fibers, applications in the build of bridges, ultrahigh-speed flywheels, and applications in fire protection.

In electromagnetic field, the applications of CNTs are briefed in respect of their uses in chemical nanowires, conductive films, electric motor brushes, magnets, optical ignition, their applications to produce light bulb filament (as an alternative for tungsten filaments), the applications related to their fine superconductivity properties, in display screens such as field emission displays (FEDs), the

applications in transistor industrial, and the electromagnetic antenna.

Other applications of CNTs are briefed in respect of their chemical applications, including air pollution filters, biotech containers, hydrogen storage, water filtration, and the mechanical applications such as using them as the faster oscillators, nanotube membrane, slick surface, carbon nanotube actuators, infrared detector, radiometric standard, and their application as the thermal radiation for space satellites.

This is worth to know that the wide range of applications of CNTs mentioned above is due to their unique mechanical, electrical, thermal, and optical properties which are briefly introduced in this section.

**3.3.1. Strength.** Carbon nanotubes (CNTs) are the strongest materials yet discovered, which is due to the covalent sp<sup>2</sup> bonds between the individual carbon atoms. In 2000, Yu et al. [168] tested a multiwalled carbon nanotube (MWCNT) to access the tensile strength up to 63 GPa. The specific strength is defined as the material's strength (force per unit area at breaking point) divided by its density. Considering the low density of CNTs (1.3 to 1.4 g cm<sup>-3</sup>), the specific strength of CNTs is obtained up to  $48 \times 10^3$  kN m kg<sup>-1</sup>. This value is dramatically the best of the known materials.

To compare the strength property of various CNTs to some other strong materials such as stainless steel and kevlar, the tensile strength and Young's modulus of these materials have been briefed in Table 3 [168–175].

The first row of Table 3 shows the data for SWNT ropes based on the “experimental” measurements by Yu et al. using the microscopy method based on AFM [171, 173]. Yu et al. [173] measured the mechanical responses of 15 SWCNT ropes under the tensile load [173]. As they have stated in their paper [173], they considered all SWNT samples as (10, 10) nanotubes, with the measured diameter of 1.36 nm [173]. According to their experiments, as it is seen in Table 3, the average breaking strength value varies from 13 to 52 GPa [173]. Furthermore, in the same evaluation, Yu et al. measured the average Young's modulus values of the SWNT rope samples equal to 1002 GP (from 320 to 1470 GPa or about 1 TP in Table 3). In the same study, the failure strains occur at 16%. In addition, Yu et al. reported the similar data for 19 samples of MWNTs. Based on their report [173], the strength and Young's modulus values for MWNT samples vary from 11 to 63 GPa and 270 to 950 GPa, respectively (Table 3). In addition, Demczyk et al. [174] observed the force required to break the samples of MCNTs directly using transition electron microscopy. Based on the conducted pulling and bending tests on individual MWNTs, the mentioned researchers have measured the tensile strength and elastic modulus of MCNTs equal to 150 GPa and 800 GPa, respectively [174].

On the other hand, the second and third rows of Table 3 show the related data as the “predicted” strength tensile values based on the analytical simulation models. Various “analytical” simulations and models have been recently applied to calculate the tensile and Young's modulus values for CNTs. An interesting model based on a molecular

TABLE 3: Comparison of the mechanical properties of various nanotubes [168–175].

Material	Tensile strength (GPa)	Young's modulus (GPa)	Failure strain (%)
SWNT	13 to 53 (measured)	1002 (~1 TPa) (measured)	16
Armchair SWNT	126.2 (predicted)	940 (predicted)	23.1
Zigzag SWNT	94.5 (predicted)	940 (predicted)	15.6–17.5
Chiral SWNT	—	920	—
MWNT	11 to 150	270 to 950	—
Stainless steel	0.38 to 1.55	186 to 214	15 to 50
Kevlar	3.6 to 3.8	60 to 180	~2

mechanics by Xiao et al. [175] predicts the maximum values of 126.2 GP and 94 GP for Armchair SWNT and Zigzag SWNT, respectively. As given in Table 3, the predicted failure strains in the study by Xiao et al. are 23.1% and within 15.6–17.5% for armchair nanotubes and zigzag nanotubes, respectively [175].

Generally, as it is seen from Table 3, both the Young modulus and tensile strength of various carbon nanotubes are significantly more elevated than those for stainless steel and kevlar. It seems that CNTs are tended to a permanent deformation under a strong tensile strain. Furthermore, due to the hollow structure and high aspect ratio of CNTs, it seems that their strength is limited under compression or bending stress. On the other hand, as it can be seen from the simple geometry of CNT, carbon nanotubes should be softer in the radial direction than along the tube axis. In 1993, Ruoff et al. studied the Radial deformation of carbon nanotubes by van der Waals forces using transmission electron microscopy (TEM) [176]. According to their suggestion, two near nanotubes can be deformed even by van der Waals forces. Furthermore, according to the studies by Yu et al. in 2000 on radial deformability of individual carbon nanotubes under controlled indentation force (Figure 7) [177] and by Palaci et al. in 2005 [178] on radial elasticity of multiwalled carbon nanotubes, as can be seen in Figure 8, carbon nanotubes are rather soft in their radial direction.

**3.3.2. Hardness.** In 2002, Popov et al. [179] reported the synthesis of a super-hard phase (SP) composed of single-wall carbon nanotubes, measured by a nanoindenter within 62–152 GPa. The synthesis treatment was performed by compressing SWNTs to above 24 GPa at room temperature. The authors considered the hardness of diamond and boron nitride samples (150 and 62 GPa, resp.) as mentioned in the references in their work [179]. The high mechanical properties of SP-SWNT, namely bulk modulus, were obtained as 462–546 GPa, surpassing the value of 420 GPa for diamond [179]. The authors have found the hardness of SP-SWNT in the range of 62 to 150 GPa and attributed SP-SWNT to the class of super-hard materials [179].

**3.3.3. Electrical Properties.** The electrical properties of a nanotube strongly depend on its structure due to the symmetrical and exceptionally electronic structure of graphene. For example, as shown in Figure 9, in a graphene crystal lattice,  $n$  and  $m$  are the number of unit vectors along

two directions in which the graphene sheet is wrapped to make nanotube, so that  $(n, m)$  is called the chiral vector. Zigzag nanotubes are formed by wrapping a graphene sheet whenever  $m = 0$ , and in the same way, the structure is called armchair nanotube if  $n = m$ ; Otherwise, they are called chiral nanotubes. In the view point of the electrical properties of CNTs, according to the model described by Lu et al. mentioned above [180], armchair nanotubes ( $n = m$ ) are metallic. On the other hand, if  $n$  is not equal to  $m$ , however,  $(n - m)$  is a multiple of 3, the nanotube is semiconducting with a very small band gap; otherwise, the nanotube is a moderate semiconductor [180].

According to the mentioned rule, the structure of  $(5, 0)$  SWNTs should be semiconductor; however, exceptionally according to the calculations, due to the curvature effects in small diameter carbon nanotubes, this structure is metallic [180]. On the other hand, zigzag and chiral SWNTs with small diameters that are expected to be metallic have actually a finite gap [180].

In general, as Zhou et al. [181] have mentioned, SWNTs show excellent electronic properties such as the carrier mobility about  $10^4 \text{ cm}^2 \text{ V}^{-1} \text{ s}^{-1}$  [182] which is higher than that of silicon. On the other hand, as Dai et al. have described [182, 183], CNTs can carry an electrical current density of about  $4 \times 10^9 \text{ Acm}^{-2}$ . Such a current density is three orders of magnitude higher than a typical metal, for example, Cu or Al [182].

Furthermore, in order to describe the electrical properties of multiwalled carbon nanotubes (MWNTs), it is worth to mention that, in 2006, Takesue et al. [184] have confirmed that the entirely end-banded MWNTs exhibit superconductivity with a transition temperature as high as 12 K which is approximately 30 times greater than that for ropes of SWNTs or for MWNTs with usually noninterconnected shells [184].

**3.3.4. Thermal Properties of CNTs.** As shown in Figure 10, the thermal conductivity of an SWNT at room temperature along its axis with the length  $L \approx 2.6 \mu\text{m}$  and the diameter  $d \approx 1.7 \text{ nm}$  was reported as  $k \approx 3500 \text{ Wm}^{-1} \text{ K}^{-1}$  by Pop et al. [185]. In order to compare the reported value by Pop et al. [185] with a good metallic thermal conductor, Cu shows a thermal conductivity about  $385 \text{ Wm}^{-1} \text{ K}^{-1}$ . Furthermore, as Thostenson et al. [186] have mentioned, SWNTs show the stability to the temperature up to  $2800^\circ \text{C}$  in vacuum and  $750^\circ \text{C}$  in air, while metallic wires in microchips are melted at  $600\text{--}1000^\circ \text{C}$  [186].

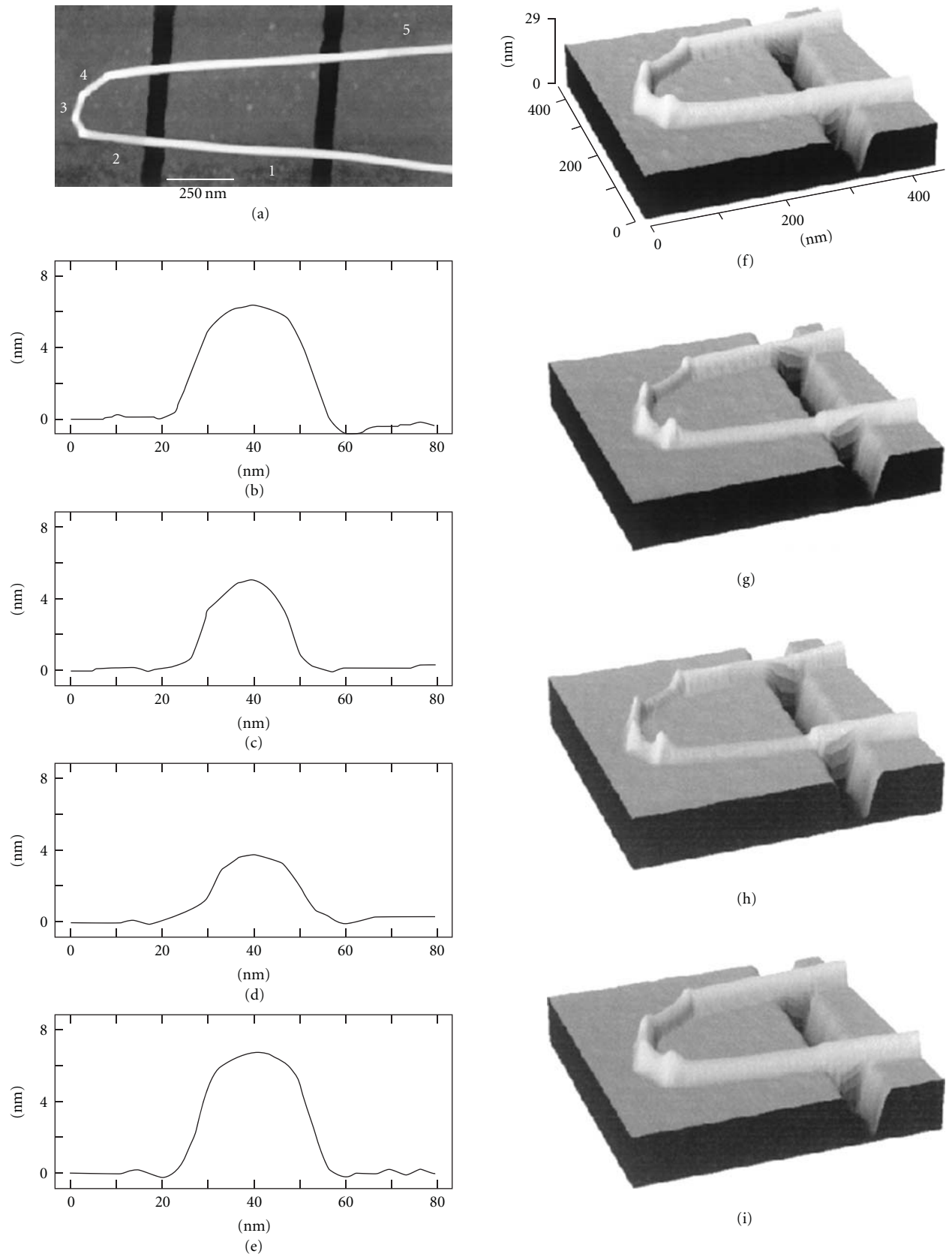


FIGURE 7: Deformability of a MWCNT deposited on an patterned silicon wafer as visualized with tapping-mode AFM operated far below mechanical resonance of a cantilever at different set points [177].

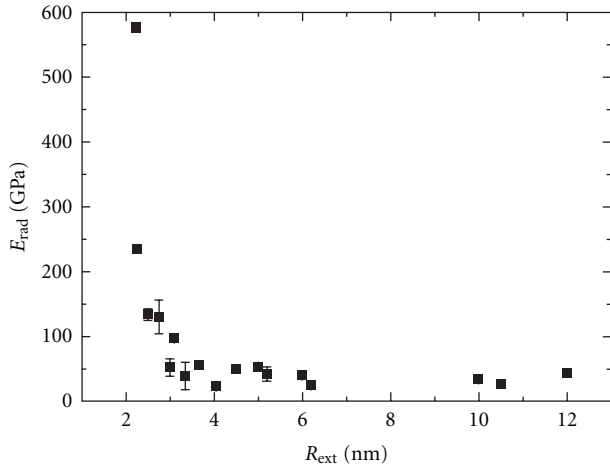


FIGURE 8: The radial Young modulus of CNTs as a function of  $R_{\text{ext}}$ , experimentally [178].

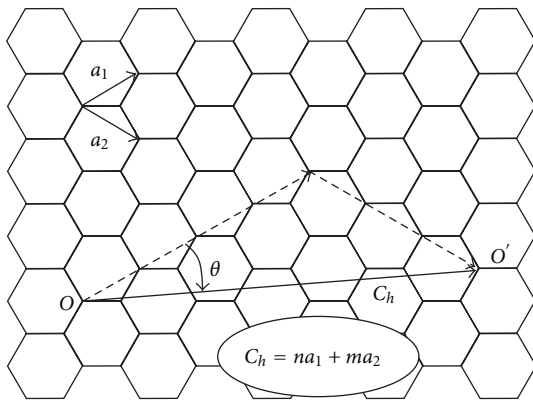


FIGURE 9: An  $(n, m)$  SWCNT: roll-up vector  $C_h = na_1 + ma_2$  and chiral angle  $\theta$  (for this special case,  $n = 5, m = 3$ ;  $a_1$  and  $a_2$  are the primitive vectors of a graphene sheet) [180].

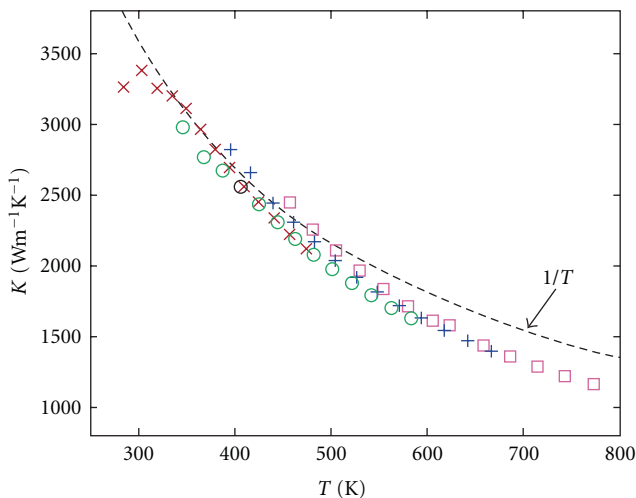


FIGURE 10: The relation between the extracted values of thermal conductivity and the average SWCNT temperature [185].

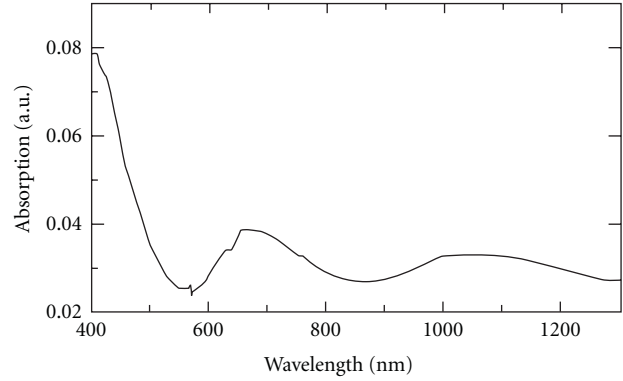


FIGURE 11: The adsorption spectrum of CNTs [172, 187].

**3.3.5. Optical Absorption.** The optical absorption in carbon nanotubes determined by Liu et al. [187] is shown in Figure 11. On the other hand, Margulis [188] has studied theoretically to indicate that zigzag SWNTs have positive low-frequency third-order susceptibilities. The Optical absorption in CNTs is occurred due to the electronic transitions from the levels  $v_2$  to  $c_2$  or  $v_1$  to  $c_1$ , and so forth [172, 189]. The mentioned transition is sharp, so it can be used to identify the type of nanotube. As it was shown by Itkis et al. [190], optical absorption is used to obtain the quality of the CNTs' powders [191].

On the other hand, according to an interesting study by Mizuno et al. in 2009 [191], SWNTs can have absorbances of 0.98–0.99 from the far-ultraviolet (200 nm) to far-infrared (200  $\mu\text{m}$ ) wavelengths. Therefore, compared to an ideal black body (with the absorbance of 1.0), a typical carbon nanotube is considered as a “practical black body” [191].

**3.4. Graphene.** In 2007, Meyer et al. [192] used transmission electron microscopy (TEM) to study the atomic structure of a single-layer graphene. As they reported, they have studied individual graphene sheets freely suspended on a micro-fabricated scaffold in vacuum or the air. The membranes were only one-atom thick, yet they still displayed long-range crystalline order [192]. According to their studies using TEM, the suspended graphene sheets are not perfectly flat. In other words, the suspended graphenes were observed as rippling of the flat sheet, with amplitude of about 1 nm [192]. As the authors explained, the atomically thin single-crystal membranes offered ample scope for fundamental research and new technologies, whereas the observed corrugations in the third dimension may provide subtle reasons for the stability of two-dimensional crystals [192].

**3.4.1. Mobility of Graphene and the Applications.** Graphene is known as a high electron mobility material at room temperature, so that the reported value is  $15,000 \text{ cm}^2\text{V}^{-1}\text{s}^{-1}$  [193]. In 2005, Novoselov et al. [194] considered graphene as a condensed-matter system in which electron transport is essentially governed by Dirac's (relativistic) equation [194]. In 2008, Morozov et al. [195] studied temperature dependences of electron transport in graphene and showed

that the electron mobility higher than  $2 \times 10^5 \text{ cm}^2 \text{ V}^{-1} \text{ s}$  is achievable if extrinsic disorder is eliminated. In the same year, Chen et al. [196] studied the intrinsic and extrinsic performance limits of graphene devices on  $\text{SiO}_2$ . According to the studies mentioned above, it seems that the electron mobility in graphene should be almost independent of the temperature between 10 K and 100 K [194–196].

Due to the high mobility of graphene, this material is known as a promising nanomaterial particularly for those applications in which transistors need to switch extremely fast. Furthermore, the high mobility of graphene involves this material in the applications related to chemical and biochemical sensing.

On the other hand, the resistivity of the graphene sheets is  $10^{-6} \Omega \text{ cm}$  which is less than the resistivity of silver as known as the lowest resistivity at room temperature. Such a unique low resistivity and also the very low thickness of graphene have made this material to have a great role in many applications such as mechanical fields, electrical conducting, and transparent films which are necessarily applicable in the field of electronics such as producing touch screens and photovoltaic cells.

#### 4. Conclusion and the Future Outlooks

As described in this paper, the unique structure and properties of low-dimensional carbon nanomaterials as the advanced materials have led them to have a strong and important potential role in various scientific fields and engineering such as nanoscale electronic devices, field emission displays, diodes, transistors, sensors, composite polymers, artificial muscles, mechanical reinforcements, capacitors, and hydrogen storage. For example, carbon nanobuds are the recently produced materials from two previously known allotropes of carbon nanotubes and fullerenes. These fullerene-like “buds” have found the unique properties of both fullerenes and CNTs which have many applications as good field emitters as well as their role to improve the mechanical properties of composites. As another example, the application of CNTs to develop the biofuel products is being noticeably growing due to their strongly deferent properties comparing to the previous products.

The list of companies which are working on the new features of carbon nanomaterials can show the importance of the use of these key materials in industry as well as the scientific areas. Taken the examples of such companies and their products, we can mention the Eagle Windpower Ltd. (windmills with lightweight blades), Easton (on bicycle components), Xintek (on Nanotube-based cathodes, AFM probes, and X-ray tubes), Nanomix (sensors for detecting chemical vapors), Nano-Proprietary, Inc. (analyzing chemicals in liquid samples), Zyvex Performance Materials (epoxy resins strengthened with carbon nanotubes), Hyperion (Nanotube-based plastic mold compounds), Nano Lab (functionalized nanotubes and nanotube arrays), Nanoledge (Nanotube-based resins), Nanocs (Functionalized nanotubes), Nanocyl (nanotube-based epoxy resins), Amroy Europe Oy (Nanotube-based epoxy resins), Bayer Material

Science (Carbon nanotubes), Cheap Tubes (Carbon nanotubes), Catalytic Materials (Carbon nanotubes and graphite nanofibers), MER Corporation (Carbon nanotubes and buckyballs), NanoCarbLab (Carbon nanotubes), NanoAmor (Carbon nanotubes, carbon nanofibers, nanowires, and nanoparticles), Nanothinx (Carbon nanotubes), Rosseter Holdings (Carbon nanotubes), and many others.

As a matter of fact, due to the unique mechanical, optical, and electronic properties of carbon nanotubes, the publication statistics show that CNTs have succeeded to attract the main body of the authors' interest since 1991 up to now. However, as described in this paper, carbon nanomaterials are not limited to CNTs. Therefore, the future outlook of applications of these materials depends on the capability of the use of each one. As an interesting bioapplication example, nanodiamonds may be capable to be used for biolistic delivery in gene therapy, drug delivery, and vaccines as a solid support matrix. Furthermore, there is a strong possibility in near future to use nanodiamonds in the medical immunoassays as either the detection tag or the solid support matrix [197].

As the definition of the low-dimensional carbon nanomaterial, these materials also cover a wide range of carbon-related nanostructures such as nanodiamonds, fibers, cones, scrolls, whiskers, and graphite polyhedral crystals. In fact, there are expectable outlooks for the use of these materials in the fields of molecular electronics, sensing, nanoelectromechanic devices, field-emission displays, energy storage, and composite materials, as well as their growing applications in medical science, health, and daily life [198].

#### Acknowledgment

This work was supported by Chang Jiang Scholars Program, China. The authors would like to express their appreciation to them. A. Mostofizadeh and Y. Li contributed equally to this work.

#### References

- [1] M. Monthieux and V. L. Kuznetsov, “Who should be given the credit for the discovery of carbon nanotubes?” *Carbon*, vol. 44, no. 9, pp. 1621–1623, 2006.
- [2] W. Bollmann and J. Spreadborough, “Action of graphite as a lubricant,” *Nature*, vol. 186, no. 4718, pp. 29–30, 1960.
- [3] A. Oberlin, M. Endo, and T. Koyama, “Filamentous growth of carbon through benzene decomposition,” *Journal of Crystal Growth*, vol. 32, no. 3, pp. 335–349, 1976.
- [4] H. W. Kroto, J. R. Heath, S. C. O'Brien, R. F. Curl, and R. E. Smalley, “C<sub>60</sub>: buckminsterfullerene,” *Nature*, vol. 318, no. 6042, pp. 162–163, 1985.
- [5] S. Subramoney, “Novel nanocarbons—structure, properties, and potential applications,” *Advanced Materials*, vol. 10, no. 15, pp. 1157–1171, 1998.
- [6] T. Seyller, A. Bostwick, K. V. Emtsev et al., “Epitaxial graphene: a new material,” *Physica Status Solidi (B)*, vol. 245, no. 7, pp. 1436–1446, 2008.
- [7] J. H. Kim, C. K. Kim, Y. H. Kim, and C. S. Yoon, “Synthesis of carbon-encapsulated gold nanoparticles in polyimide

- matrix," *Colloids and Surfaces A*, vol. 321, no. 1–3, pp. 297–300, 2008.
- [8] L. Hawelek, A. Brodka, J. C. Dore, V. Honkimaki, S. Tomita, and A. Burian, "Structural studies of nanodiamond by high-energy X-ray diffraction," *Diamond and Related Materials*, vol. 17, no. 7–10, pp. 1186–1193, 2008.
  - [9] W. Xia, D. Su, A. Birkner et al., "Chemical vapor deposition and synthesis on carbon nanofibers: sintering of ferrocene-derived supported iron nanoparticles and the catalytic growth of secondary carbon nanofibers," *Chemistry of Materials*, vol. 17, no. 23, pp. 5737–5742, 2005.
  - [10] O. Shenderova, V. Grishko, G. Cunningham, S. Moseenkov, G. McGuire, and V. Kuznetsov, "Onion-like carbon for terahertz electromagnetic shielding," *Diamond and Related Materials*, vol. 17, no. 4–5, pp. 462–466, 2008.
  - [11] S. Vizireanu, L. Nistor, M. Haupt, V. Katzenmaier, C. Oehr, and G. Dinescu, "Carbon nanowalls growth by radiofrequency plasma-beam-enhanced chemical vapor deposition," *Plasma Processes and Polymers*, vol. 5, no. 3, pp. 263–268, 2008.
  - [12] "The Nobel Prize in Chemistry 1996," Nobelprize.org, October 2010, [http://nobelprize.org/nobel\\_prizes/chemistry/laureates/1996/](http://nobelprize.org/nobel_prizes/chemistry/laureates/1996/).
  - [13] W. Krätschmer, K. Fostiropoulos, and D. R. Huffman, "The infrared and ultraviolet absorption spectra of laboratory-produced carbon dust: evidence for the presence of the C molecule," *Chemical Physics Letters*, vol. 170, no. 2–3, pp. 167–170, 1990.
  - [14] N. I. Alekseyev and G. A. Dyuzhev, "Fullerene formation in an arc discharge," *Carbon*, vol. 41, no. 7, pp. 1343–1348, 2003.
  - [15] J. B. Howard, J. T. McKinnon, Y. Makarovsky, A. L. Lafleur, and M. E. Johnson, "Fullerenes C60 and C70 in flames," *Nature*, vol. 352, no. 6331, pp. 139–141, 1991.
  - [16] J. B. Howard, A. L. Lafleur, Y. Makarovsky, S. Mitra, C. J. Pope, and T. K. Yadav, "Fullerenes synthesis in combustion," *Carbon*, vol. 30, no. 8, pp. 1183–1201, 1992.
  - [17] S. Y. Xie, R. B. Huang, L. J. Yu, J. Ding, and L. S. Zheng, "Microwave synthesis of fullerenes from chloroform," *Applied Physics Letters*, vol. 75, no. 18, pp. 2764–2766, 1999.
  - [18] R. Taylor, G. J. Langley, H. W. Kroto, and D. R. M. Walton, "Formation of C60 by pyrolysis of naphthalene," *Nature*, vol. 366, no. 6457, pp. 728–731, 1993.
  - [19] A. Koshio, M. Yudasaka, M. Ozawa, and S. Iijima, "Fullerene formation via pyrolysis of ragged single-wall carbon nanotubes," *Nano Letters*, vol. 2, no. 9, pp. 995–997, 2002.
  - [20] C. Chen and Z. Lou, "Formation of C60 by reduction of CO<sub>2</sub>," *Journal of Supercritical Fluids*, vol. 50, no. 1, pp. 42–45, 2009.
  - [21] N. Koprinarov, M. Marinov, M. Konstantinova, and B. Rangelov, "Fullerene structure synthesis by DC arc discharge in ferrocene vapours," *Vacuum*, vol. 58, no. 2, pp. 208–214, 2000.
  - [22] H. Richter, E. De Hoffmann, R. Doome et al., "Fullerene formation in acetylene/oxygen/argon/chlorine flames," *Carbon*, vol. 34, no. 6, pp. 797–803, 1996.
  - [23] L. T. Scott, "Methods for the chemical synthesis of fullerenes," *Angewandte Chemie—International Edition*, vol. 43, no. 38, pp. 4994–5007, 2004.
  - [24] R. S. Ruoff, D. C. Lorents, B. Chan, R. Malhotra, and S. Subramoney, "Single crystal metals encapsulated in carbon nanoparticles," *Science*, vol. 259, no. 5093, pp. 346–348, 1993.
  - [25] M. Tomita, Y. Saito, and T. Hayashi, "LaC encapsulated in graphite nano-particle," *Japanese Journal of Applied Physics*, vol. 32, no. 2, pp. L280–L282, 1993.
  - [26] Y. Saito, "Nanoparticles and filled nanocapsules," *Carbon*, vol. 33, no. 7, pp. 979–988, 1995.
  - [27] V. P. Dravid, J. J. Host, M. H. Teng et al., "Controlled-size nanocapsules," *Nature*, vol. 374, no. 6523, p. 602, 1995.
  - [28] J. J. Host, J. A. Block, K. Parvin et al., "Effect of annealing on the structure and magnetic properties of graphite encapsulated nickel and cobalt nanocrystals," *Journal of Applied Physics*, vol. 83, no. 2, pp. 793–801, 1998.
  - [29] J. Jiao, S. Seraphin, X. Wang, and J. C. Withers, "Preparation and properties of ferromagnetic carbon-coated Fe, Co, and Ni nanoparticles," *Journal of Applied Physics*, vol. 80, no. 1, pp. 103–108, 1996.
  - [30] J. Jiao and S. Seraphin, "Carbon encapsulated nanoparticles of Ni, Co, Cu, and Ti," *Journal of Applied Physics*, vol. 83, no. 5, pp. 2442–2448, 1998.
  - [31] J. Qiu, Y. Li, Y. Wang, Z. Zhao, Y. Zhou, and Y. Wang, "Synthesis of carbon-encapsulated nickel nanocrystals by arc-discharge of coal-based carbons in water," *Fuel*, vol. 83, no. 4–5, pp. 615–617, 2004.
  - [32] P. J. F. Harris and S. C. Tsang, "A simple technique for the synthesis of filled carbon nanoparticles," *Chemical Physics Letters*, vol. 293, no. 1–2, pp. 53–58, 1998.
  - [33] E. Flahaut, F. Agnoli, J. Sloan, C. O'Connor, and M. L. H. Green, "CCVD Synthesis and characterization of cobalt-encapsulated nanoparticles," *Chemistry of Materials*, vol. 14, no. 6, pp. 2553–2558, 2002.
  - [34] Z. H. Wang, C. J. Choi, B. K. Kim, J. C. Kim, and Z. D. Zhang, "Characterization and magnetic properties of carbon-coated cobalt nanocapsules synthesized by the chemical vapor-condensation process," *Carbon*, vol. 41, no. 9, pp. 1751–1758, 2003.
  - [35] S. H. Tsai, C. L. Lee, C. W. Chao, and H. C. Shih, "Novel technique for the formation of carbon-encapsulated metal nanoparticles on silicon," *Carbon*, vol. 38, no. 5, pp. 781–785, 2000.
  - [36] B. H. Liu, J. Ding, Z. Y. Zhong, Z. L. Dong, T. White, and J. Y. Lin, "Large-scale preparation of carbon-encapsulated cobalt nanoparticles by the catalytic method," *Chemical Physics Letters*, vol. 358, no. 1–2, pp. 96–102, 2002.
  - [37] Y. F. Zhang, Y. H. Tang, Y. Zhang, C. S. Lee, I. Bello, and S. T. Lee, "Deposition of carbon nanotubes on Si nanowires by chemical vapor deposition," *Chemical Physics Letters*, vol. 330, no. 1–2, pp. 48–52, 2000.
  - [38] Y. Lu, Z. Zhu, and Z. Liu, "Carbon-encapsulated Fe nanoparticles from detonation-induced pyrolysis of ferrocene," *Carbon*, vol. 43, no. 2, pp. 369–374, 2005.
  - [39] W. Wu, Z. Zhu, Z. Liu, Y. Xie, J. Zhang, and T. Hu, "Preparation of carbon-encapsulated iron carbide nanoparticles by an explosion method," *Carbon*, vol. 41, no. 2, pp. 317–321, 2003.
  - [40] J. N. Wang, L. I. Zhang, F. Yu, and Z. M. Sheng, "Synthesis of carbon encapsulated magnetic nanoparticles with giant coercivity by a spray pyrolysis approach," *Journal of Physical Chemistry B*, vol. 111, no. 8, pp. 2119–2124, 2007.
  - [41] H. Song and X. Chen, "Large-scale synthesis of carbon-encapsulated iron carbide nanoparticles by co-carbonization of durenene with ferrocene," *Chemical Physics Letters*, vol. 374, no. 3–4, pp. 400–404, 2003.
  - [42] J. Huo, H. Song, and X. Chen, "Preparation of carbon-encapsulated iron nanoparticles by co-carbonization of aromatic heavy oil and ferrocene," *Carbon*, vol. 42, no. 15, pp. 3177–3182, 2004.

- [43] M. Bystrzejewski, H. Lange, A. Huczko, H. I. Elim, and W. Ji, "Study of the optical limiting properties of carbon-encapsulated magnetic nanoparticles," *Chemical Physics Letters*, vol. 444, no. 1–3, pp. 113–117, 2007.
- [44] J. B. Park, S. H. Jeong, M. S. Jeong, J. Y. Kim, and B. K. Cho, "Synthesis of carbon-encapsulated magnetic nanoparticles by pulsed laser irradiation of solution," *Carbon*, vol. 46, no. 11, pp. 1369–1377, 2008.
- [45] J. Nishijo, C. Okabe, O. Oishi, and N. Nishi, "Synthesis, structures and magnetic properties of carbon-encapsulated nanoparticles via thermal decomposition of metal acetylide," *Carbon*, vol. 44, no. 14, pp. 2943–2949, 2006.
- [46] F. Maya, S. Muhl, O. Peña, and M. Miki-Yoshida, "Synthesis and characterization of silver-carbon nanoparticles produced by high-current pulsed arc," *Thin Solid Films*, vol. 518, no. 5, pp. 1484–1488, 2009.
- [47] F. P. Bundy, H. T. Hall, H. M. Strong, and R. H. Wentorf, "Man-Made diamonds," *Nature*, vol. 176, no. 4471, pp. 51–55, 1955.
- [48] A. M. Staver, N. V. Gubareva, A. I. Lyamkin et al., "The flow in a shock tube in the presence of suspended particles," *Fizika Goreniya I Vzryza*, vol. 20, no. 5, 1984.
- [49] N. R. Greiner, D. S. Phillips, J. D. Johnson, and F. Volk, "Diamonds in detonation soot," *Nature*, vol. 333, no. 6172, pp. 440–442, 1988.
- [50] K. Iakoubovskii, M. V. Baidakova, B. H. Wouters et al., "Structure and defects of detonation synthesis nanodiamond," *Diamond and Related Materials*, vol. 9, no. 3–6, pp. 861–865, 2000.
- [51] P. W. Chen, Y. S. Ding, Q. Chen, F. L. Huang, and S. R. Yun, "Spherical nanometer-sized diamond obtained from detonation," *Diamond and Related Materials*, vol. 9, no. 9, pp. 1722–1725, 2000.
- [52] T. Hamilton, E. Z. Kurmaev, S. N. Shamin, P. Y. Detkov, S. I. Chukhaeva, and A. Moewes, "Soft X-ray absorption and emission characterization of nanodiamond prepared by explosive detonation," *Diamond and Related Materials*, vol. 16, no. 2, pp. 350–352, 2007.
- [53] X. Xu, Z. Yu, Y. Zhu, and B. Wang, "Influence of surface modification adopting thermal treatments on dispersion of detonation nanodiamond," *Journal of Solid State Chemistry*, vol. 178, no. 3, pp. 688–693, 2005.
- [54] Q. Zou, M. Z. Wang, Y. G. Li, L. H. Zou, H. Yu, and Y. C. Zhao, "Analysis of structures and surface states of the nanodiamond particle synthesised by detonation," *Micro and Nano Letters*, vol. 4, no. 3, pp. 133–141, 2009.
- [55] V. Gupta, P. Scharff, and N. Miura, "Synthesis of diamond by electron irradiation of C60 intercalated graphite," *Materials Letters*, vol. 59, no. 26, pp. 3259–3261, 2005.
- [56] V. S. Purohit, D. Jain, V. G. Sathe, V. Ganesan, and S. V. Bhoraskar, "Synthesis of nanocrystalline diamonds by microwave plasma," *Journal of Physics D*, vol. 40, no. 6, pp. 1794–1800, 2007.
- [57] T. Sharda, T. Soga, T. Jimbo, and M. Umeno, "Biased enhanced growth of nanocrystalline diamond films by microwave plasma chemical vapor deposition," *Diamond and Related Materials*, vol. 9, no. 7, pp. 1331–1335, 2000.
- [58] M. Nagatsu, M. Miyake, and J. Maeda, "Plasma CVD reactor with two-microwave oscillators for diamond film synthesis," *Thin Solid Films*, vol. 506–507, pp. 617–621, 2006.
- [59] T. Hao, H. Zhang, C. Shi, and G. Han, "Nano-crystalline diamond films synthesized at low temperature and low pressure by hot filament chemical vapor deposition," *Surface and Coatings Technology*, vol. 201, no. 3–4, pp. 801–806, 2006.
- [60] L. Vandenbulcke, T. Gries, and J. N. Rouzaud, "Nanodiamonds in dusty low-pressure plasmas," *Applied Physics Letters*, vol. 94, no. 4, Article ID 044106, 2009.
- [61] L. Yang, P. W. May, L. Yin, J. A. Smith, and K. N. Rosser, "Growth of diamond nanocrystals by pulsed laser ablation of graphite in liquid," *Diamond and Related Materials*, vol. 16, no. 4–7, pp. 725–729, 2007.
- [62] C. Wen, Z. Jin, X. Liu et al., "Synthesis of diamond using nano-graphite and Fe powder under high pressure and high temperature," *Materials Letters*, vol. 60, no. 29–30, pp. 3507–3510, 2006.
- [63] L. Hawelek, A. Brodka, J. C. Dore, V. Honkimaki, S. Tomita, and A. Burian, "Structural studies of nanodiamond by high-energy X-ray diffraction," *Diamond and Related Materials*, vol. 17, no. 7–10, pp. 1186–1193, 2008.
- [64] D. Amans, A. C. Chenus, G. Ledoux et al., "Nanodiamond synthesis by pulsed laser ablation in liquids," *Diamond and Related Materials*, vol. 18, no. 2–3, pp. 177–180, 2009.
- [65] D. Ugarte, "Curling and closure of graphitic networks under electron-beam irradiation," *Nature*, vol. 359, no. 6397, pp. 707–709, 1992.
- [66] P. J. F. Harris and S. C. Tsang, "High-resolution electron microscopy studies of non-graphitizing carbons," *Philosophical Magazine A*, vol. 76, no. 3, pp. 667–677, 1997.
- [67] D. Ugarte, "Morphology and structure of graphitic soot particles generated in arc-discharge C production," *Chemical Physics Letters*, vol. 198, no. 6, pp. 596–602, 1992.
- [68] W. Kratschmer, L. D. Lamb, K. Fostiropoulos, and D. R. Huffman, "Solid C60: a new form of carbon," *Nature*, vol. 347, no. 6291, pp. 354–358, 1990.
- [69] B. S. Xu and S. I. Tanaka, "Formation of giant onion-like fullerenes under Al nanoparticles by electron irradiation," *Acta Materialia*, vol. 46, no. 15, pp. 5249–5257, 1998.
- [70] A. G. Nasibulin, A. Moisala, D. P. Brown, and E. I. Kauppinen, "Carbon nanotubes and onions from carbon monoxide using Ni(acac)<sub>2</sub> and Cu(acac)<sub>2</sub> as catalyst precursors," *Carbon*, vol. 41, no. 14, pp. 2711–2724, 2003.
- [71] J. S. Qiu, Y. Zhou, L. N. Wang, and S. C. Tsang, "Formation of carbon nanotubes and encapsulated nanoparticles from coals with moderate ash contents," *Carbon*, vol. 36, no. 4, pp. 465–467, 1998.
- [72] T. Cabioch, E. Thune, and M. Jaouen, "Carbon-onion thin-film synthesis onto silica substrates," *Chemical Physics Letters*, vol. 320, no. 1–2, pp. 202–205, 2000.
- [73] T. Cabioch, M. Jaouen, M. F. Denanot, and P. Bechet, "Influence of the implantation parameters on the microstructure of carbon onions produced by carbon ion implantation," *Applied Physics Letters*, vol. 73, no. 21, pp. 3096–3098, 1998.
- [74] H. Abe, "Nucleation of carbon onions and nanocapsules under ion implantation at high temperature," *Diamond and Related Materials*, vol. 10, no. 3–7, pp. 1201–1204, 2001.
- [75] V. L. Kuznetsov, A. L. Chuvilin, Y. V. Butenko, I. Y. Mal'kov, and V. M. Titov, "Onion-like carbon from ultra-disperse diamond," *Chemical Physics Letters*, vol. 222, no. 4, pp. 343–348, 1994.
- [76] L. G. Bulusheva, A. V. Okotrub, V. L. Kuznetsov, and D. V. Vyalikh, "Soft X-ray spectroscopy and quantum chemistry characterization of defects in onion-like carbon produced by nanodiamond annealing," *Diamond and Related Materials*, vol. 16, no. 4–7, pp. 1222–1226, 2007.
- [77] M. Bystrzejewski, M. H. Rummeli, T. Gemming, H. Lange, and A. Huczko, "Catalyst-free synthesis of onion-like carbon nanoparticles," *New Carbon Materials*, vol. 25, no. 1, pp. 1–8, 2010.

- [78] M. Zhao, H. Song, X. Chen, and W. Lian, "Large-scale synthesis of onion-like carbon nanoparticles by carbonization of phenolic resin," *Acta Materialia*, vol. 55, no. 18, pp. 6144–6150, 2007.
- [79] X. Liu, C. Wang, Y. Yang, X. Guo, H. Wen, and B. Xu, "Synthesis of nano onion-like fullerenes by using Fe/Al<sub>2</sub>O<sub>3</sub> as catalyst by chemical vapor deposition," *Chinese Science Bulletin*, vol. 54, no. 1, pp. 137–141, 2009.
- [80] A. B. Du, X. G. Liu, D. J. Fu, P. D. Han, and B. S. Xu, "Onion-like fullerenes synthesis from coal," *Fuel*, vol. 86, no. 1-2, pp. 294–298, 2007.
- [81] J. Huang, Y. Liu, and T. You, "Carbon nanofiber based electrochemical biosensors: a review," *Analytical Methods*, vol. 2, no. 3, pp. 202–211, 2010.
- [82] P. Serp, M. Corrias, and P. Kalck, "Carbon nanotubes and nanofibers in catalysis," *Applied Catalysis A*, vol. 253, no. 2, pp. 337–358, 2003.
- [83] S. Iijima, "Helical microtubules of graphitic carbon," *Nature*, vol. 354, no. 6348, pp. 56–58, 1991.
- [84] E. P. S. Tan, C. N. Goh, C. H. Sow, and C. T. Lim, "Tensile test of a single nanofiber using an atomic force microscope tip," *Applied Physics Letters*, vol. 86, no. 7, Article ID 073115, 3 pages, 2005.
- [85] E. P. S. Tan and C. T. Lim, "Mechanical characterization of nanofibers—a review," *Composites Science and Technology*, vol. 66, no. 9, pp. 1099–1108, 2006.
- [86] H. J. Qi, K. B. K. Teo, K. K. S. Lau et al., "Determination of mechanical properties of carbon nanotubes and vertically aligned carbon nanotube forests using nanoindentation," *Journal of the Mechanics and Physics of Solids*, vol. 51, no. 11-12, pp. 2213–2237, 2003.
- [87] P. E. Aderson and N. M. Rodriguez, "Influence of the support on the structural characteristics of carbon nanofibers produced from the metal-catalyzed decomposition of ethylene," *Chemistry of Materials*, vol. 12, no. 3, pp. 823–830, 2000.
- [88] A. Tanaka, S. H. Yoon, and I. Mochida, "Preparation of highly crystalline nanofibers on Fe and Fe-Ni catalysts with a variety of graphene plane alignments," *Carbon*, vol. 42, no. 3, pp. 591–597, 2004.
- [89] G. L. Bezemer, P. B. Radstake, U. Falke et al., "Investigation of promoter effects of manganese oxide on carbon nanofiber-supported cobalt catalysts for Fischer-Tropsch synthesis," *Journal of Catalysis*, vol. 237, no. 1, pp. 152–161, 2006.
- [90] S. Takenaka, M. Ishida, M. Serizawa, E. Tanabe, and K. Otsuka, "Formation of carbon nanofibers and carbon nanotubes through methane decomposition over supported cobalt catalysts," *Journal of Physical Chemistry B*, vol. 108, no. 31, pp. 11464–11472, 2004.
- [91] J. P. Tu, L. P. Zhu, K. Hou, and S. Y. Guo, "Synthesis and frictional properties of array film of amorphous carbon nanofibers on anodic aluminum oxide," *Carbon*, vol. 41, no. 6, pp. 1257–1263, 2003.
- [92] V. Z. Mordkovich, "Carbon nanofibers: a new ultrahigh-strength material for chemical technology," *Theoretical Foundations of Chemical Engineering*, vol. 37, no. 5, pp. 429–438, 2003.
- [93] A. De Lucas, P. B. García, A. Garrido, A. Romero, and J. L. Valverde, "Catalytic synthesis of carbon nanofibers with different graphene plane alignments using Ni deposited on iron pillared clays," *Applied Catalysis A*, vol. 301, no. 1, pp. 123–132, 2006.
- [94] K. Takehira, T. Ohi, T. Shishido, T. Kawabata, and K. Takaki, "Catalytic growth of carbon fibers from methane and ethylene on carbon-supported Ni catalysts," *Applied Catalysis A*, vol. 283, no. 1-2, pp. 137–145, 2005.
- [95] D. Y. Ding, J. N. Wang, and A. Dozier, "Symmetry-related growth of carbon nanocoils from Ni-P based alloy particles," *Journal of Applied Physics*, vol. 95, no. 9, pp. 5006–5009, 2004.
- [96] K. L. Klein, A. V. Melechko, P. D. Rack, J. D. Fowlkes, H. M. Meyer, and M. L. Simpson, "Cu-Ni composition gradient for the catalytic synthesis of vertically aligned carbon nanofibers," *Carbon*, vol. 43, no. 9, pp. 1857–1863, 2005.
- [97] A. R. Naghash, Z. Xu, and T. H. Etsell, "Cocprecipitation of nickel-copper-aluminum takovite as catalyst precursors for simultaneous production of carbon nanofibers and hydrogen," *Chemistry of Materials*, vol. 17, no. 4, pp. 815–821, 2005.
- [98] F. Yuan, H. K. Yu, and H. Ryu, "Preparation and characterization of carbon nanofibers as catalyst support material for PEMFC," *Electrochimica Acta*, vol. 50, no. 2-3, pp. 685–691, 2004.
- [99] W. C. Ren and H. M. Cheng, "Herringbone-type carbon nanofibers with a small diameter and large hollow core synthesized by the catalytic decomposition of methane," *Carbon*, vol. 41, no. 8, pp. 1657–1660, 2002.
- [100] Y. Qin, Z. Zhang, and Z. Cui, "Helical carbon nanofibers with a symmetric growth mode," *Carbon*, vol. 42, no. 10, pp. 1917–1922, 2004.
- [101] C. Singh, T. Queded, C. B. Boothroyd et al., "Synthesis and characterization of carbon nanofibers produced by the floating catalyst method," *Journal of Physical Chemistry B*, vol. 106, no. 42, pp. 10915–10922, 2002.
- [102] C. Pham-Huu, N. Keller, V. V. Roddatis, G. Mestl, R. Schlögl, and M. J. Ledoux, "Large scale synthesis of carbon nanofibers by catalytic decomposition of ethane on nickel nanoclusters decorating carbon nanotubes," *Physical Chemistry Chemical Physics*, vol. 4, no. 3, pp. 514–521, 2002.
- [103] G. Zou, D. Zhang, C. Dong et al., "Carbon nanofibers: synthesis, characterization, and electrochemical properties," *Carbon*, vol. 44, no. 5, pp. 828–832, 2006.
- [104] L. Yu, L. Sui, Y. Qin, and Z. Cui, "Low-temperature synthesis of carbon nanofibers by decomposition of acetylene with a catalyst derived from cupric nitrate," *Chemical Engineering Journal*, vol. 144, no. 3, pp. 514–517, 2008.
- [105] J. Zhang, I. Khatiri, N. Kishi, T. Soga, and T. Jimbo, "Synthesis of carbon nanofibers using C<sub>60</sub>, graphite and boron," *Materials Letters*, vol. 64, no. 11, pp. 1243–1246, 2010.
- [106] T. Kimura, H. Koizumi, H. Kinoshita, and T. Ichikawa, "Formation of carbon nanofibers from decacyclene by ion beam irradiation," *Nuclear Instruments and Methods in Physics Research B*, vol. 236, no. 1–4, pp. 474–481, 2005.
- [107] Y. Matsumoto, M. Than Oo, M. Nakao, K. Kamimura, Y. Onuma, and H. Matsushima, "Preparation of carbon nanofibers by hot filament-assisted sputtering," *Materials Science and Engineering B*, vol. 74, no. 1, pp. 218–221, 2000.
- [108] M. Guláš, M. Čaplovičová, M. Michalka et al., "Growth of carbon nanofibers and related structures by combined method of plasma enhanced chemical vapor deposition and aerosol synthesis," *Vacuum*, vol. 82, no. 8, pp. 805–813, 2008.
- [109] P. Ren, X. Zou, J. Cheng et al., "Synthesis of carbon nanofibers by ethanol catalytic combustion technique," *Advanced Materials Research*, vol. 24-25, pp. 731–734, 2007.
- [110] L. Ci, Y. Li, B. Wei, J. Liang, C. Xu, and D. Wu, "Preparation of carbon nanofibers by the floating catalyst method," *Carbon*, vol. 38, no. 14, pp. 1933–1937, 2000.

- [111] S. Mori and M. Suzuki, "Effect of oxygen and hydrogen addition on the low-temperature synthesis of carbon nanofibers using a low-temperature CO/Ar DC plasma," *Diamond and Related Materials*, vol. 17, no. 6, pp. 999–1002, 2008.
- [112] S. Iijima, "Helical microtubules of graphitic carbon," *Nature*, vol. 354, no. 6348, pp. 56–58, 1991.
- [113] T. W. Ebbesen and P. M. Ajayan, "Large-scale synthesis of carbon nanotubes," *Nature*, vol. 358, no. 6383, pp. 220–222, 1992.
- [114] S. Iijima and T. Ichihashi, "Single-shell carbon nanotubes of 1-nm diameter," *Nature*, vol. 363, no. 6430, pp. 603–605, 1993.
- [115] D. S. Bethune, C. H. Kiang, M. S. De Vries et al., "Cobalt-catalysed growth of carbon nanotubes with single-atomic-layer walls," *Nature*, vol. 363, no. 6430, pp. 605–607, 1993.
- [116] C. Journet, W. K. Maser, P. Bernier et al., "Large-scale production of single-walled carbon nanotubes by the electric-arc technique," *Nature*, vol. 388, no. 6644, pp. 756–758, 1997.
- [117] A. Thess, R. Lee, P. Nikolaev et al., "Crystalline ropes of metallic carbon nanotubes," *Science*, vol. 273, no. 5274, pp. 483–487, 1996.
- [118] M. Yacaman, M. Yoshida, L. Rendon, and J. G. Santiesteban, "Catalytic growth of carbon microtubules with fullerene structure," *Applied Physics Letters*, vol. 62, no. 2, pp. 202–204, 1993.
- [119] E. Flahaut, A. Govindaraj, A. Peigney, CH. Laurent, A. Rousset, and C. N. R. Rao, "Synthesis of single-walled carbon nanotubes using binary (Fe, Co, Ni) alloy nanoparticles prepared in situ by the reduction of oxide solid solutions," *Chemical Physics Letters*, vol. 300, no. 1-2, pp. 236–242, 1999.
- [120] H. Dai, "Carbon nanotubes: opportunities and challenges," *Surface Science*, vol. 500, no. 1–3, pp. 218–241, 2002.
- [121] V. N. Popov, "Carbon nanotubes: properties and application," *Materials Science and Engineering R*, vol. 43, no. 3, pp. 61–102, 2004.
- [122] P. M. Ajayan and T. W. Ebbesen, "Nanometre-size tubes of carbon," *Reports on Progress in Physics*, vol. 60, no. 10, pp. 1025–1062, 1997.
- [123] Q. Zeng, Z. Li, and Y. Zhou, "Synthesis and application of carbon nanotubes," *Journal of Natural Gas Chemistry*, vol. 15, no. 3, pp. 235–246, 2006.
- [124] E. S. Thiele and R. H. French, "Computation of light scattering by anisotropic spheres of rutile titania," *Advanced Materials*, vol. 10, no. 15, pp. 1271–1276, 1998.
- [125] W. Zhou, X. Bai, E. Wang, and S. Xie, "Synthesis, structure, and properties of single-walled carbon nanotubes," *Advanced Materials*, vol. 21, no. 45, pp. 4565–4583, 2009.
- [126] D. S. Arensburger, S. M. Zimakov, P. A. Kulu, and M. A. Oyaviir, "Coatings deposited by the high-velocity flame spraying method," *Powder Metallurgy and Metal Ceramics*, vol. 40, no. 3-4, pp. 127–134, 2001.
- [127] A. Huczko, "Synthesis of aligned carbon nanotubes," *Applied Physics A*, vol. 74, no. 5, pp. 617–638, 2002.
- [128] C. N. R. Rao, B. C. Satishkumar, A. Govindaraj, and M. Nath, "Nanotubes," *ChemPhysChem*, vol. 2, no. 2, pp. 78–105, 2001.
- [129] S. N. Bondi, W. J. Lackey, R. W. Johnson, X. Wang, and Z. L. Wang, "Laser assisted chemical vapor deposition synthesis of carbon nanotubes and their characterization," *Carbon*, vol. 44, no. 8, pp. 1393–1403, 2006.
- [130] K. S. Novoselov, A. K. Geim, S. V. Morozov et al., "Electric field in atomically thin carbon films," *Science*, vol. 306, no. 5696, pp. 666–669, 2004.
- [131] K. S. Novoselov, D. Jiang, F. Schedin et al., "Two-dimensional atomic crystals," *Proceedings of the National Academy of Sciences of the United States of America*, vol. 102, no. 30, pp. 10451–10453, 2005.
- [132] K. S. Novoselov, A. K. Geim, S. V. Morozov et al., "Chiral tunnelling and the Klein paradox in graphene," *Nature*, vol. 438, pp. 197–200, 2005.
- [133] A. K. Geim and K. S. Novoselov, "The rise of graphene," *Nature Materials*, vol. 6, no. 3, pp. 183–191, 2007.
- [134] K. S. Kim, Y. Zhao, H. Jang et al., "Large-scale pattern growth of graphene films for stretchable transparent electrodes," *Nature*, vol. 457, no. 7230, pp. 706–710, 2009.
- [135] V. Y. Aristov, G. Urbanik, K. Kummer et al., "Graphene synthesis on cubic SiC/Si wafers. Perspectives for mass production of graphene-based electronic devices," *Nano Letters*, vol. 10, no. 3, pp. 992–995, 2010.
- [136] W. S. Hummers and R. E. Offeman, "Preparation of graphitic oxide," *Journal of the American Chemical Society*, vol. 80, no. 6, p. 1339, 1958.
- [137] M. J. McAllister, J. E. L. Li, D. H. Adamson et al., "Single sheet functionalized graphene by oxidation and thermal expansion of graphite," *Chemistry of Materials*, vol. 19, no. 18, pp. 4396–4404, 2007.
- [138] J. Chattopadhyay, A. Mukherjee, C. E. Hamilton et al., "Graphite epoxide," *Journal of the American Chemical Society*, vol. 130, no. 16, pp. 5414–5415, 2008.
- [139] S. Chandra, S. Sahu, and P. Pramanik, "A novel synthesis of graphene by dichromate oxidation," *Materials Science and Engineering B*, vol. 167, no. 3, pp. 133–136, 2010.
- [140] S. Stankovich, D. A. Dikin et al., "High-yield production of graphene by liquid-phase," *Carbon*, vol. 45, pp. 1558–1565, 2007.
- [141] V. C. Tung, M. J. Allen, Y. Yang, and R. B. Kaner, "Facile synthesis and characterization of graphene nanosheets," *Nature Nanotechnology*, vol. 4, pp. 25–29, 2009.
- [142] W. Guoxiu, Y. Juan, P. Jinsoo et al., "Facile synthesis and characterization of graphene nanosheets," *Journal of Physical Chemistry C*, vol. 112, no. 22, pp. 8192–8195, 2008.
- [143] Y. Si and E. T. Samulski, "Synthesis of water soluble graphene," *Nano Letters*, vol. 8, no. 6, pp. 1679–1682, 2008.
- [144] X. Fan, W. Peng, Y. Li et al., "Deoxygenation of exfoliated graphite oxide under alkaline conditions: a green route to graphene preparation," *Advanced Materials*, vol. 20, no. 23, pp. 4490–4493, 2008.
- [145] G. Williams, B. Seger, and P. V. Kamt, "TiO<sub>2</sub>-graphene nanocomposites. UV-assisted photocatalytic reduction of graphene oxide," *ACS Nano*, vol. 2, no. 7, pp. 1487–1491, 2008.
- [146] S. Wakeland, R. Martinez, J. K. Grey, and C. C. Luhrs, "Production of graphene from graphite oxide using urea as expansion-reduction agent," *Carbon*, vol. 48, no. 12, pp. 3463–3470, 2010.
- [147] W. Chen, L. Yan, and P. R. Bangal, "Preparation of graphene by the rapid and mild thermal reduction of graphene oxide induced by microwaves," *Carbon*, vol. 48, no. 4, pp. 1146–1152, 2010.
- [148] Y. Wu, P. Qiao, T. Chong, and Z. Shen, "Carbon nanowalls grown by microwave plasma enhanced chemical vapor deposition," *Advanced Materials*, vol. 14, no. 1, pp. 64–67, 2002.
- [149] K. Shiji, M. Hiramatsu, A. Enomoto, M. Nakamura, H. Amano, and M. Hori, "Vertical growth of carbon nanowalls

- using rf plasma-enhanced chemical vapor deposition," *Diamond and Related Materials*, vol. 14, no. 3–7, pp. 831–834, 2005.
- [150] M. Hiramatsu, K. Shiji, H. Amano, and M. Hori, "Fabrication of vertically aligned carbon nanowalls using capacitively coupled plasma-enhanced chemical vapor deposition assisted by hydrogen radical injection," *Applied Physics Letters*, vol. 84, no. 23, pp. 4708–4710, 2004.
- [151] T. Itoh, S. Shimabukuro, S. Kawamura, and S. Nonomura, "Preparation and electron field emission of carbon nanowall by Cat-CVD," *Thin Solid Films*, vol. 501, no. 1–2, pp. 314–317, 2006.
- [152] S. Shimabukuro, Y. Hatakeyama, M. Takeuchi, T. Itoh, and S. Nonomura, "Effect of hydrogen dilution in preparation of carbon nanowall by hot-wire CVD," *Thin Solid Films*, vol. 516, no. 5, pp. 710–713, 2008.
- [153] T. Mori, M. Hiramatsu, K. Yamakawa, K. Takeda, and M. Hori, "Fabrication of carbon nanowalls using electron beam excited plasma-enhanced chemical vapor deposition," *Diamond and Related Materials*, vol. 17, no. 7–10, pp. 1513–1517, 2008.
- [154] S. Vizireanu, L. Nistor, M. Haupt, V. Katzenmaier, C. Oehr, and G. Dinescu, "Carbon nanowalls growth by radiofrequency plasma-beam-enhanced chemical vapor deposition," *Plasma Processes and Polymers*, vol. 5, no. 3, pp. 263–268, 2008.
- [155] A. T. H. Chuang, B. O. Boskovic, and J. Robertson, "Free-standing carbon nanowalls by microwave plasma-enhanced chemical vapour deposition," *Diamond and Related Materials*, vol. 15, no. 4–8, pp. 1103–1106, 2006.
- [156] J. J. Wang, M. Y. Zhu, R. A. Outlaw et al., "Free-standing subnanometer graphite sheets," *Applied Physics Letters*, vol. 85, no. 7, pp. 1265–1267, 2004.
- [157] G. Sato, T. Kato, W. Oohara, and R. Hatakeyama, "Production and application of reactive plasmas using helicon-wave discharge in very low magnetic fields," *Thin Solid Films*, vol. 506–507, pp. 550–554, 2006.
- [158] R. C. Haddon, A. F. Hebard, M. J. Rosseinsky et al., "Conducting films of C<sub>60</sub> and C<sub>70</sub> by alkali-metal doping," *Nature*, vol. 350, no. 6316, pp. 320–322, 1991.
- [159] A. F. Hebard, M. J. Rosseinsky, R. C. Haddon et al., "Superconductivity at 18 K in potassium-doped C<sub>60</sub>," *Nature*, vol. 350, no. 6319, pp. 600–601, 1991.
- [160] M. J. Rosseinsky, A. P. Ramirez, S. H. Glarum et al., "Superconductivity at 28 K in RbxC<sub>60</sub>," *Physical Review Letters*, vol. 66, no. 21, pp. 2830–2832, 1991.
- [161] C. C. Chen, S. P. Kelty, and C. M. Lieber, "(RbK)C superconductors: formation of a continuous series of solid solutions," *Science*, vol. 253, no. 5022, pp. 886–888, 1991.
- [162] O. Zhou, G. B. M. Vaughan, Q. Zhu et al., "Compressibility of M<sub>3</sub>C<sub>60</sub> fullerene superconductors: relation between T<sub>c</sub> and lattice parameter," *Science*, vol. 255, no. 5046, pp. 833–835, 1992.
- [163] C. M. Brown, T. Takenobu, K. Kordatos, K. Prassides, Y. Iwasa, and K. Tanigaki, "Pressure dependence of superconductivity in the Na<sub>2</sub>Rb<sub>0.5</sub>Cs<sub>0.5</sub>C<sub>60</sub> fulleride," *Physical Review B*, vol. 59, no. 6, pp. 4439–4444, 1999.
- [164] A. Y. Ganin, Y. Takabayashi, Y. Z. Khimiyak et al., "Bulk superconductivity at 38 K in a molecular system," *Nature Materials*, vol. 7, no. 5, pp. 367–371, 2008.
- [165] <http://www.nanodiamond.co.kr/>.
- [166] K. Iakoubovskii, K. Mitsuishi, and K. Furuya, "High-resolution electron microscopy of detonation nanodiamond," *Nanotechnology*, vol. 19, no. 15, Article ID 155705, 2008.
- [167] S. Ji, T. Jiang, K. Xu, and S. Li, "FTIR study of the adsorption of water on ultradispersed diamond powder surface," *Applied Surface Science*, vol. 133, no. 4, pp. 231–238, 1998.
- [168] M.-F. Yu, O. Lourie, M. J. Dyer, K. Moloni, T. F. Kelly, and R. S. Ruoff, "Strength and breaking mechanism of multiwalled carbon nanotubes under tensile load," *Science*, vol. 287, no. 5453, pp. 637–640, 2000.
- [169] S. Bellucci, "Carbon nanotubes: physics and applications," *Physica Status Solidi (c)*, vol. 2, no. 1, pp. 34–47, 2005.
- [170] H. G. Chae and S. Kumar, "Rigid-rod polymeric fibers," *Journal of Applied Polymer Science*, vol. 100, no. 1, pp. 791–802, 2006.
- [171] M. Meo and M. Rossi, "Prediction of Young's modulus of single wall carbon nanotubes by molecular-mechanics based finite element modeling," *Composites Science and Technology*, vol. 66, no. 11–12, pp. 1597–1605, 2006.
- [172] S. B. Sinnott and R. Andrews, "Carbon nanotubes: synthesis, properties, and applications," *Critical Reviews in Solid State and Materials Sciences*, vol. 26, no. 3, pp. 145–249, 2001.
- [173] M.-F. Yu, B. S. Files, S. Arepalli, and R. S. Ruoff, "Tensile loading of ropes of single wall carbon nanotubes and their mechanical properties," *Physical Review Letters*, vol. 84, no. 24, pp. 5552–5555, 2000.
- [174] B. G. Demczyk, Y. M. Wang, J. Cumings et al., "Direct mechanical measurement of the tensile strength and elastic modulus of multiwalled carbon nanotubes," *Materials Science and Engineering A*, vol. 334, no. 1–2, pp. 173–178, 2002.
- [175] J. R. Xiao, B. A. Gama, and J. W. Gillespie, "An analytical molecular structural mechanics model for the mechanical properties of carbon nanotubes," *International Journal of Solids and Structures*, vol. 42, no. 11–12, pp. 3075–3092, 2005.
- [176] R. S. Ruoff, J. Tersoff, D. C. Lorents, S. Subramoney, and B. Chan, "Radial deformation of carbon nanotubes by van der Waals forces," *Nature*, vol. 364, no. 6437, pp. 514–516, 1993.
- [177] M.-F. Yu, T. Kowalewski, and R. S. Ruoff, "Investigation of the radial deformability of individual carbon nanotubes under controlled indentation force," *Physical Review Letters*, vol. 85, no. 7, pp. 1456–1459, 2000.
- [178] I. Palaci, S. Fedrigo, H. Brune, C. Klinke, M. Chen, and E. Riedo, "Radial elasticity of multiwalled carbon nanotubes," *Physical Review Letters*, vol. 94, no. 17, Article ID 175502, 2005.
- [179] M. Popov, M. Kyotani, R. J. Nemanich, and Y. Koga, "Superhard phase composed of single-wall carbon nanotubes," *Physical Review B*, vol. 65, no. 3, pp. 334081–334084, 2002.
- [180] X. Lu and Z. Chen, "Curved Pi-conjugation, aromaticity, and the related chemistry of small fullerenes (<C<sub>60</sub>) and single-walled carbon nanotubes," *Chemical Reviews*, vol. 105, no. 10, pp. 3643–3696, 2005.
- [181] X. Zhou, J.-Y. Park, S. Huang, J. Liu, and P. L. McEuen, "Band structure, phonon scattering, and the performance limit of single-walled carbon nanotube transistors," *Physical Review Letters*, vol. 95, no. 14, Article ID 146805, 4 pages, 2005.
- [182] H. Dai, A. Javey, E. Pop, D. Mann, and Y. Lu, "Electrical transport properties and field-effect transistors of carbon nanotubes," *NANO: Brief Reports and Reviews*, vol. 1, no. 1, pp. 1–4, 2006.
- [183] A. Javey, P. Qi, Q. Wang, and H. Dai, "Ten- to 50-nm-long quasi-ballistic carbon nanotube devices obtained without complex lithography," *Proceedings of the National Academy of Sciences of the United States of America*, vol. 101, no. 37, pp. 13408–13410, 2004.

- [184] I. Takesue, J. Haruyama, N. Kobayashi et al., "Superconductivity in entirely end-bonded multiwalled carbon nanotubes," *Physical Review Letters*, vol. 96, no. 5, Article ID 057001, 2006.
- [185] E. Pop, D. Mann, Q. Wang, K. Goodson, and H. Dai, "Thermal conductance of an individual single-wall carbon nanotube above room temperature," *Nano Letters*, vol. 6, no. 1, pp. 96–100, 2006.
- [186] E. T. Thostenson, C. Li, and T. W. Chou, "Nanocomposites in context," *Composites Science and Technology*, vol. 65, no. 3-4, pp. 491–516, 2005.
- [187] X. Liu, J. Si, B. Chang et al., "Third-order optical nonlinearity of the carbon nanotubes," *Applied Physics Letters*, vol. 74, no. 2, pp. 164–166, 1999.
- [188] V. L. A. Margulis, "Theoretical estimations of third-order optical nonlinearities for semiconductor carbon nanotubes," *Journal of Physics Condensed Matter*, vol. 11, no. 15, pp. 3065–3074, 1999.
- [189] H. Kataura, Y. Kumazawa, Y. Maniwa et al., "Optical properties of single-wall carbon nanotubes," *Synthetic Metals*, vol. 103, no. 1–3, pp. 2555–2558, 1999.
- [190] M. E. Itkis, D. E. Perea, R. Jung, S. Niyogi, and R. C. Haddon, "Comparison of analytical techniques for purity evaluation of single-walled carbon nanotubes," *Journal of the American Chemical Society*, vol. 127, no. 10, pp. 3439–3448, 2005.
- [191] K. Mizuno, J. Ishii, H. Kishida et al., "A black body absorber from vertically aligned single-walled carbon nanotubes," *Proceedings of the National Academy of Sciences of the United States of America*, vol. 106, no. 15, pp. 6044–6047, 2009.
- [192] J. C. Meyer, A. K. Geim, M. I. Katsnelson, K. S. Novoselov, T. J. Booth, and S. Roth, "The structure of suspended graphene sheets," *Nature*, vol. 446, no. 7131, pp. 60–63, 2007.
- [193] A. K. Geim and K. S. Novoselov, "The rise of graphene," *Nature Materials*, vol. 6, no. 3, pp. 183–191, 2007.
- [194] K. S. Novoselov, A. K. Geim, S. V. Morozov et al., "Two-dimensional gas of massless Dirac fermions in graphene," *Nature*, vol. 438, no. 7065, pp. 197–200, 2005.
- [195] S. V. Morozov, K. S. Novoselov, M. I. Katsnelson et al., "Giant intrinsic carrier mobilities in graphene and its bilayer," *Physical Review Letters*, vol. 100, no. 1, Article ID 016602, 6 pages, 2008.
- [196] J. H. Chen, C. Jang, S. Xiao, M. Ishigami, and M. S. Fuhrer, "Intrinsic and extrinsic performance limits of graphene devices on SiO<sub>2</sub>," *Nature Nanotechnology*, vol. 3, no. 4, pp. 206–209, 2008.
- [197] M. S. Amanda, A. Suzanne, H. Ciftan, and S. A. Olga, "Nanodiamond particles: properties and perspectives for bioapplications," *Critical Reviews in Solid State and Materials Sciences*, vol. 34, no. 1-2, pp. 18–74, 2009.
- [198] Y. Gogotsi, Ed., *Carbon Nanomaterials*, CRC Press, 2006.

## Research Article

# Structural and Electronic Properties of Low-Dimensional C-Nanoassemblies and Possible Analogues for Si (and Ge)

N. H. March<sup>1,2,3</sup> and A. Rubio<sup>4</sup>

<sup>1</sup>DIPC, San Sebastian, Donosita-San Sebastian, 20078 Gipuzkoa, Spain

<sup>2</sup>Department of Physics, University of Antwerp, 2000 Antwerpen, Belgium

<sup>3</sup>Oxford University, Oxford, OX 12JD, UK

<sup>4</sup>Nano-Bio Spectroscopy Group and ETSF Scientific Development Centre, Depart Física de Materiales, Universidad del País Vasco, Centro de Física de Materiales CSIC-UPV/EHU-MPC and DIPC, Centro Joxe Mari Korta Avenida de Tolosa, Donostia-San Sebastian, 72, 20018 Gipuzkoa, Spain

Correspondence should be addressed to N. H. March, arubio@sc.ehu.es

Received 11 June 2010; Accepted 20 September 2010

Academic Editor: Teng Li

Copyright © 2011 N. H. March and A. Rubio. This is an open access article distributed under the Creative Commons Attribution License, which permits unrestricted use, distribution, and reproduction in any medium, provided the original work is properly cited.

The delocalised nature of  $\pi$ -electrons in carbon-based compounds has opened a huge path for new fundamental and technological developments using carbon-based materials of different dimensionality (from clusters, to surfaces, nanotubes and graphene, among others). The success of this field has prompted the proposal that other inorganic structures based on B and N and more recently on Si and Ge could be formed with specific structural, mechanical, and electronic properties. In this paper we provide an analysis of the similarities of the two fields starting from the analysis of the  $\text{Si}_6\text{H}_6$  molecule, the analogue of the benzene molecule but now being nonplanar. Then we move to the study of the two-dimensional (buckled) analogues of graphene but now formed by Si and Ge. Similarly, we look to nonplanar compounds based on boron and boron-carbon nitrogen composites. In particular, we focus on the mechanical properties of those new materials that exhibit a very high stiffness, resilience, and flexibility. Possible applications in the fields of catalysis, lubrication, electronic, and photonic devices now seem a likely by-product. We also address future directions triggered by the predicted superconducting properties of graphene, among other areas.

## 1. Background and Outline

Both authors have been concerned since their early researches with (somewhat different) aspects of C nanoassemblies. Thus in Section 1.1 below, work on the electron density in  $\text{C}_6\text{H}_6$  is briefly summarized while in Section 3 studies on mechanical properties of C nanotubes are considered. Thus, structural, mechanical, and electronic properties of such C assemblies will be reviewed below, drawing of course on the contributions of many authors, concerned with both theory and experiment. With the background also of the present authors on B, N, and Si being relevant again to nanoassemblies, it seemed natural from time to time to refer to these atoms (plus Ge also occasionally) in the course of present discussion, to compare and contrast with purely C-based structures.

*1.1. Electron Density in Benzene, Using Experimentally Known Geometry.* In early work [1], one of us compared the ground-state electron density of benzene at its experimentally known geometry as given by the LCAO-MO approximation with that from the semiclassical Thomas-Fermi theory [2], the forerunner of modern density functional theory [3]. Some further contact with experiment came from comparison of the calculated electron densities with available X-ray diffraction experiments of Robertson et al. [4, 5] on naphthalene, in its crystalline state.

As will be discussed in somewhat more detail in Section 3, it was considerably later that Grassi et al. [6] carried out first-principles calculations on  $\text{Si}_6\text{H}_6$ , using both restricted and unrestricted Hartree-Fock (HF) theory. While their main objective was to examine theoretically, as chemical bonds were stretched, whether there would be

a Coulson-Fischer-like point (for  $H_2$  in their example [7]) in the sense of a transition from ring currents to localized  $\pi$ -electrons, in [6] a buckled  $Si_6H_6$  structure was predicted, to obtain all real vibrational frequencies.

In connection with graphene, in a work on exfoliated monolayer  $MnO_2$  sheets, Wang et al. [8] wrote, and we quote them: “strictly speaking no perfect 2D crystalline sheet structure would exist in free space unless it became an inherent part of a bulk crystal”.

In the above context, Meyer et al. [9], and also Stankovich et al. [10], found significant local curvature within graphene. In relation to the above remarks on the planar benzene molecule and, as will be discussed a little more in connection with the distortion from planarity of the as yet unsynthesized molecule  $Si_6H_6$ , we can expect any Si or Ge analogues of graphene which may be synthesized in the future to have notable departures from planarity. These will, of course, affect molecular vibrational properties and hence mechanical behaviour.

Returning briefly to benzene [1–5], a quite recent survey of ab initio calculations can be found in Moran et al. [11].

*1.2. Strained Graphenic Fragments due to Embedded Impurity Cluster.* Dietz et al. [12] considered a variety of localized defect states (e.g., impurity defects) as well as topological defects, in two-dimensional graphite. Independently, Peeters et al. [13] have reported results on a planar  $B_{12}$  cluster embedded in graphenic fragments of different sizes. Below as we are dominantly concerned with nanomaterials, we focus on the main findings of Peeters et al. The basic motivation for their study was twofold: first, to shed light on bonding in a variety of carborazines (systems involving C, B and N atoms), either in pairs [14, 15] or with all three different types of atoms present, and second to gain understanding of the way the C nuclei relax in such two-dimensional fragments due to the stress induced when a defect structure replaces a portion of the network, so that perfect accommodation cannot be retained.

Within the first octet row of the Periodic Table where directed bonding is particularly in evidence, B, C, and N are the most highly branched nonmetal species, which are then natural combinations to build up complex networks. Further understanding of bonding involving C with B and N holds promise of important consequences for nanoscale structures and in design of materials. In addition, clusters embedded in, as well as adsorbed on, large polycyclic aromatic hydrocarbons have significance for molecular electronics (see, e.g., Stabel et al. [16]).

The  $B_{12}$  clusters discussed below are favorable for chemical bonding in free space and have been studied by Boustani (see e.g., [17, 18]). Below, we report results from Peeters et al. [13] in which two of Boustani’s more favorable  $B_{12}$  clusters are considered, surrounded first by quite a small number of C atoms. The chemical picture for such small carborane clusters was then refined by Hartree-Fock calculations in order to find (i) the stable cluster geometry and (ii) the deformation electron density distribution. Then, we summarize the effects of adding on the periphery of such

nanofragments, further C atoms, all the surface C species being bonded to peripheral H atoms.

Turning to specific B clusters and fragments, Figure 1(a) shows one  $B_{12}$  cluster to be embedded in a series of graphenic fragments. A second  $B_{12}$  cluster studied by Boustani and others is depicted in part (b) of Figure 1 and this is also treated briefly below.

A good choice for an appropriate graphenic fragment is the 16-atom “pyrene” cluster. In the small cluster studied by Peeters et al. [13], the  $B_{12}$  clusters were surrounded by just two layers of C atoms. Then H atoms, as mentioned above, are added at the periphery of these fragments. The formula for these smallest graphenic fragments is  $B_{12}C_{64}H_{22}$ . As discussed by Peeters et al., the geometry of  $B_{12}$  as in Figure 1(a) is significantly different from the geometry of an isolated molecule in the above fragment. The molecular deformation electron density distribution is shown in Figure 3 of Peeters et al. [13].

*1.2.1. Embedding of  $B_{12}$  in Larger Graphenic Fragments.* The largest Hartree-Fock computations were performed with 6 layers of C atoms surrounding the two B clusters shown in Figure 1. The geometry of  $B_{12}$  in Figure 1(a) with 2 and 6 C layers is very similar. For the cluster in part (b), the differences between the 2 and 6 C layers are larger.

In general, of course, the relaxation of the C nuclei positions in the graphenic fragments on insertion of the  $B_{12}$  impurity cluster is a function of the distance from the impurities. Table 2 in Peeters et al. records quantitative values of such relaxations. Grossly, the deviation ( $y$ ) seems to decay approximately as an inverse square root of the distance ( $r$ ) from the impurity:  $y \approx c (1/r^{1/2})$  where  $c$  is a constant. If one examines, though, the individual atomic deviations, a fair degree of scattering is in evidence, perhaps because of the outer edges of the graphenic nanofragment under discussion. The “zigzag” edges, such as those manifested in the study by Klein and Bytautus [19] give rise to “bond order” fluctuations near such edges. In [13], this was expected to be reflected as bond lengths fluctuate away from that of an infinite graphene monolayer.

We also note that the bonding electron density for the largest fragment considered by Peeters et al. [13] is shown in Figure 7 of their article. We want to conclude this subsection by emphasizing that in Section 2 below, quite a lot of attention is paid to the study of mechanical properties of graphenic fragments, that is, to observable manifestations of strains such as we have discussed microscopically above in this particular example of  $B_{12}$  embedded in graphenic nanofragments.

## 2. Nanotube Nanomechanics

Since the discovery of carbon nanotubes (CNTs) by Iijima (1991) [20], we have witnessed an explosive development of the nanotube science and technology. There is a great variety of potential applications for nanotubes, ranging from energy storage, composites, nanoelectronics, and other solid-state devices, to sensors and actuators (see for example, the reviews of Baughman et al. [21] and Loiseau et al. [22]).

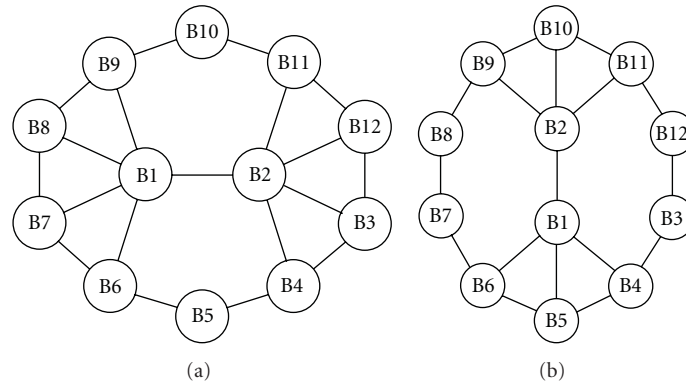


FIGURE 1: (a) Boron structure A embedded in graphenic fragments; (b) Boron structure B.

Several structural varieties of nanotubes have been identified and classified based on criteria such as helicity (also known as chirality), number of walls, and inclusion of pentagons-heptagons and. The simplest form is the singlewalled carbon nanotube (SWNT) which resembles a rolled honeycomb graphite layer into a mono-atomic-thick cylinder. Several concentrically embedded SWNTs form a multiwalled carbon nanotube (MWNT). Other nanotube varieties include nanotube bundles or ropes, intertube junctions, nanotori, coiled nanotubes, and so forth. Due to their relative simplicity and atomically precise morphology, single-walled carbon nanotubes offer the opportunity of assessing the validity of different macro- and microscopic models.

The properties of carbon nanotubes can be usefully grouped into three categories: structural, mechanical, and electronic. From the structural point of view, in most situations CNTs can be considered one-dimensional (1D) objects, with typical diameters ( $dt$ ) in the nm-range and lengths ( $L$ ) reaching several micrometers. This one-dimensionality of tubes impacts on and is visible mostly through the mechanical and electronic properties. However, the structure of nanotubes can be exploited in itself such as for instance by field emitters or gas break-down sensors, which are based on the “sharpness” of CNTs giving rise to huge local electric fields.

While the prediction of electronic properties of carbon nanotubes required relatively subtle theoretical analysis, their unique mechanical behavior could be intuitively anticipated based on several features: strength of carbon bonds, their uniform arrangement within the graphitic sheet, and the seamless folding of this network into a tubule. The mechanical properties class is encompassing the elastic, thermal, vibrational, or any other properties related to the motion of the tube’s atoms. In nanotubes, carbon is  $sp^2$ -hybridized resulting in strong  $s$ -bonds weakly reinforced by  $\pi$ -bonds. Considering the hybridization, it is natural to assume a certain overlap between nanotube and graphite (graphene) elastic properties, such as Young’s modulus, bending, tensile and torsional stiffness, and yield strength. SWNTs have tensile moduli close to 1TPa (stiff as diamond) and strengths  $\approx 50$  GPa (corresponding to 5%–10% maximal strain), which

earned them the title of ultimate fibers. Despite their stiffness, CNTs retain a high bending flexibility due to their high aspect ratios. With some exceptions, the thermal and vibrational properties of nanotubes also show similarities with graphite. Since the in-plane thermal conductivity of pyrolytic graphite is very high, it is to be expected that the on-axis thermal conductivity of defect-free tubes would be even higher.

The understanding of the mechanical response of nanotubes to external forces is of relevance for the application of nanotubes as a composite material reinforcement as well as in electronic devices, where the deformation of the tubes induced by the substrate alter locally the electronic properties of the nanotube. A broad discussion of potential applications of the nanotube can be found in existing reviews [23–26], also outlining the challenges of implementation. There are two *actual* applications already, where the carbon nanotube can *commercially* compete with other materials units, and the mechanics of carbon nanotubes plays either a central or an important secondary role in both cases.

Carbon as well as composite BN nanotubes demonstrate very high stiffness to an axial load or a bending of small amplitude, which translates in the record-high efficient *linear*-elastic moduli. At larger strains, the nanotubes (especially, the singlewalled type) are prone to buckling, kink forming, and collapse, due to the hollow shell-like structure. These abrupt changes (bifurcations) manifest themselves as singularities in the *nonlinear* stress-strain curve, but are *reversible* and involve no bond-breaking or atomic rearrangements. This resilience corresponds, quantitatively, to a very small subangstrom efficient thickness of the constituent graphitic shells. *Irreversible* yield of nanotubes begins at extremely high deformation (from several to dozens percent of in-plane strain, depending on the strain rate) and high temperature. The failure threshold (yield strength) turns out to depend explicitly on nanotube *helicity*, which thus demonstrates again the profound role of symmetry for the physical properties, either electrical conductivity or mechanical strength. Finally, the manifestation of mechanical strength in the *multiwalled* or *bundled* nanotubes (ropes) is obscured by the poor load transfer from the exterior to the core of such larger structures.

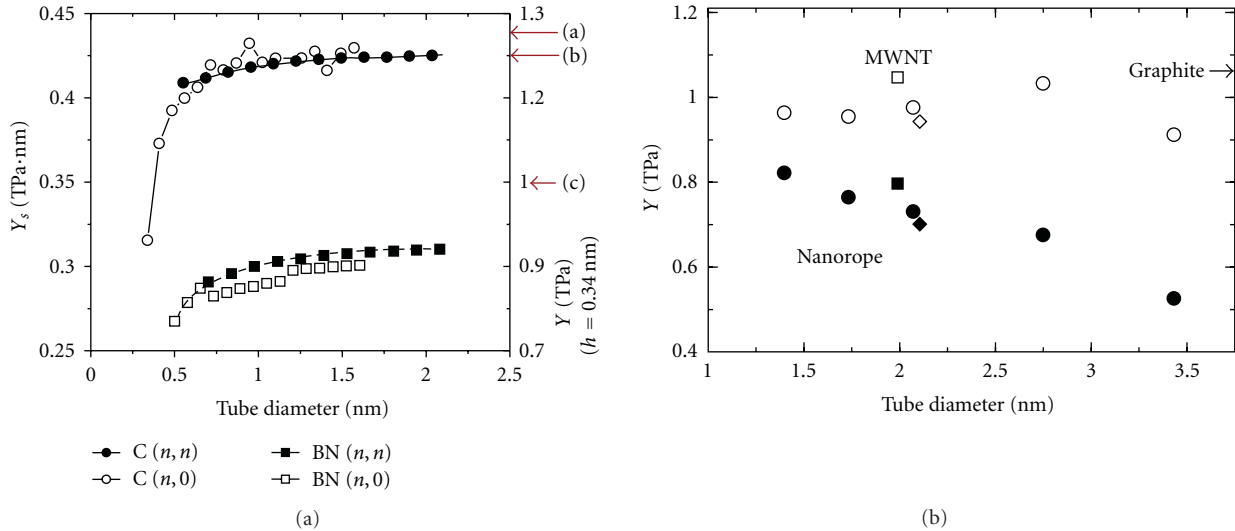


FIGURE 2: (a): Young modulus for armchair and zig-zag carbon and BN nanotubes. The values are given in the proper unit of TPa nm for SWNTs (left axis) and converted to TPa (right axis) by taking a value for the graphene thickness of 0.34 nm. The experimental values for carbon nanotubes are reported on the right-hand side: (a) 1.28 TPa [27]; (b) 1.25 TPa [28]; (c) 1 TPa for MWNTs [29]. (b): Young modulus versus tube diameter in different arrangements. Open symbols correspond to the multiwall geometry (10-layer tube with an interlayer distance of 0.34 nm), and solid symbols for the single-wall-nanotube crystalline-rope configuration. In the MWNT geometry, the value of the Young modulus does not depend on the specific number of layers. The experimental value of the  $c_{11} = 1.06$  TPa elastic constant of graphite is also shown.

The similarities among graphite and other  $sp^2$ -like bonded materials such as hexagonal boron nitride and boron-carbon-nitrogen compounds lead us to the theoretical proposition that  $B_xC_yN_z$  nanotubes would be stable [30–33]. Specific synthesis of these nanotubes was achieved afterwards: boron-nitride [34, 35] and  $BC_2N$  and  $BC_3$  [36, 37] as well as other inorganic tubular forms of  $WS_2$  and  $MoS_2$  [38, 39]. The predicted properties of these tubules are quite different from those of carbon with numerous possible technological applications in the fields of catalysis, lubrication, electronic, and photonic devices [32, 33].

Calculations of the stiffness of SWNTs demonstrated that the Young modulus shows a small dependence on the tube diameter and chirality for the experimental range of nanotube diameters (between 1.3 and 1.4 nm). It is predicted that carbon nanotubes have the highest Young's modulus of all the different types of composite tubes considered (BN,  $BC_3$ ,  $BC_2N$ ,  $C_3N_4$ , CN) [40]. Those results for the C and BN nanotubes are reproduced in the left panel of Figure 2. Furthermore, the Young modulus approaches, from below, the graphitic limit for diameters of the order of 1.2 nm. The computed value of C for the wider carbon nanotubes of 0.43 TPa nm, that corresponds to 1.26 TPa modulus in our convention, is in excellent agreement with the experimental value for SWNT's of 1.25 TPa [41]. It is also in rather good agreement with the value of 1.28 TPa reported for multiwall nanotubes (MWNT) [27]. Although this result is for MWNT, the similarity between SWNT is not surprising as the intrawall C–C bonds mainly determine the Young's modulus. From this result, we can estimate the Young modulus considering two different geometries of practical

relevance:

- (i) *multiwall* like geometry, in which the normal area is calculated using the wall-wall distance as the one in MWNTs, which is very approximately equal to the one of graphite,
- (ii) *nanorope or bundle* configuration of SWNTs, where the tubes would be arranged forming a hexagonal close-packed lattice, with a lattice constant of  $(2R+3.4)$ ,  $R$  being the tube radius.

The results for these two cases are presented in the right panel of Figure 2. The MWNT geometry gives a value that is very close to the graphitic one; however, the rope geometry shows a decrease of the Young modulus with increasing the tube radius due to the quadratic increase of the effective area in this configuration, while the number of atoms increases only linearly with the tube diameter. The computed values for the SWNT ropes experimentally observed are, however, still very high (0.5 TPa), even comparing with other known carbon fibers. This value is in quite good agreement with AFM experiments on anchored SWNTs ropes [42] ( $Y \sim 0.6$  TPa) and for stress-strain puller measurements of the Young modulus for aligned nanotube ropes of MWNTs ( $Y \sim 0.45 \pm 0.23$  TPa) [43].

For composite nanotubes, the results of [44] for the Young modulus of BN MWNT's give 1.22 TPa, which is somewhat larger than the result obtained for these tubes in the TB calculations ( $\sim 0.9$  TPa) [45], but nevertheless the agreement is close. We indicate that BN and  $BC_3$  tubes have similar values of the Young modulus (the calculated average

Young modulus is 0.9 TPa and 0.92 TPa for BN and BC<sub>3</sub>, resp.), although the latter have slightly larger values. In those studies C<sub>3</sub>N<sub>4</sub> nanotubes are shown to be much softer than any other type of tube, the reason being that for a given amount of tube surface, there is a smaller density of chemical bonds [40].

The Poisson ratio is given by the variation of the radius of the SWNT resulting from longitudinal deformations along the tube axis. In all cases, the computed Poisson ratio is positive: an elongation of the tube reduces its diameter. The *ab initio* values are 0.14 (from 0.12 to 0.16) for the armchair (*n,n*) tubes, and a little larger for other chiralities: 0.19 for (10,0) and 0.18 for (8,4). The uncertainty of the obtained values is of the order of 10%. In summary, the *ab initio* calculations indicate that the Poisson ratio retains graphitic values except for a possible slight reduction for small radii. It shows chirality dependence: (*n,n*) tubes display smaller values than (10,0) and (8,4). Similar differences are found between the *ab initio* and TB calculations for BN tubes, namely, for the (6,6) tube the *ab-initio* value for the Poisson ratio is 0.23 whereas the TB one is 0.30 [45].

**2.1. Experimental Evidence of Nanotube Resilience.** Collapsed forms of the nanotube (“nanoribbons”) have been observed in experiment, and their stability can be explained by the competition between the van der Waals attraction and elastic energy. The basic physics can be understood by noticing that the elastic curvature energy per unit length is proportional to  $1/R$  ( $R$ , radii of the tube); however, for a fully collapsed single-wall tubule with the opposite tubule walls at the typical van der Waals contact distance  $c$ , the energy per unit length would be composed of a higher curvature energy due to the edges which is independent of the initial tubule diameter, and a negative van der Waals contribution,  $\epsilon_{vdW}$  0.03–0.04 eV/atom, that is,  $\propto R$  per unit length. Collapse occurs when the latter term prevails above a certain critical tube radii  $R_c$  that depends on the number  $N$  of shells of the nanotube,  $R_c$  ( $N = 1$ )  $\sim 8c$  and  $R_c$  ( $N = 8$ )  $\sim 19c$  [46], and the thickness of the collapsed strip-ribbon is  $(2N-1)c$ . Any additional torsional strain imposed on a tube in experimental environment also favors flattening [47, 48] and facilitates the collapse.

The bending seems fully reversible up to very large bending angles despite the occurrence of kinks and highly strained tubule regions in simulations, that are in excellent morphological agreement with the experimental images [49]. Similar bent-buckled shapes have been reported by several groups [49–51], Figure 4.4. This apparent flexibility stems from the ability of the  $sp^2$  network to rehybridize when deformed out of plane, with the degree of  $sp^2$ - $sp^3$  rehybridization being proportional to the local curvature [52].

In this context, the recent work of Colombo [53, 54] is very relevant as it presents a very detailed combined continuum and atomistic approach to the elastic properties of graphene and C nanoribbons. In a little more detail, the stress-strain nonlinear constitutive equation is worked out by Colombo using continuum theory in both small-strain and large-strain circumstances. Then by atomistic simulations,

the relevant linear and non-linear elastic moduli have been computed (see also, [53]). In particular, Colombo throws light on the physical meaning of the effective non-linear elastic modulus measured by nanoindentation of a free-standing monolayer graphene sample [55]. Through a stress-strain plot, Colombo also predicts a very high failure stress, in good accordance with experimental data recorded by Lee et al. [55]. The corresponding effective 3D failure stress is found by Colombo to be  $\sim 1300$  Pa, which exceeds that in most materials, including multiwalled nanotubes.

In relation to bending elasticity, Colombo identifies the bending rigidity modulus by continuum theory and characterizes it by the local curvature of a bended ribbon. Then this bending modulus is calculated by tight-binding atomistic simulations (see also [54]). Finally, the elastic behaviour of various curved nanoribbons is studied and the onset of nanoscale features is discussed. It is shown, in particular, that atomic-scale relaxations on bending induce an additional strain field of in-plane stretching. An important issue is then raised as to the way in which to disentangle bending and stretching features for small-width nanoribbons.

### 3. Parallels between Low-Dimensional Assemblies of C and of Si and Ge Atoms

Our interest in this area has been rekindled by the very recent study of Cahangirov et al. [56]. These authors reported calculations of structure optimization, phonon modes, and finite temperature molecular dynamics. Their predictions were that both Si and Ge can have stable, two-dimensional, low-buckled honeycomb structures. Therefore, in this paper, we shall, first of all, use available work from both experiment and theory to compare especially Si–Si equilibrium bond lengths in a number of structures, both finite molecular and clusters and in honeycomb lattices, with the geometry predicted in [6] for Si<sub>6</sub>H<sub>6</sub>. It is natural here, therefore, to elaborate somewhat on the results reported in [6].

First of all, results were obtained on the equilibrium geometry of Si<sub>6</sub>H<sub>6</sub> from spin-compensated (restricted) HF (HRF) calculations. The bond lengths predicted by this method were 2.21 Å for the Si–Si bonds and for the Si–H lengths were 1.47 Å. Also binding was demonstrated with respect to 6Si and 6H isolated atoms.

But a central part of the study in [6] was to consider the stretching of chemical bonds in the (as yet unsynthesized) Si<sub>6</sub>H<sub>6</sub> molecule. Such stretching was first carried out by Grassi et al. [6] in which the stretching was uniform; that is, all Si–Si and Si–H bonds were changed by a common scale factor  $\lambda$ . Figure 1 in [6] displays before RHF and UHF potential energy curves of Si<sub>6</sub>H<sub>6</sub> as a function of  $\lambda$ .

**3.1. Itinerant versus Localized  $\pi$ -Electrons.** Since there is a sense in which a UHF treatment reflects electron “correlation” by putting  $\uparrow$  and  $\downarrow$  spins in different space orbitals, Grassi et al. [6] attempted to draw conclusions about itinerant versus localized behaviour of  $\pi$ -electrons in Si<sub>6</sub>H<sub>6</sub>. Of course, the “sister” molecule benzene is a form for comparison. In this latter system, the diamagnetic

TABLE 1: Bond-lengths for different Si-structures (Å)\*. Note that for the Si=Si double bond lengths of disilenes vary between 2.14 and 2.29 Å and are nearly 5 to 10% shorter than the Si–Si single bond lengths of corresponding disilanes. This rate of bond shortening is less than 13% in carbon compounds [57].

Si-bulk [59]	2.35
Si <sub>2</sub> (en silicon-carbene-complex) [60]	2.2294 ± 0.0011
Si-nanowire (H-terminated) [57]	2.34 to 2.36
nanocrystal: Si <sub>87</sub> H <sub>76</sub> [57]	2.35
Si <sub>6</sub> H <sub>6</sub> Si-H [6]*	1.47

\* Compare 1.07 Å for C–H length in benzene, which is the same as in the CH radical itself.

susceptibility plus properties relating to ring currents testify, from experiment, to the delocalization of the  $\pi$ -electrons. In their Figures 3 and 4, Grassi et al. [6] display the spin population magnitudes on the Si and H atoms of the Si<sub>6</sub>H<sub>6</sub> ring, as a function of uniform stretching  $\lambda$ . Their conclusion was that the  $\pi$ -electrons have their densities dominantly around the Si nuclei, with a tendency towards delocalization (ring currents) for low values of the scaling factor  $\lambda$ .

As already mentioned in Section 1.1 above, in [6] it was demonstrated that for planar Si<sub>6</sub>H<sub>6</sub> a study of the normal modes of vibration reveals that not all the vibrational frequencies are real. This led these authors to consider the effect of buckling of the planar structure on these frequencies. The minimum energy structure was obtained by an optimization procedure at the UHF-singlet level. The buckled structure was such that all vibrational mode frequencies were now real. The reader is referred to [6] if fuller details are eventually required.

To begin the above programme, we collect in Table 1 available results, which are mainly from presently available theoretical and experimental work, for Si–Si equilibrium bond lengths in some rather different environments. Thus, for the predicted buckled Si<sub>6</sub>H<sub>6</sub> molecule in [6], the restricted HF prediction is 2.21 Å (see Table 1 of [6]). One experimentally accessible Si–Si distance is from a study of an Si nanowire [57] and from gas-phase infrared spectra of cationic Si-clusters ( $n = 6-17$ ); see supplementary material in Reference [58]. Returning to theory, we next note that Si nanowires potentially have structures resembling assemblies of smaller Si clusters.

In this context, it is relevant to mention work on the silicon clathrate compound (Na, Ba)<sub>X</sub>Si<sub>46</sub> studied in Kawaji et al. [61]. As these authors stress, the Si–Si atoms are bonded tetrahedrally with approximately the same bond distances as in ordinary diamond structure of Si. These distances are recorded in Table 1. We have also added Si–Si lengths in some smaller Si free space clusters (see, e.g., Alonso’s book [62]). It is also relevant to refer to work of Phillips [63] at this point. He concluded from analyzing fragmentation and contraction experiments that Si clusters with less than ten atoms have a unique structure with little or no resemblance to the diamond lattice. It is of interest to refer to Figure 9 of Merson and Sattler [64] which depicts electron density isosurfaces of the fullerene Si<sub>24</sub>. The left-side of their Figure

9 gives a side view with a pentagonal-like surface. The right-hand side shows a hexagonal of Si atoms.

At this point, we return to the work of Cahangirov et al. [56]. In their figures, these authors first present the calculated variations of the binding energy of the relaxed honeycomb structure of Si and Ge as a function of lattice constant. In that Figure, planar (PL), low-buckled (LB), and high-buckled (HB) honeycomb structures correspond to distinct minima. They find that the PL honeycomb structure is the least energetic state and is not stable. They then address the issue as to whether these puckered LB and HB geometries correspond to real local minima in the Born-Oppenheimer surface.

The PL structure of Si has some phonon modes which have imaginary frequencies analogous to planar Si<sub>6</sub>H<sub>6</sub> reported by Grassi et al. [6].

In contrast, the phonon dispersion curves shown in Figure 1 of Cahangirov et al. [56] indicate that the 2D periodic LB honeycomb structure of Si is stable. There is an equilibrium buckling of 0.44 Å for Si and 0.64 Å for Ge. The stability of these LB structures of both Si and Ge was tested in addition by the means of extensive ab initio finite temperature molecular dynamics calculations using time steps of  $2 \times 10^{-15}$  secs. They record the facts that the 2D periodic LB structure of Si (Ge) is not lost by raising the temperature from  $T = 0$  to 1000 K (800 K) for 10 picoseconds (ps). In this paper, it is especially noteworthy that a finite size, large hexagonal LB flake of Si (Ge), with hydrogen passivated edge atoms, remains intact on raising  $T$  from 0 to 1000 K (800 K) in 100 steps, and holding it there for more than 3 ps.

Finally, we note that calculated band structures and their corresponding electronic density of states of LB Si and Ge are presented in Figure 2 of Cahangirov et al. [56]. Also their Table 1 summarizes binding energy and structural parameters calculated for the LB honeycomb structure. As to possible subsequent experiments on the synthesis of Si and Ge nanoribbons with honeycomb structures, it is of interest to add that recent work by Nakano et al. [65] reports the soft synthesis of a single Si monolayer sheet on a substrate.

## 4. Future Directions

Superconducting graphene has recently been predicted [66–68] with a high transition temperature, though at the time of writing no experimental discovery has been reported. The discussion of the possible pairing mechanism in graphite intercalated compounds (GIC) by Capone et al. [69] is also relevant in the present context (see for example, the recent work by Pellegrino et al. [70] on relevant topic of pairing symmetry). However, there is clearly an area of potential interest there, both fundamental and technological, for the future.

Also, in connection with low-dimensional C-atom structures, we want to mention work on experimental detection of plasmon modes which has been utilized to investigate the dynamical behaviour of electrons in graphene layers [71–74]. In this general area, it is also relevant here to note the very recent study of Wang and Chakraborty [75]

on Coulomb screening and collective excitations in biased bilayer graphene. The plasmon-phonon strongly coupled mode in doped graphene has been explored by Liu and Willis [76].

Additionally, in relation to our discussion of strain effects above, the study of Choi et al. [77] has reported calculations on electronic properties of graphene subjected to uniaxial and isotropic strains, respectively. As consequences of these numerical studies, the semimetallic character is predicted to persist up to a very large uniaxial strain of some 30%, except in a very narrow strain range where a tiny energy gap is predicted. The work function is studied theoretically also, and is found to increase substantially as both the uniaxial and the isotropic strains increase. The impact on the optical conductivity has been addressed by Pellegrino et al. [78, 79].

Of potential fundamental interest for the future, we note the very recent theoretical work by Novoselov et al. [80] on the theory of the quantum Hall effect (QHE) in finite graphene devices. Already, prior to this study, several experiments have examined the QHE in graphene [81–83]. In the theoretical work of Novoselov et al. [80], the QHE in graphene is studied based on the current injection model, which takes some account of the finite rectangular geometry with source and drain electrodes. In their work, the presence of disorder does not play a significant role. Instead, the boundary conditions during the injection into the graphene sheet, which are enforced by the presence of the Ohmic contacts, determine the current-voltage characteristics.

## Acknowledgments

The collaboration with many people over the years has made possible the results presented in this paper. In particular, N.H. March wishes to thank Dr. A. Peeters, professors G.G.N. Angilella, C. Van Alsenoy, I.A. Howard, and D.J. Klein for invaluable cooperation on the general area embraced by this paper. Also A. Rubio wants to thank M. Cohen, S.G. Louie, P.M. Ajayan, A. Zettl, Y. Miyamoto, P. Bernier, and C. Goze for their fundamental contributions to the results presented here. This work has been supported also by the Spanish MEC (FIS2007-65702-C02-01), ACI-Promociona (ACI2009-1036), “Grupos Consolidados UPV/EHU del Gobierno Vasco” (IT-319-07), ETORTEK and the European Union through e-13 ETSF (Contract: 211956), NANODEVICES (IST-2006-029192), and THEMA (Contract: 228539) projects. The authors acknowledge support by the Barcelona Supercomputing Center, “Red Española de Supercomputación”, SGIker ARINA (UPV/EHU), Transnational Access Programme HPC-Europe++. Finally, it is a pleasure for N. H. March to thank professor P. M. Echenique for most generous hospitality at DIPC.

## References

[1] N. H. March, “Theoretical determination of the electron distribution in Benzene by the Thomas-Fermi and the molecular-orbital methods,” *Acta Crystallographica*, vol. 5, pp. 187–193, 1952.

[2] N. H. March, *Self-Consistent Fields in Atoms*, Elsevier, Amsterdam, The Netherlands, 1975.

[3] R. G. Parr and W. Yang, *Density-Functional Theory of Atoms and Molecules*, Oxford University Press, Oxford, UK, 1989.

[4] S. C. Abrahams, J. M. Robertson, and J. G. White, “The crystal and molecular structure of naphthalene. I. X-ray measurements,” *Acta Crystallographica*, vol. 2, pp. 233–238, 1949.

[5] S. C. Abrahams, J. M. Robertson, and J. G. White, “The crystal and molecular structure of naphthalene. II. Structure investigation by the triple Fourier series method,” *Acta Crystallographica*, vol. 2, pp. 238–244, 1949.

[6] A. Grassi, G. M. Lombardo, R. Pucci, G. G. N. Angilella, F. Bartha, and N. H. March, “Stretched chemical bonds in Si<sub>6</sub>H<sub>6</sub>: a transition from ring currents to localized  $\pi$ -electrons?” *Chemical Physics*, vol. 297, no. 1-3, pp. 13–19, 2004.

[7] C. A. Coulson and I. Fischer, “Notes on the molecular-orbital treatment of the hydrogen molecule,” *Philosophical Magazine*, vol. 40, pp. 386–393, 1949.

[8] Y. Wang, C. Sun, J. Zou et al., “Oxygen vacancy induced structural variations of exfoliated monolayer MnO<sub>2</sub> sheets,” *Physical Review B*, vol. 81, no. 8, Article ID 081401, 4 pages, 2010.

[9] J. C. Meyer, A. K. Geim, M. I. Katsnelson, K. S. Novoselov, T. J. Booth, and S. Roth, “The structure of suspended graphene sheets,” *Nature*, vol. 446, no. 7131, pp. 60–63, 2007.

[10] S. Stankovich, D. A. Dikin, G. H. B. Dommett et al., “Graphene-based composite materials,” *Nature*, vol. 442, no. 7100, pp. 282–286, 2006.

[11] D. Moran, A. C. Simmonett, F. E. Leach III, W. D. Allen, P. V. R. Schleyer, and H. F. Schaefer III, “Popular theoretical methods predict benzene and arenes to be nonplanar,” *Journal of the American Chemical Society*, vol. 128, no. 29, pp. 9342–9343, 2006.

[12] F. Dietz, N. Tyutyulkov, G. Madjarova, and K. Müllen, “Is 2-D Graphite an Ultimate Large Hydrocarbon? II. Structure and Energy Spectra of Polycyclic Aromatic Hydrocarbons with Defects,” *Journal of Physical Chemistry B*, vol. 104, no. 8, pp. 1746–1761, 2000.

[13] A. Peeters, C. Van Alsenoy, N. H. March, D. J. Klein, and V. E. Van Doren, “Boron B<sub>12</sub> cluster embedded in graphitic fragments,” *Journal of Physical Chemistry B*, vol. 105, no. 43, pp. 10546–10553, 2001.

[14] H.-Y. Zhu, D. J. Klein, W. A. Seitz, and N. H. March, “BN alternants: boron nitride cages and polymers,” *Inorganic Chemistry*, vol. 34, no. 6, pp. 1377–1383, 1995.

[15] H.-Y. Zhu, D. J. Klein, N. H. March, and A. Rubio, “Small band-gap graphitic CBN layers,” *Journal of Physics and Chemistry of Solids*, vol. 59, no. 8, pp. 1303–1308, 1998.

[16] A. Stabel, P. Herwig, K. Müllen, and J. P. Rabe, “Diodelike current–voltage curves for a single molecule—tunneling spectroscopy with submolecular resolution of an alkylated, peri-condensed hexabenzocoronene,” *Angewandte Chemie*, vol. 34, no. 15, pp. 1609–1611, 1995.

[17] I. Boustani, “Systematic ab initio investigation of bare boron clusters: determination of the geometry and electronic structures of B<sub>n</sub> (n=2-14),” *Physical Review B*, vol. 55, no. 24, pp. 16426–16438, 1997.

[18] I. Boustani, “Structure and stability of small boron clusters. A density functional theoretical study,” *Chemical Physics Letters*, vol. 240, no. 1–3, pp. 135–140, 1995.

[19] D. J. Klein and L. Bytautas, “Graphitic Edges and Unpaired  $\pi$ -Electron Spins,” *Journal of Physical Chemistry A*, vol. 103, no. 26, pp. 5196–5210, 1999.

- [20] S. Iijima, "Helical microtubules of graphitic carbon," *Nature*, vol. 354, no. 6348, pp. 56–58, 1991.
- [21] R. H. Baughman, A. A. Zakhidov, and W. A. De Heer, "Carbon nanotubes—the route toward applications," *Science*, vol. 297, no. 5582, pp. 787–792, 2002.
- [22] A. Loiseau, P. Launois-Bernede, P. Petit, S. Roche, and J.-P. Salvetat, "Understanding carbon nanotubes," *Lecture Notes in Physics*, vol. 677, p. 555, 2006.
- [23] T. W. Ebbesen, *Carbon Nanotubes: Preparation and Properties*, CRC Press, Boca Raton, Fla, USA, 1997.
- [24] P. M. Ajayan and T. W. Ebbesen, "Nanometre-size tubes of carbon," *Reports on Progress in Physics*, vol. 60, no. 10, pp. 1025–1062, 1997.
- [25] B. I. Yakobson and R. E. Smalley, "Fullerene nanotubes:  $C_{1,000,000}$  and beyond," *American Scientist*, vol. 85, no. 4, pp. 324–337, 1997.
- [26] J. Bernholc, C. Roland, and B. I. Yakobson, "Nanotubes," *Current Opinion in Solid State and Materials Science*, vol. 2, no. 6, pp. 706–715, 1997.
- [27] E. W. Wong, P. E. Sheehan, and C. M. Lieber, "Nanobeam mechanics: elasticity, strength, and toughness of nanorods and nanotubes," *Science*, vol. 277, no. 5334, pp. 1971–1975, 1997.
- [28] A. Krishnan, E. Dujardin, T. W. Ebbesen, P. N. Yianilos, and M. M. J. Treacy, "Young's modulus of single-walled nanotubes," *Physical Review B*, vol. 58, no. 20, pp. 14013–14019, 1998.
- [29] J. Muster, M. Burghard, S. Roth, G. S. Duesberg, E. Hernández, and A. Rubio, "Scanning force microscopy characterization of individual carbon nanotubes on electrode arrays," *Journal of Vacuum Science and Technology B*, vol. 16, no. 5, pp. 2796–2801, 1998.
- [30] A. Rubio, J. L. Corkill, and M. L. Cohen, "Theory of graphitic boron nitride nanotubes," *Physical Review B*, vol. 49, no. 7, pp. 5081–5084, 1994.
- [31] A. Rubio, "Nanocomposite tubules: A new class of materials from theory," *Condensed Matter News*, vol. 6, p. 6, 1997.
- [32] Y. Miyamoto, A. Rubio, M. L. Cohen, and S. G. Louie, "Chiral tubules of hexagonal  $BC_2N$ ," *Physical Review B*, vol. 50, no. 7, pp. 4976–4979, 1994.
- [33] Y. Miyamoto, A. Rubio, S. G. Louie, and M. L. Cohen, "Electronic properties of tubule forms of hexagonal  $BC_3$ ," *Physical Review B*, vol. 50, no. 24, pp. 18360–18366, 1994.
- [34] N. G. Chopra, R. J. Luyken, K. Cherrey et al., "Boron nitride nanotubes," *Science*, vol. 269, no. 5226, pp. 966–967, 1995.
- [35] A. Loiseau, F. Willaime, N. Demoncey, G. Hug, and H. Pascard, "Boron nitride nanotubes with reduced numbers of layers synthesized by arc discharge," *Physical Review Letters*, vol. 76, no. 25, pp. 4737–4740, 1996.
- [36] Z. Weng-Sieh, K. Cherrey, N. G. Chopra et al., "Synthesis of  $B_xC_yN_z$  nanotubules," *Physical Review B*, vol. 51, no. 16, pp. 11229–11232, 1995.
- [37] O. Stephan, P. M. Ajayan, C. Colliex et al., "Doping graphitic and carbon nanotube structures with boron and nitrogen," *Science*, vol. 266, no. 5191, pp. 1683–1685, 1994.
- [38] R. Tenne, L. Margulis, M. Genut, and G. Hodes, "Polyhedral and cylindrical structures of tungsten disulphide," *Nature*, vol. 360, pp. 444–446, 1992.
- [39] R. Tenne, "Doped and heteroatom-containing fullerene-like structures and nanotubes," *Advanced Materials*, vol. 7, pp. 965–995, 1995.
- [40] E. Hernández, C. Goze, P. Bernier, and A. Rubio, "Elastic properties of single-wall nanotubes," *Applied Physics A*, vol. 68, no. 3, pp. 287–292, 1999.
- [41] M. M. J. Treacy, T. W. Ebbesen, and J. M. Gibson, "Exceptionally high Young's modulus observed for individual carbon nanotubes," *Nature*, vol. 381, no. 6584, pp. 678–680, 1996.
- [42] J.-P. Salvetat, G. A. D. Briggs, J.-M. Bonard et al., "Elastic and shear moduli of single-walled carbon nanotube ropes," *Physical Review Letters*, vol. 82, no. 5, pp. 944–947, 1999.
- [43] Z. W. Pan, S. S. Xie, L. Lu et al., "Tensile tests of ropes of very long aligned multiwall carbon nanotubes," *Applied Physics Letters*, vol. 74, no. 21, pp. 3152–3154, 1999.
- [44] N. G. Chopra and A. Zettl, "Measurement of the elastic modulus of a multi-wall boron nitride nanotube," *Solid State Communications*, vol. 105, no. 5, pp. 297–300, 1998.
- [45] E. Hernández, C. Goze, P. Bernier, and A. Rubio, "Elastic properties of C and  $B_xC_yN_z$  composite nanotubes," *Physical Review Letters*, vol. 80, no. 20, pp. 4502–4505, 1998.
- [46] N. G. Chopra, L. X. Benedict, V. H. Crespi, M. L. Cohen, S. G. Louie, and A. Zettl, "Fully collapsed carbon nanotubes," *Nature*, vol. 377, no. 6545, pp. 135–138, 1995.
- [47] B. I. Yakobson, C. J. Brabec, and J. Bernholc, "Nanomechanics of carbon tubes: instabilities beyond linear response," *Physics Review Letters*, vol. 76, pp. 2511–2514, 1996.
- [48] B. I. Yakobson, C. J. Brabec, and J. Bernholc, "Structural mechanics of carbon nanotubes: from continuum elasticity to atomistic fracture," *Journal of Computer-Aided Materials Design*, vol. 3, no. 1–3, pp. 173–182, 1996.
- [49] S. Iijima, C. Brabec, A. Maiti, and J. Bernholc, "Structural flexibility of carbon nanotubes," *Journal of Chemical Physics*, vol. 104, no. 5, pp. 2089–2092, 1996.
- [50] J. F. Despres, E. Daguerre, and K. Lafdi, "Flexibility of graphene layers in carbon nanotubes," *Carbon*, vol. 33, no. 1, pp. 87–89, 1995.
- [51] R. S. Ruoff and D. C. Lorents, *Bulletin of the APS*, vol. 40, p. 173, 1995.
- [52] R. C. Haddon, "Chemistry of the fullerenes: the manifestation of strain in a class of continuous aromatic molecules," *Science*, vol. 261, no. 5128, pp. 1545–1550, 1993.
- [53] E. Cadelano, P. L. Palla, S. Giordano, and L. Colombo, "Nonlinear elasticity of monolayer graphene," *Physical Review Letters*, vol. 102, no. 23, Article ID 235502, 2009.
- [54] E. Cadelano, S. Giordano, and L. Colombo, "Elastic properties of graphene and carbon nanoribbons: a combined continuum and atomistic approach," submitted for publication.
- [55] C. Lee, X. Wei, J. W. Kysar, and J. Hone, "Measurement of the elastic properties and intrinsic strength of monolayer graphene," *Science*, vol. 321, no. 5887, pp. 385–388, 2008.
- [56] S. Cahangirov, M. Topsakal, E. Aktürk, H. Şahin, and S. Ciraci, "Two- and one-dimensional honeycomb structures of silicon and germanium," *Physical Review Letters*, vol. 102, no. 23, Article ID 236804, 2009.
- [57] M. Palummo, F. Iori, R. Del Sole, and S. Ossicini, "Giant excitonic exchange splitting in Si nanowires: first-principles calculations," *Physical Review B*, vol. 81, no. 12, Article ID 121303, 4 pages, 2010.
- [58] J. T. Lyon, P. Gruene, A. Fielicke et al., "Structures of silicon cluster cations in the gas phase," *Journal of the American Chemical Society*, vol. 131, no. 3, pp. 1115–1121, 2009.
- [59] O. Madelung, Ed., *Semiconductors—Basic Data*, Springer, Berlin, Germany, 1996.
- [60] Y. Wang, Y. Xie, P. Wei et al., "A stable silicon(0) compound with a Si=Si double bond," *Science*, vol. 321, no. 5892, pp. 1069–1071, 2008.

- [61] H. Kawaji, H.-O. Horie, S. Yamanaka, and M. Ishikawa, "Superconductivity in the silicon clathrate compound  $(\text{Na}, \text{Ba})_x\text{Si}_{16}$ ," *Physical Review Letters*, vol. 74, no. 8, pp. 1427–1429, 1995.
- [62] J. A. Alonso, *Structure And Properties of Atomic Nanoclusters*, Imperial College Press, London, UK, 2006.
- [63] J. C. Phillips, "Morphology of medium-size silicon clusters," *The Journal of Chemical Physics*, vol. 88, no. 3, pp. 2090–2091, 1988.
- [64] B. Marsen and K. Sattler, "Fullerene-structured nanowires of silicon," *Physical Review B*, vol. 60, no. 16, pp. 11593–11600, 1999.
- [65] H. Nakano, T. Mitsuoka, M. Harada et al., "Soft synthesis of single-crystal silicon monolayer sheets," *Angewandte Chemie*, vol. 45, no. 38, pp. 6303–6306, 2006.
- [66] S. Pathak, V. B. Shenoy, and G. Baskaran, "Possible high-temperature superconducting state with a d+id pairing symmetry in doped graphene," *Physical Review B*, vol. 81, no. 8, Article ID 085431, 5 pages, 2010.
- [67] A. M. Black-Schaffer and S. Doniach, "Resonating valence bonds and mean-field d-wave superconductivity in graphite," *Physical Review B*, vol. 75, no. 13, Article ID 134512, 2007.
- [68] B. Uchoa and A. H. Castro Neto, "Superconducting states of pure and doped graphene," *Physical Review Letters*, vol. 98, no. 14, Article ID 146801, 2007.
- [69] M. Capone, M. Fabrizio, C. Castellani, and E. Tosatti, "Colloquium: modeling the unconventional superconducting properties of expanded A3 C60 fullerides," *Reviews of Modern Physics*, vol. 81, no. 2, pp. 943–958, 2009.
- [70] F. M. D. Pellegrino, G. G. N. Angilella, and R. Pucci, "Pairing symmetry of superconducting graphene," *European Physical Journal B*, vol. 76, no. 3, pp. 469–473, 2010.
- [71] C. Kramberger, R. Hambach, C. Giorgetti et al., "Linear plasmon dispersion in single-wall carbon nanotubes and the collective excitation spectrum of graphene," *Physical Review Letters*, vol. 100, no. 19, Article ID 196803, 2008.
- [72] Y. Liu, R. F. Willis, K. V. Emtsev, and T. H. Seyller, "Plasmon dispersion and damping in electrically isolated two-dimensional charge sheets," *Physical Review B*, vol. 78, no. 20, Article ID 201403, 2008.
- [73] A. Bostwick, T. Ohta, T. Seyller, K. Horn, and E. Rotenberg, "Quasiparticle dynamics in graphene," *Nature Physics*, vol. 3, no. 1, pp. 36–40, 2007.
- [74] X.-F. Wang and T. Chakraborty, "Collective excitations of Dirac electrons in a graphene layer with spin-orbit interactions," *Physical Review B*, vol. 75, no. 3, Article ID 033408, 2007.
- [75] X.-F. Wang and T. Chakraborty, "Coulomb screening and collective excitations in biased bilayer graphene," *Physical Review B*, vol. 81, no. 8, Article ID 081402, 4 pages, 2010.
- [76] Y. Liu and R. F. Willis, "Plasmon-phonon strongly coupled mode in epitaxial graphene," *Physical Review B*, vol. 81, no. 8, Article ID 081406, 4 pages, 2010.
- [77] S.-M. Choi, S.-H. Jhi, and Y.-W. Son, "Effects of strain on electronic properties of graphene," *Physical Review B*, vol. 81, no. 8, Article ID 081407, 4 pages, 2010.
- [78] F. M. D. Pellegrino, G. G. N. Angilella, and R. Pucci, "Strain effect on the optical conductivity of graphene," *Physical Review B*, vol. 81, no. 3, Article ID 035411, 12 pages, 2010.
- [79] T. Kramer, C. Kreisbeck, V. Krueckl, E. J. Heller, R. E. Parrott, and C. T. Liang, "Theory of the quantum Hall effect in finite graphene devices," *Physical Review B*, vol. 81, Article ID 081410, 4 pages, 2010.
- [80] K. S. Novoselov, A. K. Geim, S. V. Morozov et al., "Two-dimensional gas of massless Dirac fermions in graphene," *Nature*, vol. 438, no. 7065, pp. 197–200, 2005.
- [81] K. S. Novoselov, A. K. Geim, S. V. Morozov et al., "Two-dimensional gas of massless Dirac fermions in graphene," *Nature*, vol. 438, no. 7065, pp. 197–200, 2005.
- [82] Y. Zhang, Y.-W. Tan, H. L. Stormer, and P. Kim, "Experimental observation of the quantum Hall effect and Berry's phase in graphene," *Nature*, vol. 438, no. 7065, pp. 201–204, 2005.
- [83] Y. Zhang, Z. Jiang, J. P. Small et al., "Landau-level splitting in graphene in high magnetic fields," *Physical Review Letters*, vol. 96, no. 13, Article ID 136806, pp. 1–4, 2006.

## Research Article

# Synthesis and Characterization of Glassy Carbon Nanowires

C. M. Lentz,<sup>1</sup> B. A. Samuel,<sup>2</sup> H. C. Foley,<sup>3</sup> and M. A. Haque<sup>2</sup>

<sup>1</sup> Department of Materials Science and Engineering, The Pennsylvania State University, University Park, PA 16802, USA

<sup>2</sup> Department of Mechanical and Nuclear Engineering, The Pennsylvania State University, University Park, PA 16802, USA

<sup>3</sup> Department of Chemical Engineering, The Pennsylvania State University, University Park, PA 16802, USA

Correspondence should be addressed to M. A. Haque, mah37@psu.edu

Received 7 June 2010; Accepted 13 September 2010

Academic Editor: Teng Li

Copyright © 2011 C. M. Lentz et al. This is an open access article distributed under the Creative Commons Attribution License, which permits unrestricted use, distribution, and reproduction in any medium, provided the original work is properly cited.

The advent of carbon-based micro- and nanoelectromechanical systems has revived the interest in glassy carbon, whose properties are relatively unknown at lower dimensions. In this paper, electrical conductivity of individual glassy carbon nanowires was measured as a function of microstructure (controlled by heat treatment temperature) and ambient temperature. The semiconducting nanowires with average diameter of 150 nm were synthesized from polyfurfuryl alcohol precursors and characterized using transmission electron and Raman microscopy. DC electrical measurements made at 90 K to 450 K show very strong dependence of temperature, following mixed modes of activation energy and hopping-based conduction.

## 1. Introduction

Semiconducting amorphous materials are widely used in electronics applications due to their favorable optical and dielectric properties, tunable band gaps, and low manufacturing costs [1–3]. Amorphous or glassy carbon (a-C) is of particular interest because of the versatility of the carbon material system with a diverse range of physical properties based on the nature and the spatial arrangement of the chemical bonds [4]. A common method of glassy carbon synthesis is the pyrolysis of a polymeric precursor. Such polymer-derived carbons are considered to be either graphitizing or nongraphitizing depending on their tendency to transform to graphite when subjected to temperatures above 1000°C. Nongraphitizing carbons are globally amorphous, meaning that they are disordered and noncrystalline though they may have some small graphitic regions with local order. Though a long range graphitic structure is the most thermodynamically stable form of carbon, nongraphitizing carbons remain thermally stable and resistant to chemical attack at high temperature. This stability is attributed to crosslinking in the polymeric precursor, which results in a disordered, chaotic misalignment of graphene layers in the carbon after pyrolysis [5].

The composition of the carbon-carbon bond types in a given glassy carbon material is, along with the material

microstructure, one of the most influential parameters in determining the electrical transport properties. The presence of more delocalized  $\pi$  electrons due to  $sp^2$  bonding facilitates in-plane electron transport in graphitic carbon, which is not the case for the rigid and localized  $sp^3$  bonds in diamond-like carbons. In tetrahedral carbon systems, for instance, an increase in electrical conductivity is generally observed with increase in the  $sp^2/sp^3$  ratio in the material [6]. Therefore, even in materials with a low  $sp^2/sp^3$  ratio, it is the  $sp^2$  arrangement that determines the electrical properties of the material. A range of band gaps from 1–4 eV is seen in the literature for glassy carbon [7–9], where variations arise from the composition of  $sp^3$  and  $sp^2$  carbon and from defect induced variation in the density of states.

In this study, we investigate the role of microstructure and ambient temperature on the electrical properties of glassy carbon, which has a disordered structure with primarily  $sp^2$  carbon. Though lacking in long-range order, these carbons are regular solids; they contain structural elements of the same type that are chaotically arranged in space. This regularity is observed in their inherent nanoscale porosity, which is narrowly distributed around an average pore size of 0.5 nm [10]. Such nanoporous carbons have found applications in filtration, electrical [11–13], and electrochemical applications [14–16]. The motivation for this study comes from a resurgence of the interest in nano

[14, 17–20] and biological [21, 22] applications of glassy carbon materials. Carbon is clearly a more suitable material over silicon for biological applications because life on earth is carbon-, and not silicon-based. In particular, a new area called “carbon MEMS (micro-electro-mechanical systems) is developing rapidly. The uniqueness of the technique is that nanofabrication processes are cleverly exploited to pyrolyze polymeric nanostructures to carbon-MEMS that can range from micro- to nanoscale [23] and different aspect ratios [24]. It is important to note that all these applications require comprehensive characterization of the electrical conductivity of the nanoscale glassy carbon. The literature contains ample information on the bulk glassy carbon properties [7–9, 25, 26], but only a few studies are available that investigate the size effect on electrical properties at the nanoscale [27, 28]. For example, compared to microporous bulk glassy carbon, a nanoporous nanowire has higher surface area/volume ratio, as well as defects due to the presence of 5- and 7-membered aromatic rings and uncoordinated carbon surface atoms. Because of these defects, many of the charge carriers in the system exist in localized states in the semiconductor band gap, altering the electrical transport properties of the material.

## 2. Literature Review

**2.1. Synthesis and Structure.** Glassy carbon is typically synthesized by pyrolyzing any polymeric precursor that cross-links at elevated temperatures. Specifically, the nanowires synthesized in this study are based on polymerized furfuryl alcohol (PPFA), which is a common furanic derivative of natural biomasses [29]. Fitzer and Schäfer [30] used infrared spectroscopy (IR) to examine the mechanism for the pyrolysis of PFA, at increasing temperatures from a starting point of 130°C. The furan ring remains stable up to 275°C, only fully rupturing between 300 and 400°C. At 400°C, aromatic groups begin to form spontaneously from the fragments of the furan rings. As temperature increases above 450°C, the aromatic groups coalesce to form a final, highly unsaturated polymer network. Between 500 and 1200°C, called the dehydrogenation phase, hydrogen atoms are expelled, and the linear conjugated links coalesce to form aromatic systems. The final phase is annealing, which occurs at heat treatment above 1200°C. During this stage, structural defects such as five- and seven-membered rings are progressively removed from the system as temperature is increased. Multiple models for the structures of nongraphitizing carbons exist. The final microstructure is composed of randomly oriented graphitic crystallites connected by disordered carbon sheets, or a three-dimensional network of curved graphitic ribbons, which loop around each other in no specific orientation [31–33].

**2.2. Electrical Characterization of Glassy Carbon.** Glassy carbons are considered to be Anderson insulators, where the systemic disorder, through particle localization, induces a transition from metallic conduction to an increasingly insulating state as disorder increases [34]. This is a strong

function of structural order, which is driven by stress relaxation [35]. For heat treatment temperatures above 500°C, rapid removal of hydrogen atoms produce mobile carriers via a method in which an edge carbon atom attracts electrons from a carbon atom in the interior of the aromatic sheet, producing a negatively charged edge ion and a mobile interior hole. This results in an increase in the number of mobile carriers, causing the steep decrease in resistivity. However, this process slows down exponentially after 1000°C.

In disordered carbon the charge carrier transport occurs in three regimes—tunneling transport between the localized states in the mobility gap at very low temperatures (<20 K), hopping-based conduction between localized states at low temperatures (<250 K) and thermally-activated conduction from the Fermi level to the mobility edges at room temperature and higher [36]. The hopping-based charge transfer occurs by phonon-assisted tunneling from occupied to unoccupied electronic states. The hopping conduction model predicts a  $T^{-1/(d+1)}$  relationship with the logarithm of the conductivity, where  $d$  is the dimensionality of the hopping space [33],

$$\sigma(T) = \sigma_0 \exp\left(-\left[\frac{T_0}{T}\right]^{1/(d+1)}\right). \quad (1)$$

For glassy carbon, hopping is commonly observed to be three dimensional ( $d = 3$ ) in a range of ambient temperatures from 60 K to 300 K [37]. With hopping conduction, the conductivity approaches zero as temperature approaches zero. In addition to the effects of localized states, a Coulomb gap can have an effect on the hopping conductivity mechanism [33], resulting in a  $T^{-1/2}$  dependence of logarithm of conductivity, regardless of hopping space dimension. This is given by,

$$\sigma = \sigma_0 \exp\left[-\left(\frac{T_0}{T}\right)^{1/2}\right], \quad \text{where } T_0 = \frac{6e^2}{\pi k_B} \frac{1}{4\pi\epsilon} \frac{1}{\xi}. \quad (2)$$

Here,  $\sigma_0$  is the conductivity at  $T = \infty$ ,  $\epsilon$  is the permittivity representing screening effects on charges at small graphitic regions, and  $\xi$  is the localization length of the wave function, defined as the spatial extension of the localized energy state. The Coulomb gap is calculated to be equal to  $k_B e^4 D_0 \xi / \epsilon$ , where  $D_0$  is the density of states at the Fermi energy. The contribution of the Coulomb interactions can occur when the thermal energy is smaller than the Coulomb gap width. This occurs below a characteristic temperature,  $T_C = (e^4 D_0 \xi) / \epsilon^2$ .

At or above room temperature, thermally-activated transport mechanism is expected. Here, the relationship between  $\ln(\text{conductivity})$  and surface temperature is indicative of the activation energy gap between the Fermi level and the extended states in the disordered carbon's mobility edge, ( $\epsilon_g = \epsilon_V - \epsilon_F$ ),

$$\sigma(T) = \sigma_0 e^{-\epsilon_g/k_B T}, \quad (3)$$

where  $\sigma_0$  is a constant, and  $k_B$  is the Boltzmann constant [22].

Bulk electrical properties of glassy carbon are very well studied in the literature. Kuriyama and Dresselhaus [34]

studied the metal-insulator transition in activated phenol-derived, nongraphitizing carbon fibers. They determine that the metal-insulator transition occurs at approximately 1000°C, at which point the  $\sigma \rightarrow 0$  as  $T \rightarrow 0$  relationship begins to fail as fewer states are localized. Takai et al. [33] performed a study on a primarily  $sp^2$ , nongraphitic carbon, heat-treated over a range of 200°C to 1500°C. They observed variation in conductivity with both heat treatment temperature (HTT) and with ambient temperature over a range from 4.2 K to room temperature. With successive heat treatment at intervals of  $\sim 200^\circ\text{C}$  up to a  $\text{HTT} \leq 600^\circ\text{C}$ , the conductivity shows a drastic increase of four orders of magnitude. Wang et al. [31] observed the hopping conduction mechanism at temperatures from 75 K to 275 K.

In comparison, very little is known about the lower dimensional properties of glassy carbon, which may be due to the fact that all the applications hitherto have been macroscopic. However, the advent of carbon-based micro- and nanodevices necessitates the fundamental understanding in conduction at such reduced dimensions. Park et al. [38] studied the electrical properties of glassy carbon films derived from epoxy and phenolic resins and found the properties similar to bulk glassy carbon. Our previous study involved individual glassy carbon nanowires above room temperature to show about less than 1 order of magnitude change in conductivity as surface temperature increased from 300 K to 460 K. All the specimens were heat treated at 600°C only, therefore the study did not show the role specimen microstructure and low temperature conduction [39].

### 3. Experimental Techniques

Furfuryl alcohol was polymerized inside the pores of an anodized alumina template to form the nanowires, which were subsequently pyrolyzed at temperature ranging from 600 to 2000°C. In a typical process [10] 1 M *p*-toluenesulfonic acid solution is added to 5 ml of Triton X-100. 5 ml furfuryl alcohol (FA) is added to the resultant solution using a syringe pump at a rate of  $10 \text{ ml min}^{-1}$ . The solution is allowed to polymerize (PFA) in an ice bath for 24 h and then filled inside Anodisc anodic alumina membrane (Whatman) with 200 nm pores by capillary effect. The PFA-lled template is then pyrolyzed for 8 h and then dissolved in 6 M KOH aqueous solution to produce dispersed nanowires. High temperature treatment (HTT) was carried out in a Red Devil furnace (R.D. Webb Company, Natick, MA). The hot zone was evacuated to  $10^{-3}$  mbar for 24 h prior to annealing, then backfilled to atmospheric pressure with argon. A  $25^\circ\text{C min}^{-1}$  heating rate was employed with a 1 h soak at temperatures between 1200 and 2000°C. Figure 1 shows the nanowire synthesis technique. The nanowires are then inspected with a JEOL 2010 LaB6 transmission electron microscope to obtain information about the crystallite structure within the samples. The average diameter was found to be 150 nm ( $\pm 10$  nm), which is due to the volume shrinkage during pyrolysis.

Figure 2 shows the bright field and electron diffraction images for heat treatment temperatures of 600 and

2000°C. The 600°C treated specimens (PPFA600) show no observable short-range structure, and the diffraction pattern shows Laue rings typical of glassy carbon, primarily diffused with two expected rings corresponding to the first and second coordination shells of carbon [39]. At higher temperatures (800°C, 1200°C, 1500°C), graphitic clusters less than 10 nm in size appear, leading to ribbon-like morphology. The width of the Laue rings of the diffraction pattern appears narrower for these samples than for the lower temperature specimens. At 2000°C (PPFA 2000), we observe large ribbon-like chains ( $< 20$  nm) which are distributed in random orientation throughout the sample. The surface morphology of these nanowires also is jagged and different from all the other specimens. Therefore, from TEM microscopy we can conclude that the nanowires, while still remaining disordered, exhibit a remarkable decrease in the degree of disorder with increase in heat treatment temperature.

The TEM evidence of enhanced graphitic nanostructures at higher heat treatment temperatures is also corroborated by reflected light Raman spectroscopy performed on a clump of nanowires. The spectra were obtained on a WITec Confocal Raman instrument at an excitation wavelength of 514 nm and at 100X magnification. The results are shown in Figure 3. Peak broadening is observed at lower pyrolysis temperatures, which is indicative of bond length scatter (and disorder) at the molecular level in the form of strained bonds. With increasing heat treatment temperature some of these strains are relieved, possibly through contraction, expansion, or coalescence of C–C bonds at the atomic scale. As shown in Figure 3, a sharp increase in the intensity of G peak (compared to the D peak) is seen at 2000°C, which implies that a sizeable number of the linear  $sp^2$  carbon have coalesced to form aromatic structures [40]. This is confirmed in the TEM image as an increase in the graphitic ribbon structures in PPFA2000. Therefore, Raman spectroscopy and TEM microscopy are complementary in deducing the evolution of the morphology of the nanowires.

Because the glassy carbon nanowires exhibited photo-sensitive electrical conduction, dark DC measurements with varying surface temperature of the nanowire (from 90 K to about 400 K) were performed. Single nanowires were manipulated and bonded on microfabricated electrodes using focused-ion beam-based platinum deposition in a dual gun electron microscope (Quanta 200 3D Dual Beam FIB/SEM, FEI Company). This reduces the Schottky barrier and facilitates Ohmic conduction, as well as acting as a mechanical “glue” which both ensures that the nanowires are in contact with the surface and provides mechanical stability for the system. Measurements were carried out in a Deep Level Transient Spectroscopy (DLTS) cryogenic electronic test station, under vacuum. Conductivity measurements were made using a Keithley 236 Source-Measure Unit, sweeping voltage from  $-1$  V to  $+1$  V and measuring the resultant current. Figure 4 shows a typical specimen and electrical conductivity plot. Figure 4(b) shows a clear transition from one transport mechanism to another. However, the smooth transition of the curve indicates that multiple mechanisms work simultaneously in the transition regions.

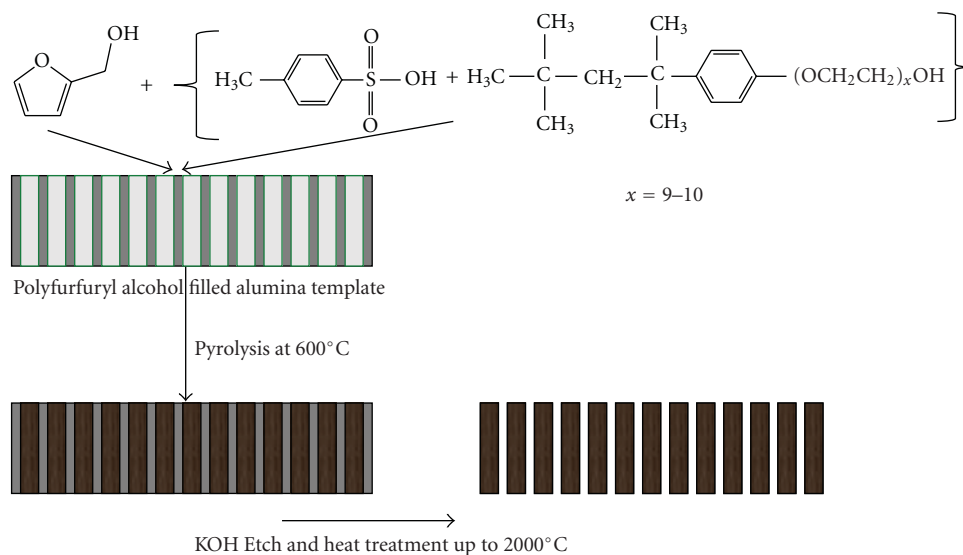


FIGURE 1: Anodized alumina template-based synthesis of poly-furfuryl alcohol nanowires. The glassy carbon nanowires are obtained by pyrolyzing the polymeric precursor nanowires and then heat treating them at desired temperatures.

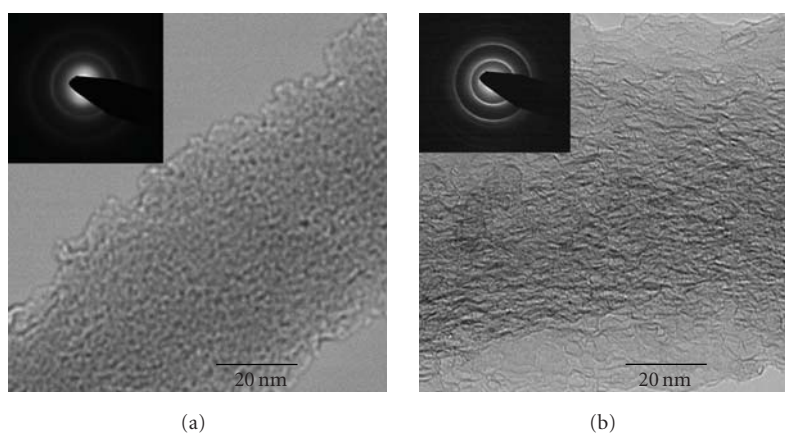


FIGURE 2: TEM bright field and diffraction patterns for glassy carbon nanowires treated at (a) 600°C and (b) 2000°C showing evolution of graphitic nanostructures.

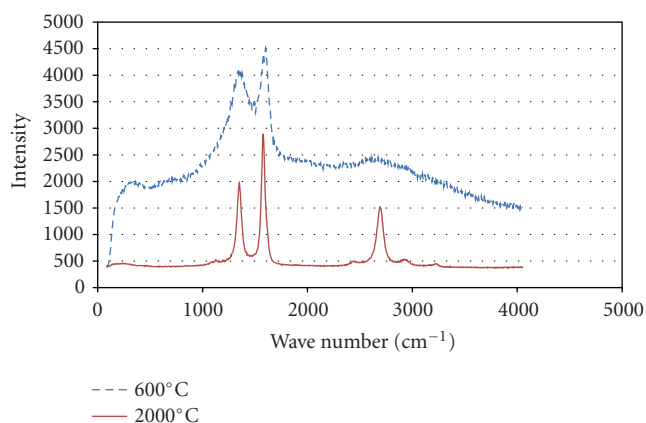


FIGURE 3: Raman spectra for nanowires heat treated at 600°C and 2000°C. The peak sharpening at 2000°C agrees very well with the TEM analysis.

#### 4. Experimental Results and Discussion

Electrical conductivity of individual glassy carbon nanowires were measured as a function of morphology and ambient temperature. The experimental results are plotted in Figure 5. As predicted by the TEM and Raman spectroscopy, the conductivity of the individual nanowires is observed to be strongly dependent on the specimen nanostructure. The increase in conductivity of the nanowires with increasing heat treatment temperature is due to the increases in aromatic  $\text{sp}^2$  ring formation, growth of curved graphitic crystallite domains and percolation networks, and the annealing of graphitic defects. Such increase in conductivity of the material by increasing the available density of charge transfer sites (and not by narrowing of the mobility gap) is analogous to an increase in doping in an extrinsic crystalline semiconductor.

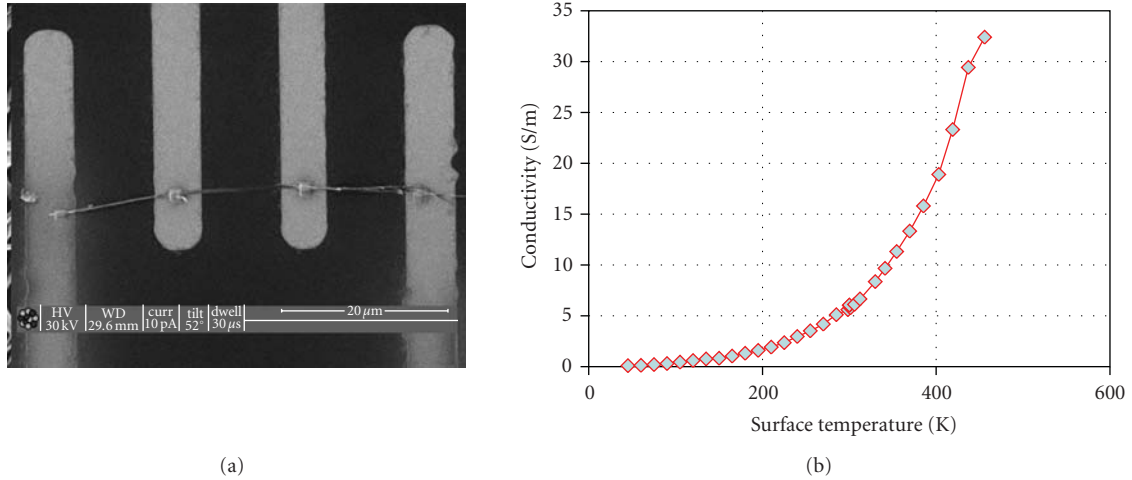


FIGURE 4: (a) Scanning electron micrograph of a single nanowire manipulated across interdigitated microelectrodes. (b) DC electrical conductivity of a nanowire.

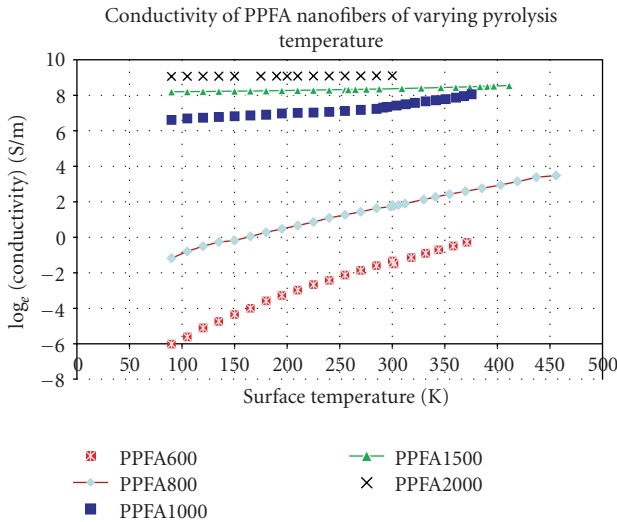


FIGURE 5: Electrical conductivity versus temperature plots for different heat treated specimens.

In Figure 5, the slope of the conductivity versus  $T$  curve is highest (6 order of magnitude change in resistivity compared to the 3 orders change observed in bulk form [25]) for the PPFA600 sample, and decreases as heat treatment temperature increases. This is seen in both the high and low temperature regions of the data and can be explained by the relative level of disorder present in the material. In glassy semiconductors, defects such as 5- and 7-membered rings cause localized states in the band gap region [41]. The greater the number of localized states, the more the conductivity is dependent on ambient temperature. This is a result of immobile charge carriers, and the activation energy required for excitation of a charge carrier is larger. The increase in ambient temperature therefore allows more charge carriers to cross the mobility gap of the material. With an increase in heat treatment temperature, the system becomes more ordered, and weak, strained bonds are allowed to relax to

a more stable  $sp^2$  graphitic state. This increase in systemic order means a decrease in the amount of localized states present, and thus more delocalized charge carriers, gradually approaching metallic conduction behavior in which conductivity would not be dependent on ambient temperature. In this situation, an increase in temperature does not provide as significant a change in the amount of electrons that are able to cross. However, the annealing effects decay quickly with the heat treatment temperature. Considering the large scatter in the electrical conductivity data originating from a wide variety of synthesis processes, the nanowire conductivities in this study are found to be marginally higher but in the same order.

To determine the dominant conduction modes in the various temperature regimes, particularly to identify the metal to insulator transition temperature, we examine Figure 6, where individual conductivity versus temperature curves for each heat treatment temperature. From these curves, we can see that for heat treatment temperatures below  $800^\circ\text{C}$  the conductivity approaches zero as the ambient temperature approaches zero. This is indicative of a hopping mechanism, however, this happens at about  $1000^\circ\text{C}$  in bulk glassy carbon.

Next, we analyze the data in the lower than room temperature region to establish the parameters for a hopping-based conduction model (1). A plot of  $\ln(\sigma)$  versus  $T^{-1/2}$  is shown in Figure 7. At higher than the room temperature, all the specimens followed a thermally activated transport mechanism. This is shown in Figure 8, where  $\ln(\sigma)$  versus  $T^{-1}$  is plotted. The slope of the conductivity versus surface temperature plots is indicative of the activation energy gap, which can be calculated using (3). The slope of this curve is equivalent to  $\varepsilon_g/k_B$ , allowing us to determine the mobility gap for the different nanowires. The activation parameters obtained are summarized in Table 1. It is interesting to note that the conductivity data for specimens heat treated at  $800^\circ\text{C}$  and below do not fit well with the thermally activated conduction mechanism, even at higher than room

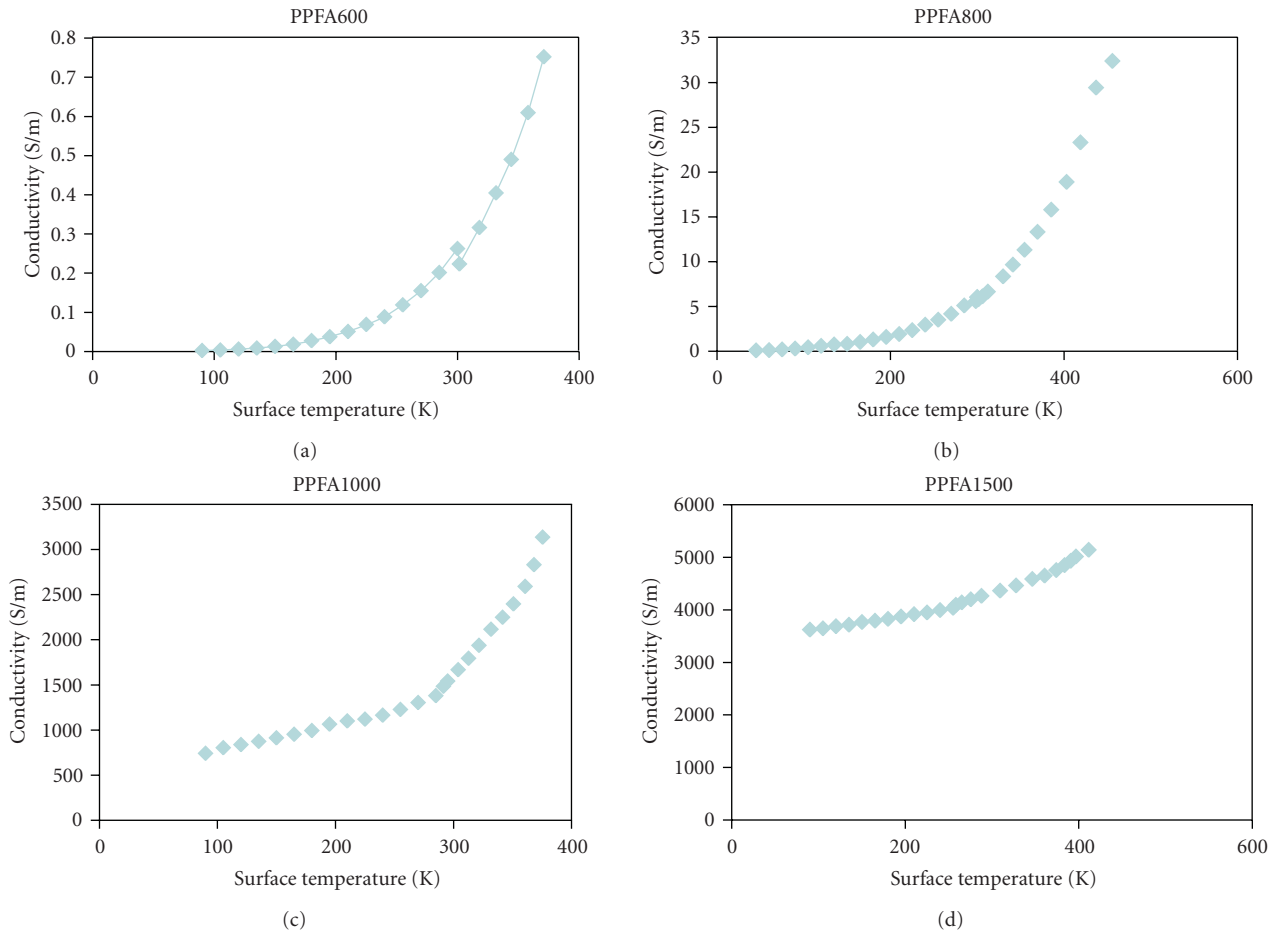


FIGURE 6: Progressive changes in the trend of conductivity with surface temperature as pyrolysis temperature is increased.

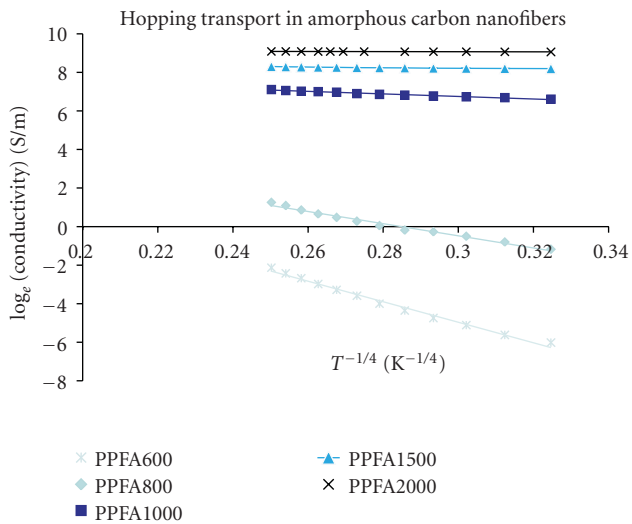


FIGURE 7: Fitting of the low temperature (<250 K) conductivity data to the hopping transport model.

temperatures. This observation is consistent with the pattern identified in Figure 6.

## 5. Discussion

TEM and Raman microscopy and DC conductivity measurements were performed on individual glassy carbon nanowires with average diameter of 150 nm in an attempt to associate the heat treatment temperature and the corresponding nanowire microstructure with the electrical properties of the material. The TEM images show a significant increase in graphitic, ribbon-like structures as the heat treatment temperature was raised from 600°C to 2000°C. The Raman spectra also qualitatively indicated similar increase in systemic order. DC conductivity measurements agree to this trend quantitatively, with 6 orders of magnitude increase in conductivity as the ambient temperature increase from 90 K to 450 K. The slope of the conductivity versus temperature curve is highest (in magnitude) for the lowest heat treatment temperature, and decreases as heat treatment temperature increases. This is seen in both the high and low temperature regions of the data and can be explained by the relative level of disorder present in the material, which determines the amount of localized states, and therefore the temperature dependence of the material. As surface temperature is increased, more localized electrons have the energy to bridge the gap. With an increase in heat treatment

TABLE 1: Parameters from the low temperature DC conductivity data fitted to both a hopping-based energy transport mechanism and a thermally activated conduction mechanism.

Sample	Slope for hopping conduction	$R^2$ for hopping conduction model	Mobility gap, $\epsilon_g$ (eV)	$R^2$ for thermally activated conduction model
PPFA600	92.607	0.98978	0.0033	0.98117
PPFA800	54.959	0.98181	0.0152	0.97261
PPFA1000	11.451	0.98183	0.0779	0.97225
PPFA1500	2.5482	0.95712	0.1309	0.9413
PPFA2000	0.5533	0.94543	0.1664	0.95255

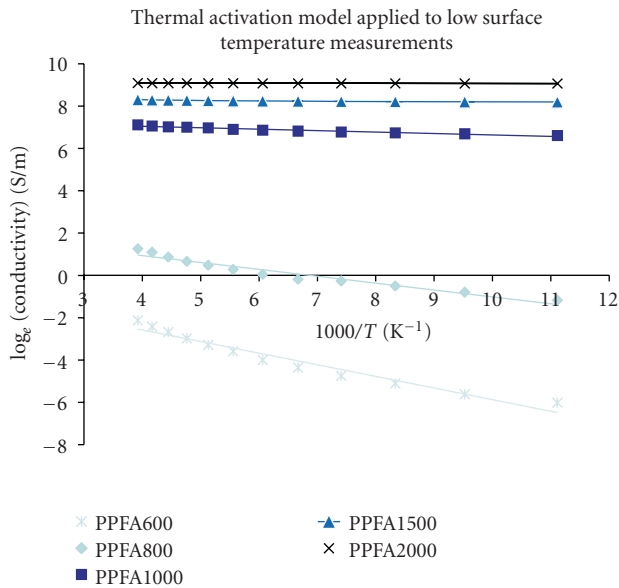


FIGURE 8: Fitting of the conductivity data for room temperature and above to a thermally activated transport model.

temperature, the system becomes more ordered, decreasing the amount of localized states present and allowing for more mobile charge carriers. With this increased electron mobility, an increase in temperature does not provide as significant a change in the amount of electrons that are able to cross, and the conductivity of the sample does not increase as rapidly with increasing surface temperature.

We conclude that it is the overall delocalized charge carrier density which determines the [41]conductivity of the system. This result can also be connected to the morphology of the nanowires. When the system is highly disordered, there are significantly fewer available charge carriers, as they are involved in the defects and strained bonds in the structure. At higher heat treatment temperatures, much of this disorder is removed from the system, which improves the conductivity of the nanowires. This is dominated by the chemical processes during heat treatment such as increases in aromatic  $sp^2$  ring formation, growth of curved graphitic crystallite domains, increase in percolation networks, and the annealing of graphitic defects.

## Acknowledgments

M.A. Haque gratefully acknowledges the support from the Center for Nanoscale Mechatronics & Manufacturing of the Korea Institute of Machinery & Materials and the National Science Foundation, USA (ECS no. 0545683).

## References

- [1] S. R. P. Silva and J. D. Carey, "Enhancing the electrical conduction in amorphous carbon and prospects for device applications," *Diamond and Related Materials*, vol. 12, no. 2, pp. 151–158, 2003.
- [2] J. Robertson, "Preparation and properties of amorphous carbon," *Journal of Non-Crystalline Solids*, vol. 137-138, no. 2, pp. 825–830, 1991.
- [3] S. R. P. Silva, Ed., *Properties of Amorphous Carbon*, vol. 29 of *EMIS Data Reviews Series*, Institution of Engineering and Technology, London, UK, 2003.
- [4] G. M. Jenkins, K. Kawamura, and L.L. Ban, "Formation and structure of polymeric carbons," *Proceedings of the Royal Society of London. Series A, Mathematical and Physical Sciences*, vol. 327, no. 1571, pp. 501–517, 1972.
- [5] C. L. Burket, R. Rajagopalan, and H. C. Foley, "Overcoming the barrier to graphitization in a polymer-derived nanoporous carbon," *Carbon*, vol. 46, no. 3, pp. 501–510, 2008.
- [6] D. G. McCulloch, J. L. Peng, D. R. McKenzie, S. P. Lau, D. Sheeja, and B. K. Tay, "Mechanisms for the behavior of carbon films during annealing," *Physical Review B*, vol. 70, no. 8, Article ID 085406, 8 pages, 2004.
- [7] D. F. Baker and R. H. Bragg, "The electrical conductivity and Hall effect of glassy carbon," *Journal of Non-Crystalline Solids*, vol. 58, no. 1, pp. 57–69, 1983.
- [8] E. P. O'Reilly, "The electronic structure of amorphous carbon," *Journal of Non-Crystalline Solids*, vol. 97-98, no. 2, pp. 1095–1102, 1987.
- [9] R. R. Saxena and R. H. Bragg, "Electrical conduction in glassy carbon," *Journal of Non-Crystalline Solids*, vol. 28, no. 1, pp. 45–60, 1978.
- [10] C. L. Burket, R. Rajagopalan, A. P. Marencic, K. Dronvajjala, and H. C. Foley, "Genesis of porosity in polyfurfuryl alcohol derived nanoporous carbon," *Carbon*, vol. 44, no. 14, pp. 2957–2963, 2006.
- [11] D. Sun, L. Zhu, and G. Zhu, "Glassy carbon ceramic composite electrodes," *Analytica Chimica Acta*, vol. 564, no. 2, pp. 243–247, 2006.
- [12] S. Shahrokhian, M. Ghalkhani, M. Adeli, and M. K. Amini, "Multi-walled carbon nanotubes with immobilised cobalt

- nanoparticle for modification of glassy carbon electrode: application to sensitive voltammetric determination of thioridazine," *Biosensors and Bioelectronics*, vol. 24, no. 11, pp. 3235–3241, 2009.
- [13] Q. Ngo, T. Yamada, M. Suzuki et al., "Structural and electrical characterization of carbon nanofibers for interconnect via applications," *IEEE Transactions on Nanotechnology*, vol. 6, no. 6, pp. 688–695, 2007.
- [14] R. Martinez-Duarte et al., "Perspectives of Micro and Nanofabrication of Carbon for Electrochemical and Microfluidic Applications," in *Microfluidics and Microfabrication*, S. Chakraborty, Ed., pp. 181–263, Springer, New York, NY, USA, 2010.
- [15] P. Yu, Y. Lin, L. Xiang, L. Su, J. Zhang, and L. Mao, "Molecular films of water-miscible ionic liquids formed on glassy carbon electrodes: characterization and electrochemical applications," *Langmuir*, vol. 21, no. 20, pp. 9000–9006, 2005.
- [16] C. Wang, L. Taherabadi, G. Jia, M. Madou, Y. Yeh, and B. Dunn, "C-MEMS for the manufacture of 3D microbatteries," *Electrochemical and Solid-State Letters*, vol. 7, no. 11, pp. A435–A438, 2004.
- [17] A. Singh, J. Jayaram, M. Madou, and S. Akbar, "Pyrolysis of negative photoresists to fabricate carbon structures for micro-electromechanical systems and electrochemical applications," *Journal of the Electrochemical Society*, vol. 149, no. 3, pp. E78–E83, 2002.
- [18] C. Wang and M. Madou, "From MEMS to NEMS with carbon," *Biosensors and Bioelectronics*, vol. 20, no. 10, pp. 2181–2187, 2005.
- [19] R. Du, S. Ssenyange, M. Aktary, and M. T. McDermott, "Fabrication and characterization of graphitic carbon nanostructures with controllable size, shape, and position," *Small*, vol. 5, no. 10, pp. 1162–1168, 2009.
- [20] C. S. Sharma, R. Vasita, D. K. Upadhyay, A. Sharma, D. S. Katti, and R. Venkataraghavan, "Photoresist derived electrospun carbon nanofibers with tunable morphology and surface properties," *Industrial and Engineering Chemistry Research*, vol. 49, no. 6, pp. 2731–2739, 2010.
- [21] S. E. Rodil, R. Olivares, H. Arzate, and S. Muhl, "Biocompatibility, cytotoxicity and bioactivity of amorphous carbon films," *Topics in Applied Physics*, vol. 100, pp. 55–75, 2006.
- [22] V.-M. Tiainen, "Amorphous carbon as a bio-mechanical coating-mechanical properties and biological applications," *Diamond and Related Materials*, vol. 10, no. 2, pp. 153–160, 2001.
- [23] R. McCreery, J. Dieringer, A. O. Solak et al., "Molecular rectification and conductance switching in carbon-based molecular junctions by structural rearrangement accompanying electron injection," *Journal of the American Chemical Society*, vol. 125, no. 35, pp. 10748–10758, 2003.
- [24] F. Anariba, S. H. DuVall, and R. L. McCreery, "Mono- and multilayer formation by diazonium reduction on carbon surfaces monitored with atomic force microscopy "scratching"" *Analytical Chemistry*, vol. 75, no. 15, pp. 3837–3844, 2003.
- [25] W. Buecker, "Preparation and DC conductivity of an amorphous organic semiconducting system," *Journal of Non-Crystalline Solids*, vol. 12, no. 1, pp. 115–128, 1973.
- [26] L. Soukup, I. Gregora, L. Jastrabik, and A. Koňáková, "Raman spectra and electrical conductivity of glassy carbon," *Materials Science and Engineering B*, vol. 11, no. 1–4, pp. 355–357, 1992.
- [27] B. Y. Park, L. Taherabadi, C. Wang, J. Zoval, and M. J. Madou, "Electrical properties and shrinkage of carbonized photoresist films and the implications for carbon microelectromechanical systems devices in conductive media," *Journal of the Electrochemical Society*, vol. 152, no. 12, pp. J136–J143, 2005.
- [28] B. A. Samuel, R. Rajagopalan, H. C. Foley, and M. A. Haque, "Temperature effects on electrical transport in semiconducting nanoporous carbon nanowires," *Nanotechnology*, vol. 19, no. 27, Article ID 275702, 2008.
- [29] R. Gonzalez, R. Martinez, and P. Ortiz, "Polymerization of furfuryl alcohol with trifluoroacetic acid: the influence of experimental conditions," *Macromolecular Chemistry*, vol. 193, no. 1, pp. 1–9, 1992.
- [30] E. Fitzer and W. Schäfer, "The effect of crosslinking on the formation of glasslike carbons from thermosetting resins," *Carbon*, vol. 8, no. 3, pp. 353–364, 1970.
- [31] Z. Wang, Z. Lu, Y. Huang, R. Xue, X. Huang, and L. Chen, "Characterizations of crystalline structure and electrical properties of pyrolyzed polyfurfuryl alcohol," *Journal of Applied Physics*, vol. 82, no. 11, pp. 5705–5710, 1997.
- [32] K. Dasgupta and D. Sathiyamoorthy, "Disordered carbon—its preparation, structure, and characterisation," *Materials Science and Technology*, vol. 19, no. 8, pp. 995–1002, 2003.
- [33] K. Takai, M. Oga, H. Sato et al., "Structure and electronic properties of a nongraphitic disordered carbon system and its heat-treatment effects," *Physical Review B*, vol. 67, no. 21, Article ID 214202, 11 pages, 2003.
- [34] K. Kuriyama and M. S. Dresselhaus, "Metal-insulator transition in highly disordered carbon fibers," *Journal of Materials Research*, vol. 7, no. 4, pp. 940–945, 1992.
- [35] J. P. Sullivan, T. A. Friedmann, and A. G. Baca, "Stress relaxation and thermal evolution of film properties in amorphous carbon," *Journal of Electronic Materials*, vol. 26, no. 9, pp. 1021–1029, 1997.
- [36] A. Tibrewala, E. Peiner, R. Bandorf, S. Biehl, and H. Lüthje, "Transport and optical properties of amorphous carbon and hydrogenated amorphous carbon films," *Applied Surface Science*, vol. 252, no. 15, pp. 5387–5390, 2006.
- [37] V. Ambegaokar, B. I. Halperin, and J. S. Langer, "Hopping conductivity in disordered systems," *Physical Review B*, vol. 4, no. 8, pp. 2612–2620, 1971.
- [38] B. Y. Park, L. Taherabadi, C. Wang, J. Zoval, and M. J. Madou, "Electrical properties and shrinkage of carbonized photoresist films and the implications for carbon microelectromechanical systems devices in conductive media," *Journal of the Electrochemical Society*, vol. 152, no. 12, pp. J136–J143, 2005.
- [39] B. A. Samuel, R. Rajagopalan, H. C. Foley, and M. A. Haque, "Temperature effects on electrical transport in semiconducting nanoporous carbon nanowires," *Nanotechnology*, vol. 19, no. 27, Article ID 275702, 2008.
- [40] A. C. Ferrari and J. Robertson, "Interpretation of Raman spectra of disordered and amorphous carbon," *Physical Review B*, vol. 61, no. 20, pp. 14095–14107, 2000.
- [41] A. Takshi, M. Mohammadi, and J. D. Madden, "Study the effect of distribution of density of states on the depletion width of organic Schottky contacts," *Solid-State Electronics*, vol. 52, no. 11, pp. 1717–1721, 2008.

## Research Article

# Fracture Toughness of Carbon Nanotube-Reinforced Metal- and Ceramic-Matrix Composites

Y. L. Chen,<sup>1,2</sup> B. Liu,<sup>1</sup> Y. Huang,<sup>3</sup> and K. C. Hwang<sup>1</sup>

<sup>1</sup>AML, Department of Engineering Mechanics, Tsinghua University, Beijing 100084, China

<sup>2</sup>Department of Mechanical Engineering, The Ohio State University, Columbus, OH 43210, USA

<sup>3</sup>Department of Civil and Environmental Engineering and Department of Mechanical Engineering, Northwestern University, Evanston, IL 60208, USA

Correspondence should be addressed to B. Liu, liubin@tsinghua.edu.cn

Received 15 July 2010; Accepted 1 November 2010

Academic Editor: Teng Li

Copyright © 2011 Y. L. Chen et al. This is an open access article distributed under the Creative Commons Attribution License, which permits unrestricted use, distribution, and reproduction in any medium, provided the original work is properly cited.

Hierarchical analysis of the fracture toughness enhancement of carbon nanotube- (CNT-) reinforced hard matrix composites is carried out on the basis of shear-lag theory and fracture mechanics. It is found that stronger CNT/matrix interfaces cannot definitely lead to the better fracture toughness of these composites, and the optimal interfacial chemical bond density is that making the failure mode just in the transition from CNT pull-out to CNT break. For hard matrix composites, the fracture toughness of composites with weak interfaces can be improved effectively by increasing the CNT length. However, for soft matrix composite, the fracture toughness improvement due to the reinforcing CNTs quickly becomes saturated with an increase in CNT length. The proposed theoretical model is also applicable to short fiber-reinforced composites.

## 1. Introduction

Carbon nanotubes (CNTs) possess exceptionally superior physical and mechanical properties, such as high strength, low density, high flexibility, and high toughness and therefore hold great promise for employment as reinforcements in advanced composites [1–10]. However, experimental and numerical studies show that the performance of such composites depends critically on the CNT/matrix interfacial characteristics [11–13]. Interface strength and interface length are two of the most important factors that affect the mechanical properties of CNT-reinforced composites and therefore have drawn the attention of many researchers.

As a type of extraordinary reinforcements, CNTs can be incorporated in a polymer, metal, or ceramic matrix. The focus of many previous studies in CNT-reinforced composites has been on polymer-matrix materials [14–21], and researchers have tried in various ways, such as nonionic surfactant and ion bombardment [11, 16, 22, 23], to form covalent bonds between CNTs and the polymer matrix to strengthen the interface. In order to know whether longer CNTs and stronger interfaces definitely result in

better mechanical properties of CNT-reinforced composites, Chen et al. [24] studied the fracture toughness enhancement of CNT-reinforced polymer-matrix composites. They found that neither longer reinforcing CNTs nor stronger CNT/matrix interfaces can definitely lead to the better fracture toughness, and the optimal interfacial chemical bond density and the optimal CNT length are those making the failure mode just in the transition from CNT pull-out to CNT break.

Meanwhile, the production and application of CNT-reinforced metal- and ceramic-matrix composites draw more and more attention. Ma and coworkers [25] formed CNT-nano-silicon-carbide (SiC)/ceramic composites and reported a 10% improvement in the strength and fracture toughness as compared to the monolithic ceramics. These modest improvements are attributed to nanotube/matrix debonding and crack deflection. The techniques to form CNT/metal-oxide composites as well as CNT/metal-matrix composites have been developed [26–31]. However, they did not provide the expected improvement in mechanical properties. Is Chen et al.'s conclusion [24] still valid for these hard matrix composites? Is there some difference between the soft matrix

and hard matrix CNT-reinforced composites? This paper will focus on the case with higher matrix stiffness and study the influence factors on the fracture toughness of CNT-reinforced composites.

## 2. Roadmap for Hierarchical Failure Analysis of CNT-Reinforced Composites

In CNT-reinforced composites with macroscopic cracks, the high strength of CNTs can retard crack propagation, and a fracture zone bridged by CNTs at the crack tip is formed, as shown in Figure 1(a). This toughening effect of bridging CNTs is equivalent to that of nonlinear springs connecting the upper and lower crack surfaces, as shown in Figure 1(b). The force-displacement relation for these springs can be obtained by studying the pulling force  $F$  and pull-out displacement  $\delta$  of a single CNT, as in Figure 1(c). This  $F - \delta$  curve depends on the interfacial atomic bond properties, that is, on the interaction between atoms, as shown in Figure 1(d). Therefore, CNT-reinforced composites have three failure mode levels: a bond break at the atomistic level, CNT fiber failure mode at the mesoscopic level, and macroscopic crack propagation at the macroscopic level. To better understand and optimize the toughness of CNT-reinforced composites, this paper presents hierarchical failure analysis. We first adopt shear-lag theory to investigate CNT fiber in Section 3 and then use fracture mechanics to study macroscopic-level failure in Section 4. Our conclusions are summarized in the last section.

## 3. Force-Displacement Relation of a Single CNT Pulled from the Matrix

There are a large number of continuum mechanics studies on the fiber-reinforced composites, especially the widely used shear-lag theory [32–37]. Chon and Sun [33] studied stress distribution along a single reinforcing fiber of a randomly oriented chopped-fiber composite under the assumption of perfect bonding. Lawrence [34] assumed the stiffness of the fiber is lower than that of the matrix and investigated fiber pull-out from an elastic matrix. For ceramic composites, Marshall et al. [35] studied the cracking in brittle matrix. Hutchinson and Jensen [36] treated debonding process as a mode 2 crack to study fiber debonding and pull-out, and based on these studies, Budiansky et al. [37] accounted for an interfacial debonding resistance and studied the effects of debonding and initial stress on overall composite toughness. Many of these models are also applicable to CNT-reinforced composites. However, for the completeness and convenience to readers, the related analysis is still briefly presented in this section.

**3.1. Shear-Lag-Model-Based Stress Analysis of the CNT and Matrix.** According to the shear-lag theory, the interaction between the CNTs and the matrix that results from the chemical bonds shown in Figure 2 is shear stress, which is related to the relative displacement between the CNT fiber and the matrix  $\Delta u$ . A bond break occurs when  $\Delta u$  reaches

the critical shear displacement  $\delta_b$ , which depends only on the type of functionalization bond at the interface, whereas the corresponding interface strength  $\tau_b$  also depends on the interface bond density. The interface shear stress  $\tau$  is assumed to be proportional to the relative displacement  $\Delta u$ , that is,

$$\tau(x) = k\Delta u(x) = k[u_m(x) - u_f(x)], \quad (1)$$

where  $k = \tau_b/\delta_b$  is the shear stiffness of the interface and  $u_m(x)$  and  $u_f(x)$  are the axial or  $x$ -direction displacements of the matrix and the CNT fiber, respectively.

Suppose the CNT and the matrix are both linear elastic, with Young's modulus  $E_f$  and  $E_m$ , respectively. A representative volume element (RVE) including a single CNT with embedded length  $L$  and diameter  $d$ , as shown in Figure 2, is adopted for analysis. With the balance conditions of the fiber and the matrix, the shear stress distribution can be derived [24]

$$\tau(x) = F \sqrt{\frac{\tau_b}{C\delta_b}} \cdot \frac{1/(E_m A_m) \cosh(x\sqrt{C\tau_b/\delta_b})}{\sinh(L\sqrt{C\tau_b/\delta_b})} + \frac{1/(E_f A_f) \cosh[(x-L)\sqrt{C\tau_b/\delta_b}]}{\sinh(L\sqrt{C\tau_b/\delta_b})}, \quad (2)$$

where  $A_f$  and  $A_m$  are the cross-section areas of the CNT and the matrix in the RVE,  $F$  is the pulling force, and  $C$  depends on the material constants and geometry parameters as

$$C = \pi d \left( \frac{1}{E_f A_f} + \frac{1}{E_m A_m} \right). \quad (3)$$

The distribution of the axial normal stress in the CNT can also be derived as

$$\sigma(x) = \frac{1}{A_f} \left[ F - \int_0^x \pi d \tau(x) dx \right]. \quad (4)$$

**3.2. Critical Pull-Out/Break Condition of CNTs.** The two main fiber-level failure modes are usually interfacial debonding and fiber break, depending on the interfacial shear stress and the axial normal stress, respectively. When the composite is under increasing tension, both the shear stress on the interface and the axial normal stress in the CNT increase.

**3.2.1. Critical Condition for CNT Fiber Break.** Obviously, the maximum axial normal stress in the CNT is located at position  $x = 0$  and can be expressed as

$$\sigma(x)|_{\max} = \sigma(0) = \frac{F}{A_f}. \quad (5)$$

CNT break occurs when the maximum axial normal stress reaches CNT strength  $\sigma_f^b$ , and the corresponding critical pulling force is

$$F_{\max}^{\sigma} = \sigma_f^b A_f. \quad (6)$$

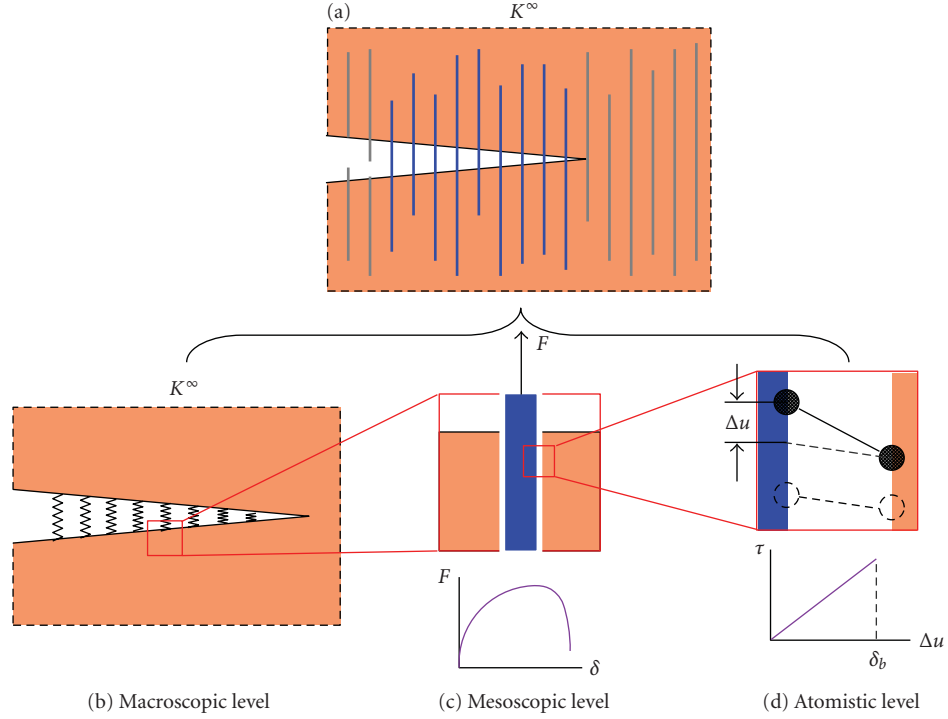


FIGURE 1: Schematic diagram of three-level failure analysis models. (a) Fracture zone bridged with CNTs at the crack tip. (b) Macroscopic-level model with equivalent bridging nonlinear springs. (c) Mesoscopic-level model for studying CNT-fiber failure and obtaining the force-displacement relation of equivalent nonlinear spring. (d) Atomistic-level failure model for characterizing CNT/matrix interfacial bond breaking.

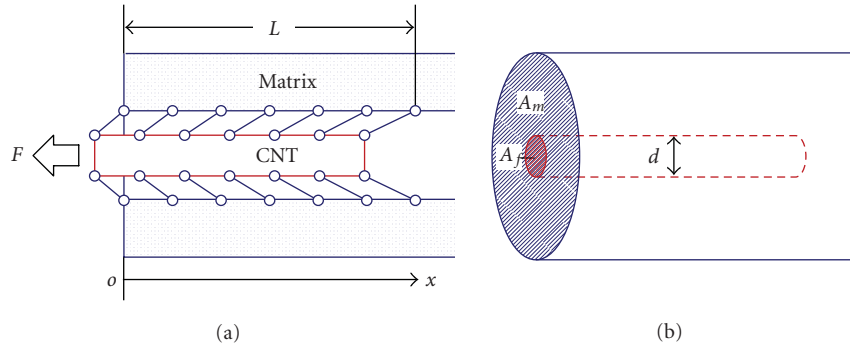


FIGURE 2: Schematic diagram of shear-lag model for the interactions between the CNT and the matrix (a), and the geometric parameters (b).

**3.2.2. Critical Condition for Interfacial Debonding.** According to (2), the maximum shear stress on the interface may appear at either  $x = 0$  for  $E_f A_f < E_m A_m$  or  $x = L$  for  $E_f A_f > E_m A_m$ . In CNT/polymer composites, the stiffness of the CNT is usually greater than that of the matrix, that is,  $E_f A_f > E_m A_m$ , as Chen et al. have previously discussed in [24], but in metal- and ceramic-matrix composites Young's modulus of the matrix is close to that of the CNTs, so the stiffness of the CNT is less than that of the matrix, that is,  $E_f A_f < E_m A_m$ . The current paper is focused on this hard matrix regime and sometimes also presents the results of soft matrix regime for comparison.

(1)  $E_f A_f < E_m A_m$  Case (Hard Matrix). From (2), the maximum shear stress on the interface can be found at the  $x = 0$  position, and

$$\begin{aligned} \tau(x)|_{\max} &= \tau(0) \\ &= F \sqrt{\frac{\tau_b}{C \delta_b}} \\ &\cdot \frac{1/(E_m A_m) + 1/(E_f A_f) \cosh(L\sqrt{C\tau_b/\delta_b})}{\sinh(L\sqrt{C\tau_b/\delta_b})}. \end{aligned} \quad (7)$$

The corresponding critical pulling force is

$$F_{\max}^{\tau 0} = \frac{\sqrt{C\tau_b\delta_b} \sinh(L\sqrt{C\tau_b/\delta_b})}{1/(E_m A_m) + 1/(E_f A_f) \cosh(L\sqrt{C\tau_b/\delta_b})}. \quad (8)$$

Together with (6) and (8), the transition condition between the pull-out and break failure modes is

$$\frac{\sigma_f^b A_f}{\sqrt{C\tau_b\delta_b}} \frac{1/(E_m A_m) + 1/(E_f A_f) \cosh(L\sqrt{C\tau_b/\delta_b})}{\sinh(L\sqrt{C\tau_b/\delta_b})} > 1 \quad (\text{interfacial debonding}), \quad (9)$$

$$\frac{\sigma_f^b A_f}{\sqrt{C\tau_b\delta_b}} \frac{1/(E_m A_m) + 1/(E_f A_f) \cosh(L\sqrt{C\tau_b/\delta_b})}{\sinh(L\sqrt{C\tau_b/\delta_b})} < 1 \quad (\text{CNT fiber breaking}),$$

that is, a weak interface results in interfacial debonding and fiber pull-out, whereas a strong interface leads to fiber break.

(2)  $E_f A_f > E_m A_m$  Case (Soft Matrix). The most important difference from the hard matrix case (i.e.,  $E_f A_f < E_m A_m$ ) is that the maximum shear stress on the interface is found at the  $x = L$  position, so the critical pulling force is [24]

$$F_{\max}^{\tau L} = \frac{\sqrt{C\tau_b\delta_b} \sinh(L\sqrt{C\tau_b/\delta_b})}{1/(E_m A_m) \cosh(L\sqrt{C\tau_b/\delta_b}) + 1/(E_f A_f)}, \quad (10)$$

and the transition condition between the pull-out and break failure modes is [24]

$$\frac{\sigma_f^b A_f}{\sqrt{C\tau_b\delta_b}} \frac{1/(E_m A_m) \cosh(L\sqrt{C\tau_b/\delta_b}) + 1/(E_f A_f)}{\sinh(L\sqrt{C\tau_b/\delta_b})} > 1 \quad \text{interfacial debonding}, \quad (11)$$

$$\frac{\sigma_f^b A_f}{\sqrt{C\tau_b\delta_b}} \frac{1/(E_m A_m) \cosh(L\sqrt{C\tau_b/\delta_b}) + 1/(E_f A_f)}{\sinh(L\sqrt{C\tau_b/\delta_b})} < 1 \quad \text{CNT fiber breaking}.$$

**3.3. Relation between Pulling Force and Pull-Out Displacement.** For different possible failure modes, there are three types of  $F - \delta$  curves, as shown in Figures 3(a), 3(b), and 3(c). Here,  $F$  is the pulling force, and  $\delta = \Delta u(0)$  is the pull-out displacement. The corresponding relations are given as below.

**3.3.1. CNT Break Case.** The  $F - \delta$  relation can be obtained as

$$F = \begin{cases} \delta \sqrt{\frac{C\tau_b}{\delta_b}} \cdot \frac{E_f A_f \sinh(L\sqrt{C\tau_b/\delta_b})}{\cosh(L\sqrt{C\tau_b/\delta_b}) + 1/\alpha}, & 0 \leq \delta \leq \delta_C^\sigma, \\ 0, & \delta > \delta_C^\sigma, \end{cases} \quad (12)$$

where  $\alpha = E_m A_m / (E_f A_f)$  is the stiffness ratio of the matrix to the CNT, and

$$\delta_C^\sigma = \sigma_f^b \sqrt{\frac{\delta_b}{C\tau_b}} \cdot \frac{\cosh(L\sqrt{C\tau_b/\delta_b}) + 1/\alpha}{E_f \sinh(L\sqrt{C\tau_b/\delta_b})}. \quad (13)$$

**3.3.2. Interface Debonding from the End of Pulling Force (Hard Matrix).** If  $E_f A_f < E_m A_m$ , the interface begins to debond at the  $x = 0$  position where the relative displacement reaches  $\delta_b$ . So the critical pull-out displacement for the interfacial debonding case is

$$\delta_C^{\tau 0} = \delta_b. \quad (14)$$

At this time, the relative displacement at the  $x = L$  position is  $\delta_b \cdot (1/\alpha)(1 + (\alpha^2 - 1)/(\alpha \cosh(L\sqrt{C\tau_b/\delta_b}) + 1))$ , which is less than  $\delta_b$ , so the interface is not debonded completely and can still stand some degree of shear stress. After this point, the  $F - \delta$  curve decreases until the interface debonds completely. In the process of debonding, the CNT and the matrix can be analyzed as a similar system but with a shorter interface length  $L_2$  ( $L_2 < L$ ). Both the pulling force  $F$  and the pull-out displacement  $\delta$  are dependent on the new interface length  $L_2$  as follows:

$$F(L_2) = \sqrt{C\tau_b\delta_b} \cdot \frac{E_f A_f \sinh(L_2\sqrt{C\tau_b/\delta_b})}{\cosh(L_2\sqrt{C\tau_b/\delta_b}) + 1/\alpha},$$

$$\delta(L_2) = \delta_b + (L - L_2) \left( \sqrt{C\tau_b\delta_b} \cdot \frac{\sinh(L_2\sqrt{C\tau_b/\delta_b})}{\cosh(L_2\sqrt{C\tau_b/\delta_b}) + 1/\alpha} \right). \quad (15)$$

Getting rid of  $L_2$  from the above two equations, we can get the relation between the pulling force  $F$  and the pull-out displacement  $\delta$  after the beginning of interface debonding as

$$\delta = \delta_b + \left\{ L - \sqrt{\frac{\delta_b}{C\tau_b}} \ln \left[ \frac{F + \sqrt{F^2 + \alpha^2 (C\tau_b\delta_b E_f^2 A_f^2 - F^2)}}{\alpha (E_f A_f \sqrt{C\tau_b\delta_b} - F)} \right] \right\} \times \left( \frac{F}{E_f A_f} \right). \quad (16)$$

So the relation between the pulling force  $F$  and the relative displacement  $\delta$  is

$$F = \begin{cases} \delta \sqrt{\frac{C\tau_b}{\delta_b}} \cdot \frac{E_f A_f \sinh(L\sqrt{C\tau_b/\delta_b})}{\cosh(L\sqrt{C\tau_b/\delta_b}) + 1/\alpha}, & 0 \leq \delta \leq \delta_b, \\ F_{\text{soften}}(\delta), & \delta_b < \delta \leq \delta_{\max}, \end{cases} \quad (17)$$

where  $F_{\text{soften}}(\delta)$  is solved from (16) and the maximum pull-out displacement  $\delta_{\max}$  is determined by

$$\frac{\partial \delta(L_2)}{\partial L_2} = 0. \quad (18)$$

This process is shown in Figure 3(b), and the critical point ( $\delta_C^{r0}$ ,  $F_{\max}^{r0}$ ) is given by (14) and (8), respectively. It is interesting to notice that after the initial debonding at  $x = 0$ , the interface first debonds gradually and steadily, with the gradual decreasing pulling force, but when the pull-out displacement reaches  $\delta_{\max}$ , the whole bonding interface debonds simultaneously and the pulling force drops down to zero suddenly.

3.3.3. *Interface Debonding from the End Away from Pulling Force (Soft Matrix)*. As discussed by Chen et al. in [24], if  $E_f A_f > E_m A_m$ , the  $F - \delta$  relation is

$$F = \begin{cases} \delta \sqrt{\frac{C\tau_b}{\delta_b}} \cdot \frac{E_f A_f \sinh(L\sqrt{C\tau_b/\delta_b})}{\cosh(L\sqrt{C\tau_b/\delta_b}) + 1/\alpha}, & 0 \leq \delta \leq \delta_C^{rL}, \\ E_m A_m \sqrt{\frac{C\tau_b}{\delta_b} \left( \frac{\delta_b^2 - \delta^2}{1 - \alpha^2} \right)}, & \delta_C^{rL} < \delta \leq \delta_b, \end{cases} \quad (19)$$

where

$$\delta_C^{rL} = \delta_b \cdot \left( \alpha + \frac{1 - \alpha^2}{\cosh(L\sqrt{C\tau_b/\delta_b}) + \alpha} \right). \quad (20)$$

The  $F - \delta$  curve is shown in Figure 3(c), and the critical point ( $\delta_C^{rL}$ ,  $F_{\max}^{rL}$ ) is given by (20) and (10), respectively. Different from the other debonding case in Section 3.3.2, the interface debonds gradually and steadily, until it goes down to zero.

## 4. Macroscopic-Level Fracture Failure Analysis

4.1. *Fracture Toughness Enhancement  $\Delta K$* . In CNT-reinforced composites, crack propagation is retarded by the pulling force of the CNTs at the crack surface, the so-called “bridge-toughening effect.” The displacement of the crack surface (i.e., half of the crack opening displacement) is [38]

$$\delta = \frac{2(1 - \nu_m^2)K_{IC}}{E_m} \sqrt{\frac{2r}{\pi}} = \eta K_{IC} \sqrt{r}, \quad (21)$$

where  $r$  is the distance to the crack tip and  $\eta = 2\sqrt{2}(1 - \nu_m^2)/(E_m\sqrt{\pi})$  depends only on Young's modulus  $E_m$  and Poisson's ratio  $\nu_m$ . According to (12), (17), and (19), for all different types of failure modes, the pulling force  $F(\delta)$  can be expressed as a function of the distance to the macroscopic crack tip  $r$ , that is,  $F(\delta) = F(\delta(r)) = F(r)$ . The homogenized traction on the crack surface is then

$$p(r) = F(r)(A_f + A_m)^{-1}, \quad (22)$$

and the fracture toughness enhancement  $\Delta K$  can be computed as [39]

$$\Delta K = \int_0^\infty \frac{\sqrt{2}p(r)}{\sqrt{\pi r}} dr. \quad (23)$$

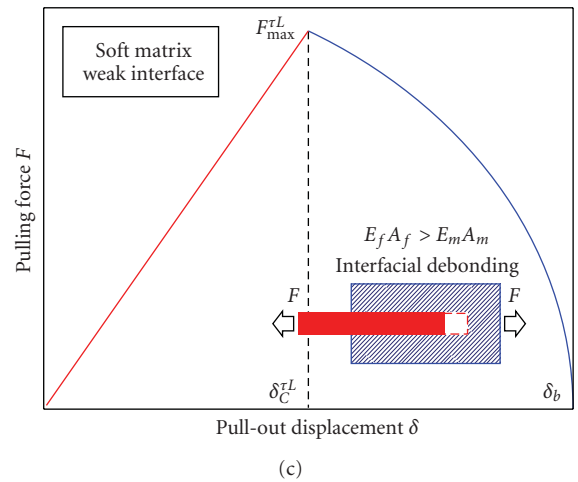
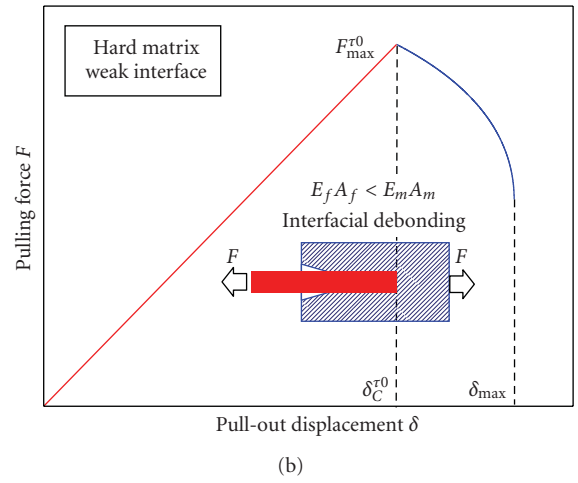
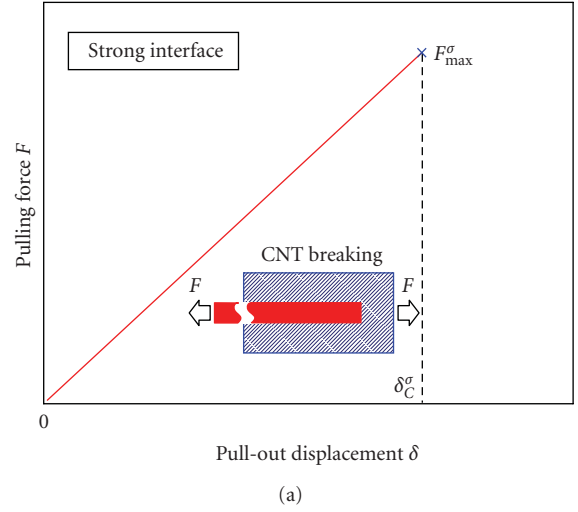


FIGURE 3: The relation between the pulling force and the pull-out displacement for the three CNT-fiber failure modes (a) CNT breaking, (b) interface failure with partial steady debonding when  $E_f A_f < E_m A_m$ , and (c) interface failure with steady debonding when  $E_f A_f > E_m A_m$ .

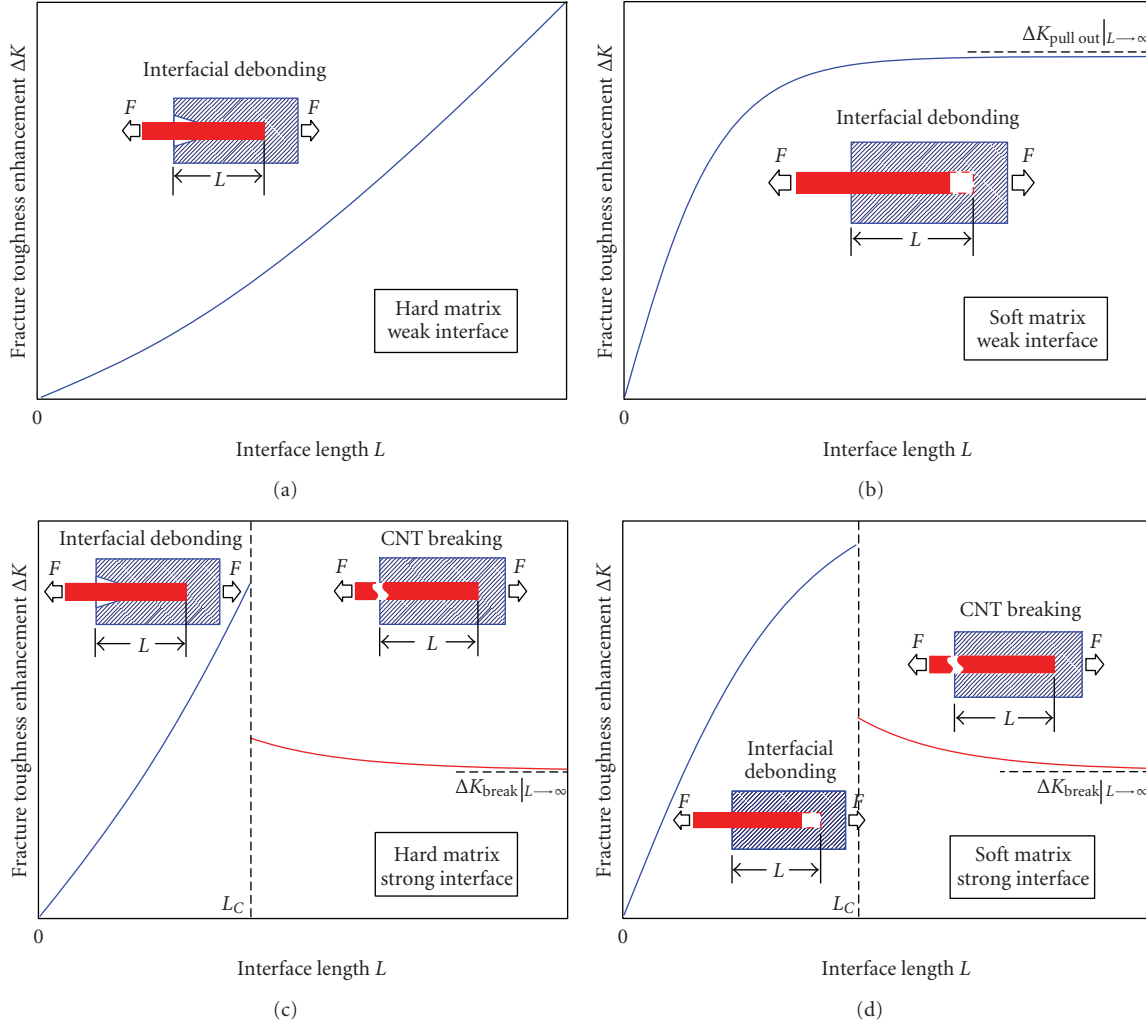


FIGURE 4: Schematic diagram for the effect of the interface length on the fracture toughness enhancement: (a) hard matrix, weak interface  $\tau_b < (\sigma_f^b)^2 / (CE_f^2 \delta_b)$ . (b) soft matrix, weak interface  $\tau_b < (C\sigma_f^b A_f)^2 / (E_m^2 A_m^2 \delta_b)$ . (c) hard matrix, strong interface  $\tau_b > (\sigma_f^b)^2 / (CE_f^2 \delta_b)$ ; (d) soft matrix, strong interface  $\tau_b > (C\sigma_f^b A_f)^2 / (E_m^2 A_m^2 \delta_b)$ .

4.2. Factors Affecting the Fracture Toughness Enhancement  $\Delta K$ . For the case of hard matrix ( $E_f A_f < E_m A_m$ ), the factors affecting the fracture toughness enhancement  $\Delta K$  are discussed below, and some results of soft matrix regime in [24] are also presented briefly for comparison.

4.2.1. Effect of Interface Length  $L$ . From the pull-out/break critical condition (9), we know that if  $\tau_b < (\sigma_f^b)^2 / (CE_f^2 \delta_b)$ , the failure mode should always be the CNT pull-out, as shown in Figure 4(a). In this case, the fracture toughness enhancement  $\Delta K$  increases with an increase in the interface length  $L$  infinitely. This phenomenon is different from the case of weak interface in the soft matrix CNT-reinforced composites shown in Figure 4(b), in which an upper limit of the fracture toughness enhancement exists so any further lengthening of the CNTs improves the fracture toughness of the composites only slightly [24].

For the case with strong interface  $\tau_b > (\sigma_f^b)^2 / (CE_f^2 \delta_b)$ , as shown in Figure 4(c), a critical length  $L_C$  exists and can be determined from the pull-out/break critical condition (9):

$$L_C = \sqrt{\frac{\delta_b}{C\tau_b}} \ln \frac{\sigma_f^b + \sqrt{C\tau_b \delta_b (\alpha E_f)^2 - (\sigma_f^b)^2 (\alpha^2 - 1)}}{\alpha (E_f \sqrt{C\tau_b \delta_b} - \sigma_f^b)}. \quad (24)$$

When  $L < L_C$ , the CNT is pulled out, and the fracture toughness enhancement  $\Delta K$  increases with an increase in the interface length  $L$ . If  $L$  is further increased beyond the critical length  $L_C$ , the failure mode is converted from CNT pull-out to CNT break and  $\Delta K$  drops significantly. In this regime, the fracture toughness enhancement  $\Delta K$  decreases with an increase in  $L$  and finally approaches the following value:

$$\Delta K_{\text{break}} |_{L \rightarrow \infty} = \sqrt{\frac{2\delta_b}{\pi C\tau_b}} \frac{(\sigma_f^b)^2 A_f}{(A_f + A_m) \eta K_{IC} E_f}. \quad (25)$$

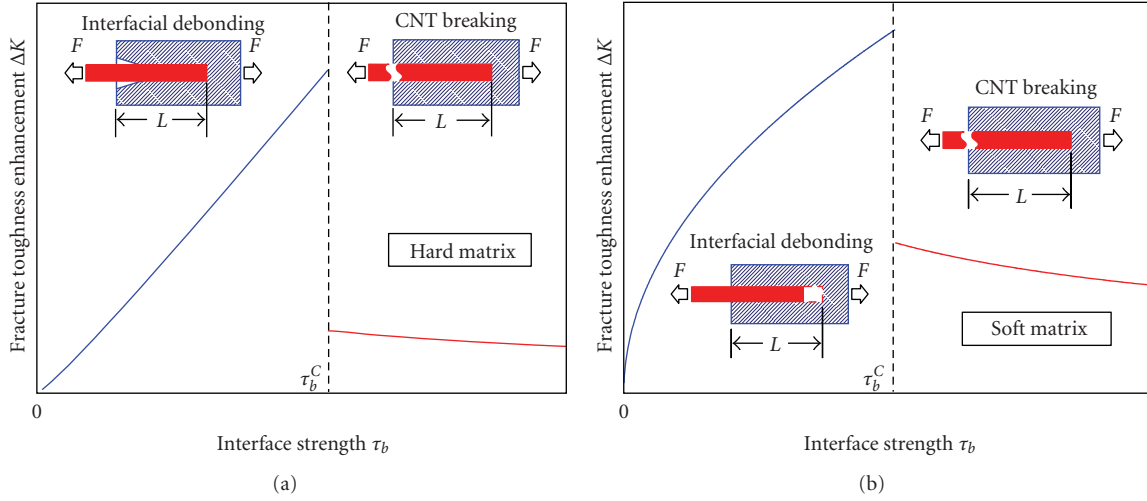


FIGURE 5: Schematic diagram for the effect of the interface strength on the fracture toughness enhancement: (a) hard matrix; (b) soft matrix.

It is interesting to note that, in this case, lengthening the interface beyond the critical length can even decrease the fracture toughness, which is very similar to the result shown in Figure 4(d) for the soft matrix CNT-reinforced composites [24].

**4.2.2. Effect of Interface Strength  $\tau_b$ .** Another important factor affecting the toughness enhancement is interface strength  $\tau_b$ , and its effect is shown in Figure 5(a). When  $\tau_b$  is small, the failure mode is CNT pull-out, and the fracture toughness enhancement  $\Delta K$  increases with an increase in  $\tau_b$ . Further increasing  $\tau_b$  beyond the critical interface strength  $\tau_b^c$ , which can be determined by the pull-out/break critical condition (9), leads the failure mode to be converted from CNT pull-out to CNT break, and  $\Delta K$  drops significantly. In this regime, the toughness enhancement  $\Delta K$  decreases with an increase in  $\tau_b$ . This result agrees with the experimental and numerical studies of Xia et al.'s work on ceramic-matrix composites [40, 41], as well as the theoretical studies for soft matrix CNT-reinforced composites in Figure 5(b) [24]. Therefore, for CNTs with a given length, the maximum fracture toughness of the composite is achieved when  $\tau_b$  is only slightly smaller than the critical interface strength  $\tau_b^c$ .

**4.3. Optimization of Fracture Toughness Enhancement.** In this subsection, we attempt to optimize the composite fracture toughness for the case of  $E_f A_f < E_m A_m$  by tailoring both the interface length  $L$  and interface strength  $\tau_b$ , which is essentially a bivariate optimization problem. For convenience, we use another group of variables, normalized interface length  $\hat{L} = L\sqrt{C\tau_b/\delta_b}$  and  $\tau_b$ , instead. According to (9), the maximum  $\Delta K$  with a given  $\hat{L}$  can be achieved when

$$\tau_b = \tau_b^{\text{optimal}}(\hat{L}) = \left( \frac{\sigma_f^b A_f}{E_m A_m} \frac{1 + \alpha \cosh(\hat{L})}{\sinh(\hat{L})} \right)^2 / (C\delta_b). \quad (26)$$

Figure 6 shows the normalized fracture toughness enhancement  $\Delta\hat{K} = \Delta K \cdot (A_f + A_m)\eta K_{IC}/\sigma_f^b A_f \delta_b$  versus  $\hat{L}$  for

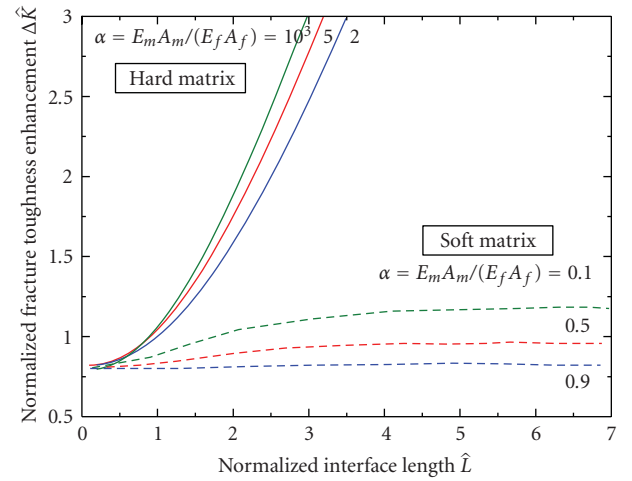


FIGURE 6: The normalized fracture toughness enhancement  $\Delta\hat{K}$  as a function of the normalized interface length  $\hat{L}$  with different stiffness ratio  $\alpha = E_m A_m / (E_f A_f)$  and optimal interface strength.

cases with different stiffness ratios:  $\alpha = E_m A_m / (E_f A_f)$ . It is found that when  $\hat{L} \rightarrow \infty$ ,  $\Delta\hat{K}$  reaches an infinite value. And according to (26), the corresponding optimal interface strength is

$$\tau_b^{\text{optimal}} \Big|_{\hat{L} \rightarrow \infty} = \frac{\alpha (\sigma_f^b)^2 A_f}{\pi d \delta_b E_f (\alpha + 1)}. \quad (27)$$

This result is different from the case of  $E_f A_f > E_m A_m$  studied by Chen et al. [24], which presents the upper limit of the fracture toughness enhancement, as shown in Figure 6 with the dashed lines. When  $E_f A_f < E_m A_m$ , the value of the dimensionless fracture toughness enhancement  $\Delta\hat{K}$  increases with  $\hat{L}$  unlimitedly, as shown in Figure 6 by the solid lines. So, there is neither upper limit for  $\Delta\hat{K}$  nor optimal value for the CNT length  $L$ . The optimal CNT length  $L$  can only depend

on the preparation level and some other factors such as the critical CNT length for clustering and self-folding [42].

## 5. Conclusions

Combining the shear-lag model and fracture mechanics, we have carried out the hierarchical failure analysis on CNT-reinforced composites with hard matrix. The following conclusions have been reached.

(1) Stronger CNT/matrix interfaces cannot definitely lead to a better fracture toughness of these composites. In contrast, the optimal interfacial chemical bond density is that making the failure mode just in the transition from CNT pull-out to CNT break.

(2) For composites with hard matrix, there exists a critical interface strength, below which the CNT is always pulled out, and the fracture toughness can be effectively improved by increasing the interface length  $L$ . However, for soft matrix composite, the fracture toughness improvement due to the reinforcing CNTs quickly becomes saturated with an increase in CNT length.

It should be noted that the theoretical analysis and conclusions drawn in this paper can also be extended to fiber-reinforced composites.

## Acknowledgments

The authors acknowledge the support of the National Natural Science Foundation of China (Grant nos. 10702034, 10732050, 90816006 and 10820101048) and the National Basic Research Program of China (973 Program), Grant nos. 2007CB936803 and 2010CB832701.

## References

- [1] M. M. J. Treacy, T. W. Ebbesen, and J. M. Gibson, "Exceptionally high Young's modulus observed for individual carbon nanotubes," *Nature*, vol. 381, no. 6584, pp. 678–680, 1996.
- [2] E. W. Wong, P. E. Sheehan, and C. M. Lieber, "Nanobeam mechanics: elasticity, strength, and toughness of nanorods and nanotubes," *Science*, vol. 277, no. 5334, pp. 1971–1975, 1997.
- [3] M.-F. Yu, O. Lourie, M. J. Dyer, K. Moloni, T. F. Kelly, and R. S. Ruoff, "Strength and breaking mechanism of multiwalled carbon nanotubes under tensile load," *Science*, vol. 287, no. 5453, pp. 637–640, 2000.
- [4] B. Vigolo, A. Penicaud, C. Coulon et al., "Macroscopic fibers and ribbons of oriented carbon nanotubes," *Science*, vol. 290, no. 5495, pp. 1331–1334, 2000.
- [5] B. I. Yakobson, M. P. Campbell, C. J. Brabec, and J. Bernholc, "High strain rate fracture and C-chain unraveling in carbon nanotubes," *Computational Materials Science*, vol. 8, no. 4, pp. 341–348, 1997.
- [6] G. Gao, T. Çağın, and W. A. Goddard III, "Energetics, structure, mechanical and vibrational properties of single-walled carbon nanotubes," *Nanotechnology*, vol. 9, no. 3, pp. 184–191, 1998.
- [7] Y. L. Chen, B. Liu, J. Wu, Y. Huang, H. Jiang, and K. C. Hwang, "Mechanics of hydrogen storage in carbon nanotubes," *Journal of the Mechanics and Physics of Solids*, vol. 56, no. 11, pp. 3224–3241, 2008.
- [8] Y. Yin, Y. L. Chen, J. Yin, and K. Huang, "Geometric conservation laws for Y-branched carbon nanotubes," *Nanotechnology*, vol. 17, pp. 1–5, 2006.
- [9] Y.-L. Chen, B. Liu, Y.-J. Yin, Y.-G. Huang, and K.-C. Hwang, "Nonlinear deformation processes and damage modes of super carbon nanotubes with armchair-armchair topology," *Chinese Physics Letters*, vol. 25, no. 7, pp. 2577–2580, 2008.
- [10] Y. Chen, Y. Yin, Y. Huang, and K.-C. Hwang, "Atomistic simulations of the nonlinear deformation and damage modes of super carbon nanotubes," *Journal of Computational and Theoretical Nanoscience*, vol. 6, no. 1, pp. 41–45, 2009.
- [11] F. H. Gojny, J. Nastalczyk, Z. Roslaniec, and K. Schulte, "Surface modified multi-walled carbon nanotubes in CNT/epoxy-composites," *Chemical Physics Letters*, vol. 370, no. 5-6, pp. 820–824, 2003.
- [12] S. J. V. Frankland, A. Caglar, D. W. Brenner, and M. Griebel, "Molecular simulation of the influence of chemical cross-links on the shear strength of carbon nanotube-polymer interfaces," *Journal of Physical Chemistry B*, vol. 106, no. 12, pp. 3046–3048, 2002.
- [13] S. J. V. Frankland and V. M. Harik, "Analysis of carbon nanotube pull-out from a polymer matrix," *Surface Science*, vol. 525, no. 1–3, pp. L103–L108, 2003.
- [14] P. M. Ajayan, O. Stephan, C. Colliex, and D. Trauth, "Aligned carbon nanotube arrays formed by cutting a polymer resin-nanotube composite," *Science*, vol. 265, no. 5176, pp. 1212–1214, 1994.
- [15] M. S. P. Shaffer and A. H. Windle, "Fabrication and characterization of carbon nanotube/poly(vinyl alcohol) composites," *Advanced Materials*, vol. 11, no. 11, pp. 937–941, 1999.
- [16] X. Gong, J. Liu, S. Baskaran, R. D. Voise, and J. S. Young, "Surfactant-assisted processing of carbon nanotube/polymer composites," *Chemistry of Materials*, vol. 12, no. 4, pp. 1049–1052, 2000.
- [17] S. Kumar, H. Doshi, M. Srinivasarao, J. O. Park, and D. A. Schiraldi, "Fibers from polypropylene/nano carbon fiber composites," *Polymer*, vol. 43, no. 5, pp. 1701–1703, 2002.
- [18] X. Tong, X.-J. He, and H.-M. Cheng, "Effect of carbon nanotubes on mechanical properties and crystallization process of high density polyethylene," *New Carbon Materials*, vol. 19, no. 4, pp. 261–267, 2004.
- [19] D. Qian, E. C. Dickey, R. Andrews, and T. Rantell, "Load transfer and deformation mechanisms in carbon nanotube-polystyrene composites," *Applied Physics Letters*, vol. 76, no. 20, pp. 2868–2870, 2000.
- [20] C. Bower, R. Rosen, L. Jin, J. Han, and O. Zhou, "Deformation of carbon nanotubes in nanotube-polymer composites," *Applied Physics Letters*, vol. 74, no. 22, pp. 3317–3319, 1999.
- [21] P. M. Ajayan, L. S. Schadler, C. Giannaris, and A. Rubio, "Single-walled carbon nanotube-polymer composites: strength and weakness," *Advanced Materials*, vol. 12, no. 10, pp. 750–753, 2000.
- [22] B. Ni and S. B. Sinnott, "Tribological properties of carbon nanotube bundles predicted from atomistic simulations," *Surface Science*, vol. 487, no. 1–3, pp. 87–96, 2001.
- [23] Y. Hu, I. Jang, and S. B. Sinnott, "Modification of carbon nanotube-polystyrene matrix composites through polyatomic-ion beam deposition: predictions from molecular dynamics simulations," *Composites Science and Technology*, vol. 63, no. 11, pp. 1663–1669, 2003.
- [24] Y. L. Chen, B. Liu, X. Q. He, Y. Huang, and K. C. Hwang, "Failure analysis and the optimal toughness design of carbon nanotube-reinforced composites," *Composites Science and Technology*, vol. 70, no. 9, pp. 1360–1367, 2010.

- [25] R. Z. Ma, J. Wu, B. Q. Wei, J. Liang, and D. H. Wu, "Processing and properties of carbon nanotubes-nano-SiC ceramic," *Journal of Materials Science*, vol. 33, no. 21, pp. 5243–5246, 1998.
- [26] E. Flahaut, A. Peigney, CH. Laurent, CH. Marlière, F. Chastel, and A. Rousset, "Carbon nanotube-metal-oxide nanocomposites: microstructure, electrical conductivity and mechanical properties," *Acta Materialia*, vol. 48, no. 14, pp. 3803–3812, 2000.
- [27] A. Peigney, C. Laurent, O. Dumortier, and A. Rousset, "Carbon nanotubes-Fe-alumina nanocomposites. Part I: influence of the Fe content on the synthesis of powders," *Journal of the European Ceramic Society*, vol. 18, no. 14, pp. 1995–1104, 1998.
- [28] C. Laurent, A. Peigney, O. Dumortier, and A. Rousset, "Carbon nanotubes-Fe-Alumina nanocomposites. Part II: microstructure and mechanical properties of the hot-Pressed composites," *Journal of the European Ceramic Society*, vol. 18, no. 14, pp. 2005–2013, 1998.
- [29] A. Peigney, CH. Laurent, and A. Rousset, "Synthesis and characterization of alumina matrix nanocomposites containing carbon nanotubes," *Key Engineering Materials*, no. 136, pp. 743–746, 1997.
- [30] X. Chen, J. Xia, J. Peng, W. Li, and S. Xie, "Carbon-nanotube metal-matrix composites prepared by electroless plating," *Composites Science and Technology*, vol. 60, no. 2, pp. 301–306, 2000.
- [31] C. L. Xu, B. Q. Wei, R. Z. Ma, J. Liang, X. K. Ma, and D. H. Wu, "Fabrication of aluminum-carbon nanotube composites and their electrical properties," *Carbon*, vol. 37, no. 5, pp. 855–858, 1999.
- [32] H. L. Cox, "The elasticity and strength of paper and other fibrous materials," *British Journal of Applied Physics*, vol. 3, no. 1, pp. 72–79, 1952.
- [33] C. T. Chon and C. T. Sun, "Stress distributions along a short fibre in fibre reinforced plastics," *Journal of Materials Science*, vol. 15, no. 4, pp. 931–938, 1980.
- [34] P. Lawrence, "Some theoretical considerations of fibre pull-out from an elastic matrix," *Journal of Materials Science*, vol. 7, no. 1, pp. 1–6, 1972.
- [35] D. B. Marshall, B. N. Cox, and A. G. Evans, "The mechanics of matrix cracking in brittle-matrix fiber composites," *Acta Metallurgica*, vol. 33, no. 11, pp. 2013–2021, 1985.
- [36] J. W. Hutchinson and H. M. Jensen, "Models of fiber debonding and pullout in brittle composites with friction," *Mechanics of Materials*, vol. 9, no. 2, pp. 139–163, 1990.
- [37] B. Budiansky, A. G. Evans, and J. W. Hutchinson, "Fiber-matrix debonding effects on cracking in aligned fiber ceramic composites," *International Journal of Solids and Structures*, vol. 32, no. 3-4, pp. 315–328, 1995.
- [38] T. L. Anderson, *Fracture Mechanics: Fundamentals and Applications*, CRC Press LLC, Boca Raton, Fla, USA, 1995.
- [39] H. Tada, P. C. Paris, and G R. Irwin, *The Stress Analysis of Cracks Handbook*, ASME Press, New York, NY, USA, 3rd edition, 2000.
- [40] Z. Xia, L. Riester, W. A. Curtin et al., "Direct observation of toughening mechanisms in carbon nanotube ceramic matrix composites," *Acta Materialia*, vol. 52, no. 4, pp. 931–944, 2004.
- [41] Z. Xia and W. A. Curtin, "Tough-to-brittle transitions in ceramic-matrix composites with increasing interfacial shear stress," *Acta Materialia*, vol. 48, no. 20, pp. 4879–4892, 2000.
- [42] W. Zhou, Y. Huang, B. Liu et al., "Self-folding of single- and multiwall carbon nanotubes," *Applied Physics Letters*, vol. 90, no. 7, Article ID 73107, 2007.

## Research Article

# Size Dependence of the Nonlinear Elastic Softening of Nanoscale Graphene Monolayers under Plane-Strain Bulge Tests: A Molecular Dynamics Study

Sukky Jun,<sup>1</sup> Tenzin Tashi,<sup>1</sup> and Harold S. Park<sup>2</sup>

<sup>1</sup>Department of Mechanical Engineering, University of Wyoming, Laramie, WY 82071, USA

<sup>2</sup>Department of Mechanical Engineering, Boston University, Boston, MA 02215, USA

Correspondence should be addressed to Sukky Jun, sjun@uwyo.edu

Received 28 May 2010; Accepted 19 October 2010

Academic Editor: Sulin Zhang

Copyright © 2011 Sukky Jun et al. This is an open access article distributed under the Creative Commons Attribution License, which permits unrestricted use, distribution, and reproduction in any medium, provided the original work is properly cited.

The pressure bulge test is an experimental technique to characterize the mechanical properties of microscale thin films. Here, we perform constant-temperature molecular dynamics simulations of the plane-strain cylindrical bulge test of nanosized monolayer graphene subjected to high gas pressure induced by hydrogen molecules. We observe a nonlinear elastic softening of the graphene with an increase in hydrogen pressure due to the stretching and weakening of the carbon-carbon bonds; we further observe that this softening behavior depends upon the size of the graphene monolayers. Our simulation results suggest that the traditional microscale bulge formulas, which assume constant elastic moduli, should be modified to incorporate the size dependence and elastic softening that occur in nanosized graphene bulge tests.

## 1. Introduction

Along with the indentation hardness test, the pressure bulge test has been one of the popular experimental techniques to characterize the mechanical properties of microscale thin films [1]. Recently, Bunch et al. [2] applied the bulge test technique to a graphene monolayer, or a one-atom-thick two-dimensional crystalline sheet of carbon atoms, in order to predict its elastic behavior, while Lee et al. [3] measured the elastic properties and intrinsic breaking strength of free-standing monolayer graphene membranes by nanoindentation in an atomic force microscope. Both experimental studies employed graphene membranes with dimensions on the order of a few microns. On the other hand, molecular dynamics (MD) simulations have often been employed for scales of length much smaller than micrometers, due to the intractable computational expense that would be incurred for a direct experimental comparison. There have been numerous examples of MD simulations of nanoindentation of a variety of nanometer materials [4–6]. However, to the authors' knowledge, no atomistic simulation of the pressure bulge test has been reported for the analysis of the nonlinear elastic properties of atomic layers, in

particular nanometer-sized graphene monolayers, which motivates the current study. We therefore perform constant-temperature MD simulations of plane-strain bulge tests of graphene monolayers to investigate their nonlinear elastic response to extremely high pressures generated by hydrogen molecules.

## 2. Simulation Method

The schematic model of the atomistic plane-strain pressure bulge test that we perform in the present work is illustrated in Figure 1, where the graphene monolayer is represented by the gray half-cylindrical sheet. Before applying the pressure, the hollow chamber underneath the undeformed flat graphene monolayer has initial dimensions of  $2a \times d \times w$ , where the cross sectional area is  $2a \times d$  and the longitudinal length along the axis of cylindrical symmetry, which is much longer than the other dimensions, is  $w$ . After a certain amount of pressure is applied by supplying hydrogen molecules ( $H_2$ ) into the chamber, the graphene monolayer is inflated upward and eventually reaches a thermally equilibrated bulge height  $h$ .

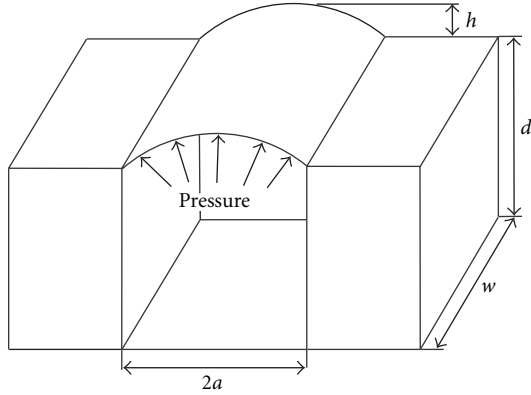


FIGURE 1: Schematic of the model employed to perform the cylindrical pressure bulge test.

Constant-temperature molecular dynamics simulations were performed by employing the Nosé-Hoover thermostat [7, 8], while the carbon-carbon interactions of the graphene monolayer are modeled using the hydrocarbon reactive empirical bond-order potential (known as AIREBO, i.e., Adaptive Intermolecular Reactive Empirical Bond-Order potential) [9] as implemented in the publicly available LAMMPS atomistic simulation package [10]. The simulation time step is fixed as 0.5 fs and the temperature is set to be 300 K. We employ a vertical slab model for the simulation box as shown in Figure 2.

Initially, we place an energy-minimized flat graphene monolayer in the simulation box and fix the positions of edge atoms closest to the two narrow side walls to represent idealized van der Waal's clamping to an underlying substrate. The slab width  $w$  is relatively small compared with the other dimensions of the box because we impose periodic boundary conditions on the front and rear faces perpendicular to the  $w$  direction to mimic an infinitely extended graphene monolayer. We impose reflecting boundary conditions on the other four-side faces [10]. While the space above the graphene monolayer is kept as vacuum, we supply sufficient hydrogen molecules into the space underneath the graphene monolayer such that the monolayer is inflated upward due to the hydrogen pressure, where the C–H and H–H interactions are also represented by the same above-mentioned AIREBO potential [9]. Hydrogen molecules were employed to induce the pressure mainly for the convenience of being able to utilize the same AIREBO interatomic potential for all (C–C, C–H, and H–H) molecular interactions.

After the graphene monolayer reaches the thermally equilibrated state, we measure the height of the bulge  $h$ . The new expanded volume underneath the graphene monolayer is calculated by simple geometrical analysis, assuming that the curve of the graphene is part of a perfect circle (i.e., pressure is homogeneously applied). The gas pressure is computed by contributions of both the kinetic energy and the virial energy, as implemented in LAMMPS [10], after excluding any contribution from the C–C interactions within the graphene monolayer. We tested four graphene monolayers of different length, that is,  $2a = 40, 80, 120$ , and

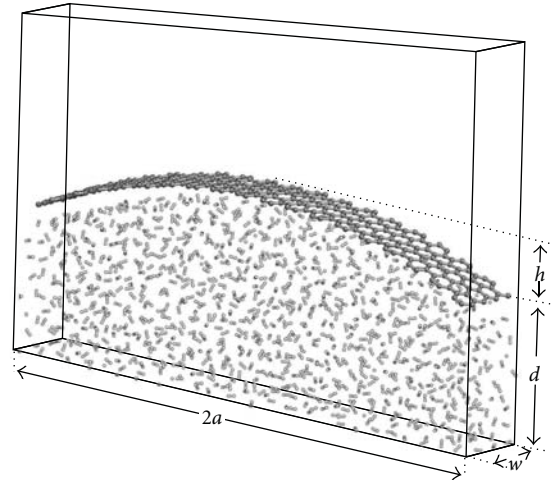


FIGURE 2: Atomistic simulation model of the nanoscale cylindrical bulge test of the graphene monolayer. The schematic shows the graphene monolayer bulged to height  $h$  due to the pressure exerted by the  $H_2$  molecules underneath it.

160 Å, where for each graphene monolayer of length  $2a$ , the above procedure was repeated several times by changing the number of hydrogen molecules to change the pressure.

### 3. Results and Discussion

We first present the typical response of a graphene monolayer using the model with length  $2a = 80$  Å and width  $w = 9.8$  Å that is composed of 300 carbon atoms. The entire simulation box is  $80.4 \text{ Å} \times 80 \text{ Å} \times 10 \text{ Å}$  including the vacuum zone, and the graphene monolayer is initially placed at a height of  $d = 20$  Å from the bottom wall, as shown in Figure 2. Figure 3(a) depicts the plot of the bulge height versus hydrogen pressure as the number of hydrogen molecules is increased. The corresponding pressure ranges from about 2407 to 5900 bar (0.24 ~ 0.59 GPa), which are very high pressures, and leads to bulge heights ranging from 4.47 Å to 21.20 Å (it is noted that extreme pressures as high as 1.3 Mbar have been reported by a recent first-principles study of fullerene nanocages filled with hydrogen molecules [11]). The fitted line in Figure 3(a) clearly exhibits softening behavior from early stage, which is in sharp contrast to the hardening obtained from the bulge test of microscale graphene [2]. Our simulation reveals that the nanosized graphene monolayer continues softening until a C–C bond is broken at a pressure of about 6600 bar.

In order to demonstrate the discrepancy between our MD simulation results and classical elasticity more clearly, we derived the analytical elasticity solution for the relationship between pressure  $p$  and bulge height  $h$  of the cylindrical bulge test, considering large deflection of the graphene, as follows:

$$p = \frac{C_1}{R} \left[ \frac{R}{a} \arcsin\left(\frac{a}{R}\right) - 1 \right] + \frac{C_2}{R} \left[ \frac{R}{a} \arcsin\left(\frac{a}{R}\right) - 1 \right]^2, \quad (1)$$

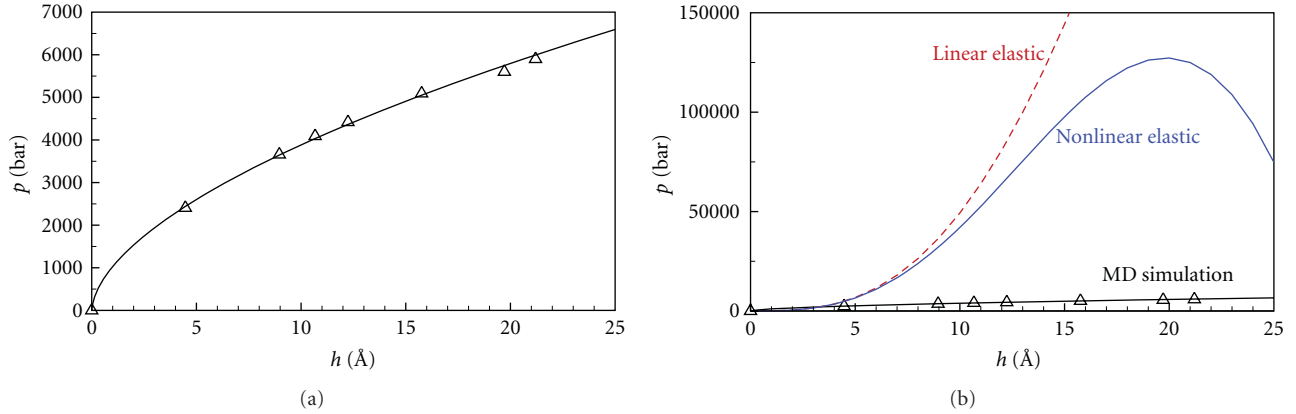


FIGURE 3: (a) The response of the  $2a = 80 \text{ \AA}$  graphene monolayer to pressure induced by hydrogen molecules. As the pressure increases, the graphene deflects more easily, indicating softening behavior. (b) MD results of (a) are compared with classical elasticity solutions for large-deflection bulge tests. Typical microscale linear elastic thin films follow  $p \propto h^3$  curves. Nanoscale MD simulation reveals that the graphene monolayer is easier to deflect at much lower pressure than elasticity solutions.

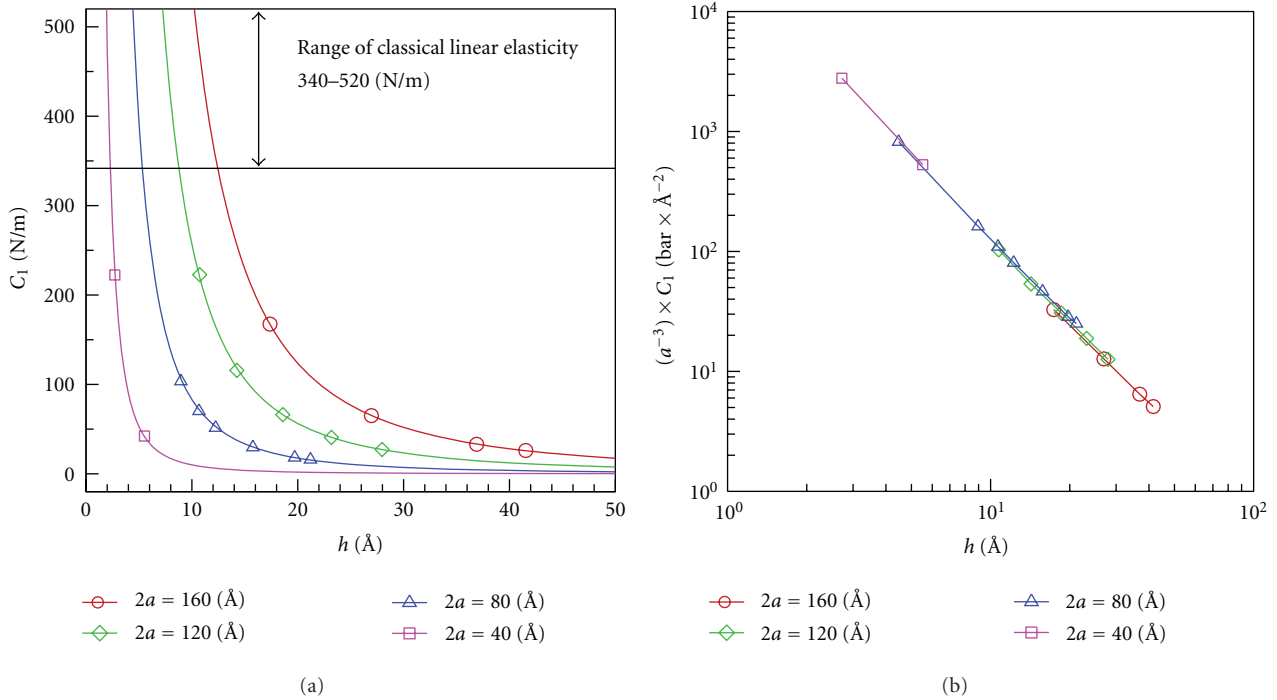


FIGURE 4: (color online) Elastic constant  $C_1(\epsilon)$  that is computed from the simulation data. (a) Illustration of the size-dependent softening behavior that is common amongst all four graphene monolayers under consideration. (b) Collapse of the size-dependent values of the elastic constant onto a single line on a log scale after multiplication by the size factor  $a^{-3}$ .

where  $R = (a^2 + h^2)/2h$ . A simple material nonlinearity,  $\sigma = C_1\epsilon + C_2\epsilon^2$ , was assumed as employed in an experimental study of microscale graphene indentation [3] where authors deduced the values of  $C_1 = 340 \text{ (N/m)}$  and  $C_2 = -690 \text{ (N/m)}$ . Using these values, we plot the elasticity solutions together with our MD results in Figure 3(b). Linear elastic curve implies  $C_2 = 0$ . It is well shown that our nanoscale graphene specimen is easier to deflect at much lower hydrogen pressure than elasticity solutions, which

exhibits the softened response. We also simulated three other graphene monolayers of different lengths, that is,  $2a = 40, 120, \text{ and } 160 \text{ \AA}$ . Under similar pressure levels, we found this softening behavior to be common amongst all the simulated graphene monolayers.

In our 300 K molecular dynamics simulations, we did not measure the bulge height when the gas pressure was relatively low. This is because the graphene monolayer exhibits thermal fluctuations such that extracting an equilibrated bulge

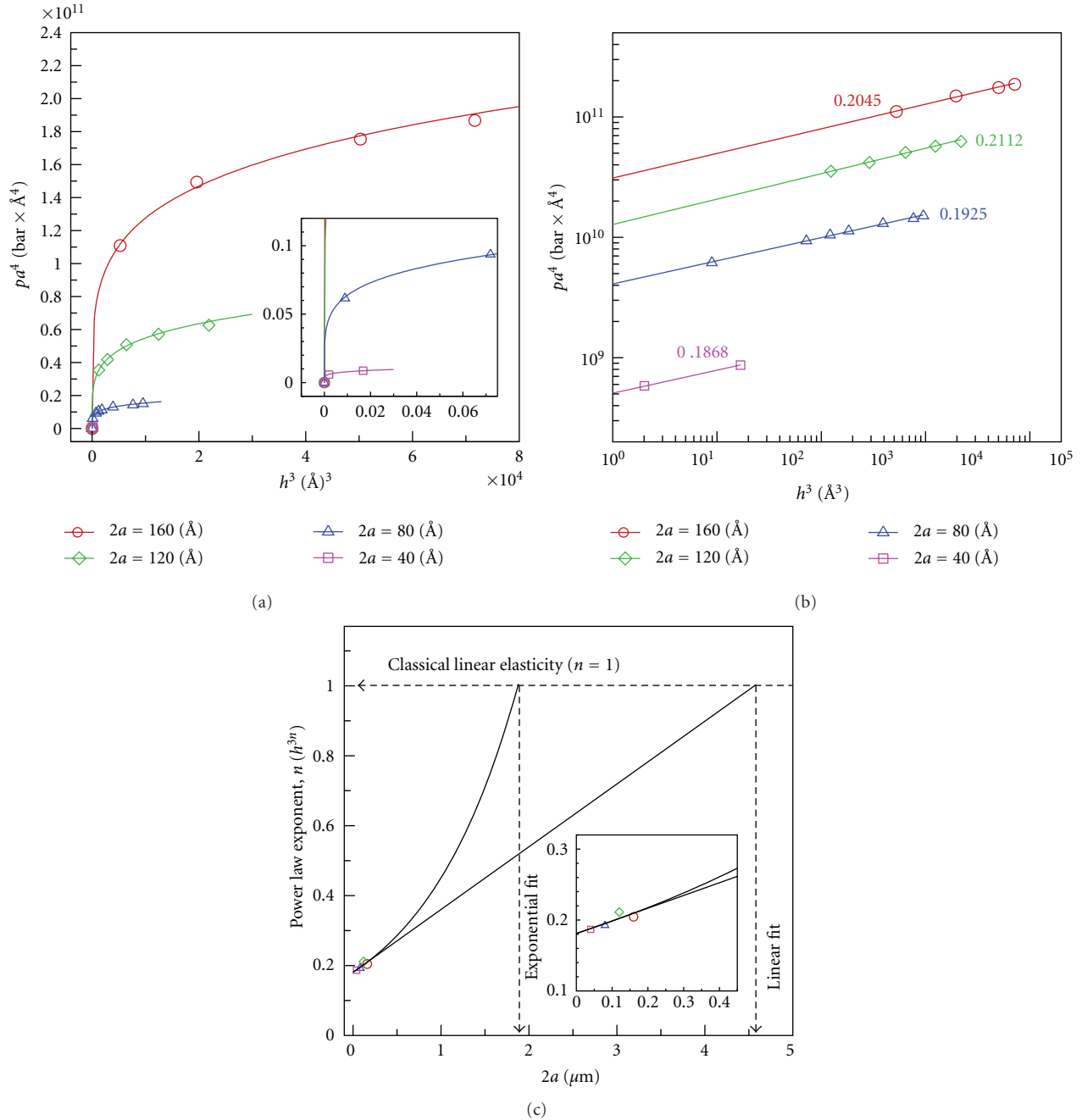


FIGURE 5: (color online) (a) The relation of  $pa^4$  and  $h^3$  follows the power law while linear elastic solution obeys a linear relation. (b) The power law exponents range  $n = 0.1868 \sim 0.2112$  that are significantly smaller than the linear elastic response of  $n = 1$ . (c) The extrapolations of the estimated power law exponents predict the nonlinear softening behavior to disappear and converge to linear elasticity around the specimen size of  $2.0 \sim 4.5 \mu\text{m}$ .

height is difficult, particularly when the bulge height (and thus graphene strain) is small. Furthermore, the graphene monolayer does not bulge or strain significantly until a large number of hydrogen molecules are supplied into the chamber. Therefore, at low pressures, the graphene monolayer does not appear to bulge or strain even though the gas pressure is increasing due to the addition of more hydrogen molecules to the chamber, which results in an

excessively stiff response from the graphene monolayer until the gas pressure reaches a sufficient value. In order to rule out this difficulty at low gas pressure, we thus collected data only after we were able to capture a noticeably well time-averaged bulge height at sufficiently high hydrogen pressure. Instead, we simply added a data point of  $p = 0$  bar at  $h = 0 \text{\AA}$  to our simulation results in order to represent the behavior of graphene under such small pressures (i.e.,

mainly for curve fittings in the vicinity of  $h = 0 \text{ \AA}$  as in Figure 3).

We demonstrate the softening behavior and size dependence in two different ways. First, we estimate the nonconstant values of the elastic constant  $C_1(\varepsilon)$  from the simulation data, using (1), in order to highlight the distinct size-dependent difference from classical linear elasticity (We here drop the higher-order elastic constant  $C_2$ .) Similar estimation can be found in the first-principles calculation of spherical fullerene nanocages filled with hydrogen molecules [11]. Figure 4 shows how the values of the elastic constant calculated from our simulation data decay as the pressure increases. For comparison, the range of the linear elastic constant ( $340 \sim 520 \text{ N/m}$ ) that is obtained from both the microscale experiments [2, 3] and theoretical estimation [12] is also marked on the figure. In Figure 4(a), the four different specimens follow different curves, which demonstrates the size effect. Due to the unrealistically stiff behavior from the low-pressure bulge simulations that was discussed above, we postulate that the four fitted curves will merge into the classical linear elastic value as the bulge height decreases to  $h = 0 \text{ \AA}$ , or equivalently as the strain in the graphene monolayer due to the hydrogen pressure decreases to zero.

Figure 4(b) demonstrates the size dependence more dramatically. We show this by multiplying the elastic constant  $C_1$  by the size factor  $a^{-3}$ , then plotting the product on the  $y$ -axis of the log scale plot shown in Figure 4(b). Interestingly, all data points from the four different specimen sizes collapse onto a single straight line. Furthermore, the four graphene specimens all exhibit decaying values of the elastic constant as the graphene bulge increases, which again verifies the nonlinear elastic softening behavior of nano-sized graphene monolayers. This softening response to extreme pressure is mainly caused by the stretching and weakening of the carbon-carbon bonds in graphene as explained in the recent first-principles simulation study of fullerene nanocages subjected to extremely high internal pressure [11]. Compared with the fullerene simulation, we obtain lower pressure-to-strain ratios. The reason for this is that in our simulation models, the graphene monolayer covers only a single side of the simulation box, which enables the graphene monolayer to deflect more severely at the same pressure than the fullerene cage that has expandable faces in all directions.

To further demonstrate the softening behavior, we present the plots of  $pa^4$  versus  $h^3$  for the four specimens in Figures 5(a) and 5(b). According to (1), the classical linear elastic response is a straight line of which the slope defines the linear elastic constant  $C_1$  of the graphene monolayer. However, our simulation results are found to be best fitted by power laws, where the power law exponent  $n$  in  $(pa^4) \sim (h^3)^n$  ranges from  $n = 0.1868 \sim 0.2112$  for the four model specimens as shown in Figure 5(b), while the exponent of classical linear elasticity is  $n = 1$ , that is,  $pa^4 \sim h^3$ . By extrapolating these four power law exponents, we can approximately predict the graphene monolayer size where this size dependence disappears and begins to follow classical elasticity. In Figure 5(c), we present two possible extrapolations; one is obtained using exponential fitting and the other is obtained using linear fitting. From these results,

we can roughly anticipate that the length scale from which classical linear elastic behavior is valid for the pressure bulge test is between about  $2.0 \sim 4.5 \mu\text{m}$ , which is comparable with the graphene monolayer sizes of about  $5 \mu\text{m}$  that were used in the experimental graphene bulge tests [2]. We therefore expect that the nanoscale softening effect will disappear as the size of graphene monolayer reaches the microscale size scales that have been tested experimentally.

## 4. Conclusions

In conclusion, molecular dynamics simulations have been performed to simulate the cylindrical bulge test of nanoscale graphene monolayers under high pressure. The graphene monolayers exhibit size-dependent nonlinear elastic softening as the applied pressure increases due to the stretching-induced weakening of the carbon-carbon bonds in graphene. Our results demonstrate that the traditional microscale bulge formulas, which assume constant elastic moduli, may need to be modified to incorporate the size dependence and elastic softening for the graphene bulge tests at the nanoscale. Our future research will focus on further investigating the size-dependent softening of graphene through theoretical models that can link the currently presented nanoscale effects to the classical microscale behavior of graphene monolayers along with the effects of temperature.

## Acknowledgments

This work was supported in part by a Faculty Grant-in-Aid program from the University of Wyoming. S. Jun acknowledges support from NSF Grant CMMI-0856250. T. Tashi was supported by the University of Wyoming Graduate School and the Government of Tibet in Exile.

## References

- [1] J. J. Vlassak and W. D. Nix, "New bulge test technique for the determination of Young's modulus and Poisson's ratio of thin films," *Journal of Materials Research*, vol. 7, no. 12, pp. 3242–3249, 1992.
- [2] J. S. Bunch, S. S. Verbridge, J. S. Alden et al., "Impermeable atomic membranes from graphene sheets," *Nano Letters*, vol. 8, no. 8, pp. 2458–2462, 2008.
- [3] C. Lee, X. Wei, J. W. Kysar, and J. Hone, "Measurement of the elastic properties and intrinsic strength of monolayer graphene," *Science*, vol. 321, no. 5887, pp. 385–388, 2008.
- [4] I. Szlufarska, "Atomistic simulations of nanoindentation," *Materials Today*, vol. 9, no. 5, pp. 42–50, 2006.
- [5] A. Gouldstone, N. Chollacoop, M. Dao, J. Li, A. M. Minor, and Y.-L. Shen, "Indentation across size scales and disciplines: recent developments in experimentation and modeling," *Acta Materialia*, vol. 55, no. 12, pp. 4015–4039, 2007.
- [6] C. Y. Wang, K. Mylvaganam, and L. C. Zhang, "Wrinkling of monolayer graphene: a study by molecular dynamics and continuum plate theory," *Physical Review B*, vol. 80, no. 15, Article ID 155445, 2009.
- [7] S. Nosé, "A unified formulation of the constant temperature molecular dynamics methods," *The Journal of Chemical Physics*, vol. 81, no. 1, pp. 511–519, 1984.

- [8] W. G. Hoover, "Canonical dynamics: equilibrium phase-space distributions," *Physical Review A*, vol. 31, no. 3, pp. 1695–1697, 1985.
- [9] D. W. Brenner, O. A. Shenderova, J. A. Harrison, S. J. Stuart, B. Ni, and S. B. Sinnott, "A second-generation reactive empirical bond order (REBO) potential energy expression for hydrocarbons," *Journal of Physics Condensed Matter*, vol. 14, no. 4, pp. 783–802, 2002.
- [10] "LAMMPS Users Manual," <http://lammmps.sandia.gov/>.
- [11] O. V. Pupyshcheva, A. A. Farajian, and B. I. Yakobson, "Fullerene nanocage capacity for hydrogen storage," *Nano Letters*, vol. 8, no. 3, pp. 767–774, 2008.
- [12] F. Liu, P. Ming, and J. Li, "Ab initio calculation of ideal strength and phonon instability of graphene under tension," *Physical Review B*, vol. 76, no. 6, Article ID 064120, 2007.

## Research Article

# Localized Quantitative Characterization of Chemical Functionalization Effects on Adhesion Properties of SWNT

Hao Lu, Jiangnan Zhang, and Jun Lou

*Department of Mechanical Engineering and Materials Science, Rice University, Houston, TX 77005, USA*

Correspondence should be addressed to Jun Lou, jlou@rice.edu

Received 8 September 2010; Accepted 8 December 2010

Academic Editor: Teng Li

Copyright © 2011 Hao Lu et al. This is an open access article distributed under the Creative Commons Attribution License, which permits unrestricted use, distribution, and reproduction in any medium, provided the original work is properly cited.

Chemical modification of single-walled carbon nanotubes (SWNT) has been found to be an excellent method to promote SWNT dispersion, and possibly to improve interaction with matrices via covalent bonding. It is thus a quite promising technique to enhance the mechanical properties of SWNT-reinforced nanocomposites. However, the underlying mechanism of SWNT chemical functionalization effects on interfacial strength is not quantitatively understood, limiting their usefulness in the design of nanocomposites. In this work, an atomic force microscopy (AFM-) based adhesive force mapping technique combined with a statistical analysis method were developed and implemented to study adhesive interactions of small SWNT bundles functionalized by amino, epoxide, and hydroperoxide groups as compared to SDS-treated SWNT in controlled environment. Finally, the importance of such localized quantitative measurements in SWNT-reinforced nanocomposites design and fabrication was also discussed.

## 1. Introduction

Single-walled carbon nanotubes have great mechanical properties that make them excellent candidate as reinforcing agent in composites. Nanoscale fillers like SWNTs have huge potential to improve strength and fracture toughness for lightweight composite, considering their extremely small size, high aspect ratio, large interface area, and impressive theoretical strength. In particular, SWNT-reinforced polymeric nanocomposites have attracted a lot of attentions in the past decade with an increasing demand to better understand the nature of the interactions between SWNT and corresponding matrices. Ajayan and colleagues have investigated local elastic behavior of individual SWNT bundle and load transfer in epoxy composite as well as pressed pellets of composites containing SWNTs and carbonaceous soot material formed during nanotube synthesis [1]. The investigation of the carbon nanotube (CNT)/epoxy nanocomposites via transmission electron microscope (TEM) provides evidences for improved interfacial interactions between the functionalized nanotubes and the corresponding epoxy matrix [2]. Tensile tests on carbon nanotube-polystyrene composite films show that 1 wt% nanotube additions result in 36%–42% and ~25%

increases in elastic modulus and breaking stress, respectively, indicating significant load transfer across the nanotube-matrix interface [3]. Scratch resistance and scratch damage were investigated using AFM tips sliding against the SWNT-reinforced nanocomposite surfaces, where nanoindentation/nanoscratch deformation and fracture behavior were carefully studied by in situ imaging of the indentation impressions/scratch tracks [4]. It was also found that polymers with a backbone structure containing aromatic rings can be used as building blocks in amphiphilic copolymers to promote increased interfacial bonding between the CNT and a polymeric matrix [5]. Li et al. have demonstrated that for SWNT-reinforced polymer composites, the covalent bonding between the nanotube and polymer matrices, crystallinity of matrices, tensile properties of the reinforcement and matrix materials, bundle effects, bundle curvature, and alignment plays important roles in mechanical reinforcement mechanisms [6]. It is now well recognized that the strength of nanotube-polymer composites depends critically on load transfers from matrix to nanotubes. Furthermore, the load transfer is closely related to the adhesion force between the matrix and the side walls of carbon nanotubes. When a composite fails, either CNTs breaks or CNTs are

TABLE 1: List of experimental conditions.

Samples with different functional groups	Temperature (F)	Relative humidity (%)
Amino	71.9	5.5
Epoxide	72.5	7.6
Hydroperoxide	71.7	0
SDS	71.9	4.3

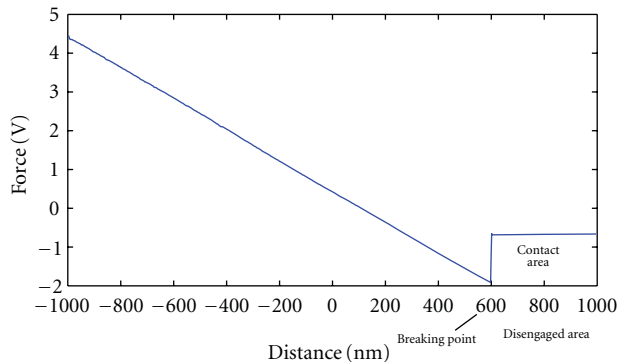
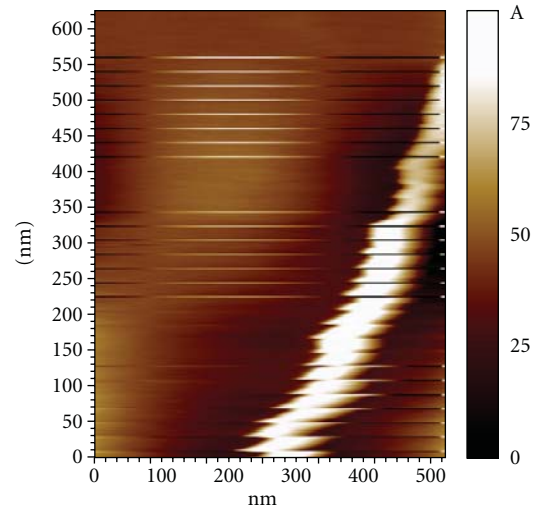


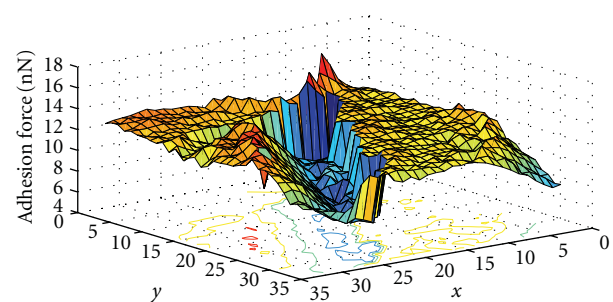
FIGURE 1: A typical force versus distance curve (the tip approaching portion of the curve was not plotted for clarity). This curve contains three parts: the disengaged area, where the AFM tip and the sample are not in contact; the contact area, where the tip and the sample are in contact; the breaking point, where the contact between the tip and the sample is just about to break.

pulled out from the matrix. The failure type depends primarily on the strength of CNTs and the interaction force between the side wall of CNTs and the matrix. The interaction force between the side walls of pristine CNTs and polymer matrix is thought to be mostly Van der Waals interaction [7], and thus the adhesion strength between pristine CNT wall and polymer is considered to be much weaker than CNTs' intrinsic strength. The composite's strength is dominated by adhesion in this scenario, and therefore enhancement of the interaction strength at the nanotube/matrix interface is being vigorously pursued.

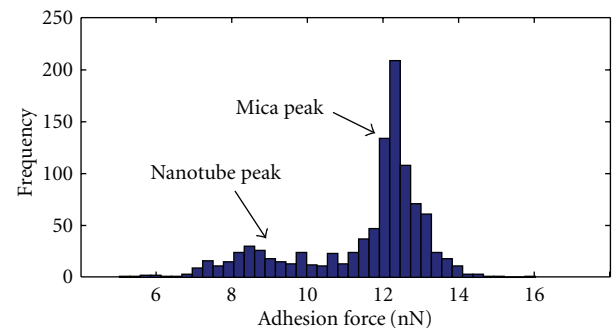
Various methods have been proposed to improve the adhesion strength. Introducing chemical bonds between side walls of CNTs, and the corresponding matrix by chemical modification of CNTs was a popular technique. A variety of functional groups have been applied to different CNTs and quantitatively understanding of adhesion enhancement by these functional groups is of great importance. Poggi et al. [8, 9] have studied the adhesion force between AFM probes and CNTs paper with different functional groups. While their results shed lights into the interfacial interactions between CNTs and AFM probes, the scenario might be quite different in real composite where CNTs are typically dispersed and distributed. Therefore, we seek to measure the adhesion properties of a small bundle of SWNTs which is more realistic for composite application compared to densely packed CNTs in CNT paper [8, 9]. SWNTs with functionalization groups of amino ( $-\text{NH}_2$ ), epoxide ( $-\text{COC}$ ), hydroperoxide ( $-\text{OOH}$ ),



(a)



(b)



■ Total of 1024 data points

(c)

FIGURE 2: (a) AFM topography and spectroscopy image; (b) Adhesion force mapping on amino-functionalized SWNTs; (c) Histogram with two peaks shows the adhesion forces on amino-functionalized SWNTs and the mica substrate, respectively.

and SWNTs physically wrapped with Sodium Dodecyl Sulfate (SDS) were studied in this work.

## 2. Materials and Experimental Procedures

Four types of SWNT samples with different functional groups and treatments ( $-\text{NH}_2$ ,  $-\text{COC}$ ,  $-\text{OOH}$ , and SDS) were obtained from NanoRidge Inc. (Houston, TX) and

TABLE 2: Adhesion forces normalized on mica. CNT with amino function group and SDS-wrapped CNT have larger adhesion force than the other two.

Functional groups	Adhesion on nanotube (Unit: nN)	Adhesion on mica (Unit: nN)	Normalized adhesion on nanotubes
Amino	$8.71 \pm 1.05$	$12.35 \pm 0.65$	0.70
Epoxide	$4.20 \pm 1.25$	$8.22 \pm 0.38$	0.51
Hydroperoxide	$7.77 \pm 1.28$	$15.61 \pm 0.88$	0.50
SDS	$5.00 \pm 0.70$	$6.98 \pm 0.57$	0.72

were tested in a our experiments. SWNTs were dispersed in Dimethylformamide (DMF) and sonicated for 5 minutes. One drop of upper layer of the sonicated solution was deposited on a freshly cleaved mica surface and dried in ambient condition. A PicoPlus 5500 AFM (Agilent Technologies) was used to obtain topography image and the corresponding adhesion force mapping. In order to obtain more accurate adhesion force mapping, the square scan area was divided into 32 by 32 subareas. A force versus distance (FD) curve was then collected in each subarea, and the corresponding adhesion force was acquired from the FD curve. The AFM cantilever used was calibrated using a standard reference cantilever method [10], and the measured spring constant is 0.043 N/m, which is very close to the manufacturer's specifications. The same AFM cantilever was used in all experiments to exclude variations caused by using different tips. Humidity of the testing environment was controlled using an environmental isolation chamber. The topography images were first obtained for every sample, and a single or a small bundle of nanotubes was then identified based on the topography information. After a series of zooming in onto the identified nanotubes (by reducing the AFM scan size), adhesion force mapping was obtained by collecting 1,024 force versus distance curves according to a 32-by-32 matrix configuration in the final scanned area. A typical FD curve is shown in Figure 1. From the FD curve, the adhesion force is defined by the difference between the force at disengaged region and the force at the breaking point. The temperature and relative humidity were carefully controlled and monitored during the experiment as listed in Table 1. The temperature variation was quite small during our experiments, and the relative humidity was maintained to be below 10% using dry nitrogen.

### 3. Results and Discussion

After locating a single SWNT or a small SWNT bundle, the above-mentioned FD spectroscopy mapping was collected on each sample. The typical mapping size was generally below  $1 \mu\text{m}$  by  $1 \mu\text{m}$ . A typical adhesion force mapping and the associated topography image for amino-functionalized SWNTs are shown in Figure 2. It should be noted that the features in the adhesion force mapping image (Figure 2(b)) nearly replicates the AFM topography image (Figure 2(a)), with the portion of lower adhesion forces in Figure 2(b) correspond to higher topography features in Figure 2(a) showing the location of the amino-functionalized SWNT

bundle. Interestingly, there still exists a slight pattern mismatch which might be caused by the hysteresis of the AFM scanner and also friction-induced small deviation between the point where spectroscopy was collected and the point where topography was measured [11]. The discontinuities of CNT topography image in Figure 2(a) seem to support this hypothesis. The associated histogram for the measured adhesive forces was also plotted in Figure 2(c). Two adhesion force peaks with one on nanotube and another on mica were very evident although the mica peak dominated over nanotube peak as shown in Figure 2(c). However, for most of other adhesion experiments, the nanotube peaks cannot be clearly identified from the histogram. For the purpose of separating adhesion forces on nanotubes from that on the mica substrate, an optimal global threshold was found using the Otsu's method [12] for each experiment. Adhesion forces below the threshold were thought to be the adhesion between the tip and the SWNTs while forces larger than the threshold were identified as the adhesion between the tip and the mica. The adhesion force mapping images of amino-functionalized SWNTs before and after the application of the Otsu's method were shown in Figure 3. Adhesion forces below the carefully chosen threshold were considered to be adhesion on SWNTs as shown in white in Figure 3(b), while forces larger than the threshold were thought to be the adhesion on mica substrate as shown in black in the same figure. Average adhesion forces and standard deviations could then be calculated and are summarized in Table 2. Although it is reasonable to assume that the adhesion forces between the AFM tip and the mica substrates should be identical since the same AFM tip was used to probe relatively homogeneous mica substrates, we have observed dissimilar absolute adhesion forces in different experiments. This has been attributed to the variations in testing environments. In order to be able to make more meaningful comparisons of the results obtained from different experiments, the adhesion forces measured on nanotubes were also normalized against the adhesion forces on mica. As shown in Table 2, the measured adhesion forces between the AFM tip and the nanotubes are typically less than 10 nN. Compared with the individual bond strength measured by Friddle et al. [13], the adhesion force measured in our experiments came from breaking of tens of bonds at the same time.

The height of the amino-functionalized nanotubes was also estimated from the topography image (Figure 4(a)). Figure 4(b) is the cross sectional line of the SWNTs shown in Figure 4(a). The height of it is determined to be 6.8 nm,

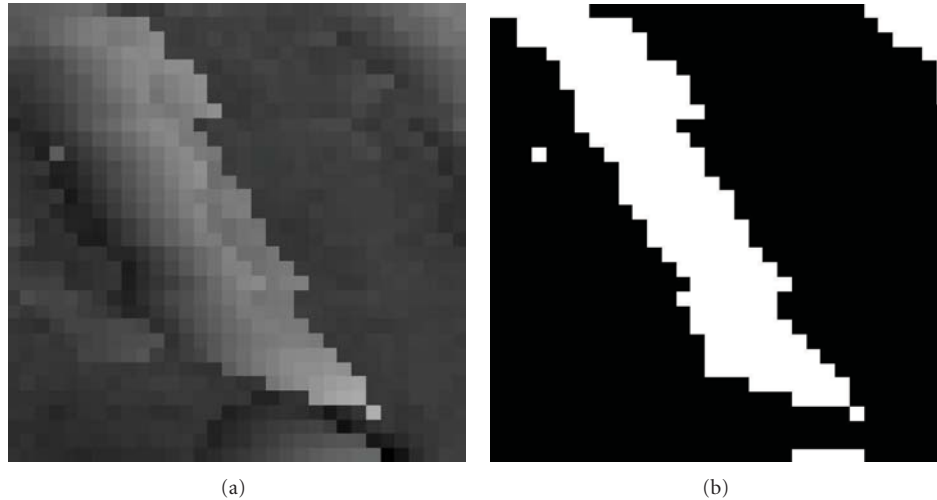


FIGURE 3: (a) Grey image of adhesion mapping for amino-functionalized CNT. (b) Black and white image after finding a global threshold with Otsu's method. White area represents CNT, and black part represents mica.

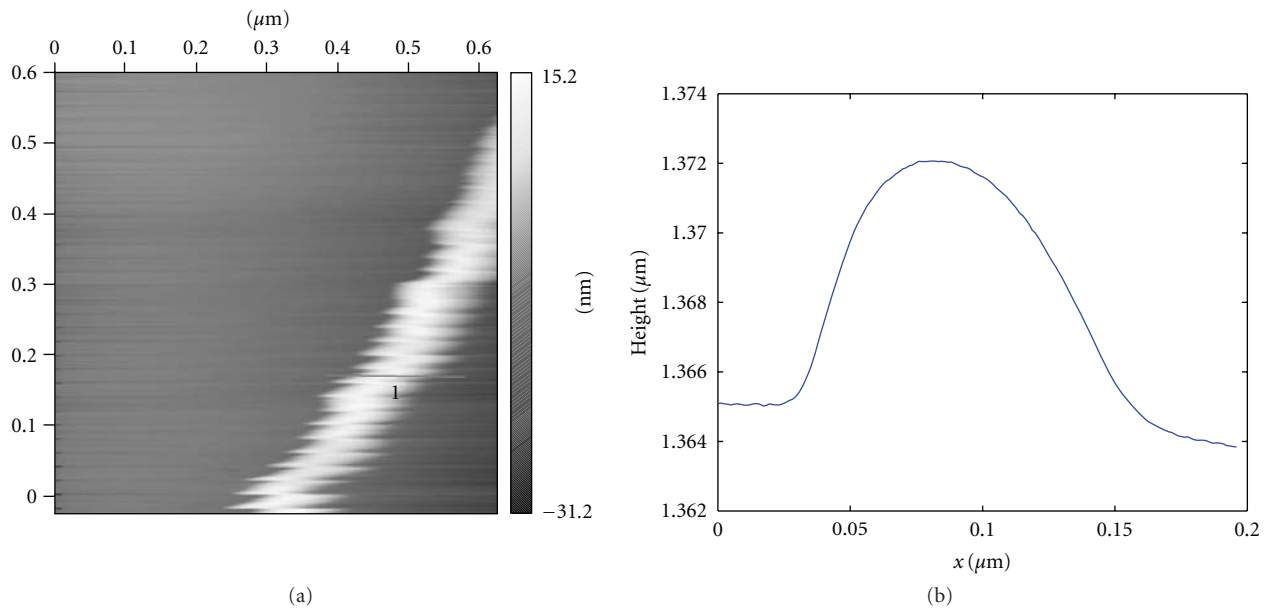


FIGURE 4: Topography image of amino-functionalized nanotubes. (b) Cross section of the SWNTs.  $x$ -axis is the lateral dimension while  $y$ -axis is the height in nanometer.

indicating that this is a small SWNT bundle with 4–6 single nanotubes. Other SWNT samples typically have height of  $\sim 10$ – $14$  nm with more than ten single nanotubes.

When comparing the normalized adhesion forces for different functionalized nanotubes (Table 2), it is found that the adhesion forces of amino-functionalized nanotube and SDS-wrapped nanotubes are larger than those of epoxide group terminated and hydroperoxide-terminated nanotubes. Such localized quantitative measurements of adhesion properties of small SWNT bundles provide an effective tool to assess the effectiveness of different chemical treatments in improving the adhesions between CNTs and matrix due to its realistic sample morphology and fast turn-around time as compared

to costly full production and evaluation cycle of producing nanocomposites. The AFM tips can be further treated with different matrix material coating or by attaching the appropriate moieties similar to the backbone structures of corresponding polymeric matrices. These improvements will be pursued in the future studies and are thus beyond the scope of current work.

#### 4. Conclusion

A localized quantitative method to measure adhesion properties of single-walled nanotubes treated with different functional groups has been reported in this paper. By carefully

analyzing collected adhesive force mapping data using the Otsu's method, we have successfully identified the adhesion forces between the AFM tip and SWNTs. The normalized adhesion on SWNTs with different functional groups is considered to be a very useful parameter to evaluate the effects of functionalization on interfacial interactions between matrices and SWNTs in nanocomposite applications.

### Authors' Contribution

H. Lu and J. Zhang contributed equally to this work.

### Acknowledgments

This work was supported by a National Science Foundation Grant CMMI no. 0800896, an Air Force Research Laboratory Grant AFRL no. FA8650-07-2-5061, and a Welch Foundation Grant no. C-1716. The authors would like to thank Dr. Jiang Zhu (NanoRidge, Inc.) and Dr. Barrera (Rice University) for providing the SWNT materials studied in this work.

### References

- [1] P. M. Ajayan, L. S. Schadler, C. Giannaris, and A. Rubio, "Single-walled carbon nanotube-polymer composites: strength and weakness," *Advanced Materials*, vol. 12, no. 10, pp. 750–753, 2000.
- [2] F. H. Gojny, J. Nastalczyk, Z. Roslaniec, and K. Schulte, "Surface modified multi-walled carbon nanotubes in CNT/epoxy-composites," *Chemical Physics Letters*, vol. 370, no. 5-6, pp. 820–824, 2003.
- [3] D. Qian, E. C. Dickey, R. Andrews, and T. Rantell, "Load transfer and deformation mechanisms in carbon nanotube-polystyrene composites," *Applied Physics Letters*, vol. 76, no. 20, pp. 2868–2870, 2000.
- [4] X. Li, H. Gao, W. A. Scrivens et al., "Nanomechanical characterization of single-walled carbon nanotube reinforced epoxy composites," *Nanotechnology*, vol. 15, no. 11, pp. 1416–1423, 2004.
- [5] M. Yang, V. Koutsos, and M. Zaiser, "Interactions between polymers and carbon nanotubes: a molecular dynamics study," *Journal of Physical Chemistry B*, vol. 109, no. 20, pp. 10009–10014, 2005.
- [6] X. Li, H. Gao, W. A. Scrivens et al., "Reinforcing mechanisms of single-walled carbon nanotube-reinforced polymer composites," *Journal of Nanoscience and Nanotechnology*, vol. 7, no. 7, pp. 2309–2317, 2007.
- [7] K. Liao and S. Li, "Interfacial characteristics of a carbon nanotube-polystyrene composite system," *Applied Physics Letters*, vol. 79, no. 25, pp. 4225–4227, 2001.
- [8] M. A. Poggi, L. A. Bottomley, and P. T. Lillehei, "Measuring the adhesion forces between alkanethiol-modified AFM cantilevers and single walled carbon nanotubes," *Nano Letters*, vol. 4, no. 1, pp. 61–64, 2004.
- [9] M. A. Poggi, P. T. Lillehei, and L. A. Bottomley, "Chemical force microscopy on single-walled carbon nanotube paper," *Chemistry of Materials*, vol. 17, no. 17, pp. 4289–4295, 2005.
- [10] M. Tortorese and M. Kirk, "Characterization of application-specific probes for SPMs," in *Micromachining and Imaging*, Proceedings of SPIE, pp. 53–60, San Jose, Calif, USA, February 1997.
- [11] J. H. Hoh and A. Engel, "Friction effects on force measurements with an atomic force microscope," *Langmuir*, vol. 9, no. 11, pp. 3310–3312, 1993.
- [12] N. Otsu, "A threshold selection Method from gray-level histograms," *IEEE Transactions on Systems, Man, and Cybernetics*, vol. 9, no. 1, pp. 62–66, 1979.
- [13] R. W. Friddle, M. C. Lemieux, G. Cicero et al., "Single functional group interactions with individual carbon nanotubes," *Nature Nanotechnology*, vol. 2, no. 11, pp. 692–697, 2007.

## Research Article

# A Molecular Mechanics Study of Morphologic Interaction between Graphene and Si Nanowires on a SiO<sub>2</sub> Substrate

Zhao Zhang<sup>1</sup> and Teng Li<sup>1,2</sup>

<sup>1</sup>Department of Mechanical Engineering, University of Maryland, College Park, MD 20742, USA

<sup>2</sup>Maryland NanoCenter, University of Maryland, College Park, MD 20742, USA

Correspondence should be addressed to Teng Li, lit@umd.edu

Received 7 September 2010; Accepted 25 October 2010

Academic Editor: Sulin Zhang

Copyright © 2011 Z. Zhang and T. Li. This is an open access article distributed under the Creative Commons Attribution License, which permits unrestricted use, distribution, and reproduction in any medium, provided the original work is properly cited.

We study the morphologic interaction between graphene and Si nanowires on a SiO<sub>2</sub> substrate, using molecular mechanics simulations. Two cases are considered: (1) a graphene nanoribbon intercalated by a single Si nanowire on a SiO<sub>2</sub> substrate and (2) a blanket graphene flake intercalated by an array of Si nanowires evenly patterned in parallel on a SiO<sub>2</sub> substrate. Various graphene morphologies emerge from the simulation results of these two cases, which are shown to depend on both geometric parameters (e.g., graphene nanoribbon width, nanowire diameter, and nanowire spacing) and material properties (e.g., graphene-nanowire and graphene-substrate bonding strength). While the quantitative results at the atomistic resolution in this study can be further used to determine the change of electronic properties of graphene under morphologic regulation, the qualitative understandings from this study can be extended to help exploring graphene morphology in other material systems.

## 1. Introduction

The experimental discovery of graphene [1] has inspired a surge of interest in developing its application toward novel nanoelectronic devices [2–7]. The atomically thin structure of graphene dictates the strong correlation between the electronic properties and the morphology of graphene [8–11]. For example, bending-induced local curvature in graphene changes the interatomic distances and angles between chemical bonds, and thus leads to changes in the graphene's band structure [9]. Therefore, the intrinsic random corrugations in freestanding graphene [12] may result in unpredictable fluctuation of electronic properties that is undesirable for graphene-based nanodevice applications. Recent experiments [13–17] and simulations [18–20] reveal that the morphology of graphene can be controlled via extrinsic regulation, which envisions a promising pathway toward tunable electronic properties of graphene. In this paper, using molecular mechanics simulations, we study the morphology of graphene nanoribbons and flakes regulated by Si nanowires on a SiO<sub>2</sub> substrate. The results from the present study can shed light on the structural design of

graphene-based field effect transistors and other nanoelectronics components.

Recent experiments [13, 14] show that the interaction between graphene and its underlying substrate can effectively suppress the intrinsic random ripples in the graphene. As a result, the graphene can partially conform to the substrate surface corrugations. Inspired by these experimental observations, recent modeling and simulations [18–21] have predicted the graphene morphology regulated by various substrates with engineered nanoscale surface features. The substrate-regulated morphology of graphene is governed by the interplay between the graphene-substrate interaction energy and the deformation energy of the graphene due to bending and stretching. Emerging from these theoretical studies is an effective approach to controlling the graphene morphology and thus its electronic properties via external regulation.

Nanowires (e.g., Si) of diameters as small as 1 nm have been successfully fabricated [22], which can be used as building blocks of nanoelectronic devices. Furthermore, ultrathin nanowires patterned on a substrate surface [23] can potentially serve as scaffolds to regulate the graphene

morphology at an even higher resolution that approaches the atomic feature size of graphene (e.g., the carbon-carbon bond length in graphene is about 0.14 nm). To this end, we recently extended our previous continuum mechanics energetic framework [19] to quantitatively determine the graphene morphology regulated by nanowires patterned in parallel on a substrate surface [20]. In the extended modeling framework, the graphene-nanowire interaction energy is incorporated into the energetic interplay. This extended continuum mechanics model can shed light on predicting the graphene morphology modulated by nanowires of diameters comparable to or modestly smaller than the spatial resolution of engineered substrate surfaces (e.g., as low as about 10 nm). It is expected that, however, the continuum mechanics model cannot capture the full characteristics of the graphene morphology regulated by ultrathin nanowires (e.g., with diameters on the order of 1 nm). Furthermore, the continuum model cannot determine the exact positions of each carbon atom in graphene at the equilibrium morphology. Such information will be needed in further first principle calculation of the electronic properties of the graphene.

To address the above concerns, in this paper, we carry out molecular mechanics (MM) simulations to study the morphological interaction between graphene nanoribbons/flakes and Si nanowires on a  $\text{SiO}_2$  substrate. The rest of the paper is organized as follows. Section 2 describes the computational model; in Section 3, we consider two simulation cases: (1) interaction between a graphene nanoribbon and a Si nanowire on a  $\text{SiO}_2$  substrate; (2) interaction between a blanket graphene flake and an array of Si nanowires patterned in parallel on a  $\text{SiO}_2$  substrate; discussions and summary are given in Section 4.

## 2. Computational Model

The nanowire-regulated morphology of graphene on a substrate is governed by the interplay among the following energies: the strain energy of the graphene due to bending and stretching, the graphene-nanowire interaction energy, and the graphene-substrate interaction energy. Both nonbonding interaction energies can be characterized by van der Waals force, which minimizes at a certain equilibrium distance between the graphene and the nanowires (or the substrate). On the other hand, the graphene strain energy minimizes when the graphene remains flat and increases monotonically as the graphene corrugates to conform to the nanowires and the substrate. As a result, the total energy of the graphene-nanowire-substrate system minimizes when the corrugated graphene reaches its equilibrium morphology.

Figure 1 depicts the two configurations simulated in this paper: (1) a graphene nanoribbon of finite width in  $y$ -direction on a  $\text{SiO}_2$  substrate with a Si nanowire intercalating in between (Figure 1(a)) and (2) a blanket graphene flake intercalated by an array of Si nanowires patterned in parallel on a  $\text{SiO}_2$  substrate (Figure 1(b)). Given the periodicity of these two configurations, only the portion of the graphene marked by dash lines and the corresponding nanowire and

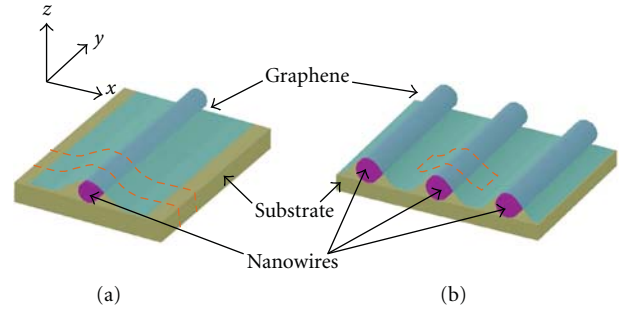


FIGURE 1: Schematics of two simulation cases. (a) A graphene nanoribbon intercalated by a Si nanowire on a  $\text{SiO}_2$  substrate; (b) a blanket graphene flake intercalated by an array of Si nanowires evenly patterned in parallel on a  $\text{SiO}_2$  substrate. The dash lines delineate the portion of graphene and the underlying nanowire and substrate simulated by molecular mechanics in each case.

TABLE 1: LJ potential parameters used in molecular mechanics simulations [25].

	$\epsilon$ (eV)	$\sigma$ (Å)
C–Si	0.00213	1.506
C–O	0.00499	2.256

substrate underneath are simulated. In the MM simulations, periodic boundary conditions are applied to the two-end surfaces in  $y$ -direction in Figure 1(a), and to the end surfaces in both  $x$ - and  $y$ -directions in Figure 1(b). The depth of the MM simulation box in  $y$ -direction is 30 Å and the substrate thickness is 15 Å, larger than the cutoff radius in calculating von der Waals force. The width of the graphene portion demarcated by the dash lines and that of the underlying substrate in  $x$ -direction, and the nanowire diameters are varied to study their effects on the graphene morphology. The C–C bonding energy in the graphene is described by the second generation Brenner potential [24]. The interaction energy between the graphene and the nanowires and that between the graphene and the substrate are computed by the sum of the van der Waals forces between all C–Si and C–O atomic pairs in the system. These two types of van der Waals forces are described by two Lennard-Jones (LJ) pair potentials, respectively, both of which take the general form of  $V(r) = 4\epsilon(\sigma^{12}/r^{12} - \sigma^6/r^6)$ , where  $\sqrt[6]{2}\sigma$  is the equilibrium distance of the atomic pair and  $\epsilon$  is the bonding energy at the equilibrium distance. Parameters in the C–Si pair potential and those in the C–O pair potential are listed in Table 1. To reduce the computation cost, the bonding energy in the Si nanowire and the  $\text{SiO}_2$  substrate, and the nonbonding Si– $\text{SiO}_2$  interaction are assumed to be constant, thus not considered in the energy minimization. This assumption is justified given the rigidity of Si and  $\text{SiO}_2$  solids compared with the out-of-plane flexibility of a graphene monolayer.

In each MM simulation case, the graphene is prescribed with an initial morphology that partially conforms to the envelop defined by the nanowire and the substrate surface (e.g., in Figure 1). The carbon atoms in the graphene then adjust their spatial positions to minimize the system

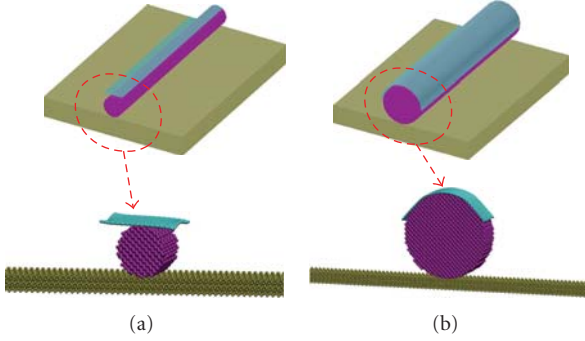


FIGURE 2: (a) On a nanowire of diameter of 4 nm, a narrow graphene nanoribbon of width of 6 nm remains nearly flat, with slight ripples along two long edges. (b) On a nanowire of diameter of 10 nm, a narrow graphene nanoribbon of width of 12 nm can fully conform to the nanowire surface.

energy, and eventually define the equilibrium morphology of the graphene. The total energy of the system is minimized using the limited-memory Broyden-Fletcher-Goldfarb-Shanno (BFGS) algorithm [26], until the total net force is less than  $10^{-6}$  eV/Å. The MM simulations are carried out by running a code in a high performance computer cluster.

### 3. Results and Discussion

**3.1. Morphological Interaction between a Graphene Nanoribbon and a Si Nanowire on a SiO<sub>2</sub> Substrate.** We consider the interaction between a graphene nanoribbon of finite width  $W$  and a Si nanowire of diameter  $d$  on a SiO<sub>2</sub> substrate. Such a structure can be fabricated by transfer printing a mechanically exfoliated graphene nanoribbon onto a SiO<sub>2</sub>-supported Si nanowire [27], with the length direction of the graphene nanoribbon parallel to the axial direction of the nanowire. As will be shown in this section, the regulated morphology of the graphene nanoribbon depends strongly on its width  $W$  and the nanowire diameter  $d$ .

If  $W$  is smaller than or comparable to  $d$ , the morphology of such a narrow graphene nanoribbon is mainly determined by the interaction between the graphene and the nanowire, and that between the graphene and the substrate becomes negligible. Depending on the relative value of  $W$  and  $d$ , the narrow graphene nanoribbon can have two different morphologies, as illustrated in Figure 2. For example, on a Si nanowire of  $d = 4$  nm, a graphene nanoribbon of  $W = 6$  nm remains nearly flat (Figure 2(a)). By contrast, on a Si nanowire of  $d = 10$  nm, a graphene nanoribbon of  $W = 12$  nm fully conforms to the surface of the Si nanowire (Figure 2(b)). These two different morphologies of the graphene nanoribbon can be explained as follows. The strain energy density of the graphene due to out-of-plane bending approximately scales with the square of the local curvature of the graphene. Therefore, the graphene strain energy due to conforming to the Si nanowire surface is roughly proportional to  $1/d^2$ . If the Si nanowire is too thin, the significant increase of the graphene strain energy

can overbalance the decrease of the graphene-nanowire interaction energy due to graphene conforming to the nanowire. As a result, the graphene nanoribbon remains nearly flat on the Si nanowire. On the other hand, if the Si nanowire is sufficiently thick, the decrease of the interaction energy outweighs the increase of the graphene strain energy. Consequently, the graphene nanoribbon conforms to the nanowire surface. Also note when the graphene nanoribbon remains nearly flat on the Si nanowire, the two free edges in  $y$ -direction form ripples due to the edge stress [28] in the graphene nanoribbon.

If  $W$  is much larger than  $d$ , the equilibrium morphology of the graphene nanoribbon takes the form as shown in Figure 3(a). The graphene portion far away from the Si nanowire conforms to the flat surface of the SiO<sub>2</sub> substrate while the middle portion of the graphene partially wraps around the Si nanowire. The geometry of the graphene-nanowire-substrate system at the equilibrium can be characterized by three parameters: the width of the corrugated portion of the graphene nanoribbon  $L$ , the width of the graphene nanoribbon  $W$ , and nanowire diameter  $d$  (Figure 3(a)). Figure 3(b) plots  $L/d$  as a function of  $d$  for various widths of graphene nanoribbon  $W/d = 6.8, 7.0, 7.2, \text{ and } 7.4$ , respectively. When the graphene nanoribbon is sufficiently wide (e.g., much larger than  $d$ ),  $L$  is roughly independent of  $W$ , as evident with the small variation among the results for the four different values of  $W$ . As shown in Figure 3(b),  $L/d$  decreases as  $d$  increases, and then approaches to a plateau of about 2.2 when  $d$  exceeds 7 nm. Such a trend can be explained by the similar argument aforementioned. If the Si nanowire is too thin, the graphene nanoribbon can only barely wrap around the nanowire, given the significant constraint of possible strain energy increase in the graphene. The corrugated portion of the graphene ribbon gradually transits to the flat portion on the substrate surface, resulting in a relatively large  $L/d$  (e.g., 3.7 for  $d = 2$  nm). If the Si nanowire is thick enough, the graphene nanoribbon can wrap more of the nanowire surface, leading to a higher slope of the graphene sagging down toward the substrate surface, and thus a smaller  $L/d$ . As the nanowire diameter is greater than  $\sim 7$  nm,  $L/d$  tends to a constant of  $\sim 2.2$ . In other words, the morphology of the corrugated portion of the graphene nanoribbon intercalated by a sufficiently thick nanowire is self-similar.

Figure 4 further plots the Brenner potential energy of the carbon atoms in the graphene nanoribbon at the equilibrium state (e.g., Figure 3(a)), which depicts the strain energy profile of the corrugated graphene. As indicated by the color shades, high strain energy states in the graphene nanoribbon occur at the regions near the top of the nanowire and where the graphene becomes flat on the substrate. At such regions the graphene nanoribbon bends the most. The inset of Figure 4 further shows the average C–C bond lengths in  $x$ -direction at three locations, as indicated by three marked lines A (where graphene remains flat on the substrate), B (in the middle of the intercalated portion of the graphene), and C (the crest of the corrugated graphene portion). Given the equilibrium C–C bond length of 1.42 Å, it is evident that the C–C bonds are stretched at B in  $x$ -direction and

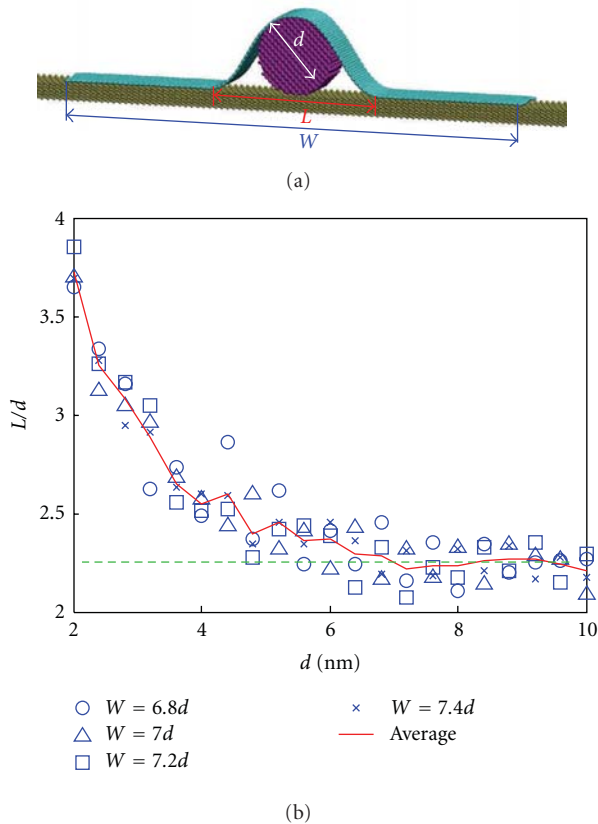


FIGURE 3: (a) Molecular mechanics simulation result of the morphology of a wide graphene nanoribbon intercalated by a Si nanowire on a  $\text{SiO}_2$  substrate. Here  $d = 6$  nm and  $W = 40$  nm. (b) Normalized width of the corrugated portion of the graphene  $L/d$  as a function of  $d$  for various widths of the graphene nanoribbon  $W = 6.8d, 7.0d, 7.2d,$  and  $7.4d$ , respectively. The solid line plots the average of the four data sets. The dash line shows the plateau value of  $L/d$  when  $d$  is sufficiently large.

un-stretched at A and C. As shown in Figure 4, comparing with the much higher energy of the carbon atoms at C due to bending, the Brenner potential energy of the carbon atoms at B is at a comparable level of that of carbon atoms at A, even though the C–C bonds at B are stretched but those at C not. Therefore, it can be estimated that the strain energy of the corrugated graphene nanoribbon is mainly due to bending, rather than stretching.

**3.2. Morphologic Interaction between a Blanket Graphene Flake and an Array of Si Nanowires Evenly Patterned in Parallel on a  $\text{SiO}_2$  Substrate.** When a blanket graphene flake is intercalated by an array of Si nanowires evenly patterned in parallel on a  $\text{SiO}_2$  substrate, the nanowire spacing  $W$  comes into play in determining the regulated morphology of the graphene flake. Emerging from the simulations are two types of morphologies of graphene at equilibrium, depending on  $W$  and  $d$ , as shown in Figure 5.

If the nanowires are widely spaced (e.g.,  $W \gg d$ ), the graphene tends to conform to the envelop of each individual nanowire (Figure 5(a)), sags down and adheres

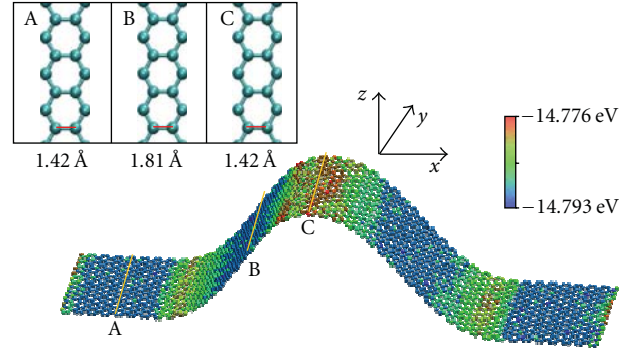


FIGURE 4: The distribution of Brenner potential energy of the carbon atoms in a graphene nanoribbon intercalated by a Si nanowire (not shown) on a  $\text{SiO}_2$  substrate (not shown). The inset shows the C–C bond lengths in  $x$ -direction at three cross-sections marked by the solid lines on graphene, indicating the graphene is under tension near location B. Here  $d = 4$  nm and  $W = 20$  nm.

to the substrate in between neighboring nanowires. The corrugated portion of the graphene is of a width of  $L$  and an amplitude of  $A_g$  ( $\approx d$  in this case). Figure 6(a) further plots  $L/d$  as a function of  $d$  for various values of  $W$ . For a given  $W$ ,  $L/d$  increases as  $d$  increases in a roughly linear manner. When compared with the case of graphene nanoribbon intercalated by a single nanowire on a substrate (e.g., Figure 3(b)), the width of the corrugated portion of the graphene intercalated by patterned nanowires on a substrate is much larger. This can be explained by the constraint of the portion of the graphene sagged in between neighboring nanowires and adhered to the substrate. Therefore, the graphene cannot slide easily on the substrate to conform to the envelop of each individual nanowire closely. As a result, the corrugated portion of the graphene is under modest stretch in  $x$ -direction. By contrast, the graphene nanoribbon intercalated by a single nanowire is shown to be able to slide on the substrate surface to conform more to the nanowire surface. As a result, the stretch in the graphene in  $x$ -direction can be nearly fully relaxed (e.g., Figure 4), leading to a much smaller value of  $L/d$ . Figure 6(a) also indicates the increase of  $L/d$  as  $W$  decreases, for a given value of  $d$ . To further clarify this trend, Figure 6(b) plots  $L/d$  as a function of  $W/d$  for various values of  $d$ , which indicates a roughly linear dependence between  $L$  and  $W$  as well as a weak dependence on  $d$ . This can be explained that, when nanowire spacing is larger, the corrugation-induced graphene stretching is accommodated by a longer graphene segment, leading to smaller strain energy of the graphene. Therefore the graphene conforms more to the nanowires. The limiting case of infinitely large nanowire spacing corresponds to that of graphene intercalated by a single nanowire (e.g., Figure 3).

If the spacing between the patterned nanowires is not sufficiently large, the graphene flake remains nearly flat, just slightly conforming to the envelop of the nanowires with a negligible amplitude  $A_g$  (Figure 5(b)), a morphology of graphene distinct from that regulated by widely distributed nanowires on a substrate (i.e., Figure 5(a)). For a given nanowire diameter  $d$ , there is a sharp transition between

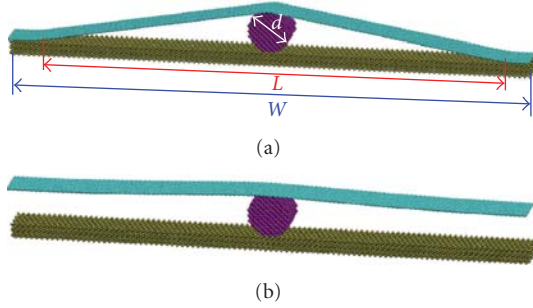
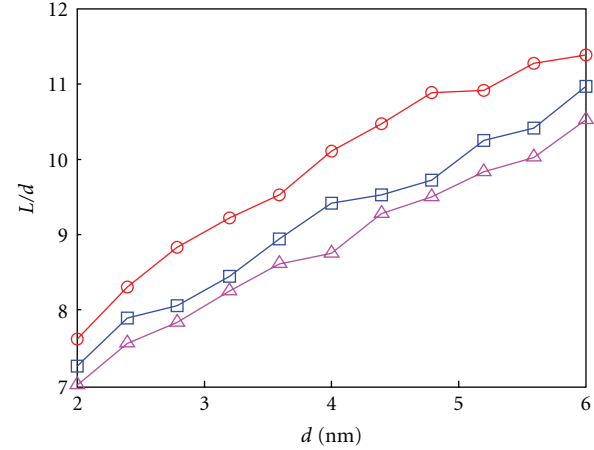


FIGURE 5: Molecular simulation results of the morphology of a blanket graphene flake intercalated by Si nanowires evenly patterned in parallel on a  $\text{SiO}_2$  substrate. (a) When the Si nanowires are widely spaced (e.g.,  $W$  is large), graphene sags in between neighboring nanowires and adheres to the substrate surface. The width of the corrugated portion of the graphene is denoted by  $L$ . (b) If the nanowire spacing is small, graphene remains nearly flat, just slightly conforming to the envelop of the nanowires. Here  $d = 4$  nm and  $W = 48$  nm in (a) and 46 nm in (b). The sharp transition between (a) and (b) as  $W$  varies indicates a snap-through instability of the graphene morphology.

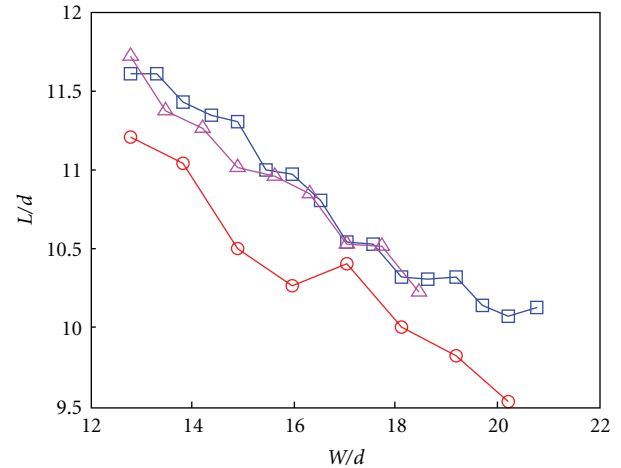
these two distinct morphologies as the nanowire spacing reaches a critical value  $W_{cr}$ . This result agrees with the snap-through instability of the graphene morphology regulated by patterned nanowires on a substrate predicted by our previous continuum model results [20]. Such a snap-through instability of the graphene morphology results from the double-well energy profile of the system [19]. For the bonding parameters given in Table 1,  $W_{cr}/d$  ranges from 12.3 to 12.8 and is approximately independent of  $d$ . In practice, it is possible to have chemical bonding or pinnings between the graphene and the substrate, and/or the nanowire surface can also be functionalized to facilitate chemical bonding with the graphene, both of which lead to an enhanced interfacial bonding energy of the graphene. Based on the energetic interplay as described in Section 2, it is expected that the resulting graphene morphology can also be tuned by the interfacial bonding energy.

To investigate the effect of graphene-substrate interfacial bonding energy on the graphene morphology, a tuning factor  $\lambda$  is used to vary the bonding energy in the LJ pair potential describing the graphene-substrate van der Waals interaction. A tuning factor  $\lambda > 1$  denotes a graphene-substrate interaction energy stronger than that described in Table 1. Here, the graphene-nanowire interaction energy remains the same. Figure 7 plots the normalized amplitude of graphene corrugation  $A_g/d$  as a function of tuning factor  $\lambda$  for  $d = 4$  nm, 4.2 nm, and 4.4 nm, respectively. Here,  $W = 46.9$  nm. For a given nanowire diameter and spacing, there exists a critical graphene-substrate interaction energy (i.e., a critical tuning factor  $\lambda_c$ ), weaker than which the graphene only slightly conforms to the envelop of the nanowires (e.g.,  $A_g/d \ll 1$ ), and stronger than which the graphene can sag in between the nanowires and adhere to the substrate (e.g.,  $A_g/d \approx 1$ ). The sharp transition between these two distinct morphologies at the critical graphene-substrate interfacial



—○—  $W = 80.9$  nm  
—□—  $W = 93.7$  nm  
—△—  $W = 106.5$  nm

(a)



—○—  $d = 2$  nm  
—□—  $d = 4$  nm  
—△—  $d = 6$  nm

(b)

FIGURE 6: (a)  $L/d$  as a function of  $d$  for various values of  $W$ . (b)  $L/d$  as a function of  $W/d$  for various values of  $d$ .

energy reveals the similar snap-through instability of the graphene morphology aforementioned. Previous studies based on continuum model [20] suggest that  $W/d \propto \lambda_c^{1/4}$ , or  $W\lambda_c^{1/4}/d$  is a constant. The results shown in Figure 7 give  $W\lambda_c^{1/4}/d = 12.40, 12.25, \text{ and } 12.26$  for  $d = 4$  nm, 4.2 nm, and 4.4 nm, respectively. In this sense, the molecular mechanics simulation results agree well with the continuum model prediction.

#### 4. Concluding Remarks

Using molecular mechanics simulations, we determine the morphologic interaction between a graphene nanoribbon

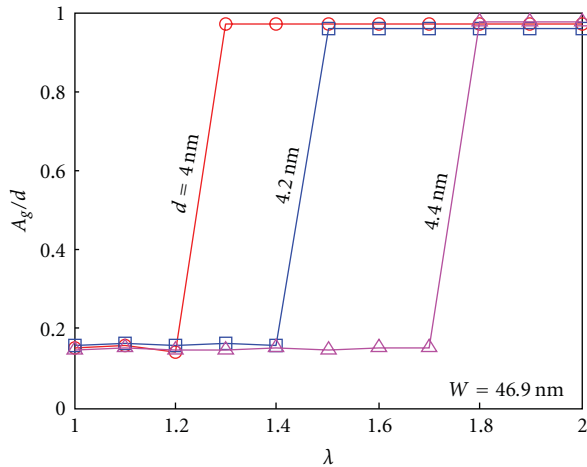


FIGURE 7:  $A_g/d$  as a function of tuning factor  $\lambda$  for various values of  $d$ . Here,  $W = 46.9$  nm. The sudden jumps of  $A_g/d$  at a critical value of  $\lambda$  indicate the snap-through instability of the graphene morphology shown in Figure 5.

and a Si nanowire on a  $\text{SiO}_2$  substrate, and that between a blanket graphene flake and an array of Si nanowires evenly patterned in parallel on a  $\text{SiO}_2$  substrate. The regulated graphene morphology is shown to be determined by the interplay between the graphene strain energy due to bending and stretching and the graphene-substrate and graphene-nanowire interaction energies. Specifically, the graphene morphology can be tuned by both geometric parameters (e.g., graphene nanoribbon width, nanowire diameter, and nanowire spacing) and material properties (e.g., graphene-nanowire and graphene-substrate bonding strength). Various simulations are conducted to quantify the relation between the graphene morphology and these parameters and properties. The present study assumes negligible deformation of the substrate under the morphologic interaction, which is justified by the rigidity of  $\text{SiO}_2$ . Recent experiments demonstrate the snap-through instability of the morphology of graphene on an elastomeric substrate[15]. Given the ultralow stiffness of such substrate materials (e.g.,  $1 \text{ s} \sim 10 \text{ s MPa}$ ), the elastomeric substrate may deform to some extent under the morphologic interaction with the graphene. To precisely predict the regulated morphology of the graphene in such a material system, the elastic energy of the substrate needs to be considered in the energetic interplay, which is additive to the present model and will be reported elsewhere. The molecular mechanics simulation results agree well with our previous continuum mechanics modeling results, and furthermore, provide atomistic scale information of each carbon atoms in the graphene. Such information can be consequently used to determine the effect of the morphologic interaction and the mechanical deformation on the electronic properties of the graphene (e.g., bandgap). Though much remains to be done to achieve fine tuning of graphene's electronic properties via morphologic interaction, the present study demonstrates the beginning steps toward this promising approach that

could potentially enable new graphene-based device applications.

## Acknowledgments

This work is supported by the Minta-Martin Foundation, a UMD General Research Board summer research award to T. Li, and National Science Foundation (Grant no. 0928278). Z. Zhang also thanks the support of the A. J. Clark Fellowship and the UMD Future Faculty Fellowship.

## References

- [1] K. S. Novoselov, A. K. Geim, S. V. Morozov et al., "Electric field in atomically thin carbon films," *Science*, vol. 306, no. 5696, pp. 666–669, 2004.
- [2] R. Murali, K. Brenner, Y. Yang, T. Beck, and J. D. Meindl, "Resistivity of graphene nanoribbon interconnects," *IEEE Electron Device Letters*, vol. 30, no. 6, pp. 611–613, 2009.
- [3] M. D. Stoller, S. Park, Z. Yanwu, J. An, and R. S. Ruoff, "Graphene-based ultracapacitors," *Nano Letters*, vol. 8, no. 10, pp. 3498–3502, 2008.
- [4] X. Li, X. Wang, L. Zhang, S. Lee, and H. Dai, "Chemically derived, ultrasmooth graphene nanoribbon semiconductors," *Science*, vol. 319, no. 5867, pp. 1229–1232, 2008.
- [5] X. Wang, L. Zhi, and K. Müllen, "Transparent, conductive graphene electrodes for dye-sensitized solar cells," *Nano Letters*, vol. 8, no. 1, pp. 323–327, 2008.
- [6] K. S. Kim, Y. Zhao, H. Jang et al., "Large-scale pattern growth of graphene films for stretchable transparent electrodes," *Nature*, vol. 457, no. 7230, pp. 706–710, 2009.
- [7] Q. Yan, B. Huang, J. Yu et al., "Intrinsic current-voltage characteristics of graphene nanoribbon transistors and effect of edge doping," *Nano Letters*, vol. 7, no. 6, pp. 1469–1473, 2007.
- [8] A. H. C. Neto, F. Guinea, N. M. R. Peres, K. S. Novoselov, and A. K. Geim, "The electronic properties of graphene," *Reviews of Modern Physics*, vol. 81, no. 1, pp. 109–162, 2009.
- [9] F. Guinea, M. I. Katsnelson, and M. A. H. Vozmediano, "Midgap states and charge inhomogeneities in corrugated graphene," *Physical Review B*, vol. 77, no. 7, Article ID 075422, 2008.
- [10] V. M. Pereira and A. H. C. Neto, "Strain engineering of graphene's electronic structure," *Physical Review Letters*, vol. 103, no. 4, Article ID 046801, 2009.
- [11] E. A. Kim and A. H. C. Neto, "Graphene as an electronic membrane," *Europhysics Letters*, vol. 84, no. 5, Article ID 57007, 2008.
- [12] A. Fasolino, J. H. Los, and M. I. Katsnelson, "Intrinsic ripples in graphene," *Nature Materials*, vol. 6, no. 11, pp. 858–861, 2007.
- [13] U. Stöberl, U. Wurstbauer, W. Wegscheider, D. Weiss, and J. Eroms, "Morphology and flexibility of graphene and few-layer graphene on various substrates," *Applied Physics Letters*, vol. 93, no. 5, Article ID 051906, 2008.
- [14] C. H. Lui, L. Liu, K. F. Mak, G. W. Flynn, and T. F. Heinz, "Ultraflat graphene," *Nature*, vol. 462, no. 7271, pp. 339–341, 2009.
- [15] S. Scharfenberg, D. Z. Rocklin, C. Chialvo, R. L. Weaver, P. M. Goldbart, and N. Mason, "Probing the mechanical properties of graphene using a corrugated elastic substrate," <http://arxiv.org/abs/1006.3037>.

- [16] A. L. V. de Parga, F. Calleja, B. Borca et al., “Periodically rippled graphene: growth and spatially resolved electronic structure,” *Physical Review Letters*, vol. 100, no. 5, Article ID 056807, 2008.
- [17] T. Tsukamoto and T. Ogino, “Morphology of graphene on step-controlled sapphire surfaces,” *Applied Physics Express*, vol. 2, no. 7, Article ID 075502, 2009.
- [18] T. Li and Z. Zhang, “Snap-through instability of graphene on substrates,” *Nanoscale Research Letters*, vol. 5, no. 1, pp. 169–173, 2010.
- [19] T. Li and Z. Zhang, “Substrate-regulated morphology of graphene,” *Journal of Physics D-Applied Physics*, vol. 43, no. 7, Article ID 075303, 2010.
- [20] Z. Zhang and T. Li, “Graphene morphology regulated by nanowires patterned in parallel on a substrate surface,” *Journal of Applied Physics*, vol. 107, no. 10, Article ID 103519, 2010.
- [21] Z. H. Aitken and R. Huang, “Effects of mismatch strain and substrate surface corrugation on morphology of supported monolayer graphene,” *Journal of Applied Physics*, vol. 107, no. 12, Article ID 123531, 2010.
- [22] D. D. D. Ma, C. S. Lee, F. C. K. Au, S. Y. Tong, and S. T. Lee, “Small-diameter silicon nanowire surfaces,” *Science*, vol. 299, no. 5614, pp. 1874–1877, 2003.
- [23] N. A. Melosh, A. Boukai, F. Diana et al., “Ultrahigh-density nanowire lattices and circuits,” *Science*, vol. 300, no. 5616, pp. 112–115, 2003.
- [24] D. W. Brenner, O. A. Shenderova, J. A. Harrison, S. J. Stuart, B. Ni, and S. B. Sinnott, “A second-generation reactive empirical bond order (REBO) potential energy expression for hydrocarbons,” *Journal of Physics Condensed Matter*, vol. 14, no. 4, pp. 783–802, 2002.
- [25] V. A. Bakaev, W. A. Steele, T. I. Bakaeva, and C. G. Pantano, “Adsorption of CO<sub>2</sub> and Ar on glass surfaces. Computer simulation and experimental study,” *Journal of Chemical Physics*, vol. 111, no. 21, pp. 9813–9821, 1999.
- [26] D. C. Liu and J. Nocedal, “On the limited memory BFGS method for large scale optimization,” *Mathematical Programming, Series B*, vol. 45, no. 3, pp. 503–528, 1989.
- [27] X. Liang, Z. Fu, and S. Y. Chou, “Graphene transistors fabricated via transfer-printing in device active-areas on large wafer,” *Nano Letters*, vol. 7, no. 12, pp. 3840–3844, 2007.
- [28] V. B. Shenoy, C. D. Reddy, A. Ramasubramaniam, and Y. W. Zhang, “Edge-stress-induced warping of graphene sheets and nanoribbons,” *Physical Review Letters*, vol. 101, no. 24, Article ID 245501, 2008.

## Research Article

# Preparation, Characterization, and Modeling of Carbon Nanofiber/Epoxy Nanocomposites

Lan-Hui Sun,<sup>1</sup> Zoubeida Ounaies,<sup>2</sup> Xin-Lin Gao,<sup>3</sup> Casey A. Whalen,<sup>2</sup> and Zhen-Guo Yang<sup>1</sup>

<sup>1</sup>Department of Materials Science, Fudan University, Shanghai 200433, China

<sup>2</sup>Department of Aerospace Engineering, Texas A&M University, College Station, TX 77843, USA

<sup>3</sup>Department of Mechanical Engineering, Texas A&M University, College Station, TX 77843, USA

Correspondence should be addressed to Zoubeida Ounaies, zounaies@tamu.edu

Received 6 July 2010; Accepted 19 October 2010

Academic Editor: Sulin Zhang

Copyright © 2011 Lan-Hui Sun et al. This is an open access article distributed under the Creative Commons Attribution License, which permits unrestricted use, distribution, and reproduction in any medium, provided the original work is properly cited.

There is a lack of systematic investigations on both mechanical and electrical properties of carbon nanofiber (CNF)-reinforced epoxy matrix nanocomposites. In this paper, an in-depth study of both static and dynamic mechanical behaviors and electrical properties of CNF/epoxy nanocomposites with various contents of CNFs is provided. A modified Halpin-Tsai equation is used to evaluate the Young's modulus and storage modulus of the nanocomposites. The values of Young's modulus predicted using this method account for the effect of the CNF agglomeration and fit well with those obtained experimentally. The results show that the highest tensile strength is found in the epoxy nanocomposite with a 1.0 wt% CNFs. The alternate-current (AC) electrical properties of the CNF/epoxy nanocomposites exhibit a typical insulator-conductor transition. The conductivity increases by four orders of magnitude with the addition of 0.1 wt% (0.058 vol%) CNFs and by ten orders of magnitude for nanocomposites with CNF volume fractions higher than 1.0 wt% (0.578 vol%). The percolation threshold (i.e., the critical CNF volume fraction) is found to be at 0.057 vol%.

## 1. Introduction

Carbon nanofibers (CNFs) are electrically and thermally conductive and have very good mechanical properties. Research on carbon nanofiber-reinforced nanocomposites has been mainly focusing on carbon nanotube (CNT)-filled nanocomposites. This is due to the fact that CNTs have fewer microstructural defects than CNFs, resulting in better overall properties as well as smaller dimensions and a lower density. However, CNFs are less expensive and can be manufactured at high yields, justifying further in-depth investigation of their impact on nanocomposites.

CNFs have a cup-stacked structure which results from the vapor deposition process used to produce them [1, 2]. The relatively low efficiency of catalyst results in microstructural defects in CNFs, which require special treatments in order for CNFs to achieve desired properties. A number of treatment methods have been used, which include acid treatment [3, 4], heat treatment (to eliminate defects) [5], plasma treatment (to purify) [6], and surface functionalization (to improve

interface adhesion) [7, 8]. Because of their high aspect ratio and high surface energy (due to nanoscale diameters), CNFs tend to agglomerate, leading to inhomogeneous dispersion. Many efforts have been made to deagglomerate CNFs using methods such as diluting the matrix with solvents [6, 9] and combining mechanical mixing with sonication [9, 10].

Good dispersion of CNFs leads to an enhancement in both strength and modulus of nanocomposites [9, 11–14]. Choi et al. [9] found that CNF/epoxy nanocomposites had a maximum tensile strength and a large Young's modulus with 5 wt% CNFs, and a reduced fracture strain with increasing filler content. In addition, both the storage modulus and the glass transition temperature ( $T_g$ ) increased due to the incorporation of CNFs. A study by Zhou and coworkers [14] indicated that the modulus of CNF/epoxy nanocomposites increased continuously with increasing CNF content, but the tensile strength decreased with further increasing CNF content beyond 2 wt% CNF. DMA studies revealed that with 3 wt% CNFs, there was a 65% enhancement in the storage modulus at room temperature and a 6°C increase

in  $T_g$ . Xu et al. [15] demonstrated that there was only very little increase in mechanical properties of CNF/epoxy nanocomposites, even though they used GCNF-ODA reactive linkers to improve the interface of CNFs and epoxy.

Because of their high electrical conductivity, CNFs have been used as fillers to improve electrical properties of polymeric composites in a number of studies [3, 4, 10, 16–19]. A remarkable increase in electrical conductivity was observed when CNF volume fraction exceeded the percolation threshold. For CNF/epoxy nanocomposites, Allaoui et al. [10] found a percolation threshold at a very low critical CNF weight fraction of 0.064%. The insulator-to-conductor transition region spanned about one order of magnitude of the CNF weight fraction from 0.1 to 1.2%. Far from the transition, the conductivity increased by two orders of magnitude. Other studies on electrical properties of CNF/epoxy nanocomposites did not focus on the percolation behavior, but rather on the effect of CNFs' heat treatment [5] or on the effect of the viscosity of epoxy matrix [9] on the electrical conductivity of CNF/epoxy nanocomposites. Moreover, none of these papers discussed the dielectric properties of CNF/epoxy nanocomposites.

So far, there has been no study that specifically focuses on the simultaneous characterization of mechanical and electrical properties of solvent-processed CNF/epoxy nanocomposites. In addition, the existing results concerning the impact of CNFs on mechanical behavior of epoxy nanocomposites appear to be inconsistent, as reviewed above. This motivated the current study.

In this paper, CNF/epoxy nanocomposites with various contents of CNFs were prepared. Both static and dynamic mechanical properties as well as electrical and dielectric properties of the nanocomposites were investigated, and fracture surfaces were observed in order to better understand the fracture mechanisms. Also, the Young's modulus and storage modulus were predicted using a modified Halpin-Tsai equation, which fitted the experimental results well.

## 2. Experimental Study

**2.1. Preparation of Nanocomposites.** Carbon nanofibers (Pyrograf-III) were supplied by Applied Science, Inc. (ASI). The carbon nanofibers have diameters ranging from 100 to 200 nm and lengths from 30 to 100  $\mu\text{m}$ . The acquired carbon nanofibers were heat treated up to 3000°C. A purification process was also utilized to remove the undesirable impurities. The purification process consisted of refluxing the CNFs in dichloromethane— $\text{CH}_2\text{Cl}_2$  (Aldrich, Co.) for five days at 35°C, followed by several deionized  $\text{H}_2\text{O}$  washes and second-time refluxing for 24 hours. The nanofibers were rinsed again, vacuum filtered for 24 hours and dried at 110°C for at least 24 hours, and then examined for water content. The purified CNFs were properly stored in closed hygroscopic containers, since retained moisture could prevent proper mixing.

CNF/epoxy nanocomposites with CNF content ranging from 0 to 2 wt% were fabricated. First, a desired amount of CNFs was immersed into Dimethylacetamide (DMAC).

The solution was sonicated and mechanically stirred for 1 hour. Epoxy resin (Epon 862, Hexion Specialty Chemicals, Inc.) was then added, and the new solution was sonicated and mechanically stirred for another 3 hours. The solution was then evaporated in an enclosed vacuum at 80°C overnight to eliminate all the DMAC. Curing agent (EpiKure W, Hexion Specialty Chemicals, Inc.) was then used, and the new solution was sonicated and mechanically mixed for half an hour. Before casting, the solution was degassed in a vacuum overnight to remove trapped gasses. Finally, the solution was cast into different molds to get samples for mechanical and electrical tests. The samples were heated and cured for 2 hours at 125°C and another 2 hours at 177°C.

**2.2. Tensile Tests and SEM.** Mechanical properties were measured on an MTS universal testing machine at a constant displacement rate of 0.5 mm/min. The specimen had a width of 13 mm and a thickness of 2.5 mm. The gauge length was 60 mm. The tensile strength and Young's modulus were calculated from the recorded stress levels at the constant displacement rate. All tensile tests were performed at room temperature, and three specimens (or more) were used for each CNF content. The average value for each specimen type was recorded. The tensile stress-strain curves were plotted after calculating the engineering stress and engineering strain.

Fracture surfaces of the tensile specimens were observed using a scanning electron microscope (SEM, JEOL JSM-6400) to study the failure mechanisms and the post-fracture dispersion of CNFs. Before the SEM observations, the specimens were coated with a thin layer of platinum.

**2.3. Dynamic Mechanical Analysis.** Dynamic mechanical analysis (DMA) was performed on a RSA-III DMA from 25 to 200°C at a temperature scanning rate of 3°C/min. The tests were operated in the three-point bending mode at an oscillation frequency of 1 Hz. The rectangular specimens were 30 mm long, 9 mm, wide and 3 mm thick. Three samples of each CNF content were tested. The glass transition temperature ( $T_g$ ) was assigned as the temperature where the loss factor was recorded as a maximum.

**2.4. Electrical Measurements.** Alternate-current (AC) conductivity and dielectric constant of pure epoxy and CNF/epoxy nanocomposites were measured using an impedance analyzer (Novocontrol Alpha Analyzer) in a frequency range of  $10^{-2}$ – $10^7$  Hz. The specimens were coated with an electro-deposited silver layer (100 nm thick) on the two opposite surfaces to ensure a good electrical contact area between the electrodes and specimen. The samples had a bulk size of 1.5 cm  $\times$  1.5 cm. The silver electrode area was circular with a diameter of 0.5 cm. Each measurement shown was an average of 3 to 4 samples. The setup was based on a parallel plate configuration, where the parallel capacitance ( $C_p$ ) was measured at each frequency and was then converted to dielectric constant  $\epsilon = C_p t / (A \epsilon_0)$ , where  $t$  is the thickness of the sample ( $\sim 0.5$  mm),  $A$  is the electrode area, and  $\epsilon_0$  is the permittivity of free space ( $= 8.85 \times 10^{-12}$  F/m).

TABLE 1: Tensile properties of CNF/epoxy nanocomposites.

Sample	Tensile strength (MPa)	Toughness (MJ/m <sup>3</sup> )	Young's Modulus (GPa)
Pure Epon862	68.7 ± 2.5	397.6 ± 33.2	1.04 ± 0.04
0.05% CNF	70.9 ± 2.6	418.2 ± 41.9	1.06 ± 0.06
0.1% CNF	71.0 ± 3.7	550.0 ± 23.6	1.09 ± 0.01
0.5% CNF	73.0 ± 1.4	610.2 ± 39.3	1.16 ± 0.01
1% CNF	74.4 ± 2.4	562.7 ± 28.0	1.22 ± 0.01
2% CNF	62.1 ± 2.5	244.5 ± 30.8	1.29 ± 0.02

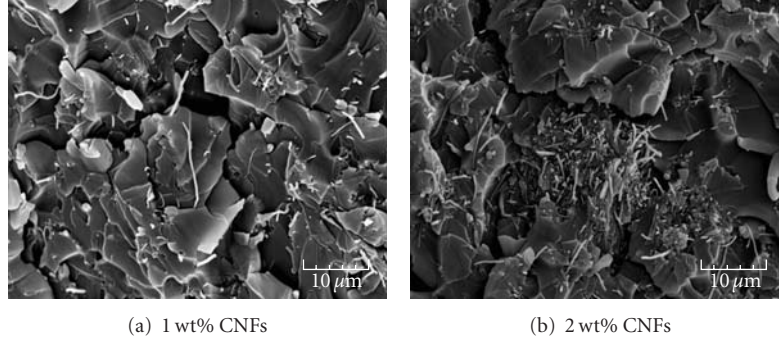


FIGURE 1: Dispersion of CNFs in epoxy.

### 3. Results and Discussion

**3.1. Tensile Properties.** The tensile properties of the CNF/epoxy nanocomposites with the CNF content varying from 0 to 2 wt% are shown in Table 1. It is seen that the tensile strength increases with increasing content of CNFs until 1 wt%, beyond which the tensile strength decreases. Figure 1 shows the dispersion of CNFs in the nanocomposites with 1 wt% and 2 wt% CNFs. For the 1 wt% CNF/epoxy nanocomposite, the CNFs are homogeneously dispersed as individual fibers. However, the CNFs in the 2 wt% CNF/epoxy nanocomposite are agglomerated and clustered as bundles with a diameter of about 10  $\mu\text{m}$ . These bundles act as stress concentration sites, leading to the nonuniform stress distribution and high stresses near the bundles. During the tensile test, the epoxy matrix around these bundles breaks quickly due to the elevated stresses, resulting in the decrease in tensile strength of this nanocomposite.

The area under the stress-strain curve is known as toughness, which represents the total strain energy per unit volume in the material induced by the applied stress. The addition of uniformly dispersed CNFs can significantly increase the toughness of the epoxy, as indicated in Table 1. The toughness increases by 42% with the addition of 1 wt% CNFs and decreases by 39% with the addition of 2 wt% CNFs, both relative to the pure epoxy (Epon 862). To better understand the toughening mechanism of the CNF/epoxy nanocomposites, SEM is used to observe the fracture surfaces.

From the fracture surface of the pure epoxy (Figure 2(a)), it can be seen that large and flat cleavage planes indicate typical characteristic of brittle fracture. For a 0.05 wt%

CNF/epoxy nanocomposite (Figure 2(b)), the fracture surface becomes more rough, and the cleavage planes become smaller than those of the pure epoxy. Large cracks propagate along low CNF density areas, leading to ridges. Cleavage planes are evenly distributed and are the smallest for a 1 wt% CNF/epoxy nanocomposite (Figure 2(c)). The increased number of cleavage planes results in more areas capable of absorbing the fracture energy, which leads to a higher crack propagation resistance. An inspection of Figure 1(a) again reveals some fiber pullout, indicating that the fiber-matrix adhesion is not optimal. From these observations, it appears that this nanocomposite has the highest toughness. However, matrix cracks are evident on the fracture surface of the 2 wt% CNF/epoxy nanocomposite (Figure 2(d)). This suggests that a lot of microcracks may have started from the clusters of CNFs. With the increase of the applied load, these microcracks would quickly connect with each other to form macrocracks, leading to fracture of the nanocomposite.

The Halpin-Tsai equation links the modulus of a unidirectional fiber composite to the fiber volume fraction [20, 21]. Many studies have been conducted to predict the modulus of a fiber-reinforced composite with randomly aligned discontinuous fibers by using variants of the Halpin-Tsai equation. In most of these studies, an orientation factor,  $\alpha$ , was introduced to account for the random fiber orientation. In [22], the Halpin-Tsai equation was modified to be

$$\frac{E_c}{E_m} = \frac{1 + c\eta\nu_f}{1 - \eta\nu_f} \quad \text{with} \quad \eta = \frac{(\alpha E_f/E_m) - 1}{(\alpha E_f/E_m) + c}, \quad (1)$$

where  $E_c$ ,  $E_m$ , and  $E_f$  are, respectively, the moduli of the composite, matrix, and fiber (carbon nanotubes),  $\nu_f$  is

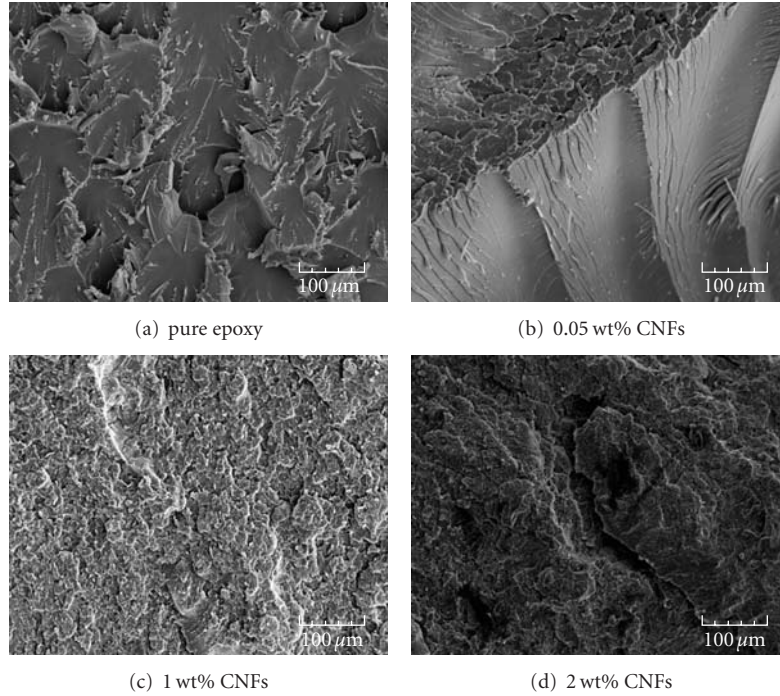


FIGURE 2: Fracture surface morphology.

the fiber volume fraction, and  $c = 2l/d$  is the shape factor relating to the aspect ratio of the reinforcement length ( $l$ ) over the diameter ( $d$ ). They further modified the Halpin-Tsai equation by changing the shape factor  $c$  to  $\xi = (2l/d)e^{-av_f-b}$ , which is an exponential relation, with  $a$  and  $b$  being constants that are related to the degree of CNF agglomeration.

In this study, the Young's moduli of the epoxy matrix and CNF are 1.04 GPa and 400 GPa, respectively. The orientation factor  $\alpha$  is taken to be 0.184 (after [23]). The aspect ratio of the CNFs is about 150. The effects of the constants  $a$  and  $b$  on the Young's modulus predicted using the modified Halpin-Tsai equation are shown in Figures 3(a) and 3(b). It can be seen that increasing the constant  $a$  tends to bend the curves, while increasing the constant  $b$  lowers the height of the curves.

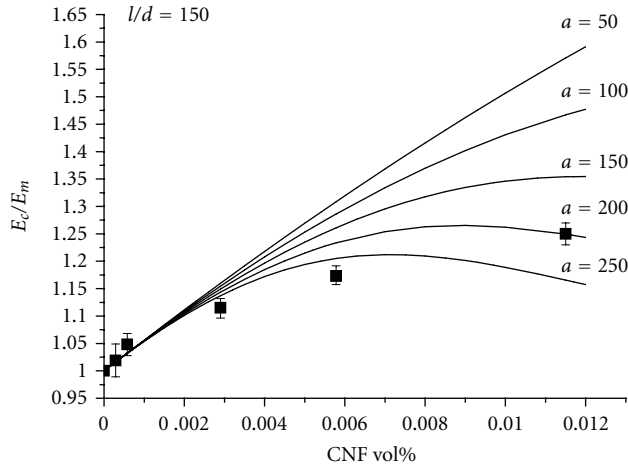
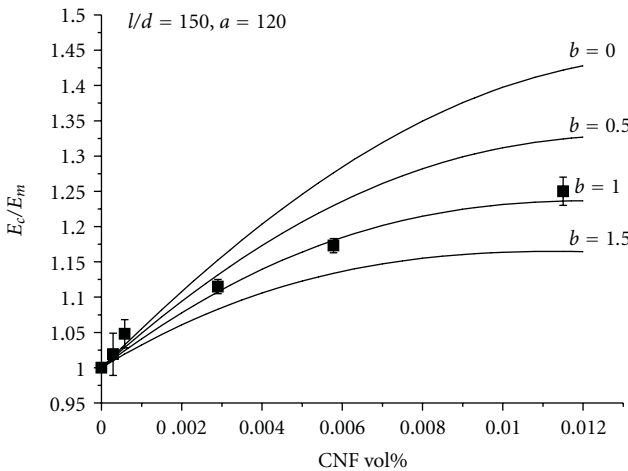
By varying the values of  $a$  and  $b$ , a best fit to the experimentally obtained Young's modulus is found when  $a = 120$  and  $b = 1$ . This best fit is displayed in Figure 3(b), for which  $\xi = 300e^{-120v_f-1}$ . Good agreement between the experimental data and predicted results over the range of fiber volume fractions investigated indicates that CNF/epoxy nanocomposites are 3D randomly oriented systems with agglomeration of CNFs at higher volume fractions.

**3.2. Dynamic Mechanical Analysis.** The effects of CNFs on the storage modulus of the CNF/epoxy nanocomposites are illustrated in Figure 4. The addition of CNFs increases the storage modulus of epoxy at temperatures both below and above the glass transition temperature ( $T_g$ ). The maximum storage modulus is observed in the nanocomposite with 1 wt% CNFs, which is, respectively, about 18% and 70% higher than that of the pure epoxy below and above the

glass transition temperature. The presence of CNFs inhibits the movement of molecular chains around the CNFs. This is due to the high surface energy of CNFs absorbing the motion of the molecular chains around them. Because of this interaction between CNFs and the molecular chains, the force imposed on the CNF/epoxy nanocomposites transfers to the stiff CNFs and leads to the increased storage modulus. The storage modulus starts to decrease at 2 wt% CNF content. This is due to the poor dispersion of CNFs at higher contents, which can be seen from the SEM images in Figure 1.

$T_g$  represents a major transition for many polymers, as physical properties change significantly when the material goes from the glassy state to the rubber-like state. For cured polymers it appears that DMA is 10 to 100 times more sensitive to the changes occurring near  $T_g$  than differential scanning calorimetry [24].  $T_g$  is usually determined from the peak of the loss factor ( $\tan \delta$ ) curves. Figure 5 shows the loss factor curves of the pure epoxy and the CNF/epoxy nanocomposites. A small increase in  $T_g$  is found at CNF content lower than 2 wt%. CNFs restrict the segmental movement of molecular chains, resulting in a higher  $T_g$ . The peak height of the loss factor of the nanocomposites decreases with the increasing content of CNFs. As mentioned in [25], the relative heights in  $T_g$  are inversely proportional to the volume fraction of confined segments in the interface layer. On the other hand, with the increasing content of the uniformly dispersed CNFs, more interactions between molecular chains and CNFs occur.

For the nanocomposite with 2 wt% CNFs, there are a decrease in  $T_g$  and a broadening of the peak. The decrease in  $T_g$  is due to the agglomeration of the CNFs in the

(a) Effect of the constant  $a$ (b) Effect of the constant  $b$ FIGURE 3: Effects of  $a$  and  $b$  on the predicted Young's modulus.

epoxy matrix. There is a hump on the loss factor curve, which further confirms the non-uniformly distributed CNFs. Figure 1(b) clearly shows the dispersion of CNFs in epoxy: large clusters of CNFs are found, but individual fibers are still present. Since the samples of DMA are randomly chosen from the bulk nanocomposite, it is believed that some samples have more CNF clusters, while other samples have more individually dispersed CNFs for the 2 wt% CNF/epoxy nanocomposite. The mobility of molecular chains around CNF clusters is different from that around individual CNFs. Thus, the average value of the loss factor of this nanocomposite has two blunt peaks, indicating two different molecular mobilities around CNF clusters and individual CNFs. Also, the presence of CNF clusters may inhibit the curing of epoxy, thereby decreasing the crosslink density, so that  $T_g$  decreases.

The modified Halpin-Tsai equation is also used to fit the experimental data of the storage modulus both below and above  $T_g$ . The results are shown in Figure 6. The fitting to the storage modulus is still good for temperatures both below

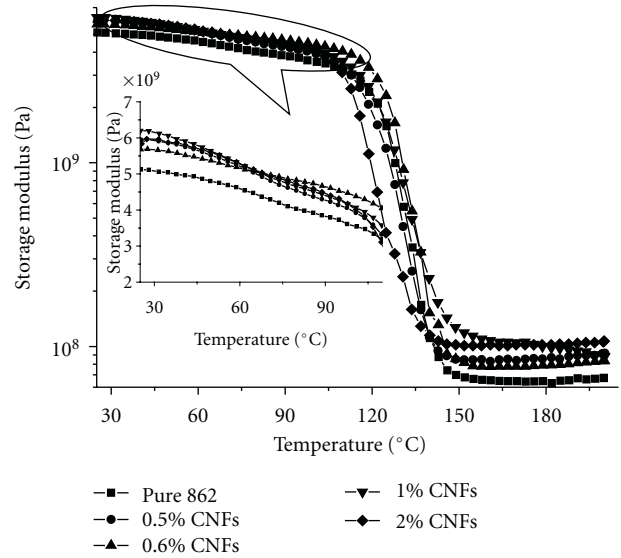


FIGURE 4: Storage modulus of the pure epoxy and CNF/epoxy nanocomposites.

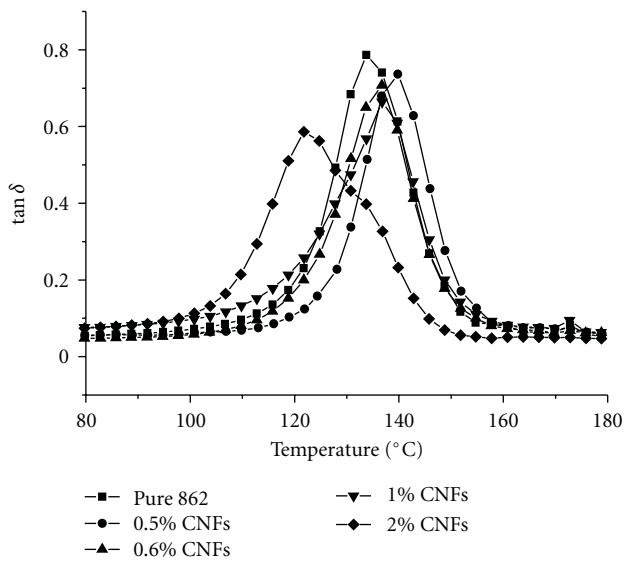


FIGURE 5: Loss factor of the pure epoxy and CNF/epoxy nanocomposites.

and above  $T_g$ . The constants  $a$  and  $b$  tend to affect the shape of each predicted curve although they do not have clear physical meaning. Figure 6 shows that  $a$  and  $b$  seem to be higher for high temperatures than those for low temperatures. Also, it is worth pointing out that the deviation of the storage modulus between the samples with the same content of CNFs is relatively large. With the difficulties involved in achieving a uniformly distributed CNF/epoxy nanocomposite, the dispersion of the CNFs is a likely source of error.

**3.3. Electrical Properties.** Figure 7 shows the electrical conductivity of the pure epoxy and the CNF/epoxy nanocomposites changing with frequency. Conductivity of the pure

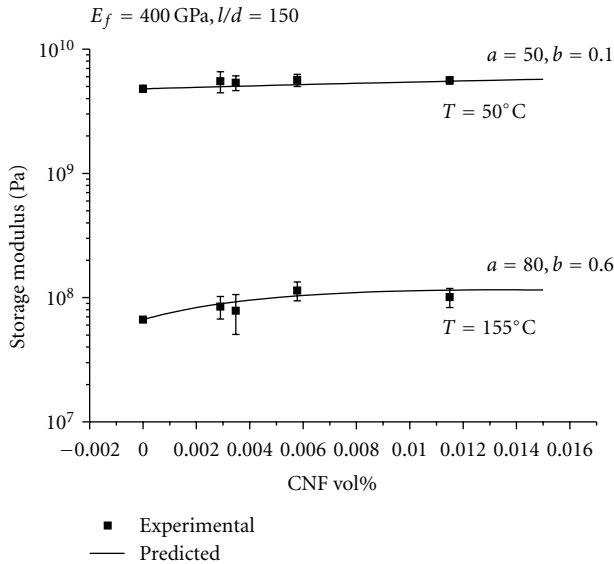


FIGURE 6: Storage modulus predicted using the modified Halpin-Tsai equation and fitted to the experimental data.

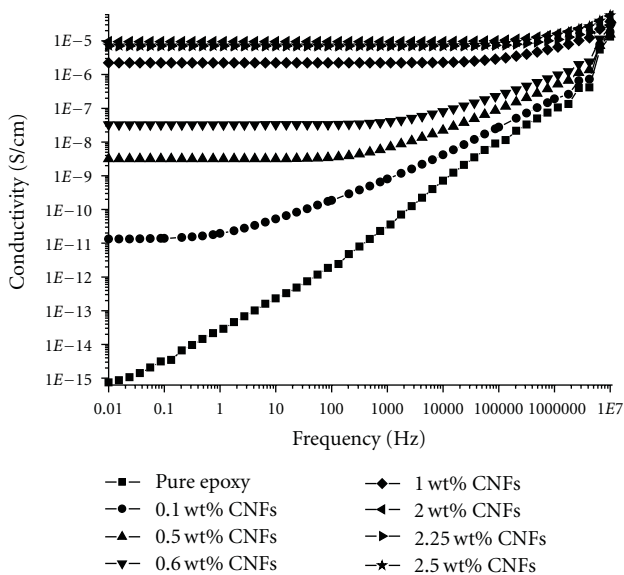


FIGURE 7: Conductivity of the epoxy nanocomposites with various volume fractions of CNFs as a function of frequency.

epoxy is seen to increase almost linearly with increasing frequency, indicating a behavior of a non-conductive material. For the CNF/epoxy nanocomposites, the conductivity is independent of frequency at low frequencies but increases with the frequency after critical value is surpassed. The critical frequency at which the conductivity begins to rise increases with the CNF volume fraction. The frequency dependence of the electrical conductivity of the nanocomposites results from the electrons in finite-size clusters with fractal nature that can be scanned at frequencies higher than the critical frequency [10].

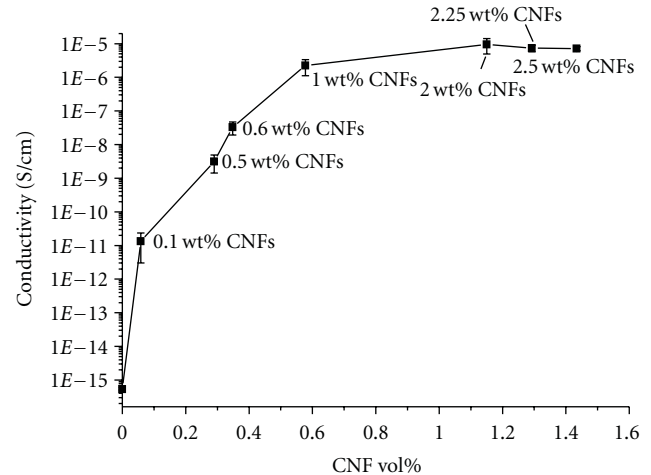


FIGURE 8: Conductivity varying with the CNF volume fraction.

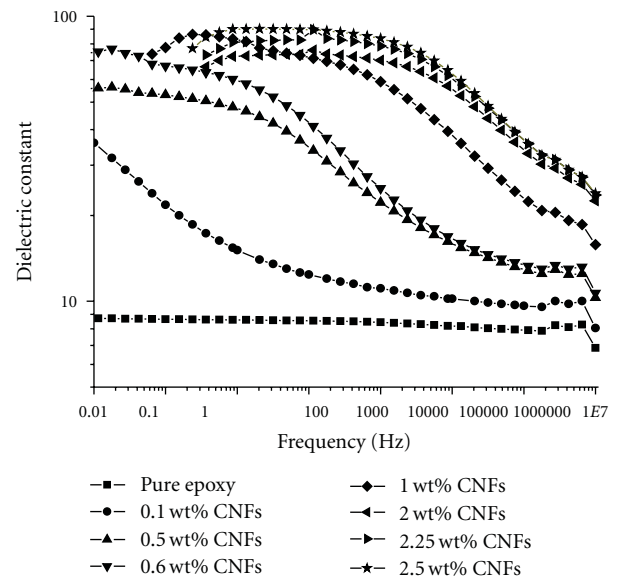


FIGURE 9: Dielectric constant of the epoxy nanocomposites with various volume fractions of CNFs as a function of frequency.

The direct-current (DC) conductivities are obtained by extrapolating the conductivity curves of the alternate-current (AC) data. The conductivity is plotted versus the CNF volume fraction ( $p$ ), as shown in Figure 8. The conductivity increases by four orders of magnitude with the addition of 0.1 wt% (0.058 vol%) CNFs due to the tunneling conduction between CNFs. The value of the CNF volume fraction at which tunneling occurs is called the percolation threshold ( $p_c$ ). According to percolation theory, the direct-current electrical conductivity  $\sigma$  (at  $p > p_c$ ) of a percolating system should exhibit a power-law dependence:  $\sigma \propto (p - p_c)^t$ . A best fit to the experimental data reveals that the percolation threshold is 0.057 vol% with the exponent  $t = 1.83$ . The exponent  $t$  is in the range of 1.6 to 2.0, which has been typically used in percolation theory [26–29]. The conductivity increases by ten orders of magnitude for nanocomposites

with CNF volume fractions higher than 1 wt% (0.578 vol%) and then plateaus. This is because CNFs come into contact with each other and form conductive pathways throughout the composites at high CNF volume fractions.

The dielectric constant of the nanocomposites with various volume fractions of CNFs was measured as a function of frequency (Figure 9). The addition of CNFs greatly increases the dielectric constant, and the dielectric constant increases with increasing amount of CNF volume fraction at a given frequency. The dielectric constant of the pure epoxy is independent of frequency, which is the typical behavior of a capacitor. Once CNFs have been added, the dielectric constant of the nanocomposite decreases with frequency. The frequency dependence of dielectric constant results from two effects: one is the polarization effect between clusters inside the solution, and the other is anomalous diffusion within each cluster [30]. At higher frequencies, it is hard for either the polarization or the diffusion to occur because the electrical field changes so fast that they are not able to follow the field variation.

#### 4. Conclusion

CNF/epoxy nanocomposites with various contents of CNFs are processed and studied. Static and dynamic mechanical testing and AC electrical measurements are conducted to investigate the effects of CNFs on the effective properties of the CNF/epoxy nanocomposites. The nanocomposite with 1 wt% CNFs exhibits good dispersion and has the highest tensile strength. The tensile strength decreases with further increase in the CNF content due to agglomeration of CNFs. The maximum storage modulus is also observed in the nanocomposite with 1 wt% CNFs, which is about 18% and 70% higher than that of the pure epoxy below and above the glass transition temperature, respectively. The predicted values of the Young's modulus and storage modulus using a modified Halpin-Tsai equation that accounts for the effect of the CNF agglomeration compares fairly well with those obtained experimentally.

The AC electrical behavior of the CNF/epoxy nanocomposites exhibits a typical insulator-conductor transition. The conductivity increases by four orders of magnitude with the addition of 0.1 wt% (0.058 vol%) CNFs, and by ten orders of magnitude for nanocomposites with CNF volume fractions higher than 1 wt% (0.578 vol%). The measured values of the conductivity of the nanocomposites conform to percolation theory and show a low percolation threshold at 0.057 vol%.

#### Acknowledgments

The research reported here was conducted in the Electroactive Materials Characterization Laboratory at Texas A&M University. Z. Ounaies acknowledges financial support from NSF (Grant no. CMMI 0514265) and AFOSR (Grant no. FA9550-06-1-0422). X. L. Gao thanks the U.S Army-Soldier Equipment Program for supporting the effort. L. H. Sun and Z. G. Yang are grateful for the support from China

Scholarship Council (no. 20083019) and Shanghai Leading Academic Discipline Project (Project no. B113).

#### References

- [1] G. G. Tibbetts, M. L. Lake, K. L. Strong, and B. P. Rice, "A review of the fabrication and properties of vapor-grown carbon nanofiber/polymer composites," *Composites Science and Technology*, vol. 67, no. 7-8, pp. 1709–1718, 2007.
- [2] T. Hashishin, H. Iwanaga, M. Ichihara, and S. R. Mukai, "Core structure of vapor grown carbon fibers and morphology dependence of tensile strength," *Carbon*, vol. 41, no. 2, pp. 343–349, 2003.
- [3] P. Cortés, K. Lozano, E. V. Barrera, and J. Bonilla-Rios, "Effects of nanofiber treatments on the properties of vapor-grown carbon fiber reinforced polymer composites," *Journal of Applied Polymer Science*, vol. 89, no. 9, pp. 2527–2534, 2003.
- [4] S. Kumar, T. Rath, R. N. Mahaling et al., "Study on mechanical, morphological and electrical properties of carbon nanofiber/polyetherimide composites," *Materials Science and Engineering B*, vol. 141, no. 1-2, pp. 61–70, 2007.
- [5] K. Lafdi, W. Fox, M. Matzek, and E. Yildiz, "Effect of carbon nanofiber heat treatment on physical properties of polymeric nanocomposites—part I," *Journal of Nanomaterials*, vol. 2007, Article ID 52729, 6 pages, 2007.
- [6] R. D. Patton, C. U. Pittman Jr., L. Wang, and J. R. Hill, "Vapor grown carbon fiber composites with epoxy and poly(phenylene sulfide) matrices," *Composites Part A*, vol. 30, no. 9, pp. 1081–1091, 1999.
- [7] S.-N. Ahn, H.-J. Lee, B.-J. Kim, L.-S. Tan, and J.-B. Baek, "Epoxy/amine-functionalized short-length vapor-grown carbon nanofiber composites," *Journal of Polymer Science, Part A*, vol. 46, no. 22, pp. 7473–7482, 2008.
- [8] K. Lozano and E. V. Barrera, "Nanofiber-reinforced thermoplastic composites. I. Thermoanalytical and mechanical analyses," *Journal of Applied Polymer Science*, vol. 79, no. 1, pp. 125–133, 2001.
- [9] Y.-K. Choi, K.-I. Sugimoto, S.-M. Song, Y. Gotoh, Y. Ohkoshi, and M. Endo, "Mechanical and physical properties of epoxy composites reinforced by vapor grown carbon nanofibers," *Carbon*, vol. 43, no. 10, pp. 2199–2208, 2005.
- [10] A. Allaoui, S. V. Hoa, and M. D. Pugh, "The electronic transport properties and microstructure of carbon nanofiber/epoxy composites," *Composites Science and Technology*, vol. 68, no. 2, pp. 410–416, 2008.
- [11] J. Sandler, P. Werner, M. S. P. Shaffer, V. Demchuk, V. Altstädt, and A. H. Windle, "Carbon-nanofibre-reinforced poly(ether ether ketone) composites," *Composites Part A*, vol. 33, no. 8, pp. 1033–1039, 2002.
- [12] H. Ma, J. Zeng, M. L. Realff, S. Kumar, and D. A. Schiraldi, "Processing, structure, and properties of fibers from polyester/carbon nanofiber composites," *Composites Science and Technology*, vol. 63, no. 11, pp. 1617–1628, 2003.
- [13] Y. K. Choi, K. I. Sugimoto, S. M. Song, and M. Endo, "Mechanical and thermal properties of vapor-grown carbon nanofiber and polycarbonate composite sheets," *Materials Letters*, vol. 59, no. 27, pp. 3514–3520, 2005.
- [14] Y. Zhou, F. Pervin, and S. Jeelani, "Effect vapor grown carbon nanofiber on thermal and mechanical properties of epoxy," *Journal of Materials Science*, vol. 42, no. 17, pp. 7544–7553, 2007.

- [15] L. R. Xu, V. Bhamidipati, W.-H. Zhong et al., "Mechanical property characterization of a polymeric nanocomposite reinforced by graphitic nanofibers with reactive linkers," *Journal of Composite Materials*, vol. 38, no. 18, pp. 1563–1582, 2004.
- [16] Y. Bin, M. Mine, A. Koganemaru, X. Jiang, and M. Matsuo, "Morphology and mechanical and electrical properties of oriented PVA-VGCF and PVA-MWNT composites," *Polymer*, vol. 47, no. 4, pp. 1308–1317, 2006.
- [17] G. D. Liang and S. C. Tjong, "Electrical properties of percolative polystyrene/carbon nanofiber composites," *IEEE Transactions on Dielectrics and Electrical Insulation*, vol. 15, no. 1, pp. 214–220, 2008.
- [18] T. Natsuki, Q.-Q. Ni, and S.-H. Wu, "Temperature dependence of electrical resistivity in carbon nanofiber/unsaturated polyester nanocomposites," *Polymer Engineering and Science*, vol. 48, no. 7, pp. 1345–1350, 2008.
- [19] R. J. Kuriger, M. K. Alam, D. P. Anderson, and R. L. Jacobsen, "Processing and characterization of aligned vapor grown carbon fiber reinforced polypropylene," *Composites Part A*, vol. 33, no. 1, pp. 53–62, 2002.
- [20] J. C. Halpin and J. L. Kardos, "The Halpin-Tsai equations: a review," *Polymer Engineering and Science*, vol. 16, no. 5, pp. 344–352, 1976.
- [21] C. L. Tucker III and E. Liang, "Stiffness predictions for unidirectional short-fiber composites: review and evaluation," *Composites Science and Technology*, vol. 59, no. 5, pp. 655–671, 1999.
- [22] M.-K. Yeh, N.-H. Tai, and J.-H. Liu, "Mechanical behavior of phenolic-based composites reinforced with multi-walled carbon nanotubes," *Carbon*, vol. 44, no. 1, pp. 1–9, 2006.
- [23] M. Van Es, F. Xiqiao, J. Van Turhout, and E. van der Giessen, "Comparing polymer-clay nanocomposites with conventional composites using composite modeling," in *Speciality Polymer Additives: Principles and Applications*, S. Al-Malaika, A. Golovoy, and C. A. Wilkie, Eds., vol. 484, chapter 21, Blackwell Science, Malden, Mass, USA, 2001.
- [24] H. P. Menard, *Dynamic Mechanical Analysis, A Practical Introduction*, CRC Press, Taylor & Francis, Boca Raton, Fla, USA, 2008.
- [25] Y. Pan, Y. Xu, L. An et al., "Hybrid network structure and mechanical properties of rodlike silicate/cyanate ester nanocomposites," *Macromolecules*, vol. 41, no. 23, pp. 9245–9258, 2008.
- [26] D. Stauffer and A. Aharony, *An Introduction to Percolation Theory*, CRC Press, Taylor & Francis, Boca Raton, Fla, USA, 1994.
- [27] Z. Ounaies, C. Park, K. E. Wise, E. J. Siochi, and J. S. Harrison, "Electrical properties of single wall carbon nanotube reinforced polyimide composites," *Composites Science and Technology*, vol. 63, no. 11, pp. 1637–1646, 2003.
- [28] H. M. Ma and X.-L. Gao, "A three-dimensional Monte Carlo model for electrically conductive polymer matrix composites filled with curved fibers," *Polymer*, vol. 49, no. 19, pp. 4230–4238, 2008.
- [29] K. Li, X. L. Gao, J. C. Fielding, and T. B. Tolle, "Modeling of electrical conductivity of nickel nanostrand filled polymer matrix composites," *Journal of Computational and Theoretical Nanoscience*, vol. 6, no. 3, pp. 494–504, 2009.
- [30] Y. Song, T. W. Noh, S.-I. Lee, and J. R. Gaines, "Experimental study of the three-dimensional ac conductivity and dielectric constant of a conductor-insulator composite near the percolation threshold," *Physical Review B*, vol. 33, no. 2, pp. 904–908, 1986.

## Research Article

# Effect of Source, Surfactant, and Deposition Process on Electronic Properties of Nanotube Arrays

Dheeraj Jain,<sup>1</sup> Nima Rouhi,<sup>1</sup> Christopher Rutherglen,<sup>1</sup> Crystal G. Densmore,<sup>2</sup>  
Stephen K. Doorn,<sup>2</sup> and Peter J. Burke<sup>1,3</sup>

<sup>1</sup>Integrated Nanosystems Research Facility, Department of Electrical Engineering and Computer Science, University of California, Irvine, CA 92697, USA

<sup>2</sup>Chemical Diagnostics and Engineering (C-CDE) Group, Chemistry Division, Los Alamos National Laboratory, Los Alamos, NM 87545, USA

<sup>3</sup>Department of Printed Electronics, Suncheon National University, Suncheon, Jeonnam 540-742, Republic of Korea

Correspondence should be addressed to Peter J. Burke, pburke@uci.edu

Received 6 May 2010; Accepted 27 September 2010

Academic Editor: Sulin Zhang

Copyright © 2011 Dheeraj Jain et al. This is an open access article distributed under the Creative Commons Attribution License, which permits unrestricted use, distribution, and reproduction in any medium, provided the original work is properly cited.

The electronic properties of arrays of carbon nanotubes from several different sources differing in the manufacturing process used with a variety of average properties such as length, diameter, and chirality are studied. We used several common surfactants to disperse each of these nanotubes and then deposited them on Si wafers from their aqueous solutions using dielectrophoresis. Transport measurements were performed to compare and determine the effect of different surfactants, deposition processes, and synthesis processes on nanotubes synthesized using CVD, CoMoCAT, laser ablation, and HiPCO.

## 1. Introduction

*1.1. Motivation.* Carbon nanotubes can be used for high-performance electronics [1] (defense), printed electronics [2] (commercial), and molecular sensors [3] (security) as well as a host of other potentially exotic applications such as nanoantennas [4, 5] and molecular beacons [6]. However, a scalable manufacturing technology for nanotube devices with appropriate yield, reproducibility, and performance in various metrics (mobility, on/off ratio, cost, chemical sensitivity, sensor specificity, etc.) is currently lacking. This is, in part, due to the variety of synthesis and deposition techniques and challenges due to the inherence in nanotube physical properties.

Of these challenges, nanotube dispersion in solution followed by deposition into arrays or mats that preserves the intrinsic, high performance is the largest, unmet challenge. Thus, there is a great need for an integrated, comprehensive study of the effect of nanotubes synthesis procedures, dispersion procedures, and deposition processes on the electronic properties of nanotube arrays. In this paper, we provide the first attempt at such a comprehensive study. While a

complete understanding of the physical processes involved in these complex manufacturing steps is still lacking, our work provides the first, raw set of empirical guidelines to guide future technology development in this area.

*1.2. Dispersion.* It is well known that synthesized carbon nanotubes (especially single-walled carbon nanotubes SWNTs) exist in the form of bundles and that to exploit their electronic properties to the fullest; a postprocessing technology is required to separate them into individual nanotubes. A common approach to achieve this is by stabilizing the hydrophobic nature of nanotube surface with the use of a surfactant that overcomes the van der Waals forces among the nanotubes and results in suspensions of individual SWNTs.

It is also well known that all known synthesis methods for single-walled carbon nanotubes result in a mixture of chiralities and diameters, resulting in heterogeneous electrical properties, particularly a mixture of semiconducting and metallic nanotubes. In general, it is assumed to be an even distribution of folding chiralities, 1/3 of all SWNTs in

a sample being metallic with the remaining 2/3 exhibiting semiconducting characteristics. The chemistry community has led a successful effort aimed at sorting and purifying nanotubes in solution post-synthesis [7].

To date, a wide variety of surfactants have been reported to be able to disperse the nanotube in bundles into their individual form in an aqueous media successfully [7, 8]. Several commercial surfactants such as sodium dodecyl sulfate (SDS), sodium cholate (SC), and sodium dodecylbenzenesulfonate (SDBS) are among the most reported for an efficient dispersion. Most dispersion studies have been directed toward chemical modification of the nanotube surface. Although many researchers have tried to solubilize nanotube ends and exterior walls through various functionalization routes [9], dispersion via functionalization has found limited success. Furthermore, covalent functionalization disturbs the extended  $\pi$ -electron systems ( $sp^2$  orbitals) of the nanotube surface, responsible for many attractive attributes of SWNTs. Therefore, noncovalent surfactants are desired.

At present, it is not known how these surfactants are used since both the dispersion and metallic/semiconducting nanotube separation affect the electronic properties of nanotube arrays and films made from depositing nanotubes using various techniques. Adsorption of ionic surfactants on the surface could significantly modulate the device characteristics and affect the conductance of the devices [10]. It is critical to compare the electronic nature of the nanotube-surfactant conjugates versus intact nanotubes, since these reagents are increasingly being used in industry and laboratories. It is the purpose of this work to investigate the effect of various surfactant and deposition techniques on nanotube electronic properties using carbon nanotubes synthesized and purified using a variety of methods from a variety of academic and industrial institutions.

**1.3. Dielectrophoresis.** Several postsynthesis processes involve solution-based processing of nanotubes such as spin coating [11] or dielectrophoresis (DEP) deposition [12, 13]. Spin-coating is probably the best long-term approach but is not yet mature enough for ultradense arrays. Dielectrophoresis allows selective alignment of nanotubes into controlled locations, and so it is used in this work as a test bed for systematic studies of the effect of alignment, source, and surfactants on electronic properties of nanotube arrays.

In DEP deposition steps, the presence of both metallic and semiconducting carbon nanotubes in solution is the main hurdle to form single-nanotube conductance channels. When an AC field is applied to the electrodes with nanotubes between the gap, the induced dipole moment of SWNTs interacts with nonuniform field resulting in a dielectrophoretic force which is influenced by the electronic properties of the SWNTs and in turn causes a separation of metallic and semiconducting nanotubes [14]. Assuming carbon nanotubes to be small cylindrical dipoles for simplifying the equations, the dielectrophoretic force can be expressed as  $F \sim (\epsilon_p - \epsilon_m)/\epsilon_m$ , where  $\epsilon_p$  is the dielectric constant of the carbon nanotubes and  $\epsilon_m$  is the dielectric constant of the solvent [15]. At higher frequencies, this force

is basically proportional to the difference between dielectric constant of the carbon nanotubes and dielectric constant of the solvent. The force observed by metallic nanotubes is significantly larger than that on semiconducting nanotubes because of the high dielectric constant of metallic SWNTs and the low dielectric constant of semiconducting SWNTs [14]. When a solvent with a dielectric constant between those values is used, separation of SWNTs will occur with metallic SWNTs attracted towards the field source (positive DEP) and semiconducting SWNTs repelled from the source (negative DEP). This physical effect causes separation of nanotubes due to metallic nanotubes being attracted towards field source electrodes while leaving behind semiconducting nanotubes in solution.

In this work, we use DEP for the deposition process. Therefore, our studies tend to elucidate arrays of metallic SWNTs primarily. However, these initial pioneering studies are meant to provide qualitative guidelines for the effects of surfactants and synthesis recipes on all types of SWNT arrays, including random and aligned arrays of all-semi, all-metal, or mixed species of SWNTs. Such studies are urgently needed if nanotube electronics is to progress from science to technology.

## 2. Device Fabrication

Single-walled carbon nanotubes were obtained from several different sources. Nanotubes obtained differ in terms of synthetic procedure used for their fabrication. Table 1 contains a list of the nanotube sources that we used with some details of their basic properties.

Nanotube diameters as mentioned in this table are obtained from the datasheets provided by their supplier and are also listed on their websites.

Each of these nanotubes (except semienriched samples from Los Alamos [16] and semienriched (90% semiconducting) solution obtained from Nanointegris was first dispersed in surfactant solutions. Surfactants used for the comparison in our experiments were SDS, SC, and SDBS. The protocol used for the dispersion of each sample is as follows.

- (1) 5% w/v solutions of surfactants were prepared in deionized water.
- (2) 5 mg of nanotube sample was dispersed in 10 mL of surfactant solution.
- (3) Suspensions formed after addition of nanotubes were then sonicated for 3 hours.
- (4) Mixtures were then centrifuged at 16,400 rpm (at 30°C) for 1 hour, 6 times repeatedly.

Dispersions obtained after 6 times centrifugation were then used for the deposition. Purified nanotubes obtained from Las Alamos were first dialyzed with 1% SDS solution in deionized water prior to their use. Nanointegris nanotube solution was used as received.

Using a glass micropipette with a tip diameter of  $\sim 20 \mu\text{m}$ , the supernatant was placed on the electrodes and DEP was used to accumulate the solubilized SWNTs within

TABLE 1: Nanotube sources and their properties.

Company	Synthetic process used	Avg. diameter as reported by provider
CNI/Unidym	HiPCO	0.81–0.85 nm
SouthWest Nanotechnologies	CoMoCAT	0.8–1 nm
Carbon Solutions	Arc discharge	1–1.4 nm
Las Alamos (semi-enriched)	HiPCO	0.81–0.85 nm
Cheap Tubes	CVD	1–2 nm
Nanointegris (semienriched, 90%)	Arc discharge	1.2–1.6 nm

TABLE 2: Summary of results.

SWNT Sources	Electrode spacing	Avg. length after deposition (in SEM)	DC resistance (1000's of SWNTs in parallel)	On/off ratio
Cheap Tubes	3 $\mu\text{m}$	>3 $\mu\text{m}$	<50 $\Omega$	2–8%
SWeNT	1 $\mu\text{m}$	<1 $\mu\text{m}$	50–100 $\Omega$	2–6%
CSI	1 $\mu\text{m}$	<1.5 $\mu\text{m}$	100–200 $\Omega$	<1%
CNI/Unidym	1 $\mu\text{m}$	<1 $\mu\text{m}$	100–500 $\Omega$	<1%
Las Alamos	1 $\mu\text{m}$	<1.5 $\mu\text{m}$	120–150 $\Omega$	<1%
Nanointegris (semi-enriched, 90%)	1 $\mu\text{m}$	<1.5 $\mu\text{m}$	150–180 $\Omega$	<1%

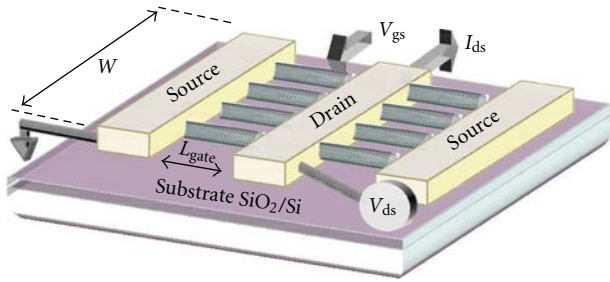


FIGURE 1: Diagram of RF probing and dual coplanar waveguide/electrode structure.

the electrode gap. This was accomplished using a 1–5  $V_{pp}$ , 300 KHz–25 MHz sine wave voltage signal applied to the electrodes. The drop was then air dried, and the residue from the solution left after evaporation was gently washed away with deionized water.

Figure 1 shows the layout for our measurements. Device fabrication for these experiments was done using a similar protocol described in our earlier work [13]. Using electron beam lithography, electrodes with a pair of gaps were patterned and evaporated with Ti/Au 5 nm/50 nm on high resistivity Si wafers (8000  $\Omega\text{-cm}$ ) with a 500 nm thermal oxide layer. Coplanar waveguide electrode geometries were patterned with photolithography and evaporated with 25 nm Ti/250 nm Au to form a dual waveguide/electrode structure with a pair of electrode gaps and with widths of 100  $\mu\text{m}$ . After accumulation of aligned SWNTs within the gap by DEP, as described further in this paper, contact electrodes were patterned using e-beam lithography and evaporated with 70 nm of Pd producing a new electrode gap of 1  $\mu\text{m}$ . The devices were RF-contacted electrically using a commercially available probe. Figure 2 shows a schematic diagram of

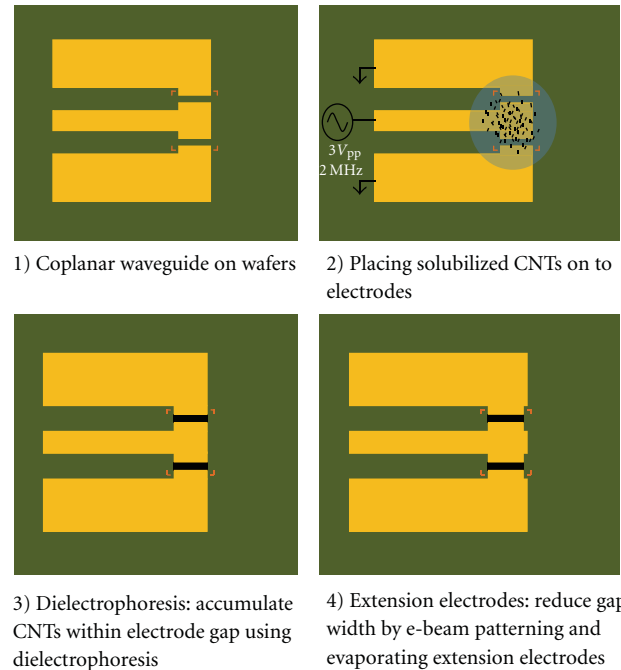


FIGURE 2: Schematic diagram of steps used in deposition of nanotubes on Si wafers.

several steps involved in the process of making a device with nanotubes deposited in the gaps.

Rather than characterize each device in full detail, we opted for a simplified, higher throughput measurement procedure in order to maximize the number of deposition conditions we could perform. For all the DC resistance measurements, a low source-drain bias voltage (+1 V to –1 V) was used. Gate voltages of –9, 0 and +9 V were applied to the Si Substrate (bottom gate) to modulate the

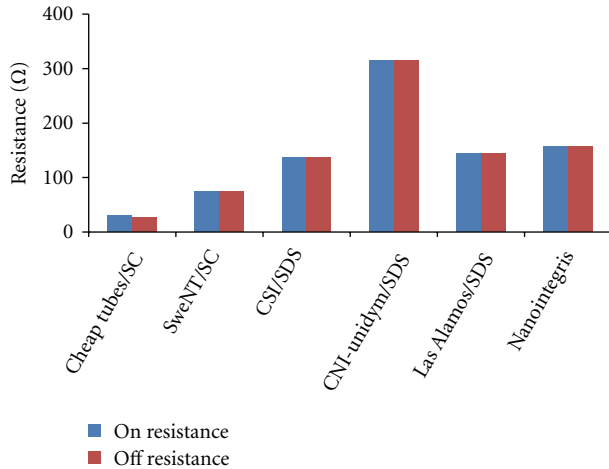


FIGURE 3: Results of DC resistance measurements done on nanotubes obtained from various sources that differ in synthetic process used (HiPCO/CoMoCat/Arc/CVD).

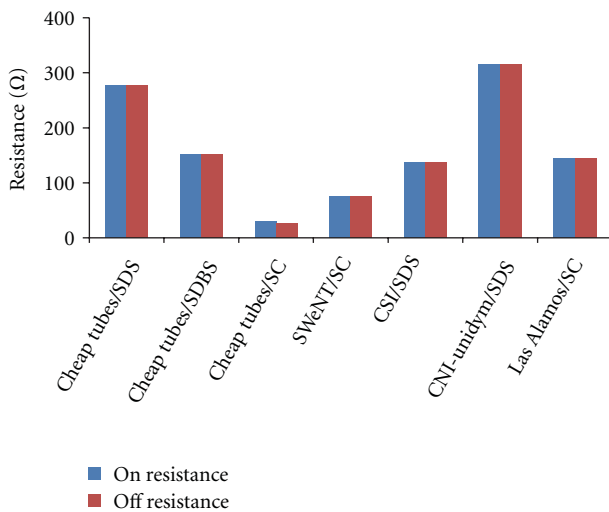


FIGURE 4: Results of DC resistance measurements done on nanotubes solubilized using variety of surfactants SDS, SC, and SDBS.

conductance and measure the on/off ratio for the nanotube devices. Because the full depletion curve was not measured, the on/off ratio is qualitative, not quantitative. (The devices may not have been completely “on” or “off” in our simplified measurement scheme.)

### 3. Experimental Results

Electronic measurements were performed on several devices fabricated by keeping some factors common for comparison. Based on our experiments, we have identified the role of frequency and amplitude used in DEP for the deposition of nanotubes. We were able to optimize these factors to make such device fabrication reproducible to a certain extent. Studies shown in this article would help researchers to

establish a similar protocol for optimized deposition when nanotubes are obtained from different sources.

The following comparison results are based on the data obtained by averaging results for several similarly formed devices. DC-resistance values are normalized for a device with a width of  $100\ \mu\text{m}$ . The length of devices was kept in the range of the length of nanotubes from respective sources (Table 2). This would ensure that the comparison is based on the nanotubes similarly distributed over the length of devices and not over the width.

**3.1. Comparison on Nanotube Sources.** Nanotubes obtained from various sources were deposited on wafers, and electronic measurements done for them are summarized below. Nanotubes obtained from Unidyn (formerly Carbon Nanotechnologies Inc, HiPCO,  $0.81\text{--}0.85\ \text{nm}$  diameter, length  $<1\ \mu\text{m}$ ) were found to show greater resistance as compared to the lowest shown by nanotubes from Cheap Tubes Inc. (Arc discharge,  $1\text{--}2\ \text{nm}$  diameter, length  $>3\ \mu\text{m}$ ). Figure 3 shows a cumulative chart on DC resistance studies done on nanotubes that differ in their synthetic process. For our experiments, we obtained nanotubes from different sources to accommodate nanotubes produced by HiPCO, CoMoCAT, Arc, and CVD methods. In these experiments,  $4\ V_{pp}$ ,  $25\ \text{MHz}$  sine wave voltage signal was applied for 3 minutes to the electrodes for the deposition of nanotubes.

**3.2. Comparison on Using Different Surfactants.** Three different surfactants—sodium cholate (SC), sodium dodecyl sulfate (SDS), and sodium dodecyl benzene sulfonate (SDBS) were used to solubilize nanotubes in aqueous solution. SC was found to be the most effective surfactant for solubilizing most of the nanotubes. Figure 4 shows the on/off DC resistance of nanotube devices where nanotubes from several sources were dissolved using different surfactants and deposited on wafers using DEP. In all the experiments,  $4\ V_{pp}$ ,  $25\ \text{MHz}$  sine wave voltage signal was applied for 3 minutes to the electrodes for the deposition of nanotubes.

**3.3. Comparison on Using Different Frequencies.** When different frequencies were used for the deposition, it was observed that nanotubes deposited using a frequency less than  $15\ \text{MHz}$  were not aligned, while when a frequency above  $25\ \text{MHz}$  was used, deposited nanotubes were found to be well aligned. Figure 5 shows some representative images of nanotubes deposited under various different conditions. Several different patterns of alignments owing to different DEP parameters were observed. In one case, it was also observed that when a nanotube solution (nanotube dispersed in  $1\% \text{ w/v}$  solution of SC) was left standing prior to its use for DEP deposition for several days, nanotubes formed bigger bundles, which were apparent in their SEM images.

**3.4. Comparison on Using Different Amplitude.** Nanotube samples (Cheap Tubes, dissolved using SC) were deposited by applying several different voltages for DEP at a constant frequency of  $25\ \text{MHz}$ . In general, it was observed that when an amplitude above  $3\ \text{V}$  was applied, 2 minutes or more

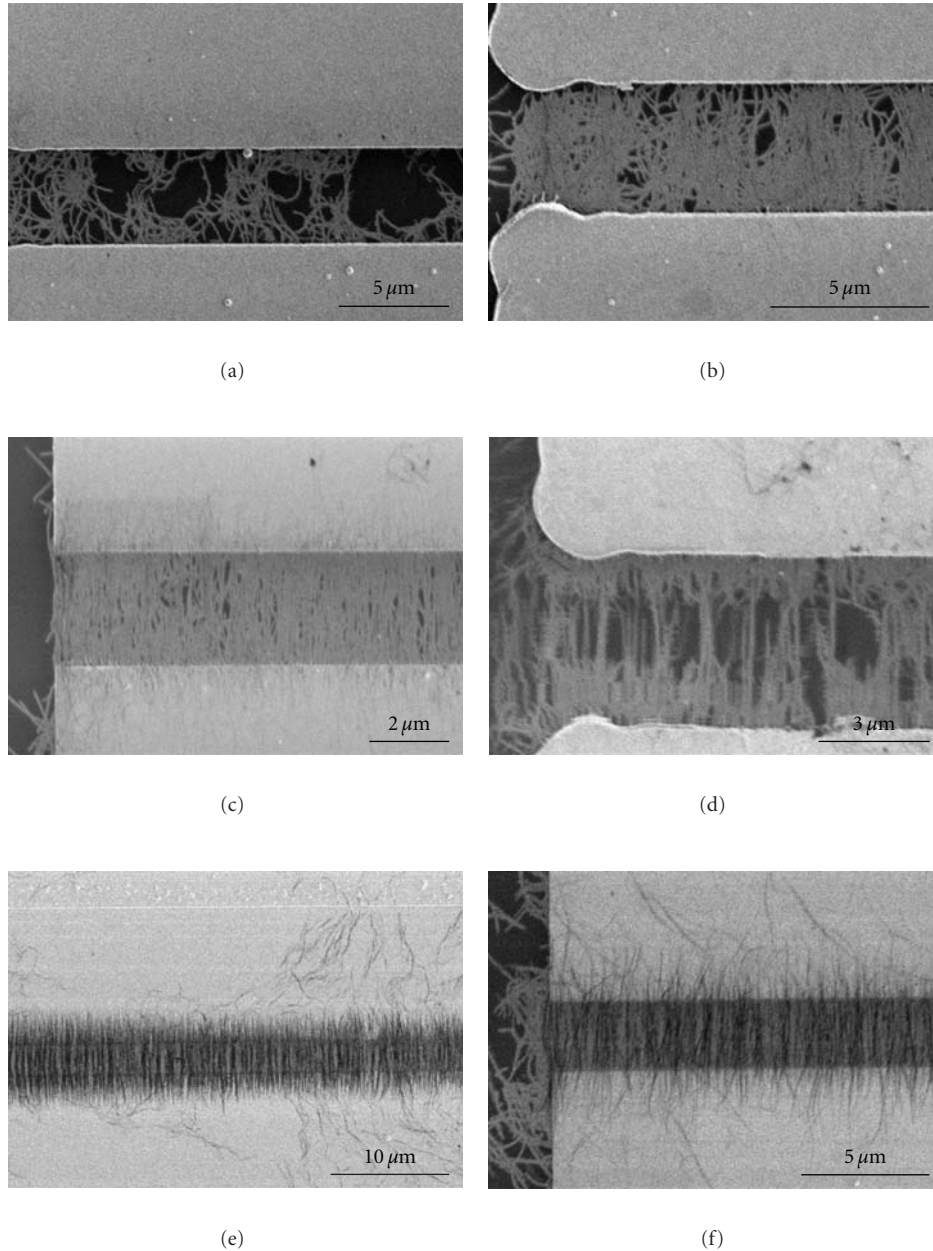


FIGURE 5: Nanotubes (Cheap Tubes) deposited on Si wafers at 2 MHz (Figures 5(a), 5(b)) and 25 MHz (Figures 5(c), 5(d)). The difference in their alignment is apparent. Figure 5(d) represents deposited nanotubes (at 25 MHz) shorter in length ( $<2\ \mu\text{m}$ ); it can be seen that even shorter nanotubes were amazingly aligned in the gap. Figures 5(e), 5(f) show nanotubes deposited from a solution that was sonicated for a short time (5 min) and then left standing for a few days prior to use; formation of bigger bundles of nanotubes is apparent in the images.

was sufficient to fill the gap up to almost 100%. When a voltage less than 1 was used, no nanotubes were apparently deposited. Using a dilute solution and giving more time for the deposition or using a comparatively concentrated solution with less time yielded the devices with similar properties. Also using any amplitude above 3 V did not make much difference on device characteristics.

Figure 7 shows a typical Raman spectrum from a device (with nanotubes from Cheap Tubes), indicating that indeed SWNTs are being deposited.

**3.5. Reproducibility.** In Figure 8 is shown a histogram plotted for DC-resistance measurement done on several devices that had different gap width. Most of the devices having the same width had shown DC resistance in similar range (Figure 8(a)), which shows the reproducibility of our experiments. Figure 8(b) is a plot of averaged DC resistance observed for the devices plotted against their width. Increasing the width 10 times in fact lowered the resistance with an order of 10 too, which shows the reliability of the process in terms of reproducing the results over the repeated experiments.

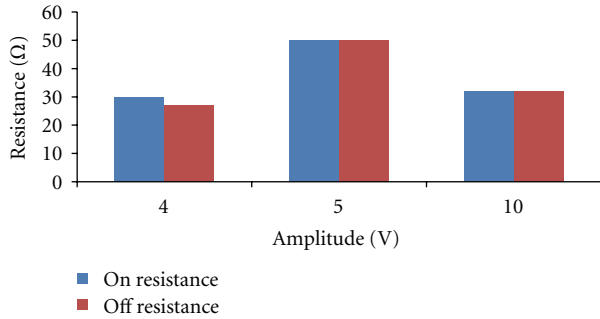


FIGURE 6: DC-resistance measurements done on nanotubes devices fabricated by depositing nanotubes using different amplitudes.

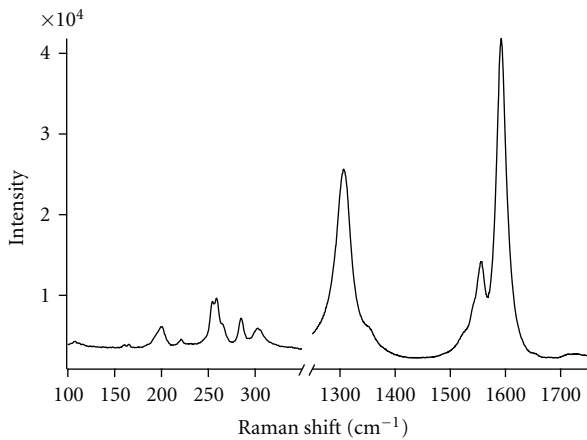


FIGURE 7: A typical Raman spectra from a device representative to the one shown in Figure 6 confirm the presence of nanotubes.

#### 4. Discussion

The use of ionic surfactant to solubilized nanotubes is known to modulate the surface conductance of nanotubes that will eventually affect the dielectrophoresis force applied for the deposition of nanotubes. Strano's group studied effects of surface conductivity of semiconducting SWNTs induced by ionic surfactants on the sign of dielectrophoretic force [17]. They were able to modulate the surface conductance by changing the ionic strength of medium. Also, by neutralizing the surface charge using an equimolar mixture of anionic and cationic surfactant, they observed negative DEP of semiconducting species at 10 MHz. They suggested 10 MHz to be the crossover frequency for their semiconducting nanotube. From our experiments we found that in most of the cases when nanotubes were deposited at frequencies higher than 5 MHz, only metallic behavior of deposited nanotubes was observed in their electronic measurements. Even when the solution enriched in semiconducting nanotube was used, dielectrophoretic deposition at any frequencies higher than 5 MHz resulted in devices with extremely low or no on/off ratio. We believe this is because even if above crossover frequencies, semiconducting nanotubes might have observed positive DEP, amount of metallic nanotubes that were deposited in the process was much larger than semiconducting nanotubes.

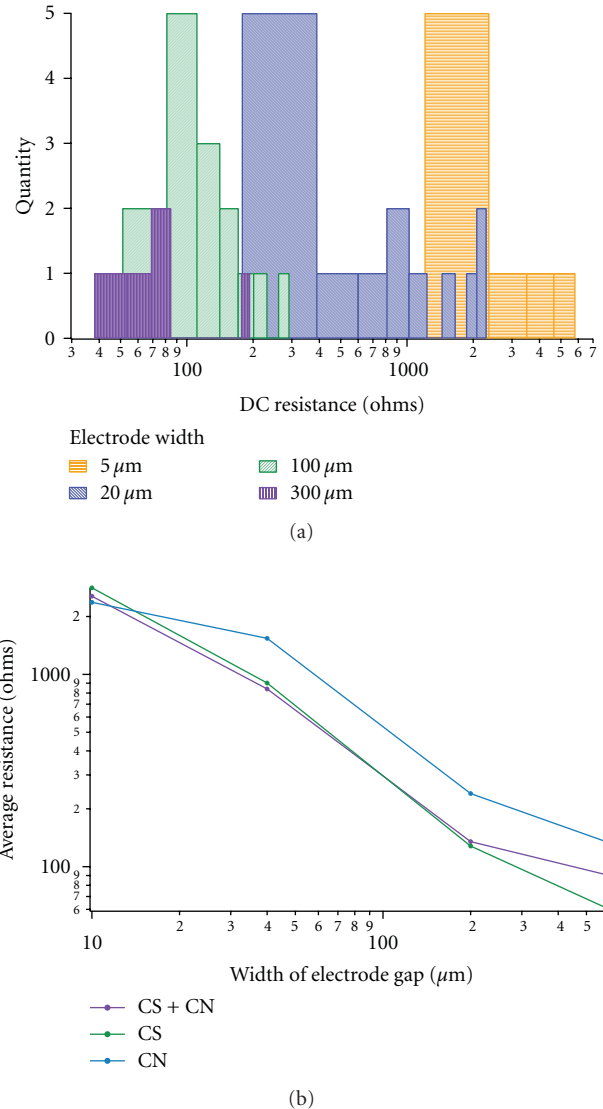


FIGURE 8: An averaged DC-resistance measurement done on devices having different electrode width.

The on/off ratios reported here are consistent with Happy et al. who found that when a conventional SWNT solution with  $\sim 2/3$  of semiconducting nanotubes is deposited using DEP, major part of the DC current (90–95%) is produced by metallic nanotubes [18, 19]. They also found that when 99% semi-enriched solution was used for deposition with DEP along with substrate's surface modification, the devices did not go to complete off state, most likely because a small number of metallic nanotubes were preferentially deposited by DEP [19]. In another recent experiments [20], we used same semi-enriched solution (90%, "IsoNanotubes-S", Nanointegris) and deposited them without DEP by using only surface modification [21] which resulted in devices with better mobility and also higher on/off ratios than the current DEP method. An on/off ratio of up to 110000 was achieved when nanotubes were deposited using only surface modification.

## 5. Conclusion

We have performed the first systematic study of the effects of surfactants, source, and deposition procedure on the electronic properties of nanotube devices. From our experience we believe, neither the surfactant used nor the source has a significant impact on the on-resistance. The alignment is much affected by the frequency of the AC voltage used to align the nanotubes. On the other hand, a consistent scaling of device resistance with width is observed for samples from different sources, indicating that the procedure can be empirically adjusted to give reasonably tight tolerances. Using this technique, the on/off ratio was never large, indicating that in most of the cases, metallic nanotubes were deposited preferentially. Finally, we consistently (with almost perfect yield) were able to achieve devices with resistance of order 50  $\Omega$ , regardless of nanotubes source or surfactant, which holds promise for future RF devices with nanotube arrays.

## Acknowledgments

The authors would like to thank Jie Liu from Duke University for Raman spectroscopy. This work was funded by the National Science Foundation, Army Research Office, Office of Naval Research, Northrop Grumman, and Korean National Science Foundation (KOSEF) World Class University (WCU) program.

## References

- [1] C. Rutherglen, D. Jain, and P. Burke, "Nanotube electronics for radiofrequency applications," *Nature Nanotechnology*, vol. 4, pp. 811–819, 2009.
- [2] Q. Cao and J. A. Rogers, "Ultrathin films of single-walled carbon nanotubes for electronics and sensors: a review of fundamental and applied aspects," *Advanced Materials*, vol. 21, no. 1, pp. 29–53, 2009.
- [3] P. G. Collins, K. Bradley, M. Ishigami, and A. Zettl, "Extreme oxygen sensitivity of electronic properties of carbon nanotubes," *Science*, vol. 287, no. 5459, pp. 1801–1804, 2000.
- [4] P. J. Burke, S. Li, and Z. Yu, "Quantitative theory of nanowire and nanotube antenna performance," *IEEE Transactions on Nanotechnology*, vol. 5, no. 4, pp. 314–334, 2006.
- [5] P. J. Burke, C. Rutherglen, and Z. Yu, "Carbon nanotube antennas," in *Proceedings of the 9th International Conference on Electromagnetics in Advanced Applications*, p. 937, 2005.
- [6] H. Jin, D. A. Heller, and M. S. Strano, "Single-particle tracking of endocytosis and exocytosis of single-walled carbon nanotubes in NIH-3T3 cells," *Nano Letters*, vol. 8, no. 6, pp. 1577–1585, 2008.
- [7] M. C. Hersam, "Progress towards monodisperse single-walled carbon nanotubes," *Nature Nanotechnology*, vol. 3, no. 7, pp. 387–394, 2008.
- [8] V. C. Moore, M. S. Strano, E. H. Haroz et al., "Individually suspended single-walled carbon nanotubes in various surfactants," *Nano Letters*, vol. 3, no. 10, pp. 1379–1382, 2003.
- [9] C. A. Dyke and J. M. Tour, "Covalent functionalization of single-walled carbon nanotubes for materials applications," *Journal of Physical Chemistry A*, vol. 108, no. 51, pp. 11151–11159, 2004.
- [10] Q. Fu and J. Liu, "Effects of ionic surfactant adsorption on single-walled carbon nanotube thin film devices in aqueous solutions," *Langmuir*, vol. 21, no. 4, pp. 1162–1165, 2005.
- [11] M. C. LeMieux, M. Roberts, S. Barman, W. J. Yong, M. K. Jong, and Z. Bao, "Self-sorted, aligned nanotube networks for thin-film transistors," *Science*, vol. 321, no. 5885, pp. 101–104, 2008.
- [12] R. Krupke, F. Hennrich, H. B. Weber, M. M. Kappes, and H. V. Löhneysen, "Simultaneous deposition of metallic bundles of single-walled carbon nanotubes using ac-dielectrophoresis," *Nano Letters*, vol. 3, no. 8, pp. 1019–1023, 2003.
- [13] C. Rutherglen, D. Jain, and P. Burke, "Rf resistance and inductance of massively parallel single walled carbon nanotubes: direct, broadband measurements and near perfect 50 impedance matching," *Applied Physics Letters*, vol. 93, no. 8, Article ID 083119, 2008.
- [14] R. Krupke, F. Hennrich, H. V. Löhneysen, and M. M. Kappes, "Separation of metallic from semiconducting single-walled carbon nanotubes," *Science*, vol. 301, no. 5631, pp. 344–347, 2003.
- [15] M. Dimaki and P. Bøggild, "Dielectrophoresis of carbon nanotubes using microelectrodes: a numerical study," *Nanotechnology*, vol. 15, no. 8, pp. 1095–1102, 2004.
- [16] S. Niyogi, C. G. Densmore, and S. K. Doorn, "Electrolyte tuning of surfactant interfacial behavior for enhanced density-based separations of single-walled carbon nanotubes," *Journal of the American Chemical Society*, vol. 131, no. 3, pp. 1144–1153, 2009.
- [17] Y. Kim, S. Hong, S. Jung, M. S. Strano, J. Choi, and S. Baik, "Dielectrophoresis of surface conductance modulated single-walled carbon nanotubes using cationic surfactants," *Journal of Physical Chemistry B*, vol. 110, no. 4, pp. 1541–1545, 2006.
- [18] A. Le Louarn, F. Kapche, J.-M. Bethoux et al., "Intrinsic current gain cutoff frequency of 30 GHz with carbon nanotube transistors," *Applied Physics Letters*, vol. 90, no. 23, Article ID 233108, 2007.
- [19] L. Nougaret, H. Happy, G. Dambrine et al., "80 GHz field-effect transistors produced using high purity semiconducting single-walled carbon nanotubes," *Applied Physics Letters*, vol. 94, no. 24, Article ID 243505, 2009.
- [20] N. Rouhi, D. Jain, K. Zand, and P. J. Burke, "All-semiconducting nanotube devices for RF and microwave applications," in *Proceedings of the IEEE MTT International Microwave Symposium*, May 2009.
- [21] S. Auvray, V. Derycke, M. Goffman, A. Filoramo, O. Jost, and J.-P. Bourgoin, "Chemical optimization of self-assembled carbon nanotube transistors," *Nano Letters*, vol. 5, no. 3, pp. 451–455, 2005.

## Research Article

# Fabrication and Electrical Characterization of Multiwalled Carbon Nanotube-Based Circuit at Room Temperature

Yitian Peng,<sup>1,2</sup> Yuanzhong Hu,<sup>3</sup> and Weibing Lu<sup>4</sup>

<sup>1</sup> Jiangsu Key Laboratory of Design and Manufacture of Micro/Nano Biomedical Instrument, Southeast University, Nanjing 211189, China

<sup>2</sup> State Key Laboratory of Mechanical Transmission, Chongqing University, Chongqing 400044, China

<sup>3</sup> State Key Laboratory of Tribology, Tsinghua University, Beijing 100084, China

<sup>4</sup> State Key Laboratory of Millimeter Waves, School of Information Science and Engineering, Southeast University, Nanjing 211189, China

Correspondence should be addressed to Yitian Peng, pengyitian@gmail.com

Received 27 March 2010; Revised 25 April 2010; Accepted 17 May 2010

Academic Editor: Jianyu Huang

Copyright © 2011 Yitian Peng et al. This is an open access article distributed under the Creative Commons Attribution License, which permits unrestricted use, distribution, and reproduction in any medium, provided the original work is properly cited.

Multiwalled carbon nanotube (MWCNT) deposited on a pair of predetermined aluminum electrodes treated with the (3-Aminopropyl)-triethoxysilane (APTES) self-assembled monolayers (SAMs). The MWCNT bridges electrodes and forms electrode/MWCNT/electrode circuit on silicon with 500 nm silicon dioxide. Then the Metal (Ti/Au) pads were fabricated on MWCNT to bury the MWCNT into metal electrodes. The electrical properties of MWCNT-based circuits before and after the fabrication of metal pads were characterized. Results indicate that metal pads on MWCNT improved the electrical properties MWCNT-based circuit largely.

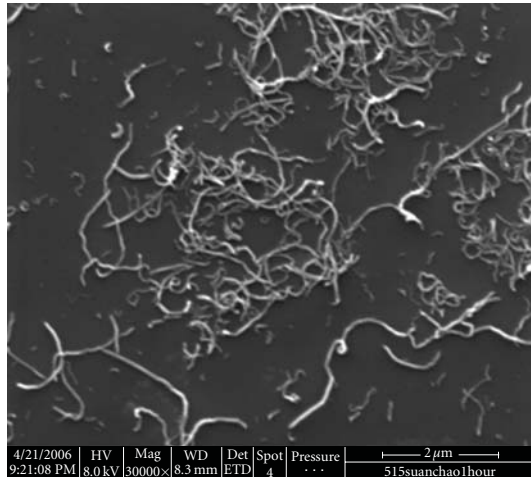
## 1. Introduction

Carbon nanotubes (CNTs) have exhibited a rich variety of intriguing electronic properties, such as metallic and semi-conducting behavior, exhibiting ballistic transport along the tubes, and sustaining current density as high as  $10^9$  A/cm<sup>2</sup>. These properties suggest that CNTs are potential candidates for nanoelectronic applications such as field-effect transistors, electrical interconnect, and sensors. Nevertheless, difficulties in handling an individual CNT and positioning it at a desired location hamper the absolute exploration of CNT properties and also devices for practical applications. Large efforts are underway worldwide to address these challenges. Early CNT devices were fabricated by depositing CNTs from liquid suspension randomly, either on top of prepatterned electrodes or directly onto a substrate prior to electrode patterning [1]. This process has the advantages of low cost, scalability and compatibility with many kinds of substrate materials. However, it has significant disadvantage with too much randomness on the placement of CNT. High-density selective placement methods for CNTs have been developed

by preparing the aminopropyltriethoxysilane (APTES) SAMs on the prepatterned electrodes [2, 3]. However, the contact resistance between the CNTs and electrodes is too big and hinder the effective connection between the CNT and the external world. It means that the MWCNT is not easy to function as an active component in device [4, 5]. In this paper, multi-walled carbon nanotubes (MWCNTs) were placed on prepatterned aluminum electrodes by chemical method using self-assembled monolayers and the metal pads were fabricated on MWCNT to improve the electrical contact between electrodes and MWCNT. Electrical properties of MWCNT-based circuits with and without metal pads on MWCNT were investigated.

## 2. Experiment and Analysis

The MWCNTs used in our study were obtained from Shenzhen Nanotech Port Co. Ltd in China. The purity of MWCNTs is greater than 95%. The axial dimension and diameter of the MWCNTs were 5–15  $\mu$ m and 10–20 nm, respectively. The MWCNT suspensions were prepared by



(a)



(b)

FIGURE 1: SEM (a) and TEM (b) image of dispersed MWCNTs.

ultrasonically dispersing the MWCNT in dimethylformamide (DMF) solution for half an hour. The MWCNT suspension was centrifuged to remove large particles and CNT bundles. To examine the dispersion of MWCNTs in DMF solution, we dropped the dispersion onto a copper grid and silicon substrate, while being dried by nitrogen gas. The configuration of dispersed MWCNTs was observed through Transmission electron microscope (TEM, JEM-200CX) and Field-emission scanning electron microscope (FESEM). The representative TEM and SEM image is shown in Figure 1, from which we can see the MWCNTs were well dispersed appropriate to the fabrication of MWCNT-based circuits.

A scheme for the deposition of MWCNTs on patterned aluminum electrodes with self-assembled monolayers is illustrated in Figure 2(a). Lightly n-doped Silicon (100) wafer with 500 nm of thermal dioxide silicon was used as the substrate for the fabrication of patterned electrodes. The substrate was cleaned as follows: firstly they were ultrasonicated in acetone and ethanol for 10 minutes each and then immersed into a Piranha solution at 80°C for 30 minutes.

To fabricate the patterned metal electrodes, the silicon wafers were metalized by evaporating 60 nm-thick aluminum. A thin layer of hydrophobic photo resist (S1813) was coated on the top of the aluminum layer. The pattern which had been pre-designed for the electrical characterization was created by photolithography and development. Then the aluminum at the exposed areas was etched away subsequently and the patterned electrodes were created. The amine-terminated SAMs on exposed area between the electrodes were prepared by immersing the substrates into the solution for the formation of (3-Aminopropyl)-triethoxysilane (APTES) SAMs. The solution is composed as follows: 1 cm<sup>3</sup> of acetic acid, 1 cm<sup>3</sup> of de-ionized water, 25 cm<sup>3</sup> of absolute methanol, and 0.5 cm<sup>3</sup> of APTES (99% purity) [6]. Then the substrate was immersed in acetone to remove the remained photoresist on the metal electrodes. The processed patterned substrate was rinsed with chloroform and alcohol. Afterward, the substrate with patterned electrodes was immersed into the dispersion of MWCNTs. Modestly hydrophilic amine-terminated (-NH<sub>2</sub>) SAMs (contact angle of 30–40 degrees) produce strong attractions to MWCNTs. As a result, the MWCNT was induced to deposit on the surface of amine-terminated SAMs. The MWCNTs deposited in the vicinity of the electrodes can bridge two separated electrodes and create MWCNT-based circuit. The MWCNT is hard to be removed just by rinsing because the bonding is strong enough due to the interaction between amine-terminated SAMs and dispersed MWCNT [7, 8].

In order to improve the electrical contact between the MWCNT and aluminum electrodes, metal pads were fabricated on the MWCNT using electron beam lithography. A scheme for the fabrication of metal pads on MWCNT is illustrated in Figure 2(b). The detailed process for the fabrication of metal pads on MWCNT can be demonstrated as follows: firstly, it was conducted by spinning single layer of PMMA 950 C4 onto the substrate. The thickness of the PMMA 950 C4 was about 120 nm controlled according to the curve of thickness versus spin speed. After the e-beam writing, the pattern development was accomplished by soaking the substrate into a mixed solution of MIBK (methyl isobutyl ketone) and isopropanol (1:3) for 90 seconds and rinsing with isopropanol for 30 seconds. After rinsing and drying, 8 nm Ti and 50 nm Au film was evaporated on the substrate by electron beam evaporation method. The substrate was soaked in acetone for 15 minutes to lift-off the Ti/Au and the metal pads on the MWCNT formed.

Figures 3(a) and 3(b) show the FE-SEM pictures of MWCNT-aligned on aluminum electrode patterns at lower and higher magnification, respectively. The MWCNT in the circuit is about 3 μm long and placed at the center of the patterned electrodes. The distance of two electrodes is about 2 μm. The MWCNTs are large enough to fill the electrode spacing, allowing for possible current flow. At some other places, several MWCNTs aligned at only one electrode edge and linked up to other electrode. But there were few MWCNT in the area without SAMs. It can be concluded that the SAMs induced the deposition of MWCNT and improve the efficiency of the fabrication of MWCNT-based circuits.

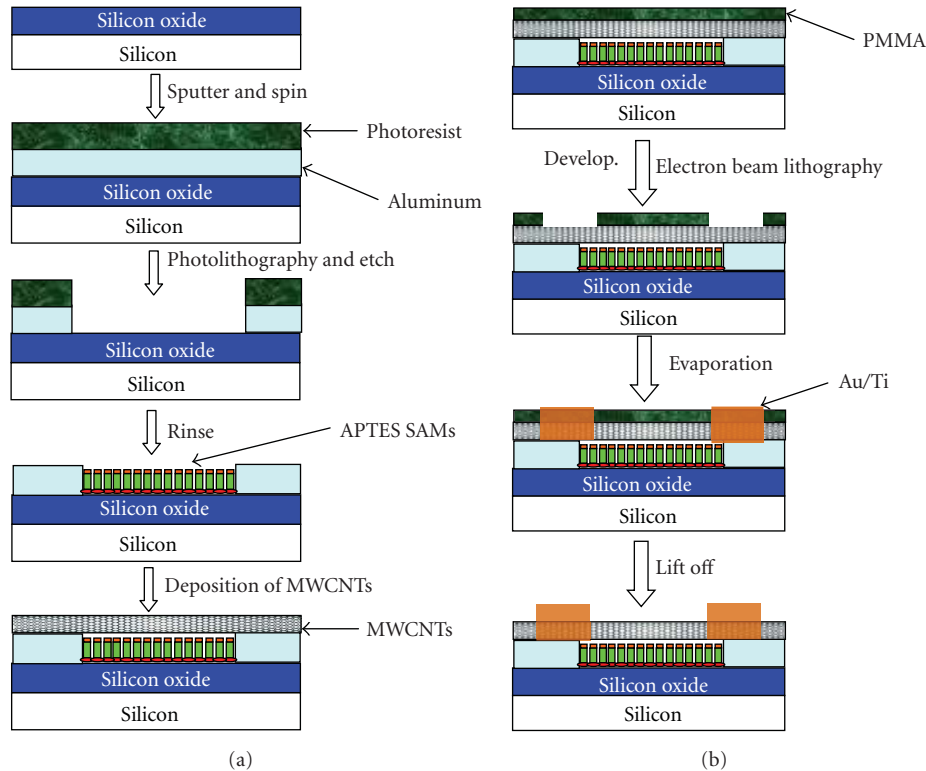


FIGURE 2: (a) Scheme of the Deposition of MWCNTs on patterned Aluminum electrode. (b) Fabrication of metal pads on MWCNT.

Figures 3(c) and 3(d) show the SEM image of MWCNT-based circuits after the fabrication of metal pads on MWCNT. The two ends of MWCNT were buried in the Ti/Au metal pads. The contact between MWCNT and electrodes changed from side contact to end contact. The Ti/Au metal pads are more resistant to oxidation and easy to form lower-resistance ohmic contact between MWCNTs and electrodes [9].

Current versus bias voltage ( $I$ - $V$ ) measurements at room temperature were conducted to evaluate the electrical properties of the placed MWCNT on the prepatterned aluminum electrodes. Figure 4(a) shows the measured current between electrodes in Figures 2(a) and 2(b) as a function of applied voltage. The MWCNT was considered as the main current passing between two electrodes and the resistance of the MWCNT is calculated. The result corresponds to a very high resistance in the order of  $P\Omega$ . This value is considerably larger than the results previously reported [9]. The MWCNTs do contribute to the current between two electrodes [10, 11]. But Aluminum has a low work function at 3.9–4.2 eV and the contacts have equal barriers for both electrons and holes. It is hard to obtain ohmic contact behavior between the CNT and Aluminum interfaces. Another phenomenon associated with this kind of MWCNT-based circuits known as the side contacts, meaning that MWCNTs are electrically contacted only along the circumference of the nanotube. Such contacts result in weak interaction between the carbon and the metal atoms [12]. Generally defect is more easy to form on the outer layer during the purify process of MWCNT. This also may result from the interface between the MWCNT and

aluminum which is due to the oxidation of the aluminum before the deposition of MWCNT [13].

Figure 4(b) shows the measured  $I$ - $V$  electrical conductance of Figures 3(c) and 3(d) after the fabrication of the metal pads on MWCNT. The current transport between the electrodes shows a nonlinear dependence of applied voltage with the presence of an alumina layer on the aluminum electrodes. It is evident that the electrical pads lying on MWCNTs allow for considerable improvement in the electrical properties of MWCNT-based circuits by many orders of magnitude.

The resistances between the two terminals have been lowered to several  $M\Omega$  by applying contact metal on the top of MWCNTs. The reason for this is very complicated because not only the contact resistance could be lowered but also the multilayers of the MWCNT could contact with the Ti/Au electrodes. The remarkable decrease of the two-terminal resistance has three possible origins as follows: Firstly, Several layers of MWCNT could be carrying the current simultaneously after the MWCNT was buried in the metal pads. The inner layers of MWCNT have better conductive property than the outer layer because the inner layer more perfect crystalline structure. Secondly, the electrical contacts between the MWCNT and the Ti/Au electrodes may improve considerably than Al electrodes. Finally, the MWCNT may be modified by exposure to PMMA with a resulting resistance decreases [14, 15].

Figure 5 shows the electrical conductance measured between electrodes from  $-5$  V through  $5$  V. The maximum

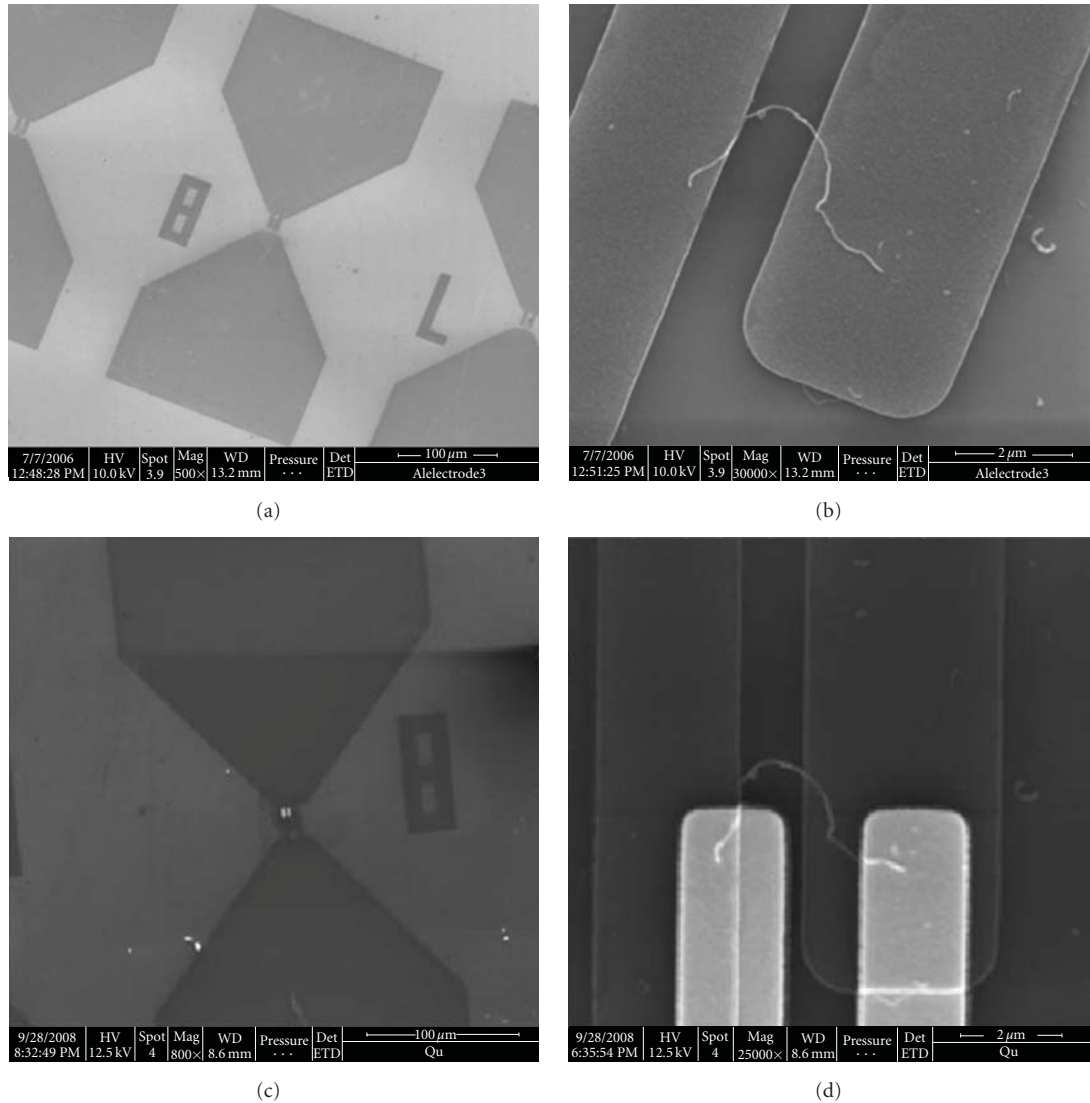


FIGURE 3: SEM image of (a) Pattern aluminum electrodes, (b) MWCNT bridging the patterned aluminum electrodes, (c) pattern electrodes with metal pads on MWCNT at low magnification, and (d) MWCNT-based circuits with metal pads on MWCNT at high magnification.

current that the MWCNT stand during the measurement was about  $10^7$  A/cm<sup>2</sup> and it is close to the maximum current density of MWCNT reported. It indicates that the electrical contact between the MWCNT and electrodes have been improved by burying the MWCNT into Ti/Au electrodes. Also the resistance can be lowered under larger voltage. The advantage of the technology is to construct devices out of preselected MWCNT which will provide a possibility to build a great variety of complex CNT-based devices.

### 3. Conclusion

The MWCNTs were induced and placed on prepatterned aluminum electrodes by self-assembled monolayers to fabricate the MWCNT-based circuit. This process improved the efficiency of fabrication of MWCNT electronic circuits. Then metal pads on MWCNT were fabricated by electron

beam lithography method. The electrical properties of MWCNT-based circuits were characterized with two probe system before and after the fabrication of metal pads on MWCNT. Electrical properties of MWCNT-based circuits were improved largely after two metal pads were fabricated on the MWCNT.

### Acknowledgments

This work is supported by State Key Laboratory of Mechanical Transmission, Chongqing University (Grant no. SKLMT-KFKT-200904). This work also is supported partly by the Natural Science Foundation of Jiangsu Province under grant No. bk2009265, in part by the New Century Training Program Foundation for the Talents by the State Education Commission under Grant no. NCET080107, in part by the Key Project of Chinese Ministry of Education under

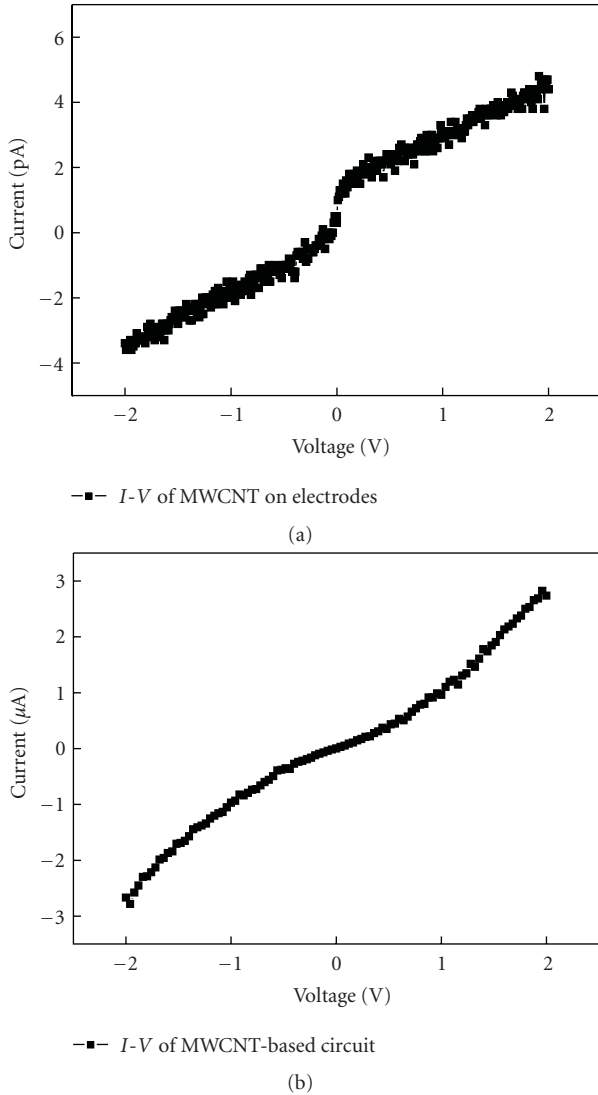


FIGURE 4: *I-V* behavior of MWCNTs-based circuits before (a) and after (b) the fabrication of metal pads on MWCNT.

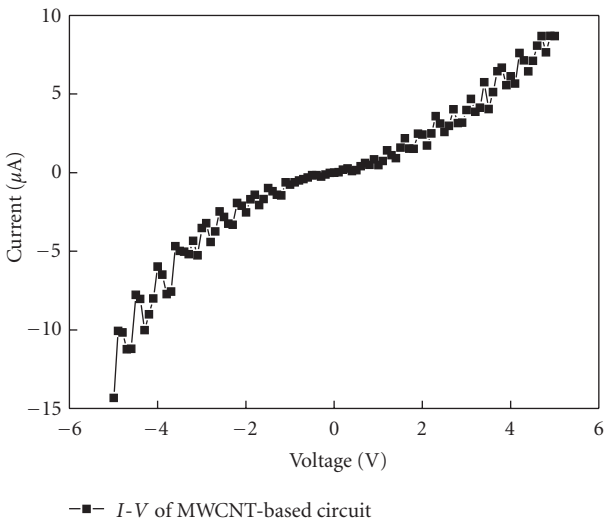


FIGURE 5: *I-V* behavior of MWCNTs-based circuits that the voltage varied from  $-5\text{ V}$  to  $5\text{ V}$ .

Grant no. 109074, in part by National Aerospace Science Foundation of China 20080169002.

## References

- [1] L. A. Nagahara, I. Amlani, J. Lewenstein, and R. K. Tsui, "Directed placement of suspended carbon nanotubes for nanometer-scale assembly," *Applied Physics Letters*, vol. 80, no. 20, pp. 3826–3829, 2002.
- [2] S. Lu, J. Chung, and R. S. Ruoff, "Controlled deposition of nanotubes on opposing electrodes," *Nanotechnology*, vol. 16, no. 9, pp. 1765–1770, 2005.
- [3] J. Liu, M. J. Casavant, M. Cox et al., "Controlled deposition of individual single-walled carbon nanotubes on chemically functionalized templates," *Chemical Physics Letters*, vol. 303, no. 1-2, pp. 125–129, 1999.
- [4] M. Burghard, G. Duesberg, G. Philipp, J. Muster, and S. Roth, "Controlled adsorption of carbon nanotubes on chemically modified electrode arrays," *Advanced Materials*, vol. 10, no. 8, pp. 584–588, 1998.
- [5] X. M. H. Huang, R. Caldwell, L. Huang et al., "Controlled placement of individual carbon nanotubes," *Nano Letters*, vol. 5, no. 7, pp. 1515–1518, 2005.
- [6] Y. Peng, Y. Hu, and H. Wang, "Patterned deposition of multi-walled carbon nanotubes on self-assembled monolayers," *Chinese Science Bulletin*, vol. 51, no. 2, pp. 147–150, 2006.
- [7] K. H. Choi, J. P. Bourgoïn, S. Auvray et al., "Controlled deposition of carbon nanotubes on a patterned substrate," *Surface Science*, vol. 462, no. 1, pp. 195–202, 2000.
- [8] J. C. Lewenstein, T. P. Burgin, A. Ribayrol, L. A. Nagahara, and R. K. Tsui, "High-yield selective placement of carbon nanotubes on pre-patterned electrodes," *Nano Letters*, vol. 2, no. 5, pp. 443–446, 2002.
- [9] P. S. Na, H. Kim, H.-M. So et al., "Investigation of the humidity effect on the electrical properties of single-walled carbon nanotube transistors," *Applied Physics Letters*, vol. 87, Article ID 093101, 3 pages, 2005.
- [10] M. H. Yang, K. B. K. Teo, W. I. Milne, and D. G. Hasko, "Carbon nanotube Schottky diode and directionally dependent field-effect transistor using asymmetrical contacts," *Applied Physics Letters*, vol. 87, no. 25, Article ID 253116, 3 pages, 2005.
- [11] H. Watanabe, K. Shimotani, T. Shigematu, and C. Manabe, "Electric measurements of nano-scaled devices," *Thin Solid Films*, vol. 438-439, pp. 462–466, 2003.
- [12] K. Ojima, Y. Otsuka, T. Matsumoto, T. Kawai, K. Nakamatsu, and S. Matsui, "Printing electrode for top-contact molecular junction," *Applied Physics Letters*, vol. 87, no. 23, Article ID 234110, pp. 1–3, 2005.
- [13] A. Bachtold, M. Henny, C. Terrier et al., "Contacting carbon nanotubes selectively with low-ohmic contacts for four-probe electric measurements," *Applied Physics Letters*, vol. 73, no. 2, pp. 274–276, 1998.
- [14] J. Chung and J. Lee, "Nanoscale gap fabrication and integration of carbon nanotubes by micromachining," *Sensors and Actuators A*, vol. 104, no. 3, pp. 229–235, 2003.
- [15] T. Shimizu, H. Abe, A. Ando, Y. Nakayama, and H. Tokumoto, "Electrical conductivity measurements of a multi-walled carbon nanotube," *Surface and Interface Analysis*, vol. 37, no. 2, pp. 204–207, 2005.

## Research Article

# Purity and Defect Characterization of Single-Wall Carbon Nanotubes Using Raman Spectroscopy

Yasumitsu Miyata,<sup>1,2</sup> Kohei Mizuno,<sup>3</sup> and Hiromichi Kataura<sup>1,4</sup>

<sup>1</sup>Nanosystem Research Institute (NRI), National Institute of Advanced Industrial Science and Technology (AIST), 1-1-1 Higashi, Tsukuba 305-8562, Japan

<sup>2</sup>Department of Chemistry, Nagoya University, Nagoya 464-8602, Japan

<sup>3</sup>Nanotube Research Center, National Institute of Advanced Industrial Science and Technology (AIST), 1-1-1 Higashi, Tsukuba 305-8565, Japan

<sup>4</sup>JST, CREST, Kawaguchi 330-0012, Japan

Correspondence should be addressed to Hiromichi Kataura, h-kataura@aist.go.jp

Received 15 June 2010; Accepted 23 November 2010

Academic Editor: Teng Li

Copyright © 2011 Yasumitsu Miyata et al. This is an open access article distributed under the Creative Commons Attribution License, which permits unrestricted use, distribution, and reproduction in any medium, provided the original work is properly cited.

We investigated the purity and defects of single-wall carbon nanotubes (SWCNTs) produced by various synthetic methods including chemical vapor deposition, arc discharge, and laser ablation. The SWCNT samples were characterized using scanning electron microscopy (SEM), thermogravimetric analysis (TGA), and Raman spectroscopy. Quantitative analysis of SEM images suggested that the G-band Raman intensity serves as an index for the purity. By contrast, the intensity ratio of G-band to D-band (G/D ratio) reflects both the purity and the defect density of SWCNTs. The combination of G-band intensity and G/D ratio is useful for a quick, nondestructive evaluation of the purity and defect density of a SWCNT sample.

## 1. Introduction

Evaluating the quality of single-wall carbon nanotubes (SWCNTs) is very important, both in basic research and industrial application. To evaluate quality, we must consider two independent parameters: purity and defect density. Purity can be defined as a content ratio of SWCNTs to impurities, and the defect density can be defined as the abundance of structural defects on the nanotube walls. Raman spectroscopy has often been applied for the purity evaluation because a Raman mode around  $1350\text{ cm}^{-1}$  (the “D-band”) is sensitive to structural defects in the graphitic  $\text{sp}^2$  network typical of carbonaceous impurities, such as amorphous carbon particles [1]. In previous studies, the intensity ratio of the tangential mode of SWCNTs (G-band) to the D-band was used to discuss the purity [2–5]. Because a pure SWCNT is also thought to have considerable D-band intensity due to structural defects, however, the evaluation based on the G/D ratio has uncertainty as to whether the D-band intensity reflects the amount of impurity particles or

the defect density on the sidewalls of SWCNTs. For example, when the D-band mainly reflects carbonaceous impurities in a sample, the G/D ratio becomes a good index of SWCNT purity. Meanwhile, when there are fewer carbon impurities in the sample, the G/D ratio can be used to discuss SWCNT defects. To resolve this uncertainty in the evaluation due to the double meaning of the D-band, a clearer scale reflecting either the purity or the defect density is required.

The Raman intensity of the G-band and radial breathing modes (RBMs) has been applied to the purity evaluation of SWCNTs [3, 6, 7]. Recently, Itkis et al. reported that the G-band area is proportional to the relative purity, as determined by optical absorption spectroscopy, for samples produced by arc discharge [3]. In this paper, we show that the G-band peak intensity around  $1593\text{ cm}^{-1}$  serves as a good index for the purity of as-grown SWCNTs produced by various synthetic methods, such as chemical vapor deposition (CVD), arc discharge, and laser ablation, even though their mean diameters differed. SWCNT purity was characterized using scanning electron microscopy (SEM)

and compared to the G-band intensity and the G/D ratio of the samples. Quantitative analysis of SEM images suggested that the G-band intensity obtained from 2.31 eV laser excitation is associated with the purity of SWCNTs with mean diameters ranging from 1.0 to 2.0 nm. An improved method of purity and defect evaluation using Raman spectroscopy is proposed.

## 2. Experimental

The SWCNT samples used in this work and the measurement conditions for the purity evaluation were as follows. The six SWCNT samples are referred to as (1) HiPco (raw material produced by the HiPco process, lot no. R0546, Carbon Nanotechnologies Inc.), (2) CoMoCAT (purified material produced by the CoMoCAT method, Southwest Nanotechnologies Inc.), (3) Meijo (raw material produced by arc discharge, AP-J grade, Meijo Nano Carbon Inc.), (4) Carbolex (raw material produced by arc discharge, Carbolex Inc.), (5) Laser (raw material produced by laser ablation in our laboratory), and (6) DIPS (raw material produced by direct injection pyrolytic synthesis (DIPS), Nikkiso Co., Ltd.). Raman spectra were measured in the back-scattering geometry using a single monochromator with a microscope (LabRam Aramis, Horiba Jobin Yvon) equipped with a charge-coupled device detector and a notch filter. The sample was excited by the continuous wave second harmonic of an Nd:YAG laser at 2.31 eV (532 nm). To avoid laser heating, a 0.1 mW laser beam was focused onto the sample using an objective lens ( $\times 10$ ). Raman spectra were obtained by averaging 20~30 spectra obtained from different locations on the sample. All Raman measurements were carried out under the same conditions for all samples to maintain high uniformity of the intensity. Thermogravimetric analysis (TGA) profiles were recorded from room temperature to 900°C in air flow (50 ccm) at a heating rate of 10°C/min with a microthermobalance (TGA-50, Shimadzu). Samples weighing 1~2 mg were used for the TGA measurements. The corresponding SEM images of the samples were obtained using JEOL JSM-7500F, operated at 15 kV.

## 3. Results and Discussion

The purity of the samples was first characterized quantitatively using SEM, which provided visual information of the ratio of SWCNTs to carbonaceous impurities. The SEM images and corresponding image analysis results of the samples are shown in Figure 1. We presumed that Fiber-like areas correspond to bundled SWCNTs, while the other particles and lumps correspond to carbonaceous impurities. The area counting of SWCNTs and carbonaceous impurities in the SEM images was carried out using image-processing software, ImageJ (NIH; <http://rsb.info.nih.gov/ij/>), as shown in Figure 1. The ratio of SWCNT area to particle area was assumed to relate to the purity of SWCNTs. The results for each sample are presented in Table 1 and Figure 2(a). Image analysis determined that the DIPS sample possessed the highest purity, and the HiPco sample had a higher purity than the Meijo, Laser, and Carbolex samples.

TABLE 1: Relative area of SWCNTs in a SEM image,  $R_{\text{Area}}$  (%), weight ratio of carbon to sample,  $R_{\text{Carbon/Sample}}$  (wt%), average diameter of SWCNTs,  $Dt$  (nm), normalized G-band Raman intensity,  $I_G/I_{\text{DIPS}}$ , and the G/D ratio,  $I_G/I_D$ , for DIPS, HiPco, Meijo, Laser, Carbolex, and CoMoCAT samples.

Sample	$R_{\text{Area}}$ (%)	$R_{\text{Carbon/Sample}}$ (wt%)	$Dt$ (nm)	$I_G/I_{\text{DIPS}}$	$I_G/I_D$
DIPS	98	95	2.0	1	164
HiPco	83	73	1.0	0.60	25
Meijo	57	73	1.5	0.53	31
Laser	48	91	1.4	0.41	60
Carbolex	47	53	1.5	0.21	13
CoMoCAT	—	84	0.8	0.14	20

Image analysis of the as-purchased CoMoCAT sample was unsuccessful because the SWCNTs were fully covered with carbonaceous impurities, probably due to the purification process. As a result, the SEM image could not be separated into SWCNT and impurity regions for analysis. The Raman and TGA results from the CoMoCAT sample were nevertheless included for reference.

It is well known that the G-band of SWCNTs shows multiplexes around 1580  $\text{cm}^{-1}$ . For purity evaluation using Raman spectroscopy, the G-band peak around 1593  $\text{cm}^{-1}$ , which derives from the longitudinal optical (LO) phonons of semiconducting SWCNTs [8], was used for two reasons: First, the G-band intensity is less sensitive to excitation laser energy than the RBM intensity, because of a loose resonance condition due to the large phonon energy. Second, a recent theoretical study predicted that there is no significant diameter dependence of the G-band intensity for the LO phonon of semiconducting SWCNTs, while the RBM intensity is more sensitive to the diameter and chirality for SWCNTs with diameter of 0.8~2.0 nm [8]. The overtone of the D-band, the so-called  $G'$ -band, was also predicted to depend on the chirality [9]. Thus, the G-band around 1593  $\text{cm}^{-1}$  is more appropriate than the other Raman modes for the comparison of purity of SWCNTs with different diameter distributions.

Raman spectra of the samples are presented in Figure 3. In the spectra, radial breathing modes (RBMs), the D-band, and the G-band were observed between 100~400  $\text{cm}^{-1}$ , 1250~1350  $\text{cm}^{-1}$ , and 1500~1600  $\text{cm}^{-1}$ , respectively [1, 10]. The average nanotube diameter of each sample was estimated using the relation of RBM frequency  $\omega_{\text{RBM}}$  to nanotube diameter  $Dt$ ,  $Dt$  (nm) =  $227/\omega_{\text{RBM}}$  ( $\text{cm}^{-1}$ ) [11]. The G-band and the D-band intensities were obtained from their maximum peak counts. The G-band intensity and G/D ratio are shown in Table 1 and Figures 2(c) and 2(d).

In Figures 2(b) and 2(c), it can be seen that there was poor correlation between the G-band intensity and the G/D ratio. For the DIPS sample, which had the highest purity of the samples used, according to the SEM image analysis, both the G-band intensity and the G/D ratio were the highest of all samples. However, the G/D ratio of the Laser sample was 2.4 times higher than that of the HiPco sample, while the G-band intensity of the Laser sample was only 0.7 times of that of the HiPco sample. In the previous study, a linear relationship between the G/D ratio and the G-band was observed for

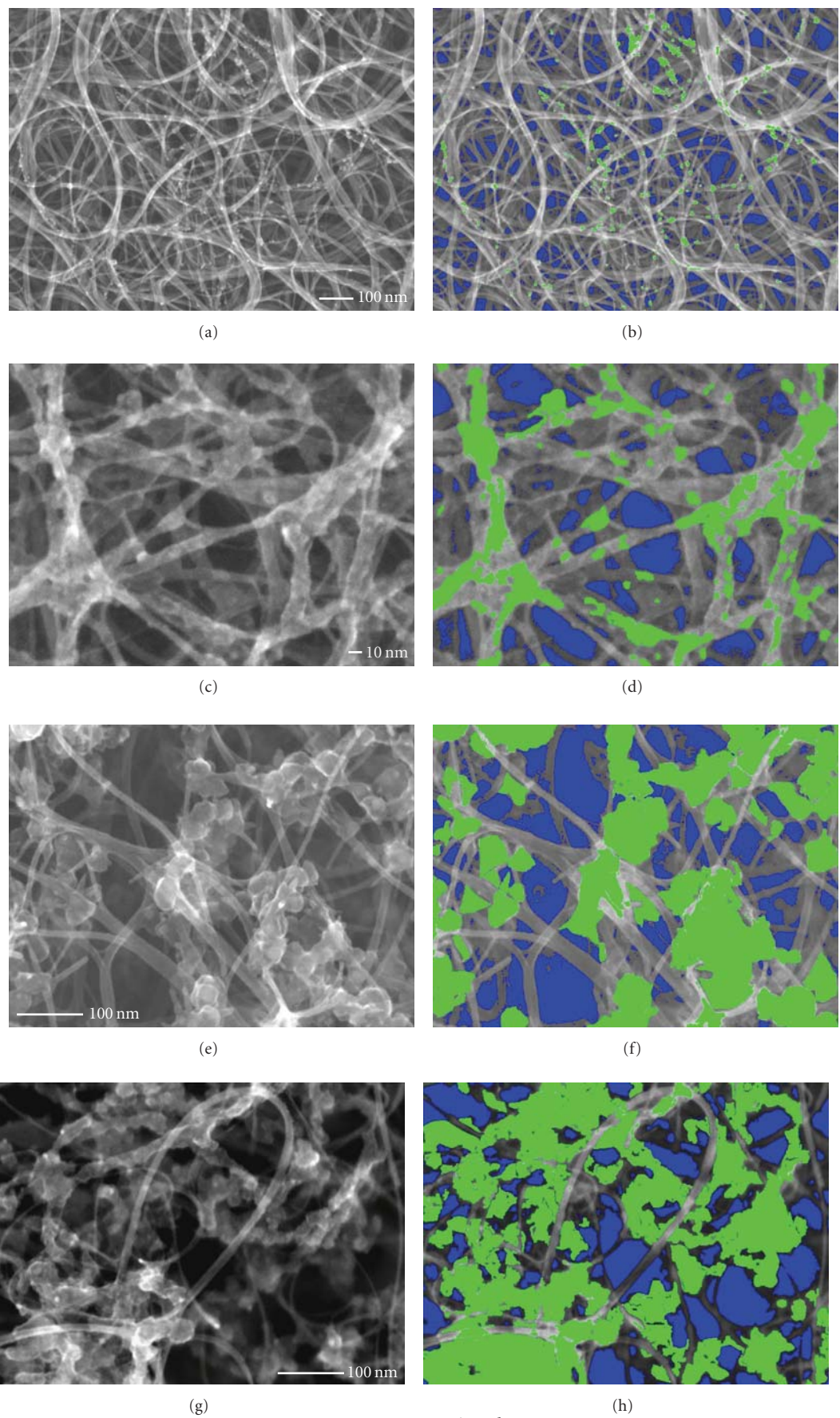


FIGURE 1: Continued.

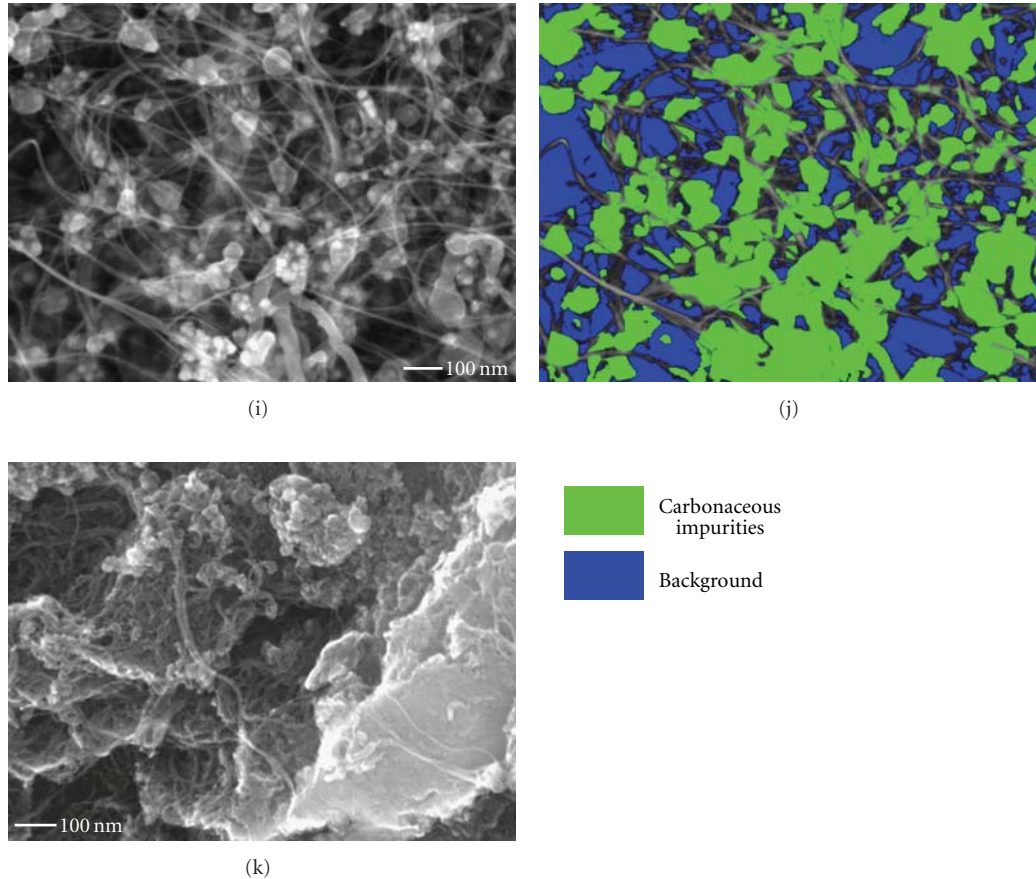


FIGURE 1: SEM images and corresponding image analysis results of (a)-(b) DIPS, (c)-(d) HiPco, (e)-(f) Meijo, (g)-(h) Laser, (i)-(j) Carbolex, and (k) CoMoCAT samples. In the image analysis, the carbonaceous impurities were painted green and background was painted blue for the area counting.

samples produced by arc discharge [3]. The present results show that such a relationship does not hold true for samples produced by different synthetic methods.

In contrast to the poor relationship between the G/D ratio and G-band intensity, the G-band intensity was well associated with the SWCNT purity estimated by SEM image analysis, as shown in Figures 2(a) and 2(b). Usually, as-produced SWCNT samples contain carbonaceous impurities, such as graphitic and/or amorphous carbon particles. Because both the SWCNTs and carbonaceous impurities have the same  $\pi$  electron system, the carbonaceous impurities also exhibit a black color and absorb visible light similarly to the SWCNTs. However, their contribution to the G-band Raman intensity is significantly different. Actually, the Raman signal from SWCNTs in a raw soot is about 30 times higher than that of carbonaceous impurities due to a resonance effect [3]. Thus, it is reasonable to suppose that carbonaceous impurities act as an optical absorber and any observed difference in the G-band intensity can be mainly attributed to a difference in the amount of carbonaceous impurities present.

The G-band intensity may also be affected by additional factors such as excitation laser wavelength and nanotube diameter. It is known that the Raman intensity of SWCNTs

is significantly enhanced by a resonance effect when the excitation energy matches the absorption bands of SWCNTs [12]. The optical transition energy is inversely proportional to the nanotube diameter [13]. According to the relationship between the diameter and optical transition energy of SWCNTs [13], the measured Raman spectra were on the resonance of the  $E_{33}$  or  $E_{44}$  optical transition of semiconducting SWCNTs, except for the CoMoCAT sample. Because the  $E_{33}$  and  $E_{44}$  transitions have broader spectral features than the  $E_{22}$  transition [12, 14], under the specific laser excitation, the difference in resonance conditions for each chirality is not significant. Thus, many types of SWCNTs can be excited by a single-wavelength laser. The resonance of semiconducting SWCNTs was confirmed by the sharp G-band peak around  $1593\text{ cm}^{-1}$ . Consequently, the difference in the resonance effect and nanotube diameter did not significantly affect the G-band Raman intensities of SWCNTs samples having different mean diameters, except for the CoMoCAT sample. In other words, the G-band intensity measured with 2.31 eV laser excitation can be used to indicate the purity of SWCNTs with average diameter distribution ranging from 1.0 to 2.0 nm. Because the absolute Raman intensity depends on the equipment and the specific measurement method, use of the G-band intensity to measure purity requires a common

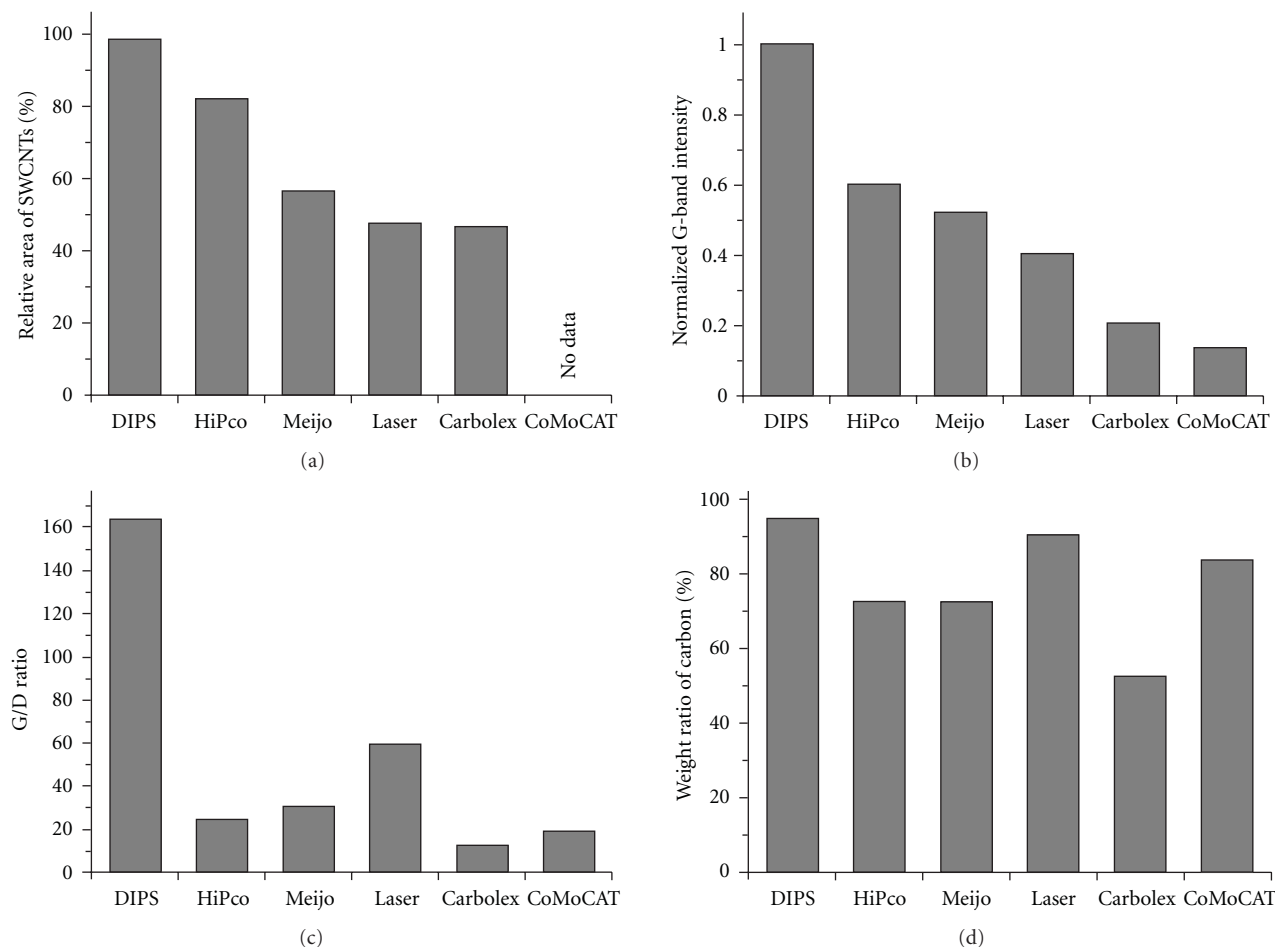


FIGURE 2: (a) relative area of SWCNTs in an SEM image, (b) normalized G-band Raman intensity, (c) G/D ratio, and (d) weight ratio of carbon in a sample for DIPS, HiPco, Meijo, Laser, Carbolex, and CoMoCAT samples.

standard sample that gives a stable, uniform purity. As shown in Figures 1(a) and 3(a), the DIPS sample had extremely high purity and a highly stable G-band intensity. In this study, we used the DIPS sample as the standard to obtain the relative purity of the other samples.

Although we primarily discuss as-grown samples, it is noteworthy that the Raman intensity of SWCNTs is sensitive to their aggregation [15] and to charge transfer, such as that induced by molecular adsorption [16]. Because of these effects, it is important to monitor the purity of SWCNTs at each purification step. In the purification process, we often use acid, which easily induces charge transfer [16], and after the purification, SWCNTs tend to form thick bundles or sometimes aggregate with impurities. To avoid misleading results, it is necessary to check for aggregation of SWCNTs by SEM and to remove adsorbed chemicals from the purified materials, using vacuum annealing or some other process. In the present study, therefore, we have not used “purified samples” but “as-grown samples” which have a scarce charge transfer and randomly oriented bundles with the size from few nanometers to several tens nanometers. We note that these samples do not have specific orientations of nanotube which should be avoided because the resonance Raman

intensity of SWCNTs has strong polarization dependence to the nanotube axis.

Once the purity of a sample is assessed from the G-band intensity, the G/D ratio can be used to discuss the relative abundance of SWCNT defects. The mismatch between the purity (Figure 2(a)) and the G/D ratio (Figure 2(c)) was caused by the difference in the main contribution to D-band intensity for each sample. It is known that the D-band derives from the structural defects of the graphitic  $sp^2$  network in both SWCNTs and carbonaceous impurities, so the simple use of only the G/D ratio is not suitable to determine purity and quality. The HiPco sample, for example, possessed a higher purity than the Laser sample but had a lower G/D ratio. This suggests that the HiPco sample had more defects than the Laser sample. The combination of the G-band intensity and the G/D ratio can be highly useful to determine both the purity and the defect density, which has been difficult to accomplish by means other than Raman spectroscopy.

Raman and SEM were used for purity evaluation and could be associated with the ratio of SWCNTs and carbonaceous impurities in a sample. On the other hand, TGA was used to measure the content ratio of noncarbonaceous

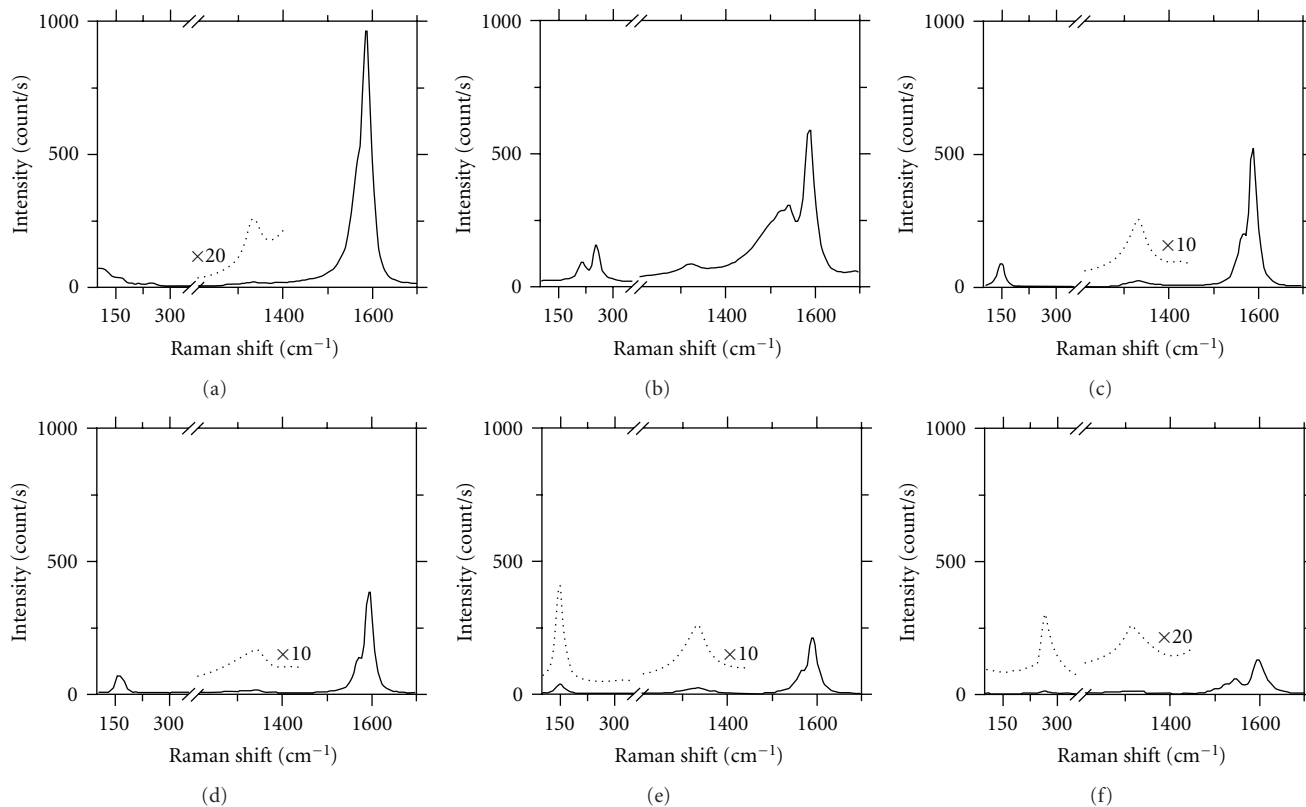


FIGURE 3: Raman spectra of (a) DIPS, (b) HiPco, (c) Meijo, (d) Laser, (e) Carbolex, and (f) CoMoCAT samples.

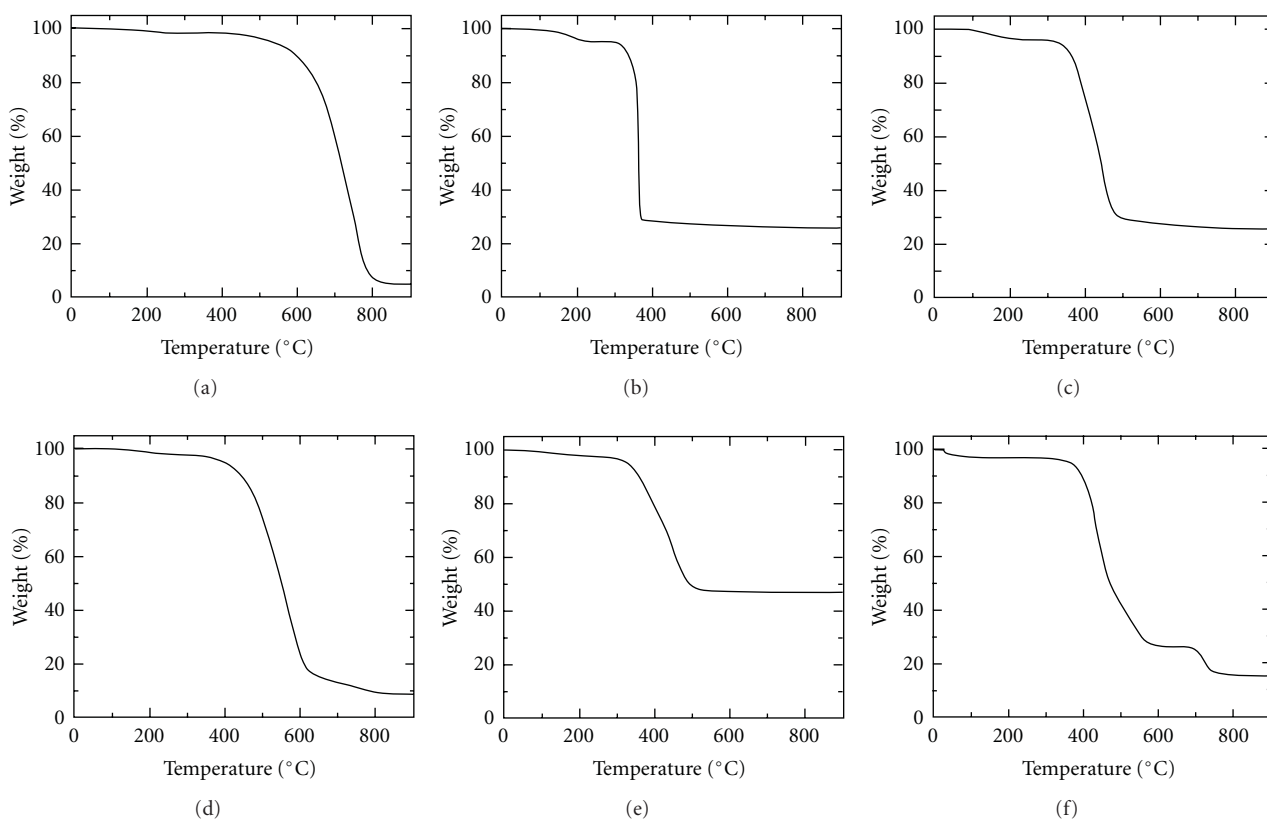


FIGURE 4: TGA profiles of (a) DIPS, (b) HiPco, (c) Meijo, (d) Laser, (e) Carbolex, and (f) CoMoCAT samples.

impurities in a sample by monitoring the weight decrease of samples during combustion in air. TGA profiles of the samples are presented in Figure 4. The weight ratio of carbon in the samples is shown in Figure 2(d). It can be seen that the weight ratio was different from the purity evaluated by SEM. Because the density of metal catalyst is much higher than that of carbon materials, evaluation of the weight ratio of the metal impurities to carbonaceous material is difficult, even by SEM image analysis. These methods complement each other. Thus, we conclude that it is better to combine Raman, SEM, and TGA for SWCNT purity evaluation and to compare the results in accordance with their intended use.

#### 4. Conclusion

A comparative study of purity and Raman intensity was carried out for SWCNTs produced by various synthetic methods. The detailed comparison of Raman intensity and SEM observations suggested that the G-band intensity is a better indicator of SWCNT purity than the G/D ratio. The G/D ratio is not suitable for determination of the purity of various samples produced by different synthetic methods. The present results indicate that a combination of the G-band intensity and the G/D ratio is useful to evaluate the purity and defect density of SWCNTs. The evaluation conditions employed in this study can be applied to SWCNTs with an average diameter of 1~2 nm, which covers most commercially available SWCNTs. If a consistent standard sample were available, evaluation based on the G-band and the D-band intensities could provide an easy means of determining the quality of SWCNTs for all users and suppliers of SWCNTs.

#### Acknowledgments

The authors thank K. Ogura of JEOL Ltd., Y. Nakata and H. Matsumoto of HORIBA Ltd., and Y. Suzuki of SHIMADZU CO. for providing experimental data; S. Shiraki and Y. Nakagawa of NIKKISO CO., LTD., for supplying the DIPS sample; and T. Okazaki, T. Saito, and D. Nishide of AIST for helpful discussions. They acknowledge the support from the Nanotechnology Program “Carbon Nanotube Capacitor Development Project” (2006–2010) by the New Energy and Industrial Technology Development Organization (NEDO).

#### References

- [1] S. Reich, C. Thomsen, and J. Maultzsch, *Carbon Nanotubes: Basic Concepts and Physical Properties*, John Wiley & Sons, Berlin, Germany, 2004.
- [2] A. C. Dillon, T. Gennett, K. M. Jones, J. L. Alleman, P. A. Parilla, and M. J. Heben, “Simple and complete purification of single-walled carbon nanotube materials,” *Advanced Materials*, vol. 11, no. 16, pp. 1354–1358, 1999.
- [3] M. E. Itkis, D. E. Perea, R. Jung, S. Niyogi, and R. C. Haddon, “Comparison of analytical techniques for purity evaluation of single-walled carbon nanotubes,” *Journal of the American Chemical Society*, vol. 127, no. 10, pp. 3439–3448, 2005.
- [4] D. Nishide, H. Kataura, S. Suzuki, K. Tsukagoshi, Y. Aoyagi, and Y. Achiba, “High-yield production of single-wall carbon nanotubes in nitrogen gas,” *Chemical Physics Letters*, vol. 372, no. 1-2, pp. 45–50, 2003.
- [5] H. Kataura, Y. Kumazawa, Y. Maniwa et al., “Diameter control of single-walled carbon nanotubes,” *Carbon*, vol. 38, no. 11-12, pp. 1691–1697, 2000.
- [6] M. Takizawa, S. Bandow, M. Yudasaka, Y. Ando, H. Shimoyama, and S. Iijima, “Change of tube diameter distribution of single-wall carbon nanotubes induced by changing the bimetallic ratio of Ni and Y catalysts,” *Chemical Physics Letters*, vol. 326, no. 3-4, pp. 351–357, 2000.
- [7] K. A. Williams, M. Tachibana, J. L. Allen et al., “Single-wall carbon nanotubes from coal,” *Chemical Physics Letters*, vol. 310, no. 1-2, pp. 31–37, 1999.
- [8] V. N. Popov and P. Lambin, “Resonant Raman intensity of the totally symmetric phonons of single-walled carbon nanotubes,” *Physical Review B*, vol. 73, no. 16, Article ID 165425, 2006.
- [9] K. K. Kim, J. S. Park, S. J. Kim et al., “Dependence of Raman spectra G' band intensity on metallicity of single-wall carbon nanotubes,” *Physical Review B*, vol. 76, no. 20, Article ID 205426, 2007.
- [10] A. Jorio, M. A. Pimenta, A. G. Souza Filho, R. Saito, G. Dresselhaus, and M. S. Dresselhaus, “Characterizing carbon nanotube samples with resonance Raman scattering,” *New Journal of Physics*, vol. 5, pp. 139.1–139.17, 2003.
- [11] P. T. Araujo, I. O. Maciel, P. B.C. Pesce et al., “Nature of the constant factor in the relation between radial breathing mode frequency and tube diameter for single-wall carbon nanotubes,” *Physical Review B*, vol. 77, no. 24, Article ID 241403, 4 pages, 2008.
- [12] A. Jorio, A. G. Souza Filho, G. Dresselhaus et al., “Joint density of electronic states for one isolated single-wall carbon nanotube studied by resonant Raman scattering,” *Physical Review B*, vol. 63, no. 24, Article ID 245416, pp. 2454161–2454164, 2001.
- [13] H. Kataura, Y. Kumazawa, Y. Maniwa et al., “Optical properties of single-wall carbon nanotubes,” *Synthetic Metals*, vol. 103, no. 1–3, pp. 2555–2558, 1999.
- [14] E. H. Haroz, S. M. Bachilo, R. B. Weisman, and S. K. Doorn, “Curvature effects on the  $E_{33}$  and  $E_{44}$  exciton transitions in semiconducting single-walled carbon nanotubes,” *Physical Review B*, vol. 77, no. 12, Article ID 125405, 9 pages, 2008.
- [15] D. A. Heller, P. W. Barone, J. P. Swanson, R. M. Mayrhofer, and M. S. Strano, “Using Raman spectroscopy to elucidate the aggregation state of single-walled carbon nanotubes,” *Journal of Physical Chemistry B*, vol. 108, no. 22, pp. 6905–6909, 2004.
- [16] W. Zhou, J. Vavro, N. M. Nemes et al., “Charge transfer and Fermi level shift in  $p$ -doped single-walled carbon nanotubes,” *Physical Review B*, vol. 71, no. 20, Article ID 205423, 7 pages, 2005.

## Research Article

# Field Emission Properties of the Dendritic Carbon Nanotubes Film Embedded with ZnO Quantum Dots

Shu Zuo, Xin Li, Weihua Liu, Yongning He, Zhihao Xiao, and Changchun Zhu

*The School of Electronic and Information Engineering, Xi'an Jiaotong University, Xi'an 710049, China*

Correspondence should be addressed to Xin Li, lx@mail.xjtu.edu.cn

Received 15 April 2010; Accepted 27 June 2010

Academic Editor: Jianyu Huang

Copyright © 2011 Shu Zuo et al. This is an open access article distributed under the Creative Commons Attribution License, which permits unrestricted use, distribution, and reproduction in any medium, provided the original work is properly cited.

Response on the effects of individual differences of common carbon nanotubes on the field emission current stability and the luminescence uniformity of cathode film, a new type of cathode film made of dendritic carbon nanotubes embedded with Zinc oxide quantum dots is proposed. The film of dendritic carbon nanotubes was synthesized through high-temperature pyrolysis of iron phthalocyanine on a silicon substrate coated with zinc oxide nanoparticles. The dendritic structure looks like many small branches protrude from the main branches in SEM and TEM images, and both the branch and the trunk are embedded with Zinc oxide quantum dots. The turn-on field of the dendritic structure film is  $\sim 1.3 \text{ V}/\mu\text{m}$  at a current of  $2 \mu\text{A}$ , which is much lower than that of the common carbon nanotube film, and the emission current and the luminescence uniformity are better than that of the common one. The whole film emission uniformity has been improved because the multi-emission sites out from the dendritic structure carbon nanotubes cover up the failure and defects of the single emission site.

## 1. Introduction

Carbon nanotubes have attracted wide concern due to their excellent physical, chemical, and electrical properties since they were firstly discovered by Iijima [1] in 1991. With its nanoscale emitter, high-aspect ratio, good thermal stability and conductivity carbon nanotubes are very appropriate materials for field emission. Field Emission Display based on Carbon nanotubes which have advantages in high brightness, high resolution, long life, easy working in electromagnetic radiation, and other extreme environment, is expected to be applied in the military display. However, there is still a long way for the commercial, for some critical technical problems needed to be resolved, such as emission current stability, luminescence uniformity, and long life. Some research groups had tried to improve the cathode film field emission property by optimizing the growth process of carbon nanotube on substrate [2–5]. Li research group improved contact performance by inserting a transition layer between carbon nanotubes and substrate [6–9]. Chen group [10, 11] discovered that the electron tunneling would be affected by the contact surface barrier between carbon

nanotubes and substrate. Different Fowler-Nordheim curves have been attributed for different kinds of Ohmic and Schottky contacts in their research. Shiroishi [11] research group decreased the turn-on voltage from 2.1 to  $1.4 \text{ V}/\mu\text{m}$  and improved the field emission characteristics by laser post-treatment on the carbon nanotubes. Yu [13] group selectively etched the carbon nanotubes film prepared through screen-printing, so as to remove the inorganic binder within the CNT cathode film and to enhance emission performance effectively. A novel dendritic structure carbon nanotube cathode film was proposed in this paper. Zinc oxide nanoparticles film is coated on the silicon wafer through screen-printing process, which served as the growth substrate. The dendritic carbon nanotubes were then synthesized through high-temperature pyrolysis of iron phthalocyanine on the ZnO nanoparticle film. The dendritic carbon nanotube cathode film was embedded with ZnO quantum dots to bring up more emission spots. The defects in that of the single emission site type could be covered up and hid by the dendritic structure with multiemission sites, and the luminescence uniformity of the cathode film field emission could be improved.

## 2. Experiment

In the experiment, the cathode film with dendritic structure carbon nanotubes embedded with zinc oxide quantum dots was prepared on the silicon substrates. Firstly, 10 gram ball milling zinc oxide nano particles were dispersed into 30 ml terpineol solution. Secondly, 4 gram ethyl cellulose was dispersed in the above solution assistant with the ultrasonic so as to form the composite paste. Finally the composite paste was then heated at 200°C. After that the zinc oxide nanoparticles film was printed on the substrate through screen-printing process. The film thickness was about 10 microns. The film was sintered in the furnace at 560°C to be growth substrate. Dendritic structure carbon nanotubes were grown on the composite film substrate through high-temperature pyrolysis of iron phthalocyanine chemical vapor deposition process. At last a new black film, which is about 1.5×1.5 square centimeter, was grown on the top of the substrate surface as the cathode. The schematic diagram of test setup and equivalent circuit were shown in Figure 1. The phosphor coated ITO glass is the anode that has the same size with that of the cathode. The space between the anode and the cathode is about 300 μm. The type of the silicon substrate is N (100) type that the resistivity is  $10^{-2} \sim 10^{-3} \Omega \cdot \text{cm}$ . The vacuum level is  $1.5 \times 10^{-4}$  Pa and temperature is the room temperature of the chamber for FE measurement. Field emission characteristics of the samples had been tested with self-developed high-vacuum field emission test equipment, and the luminous pictures were recorded by a digital camera.

## 3. Results and Discussion

The SEM images of the common carbon nanotube film grown on the silicon substrate and the dendritic structure carbon nanotube film grown on the Si/ZnO composite substrate are shown in Figures 2(a) and 2(b), respectively. The two samples have been analyzed by JSM6700F scanning electron microscopy (SEM). The diameters of the carbon nanotube on the silicon substrate are from 20 to 40 nm, and the thickness of the films is near 20 microns as shown in Figure 2(a). These carbon nanotube bundles were aligned perpendicular to the substrate in the form of high-density, and the contact between their roots and the substrate is so weak that some of them are separated from the substrate. The diameter of the samples of the dendritic structure carbon nanotubes on the Si/ZnO composite film substrate is about 100 nm, and the thickness of dendritic structure film is about 30 to 40 μm as shown in Figure 2(b), where the perspective angle is greater than 45 degrees whereas the angle from Figure 2(a) is the level perspective (0 degrees).

The dendritic structure carbon nanotubes are perpendicular to the substrate, and the contact between their roots and the substrate is so strong that their roots are almost completely buried in the substrate. The space between the dendritic carbon nanotubes is much larger than that of the samples of the common carbon nanotubes, which means the density of the former film is smaller than that of the latter one. As a field emission display cathode, if the space

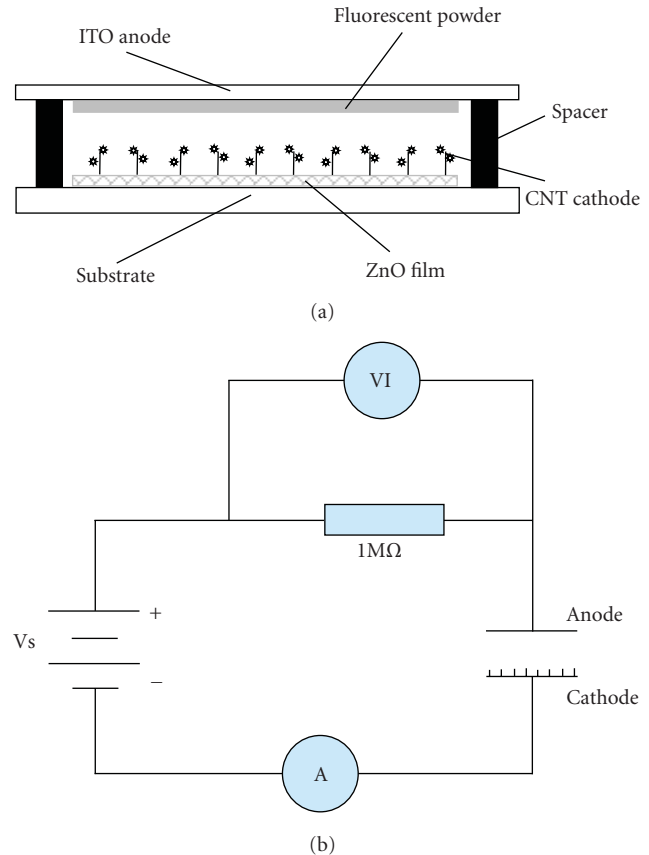


FIGURE 1: The schematic diagram (a) and equivalent circuit (b) of testing setup.

between carbon nanotubes of the film is too small to avoid shielding effect among the emission site, the emission current of the cathode film will be decreased because the local electric field of the nanotubes emission site reduced. On the other hand, keeping a certain space between emission sites will help to increase the emission current. The cathode film of the dendritic carbon nanotubes, which grow on the Si/ZnO composite film substrate, have relative larger space in between than those grow on silicon substrate, can avoid the emission site shielding effect. When the high-emission current pass through the contact site between the roots of the each nanotube and the substrate, the contact resistances are rebuilt, changed, and become uneven because of the contact interface between of the nanotube and the substrate are uneven, so that the subsequent emission current density distribution is uneven. Because the roots of the dendritic carbon nanotubes are deeply buried in the Si/ZnO composite film substrate, the contact resistance uniformity of each nanotube and the substrate is much better, so is the field emission current.

The higher resolution microscopic images of the dendritic carbon nanotubes are shown in Figure 3. There are many smaller nanotubes and nanoparticles covered the outer wall of the dendritic carbon nanotube. This kind of structures, which are called dendritic structure, looks like

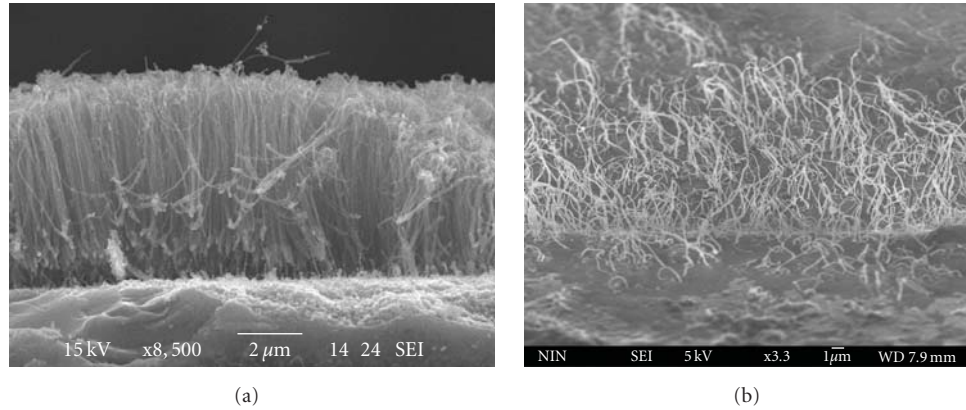


FIGURE 2: The SEM of the carbon nanotubes on (a) silicon substrates and (b) Si/ZnO substrate.

many small branches protruding from the main branches. Both the electronic transmission channels and the ratio surface area of the material increased in this kind of special dendritic structure. The nanostructure of zinc oxide particles (XRD was reported in previous work [6–9]) covered the dendritic carbon nanotube surface evenly as shown in Figures 3(a) and 3(b). The further TEM analysis also indicated that there are some zinc oxide quantum dots, which are less than 20 nm, embedded in the nanotubes as shown in Figure 3(c). The electrons will meet the suspending ZnO quantum dots while they are moving along the outer layer of the dendritic carbon nanotubes from the cathode in the electric field. The electron can pass through the covalent bond between carbon nanotubes and the ZnO quantum dots and go into conduction band of ZnO quantum dots if the electric field is high enough, so that the carrier number increased a lot because of the ZnO quantum size effect. Both the emission current density and the field emission uniformity are improved because of the multi emission sites of the dendritic structure.

A group of field emission property tests have been carried out to know if the ZnO quantum dots would affect the emission current. The field emission I-V curves (Figure 4) and luminescence pictures (Figure 5) of the two samples, which are the dendritic structure carbon nanotube film 1 embedded with zinc oxide quantum dots and the common carbon nanotubes film 2 on the silicon substrate, were acquired. The vertical line corresponds to the current of  $50 \mu\text{A}$ , and the horizontal line corresponds to voltage 500 V as shown in Figure 4. The turn-on voltage of the film 1 is 420 V, and the film 2 is 749 V. Since the space between the cathode and the anode is  $300 \mu\text{m}$ , the turn-on field of the film 1 and film 2 are  $1.3 \text{ V}/\mu\text{m}$  and  $2.5 \text{ V}/\mu\text{m}$  at a current of  $2 \mu\text{A}$ , respectively. The turn-on field of the dendritic carbon nanotubes film cathode is lower, because there is enough space between emission sites to decrease the shielding effect, and its local field of the emission site is high enough for the electronic overflow at lower voltage. The film 2 need higher electric field to produce the same emission current with that of the film 1, for example, the voltage applied on film 1 is 1060 V and film 2 is 1209 V when the current is  $100 \mu\text{A}$ . The

electrons were transported through the carbon nanotube and the dendritic carbon nanotube embedded with zinc oxide, respectively, under the same electric field. For the latter, electrons transported through the covalent bond between the dendritic carbon nanotubes and ZnO quantum dots into the conduction band of zinc oxide quantum dots, cause the increasing carriers to enhance the field emission current density. Meanwhile, many new emission sites are produced by the defects that number of were formed on the surface of carbon nanotube by the zinc oxide quantum dots embedded. When the electrical field reaches turn-on field, most of the emission sites would be the current contributions. With the help of the dendritic structure carbon nanotubes embedded with zinc oxide quantum dots, the defects provoked by single site would be covered up and hid by multispot emission, so as to enhance the current and improve the emission uniformity of the whole cathode film.

Figure 5 shows the luminous pictures of the dendritic structure carbon nanotubes film cathode at different times and the same applied voltage, the emission current is about  $50 \mu\text{A}$ . The luminescence picture of common CNTs film is shown in previous work [14]. Figure 5(a), which is the situation that just achieve this current, can be seen relatively light at lower left part, and relatively dark at the upper right corner. The pictures after 10 seconds and 20 seconds are shown in Figures 5(b) and 5(c), respectively. The initial brightness of bright areas weakened, the dark area brightness is enhanced, and the brightness of the whole region became uniform. When the ZnO quantum dots are embedded into the surface of carbon nanotubes, the surface of the carbon tube defects, which constitute a new emission site, each carbon nanotube is no longer a single emission site. When the electric field reach a certain value, the electrons transport into the ZnO conduction band through carbon nanotubes and ZnO quantum dots covalent bond between the quantum dots, and provoke carriers number increasing, resulting in multiemission site. The work function of ZnO is about 3.3 eV that is a little lower than that of the CNT, but it is not the critical point that has improved the emission current density. The ZnO tip with the nano structure can emit the electrons under the lower field in previous work [15], so that the

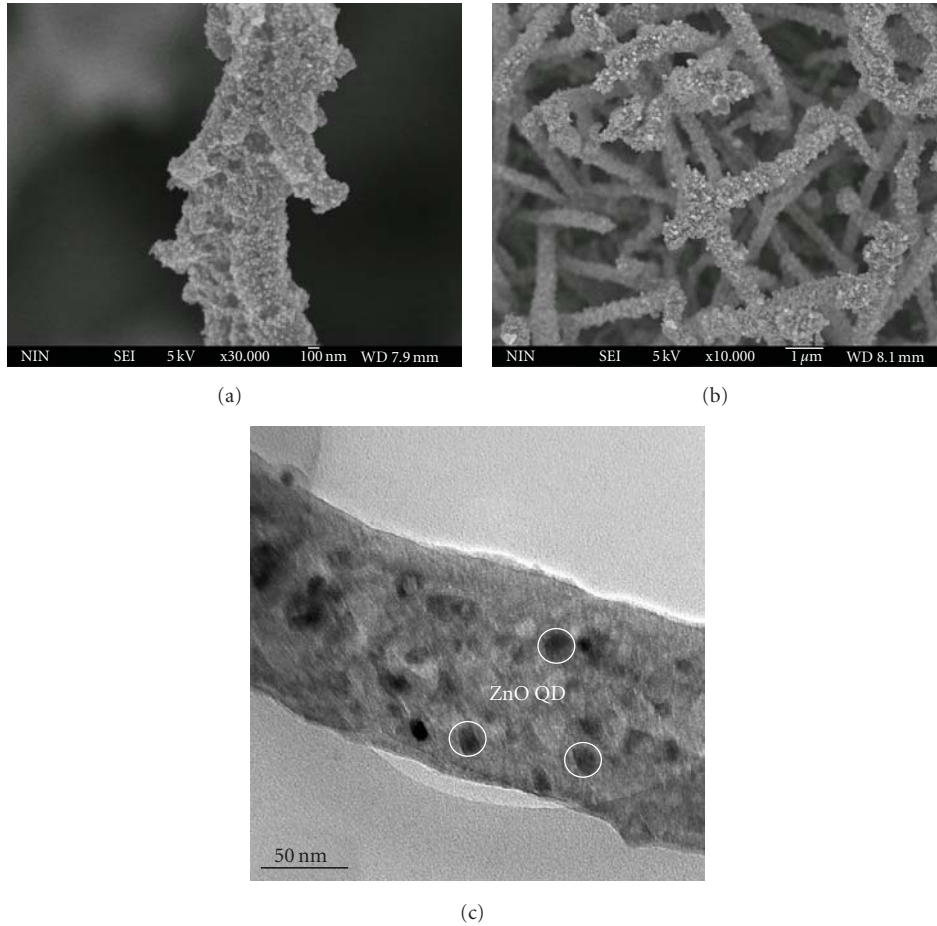


FIGURE 3: The SEM and TEM of the dendritic structure carbon nanotubes embedded with zinc oxide quantum dots. SEM of (a) one and (b) many dendritic structure carbon nanotubes; (c) TEM of the dendritic structure carbon nanotubes.

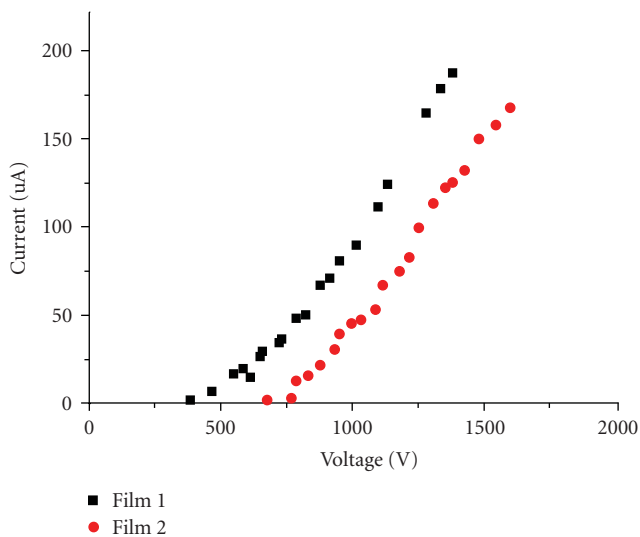


FIGURE 4: field emission I-V curves of samples on two different kinds of substrates. film 1: the dendritic structure carbon nanotubes embedded with zinc oxide quantum dots on the ZnO composite substrates; film 2: the carbon nanotubes on the silicon substrate.

embedded ZnO QDs can indeed act as multiemission sites under this field.

Multi emission sites will cover up the failure and defects of the single site, and improve the overall emission uniformity of the cathode film. The field emission current will soon enter the saturation, and achieve field emission current stability while the applied voltage remains. The uniformity has greatly improved from the luminescence pictures.

#### 4. Conclusion

Response on the effects of individual differences of common carbon nanotubes on the field emission current stability and the luminescence uniformity, zinc oxide quantum dots and nanoparticles have been proposed to modify the carbon nanotubes, so as to increase the emission sites and cover up the defects caused by initial single sites. A zinc oxide nanoparticle film was prepared on the silicon substrate through screen-printing process, the dendritic structure carbon nanotubes were synthesized on it as the cathode film. The cathode film is found to be made up of the

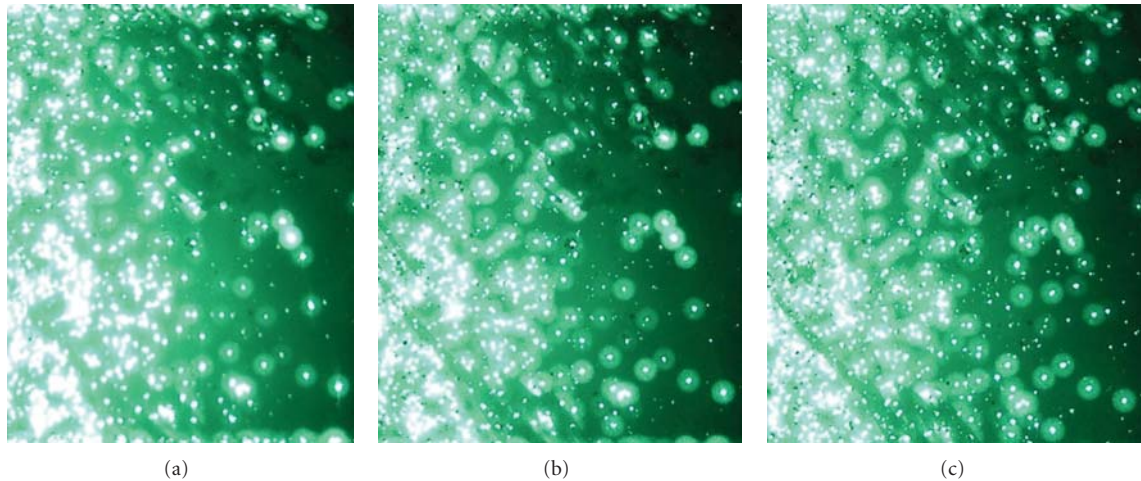


FIGURE 5: Field emission luminescence pictures when the emission current is  $50 \mu\text{A}$ : (a) just reached the current  $50 \mu\text{A}$ ; (b) after 10 second, (c) after 20 second at this current.

dendritic structure carbon nanotubes embedded with zinc oxide quantum dots, and there is enough space between emission sites to decrease the shielding effect, and its local field of the emission site is high enough for the electronic overflow at lower voltage. The contact between the root and the substrate is stronger because the roots are buried in the substrate. The turn-on field of the dendritic structure film is lower than that of the common film, and the emission current of the dendritic structure is higher than that of the common one. The additional emission sites, which are produced by the zinc oxide quantum dots embedded into the surface of carbon nanotubes, covered up the failure and defects of the single site, and improved effectively the field emission current and luminescence uniformity of the whole cathode film.

## Acknowledgments

This paper was supported by the Innovation Foundation of Xi'an Applied material, Xi'an Science and Technology Program, National 863 Key Project of Panel Display, and National Science Foundation of China.

## References

- [1] S. Iijima, "Helical microtubules of graphitic carbon," *Nature*, vol. 354, no. 6348, pp. 56–58, 1991.
- [2] Q. H. Wang, M. Yan, and R. P. H. Chang, "Flat panel display prototype using gated carbon nanotube field emitters," *Applied Physics Letters*, vol. 78, no. 9, pp. 1294–1296, 2001.
- [3] J. S. Suh, K. S. Jeong, J. S. Lee, and I. Han, "Study of the field-screening effect of highly ordered carbon nanotube arrays," *Applied Physics Letters*, vol. 80, no. 13, 2002.
- [4] S. H. Jo, Y. Tu, Z. P. Huang, D. L. Carnahan, D. Z. Wang, and Z. F. Ren, "Effect of length and spacing of vertically aligned carbon nanotubes on field emission properties," *Applied Physics Letters*, vol. 82, no. 20, pp. 3520–3522, 2003.
- [5] S. Y. Lee, W. C. Choi, C. Jeon, C.-Y. Park, J. H. Yang, and M. H. Kwon, "Field emitter density control effect on emission current density by Ag-Cu alloy coating on carbon nanotubes," *Applied Physics Letters*, vol. 93, no. 10, Article ID 103101, 2008.
- [6] X. Li, F. Ding, W. Liu, Y. He, and C. Zhu, "Luminescence uniformity studies on dendrite bamboo carbon submicron-tube field-emitter arrays," *Journal of Vacuum Science and Technology B*, vol. 26, no. 1, pp. 171–174, 2008.
- [7] J. Y. Pan, C. C. Zhu, and Y. L. Gao, "Enhanced field emission characteristics of zinc oxide mixed carbon nano-tubes films," *Applied Surface Science*, vol. 254, no. 13, pp. 3787–3792, 2008.
- [8] Y. X. Liu, J. H. Liu, and C. C. Zhu, "Flame synthesis of carbon nanotubes for panel field emission lamp," *Applied Surface Science*, vol. 255, no. 18, pp. 7985–7989, 2009.
- [9] L.-M. Yu and C.-C. Zhu, "Field emission characteristics study for ZnO/Ag and ZnO/CNTs composites produced by DC electrophoresis," *Applied Surface Science*, vol. 255, no. 20, pp. 8359–8362, 2009.
- [10] H. F. Chen, H. Song, L. Z. Cao, et al., "Effect of intergate barrier between carbon nanotube film and substrate on field emission," *Applied Physics*, vol. 106, Article ID 033703, 2009.
- [11] T. Shiroishi, A. Hosono, A. Sono et al., "Improvement of emission characteristics uniformity of carbon nanotube field emission display by surface treatment," *Journal of Vacuum Science and Technology B*, vol. 24, no. 2, pp. 979–982, 2006.
- [12] K. Ohsumi, T. Honda, W. S. Kim et al., "KrF laser surface treatment of carbon nanotube cathodes with and without reactive ion etching," *Journal of Vacuum Science and Technology B*, vol. 25, no. 2, pp. 557–560, 2007.
- [13] J. Yu, J. Chen, S. Z. Deng, J. C. She, and N. S. Xu, "Post-treatment of screen-printed carbon nanotube emitter by selective plasma etching," *Journal of Vacuum Science and Technology B*, vol. 25, no. 2, pp. 552–556, 2007.
- [14] W. Liu, F. Zeng, L. Xin, C. Zhu, and Y. He, "Turn-on field distribution of field-emitting sites in carbon nanotube film: study with luminescent image," *Journal of Vacuum Science and Technology B*, vol. 26, no. 1, pp. 32–35, 2008.
- [15] L.-M. Yu and C.-C. Zhu, "Electrophoresis deposition and field emission properties of composites films ZnO nanoneedles/CNTs," in *Proceedings of the 4th IEEE International Conference on Nano/Micro Engineered and Molecular Systems (NEMS '09)*, pp. 9–12, Shenzhen, China, January 2009.

## Research Article

# Large Deflections Mechanical Analysis of a Suspended Single-Wall Carbon Nanotube under Thermoelectrical Loading

Assaf Ya'akovovitz,<sup>1</sup> Slava Krylov,<sup>1</sup> and Yael Hanein<sup>2</sup>

<sup>1</sup> School of Mechanical Engineering, Faculty of Engineering, Tel Aviv University, Ramat Aviv, Tel Aviv 69978, Israel

<sup>2</sup> School of Electrical Engineering, Faculty of Engineering, Tel Aviv University, Ramat Aviv, Tel Aviv 69978, Israel

Correspondence should be addressed to Assaf Ya'akovovitz, assafyaa@eng.tau.ac.il

Received 14 July 2010; Revised 17 October 2010; Accepted 3 January 2011

Academic Editor: Sulin Zhang

Copyright © 2011 Assaf Ya'akovovitz et al. This is an open access article distributed under the Creative Commons Attribution License, which permits unrestricted use, distribution, and reproduction in any medium, provided the original work is properly cited.

Following the recent progress in integrating single-wall carbon nanotubes (SWCNTs) into silicon-based micro-electromechanical systems (MEMS), new modeling tools are needed to predict their behavior under different loads, including thermal, electrical and mechanical. In the present study, the mechanical behavior of SWCNTs under thermoelectrical loading is analyzed using a large deflection geometrically nonlinear string model. The effect of the resistive heating was found to have a substantial influence on the SWCNTs behavior, including significant enhancement of the strain (up to the millistrains range) and buckling due to the thermal expansion. The effect of local buckling sites was also studied and was found to enhance the local strain. The theoretical and numerical results obtained in the present study demonstrate the importance of resistive heating in the analysis of SWCNTs and provide an additional insight into the unique mechanics of suspended SWCNTs.

## 1. Introduction

Integration of carbon nanotubes (CNTs), and especially single-wall carbon nanotubes (SWCNTs) into larger scale microelectromechanical (MEMS) silicon structures, is attractive due to the unique physical properties of CNTs. CNT technology appears to be beneficial in applications such as SWCNTs transistor [1], SWCNTs resonators [2], and SWCNTs-based biological, chemical [3], and mechanical sensors [4, 5].

The progress achieved in integrating methods of SWCNTs into silicon structures, including MEMS devices [4–6], set the groundwork for the creation of a new generation of MEMS sensors, which exploit the high sensitivity of SWCNTs along with the robustness and flexibility of the already well established MEMS technology. Several SWCNT-MEMS sensors were reported in the literature. In these device physical stimuli (mechanical, electrical, magnetic, etc.) are applied to the MEMS device. The MEMS structures deform along with the SWCNT that serves as the sensing element. Due to the small dimensions the SWCNTs, even small

deformations of a microstructure may generate a significant strain in an anchored nanotube, which results in a change in their electrical properties [4, 7]. The sensors reported to date demonstrated high sensitivity and can be used as high end pressure sensors [5], displacement sensors [4], mass sensors [8] and strain sensors [9, 10]. Understanding the physics of suspended SWCNTs is, therefore, an important task towards the successful design of SWCNT-based devices.

Numerous studies were devoted to understanding SWCNT mechanics, including extensive experimental, as well as theoretical studies [11–14]. Several studies analyzed the effect of the mechanical deformation on the electrical [4, 15] or optical [16] properties of SWCNTs. A variety of approaches were used in modeling SWCNT mechanics, ranging from atomistic approaches, through mesoscale approaches, up to large scale continuum mechanics (CM) approaches. The most widely used atomistic approaches are molecular dynamics (MD) methods, which provide credible results [17]. However, MD methods are computationally expensive and thus limited to the modeling of very short SWCNTs (i.e., SWCNTs of several nanometers

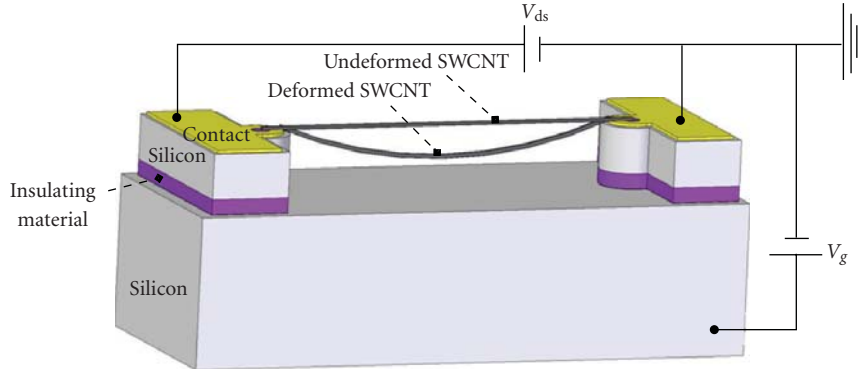


FIGURE 1: Schematics of the device under consideration. A SWCNT is suspended between two silicon anchors and is electrically insulated from the gate electrode.

in length [18]). Mesoscale approaches, such as coarse grained methods or the dissipative particle dynamics [19], enable the modeling of larger scale SWCNTs, but are still computationally expensive. The well established CM methods, on the other hand, are computationally cheaper and are not limited by the dimensions of the SWCNTs [11, 20]. In addition, CM approaches often result in relatively simple and compact models allowing analytical treatment and provides an insight into the behavior of CNTs. Although CM models do not take into account interatomic interactions within CNTs, several comparative studies have shown that CM results are in close agreement with results obtained from MD simulations [18] or experiments [11, 21].

In spite of the vast variety of reported SWCNT modeling approaches, the effect of resistive heating on the mechanical deformation of a suspended SWCNT under electrostatic loading has yet to be analyzed. As we will show below, this effect has substantial influence on the SWCNT mechanics. Due to poor heat transfer mechanisms in suspended SWCNTs, the temperature of SWCNTs can rise by hundreds of degrees even with relatively small electrical currents [22].

In the present study, a large deflection, nonlinear string model was used in order to simulate the behavior of suspended SWCNTs. Contrary to most previously reported studies in which SWCNTs were modeled as a beam, in the current study, SWCNTs were modeled as a string. A string model is justified by the high slenderness of realistic nanotube devices [6, 23, 24]. We begin with considering the nonlinear large deflection equation of equilibrium, followed by discussing the solution to this equation for a specific geometry. The effect of the resistive heating is then analyzed using the string model, followed by nonlinear finite element (FE) simulation to study of the influence of the local buckling sites on the strain arising in the SWCNTs. Finally, discussion and conclusions are presented.

## 2. Formulation

In the present study, the problem of a suspended SWCNT under resistive heating and electrostatic force was analyzed. The configuration of the device is shown schematically in Figure 1. The SWCNT is suspended on a silicon structure.

The undeformed configuration of the SWCNT can be either taut or slacked, as a function of the temperature and the pre-stress, as will be discussed below. Drain-source voltage,  $V_{ds}$ , is applied to the SWCNT and generates the resistive heating. In addition, gate voltage,  $V_g$ , is applied to the SWCNT by a silicon electrode which is electrically insulated from the SWCNT by a dielectric material, such as silicon dioxide or silicon nitride. The electrode is located at a relatively large distance from the SWCNT (several micrometers). The distance between the anchors (attachment points) is  $L_0$ . Such an experimental setup was reported by us in [6, 23, 24].

Two main simplifying assumptions were made while developing the device model. First, we consider a SWCNT of high aspect ratio (long with respect to its cross-section). In this case, the SWCNT under consideration has low bending stiffness, the stiffness resulting from the axial tension of the SWCNT is dominant, and the device can be considered as a string. Second, we assume that the electrostatic force applied to the string is independent of its deflection. Strictly speaking, the electrostatic force applied to the SWCNT depends nonlinearly on the gap between the SWCNT and the electrode [25]. However, since the displacements of the SWCNT (in the order of hundreds of nanometers) are significantly smaller than the initial electrostatic gap (in the order of several micrometers or even tens of micrometers), we assume the electrostatic force to be displacement independent. In addition, since the gate voltage (in the order of tens of Volts) is significantly higher than the drain-source voltage (in the order of tenth of Volts), we consider the actuation voltage  $V$  to be equal to the gate voltage ( $V = V_g$ ) and disregard the voltage difference along the SWCNT. Under these assumptions and taking into account the fact that the electrostatic force is perpendicular to the SWCNT axis, the deformed SWCNT has the form of a circular arc. Therefore, the governing equilibrium equation is

$$N\kappa = q, \quad (1)$$

where  $N$  is the tension force,  $q$  is the electrostatic force per unit length applied to the SWCNT, and  $\kappa$  is the curvature of the deformed SWCNT.

The electrostatic force per unit length,  $q$ , was derived by calculating the derivative of the electrostatic coenergy

$E = -CV^2/2$ , where  $C$  is the capacitance per unit length of the straight tube and  $V$  is the actuation voltage, with respect to the tube deflection. This capacitance was calculated as a capacitance of a wire of a diameter  $d$ , a length  $L_0$  and an electrostatic gap  $h$ , located above an infinite plane [26]. The capacitance  $C$  is given by

$$C = \frac{2\pi\epsilon_0}{\ln\left(L_0^2\left(\sqrt{1+16h^2/L_0^2}-1\right)/2dh\right)}, \quad (2)$$

where  $\epsilon_0$  is the dielectric permittivity of air.

The tension force,  $N$ , includes an initial pretension,  $N_0$ , which is related to the fabrication process, a tension resulting from the elongation (stretch) in the SWCNT during the deformation and a thermal compression force, namely,

$$N = N_0 + EA\epsilon - EA\alpha\Delta T. \quad (3)$$

Here  $E$  and  $A = \pi dt$  are the Young's modulus and the SWCNT cross-section area, respectively (with  $d$  and  $t$  are the diameter and thickness of the SWCNT, resp.),  $\alpha$  is the coefficient of thermal expansion (see [27]) and  $\Delta T$  is the temperature difference with respect to a reference temperature, for example, ambient room temperature. We note that (3), which is the constitutive relation of the tube, incorporates an assumption that the strain within the SWCNT is small, the stress-strain relation is linear, and the nonlinearity is only of a geometric nature. The average strain induced by deformation is defined as follows:

$$\epsilon = \frac{L}{L_0} - 1, \quad (4)$$

where  $L_0$  and  $L$  are the undeformed and the deformed lengths of the tube, respectively. Note that  $L_0$  corresponds to a state when the SWCNT has an initial tension of  $N_0$  rather than being a stress-free SWCNT.

We note that due to the resistive heating, the string expands and the strain decreases below the initial pretension. For temperature differences higher than a certain value,  $\Delta T_{cr} = N_0/\alpha EA$ , the thermal strain and the initial tensile strain eliminate each other. Since the string cannot sustain a compressive force, a deflection (slackness) appears. In this case, the only tension force that governs the behavior of the SWCNT is the stretch (see (3)) due to the transversal electrostatic force. Therefore, we define two regimes of the SWCNT behavior. In the first, also referred to as the prebuckling regime, the temperature is below its critical value  $\Delta T \leq \Delta T_{cr}$ , the SWCNT has initial length of  $L_0$ , and the constitutive relation and strain are governed by (3) and (4), respectively. In the second regime, also referred to as the postbuckling regime the axial tension is due to stretch, namely, the constitutive relation is

$$N = EA\epsilon. \quad (5)$$

Contrary to the prebuckling regime, where a temperature increase results in a decrease in the axial force, under the postbuckling regime, an increase in the temperature results in elongation of the SWCNT and a larger slackness.

We emphasize that for temperature differences lower than  $\Delta T_{cr}$  (prebuckling regime) and in the absence of a transverse loading, the string is initially straight and the undeformed length  $L_0$  is used in the calculation of the strain, in accordance with (4). However, for temperature differences higher than  $\Delta T_{cr}$  (postbuckling regime), the SWCNT has an initial deflection (slackness). In this case, the strain is calculated in accordance with the expression

$$\epsilon = \frac{L}{L_T} - 1. \quad (6)$$

Here,  $L_T$  is the SWCNT length for zero force and it is calculated as follows:

$$L_T = L_0[1 + \alpha(\Delta T - \Delta T_{cr})]. \quad (7)$$

In this work the strain in the prebuckling regime is calculated using (4) while in the postbuckling regime it was calculated using (6). Note that the strain is commonly calculated with respect to the stress-free reference length. However, since in experimental characterization of such systems the measured electrical resistance is related to elongation, we calculate the strain with respect to the length corresponding to zero force.

The geometrical relation between the undeformed ( $L_0$ ), the deformed ( $L$ ) lengths of the stretched SWCNT and the curvature ( $\kappa$ ), for both aforementioned regimes, is expressed as follows:

$$L_0 = \frac{2}{\kappa} \sin\left(\frac{L\kappa}{2}\right). \quad (8)$$

Substituting the expression for the tension  $N$  (the constitutive relation of (3) for prebuckling regime and (5) for the postbuckling regime) with strain (given by (4) for prebuckling regime and (6) for postbuckling regime) into the equilibrium (1) results in the following equilibrium equation for the case of prebuckling:

$$\left(N_0 + EA\left(\frac{L}{L_0} - 1\right) - EA\alpha\Delta T\right)\kappa = q, \quad (9)$$

whereas in the case of postbuckling, the equilibrium equation is

$$EA\left(\frac{L}{L_T} - 1\right)\kappa = q. \quad (10)$$

By expressing the term for the deformed length  $L$  from (9) and (10) and substituting them into (8), we obtain the nonlinear algebraic equations relating the curvature of the string to the applied electrostatic force. Under prebuckling regime, the equation has the form of

$$L_0 = \frac{2}{\kappa} \sin\left(\frac{L_0\kappa}{2EA}\left(\frac{q}{\kappa} - N_0\right) + \frac{L_0\kappa}{2}(1 + \alpha\Delta T)\right), \quad (11)$$

whereas under postbuckling regime the following equation is obtained

$$L_0 = \frac{2}{\kappa} \sin\left(\frac{L_T\kappa}{2}\left(\frac{q}{\kappa EA} + 1\right)\right). \quad (12)$$

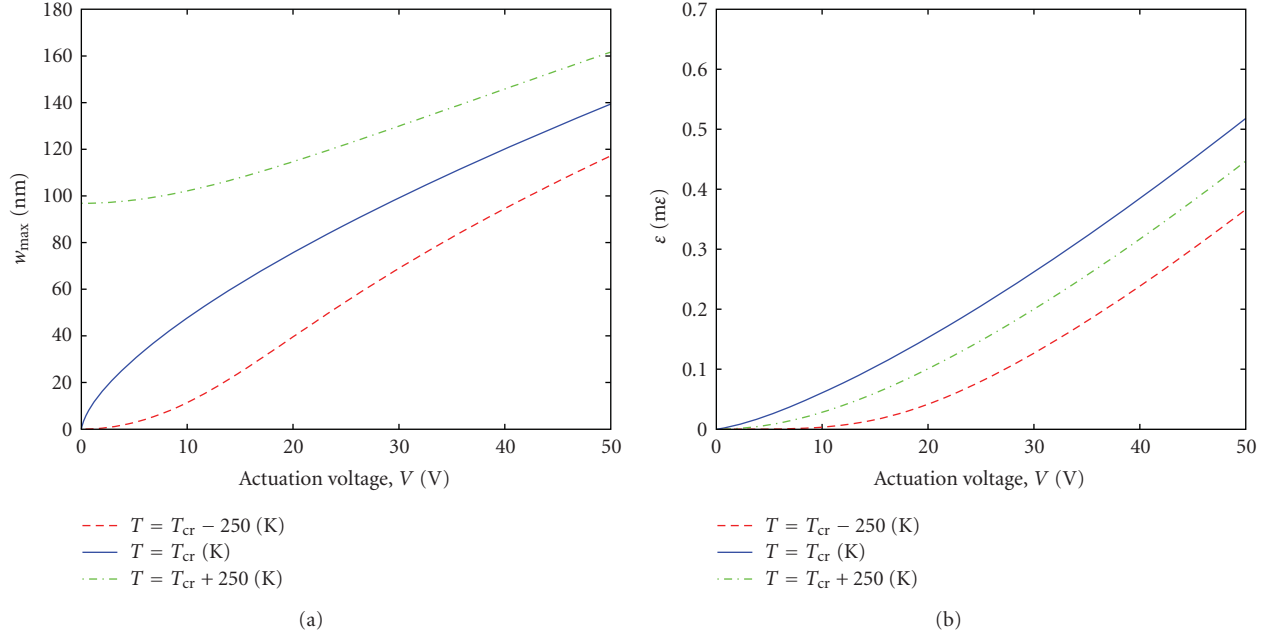


FIGURE 2: Forced response for a SWCNT with parameters listed in Tables 1 and 2 at different temperatures. (a) Maximum displacement. (b) Average axial strain.

TABLE 1: SWCNT geometrical parameters used in the calculations.

Parameter	Value
Initial (unbuckled) length	10 $\mu\text{m}$
Thickness	0.34 nm
Diameter	4 nm
Electrostatic gap	10 $\mu\text{m}$

TABLE 2: Material properties used in the calculations.

Parameter	Value
SWCNT Young's modulus, $E$	1 TPa
SWCNT initial tension, $N_0$ (see [23])	1 nN
Dielectric permittivity of the air, $\varepsilon_0$	$8.854 \cdot 10^{-12}$ F/m
Thermal expansion coefficient, $\alpha$ (see [27])	$1 \cdot 10^{-6}$ K $^{-1}$

We note that the above mentioned model is nonlinear. This model takes into account large SWCNTs deflections, as well as a tension force,  $N$ , which depends on the SWCNT deflection. In general, the electrostatic load is also not linear. For simplicity, in the present study, it is considered to be deflection independent. We emphasize that several studies reported experiments which agree with the assumption presented above [6, 23, 24].

### 3. Model Results

Equation (11) (for the case of  $\Delta T \leq \Delta T_{cr}$ ) or (12) (for the case of  $\Delta T > \Delta T_{cr}$ ) is solved in terms of the curvature  $\kappa$  using the Newton-Raphson-based solver incorporated into the MATLAB package. The geometrical dimensions as well

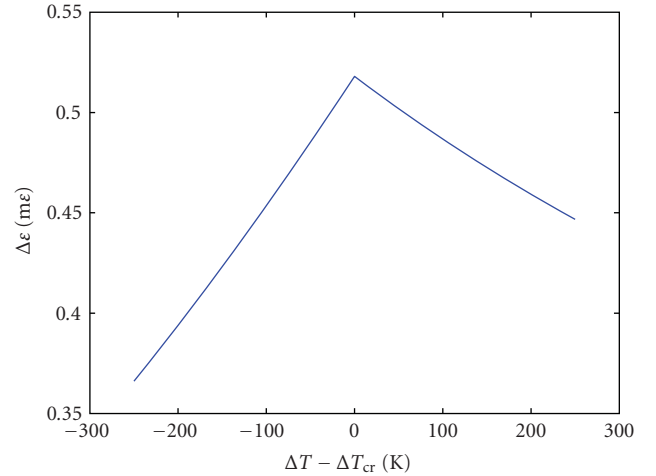


FIGURE 3: Average axial strain versus temperature with respect to the temperature difference  $\Delta T - \Delta T_{cr}$  for a SWCNT with parameters listed in Tables 1 and 2. Constant actuation voltage of 50 V was applied to the SWCNT. Note that for negative  $\Delta T - \Delta T_{cr}$  the strain was calculated using (4) while for positive  $\Delta T - \Delta T_{cr}$  the strain was calculated using (6).

as the material constants used in the calculations are listed in Tables 1 and 2, respectively. After the deformed lengths were calculated using (8), deflections were calculated using geometrical relations and the average strain was calculated over the whole length of the SWCNT using (4) and (6).

The influence of the temperature on the SWCNT behavior was analyzed in Figures 2 and in 3. As mentioned, at the critical temperature,  $\Delta T = \Delta T_{cr}$ , and at temperatures lower than the critical value,  $\Delta T < \Delta T_{cr}$  (prebuckling

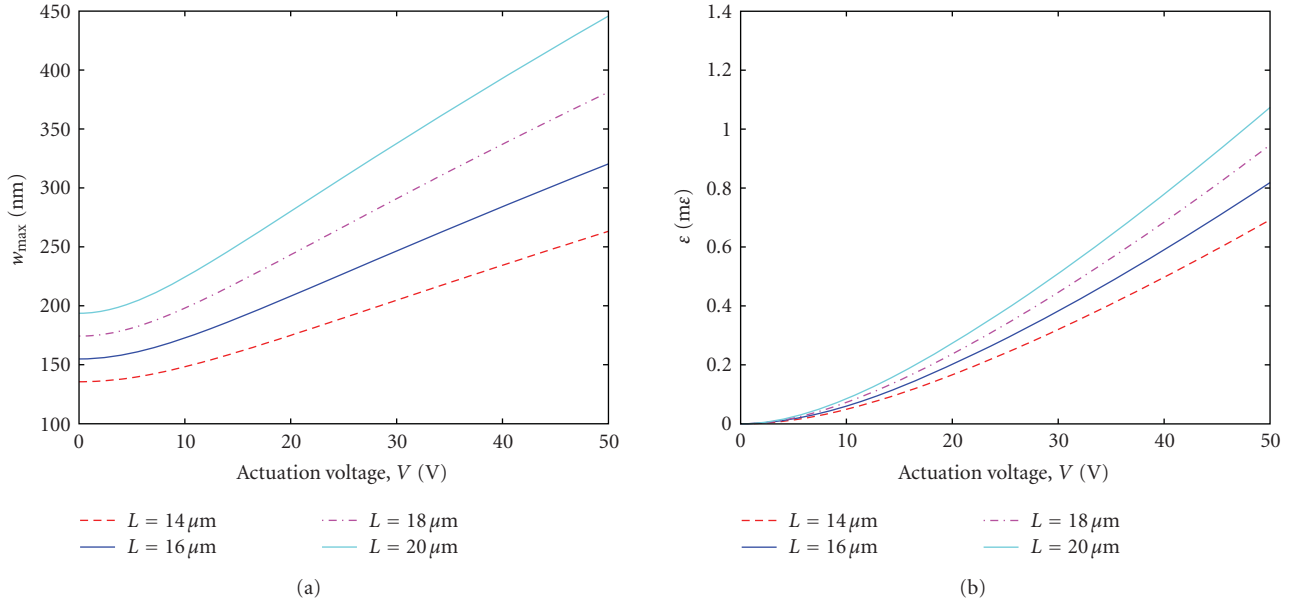


FIGURE 4: Forced response for SWCNT with parameters listed in Tables 1 and 2,  $\Delta T_K = \Delta T_{cr} + 250$  [K] and different lengths. (a) Maximum displacement. (b) Average axial strain.

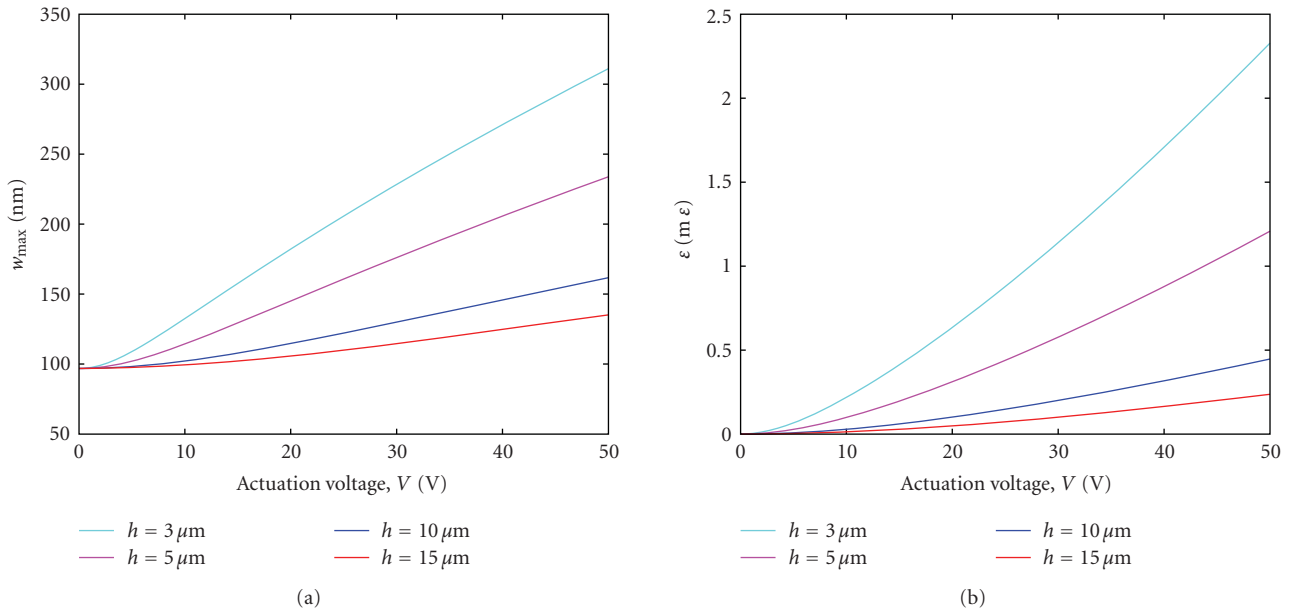


FIGURE 5: Forced response for SWCNT with parameters listed in Tables 1 and 2,  $\Delta T_K = \Delta T_{cr} + 250$  [K] and different electrostatic gaps. (a) Maximum displacement. (b) Average axial strain.

regime), the initial displacement of the SWCNT is zero. However, for temperatures higher than the critical temperature (postbuckling regime), a thermal buckling appears and the SWCNT has an initial nonzero displacement corresponding to infinitesimally small external load, Figure 2(a). Note that the maximum displacement (the displacements corresponding to the midpoint of the SWCNT) is in the order of hundreds of nanometers.

Figure 3 represents the strain of the SWCNT under a constant actuation voltage of 50 V. It can be noticed

that in the pre-buckled regime, the strain increases with temperature, namely, the temperature has a softening effect on the SWCNT. This can be explained by the fact that the compressive component of the axial force increases with the temperature, so that high temperatures are associated with SWCNT of lower tension. However, when thermal buckling takes place, an opposite trend of stiffening of the SWCNT was noticed. In this case, the SWCNT has initial slackness which results in higher stiffness since the axial force, which is horizontal before buckling takes place, has a component



FIGURE 6: An illustrative image of a SWCNT buckling site.

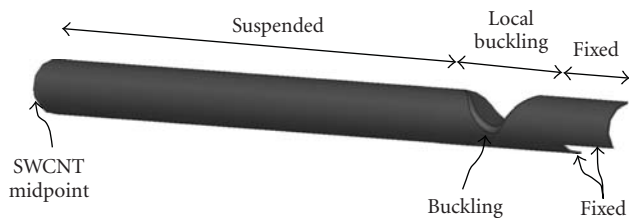


FIGURE 7: Schematic view of the FE model after the creation of the local buckling site. The three region of the SWCNT (fixed, hinge, and suspended areas) are shown.

in the lateral direction. As the slackness increases, this lateral component increases as well due to the larger slope of the SWCNT.

Next, the behavior of SWCNTs with different lengths and electrostatic gaps is shown in Figures 4 and 5, respectively, for  $\Delta T = \Delta T_{cr} + 250[K]$ . Note that due to the geometric nonlinearity, the dependence between the force and the maximum deflection is nonlinear. We emphasize that the strains plotted in Figures 2(b), 4(b), and 5(b) can be as high as several millistrains. Such a significant strain was reported to have substantial effect on SWCNT electrical behavior [5, 7, 9, 18].

#### 4. Influence of the Loading on Local Buckling Sites

The results shown in Section 3 demonstrate that resistive heating can cause the deflections to be in the order of hundreds of nanometers. The influence of such significant deflections was analyzed in this section. Here, we analyze how this thermal heating, and resulting large deflections, influence local buckling sites previously reported in suspended SWCNTs [28]. These buckling sites, shown schematically in Figure 6, may result either from intentional SWCNT loading or unintentional bending during the fabrication process. Buckling in the fabrication process originates mainly due to strong van der Waals forces, which are dominant surface forces in nanoscale structures (see [13, 17, 28] for more information regarding surface forces and buckling in SWCNTs).

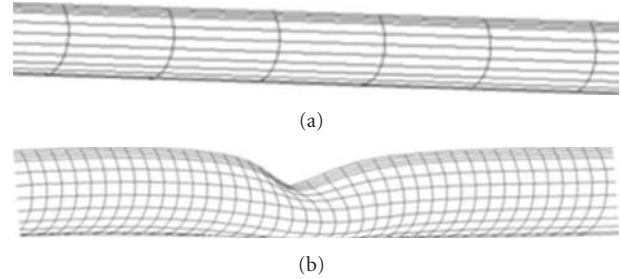


FIGURE 8: Finite element model built in ADINA software. (a) Site with no buckling. (b) Local buckling site.

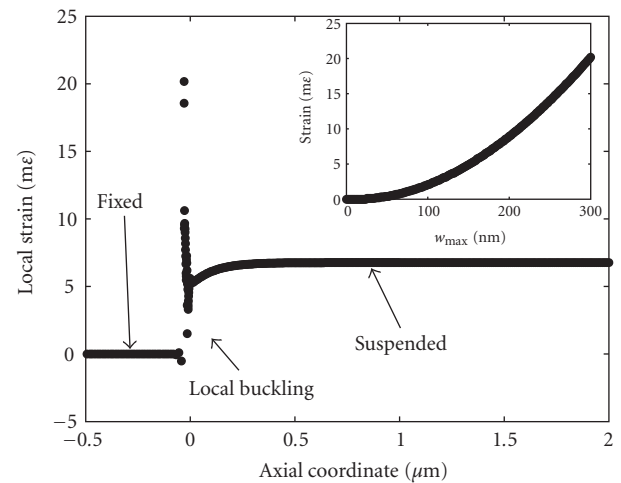


FIGURE 9: Strain versus the axial coordinate obtained from FE simulation for maximum SWCNT displacement of 300 nm. Three regions are defined. The region where the SWCNT is fixed, the region which surrounds the buckling site, and the region where the SWCNT is suspended. Inset: local strain versus the maximum SWCNT displacement for the node of maximum strain.

To understand the effect of these buckling sites on SWCNT mechanics, an FE model was built in ADINA software. The SWCNT was meshed with large displacement shell elements. The symmetries of the problem were exploited to build compact model. Due to the transverse and longitudinal symmetries, only a quarter of a SWCNT was taken into the FE model. In addition, the boundary conditions include a  $0.5\mu\text{m}$  long segment which is anchored (fixed) at its bottom. The other end, which represents the midpoint of the SWCNT, was free to deflect but was enforced to have a zero angle. A schematic description of the FE model is shown in Figure 7.

Initially, a SWCNT without buckling sites was built (Figure 8(a)). The simulation had two parts. In the first part, a displacement was enforced and remained constant in the area of the buckling site in order to create a structure similar to buckling sites observed in SWCNTs (Figure 8(b)). Next, displacements were applied to the midpoint of the SWCNT and were gradually increased until displacements of hundreds of nanometers were achieved. Strain presented in Figure 9 was calculated with respect to the state of

zero displacement applied to the midpoint of the SWCNT, namely, with respect to the initial strain of the second part of the simulation.

The results of the FE simulation are shown in Figure 9. Three main regions are clearly identified. The first is the region that represents the strain in part of the SWCNT which is fixed (marked as “fixed” in Figures 7 and in 9), the second region is the part that surrounds the local buckling site (marked as “local buckling” in Figures 7 and in 9), and the last part is the suspended part of the SWCNT (marked as “suspended” in Figures 7 and in 9). We emphasize that the region that surrounds the local buckling site underwent a significant strain in the order of several tens of milli-strain. The relation between the local strain and the maximum SWCNT displacement is shown in the inset of Figure 9 for the node that demonstrated the maximum strain. Therefore, one can conclude that the local buckling sites can have an enhancing effect on strain generated in SWCNTs.

## 5. Conclusions

The mechanical behavior of SWCNT under resistive heating and electrostatic loading was analyzed. A SWCNT was modeled as a string, and a large displacement, nonlinear model was developed. The governing equations were solved, and model results show that with sufficient large resistive heating, SWCNT can buckle and thus may demonstrate significantly different mechanical behavior. The effect of the geometrical parameters (length and electrostatic gap) on the SWCNT behavior were also analyzed. Finally, the influence of local buckling sites was analyzed and was found to have an enhancing effect on the SWCNTs local strain. Therefore, the presented results provide an important insight into the unique mechanics of suspended SWCNTs.

## Acknowledgments

The authors thank Eran Bahana for his help in schematics and Dr. Lior Kogut for helpful discussion.

## References

- [1] Y. A. Tarakanov and J. M. Kinaret, “A carbon nanotube field effect transistor with a suspended nanotube gate,” *Nano Letters*, vol. 7, no. 8, pp. 2291–2294, 2007.
- [2] A. K. Hüttel, G. A. Steele, B. Witkamp, M. Poot, L. P. Kouwenhoven, and H. S. J. Van Der Zant, “Carbon nanotubes as ultrahigh quality factor mechanical resonators,” *Nano Letters*, vol. 9, no. 7, pp. 2547–2552, 2009.
- [3] P. Hu, J. Zhang, L. E. Li, Z. Wang, W. O’Neill, and P. Estrela, “Carbon nanostructure-based field-effect transistors for label-free chemical/biological sensors,” *Sensors*, vol. 10, no. 5, pp. 5133–5159, 2010.
- [4] C. Stampfer, A. Jungen, R. Linderman, D. Oberfell, S. Roth, and C. Hierold, “Nano-electromechanical displacement sensing based on single-walled carbon nanotubes,” *Nano Letters*, vol. 6, no. 7, pp. 1449–1453, 2006.
- [5] R. C. Stampfer, T. Helbling, D. Oberfell et al., “Fabrication of single-walled carbon-nanotube-based pressure sensors,” *Nano Letters*, vol. 6, no. 2, pp. 233–237, 2006.
- [6] G. A. Karp, A. Ya’Akobovitz, M. David-Pur et al., “Integration of suspended carbon nanotubes into micro-fabricated devices,” *Journal of Micromechanics and Microengineering*, vol. 19, no. 8, Article ID 085021, 2009.
- [7] E. D. Minot, Y. Yaish, V. Sazonova, JI. Y. Park, M. Brink, and P. L. McEuen, “Tuning carbon nanotube band gaps with strain,” *Physical Review Letters*, vol. 90, no. 15, pp. 1–4, 2003.
- [8] H. Y. Chiu, P. Hung, H. W. C. Postma, and M. Bockrath, “Atomic-scale mass sensing using carbon nanotube resonators,” *Nano Letters*, vol. 8, no. 12, pp. 4342–4346, 2008.
- [9] N. K. Chang, C. C. Su, and S. H. Chang, “Fabrication of single-walled carbon nanotube flexible strain sensors with high sensitivity,” *Applied Physics Letters*, vol. 92, no. 6, Article ID 063501, 2008.
- [10] H. Maune and M. Bockrath, “Elastomeric carbon nanotube circuits for local strain sensing,” *Applied Physics Letters*, vol. 89, no. 17, Article ID 173131, 2006.
- [11] K. I. Tserpes and P. Papanikos, “Finite element modeling of single-walled carbon nanotubes,” *Composites Part B: Engineering*, vol. 36, no. 5, pp. 468–477, 2005.
- [12] D. A. Walters, L. M. Ericson, M. J. Casavant et al., “Elastic strain of freely suspended single-wall carbon nanotube ropes,” *Applied Physics Letters*, vol. 74, no. 25, pp. 3803–3805, 1999.
- [13] Q. Wang, K. M. Liew, X. Q. He, and Y. Xiang, “Local buckling of carbon nanotubes under bending,” *Applied Physics Letters*, vol. 91, no. 9, Article ID 093128, 2007.
- [14] J. P. Salvetat, G. A. D. Briggs, J. M. Bonard et al., “Elastic and shear moduli of single-walled carbon nanotube ropes,” *Physical Review Letters*, vol. 82, no. 5, pp. 944–947, 1999.
- [15] J. Cao, Q. Wang, and H. Dai, “Electromechanical properties of metallic, quasimetallic, and semiconducting carbon nanotubes under stretching,” *Physical Review Letters*, vol. 90, no. 15, pp. 1–4, 2003.
- [16] S. W. Lee, G. H. Jeong, and E. E. B. Campbell, “In situ raman measurements of suspended individual single-walled carbon nanotubes under strain,” *Nano Letters*, vol. 7, no. 9, pp. 2590–2595, 2007.
- [17] T. Hertel, R. E. Walkup, and P. Avouris, “Deformation of carbon nanotubes by surface van der Waals forces,” *Physical Review B*, vol. 58, no. 20, pp. 13870–13873, 1998.
- [18] G. Cao and X. I. Chen, “Buckling of single-walled carbon nanotubes upon bending: molecular dynamics simulations and finite element method,” *Physical Review B*, vol. 73, no. 15, Article ID 155435, 2006.
- [19] O. Liba, Y. Hanein, D. Kauzlaric, A. Greiner, and J. G. Korvink, “Investigation of the dynamic behavior of bridged nanotube resonators by dissipative particle dynamics simulation,” *International Journal for Multiscale Computational Engineering*, vol. 6, no. 6, pp. 549–562, 2008.
- [20] L. Y. Chan and B. Andrawes, “Finite element analysis of carbon nanotube/cement composite with degraded bond strength,” *Computational Materials Science*, vol. 47, no. 4, pp. 994–1004, 2010.
- [21] Y. Kuronuma, Y. Shindo, T. Takeda, and F. Narita, “Fracture behaviour of cracked carbon nanotube-based polymer composites: experiments and finite element simulations,” *Fatigue and Fracture of Engineering Materials and Structures*, vol. 33, no. 2, pp. 87–93, 2010.
- [22] V. V. Deshpande, S. Hsieh, A. W. Bushmaker, M. Bockrath, and S. B. Cronin, “Spatially resolved temperature measurements of electrically heated carbon nanotubes,” *Physical Review Letters*, vol. 102, no. 10, Article ID 105501, 2009.

- [23] A. Ya'akovovitz, G. Karp, M. David-Pur, S. Krylov, and Y. Hanein, "Carbon nanotube self-assembled high frequency resonator," in *Proceedings of the IEEE 23rd International Conference on Micro Electro Mechanical Systems (MEMS '10)*, Hong-Kong, China, 2010.
- [24] A. Ya'akovovitz, G. Karp, Y. Hanein, and S. Krylov, "Electromechanical behavior of suspended taut single-walled carbon nanotubes," in *Proceedings of the International IEEE Conference on Microwaves, Communications, Antennas and Electronic Systems (COMCAS '09)*, Tel-Aviv, Israel, 2009.
- [25] S. Senturia, *Microsystem Design*, Kluwer Academic, Boston, Mass, USA, 2001.
- [26] E. Weber, *Electromagnetic Theory : Static Fields and Their Mapping*, Dover, New York, NY, USA, 1965.
- [27] H. Jiang, B. Liu, Y. Huang, and K. C. Hwang, "Thermal expansion of single wall carbon nanotubes," *Journal of Engineering Materials and Technology, Transactions of the ASME*, vol. 126, no. 3, pp. 265–270, 2004.
- [28] Z. R. Abrams, Y. Lereah, and Y. Hanein, "Transmission electron microscope imaging of single-walled carbon nanotube interactions and mechanics on nitride grids," *Nanotechnology*, vol. 17, no. 18, pp. 4706–4712, 2006.

## Research Article

# Ferromagnetic Property and Synthesis of Onion-Like Fullerenes by Chemical Vapor Deposition Using Fe and Co Catalysts Supported on NaCl

Yongzhen Yang,<sup>1,2</sup> Xuguang Liu,<sup>1,3</sup> Yanxing Han,<sup>1,3</sup> Wenfang Ren,<sup>1,3</sup> and Bingshe Xu<sup>1,2</sup>

<sup>1</sup> Key Laboratory of Interface Science and Engineering in Advanced Materials, Taiyuan University of Technology, Ministry of Education, Taiyuan 030024, China

<sup>2</sup> College of Materials Science and Engineering, Taiyuan University of Technology, Taiyuan 030024, China

<sup>3</sup> College of Chemistry and Chemical Engineering, Taiyuan University of Technology, Taiyuan 030024, China

Correspondence should be addressed to Xuguang Liu, liuxuguang@tyut.edu.cn

Received 31 May 2010; Accepted 23 July 2010

Academic Editor: Jianyu Huang

Copyright © 2011 Yongzhen Yang et al. This is an open access article distributed under the Creative Commons Attribution License, which permits unrestricted use, distribution, and reproduction in any medium, provided the original work is properly cited.

Metal-encapsulating onion-like fullerenes (M@OLFs) were synthesized by CVD at relatively low temperature (420°C) using Fe and Co nanoparticles impregnated into NaCl as catalyst. The morphology and structure of the products were characterized by field emission scanning electron microscopy, high-resolution transmission electron microscopy, X-ray diffraction, and Raman spectroscopy. The results show that Fe@OLFs and Co@OLFs with stacked graphitic fragments were prepared using Fe/NaCl or Co/NaCl as catalysts; after Co@OLFs were immersed in concentrated HCl for 48 hours, Co nanoparticles encapsulated by carbon shells were not removed, meaning that carbon shells can protect the encapsulated Co cores against environmental degradation. The coercivity value (750.23 Oe) of Co@OLFs showed an obvious magnetic property.

## 1. Introduction

Since the report by Ugarte in 1992 [1], onion-like fullerenes (OLFs) have been expected to have good prospects in some aspects of energy materials, high-performance/high temperature wear-resistance materials, superconductive materials, and biomaterials [2]. Metal-encapsulating OLFs (M@OLFs) have potential application in many fields such as magnetic data storage, xerography, and magnetic resonance imaging [3]. At present, M@OLFs have been prepared by various techniques, such as electron irradiation [4], arc discharge [5], plasma [6], explosive decomposition of organometal [7], and chemical vapor deposition (CVD) [8, 9]. Among these methods, CVD appears promising because of its relatively low cost and potentially high yield. The catalyst, which can be categorized into floating catalyst and supported catalyst, plays essential role in CVD. Compared with the floating precursors, the supported catalyst plays the role of dispersing active components and adjusting catalyst properties via the chemical or physical interaction of support with metal

nanoparticles. Various kinds of catalyst supports such as Al<sub>2</sub>O<sub>3</sub>, MgO, CaCO<sub>3</sub>, and zeolite were used to synthesize nanocarbon materials [10–13]. However, it is difficult to separate these supports from the final products. On the other hand, water-soluble materials as catalyst supports can be easily separated from the product. Soluble silicate, carbonate, and chloride were employed as catalyst supports to synthesize carbon nanofibers or carbon nanotubes (CNTs) [14–16]. However, little attention was paid to the synthesis of M@OLFs using water-soluble materials as catalyst supports. Liu et al. [17] employed cobalt supported on NaCl prepared by mechanical milling as catalyst to synthesize carbon-encapsulated cobalt nanoparticles, but the method to fabricate catalyst was somewhat complicated.

In the present study, M@OLFs were synthesized by CVD at relatively low temperature (420°C) using Fe and Co nanoparticles impregnated into NaCl support as catalysts, and the magnetic property of Co@OLFs was also studied. This work is of interest for the low cost production of OLFs.

## 2. Experimental

**2.1. Synthesis of Fe/NaCl and Co/NaCl Catalysts.** Fe/NaCl and Co/NaCl with about 2 wt% Fe or Co were prepared by means of impregnation. First, 1.76 g of  $\text{Fe}(\text{NO}_3)_3 \cdot 9\text{H}_2\text{O}$  or 1.49 g of  $\text{Co}(\text{NO}_3)_2 \cdot 6\text{H}_2\text{O}$  was dissolved in an appropriate amount of distilled water. Then 14.85 g of NaCl was added into  $\text{Fe}(\text{NO}_3)_3$  or  $\text{Co}(\text{NO}_3)_2$  solution. To get homogeneous mixture, the mixture was stirred for 1 h and then dried at  $120^\circ\text{C}$ . The obtained catalysts were ground into fine particles.

**2.2. Synthesis of  $M@$ OLFs.** The catalytic decomposition of  $\text{C}_2\text{H}_2$  was carried out at  $420^\circ\text{C}$  in a horizontal furnace, using Fe/NaCl and Co/NaCl as catalysts separately. An 18 mm-long quartz boat with about 2.50 g of catalyst was placed at the isothermal zone in a horizontal quartz tube reactor. Initially, the tube was heated up to  $420^\circ\text{C}$  in  $100 \text{ ml} \cdot \text{min}^{-1}$  of steady Ar flow. The catalysts were reduced at  $420^\circ\text{C}$  in a hydrogen atmosphere for 1 h. Then synthesis reactions were carried out at  $420^\circ\text{C}$  by introducing a mixture of  $\text{C}_2\text{H}_2$ -Ar ( $\text{C}_2\text{H}_2$ :  $30 \text{ ml} \cdot \text{min}^{-1}$ , Ar:  $300 \text{ ml} \cdot \text{min}^{-1}$ ) into the reactor. After 1 h, the reactor was cooled to room temperature in Ar atmosphere ( $80 \text{ ml} \cdot \text{min}^{-1}$ ) and the black powders were collected.

**2.3. Purification of  $M@$ OLFs.** To separate NaCl, the products were dissolved in an appropriate amount of distilled water and filtered, which are denoted as  $\text{H}_2\text{O}$ -washed samples. In addition, to remove the residual metal catalyst, the as-synthesized samples were immersed in concentrated HCl solution at room temperature for 48 h, and then washed and filtrated with distilled water, which are denoted as HCl-washed OLFs.

**2.4. Characterization of  $M@$ OLFs.** The morphology and structure of the samples were characterized using field emission scanning electron microscope (FESEM, JSM-6700F, operated at 10 kV), high resolution transmission electron microscope (HRTEM, JEM-2010, working at an accelerating voltage of 200 kV), X-ray powder diffractometer (XRD, D/Max-3C, Cu- $K\alpha$  radiation,  $\lambda = 1.54018 \text{ \AA}$ ), and thermogravimetric analyzer (TGA, Netzsch TG 209 F3, between room temperature and  $900^\circ\text{C}$  in air atmosphere at heating rate of  $10^\circ\text{C}/\text{min}$ ). The magnetic property measurement was conducted with a vibrating sample magnetometer (VSM, Lake Shore 7307).

## 3. Results and Discussion

FESEM was used to investigate the morphologies of the products (Figure 1). It can be obviously observed that there were large quantities of nanoparticles in the products without accompanying CNTs or nanofibers (Figure 1(a)). To analyze the elemental composition for the products, the EDS spectra were shown in the insert. From the insert in Figure 1(a), C, Fe, and O signals were observed. And from the insert in Figure 1(b), C, Co, and O signals were clearly

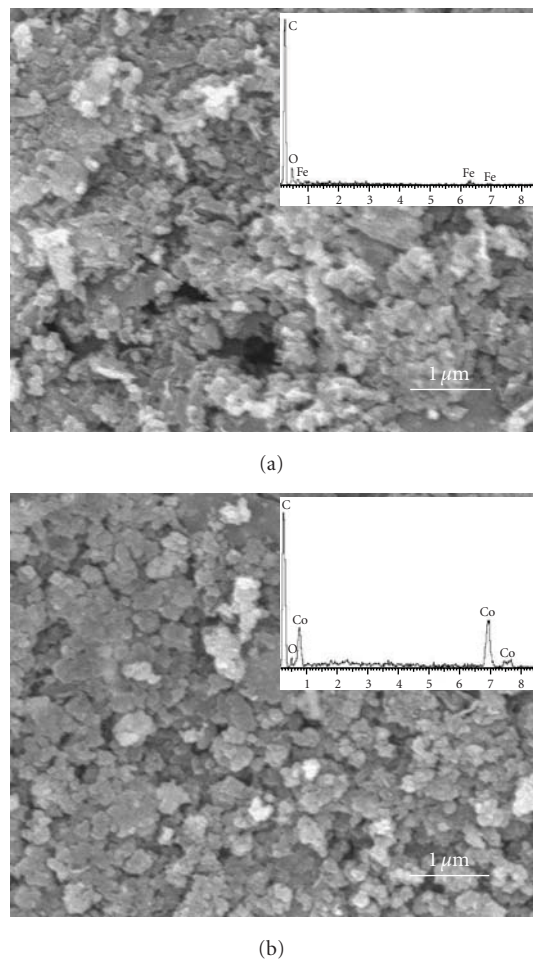


FIGURE 1: FESEM images of  $\text{H}_2\text{O}$ -washed products prepared on different catalysts. (a) Fe/NaCl, (b) Co/NaCl.

observed. No Na and Cl signals were exhibited, indicating the complete removal of NaCl.

The products were further characterized by HRTEM to study the particle size and structure. Figure 2(a) shows the TEM image of  $\text{H}_2\text{O}$ -washed OLFs synthesized using Fe/NaCl as catalyst. Most metal nanoparticles were wrapped by carbon layers, and the sizes were in the range of 10–50 nm. The diversity in the shapes of the carbon nanocages encapsulating metallic particle reflects the shapes of the encapsulated metallic particles. Figure 2(b) shows the TEM image of  $\text{H}_2\text{O}$ -washed OLFs synthesized using Co/NaCl as catalyst. A mass of metal-encapsulating carbon nanoparticles can be seen ranging in diameter from 10 to 60 nm besides little hollow carbon indicated by an arrow. Figures 2(c) and 2(d) show the TEM images of HCl-washed OLFs synthesized using Fe/NaCl and Co/NaCl as catalysts, respectively. The metal nanoparticles encapsulated by carbon shells were not removed after immersing in concentrated HCl for 48 h. It means that carbon shells can protect the encapsulated metal cores against environmental degradation. The HRTEM images of HCl-washed OLFs synthesized using Fe/NaCl and Co/NaCl as catalysts (Figures 2(e) and 2(f)) indicate that the

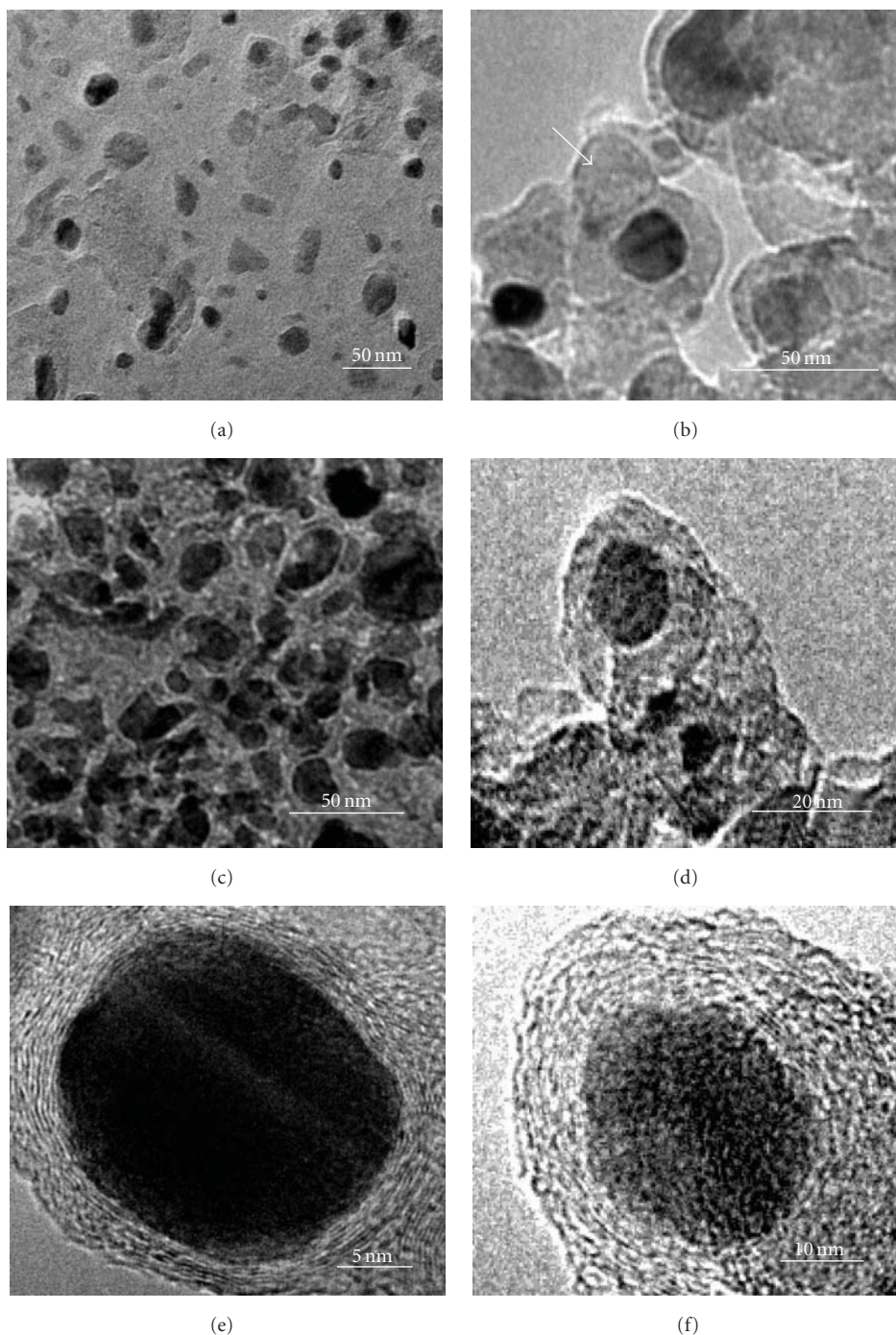


FIGURE 2: TEM images of  $\text{H}_2\text{O}$ -washed OLFs synthesized using Fe/NaCl (a) and Co/NaCl (b) as catalysts, hollow OLF as indicated by an arrow; TEM images of HCl-washed OLFs synthesized using Fe/NaCl (c) and Co/NaCl (d) as catalysts; HRTEM images of HCl-washed OLFs synthesized using Fe/NaCl (e) and Co/NaCl (f) as catalysts.

metallic cores were encapsulated by graphitic sheets. This implied that both Fe/NaCl and Co/NaCl can be used as catalysts to synthesize M@OLFs by CVD using acetylene as carbon resource at  $420^\circ\text{C}$ , and carbon shells can protect the encapsulated metallic cores.

Based on our experimental results and previous investigations, a vapor solid (VS) growth model of M@OLFs

at low temperature was suggested [18]. Firstly,  $\text{C}_2\text{H}_2$  was absorbed onto metal nanoparticle surface and decomposed into carbon atoms; secondly, assembled carbon atom clusters began to diffuse in the crystal lattice of metal particles until carbon species got supersaturated; thirdly, carbon species precipitated and nucleated on catalyst nanoparticle surface, resulting in the formation of small graphitic fragments with

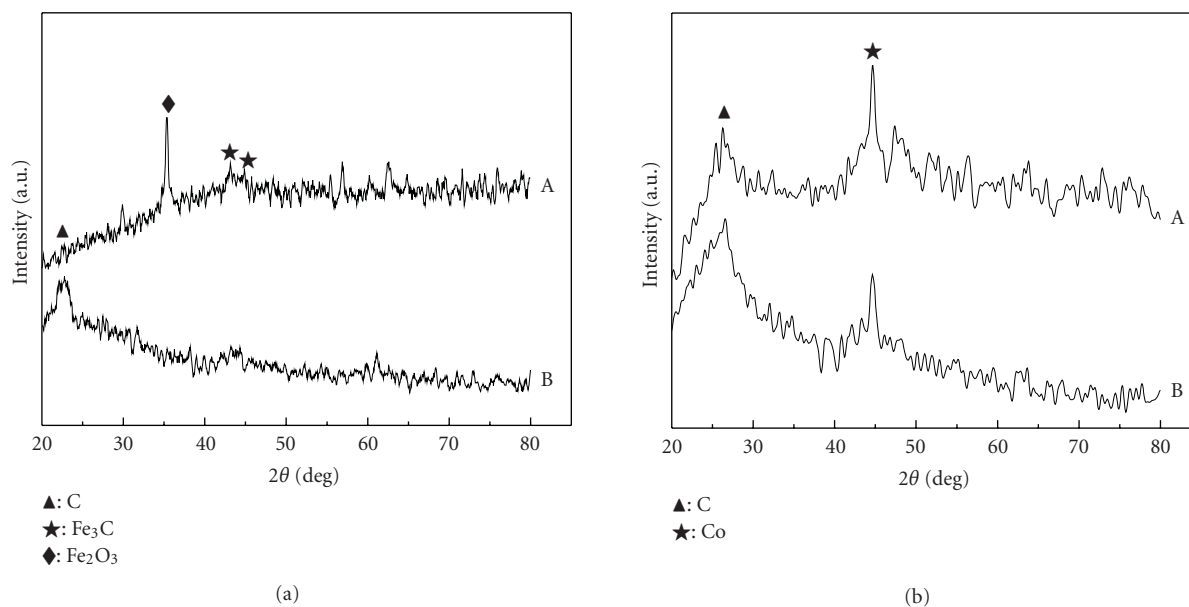


FIGURE 3: (a) XRD patterns of H<sub>2</sub>O-washed OLFs (A) and HCl-washed OLFs (B) synthesized using Fe/NaCl as catalyst; (b) XRD patterns of H<sub>2</sub>O-washed OLFs (A) and HCl-washed OLFs (B) synthesized using Co/NaCl as catalyst.

a lot of defects. The small graphitic fragments combined with each other by their dangling bonds in order to reach a more stable state, and at the same time, the defects on the surface of the graphitic fragments might act as nucleation sites for the deposition of decomposed carbon species followed by the nucleation of pentagonal or hexagonal rings. Thus OLFs grew in isotropic way continuously until no carbon source was supplied. Because the reaction temperature was too low to supply enough energy to induce the rearrangement of carbon atoms in the graphitic fragments, the formed OLFs had a structure of stacked graphitic fragments.

The products were further characterized by XRD (Figure 3). Figure 3(a) shows the XRD patterns of Fe@OLFs synthesized using Fe/NaCl. The peak attributed to the diffraction of carbon at  $2\theta = 22.6^\circ$  indicates that OLFs had a structure of stacked graphitic fragments, which was between amorphous carbon and concentric graphitic layers. The peaks at  $2\theta = 43.75^\circ$  and  $44.95^\circ$  can be ascribed to the diffraction of Fe<sub>3</sub>C, indicating that the metallic cores inside the OLFs were Fe<sub>3</sub>C. And the peak attributed to the diffraction of Fe<sub>2</sub>O<sub>3</sub> at  $2\theta = 35.4^\circ$  was also observed. After immersing the products in concentrated HCl for 48 h, the peak attributed to the diffraction of Fe<sub>2</sub>O<sub>3</sub> disappeared. It means that some catalyst nanoparticles were not encapsulated completely and converted to Fe<sub>2</sub>O<sub>3</sub> when exposed to air. Figure 3(b) shows the XRD patterns of H<sub>2</sub>O-washed OLFs (A) and HCl-washed OLFs (B) synthesized using Co/NaCl as catalyst. A broad diffraction peak at about  $26.3^\circ$  was assigned to the (002) planes of hexagonal graphite structure. The peak at  $2\theta = 44.9^\circ$  was identified to the (111) planes of Co with a face-centered cubic (fcc) structure, indicating that the metallic cores inside the OLFs were Co. After immersing the products in concentrated HCl for 48 h, the

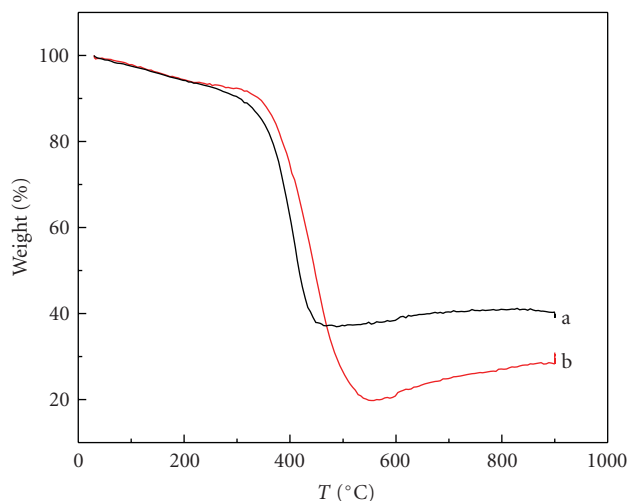


FIGURE 4: TG curves of H<sub>2</sub>O-washed Co@OLFs (a) and HCl-washed Co@OLFs (b).

peaks attributed to the diffraction of Co became weaker, indicating the removal of bare Co nanoparticles.

Co@OLFs synthesized using Co/NaCl as catalysts were further investigated by TG. The content of Co in H<sub>2</sub>O-washed and HCl-washed OLFs was calculated as 25.6 wt% and 14.2 wt%, respectively, in accordance with the XRD measurement.

The magnetic property of the HCl-washed Co@OLFs at room temperature is shown by the magnetization hysteresis loop (Figure 5). For magnetic nanoparticles, the magnetic properties, especially the saturation magnetization  $M_s$  and

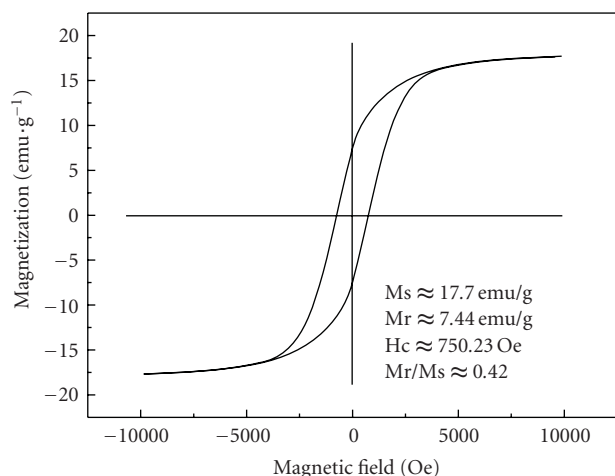


FIGURE 5: Hysteresis loops of HCl-washed Co@OLFs.

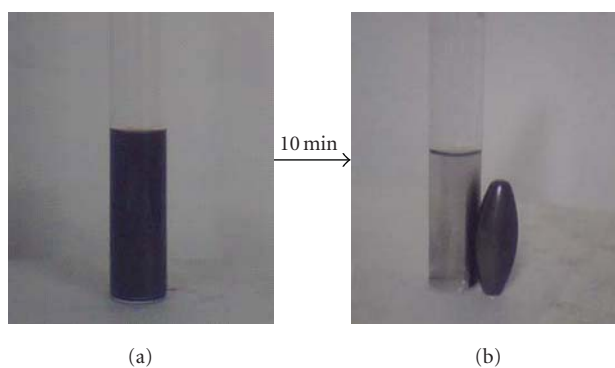


FIGURE 6: Magnetically separable HCl-washed Co@OLFs in alcohol. Before (a) and after (b) a magnet was placed on the outer wall of tube for 10 min.

coercive force  $H_c$ , are dependent upon chemical composition and particle size [19]. The curve is symmetric around  $H = 0$ , with a saturation magnetization ( $M_s$ ) of 17.70 emu/g and a coercivity ( $H_c$ ) of 750.23 Oe. Here, the  $M_s$  of Co@OLFs is much lower than that of bulk Co ( $M_s = 162.5$  emu/g) [19]. The decrease of the saturation magnetization may be attributed to the inclusive phases of carbon (e.g., carbon's diamagnetic contribution), and the surface coating effects [19], in view of the fact that Co nanoparticles were entirely encapsulated by carbon. These effects are expected to become more prominent for smaller particles owing to their larger surface-to-volume ratio. Moreover, the data for the ratio of remanence to saturation magnetization ( $M_r/M_s = 0.42$ ) indicates the good ferromagnetism of Co@OLFs at room temperature.

The magnetic property of the Co@OLFs can also be tested qualitatively, as shown in Figure 6. The Co@OLFs were dispersed homogeneously in ethanol solution in a colorimetric tube by ultrasonic vibration (Figure 6(a)). After a magnet was placed on the outer wall of colorimetric tube for 10 min, the black products were aggregated on the inner wall of tube (Figure 6(b)), suggesting the ferromagnetic property

of Co@OLFs, which may be of potential application in electronic devices, high-density magnetic memories, sensors, and electrochemical energy storage.

#### 4. Conclusions

Fe/NaCl or Co/NaCl were used as catalysts to fabricate Fe@OLFs with diameters of 10–50 nm or Co@OLFs with diameters of 10–60 nm by CVD using acetylene as carbon resource at 420°C. NaCl was easily separable from the product just by a washing process. The metallic cores inside the OLFs were  $Fe_3C$  when Fe/NaCl was used as catalyst and Co nanoparticles when Co/NaCl was used as catalyst. After immersing the as-synthesized products in concentrated HCl for 48 h, bare metal nanoparticles were removed while the metal nanoparticles encapsulated by carbon shells were unaffected. It means that carbon shells can protect the encapsulated metallic cores against environmental degradation. The coercivity value (750.23 Oe) of Co@OLFs showed an obvious magnetic property.

#### Acknowledgments

The authors acknowledge financial support from Program for Changjiang Scholar and Innovative Research Team in University (IRT0972), National Natural Science Foundation of China (20971094), International S&T Co-operation Program (2007DFA50940), International S&T Cooperation Program of Shanxi Province (2009081018, 2010081017), Natural Science Foundation of Shanxi Province (2009011012-4), and Shanxi Research Fund for Returned Scholars (2008-31).

#### References

- [1] D. Ugarte, "Curling and closure of graphitic networks under electron-beam irradiation," *Nature*, vol. 359, no. 6397, pp. 707–709, 1992.
- [2] B.-S. Xu, "Prospects and research progress in nano onion-like fullerenes," *Xinxing Tan Cailiao/ New Carbon Materials*, vol. 23, no. 4, pp. 289–301, 2008.
- [3] S. Seraphin, D. Zhou, and J. Jiao, "Filling the carbon nanocages," *Journal of Applied Physics*, vol. 80, no. 4, pp. 2097–2104, 1996.
- [4] B. S. Xu and S.-I. Tanaka, "Formation of giant onion-like fullerenes under Al nanoparticles by electron irradiation," *Acta Materialia*, vol. 46, no. 15, pp. 5249–5257, 1998.
- [5] B. Xu, J. Guo, X. Wang, X. Liu, and H. Ichinose, "Synthesis of carbon nanocapsules containing Fe, Ni or Co by arc discharge in aqueous solution," *Carbon*, vol. 44, no. 13, pp. 2631–2634, 2006.
- [6] A.-B. Du, X.-G. Liu, D.-J. Fu, P.-D. Han, and B.-S. Xu, "Onion-like fullerenes synthesis from coal," *Fuel*, vol. 86, no. 1-2, pp. 294–298, 2007.
- [7] Y. Lu, Z. Zhu, and Z. Liu, "Carbon-encapsulated Fe nanoparticles from detonation-induced pyrolysis of ferrocene," *Carbon*, vol. 43, no. 2, pp. 369–374, 2005.
- [8] Y. Yang, X. Liu, and B. Xu, "Fe-encapsulating carbon nano onionlike fullerenes from heavy oil residue," *Journal of Materials Research*, vol. 23, no. 5, pp. 1393–1397, 2008.

- [9] B. Xu, T. Li, P. Han, X. Liu, and I. Hideki, "Several features of the iron-included onion-like fullerenes," *Materials Letters*, vol. 60, no. 16, pp. 2042–2045, 2006.
- [10] G. Gulino, R. Vieira, J. Amadou et al., "C<sub>2</sub>H<sub>6</sub> as an active carbon source for a large scale synthesis of carbon nanotubes by chemical vapour deposition," *Applied Catalysis A*, vol. 279, no. 1-2, pp. 89–97, 2005.
- [11] H. Kathyayini, N. Nagaraju, A. Fonseca, and J. B. Nagy, "Catalytic activity of Fe, Co and Fe/Co supported on Ca and Mg oxides, hydroxides and carbonates in the synthesis of carbon nanotubes," *Journal of Molecular Catalysis A*, vol. 223, no. 1-2, pp. 129–136, 2004.
- [12] T. C. Schmitt, A. S. Biris, D. W. Miller et al., "Analysis of effluent gases during the CCVD growth of multi-wall carbon nanotubes from acetylene," *Carbon*, vol. 44, no. 10, pp. 2032–2038, 2006.
- [13] A. K. Sinha, D. W. Hwang, and L.-P. Hwang, "A novel approach to bulk synthesis of carbon nanotubes filled with metal by a catalytic chemical vapor deposition method," *Chemical Physics Letters*, vol. 332, no. 5-6, pp. 455–460, 2000.
- [14] E. S. Steigerwalt and C. M. Lukehart, "Preparation of graphitic carbon nanofibers with the use of water-soluble supports," *Journal of Nanoscience and Nanotechnology*, vol. 2, no. 1, pp. 25–28, 2002.
- [15] J. Geng, I. A. Kinloch, C. Singh et al., "Production of carbon nanofibers in high yields using a sodium chloride support," *Journal of Physical Chemistry B*, vol. 109, no. 35, pp. 16665–16670, 2005.
- [16] A. Eftekhari, P. Jafarkhani, and F. Moztarzadeh, "High-yield synthesis of carbon nanotubes using a water-soluble catalyst support in catalytic chemical vapor deposition," *Carbon*, vol. 44, no. 7, pp. 1343–1345, 2006.
- [17] B. H. Liu, J. Ding, Z. Y. Zhong, Z. L. Dong, T. White, and J. Y. Lin, "Large-scale preparation of carbon-encapsulated cobalt nanoparticles by the catalytic method," *Chemical Physics Letters*, vol. 358, no. 1-2, pp. 96–102, 2002.
- [18] X. Liu, C. Wang, Y. Yang, X. Guo, H. Wen, and B. Xu, "Synthesis of nano onion-like fullerenes by using Al<sub>2</sub>O<sub>3</sub> as catalyst by chemical vapor deposition," *Chinese Science Bulletin*, vol. 54, no. 1, pp. 137–141, 2009.
- [19] E. Flahaut, F. Agnoli, J. Sloan, C. O'Connor, and M. L. H. Green, "CCVD Synthesis and characterization of cobalt-encapsulated nanoparticles," *Chemistry of Materials*, vol. 14, no. 6, pp. 2553–2558, 2002.

## Research Article

# Diameter Tuning of Single-Walled Carbon Nanotubes by Diffusion Plasma CVD

**Toshiaki Kato, Shunsuke Kuroda, and Rikizo Hatakeyama**

*Department of Electronic Engineering, Tohoku University, Sendai 980-8579, Japan*

Correspondence should be addressed to Toshiaki Kato, kato12@ecei.tohoku.ac.jp

Received 22 June 2010; Accepted 16 August 2010

Academic Editor: Jianyu Huang

Copyright © 2011 Toshiaki Kato et al. This is an open access article distributed under the Creative Commons Attribution License, which permits unrestricted use, distribution, and reproduction in any medium, provided the original work is properly cited.

We have realized a diameter tuning of single-walled carbon nanotubes (SWNTs) by adjusting process gas pressures with plasma chemical vapor deposition (CVD). Detailed photoluminescence measurements reveal that the diameter distribution of SWNTs clearly shifts to a large-diameter region with an increase in the pressure during plasma CVD, which is also confirmed by Raman scattering spectroscopy. Based on the systematical investigation, it is found that the main diameter of SWNTs is determined by the pressure during the heating in an atmosphere of hydrogen and the diameter distribution is narrowed by adjusting the pressure during the plasma generation. Our results could contribute to an application of SWNTs to high-performance thin-film transistors, which requires the diameter-controlled semiconductor-rich SWNTs.

## 1. Introduction

Single-walled carbon nanotubes (SWNTs) [1] have attracted intense attention due to their prominent electrical and optical properties [2–6]. One of the most promising electrical applications of SWNTs is to fabricate a thin-film field-effect transistor (FET) exploiting their flexible structure and high carrier mobility [7–9]. Since the mixture of metallic SWNTs in the FET channel increases leak currents between source and drain electrodes, which results in low on/off ratios, the selective growth of semiconducting SWNTs is urgently required. The band gap of SWNTs and contact resistance between nanotubes and electrodes are strongly influenced by the tube diameter [10, 11]. Thus, it is indispensable to grow diameter-controlled semiconductor-rich SWNTs for realizing high-performance SWNTs-based thin-film FETs. It is known that the SWNTs grown by plasma chemical vapor deposition (CVD) show a tendency to contain semiconducting SWNTs with concentration higher than that by the other growth methods such as arc discharge, laser ablation, and thermal CVD, while their detailed mechanisms are still under investigation [12–15]. Although plasma CVD can be one of the promising approaches to obtain the abovementioned well-diameter-controlled semiconductor-rich SWNTs, the

difficulty in controlling the plasma conditions has gotten in the way of realizing the precise diameter tuning of SWNTs.

Here, we demonstrate the diameter tuning of SWNTs by changing the gas pressure during the CVD process. Detailed photoluminescence (PL) and Raman scattering spectroscopy analyses reveal that the main diameter of SWNTs becomes large with an increase in the gas pressure. The systematic investigation is also carried out to figure out the mechanism of the diameter variation.

## 2. Experimental

**2.1. SWNTs Growth.** A home-made diffusion plasma CVD system was utilized for the growth of freestanding SWNTs [16, 17]. The Fe (thickness ( $t$ ): 0.5~1 nm)/Al<sub>2</sub>O<sub>3</sub> ( $t$ : 20 nm) multilayer catalyst was formed on an Ag substrate ( $t$ : 0.2 mm) by a vacuum evaporation and a sputtering method, respectively. A capacitively coupled plasma was generated by supplying a radio-frequency (RF: 13.56 MHz) power ( $P_{RF}$ ) to an upper electrode. A mesh grid was used as an anode to promote spatial diffusion of plasmas. A substrate was placed on a heater which was located underneath the lower anode-electrode. The distance between the lower electrode and the substrate was fixed at 70 mm. The growth

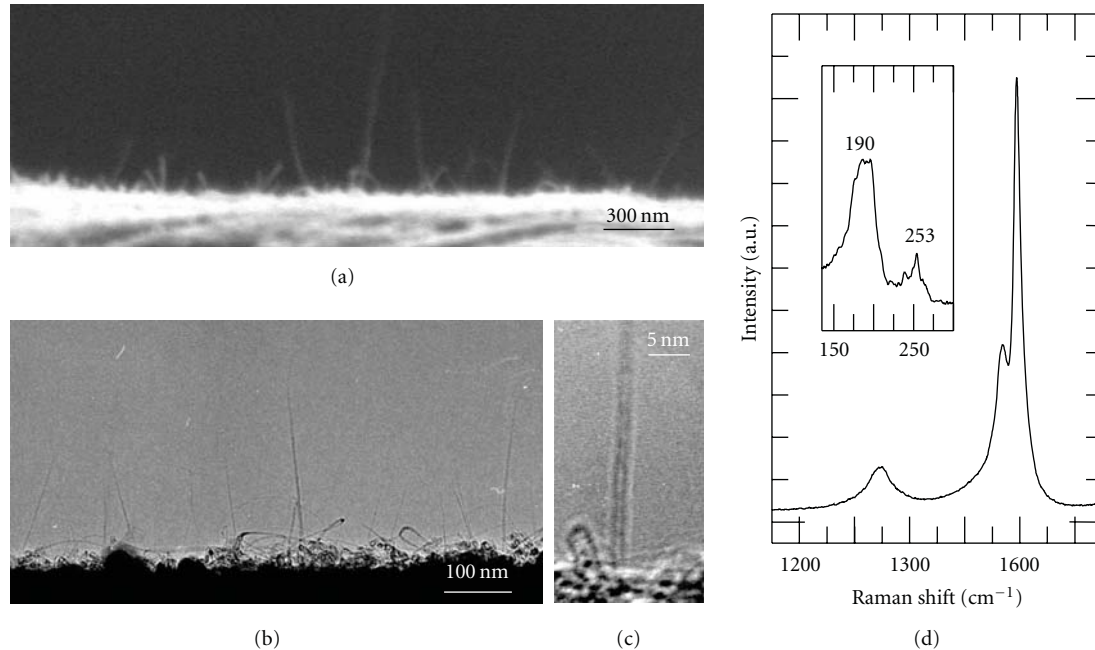


FIGURE 1: (a) SEM and (b), (c) TEM images of freestanding individual SWNTs. (d) Raman scattering spectrum (488 nm excitation) of freestanding individual SWNTs. Inset of (d) is emphasis of the RBM region.

of SWNTs by plasma CVD was carried out with the following procedures. First, the system was pumped down to a base pressure of  $10^{-2}$  Pa with rotary and diffusion pumps. The substrate was heated up to  $600^{\circ}\text{C}$  under an Ar flow, and then the Ar gas was immediately switched to a methane and hydrogen mixture gas (3 : 7 mixture ratio). Note that a total pressure during the heating process was set to be as the same as that during the growth unless otherwise specified. When the total pressure reached a desired pressure (20–650 Pa), the  $P_{\text{RF}}$  of 80 W was supplied to generate plasmas and the SWNT growth was started. The growth time was 20 sec. After the SWNT growth, the methane and hydrogen gases were pumped out and an Ar gas was introduced into the system in order to cool down the substrate.

**2.2. Electron Microscope Analysis.** As-grown states of freestanding SWNTs were analyzed with a scanning electron microscope (SEM, Hitachi 4100) and a transmission electron microscope (TEM, Hitachi HF-2000). A thin Cu wire (dia. =  $100\ \mu\text{m}$ ) covered by the Fe/ $\text{Al}_2\text{O}_3$  catalyst was utilized as a substrate, which was able to be directly set in a TEM holder without any conventional TEM grid.

**2.3. Photoluminescence Analysis.** Photoluminescence-excitation (PLE) measurements were performed with a JY (Horiba) Fluorolog-3 system. The excitation wavelength was varied from 500 to 828 nm in 4 nm step, and emission signals were accumulated for 20 sec in each excitation step. Excitation and emission slit widths were fixed at 10 nm. In order to cut the Rayleigh scattering, optical filters (Sigmakoki, ITF-50S-83IR, ITF-50S-85IR) were set in front of a liquid-nitrogen-cooled InGaAs array detector.

**2.4. Raman Scattering Spectroscopy Analysis.** Raman scattering spectra were taken with 488 nm Ar laser and 632.8 nm He-Ne laser excitations. As-growth SWNTs were used for this Raman scattering analysis.

### 3. Results and Discussion

Figures 1(a)–1(c) show typical SEM (a) and TEM (b, c) images of the as-grown SWNTs produced by diffusion plasma CVD. SWNTs are found to be grown in the freestanding form [17]. The existence of SWNTs is also confirmed by a Raman scattering spectrum as shown in Figure 1(d). In general, electrostatic potentials in plasmas sharply drop in the interface between the plasmas and solid materials, forming strong electric fields on the surface of the solid materials. Since the polarization constant of SWNTs in an axial direction is extremely high, the strong dipole moment is induced in the axial tube direction in the presence of electric fields. Due to the energy stability of the dipole moments under the electric fields, SWNTs tend to align with the electric fields. This is a possible explanation for the freestanding growth of SWNTs in the case of plasma CVD [18].

PL spectroscopy is a powerful tool to assign each chirality of semiconducting SWNTs [19, 20]. Since excited excitons in the semiconducting SWNTs are easily quenched through the metallic SWNTs, each SWNT has to be well isolated to observe the occurrence of the optical emission. Thus, PL measurements of SWNTs are usually carried out with the dispersed SWNTs in the specific chemical solution. Owing to the unique freestanding as-grown state of SWNTs grown by diffusion plasma CVD, it is possible to obtain the PL signal

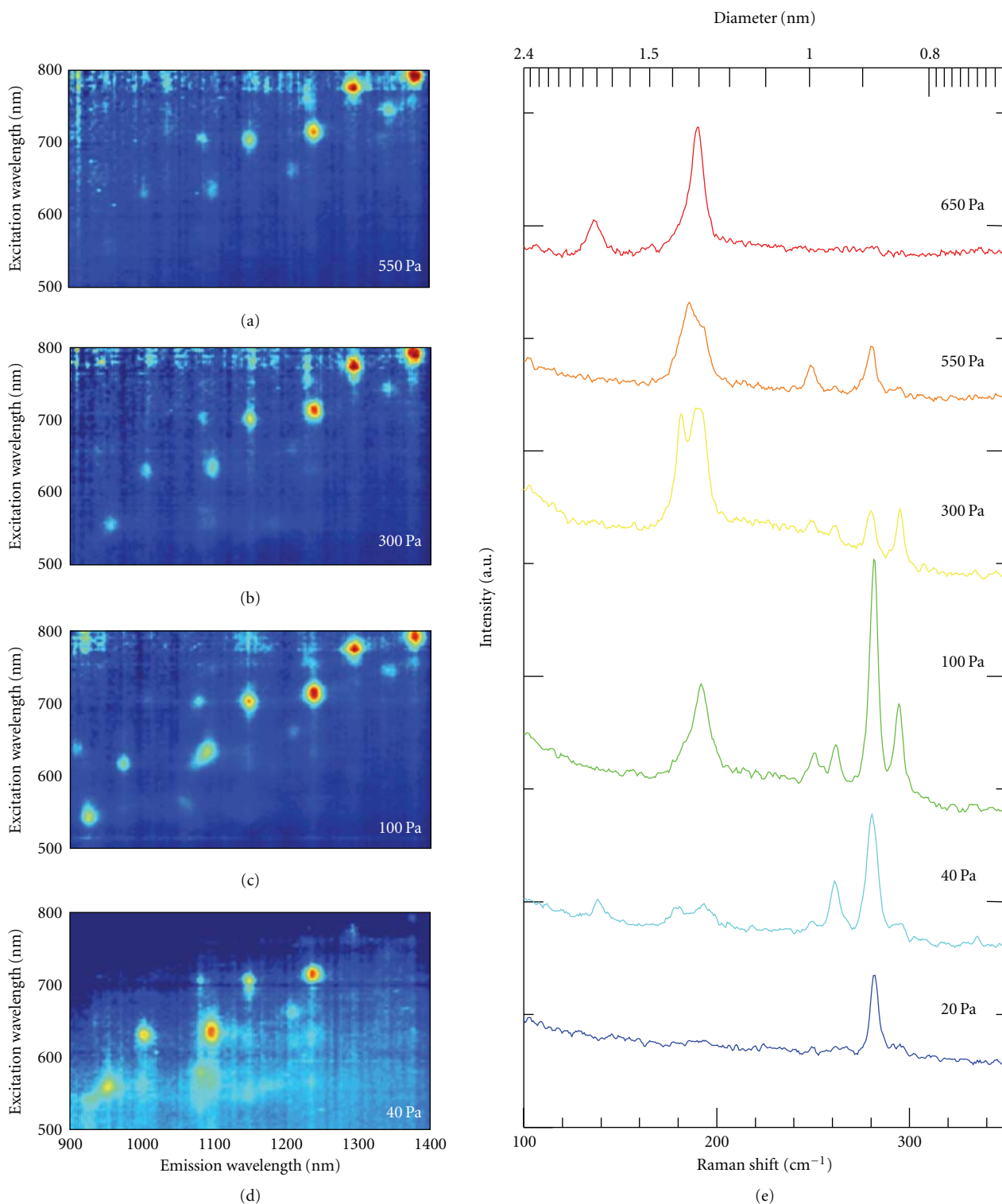


FIGURE 2: (a–d) PLE maps of as-grown freestanding SWNTs grown at the different pressures: (a) 550 Pa, (b) 300 Pa, (c) 100 Pa, and (d) 40 Pa, respectively. (e) Growth pressure dependence of RBM in Raman scattering spectra (632.8 nm excitation) of as-grown freestanding SWNTs.

from the as-grown SWNTs without any chemical dispersion [21].

Figures 2(a)–2(d) give PLE maps of as-grown SWNTs produced at different gas pressures. It is to be noted that all the PLE measurements are carried out immediately after

the growth process in order to prevent the freestanding SWNTs from forming bundles, which causes significant PL changes [21]. It is found that peaks in the PLE map at the high growth pressure (Figure 2(a)) tend to appear in the range of long excitation and emission wavelengths. The peak

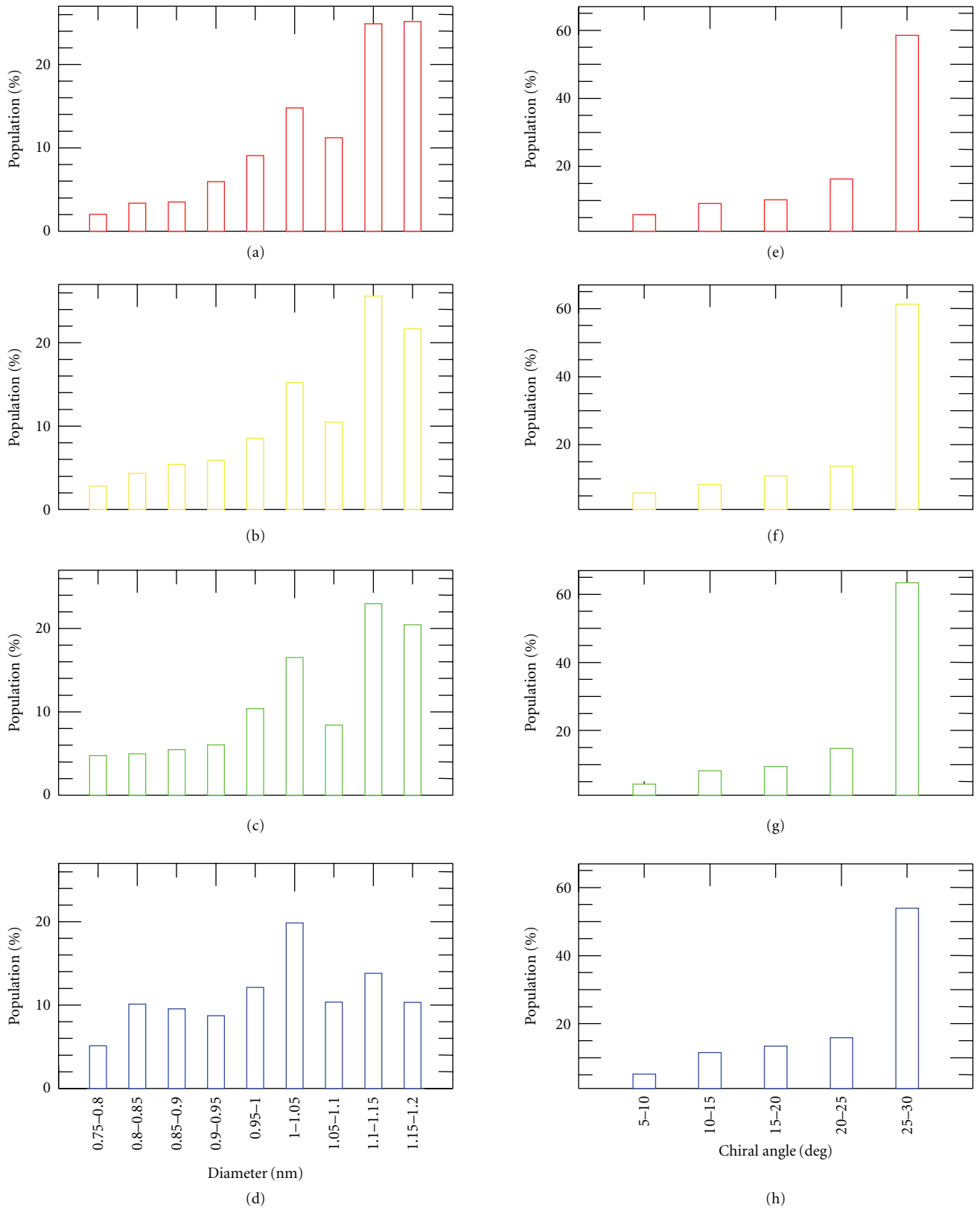


FIGURE 3: Population histograms as functions of (a–d) SWNTs diameters and (e–h) chiral angles, which are grown at the different pressures: (a, e) 550 Pa, (b, f) 300 Pa, (c, g) 100 Pa, and (d, h) 40 Pa, respectively.

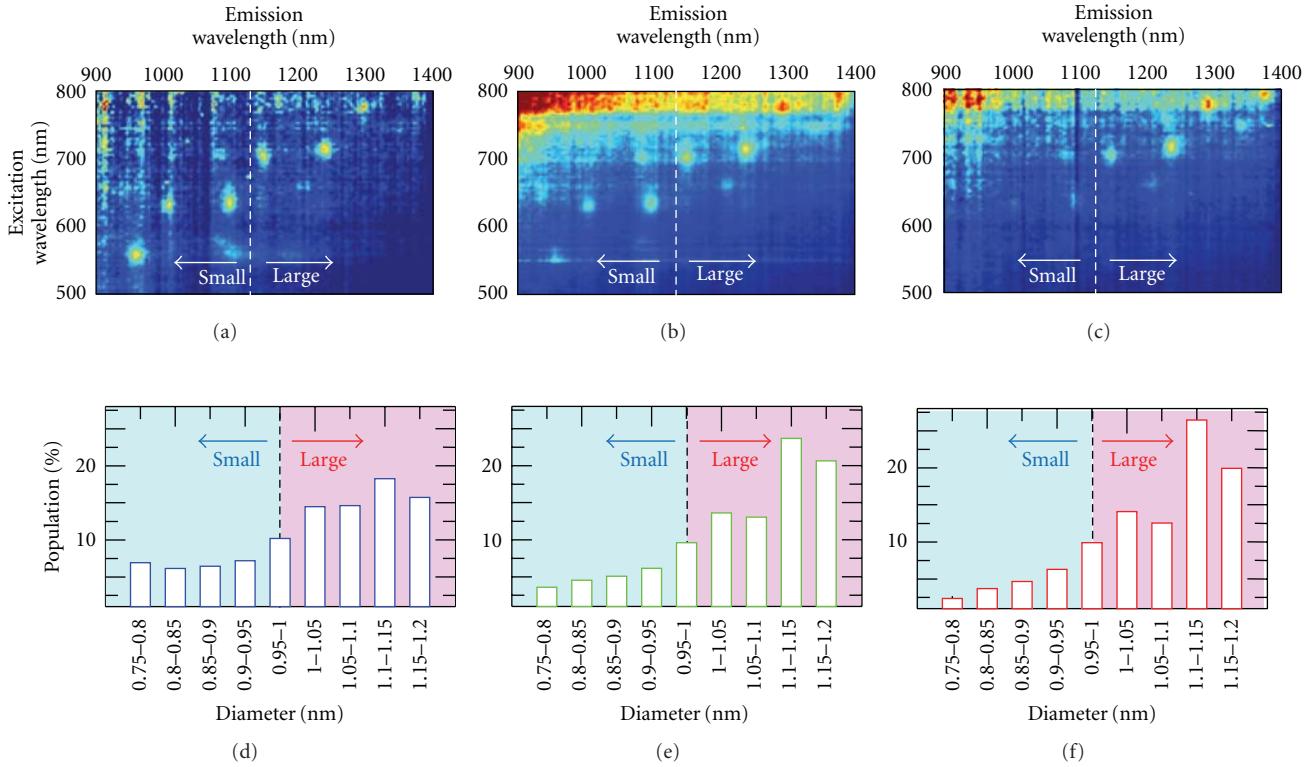


FIGURE 4: (a–c) PLE maps and (d–f) population-diameter histograms of as-grown freestanding SWNTs. The pressures during heating and growth are (a, d) both 60 Pa, (b, e) 500 Pa and 60 Pa, and (c, f) both 500 Pa, respectively.

positions shift to the region of short excitation and emission wavelengths with a decrease in the growth pressure (Figures 2(b)–2(d)). Since each peak corresponds to each chirality in the sample and smaller-diameter SWNTs are positioned in the shorter wavelength region, the peak-position shift in the PLE map indicates that the diameter distribution of produced SWNTs is strongly influenced by the growth pressure. Thus, lower pressure enables the SWNTs diameter to become smaller. This diameter dependence on the growth pressure is also reflected in Raman scattering spectra of SWNTs grown at the different growth pressures. Figure 2(e) demonstrates that peak positions of the radial breathing mode (RBM) clearly shift from higher to lower values of wave number with an increase in the growth pressures. Here the RBM peak position and the SWNTs diameter are known to have a close correlation, which is  $\omega = 248/d$  [22], where  $\omega$  and  $d$  are RBM peak position ( $\text{cm}^{-1}$ ) and diameter (nm), respectively. This result is fairly consistent with the PLE result shown in Figures 2(a)–2(d). The typical pressure range where SWNTs can be grown is from 30 Pa to 650 Pa, which depends on the  $P_{\text{RF}}$  used for the plasma generation. Although the absolute intensity of G-band in Raman scattering spectra decreases in the low or high pressure range, the G-band to D-band ratio is almost the same. This indicates that the quality of SWNTs should be the same in any pressure range whereas the density of SWNTs depends on the pressure. When we increase the input  $P_{\text{RF}}$ , it is possible to grow SWNTs

even below 30 Pa, which means that the lack of hydrocarbon supply is significant under the lower pressure condition, and hence additional input  $P_{\text{RF}}$  is required to increase the density of active species used for the growth of SWNTs.

Since the optical absorption and emission efficiency of each SWNT depend on its chirality, the PL emission intensity does not directly correspond to the population of each chirality SWNT. To discuss the population of SWNTs, it is therefore required to inspect the optical absorption and emission efficiency of each chirality SWNT. Figures 3(a)–3(d) and 3(e)–3(h) are SWNTs population histograms as the functions of diameter and chiral angle of SWNTs produced at the different growth pressures. These data are calculated from the absolute PL intensities shown in Figures 2(a)–2(d) and the optical efficiencies obtained from the theoretical calculation [23]. It is worthy of being noted that the detectable diameter range is 0.75–1.2 nm in this study due to the limitation of the PL detector used. The larger diameters of SWNTs (1.1–1.2 nm) are confirmed to be dominant in the samples grown at the high pressures, and the main diameter shifts to around 1.0 nm with a decrease in the growth pressure. In contrast, there is no clear difference of chiral angle among the growth pressures. In all the cases, near-armchair (25–30 deg) SWNTs show the highest population, which is similar to the SWNTs grown by the other methods [24]. The mechanism of the near-armchair rich growth is still unclear. In general, the chirality can be determined by the initial cap structure formed

on the catalyst particle surface. For the stable cap formation, it is required to satisfy the isolated pentagon rule [25]. This cap structure stability might have effects on the higher population of near-armchair SWNTs than the other types of SWNTs.

In order to understand the mechanism of diameter shift depending on the process pressure, we carried out the systematic investigation. Since the pressures during the heating and growth are the same in our growth process, the process pressure affects both the heating and growth process. In order to clarify which exercises a critical effect on the diameter tuning of SWNTs, we performed experiments on the SWNTs growth under the following conditions; the pressures during the heating and growth are (1) both 60 Pa, (2) 500 Pa and 60 Pa, and (3) both 500 Pa, respectively. Figures 4(a)–4(c) and 4(d)–4(f) are PLE maps and population-diameter histograms of SWNTs produced under the conditions (1) (a and d), (2) (b and e), and (3) (c and f), respectively. For the simplification, we define the diameter ranges 0.75–1.0 nm and 1.0–1.2 nm as “small” and “large,” respectively. When we compare the conditions (1) and (2), it is found that the population of small-diameter SWNTs decreases but the population of large-diameter SWNTs increases. Although we do not have any evidence about the catalyst particle size change after the high-pressure annealing, we believe that the catalyst size becomes large due to their aggregation after the high-pressure annealing, which results in the growth of larger-diameter SWNTs because the other growth conditions are completely the same for these two samples. Interestingly, the clear difference is also found between the conditions (2) and (3). Although the population of large-diameter SWNTs is almost the same, the growth of small-diameter SWNTs is obviously suppressed. This can be explained as follows. The density of reactive hydrocarbon radicals and ions should increase under the higher growth-pressure conditions. In the high carbon-supply condition, the small catalyst can be deactivated due to the oversupply of hydrocarbons, and hence the population of small-diameter SWNTs decreases. These indicate that the heating pressure is important to control the catalyst size distribution, which directly influences the main diameter of SWNTs, and that the pressure during plasma CVD is also important to narrow the SWNTs diameter distribution.

#### 4. Conclusions

We have investigated the diameter distributions of plasma CVD-grown SWNTs in their as-grown state by PLE mapping and Raman scattering spectroscopy analyses. The pressure dependence study reveals that the process pressures strongly influence the SWNTs diameter distribution in plasma CVD. Furthermore, it is found that the catalyst particle size distribution can determine the main diameter of SWNTs and that their distribution can be narrowed by adjusting the plasma conditions. Our results could contribute to precisely and perfectly controlling the structure of as-grown SWNTs in the near future.

#### References

- [1] S. Iijima and T. Ichihashi, “Single-shell carbon nanotubes of 1-nm diameter,” *Nature*, vol. 363, no. 6430, pp. 603–605, 1993.
- [2] S. J. Tans, M. H. Devoret, H. Dai et al., “Individual single-wall carbon nanotubes as quantum wires,” *Nature*, vol. 386, no. 6624, pp. 474–477, 1997.
- [3] S. J. Tans, A. R. M. Verschueren, and C. Dekker, “Room-temperature transistor based on a single carbon nanotube,” *Nature*, vol. 393, no. 6680, pp. 49–52, 1998.
- [4] A. Bachtold, P. Hadley, T. Nakanishi, and C. Dekker, “Logic circuits with carbon nanotube transistors,” *Science*, vol. 294, no. 5545, pp. 1317–1320, 2001.
- [5] A. Javey, J. Guo, Q. Wang, M. Lundstrom, and H. Dai, “Ballistic carbon nanotube field-effect transistors,” *Nature*, vol. 424, no. 6949, pp. 654–657, 2003.
- [6] M. Freitag, J. C. Tsang, J. Kirtley et al., “Electrically excited, localized infrared emission from single carbon nanotubes,” *Nano Letters*, vol. 6, no. 7, pp. 1425–1433, 2006.
- [7] Z. Wu, Z. Chen, X. Du et al., “Transparent, conductive carbon nanotube films,” *Science*, vol. 305, no. 5688, pp. 1273–1276, 2004.
- [8] M. C. LeMieux, M. Roberts, S. Barman, Y. W. Jin, J. M. Kim, and Z. Bao, “Self-sorted, aligned nanotube networks for thin-film transistors,” *Science*, vol. 321, no. 5885, pp. 101–104, 2008.
- [9] M. Engel, J. P. Small, M. Steiner et al., “Thin film nanotube transistors based on self-assembled, aligned, semiconducting carbon nanotube arrays,” *ACS Nano*, vol. 2, no. 12, pp. 2445–2452, 2008.
- [10] R. Saito, G. Dresselhaus, and M. S. Dresselhaus, *Physical Properties of Carbon Nanotubes*, Imperial College Press, London, UK, 1998.
- [11] W. Kim, A. Javey, R. Tu, J. Cao, Q. Wang, and H. Dai, “Electrical contacts to carbon nanotubes down to 1 nm in diameter,” *Applied Physics Letters*, vol. 87, no. 17, Article ID 173101, 3 pages, 2005.
- [12] Y. Li, D. Mann, M. Rolandi et al., “Preferential growth of semiconducting single-walled carbon nanotubes by a plasma enhanced CVD method,” *Nano Letters*, vol. 4, no. 2, pp. 317–321, 2004.
- [13] L. Qu, F. Du, and L. Dai, “Preferential syntheses of semiconducting vertically aligned single-walled carbon nanotubes for direct use in FETs,” *Nano Letters*, vol. 8, no. 9, pp. 2682–2687, 2008.
- [14] U. J. Kim, E. H. Lee, J. M. Kim, Y.-S. Min, E. Kim, and W. Park, “Thin film transistors using preferentially grown semiconducting single-walled carbon nanotube networks by water-assisted plasma-enhanced chemical vapor deposition,” *Nanotechnology*, vol. 20, no. 29, Article ID 295201, 2009.
- [15] T. Mizutani, H. Ohnaka, Y. Okigawa, S. Kishimoto, and Y. Ohno, “A study of preferential growth of carbon nanotubes with semiconducting behavior grown by plasma-enhanced chemical vapor deposition,” *Journal of Applied Physics*, vol. 106, no. 7, Article ID 073705, 5 pages, 2009.
- [16] T. Kato, G.-H. Jeong, T. Hirata, R. Hatakeyama, K. Tohji, and K. Motomiya, “Single-walled carbon nanotubes produced by plasma-enhanced chemical vapor deposition,” *Chemical Physics Letters*, vol. 381, no. 3–4, pp. 422–426, 2003.
- [17] T. Kato, R. Hatakeyama, and K. Tohji, “Diffusion plasma chemical vapour deposition yielding freestanding individual single-walled carbon nanotubes on a silicon-based flat substrate,” *Nanotechnology*, vol. 17, no. 9, pp. 2223–2226, 2006.

- [18] T. Kato and R. Hatakeyama, "Formation of freestanding single-walled carbon nanotubes by plasma-enhanced CVD," *Chemical Vapor Deposition*, vol. 12, no. 6, pp. 345–352, 2006.
- [19] M. J. O'Connell, S. M. Bachilo, C. B. Huffman et al., "Band gap fluorescence from individual single-walled carbon nanotubes," *Science*, vol. 297, no. 5581, pp. 593–596, 2002.
- [20] S. M. Bachilo, M. S. Strano, C. Kittrell, R. H. Hauge, R. E. Smalley, and R. B. Weisman, "Structure-assigned optical spectra of single-walled carbon nanotubes," *Science*, vol. 298, no. 5602, pp. 2361–2366, 2002.
- [21] T. Kato and R. Hatakeyama, "Exciton energy transfer-assisted photoluminescence brightening from freestanding single-walled carbon nanotube bundles," *Journal of the American Chemical Society*, vol. 130, no. 25, pp. 8101–8107, 2008.
- [22] A. Jorio, R. Saito, J. H. Hafner et al., "Structural (n, m) determination of isolated single-wall carbon nanotubes by resonant Raman scattering," *Physical Review Letters*, vol. 86, no. 6, pp. 1118–1121, 2001.
- [23] Y. Oyama, R. Saito, K. Sato et al., "Photoluminescence intensity of single-wall carbon nanotubes," *Carbon*, vol. 44, no. 5, pp. 873–879, 2006.
- [24] Y. Miyauchi, S. Chiashi, Y. Murakami, Y. Hayashida, and S. Maruyama, "Fluorescence spectroscopy of single-walled carbon nanotubes synthesized from alcohol," *Chemical Physics Letters*, vol. 387, no. 1–3, pp. 198–203, 2004.
- [25] H. W. Kroto, "The stability of the fullerenes  $C_n$ , with  $n = 24, 28, 32, 36, 50, 60$  and  $70$ ," *Nature*, vol. 329, no. 6139, pp. 529–531, 1987.

## Research Article

# Homogeneous Carbon Nanotube/Carbon Composites Prepared by Catalyzed Carbonization Approach at Low Temperature

Hongjiang Li, Changhong Liu, and Shoushan Fan

*Department of Physics, Tsinghua-Foxconn Nanotechnology Research Center, Tsinghua University, Beijing 100084, China*

Correspondence should be addressed to Changhong Liu, [chliu@tsinghua.edu.cn](mailto:chliu@tsinghua.edu.cn)

Received 17 May 2010; Revised 17 August 2010; Accepted 26 August 2010

Academic Editor: Jianyu Huang

Copyright © 2011 Hongjiang Li et al. This is an open access article distributed under the Creative Commons Attribution License, which permits unrestricted use, distribution, and reproduction in any medium, provided the original work is properly cited.

We synthesize carbon nanotube (CNT)/carbon composite using catalyzed carbonization of CNT/Epoxy Resin composite at a fairly low temperature of about 400°C. The microstructure of the composite is characterized by scanning electron microscope (SEM), transmission electron microscope (TEM), and X-ray diffraction (XRD). The results indicate that CNTs and pyrolytic carbon blend well with each other. Pyrolytic carbon mainly stays in an amorphous state, with some of it forming crystalline structures. The catalyst has the effect of eliminating the interstices in the composites. Remarkable increases in thermal and electrical conductivity are also reported.

## 1. Introduction

Owing to the superior thermal, electrical, and mechanical properties, carbon nanotube (CNT) has been widely used in composite materials, especially in polymer based composites [1–9]. Carbon nanotube/carbon (CNT/C) is a promising new composite to make a better contact between CNT and the matrix material. For one thing, CNT and carbon have the same constituent atoms, which will tend to make a better connection between them. For another, carbon itself is a kind of material with better conduct properties than most of polymers, so the CNT/C composite has the potential to gain higher conducting performance than CNT/polymer composites.

Some attempts have already been made on the synthesis of CNT/C composites; many of which are inspired by the processing methods of carbon/carbon (C/C) composites, using either chemical vapor infiltration (CVI) method [10, 11] or high pressure impregnation carbonization method [12–15]. High temperature or high pressure is needed in such processes. In the field of application, CNT/C composites can be utilized in many aspects, as structural or functional materials. Researchers have added CNTs into carbon to promote the tribological behavior [10, 16], to improve the absorption property [17, 18], to make electrodes [19, 20] for electrochemistry, and so on.

In our previous work [21], we proposed a facile postprocessing way to fabricate aligned CNT array/carbon composites at relatively low temperature and pressure. In this paper, we follow the in-situ method, using catalyzed carbonization of organic material to make homogenous CNT/C composite, making it a promising method for large-scale production. Instead of aligned CNT array and glucose, we utilize dispersed multiwalled CNTs and epoxy resin in the process, making it a more general situation. We believe that by this method the material structures can be tuned a lot. We did contrast experiment to analyze the role of the catalyst in the carbonization process. In addition, we measured the thermal properties of the composite and found a remarkable increase in the thermal conductivity and decrease in the contact thermal resistance. Electrical conducting property is also tested.

## 2. Experimental

The raw multi-walled CNTs were grown by chemical vapor deposition (CVD). The purity of the CNTs is 95%, with diameter about 20 nm and length around 10  $\mu\text{m}$ . Epoxy resin is chosen as carbon resource to produce pyrolytic carbon. The catalyst of carbonization is ferrocene. We first synthesize CNT/Epoxy resin composite, with around 2 wt % of

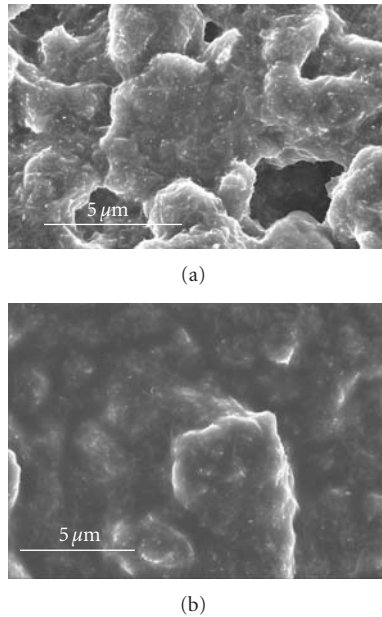


FIGURE 1: SEM top view of as-prepared CNT/C composites (a) without and (b) with ferrocene catalyst.

multi-walled CNTs and 0.1 wt % of ferrocene. The process is as follows: we put CNTs into epoxy monomer and add some ethanol to enhance fluidity. After that the mixture is stirred for 1 hour before another hour of ultrasonic treatment. Then it is cooled down and added into the catalyst and curing agent, which in our case is polyamide resin. Another hour of stirring will be needed before we put the mixture into the mold and wait about 12 hours for complete curing. Then the sample was heated in a vacuum tube furnace, which was gradually elevated to 400°C from room temperature and maintained this temperature for 1 hour before cooling. Nitrogen atmosphere was used in this treatment to protect the sample from oxidation. We had tried this temperature in the range 200–600°C. We found that 400°C was more favorable.

Scanning electron microscopy (SEM, Sirion 200, resolution 1.0 nm) and high resolution transmission electron microscopy (HRTEM, Tecnai G2 F20 S-Twin, resolution 2.4 nm) were used for characterization of microstructures. Thermal conductivity and contact resistance were measured by the static method, using an apparatus designed according to ASTM D5470, which was described elsewhere [8]. The samples have two kinds of shapes, plates with a diameter of 11.5 mm and 25 mm. They have different thickness, ranging from 0.5 mm to 2 mm. Electrical conductivity was measured by a four-point method, using Keithley's Model 2410 High-Voltage SourceMeter.

### 3. Results and Discussion

Since the temperature of carbonization was fairly low, the weight loss of the material was as low as about 20%. The density of the obtained CNT/C sample was 0.98 g/cm<sup>3</sup>,

which was remarkably higher than the typical pristine CNTs tablet (0.65 g/cm<sup>3</sup>). The enhancement in density shows that pyrolytic carbon fills the interstices between the CNTs, and instead of increasing the volume, the pyrolytic carbon holds the CNTs closer, forming a much denser material.

The microstructure of as-prepared CNT/C composites is shown in Figure 1. The sample in Figure 1(a) is synthesized by directly carbonizing CNT/Epoxy resin while the other sample made by catalyzed carbonization of CNT/Epoxy resin is shown in Figure 1(b), with ferrocene as a catalyst. We can see from the two pictures that CNTs blend well with the pyrolytic carbon, forming block structures. The dispersed CNTs are buried under the surface of pyrolytic carbon, establishing the framework of the blocks while the pyrolytic carbon closely surrounds the CNTs, making a compact compound structure. Such blocks stack with one another, building up the composite. The catalyst, ferrocene, plays an important role in the formation of the composite. In comparison Figures 1(a) and 1(b), we can see that there are many gaps between the blocks in Figure 1(a); however, with catalyst in Figure 1(b), such gaps disappear. So the ferrocene can improve the connections between the blocks, which will be beneficial to the conduct properties of the material. All the CNT/C composites talked about afterwards are made by catalyzed carbonization.

Figure 2 is the TEM image of the CNT/C composite. The close contact between the CNT and pyrolytic carbon is shown in Figure 2(a). We can see that the CNT is surrounded by the pyrolytic carbon; most of which is in an amorphous state. Their connection is so strong that we can hardly find the interface between them. In order to prepare the TEM sample uniformly, we treated the composite flake with ultrasonic for more than 2 hours; the power of which is 500 W. However, it is still hard to separate the CNT and pyrolytic carbon apart. Most of them intertwine together, forming big blocks in the pictures. It shows that the two components have strong interaction between them. Figure 2(b) gives us an enlarged view of the pyrolytic carbon. Most of the pyrolytic carbon is in an amorphous state, but on the edge of the sample, we can see some crystal texture (shown in the inset picture), where the interplaner spacing is about 0.34 nm, the same as graphite. Unfortunately, such crystalline structures do not extend over a long distance. Because of the large amount of amorphous carbon, and the strong interaction between the two components, it is hard for us to find more CNT feature under the cover of amorphous carbon.

X-ray diffraction (XRD) pattern of MWNT and MWNT/C are presented in Figure 3. The characteristic peak of MWNT is around 25.9 degree. For the latter, the peak is widened a lot, which indicates the existence of a large amount of small particles of amorphous carbon. This result is consistent with the microstructure characterization. Besides, although the MWNT is only a little proportion in the composite, the characteristic peak is still seen, showing that the CNTs maintain their structure well after carbonization process.

We measured the thermal properties of three different samples: MWNT/Epoxy Resin composite, MWNT tablet and

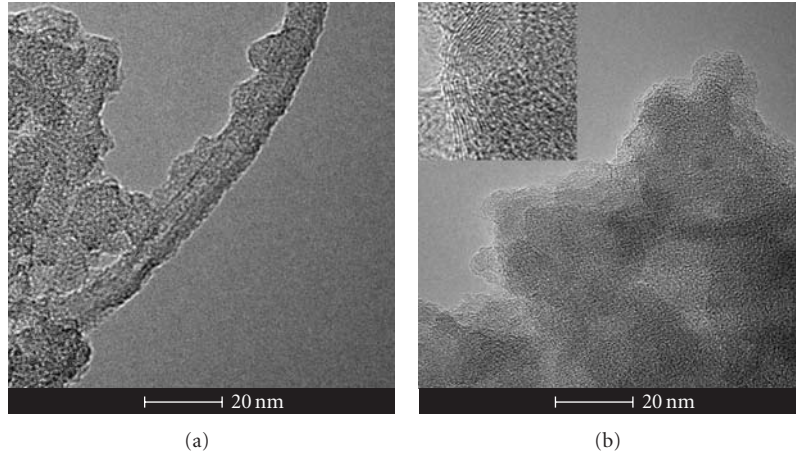


FIGURE 2: TEM image of CNT/C composite: (a) the image showing the close contact of CNT and pyrolytic carbon. (b) the microstructure of the pyrolytic carbon. The inset shows an enlarged feature of the image.

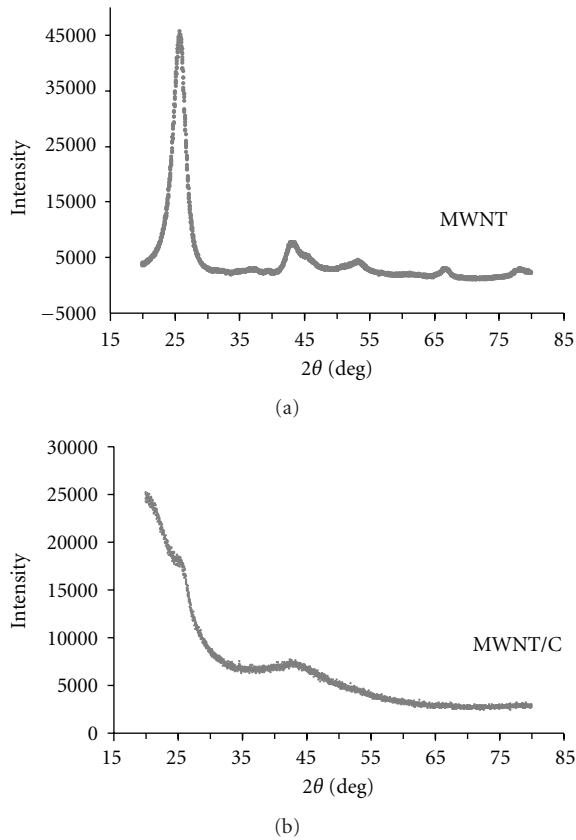


FIGURE 3: The XRD patterns of (a) MWNT tablet and (b) the MWNT/C composite. The characteristic peak of the MWNTs was around 25.9 degree.

MWNT/C composite. The thermal conductivity and thermal contact resistance are shown in Figure 4. The shown data was the average of multiple tests (three times) for each sample, and the standard deviation for the results was below 10%. The white bars represent the thermal conductivity while the black ones represent the thermal contact resistance.

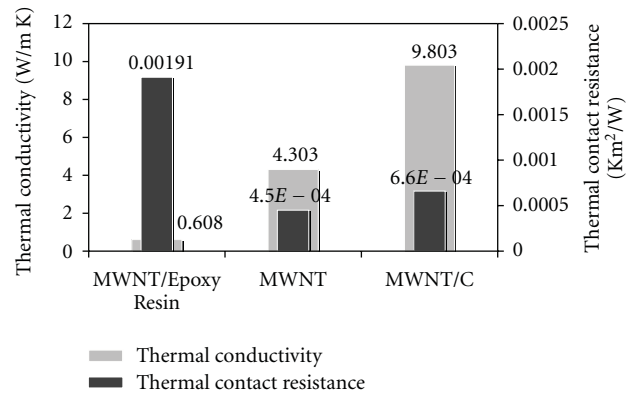


FIGURE 4: The thermal conductivity and thermal contact resistance of MWNT/Epoxy Resin composite, MWNT tablet, and MWNT/C composite. The white bars represent thermal conductivity, while the black ones are the thermal contact resistance.

From the white bars, we see that the thermal conductivity of MWNT/C composites, which is more than twice the value of pure MWNT tablet, can increase remarkably by one magnitude than MWNT/Epoxy Resin composite. This increase is attributed to the good connections between the CNTs and pyrolytic carbon as well as the relatively high thermal conductivity of pyrolytic carbon, which, instead of the air, fills in the interstices among the CNTs. The black bars give us evident information that the thermal contact resistance of MWNT/C composites remains a small value, a little higher than pure MWNT but only about 1/3 of the value of MWNT/Epoxy Resin composite. We believe that the amorphous carbon in the pyrolytic carbon plays an important role in decreasing of the thermal contact resistance, for the small blocks can easily get into the gaps between the two testing probes, squeeze the air in them, and get a better thermal connection.

The MWNT/C composite has much higher thermal conductivity and fairly low thermal contact resistance, which

is appropriate for thermal interface materials (TIMs). TIMs are important materials for thermal conduction between interfaces and are being widely used in electronic packing. As the electronics and information industry is progressing, higher standard of thermal conduction will be needed for a higher integrated density. MWNT/C composites are one kind of potential material for future thermal conduction. Besides, although the controlled growth of CNTs is still being studied, MWNTs are easily fabricated by CVD method, which will help to reduce the cost of this industry.

In addition, we measured the electrical resistivity of the MWNT/Epoxy Resin and MWNT/C composites. The value decreased a little from  $3.1 \times 10^7 \Omega \cdot \text{m}$  to  $2.5 \times 10^6 \Omega \cdot \text{m}$  after the carbonization. It shows that pyrolytic carbon has a better electrical conducting property than Epoxy Resin. However, because of the low carbonization temperature, the increase in conductivity is not so remarkable. Other characterizations are still on the way.

#### 4. Conclusions

In this paper, we fabricate MWNT/C composites by the method of catalyzed carbonization of MWNT/Epoxy Resin composite. The microstructure shows that the CNTs and the pyrolytic carbon make a compact compound material, with CNTs and carbon evenly distributed. The catalyst, ferrocene, plays an important role in making a denser composite structure. From the high-resolution TEM images, we see that pyrolytic carbon wraps around the MWNTs. Pyrolytic carbon is made up of amorphous carbon and crystal carbon, with amorphous carbon as the majority. The crystalline structure can be found on the edge of the amorphous carbon. The measurements of thermal properties of this composite indicate that the MWNT/C composite has a much higher thermal conductivity and a fairly low thermal contact resistance, which make it a good choice for the TIMs. The electrical conducting properties of the composite are also improved, increasing by one order of magnitude as to CNT/Epoxy Resin composite.

#### Acknowledgments

This paper was supported by the National Basic Research Program of China (2005CB623606) and the National Natural Science Foundation of China (50673049).

#### References

- [1] B.-K. Zhu, S.-H. Xie, Z.-K. Xu, and Y.-Y. Xu, "Preparation and properties of the polyimide/multi-walled carbon nanotubes (MWNTs) nanocomposites," *Composites Science and Technology*, vol. 66, no. 3-4, pp. 548-554, 2006.
- [2] Q. Zhang, S. Rastogi, D. Chen, D. Lippits, and P. J. Lemstra, "Low percolation threshold in single-walled carbon nanotube/high density polyethylene composites prepared by melt processing technique," *Carbon*, vol. 44, no. 4, pp. 778-785, 2006.
- [3] E. T. Thostenson and T.-W. Chou, "Processing-structure-multi-functional property relationship in carbon nanotube/epoxy composites," *Carbon*, vol. 44, no. 14, pp. 3022-3029, 2006.
- [4] X. J. He, J. H. Du, Z. Ying, and H. M. Cheng, "Positive temperature coefficient effect in multiwalled carbon nanotube/high-density polyethylene composites," *Applied Physics Letters*, vol. 86, no. 6, Article ID 062112, 3 pages, 2005.
- [5] A. R. Bhattacharyya, T. V. Sreekumar, T. Liu et al., "Crystallization and orientation studies in polypropylene/single wall carbon nanotube composite," *Polymer*, vol. 44, no. 8, pp. 2373-2377, 2003.
- [6] R. Haggenueller, H. H. Gommans, A. G. Rinzler, J. E. Fischer, and K. I. Winey, "Aligned single-wall carbon nanotubes in composites by melt processing methods," *Chemical Physics Letters*, vol. 330, no. 3-4, pp. 219-225, 2000.
- [7] R. Andrews, D. Jacques, A. M. Rao et al., "Nanotube composite carbon fibers," *Applied Physics Letters*, vol. 75, no. 9, pp. 1329-1331, 1999.
- [8] H. Huang, C. Liu, Y. Wu, and S. Fan, "Aligned carbon nanotube composite films for thermal management," *Advanced Materials*, vol. 17, no. 13, pp. 1652-1656, 2005.
- [9] C. H. Liu, H. Huang, Y. Wu, and S. S. Fan, "Thermal conductivity improvement of silicone elastomer with carbon nanotube loading," *Applied Physics Letters*, vol. 84, no. 21, pp. 4248-4250, 2004.
- [10] Q.-M. Gong, Z. Li, Z. Zhang et al., "Tribological properties of carbon nanotube-doped carbon/carbon composites," *Tribology International*, vol. 39, no. 9, pp. 937-944, 2006.
- [11] Q.-M. Gong, Z. Li, D. Li, X.-D. Bai, and J. Liang, "Fabrication and structure: a study of aligned carbon nanotube/carbon nanocomposites," *Solid State Communications*, vol. 131, no. 6, pp. 399-404, 2004.
- [12] B. Wu, Z. Wang, Q. M. Gong, H. H. Song, and J. Liang, "Fabrication and mechanical properties of in situ prepared mesocarbon microbead/carbon nanotube composites," *Materials Science and Engineering A*, vol. 487, no. 1-2, pp. 271-277, 2008.
- [13] Z. Wang, B. Wu, Q. Gong, H. Song, and J. Liang, "In situ fabrication of carbon nanotube/mesocarbon microbead composites from coal tar pitch," *Materials Letters*, vol. 62, no. 20, pp. 3585-3587, 2008.
- [14] Y. Song, G. Zhai, J. Shi, Q. Guo, and L. Liu, "Carbon nanotube: carbon composites with matrix derived from oxidized mesophase pitch," *Journal of Materials Science*, vol. 42, no. 22, pp. 9498-9500, 2007.
- [15] Z. Li, Q.-M. Gong, Z.-Y. Zhang, J. Liang, Q.-Z. Huang, and B.-Y. Huang, "Fabrication and characterization of a new pitch-based ACNT/C nanocomposites," *Chinese Journal of Inorganic Chemistry*, vol. 22, no. 10, pp. 1755-1760, 2006.
- [16] Q.-M. Gong, Z. Li, X.-D. Bai, D. Li, Y. Zhao, and J. Liang, "Thermal properties of aligned carbon nanotube/carbon nanocomposites," *Materials Science and Engineering A*, vol. 384, no. 1-2, pp. 209-214, 2004.
- [17] K. Dai, L. Shi, D. Zhang, and J. Fang, "NaCl adsorption in multi-walled carbon nanotube/active carbon combination electrode," *Chemical Engineering Science*, vol. 61, no. 2, pp. 428-433, 2006.
- [18] C. Ye, Q.-M. Gong, F.-P. Lu, and J. Liang, "Preparation of carbon nanotubes/phenolic-resin-derived activated carbon spheres for the removal of middle molecular weight toxins," *Separation and Purification Technology*, vol. 61, no. 1, pp. 9-14, 2008.

- [19] J. Luo, J. Zhu, Z. Huang, and L. Zhang, "Arrays of Ni nanowire/multiwalled carbon nanotube/amorphous carbon nanotube heterojunctions containing Schottky contacts," *Applied Physics Letters*, vol. 90, no. 3, Article ID 033114, 2007.
- [20] P. Deng, J. Fei, J. Zhang, and J. Li, "Determination of trace copper by adsorptive voltammetry using a multiwalled carbon nanotube modified carbon paste electrode," *Electroanalysis*, vol. 20, no. 11, pp. 1215–1219, 2008.
- [21] H. Li, C. Liu, and S. Fan, "Catalyzed filling of carbon nanotube array with graphite and the thermal properties of the composites," *Journal of Physical Chemistry C*, vol. 112, no. 15, pp. 5840–5842, 2008.

## Research Article

# Humidity Sensor Based on Multi-Walled Carbon Nanotube Thin Films

C. L. Cao,<sup>1,2</sup> C. G. Hu,<sup>1</sup> L. Fang,<sup>1</sup> S. X. Wang,<sup>1</sup> Y. S. Tian,<sup>2</sup> and C. Y. Pan<sup>2</sup>

<sup>1</sup>Department of Applied Physics, Chongqing University, Chongqing 400044, China

<sup>2</sup>Department of physics, Chongqing Communication College, Chongqing 400035, China

Correspondence should be addressed to C. L. Cao, caochunlan0812@163.com and C. G. Hu, hucg@cqu.edu.cn

Received 26 April 2010; Accepted 1 September 2010

Academic Editor: Teng Li

Copyright © 2011 C. L. Cao et al. This is an open access article distributed under the Creative Commons Attribution License, which permits unrestricted use, distribution, and reproduction in any medium, provided the original work is properly cited.

The properties of the humidity sensors made of chemically treated and untreated multi-walled carbon nanotube (MWCNT) thin films are investigated systematically. It shows that both the chemically treated and untreated MWCNT thin films demonstrate humidity sensitive properties, but the former have stronger sensitivity than the latter. In the range of 11%–98% relative humidity (RH), the resistances of the chemically treated and untreated MWCNT humidity sensors increase 120% and 28%, respectively. Moreover, the treated humidity sensors showed higher sensitivity and better stability. In addition, the response and recover properties, and stabilization of the humidity sensors are measured, and the humidity sensitive mechanisms of the sensors are analyzed. The humidity sensitivity of carbon nanotube thin films indicates it promise as a kind of humidity sensitive material.

## 1. Introduction

Humidity sensors are widely applied in process control, environment monitoring, storage, electrical devices, and so forth, and the research to develop some new materials for sensor device attracts more and more attention. Carbon nanotubes (CNTs) is a kind of carbon allotrope, which was found in 1991 by Iijima [1]. Owing to its very large surface area to volume ratio [2], nanoscale structure and hollow center, CNTs can absorb large amounts of foreign molecules on its surface [3]. With the presence of these molecules, many properties associated with CNTs would change. Due to these reasons nanotubes have been explored for many sensors [4–6]. Zahab et al. [7] reported that water vapor has a great effect on the electrical conductivity of a single-walled carbon nanotube (SWCNT) mat, and p-type carbon nanotube would turn into n-type if water molecules added. It means that CNTs may be a kind of humidity sensing materials. Some studies of humidity sensitivity on SWCNTs have been reported [7, 8], and Varghese et al. [5], Valentini et al. [6], and Cantalini et al. [9] have investigated the gas sensitive characteristics of MWCNTs systematically and observed humidity sensitivity of MWCNTs briefly, and they have found that the humidity sensor impedance increases

with increasing humidity [5, 6, 9]. But the humidity sensitive properties of MWCNTs have seldom been studied deeply and systematically.

Here we report the humidity sensing properties of both untreated and chemically treated MWCNT thin films systematically, including the sensitivity, the response and recover properties, and stabilization. The different properties of the two types of sensors are compared and the humidity sensing mechanisms of the sensors are discussed.

## 2. Experimental

In this experiment, carbon nanotubes were produced by hot filament chemical vapor deposition (CVD) [10] using  $C_2H_2$  and Ni/Fe as the carbon source and catalyst, respectively. The obtained carbon nanotubes were characterized by the scanning electron microscopy (SEM) and transmission electron microscopy (TEM).

The CNTs used to prepare the humidity sensors were classified into two types, untreated and chemically treated sample, respectively. In the chemical treatment process, MWCNTs were undergone a ultrasonic treatment for 150 minutes in a mixture of 98% sulphuric acid and 79% nitric

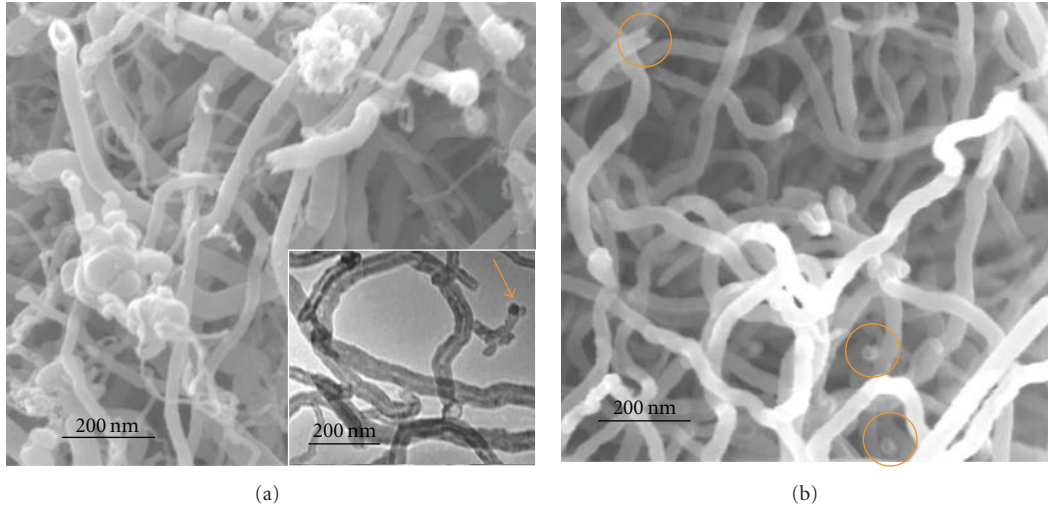


FIGURE 1: SEM images of pristine (a) and chemically treated (b) carbon nanotubes, and TEM image of carbon nanotubes (inset).

acid in ratio of 3:1. The treated nanotubes were rinsed in deionized water and then let to dry. The thin films of humidity sensors are prepared by spraying on top of pre-deposited Au electrodes on quartz plate using an airbrush with untreated and chemically treated MWCNTs dispersed in ethanol, respectively. The dimensions of samples were  $1 \times 10^{-2}$  m in length,  $5 \times 10^{-3}$  m in width, and  $1 \times 10^{-4}$  m in thickness.

The electrical characteristic of the sensors were measured by a multifunctional digital multimeter (FLUKE-45 model, made in the US America) at variant humidity environments at constant temperature ( $20^\circ\text{C}$ ). The sensors were successively put into several chambers with different RH levels obtained by saturation salt solution method. RH values varied from 11% to 98%. The uncertainty of the RH values is about  $\pm 1\%$ . All samples were dried at 373 K for 30 minutes prior to electrical measurements. The measurement was done after 30 minutes when the temperatures inside and outside the chambers became the same.

### 3. Results and Discussion

**3.1. Microstructure.** Figures 1(a) and 1(b) show the SEM images of the pristine and the chemically treated carbon nanotubes. From the SEM images, the diameter of carbon nanotubes ranges from 40 to 60 nm. TEM image of the pristine carbon nanotubes is shown in the inset, indicating tube-like morphology. Before chemical treatment, carbon nanotubes are impure with some carbon particles, and some ends of the nanotubes are closed as is pointed by the arrow. However, after chemical treatment, the carbon nanotubes are more pure, and almost all the ends of the nanotube are open (marked in circles).

**3.2. Humidity-Resistance Characteristic.** Figures 2(a) and 2(b) give the D.C. resistance versus RH plots of untreated

and treated MWCNT humidity sensors, respectively. The solid lines in the figures are measured in the humidification process (increasing RH), corresponding to the adsorption process, while the dashed lines are measured in the desiccation process (decreasing RH), corresponding to the desorption process. It shows that the resistance of both the untreated and treated samples changes almost linearly with the relative humidity. When RH increases from 11% to 98%, the resistance of the untreated and treated samples increases 28% and 120%, respectively, means, the treated samples have stronger sensitivity than the untreated.

The sensitivity factor  $S$  can be defined as

$$S = \frac{R_{RH} - R_0}{R_0} \times 100\%, \quad (1)$$

where  $R_{RH}$  and  $R_0$  are the resistance in the humidity state and 11% RH, respectively.

As shown in Figure 3, the sensitivity factor  $S$  increases linearly with RH, and can be fitted linearly to (2) and (3) for the untreated and chemically treated MWCNTs humidity sensor, respectively,

$$S = -4.70 + 0.32 * RH, \quad (2)$$

$$S = -15.47 + 1.34 * RH. \quad (3)$$

It can be seen that the slope of chemically treated MWCNTs humidity sensor (1.34) is far greater than that of untreated MWCNTs humidity sensor (0.32), meaning that the sensitivity of the former is much higher than the latter. The higher sensitivity of the chemically treated sensor is attributed to its purity of nanotubes and higher surface sites available for the adsorption of water molecules resulting from its shorter length and more open ends.

However, a hysteresis of resistance versus RH in the desiccation process (Figure 2) is found in both chemically treated and untreated sensors. This is probably due to the different

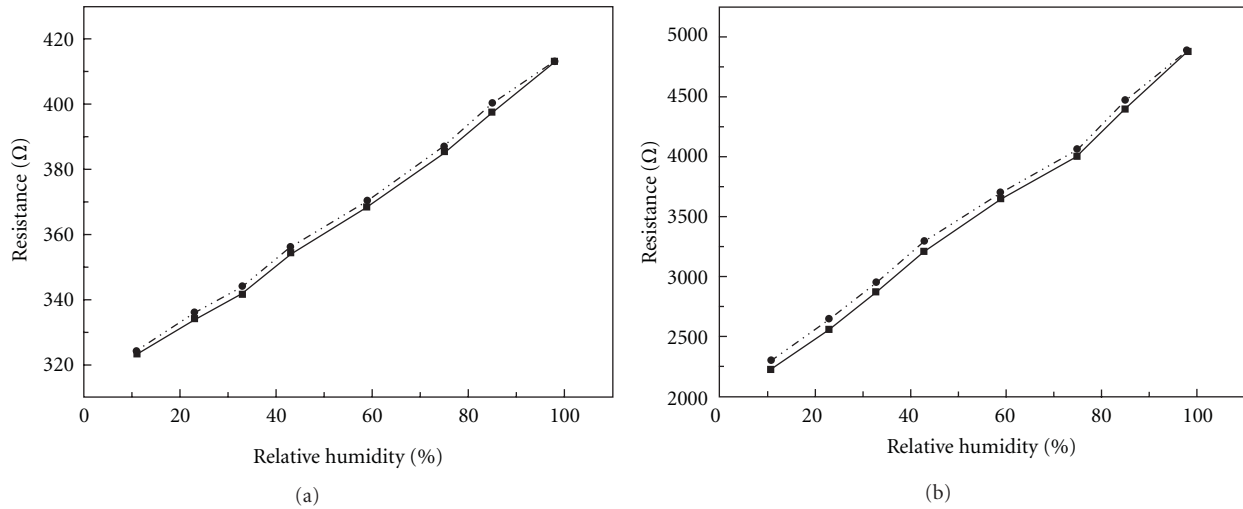


FIGURE 2: Resistance versus RH characteristics of (a) untreated and (b) treated MWCNT humidity sensors.

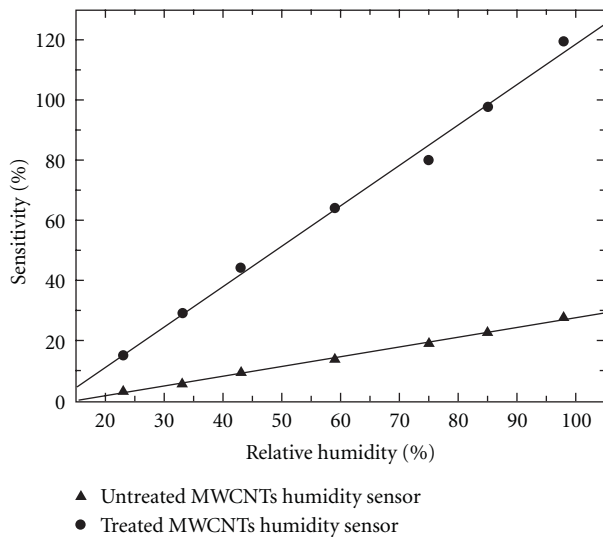


FIGURE 3: The sensitivity factor  $S$  of untreated and treated MWCNT humidity sensors.

amount of water molecules adsorbed on CNTs between the humidification process and the desiccation process at a same ambient RH, causing the different resistance at a same RH.

**3.3. Response and Recover Properties.** Several important parameters for sensor devices are response time, recover time, and reproducibility. To investigate these properties, the dynamic testing of the untreated and chemically treated MWCNT sensors at a constant RH is performed. The response time for the adsorption and desorption curves measured at 20°C for the sensors is shown in Figure 4. The response time to continuous humidification from 33% to 98% RH is 20 and 50 s for the untreated and treated MWCNT sensors, respectively. While the recover time from 98% to 33% RH is 40 and 140 s for the treated and untreated MWCNT sensors, respectively. Further testing after three

additional cycles demonstrates good reproducibility of the treated MWCNT sensors. The response and recovery time are much shorter than that of other sensors made of complex oxides, such as In-doped  $\text{CaZrO}_3$  [11] which works at high temperature (700°C),  $\text{Ba}_{1-x}\text{La}_x\text{SnO}_3$  (both 60 s) [12] and Sr added  $\text{BaAl}_2\text{O}_4$  (120 S and 50 s) [13] and other materials [14–16]. Therefore, the sensor made of the treated MWCNTs can be regarded as a fast response humidity sensor.

In case of humidity sensors, the recovery time is always higher than the response time [5, 9, 17], agreeing with our results. The long recover time can be attributed to slow desorption process of water molecules from CNTs at ambient temperature. As the usual response and recover time are tens and hundreds seconds, the quick response and recover property of the treated MWCNTs sensor has an advantage for practical applications.

**3.4. Stabilization.** The resistance variations with time for two kinds of samples are shown in Figure 5. The measurements were repeated at 20°C, every 5 days for one month. Slight or little resistance variation have been observed in both untreated and treated samples at each humidity region for one month, indicating that both the treated and untreated MWCNTs sensors are relatively stable to exposure to water vapor in air.

**3.5. Humidity Sensing Mechanism.** The origin of the humidity sensing effect in MWCNTs films may be caused by adsorption to water molecules. Before our experiment, the MWCNTs appear p-type semiconductor behavior tested by Hall effect experiment. For p-type MWCNTs, the adsorbed water molecules donate electrons to the valence band, thereby decreasing the number of holes and increasing the separation between the Fermi level and valence band [4, 7], and resulting in increase of the electrical resistance (see Figure 2). Although there is a humidity sensing effect to untreated MWCNTs, it is much weaker than that of treated MWCNTs. Chemical treatment makes carbon nanotubes

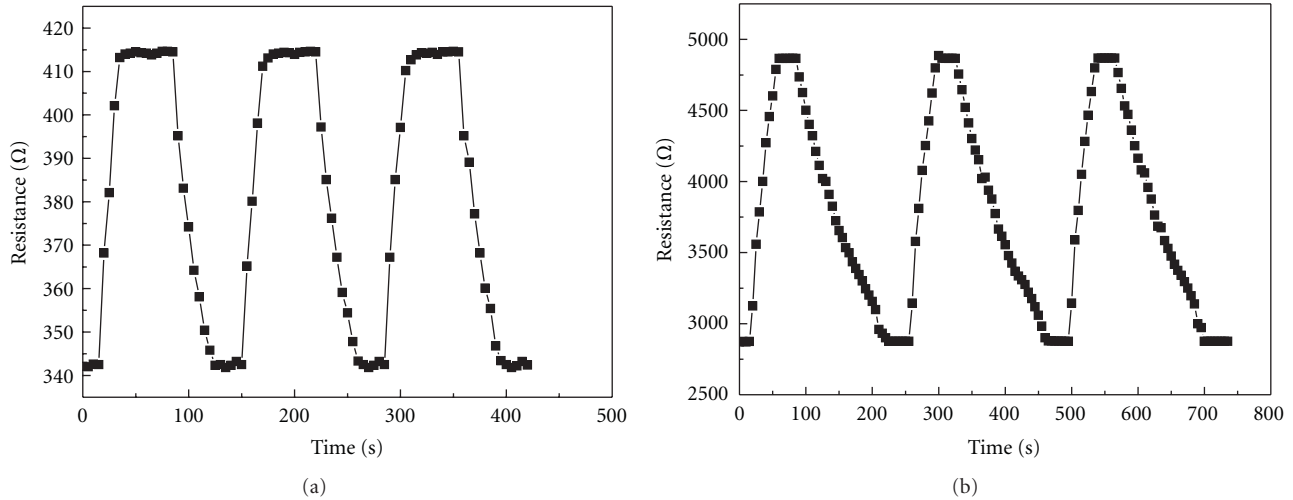


FIGURE 4: Dynamic response of untreated (a) and treated (b) MWCNT humidity sensors to humidity.

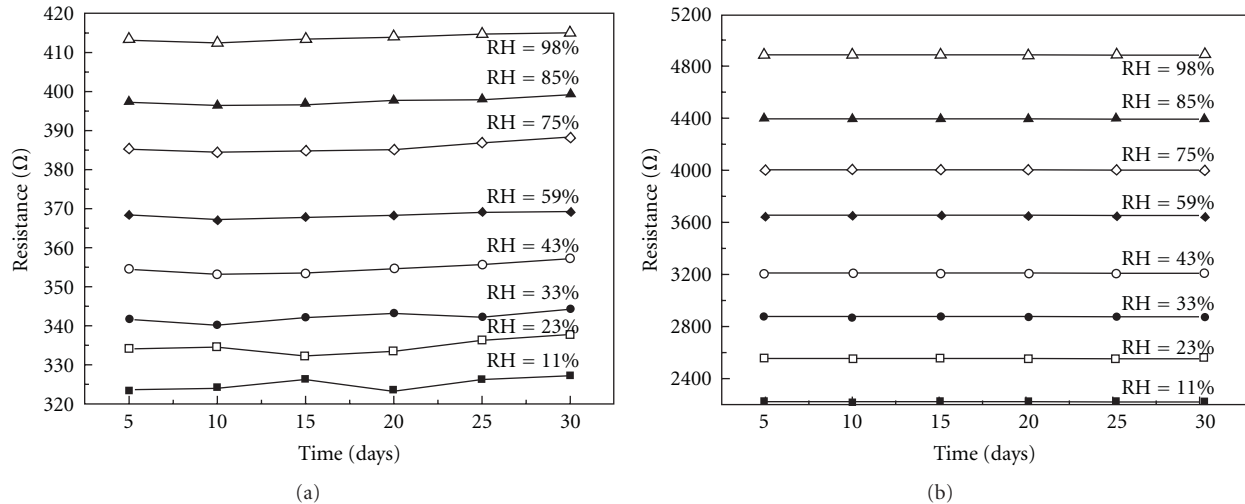


FIGURE 5: Resistance variations with time for the sensors at various RH levels: untreated (a) and treated (b) MWCNT humidity sensor.

shorten, more ends open, and more defects, which makes water molecules adsorb tubes easily. As MWCNTs could connect with lots of hydroxyl on its defects and open ends by chemical treatment, they could act as sites of adsorption to water molecules. Water molecules could be adsorbed on MWCNTs for the hydrogen in  $H_2O$  molecule could form a weak bond with one of the surface C atoms. Pati et al. [8] reported that charge can transfer between the adsorbate and the CNTs. A quantitative analysis based on Mulliken approach shows a charge transfer of  $0.03e^-$  from the single  $H_2O$  molecule to the CNTs [7]. The more water molecules can be adsorbed on the surface, intertubes, and ends after chemical treatment, the more charge transfer happens between the water molecules and CNTs. The presence of defects after chemical treatment may also reduce the conductivity of MWCNTs. Therefore, the humidity sensing characteristics of MWCNTs films is greatly enhanced after chemical treatment.

## 4. Conclusions

CNTs have been investigated as a new humidity sensitive material. The properties of the chemically treated CNT humidity sensors are discussed and compared with that of the untreated CNT sensors. The sensitivity of CNTs to humidity can be enhanced with chemical treatment. The charge transfer from absorbed water molecules to CNTs is a main reason for the humidity sensing properties. The treated CNT humidity sensor exhibited good sensitivity, linear and quick response, and excellent stability in different RH atmosphere, which demonstrate that it could be used as a good humidity sensor in practice applications.

## Acknowledgments

This work has been funded by the NSFC (60976055), and Postgraduates' Innovative Training Project (S-09109) of the

3rd-211 Project, and the large-scale equipment sharing fund of Chongqing University.

[17] Z.-H. Wu, W.-L. Wang, K.-J. Liao et al., "Study on the humidity sensitive behavior of multiwalled carbon nanotubes," *Chinese Physical Society*, vol. 53, no. 10, pp. 3462–3466, 2004.

## References

- [1] S. Iijima, "Helical microtubules of graphitic carbon," *Nature*, vol. 354, pp. 56–58, 1991.
- [2] M. Cinke, J. Li, B. Chen et al., "Pore structure of raw and purified HiPco single-walled carbon nanotubes," *Chemical Physics Letters*, vol. 365, no. 1-2, pp. 69–74, 2002.
- [3] C. K. W. Adu, G. U. Sumanasekera, B. K. Pradhan, H. E. Romero, and P. C. Eklund, "Carbon nanotubes: a thermoelectric nano-nose," *Chemical Physics Letters*, vol. 337, no. 1–3, pp. 31–35, 2001.
- [4] J. Kong, N. R. Franklin, C. Zhou et al., "Nanotube molecular wires as chemical sensors," *Science*, vol. 287, no. 5453, pp. 622–625, 2000.
- [5] O. K. Varghese, P. D. Kichambre, D. Gong, K. G. Ong, E. C. Dickey, and C. A. Grimes, "Gas sensing characteristics of multi-wall carbon nanotubes," *Sensors and Actuators B*, vol. 81, no. 1, pp. 32–41, 2001.
- [6] L. Valentini, I. Armentano, J. M. Kenny, C. Cantalini, L. Lozzi, and S. Santucci, "Sensors for sub-ppm NO<sub>2</sub> gas detection based on carbon nanotube thin films," *Applied Physics Letters*, vol. 82, no. 6, pp. 961–963, 2003.
- [7] A. Zahab, L. Spina, P. Poncharal, and C. Marlière, "Water-vapor effect on the electrical conductivity of a single-walled carbon nanotube mat," *Physical Review B*, vol. 62, no. 15, pp. 10000–10003, 2000.
- [8] R. Pati, Y. Zhang, S. K. Nayak, and P. M. Ajayan, "Effect of H<sub>2</sub>O adsorption on electron transport in a carbon nanotube," *Applied Physics Letters*, vol. 81, no. 14, pp. 2638–2640, 2002.
- [9] C. Cantalini, L. Valentini, I. Armentano, L. Lozzi, J. M. Kenny, and S. Santucci, "Sensitivity to NO<sub>2</sub> and cross-sensitivity analysis to NH<sub>3</sub>, ethanol and humidity of carbon nanotubes thin film prepared by PECVD," *Sensors and Actuators B*, vol. 95, no. 1–3, pp. 195–202, 2003.
- [10] C. J. Lee, J. Park, S. Han, and J. Ihm, "Growth and field emission of carbon nanotubes on sodalime glass at 550°C using thermal chemical vapor deposition," *Chemical Physics Letters*, vol. 337, no. 4–6, pp. 398–402, 2001.
- [11] M. H. Zhou and A. Ahamad, "Sol–gel processing of in-doped CaZrO<sub>3</sub> solid electrolyte and the impedimetric sensing characteristics of humidity and hydrogen," *Sensors and Actuators B*, vol. 129, pp. 205–209, 2008.
- [12] S. Upadhyay and P. Kavitha, "Lanthanum doped barium stannate for humidity sensor," *Materials Letters*, vol. 61, no. 8-9, pp. 1912–1915, 2007.
- [13] J. J. Vijaya, L. J. Kennedy, G. Sekaran, and K. S. Nagaraja, "Synthesis, characterization and humidity sensing properties of Sr(II)-added BaAl<sub>2</sub>O<sub>4</sub> composites," *Sensors and Actuators B*, vol. 124, no. 2, pp. 542–548, 2007.
- [14] Z. Zhang, C. Hu, Y. Xiong, R. Yang, and Z. L. Wang, "Synthesis of Ba-doped CeO<sub>2</sub> nanowires and their application as humidity sensors," *Nanotechnology*, vol. 18, no. 46, Article ID 465504, 2007.
- [15] W. Yan, C. Hu, Y. Xi et al., "ZnSe nanorods prepared in hydroxide-melts and their application as a humidity sensor," *Materials Research Bulletin*, vol. 44, no. 6, pp. 1205–1208, 2009.
- [16] M. Zhang, C. Hu, H. Liu, Y. Xiong, and Z. Zhang, "A rapid-response humidity sensor based on BaNbO<sub>3</sub> nanocrystals," *Sensors and Actuators B*, vol. 136, no. 1, pp. 128–132, 2009.

## Research Article

# Single Nucleotide Polymorphism Detection Using Au-Decorated Single-Walled Carbon Nanotube Field Effect Transistors

Keum-Ju Lee,<sup>1</sup> Hye-Mi So,<sup>1</sup> Byoung-Kye Kim,<sup>1,2</sup> Do Won Kim,<sup>3</sup> Jee-Hwan Jang,<sup>3,4</sup>  
Ki-Jeong Kong,<sup>1</sup> Hyunju Chang,<sup>1</sup> and Jeong-O Lee<sup>1</sup>

<sup>1</sup>NanoBio Fusion Research Center, Korea Research Institute of Chemical Technology, Daejeon 305-343, Republic of Korea

<sup>2</sup>Regional Innovation Agency, Jeonbuk Technopark, Jeonju 561-844, Republic of Korea

<sup>3</sup>Panagene Inc., Daejeon 305-510, Republic of Korea

<sup>4</sup>Ucaretron Inc., Dongiltechno Building C, Anyang 431-716, Republic of Korea

Correspondence should be addressed to Jeong-O Lee, jolee@kriect.re.kr

Received 14 June 2010; Revised 3 September 2010; Accepted 10 September 2010

Academic Editor: Jianyu Huang

Copyright © 2011 Keum-Ju Lee et al. This is an open access article distributed under the Creative Commons Attribution License, which permits unrestricted use, distribution, and reproduction in any medium, provided the original work is properly cited.

We demonstrate that Au-cluster-decorated single-walled carbon nanotubes (SWNTs) may be used to discriminate single nucleotide polymorphism (SNP). Nanoscale Au clusters were formed on the side walls of carbon nanotubes in a transistor geometry using electrochemical deposition. The effect of Au cluster decoration appeared as hole doping when electrical transport characteristics were examined. Thiolated single-stranded probe peptide nucleic acid (PNA) was successfully immobilized on Au clusters decorating single-walled carbon nanotube field-effect transistors (SWNT-FETs), resulting in a conductance decrease that could be explained by a decrease in Au work function upon adsorption of thiolated PNA. Although a target single-stranded DNA (ssDNA) with a single mismatch did not cause any change in electrical conductance, a clear decrease in conductance was observed with matched ssDNA, thereby showing the possibility of SNP (single nucleotide polymorphism) detection using Au-cluster-decorated SWNT-FETs. However, a power to discriminate SNP target is lost in high ionic environment. We can conclude that observed SNP discrimination in low ionic environment is due to the hampered binding of SNP target on nanoscale surfaces in low ionic conditions.

## 1. Introduction

The ability to detect small sequence differences in DNA molecules is very important in molecular biology, especially in the context of personalized diagnostics and therapy [1]. PCR combined with fluorescence detection is the most widely used and commercialized technique to date; however, this method requires expensive, bulky instruments, which has hindered the popularization of DNA-based diagnostics. There is a great demand for cost-effective, miniaturized DNA diagnostic sensors. Electronic detection platforms such as electrochemical or field-effect transistor sensors may be ideal, because electronic sensors do not require expensive instrumentation, and large-scale production is easy using microfabrication technology. Extensive efforts have been made to develop such DNA sensors. Two distinct approaches have been taken. In one approach, oligomers are used to mea-

sure hybridization of target DNA, while in the other, mutations are probed using enzymes recognizing single nucleotide polymorphisms (SNPs), deletions, translocations, or inversions [2, 3]. The first method (hybridization detection) using hairpin probe DNAs with redox or enzyme tags has been quite effective in development of electrochemical sensors [4–6], and most reported DNA sensors of the FET type use this method. For example, Hahm and Lieber reported real-time detection of DNA using peptide nucleic acid (PNA-) modified Si nanowire devices [7], and DNA sensors based on single-walled carbon nanotube field effect transistors (SWNT-FETs) have also been reported [8]. Silicon nanowire devices have the advantage of well-established surface chemistry techniques borrowed from the silicon industry. However, immobilization of probe molecules onto carbon nanotubes remains challenging. If probe molecules are covalently bound to the nanotubes, the carbon bonds will be broken,

thus destroying the excellent electrical transport characteristics of individual nanotubes. Thus, biosensors using SWNT-FETs bearing noncovalently attached linkers such as pyrene or CDI-Tween 20 have been developed [9, 10]. However, the successful use of noncovalent binding linkers for hydrophilic molecules such as DNA remains to be demonstrated.

Recently, Star et al. showed label-free detection of DNA hybridization using nanotube network transistors [8]. In their example, probe single-stranded DNAs (ssDNAs) were nonspecifically adsorbed onto carbon nanotubes by  $\pi$ -stacking between DNA bases and the sidewalls of SWNTs. Such nonspecifically adsorbed molecules cannot easily bind with complementary strands; it has been shown that ssDNA forms a complex with an SWNT by wrapping around the SWNT [11, 12]. Jeng et al. showed that although target DNA could hybridize with probe ssDNA on SWNTs, the process was relatively slow (13 hours at 25°C, compared to less than 10 minutes for free DNA hybridization) [13]. Therefore, an immobilization method better than that offered by simple nonspecific binding is required. To that end, we developed Au-nanoparticle-decorated SWNT-FETs as sensor platforms for label-free detection of DNA hybridization. Thiolated DNA capture probes bind to the Au nanoparticles on SWNTs, but the nanoparticles do not disturb the excellent electrical properties of SWNTs. Thus, we may covalently attach DNA capture probes and measure electrical responses upon hybridization. Metallic nanoparticles may offer a solid support for molecular recognition elements, and incorporating metal nanoparticles into SWNT sensors has been shown to effectively enhance the sensitivity [14–16].

## 2. Results and Discussion

The fabrication of devices using patterned growth techniques and the fabrication details are described in the Method section. Figure 1(a) shows an atomic force micrograph of a device decorated with Au nanoparticles. Devices with only one or two nanotubes between electrodes were used for all experiments. Figure S1(b) (in Supplementary Material available online at doi:10.1155/2011/105138) shows the change in  $I$ - $V_g$  characteristics upon Au decoration by electrochemical deposition. Several different approaches are available for Au nanoparticle decoration of SWNTs. For example, SWNTs may be decorated by chemical modification [17]. However, a “physical” decoration method is preferable. We have explored a simple evaporation method as well as spontaneous reduction [18]. With physical evaporation, nonspecific probe immobilization is problematic, and it is difficult to control Au nanoparticle size with spontaneous reduction. Therefore, we used electrochemical deposition [19–21].

Unlike the electroless deposition method, electrodeposition of Au nanoparticles does not require oxidative consumption of nanotubes. Therefore, the observed hole-doping effect may be explained by the work function difference between the metal and the SWNT. When the high-work-function metal Au ( $\approx 5.2$  eV) is brought into contact with an SWNT, electrons will be transferred from the SWNT to the Au by virtue of the work function difference [22]. One of

the advantages with metal decoration on SWNTs is that the reactions can be observed with optical microscope. A single SWNT decorated with Au nanoparticles larger than 50 nm can be directly imaged with optical microscopes, and dye molecules immobilized on Au nanoparticles can be imaged with confocal laser microscope. As shown in Figure 1(b) and Figure S2 in Supplementary Material, strong fluorescence signals observed upon Cy-3-labeled PNA binding. Usually, fluorescence signals from metal surfaces are low because of surface energy transfer [23]. The enhanced fluorescence that we observed presumably arose from coupling between Au nanoparticles [24].

As a probe, we used PNA rather than DNA. PNA is an artificially synthesized polymer similar to DNA and is used in both biological research and medical treatment [25]. Whereas DNA has a negatively charged phosphate backbone, the PNA backbone is composed of repeating N-(2-aminoethyl)-glycine units linked by peptide bonds. PNA has remarkable thermal, chemical, and enzymatic stability, and unique ionic strength effects relative to the natural analog, DNA. Hybridization of ssDNA with complementary target DNA can be performed only in an ionic environment that stabilizes the negatively charged backbones, because of Coulombic repulsion between negatively charged molecules. However, as PNA has a neutral peptide backbone, constraints on hybridization conditions are less severe than with DNA-DNA hybridization [26].

PNA probe sequences can be covalently immobilized to Au nanoparticles decorated on SWNT-FETs using Au-S binding. In our experiment, 5'-HS-GAC ATT ACT CAC C-CG-Cy3-3', with the 5' end terminated by a thiol, was used as a probe PNA, whereas 5'-CGG GTG AGT AAT GTC-3' was the target. The DNA sequences were chosen from an *Escherichia coli* library and synthesized by Bioneer Inc (Daejeon, Korea). Probe PNA solution was deposited on SWNT-FETs decorated with Au-nanoparticles and allowed to react for 6 hours in a humidified chamber at room temperature (Figure S2 in Supplementary Material). To confirm successful immobilization, Cy-3-labeled probe PNA was employed. Figures 1(a) and 1(b) show an AFM image and a confocal microscope image of an Au-decorated SWNT-FET bearing Cy-3-labeled PNA.

To measure hybridization of target DNA electronically, we first immersed the PNA-immobilized, Au-decorated SWNT-FET in DI water with an Ag/AgCl reference electrode as a liquid gate and applied bias voltages (100–300 mV) to the device with measurement of current in real time. Positive bias voltages were applied to enhance the hybridization of target DNA [27]. When device signals became stabilized, we added 5  $\mu$ L of 100 pmol/ $\mu$ L target DNA solution in DI water. Figure 2(a) shows real-time measurements from the device. A decrease in conductance was observed as soon as complementary target DNA was added. After about 20 minutes, the conductance saturated at 40% of the original value. The inset of Figure 2(a) shows an AFM image of the Au-decorated device. Figure 2(b) shows the evolution of  $I$ - $V_g$  characteristics upon immobilization of PNA and hybridization of DNA.

The original device had ambipolar characteristics, and, as is clear from the graph, the gate threshold voltage showed

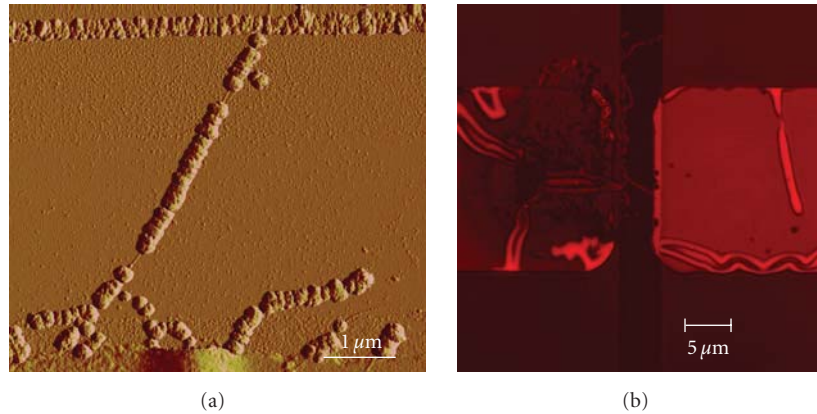


FIGURE 1: Immobilization of Cy-3-labeled probe PNA. (a) AFM image of a Au-decorated SWNT-FET. (b) Confocal micrograph of the SWNT-FET in Figure 1(a) after immobilizing Cy3-labeled probe PNA. All confocal micrographs were taken with the Zeiss LSM Exciter, with excitation at 543 nm.

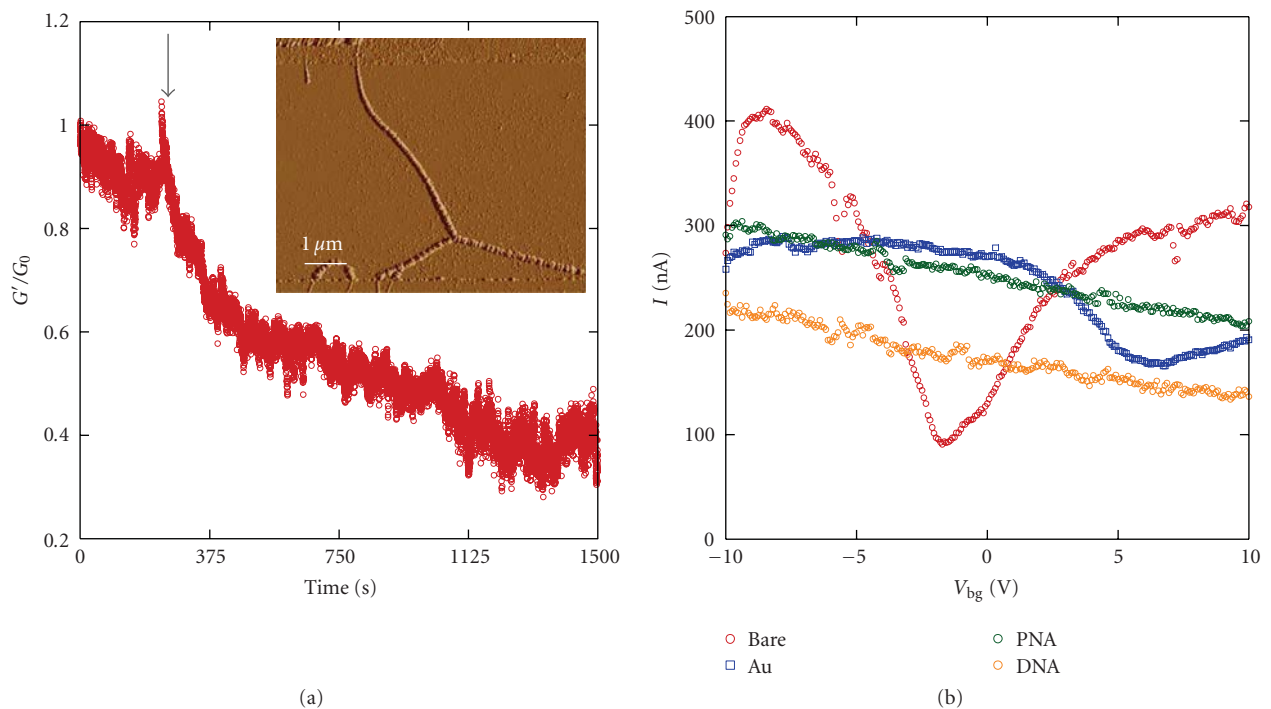


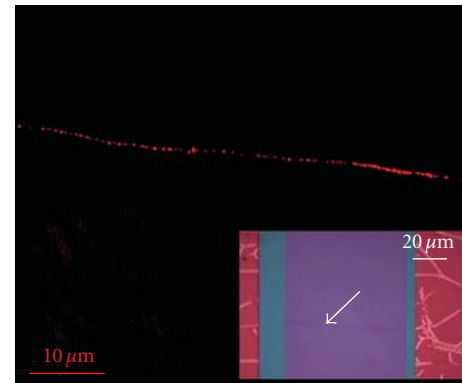
FIGURE 2: (a) The effect of hybridization on real-time conductance measured using a PNA-immobilized, Au-decorated SWNT-FET. Target DNA of a perfect match was added to the sample at the time marked with the arrow. Inset shows an AFM image of the device used for this experiment. (b) Evolution of electrical characteristics upon hybridization at  $V_{sd} = 100$  mV.

a further positive shift after Au decoration, which may be explained by the hole-doping effect of Au nanoparticles. The decrease in the on-current observed after decoration is possibly attributable to enhanced scattering at the nanotube surface [15], but the change of electrical characteristics upon Au decoration is also dependent upon decoration condition (particle size, density, etc.). Immobilization of probe PNA results in a decrease in conductance, presumably because of a reduction in the Au work function upon Au-S binding [28, 29]. However, evolution of gate threshold is not clear

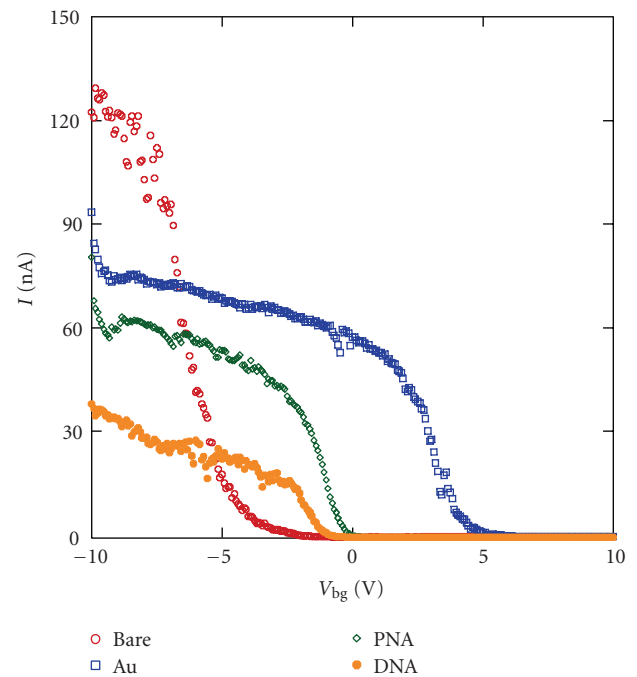
in these  $5\ \mu\text{m}$ -long channel Au-decorated SWNT-FETs after PNA immobilization. We can also consider the effect of capacitance change as a dominant mechanism behind the observed conductance change. It is known that capacitance mechanism plays a major role only in the case of nearly-full covered biomolecules [30], and we expect highly packed PNA molecules on Au nanoparticles with 6 hours incubation. Hybridization of target DNA results in a further conductance decrease, again probably arising from a drop in the Au work function upon hybridization or decreased capacitance.

Recently, lowering of the Au work function after immobilization of probe DNA and hybridization with target DNA has been observed by Kelvin probe microscopy (KPFM) [31]. Also, DNA sensors based on nanotube Schottky transistors showed decreased conductance upon hybridization related to falls in Au work function [32, 33].

To confirm that the observed change of conductance indeed originated from hybridization of target DNA, we fabricated Au-decorated ultralong SWNT-FETs. Ultralong SWNTs were grown on SiO<sub>2</sub>/Si substrates [34], and electrical leads were patterned using photolithography and liftoff. Immobilization of PNA and hybridization of DNA were performed as in the case of 5  $\mu\text{m}$ -channel devices. Figure 3(a) shows a confocal microscope image of an Au-decorated ultralong SWNT-FET after hybridization of Cy-3 labeled target DNA. Inset of Figure 3(a) is an optical micrograph of the sample, and the white arrow indicates Au-decorated SWNT. The channel length of this device is 100  $\mu\text{m}$ , and the active channel length decreased to 80  $\mu\text{m}$  after electrode passivation. Note that SWNT is visible with normal optical microscope after Au decoration. As shown in the confocal micrograph of Figure 3(a), clear fluorescence signal observed from Au nanoparticles after hybridization of Cy-3-labeled DNA. We also confirmed that hybridization occurred mainly on Au nanoparticles by using an ultralong nanotube decorated with only a few Au nanoparticles (Figure S3 in Supplementary Material). Figure 3(b) shows an evolution of gate-transfer characteristics from ultralong SWNT. Again, decoration of Au nanoparticles appears as hole doping (positive shift of gate threshold voltages), and immobilization of PNA appears as decrease of conductance as well as negative shift of gate threshold voltages. Hybridization of target DNA yields further decrease of conductance. Since the active channel length is much longer in ultralong SWNTs, we may expect that pronounced doping effect (gating effect) plays a role in them. Decrease of conductance upon hybridization of matching sequence was universal for both short-channel (5  $\mu\text{m}$ ) and long-channel (80  $\mu\text{m}$ ) devices. In Figure S4 in Supplementary Material, we showed electronic transfer characteristics of 5 different devices [(a), (b), and (c) from short-channel devices, while (d) and (e) are from long-channel devices]. As is clear from the graphs, decoration of Au nanoparticles appears as hole doping, and immobilization of probe PNA causes decrease of conductance, as well as negative shift of gate threshold voltages. Hybridization of target DNA appears as a decrease of conductance and negative shift of gate threshold voltage in all five samples, though conductance change  $\Delta I$  could vary 20~50% from different devices. To test the advantages of Au-decorated SWNT-FET, we performed the same experiment with nonspecifically bound probe PNA molecules. Bare SWNT-FET devices were incubated with PNA solution for 6 hours, and hybridization experiment was followed after thorough washing. However, devices with nonspecifically bound PNAs show little consistency. As shown in Figure S5 of Supplementary Material, 60% of the devices showed decrease of conductance, 30% of the devices did not show any change of conductance, and the rest showed increase of conductance. Since the nonspecific binding of probe PNA (DNA) depends



(a)



(b)

FIGURE 3: Hybridization of DNA on PNA-grafted, Au-decorated ultralong SWNT-FET. (a) Confocal micrograph of the Au-decorated, PNA grafted ultralong SWNT after the hybridization of Cy-3 labeled target DNA. Inset shows an optical microscope image of the device, and the white arrow indicates Au-decorated ultralong SWNT. (b) Evolution of electrical characteristics upon hybridization at  $V_{sd} = 1$  V. Clear decrease of conductance and negative shift of gate threshold voltages observed upon hybridization.

heavily on the chirality of individual nanotubes, it may be difficult to have consistency with individual SWNT devices that have random chirality.

To determine whether the Au-decorated SWNT-FET could detect an SNP, we used 5'-CGG GTG AAT AAT GTC-3' as target ssDNA. Figure 4(a) shows real-time conductance values from this experiment. In contrast to the current change seen when a perfectly matched target was added, use of target ssDNA with a single mismatch did not alter the device current. After incubation for 20 minutes, the

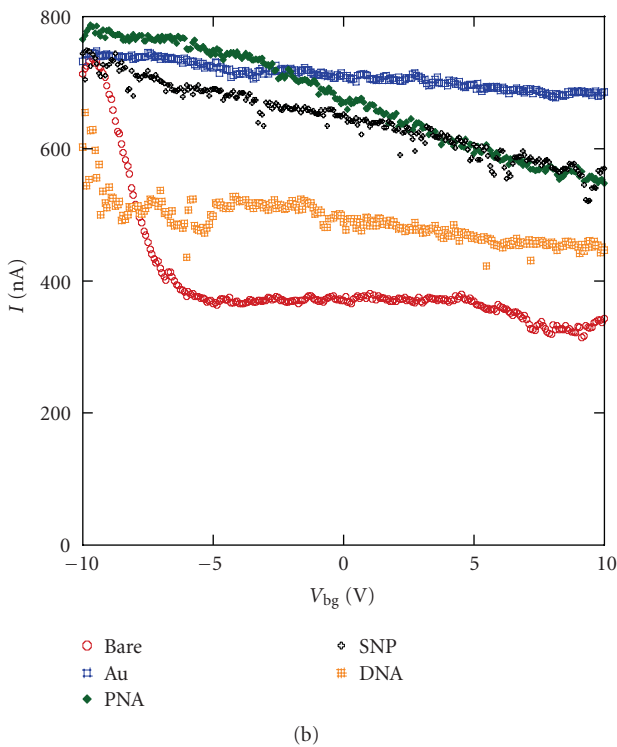
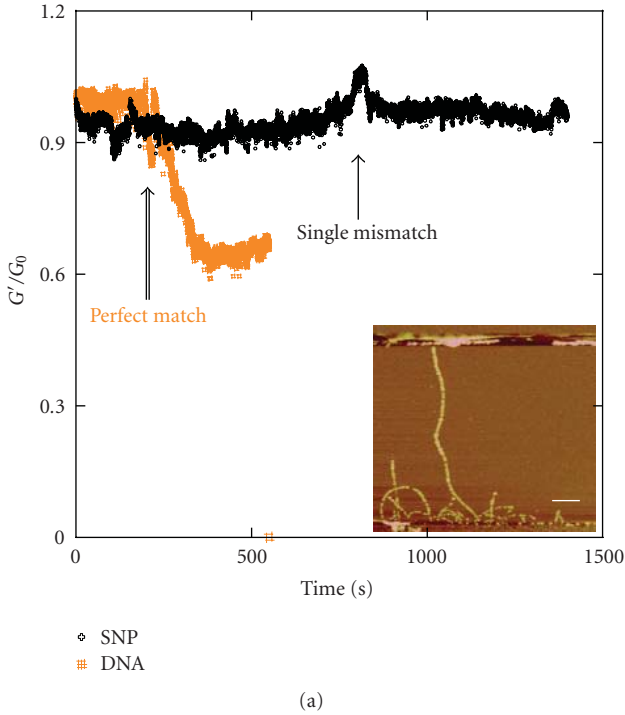


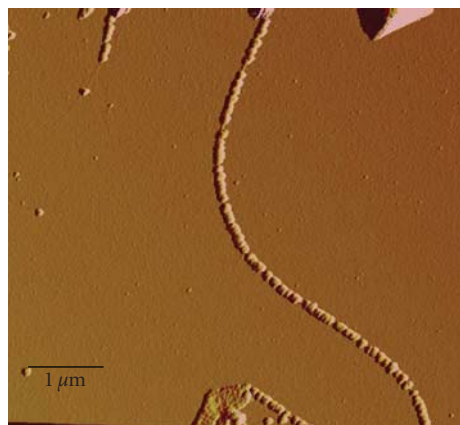
FIGURE 4: The effect of a single base mismatch. (a) Real-time conductance change upon adding target DNA with an SNP (black curve) and target ssDNA with perfect match (orange). Inset shows an AFM image of the device used for the measurement. Scale bar; 1  $\mu\text{m}$ . (b)  $I$ - $V_g$  characteristics of the device at each functionalization and hybridization step.

device was washed with an ample amount of DI water and blown dry with dry  $\text{N}_2$  gas.  $I$ - $V_g$  measurements taken after this did not show large changes either (Figure 4(b), black curve). Then, target ssDNA with perfect match was introduced to the same device baring 5  $\mu\text{L}$  DI water. As shown in Figure 4(a), clear decrease of conductance was observed upon introduction of matching DNA. Since we used the same concentration of target DNA in both SNP targets and matching targets (100 pmole/ $\mu\text{L}$ ), we may assume that observed change of conductance is not due to the change of ionic conditions or change of pH.  $I$ - $V_g$  measurement taken after washing and drying shows a clear decrease of conductance as well (Figure 4(b), orange curve).

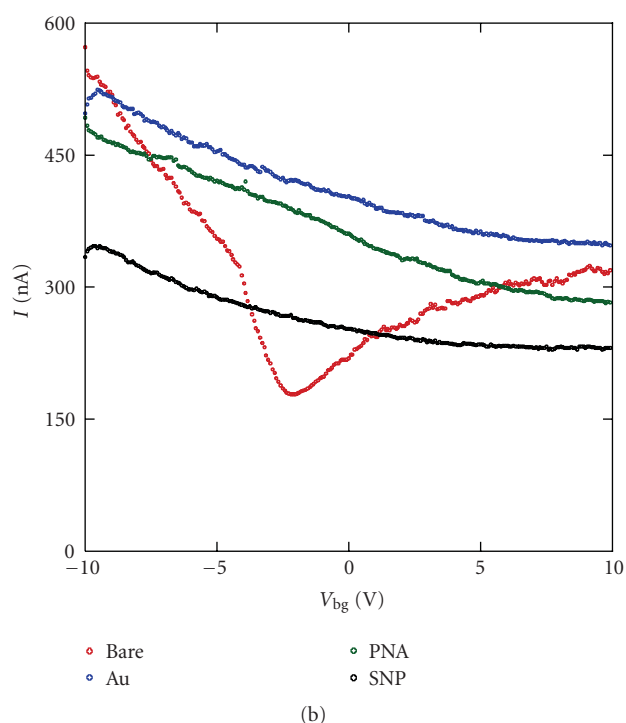
We next employed a hybrid buffer to improve hybridization between probe PNA and target DNA sequence with an SNP to determine whether a single mismatch could really alter electrical characteristics. The hybrid buffer was 3 M NaCl, 10 mM ethylenediaminetetraacetic acid (EDTA), and 380 mM 4-(2-hydroxyethyl)-1-piperazineethanesulfonic acid (HEPES). Target DNA oligomers in the hybridization buffer were allowed to react with PNAs immobilized on Au-decorated SWNT-FETs for 20 minutes. The chip was then washed with an ample amount of DI water to eliminate nonspecific binding and blown dry with  $\text{N}_2$  prior to further electrical characterization. We did not measure real-time changes in conductance as the high salt concentration of hybrid buffer made such assessment impossible. Figure 5(b) shows  $I$ - $V_g$  characteristics of the device before and after hybridization. In contrast to the absence of  $I$ - $V_g$  characteristic changes after hybridization in DI water, a clear decrease of conductance was observed after reaction in the hybrid buffer, as seen when sequences matched perfectly.

We thus conclude that the observed single-base mismatch discrimination shown by our device is likely not attributable to an SNP charge effect, as is the case in strain sensors [35, 36], but rather because hybridization of the SNP target is more difficult in DI water. To verify this, we labeled target SNP-bearing ssDNA with Cy-3 and hybridized this material to PNAs immobilized on Au-decorated SWNT-FETs in DI water for 20 minutes. No fluorescent signal was seen, in contrast to the result when perfectly matched target DNA was used for hybridization (data not shown). Park et al. have shown that ionic strength can affect PNA-DNA surface hybridization, although the influence of ionic strength is not as great as seen with DNA-DNA hybridization [37]. As we expect that probe PNAs are fully packed on Au nanoparticles, hybridizing sequences can communicate electrostatically with their neighbors, thereby hindering the hybridization of mismatched sequences.

In summary, we combined electrical transport in Au-decorated SWNT-FET with confocal microscopy to measure hybridization of target ssDNA with PNAs. Uniform-sized Au nanoparticles were formed on sidewalls of SWNTs by electrochemical deposition, and the effect of Au-decoration appears as hole doping in most cases. By addition of thiolated PNA probes to such a device, we achieved stable immobilization of molecular recognition elements with minimal effects on electrical properties. Hybridization of complementary DNA



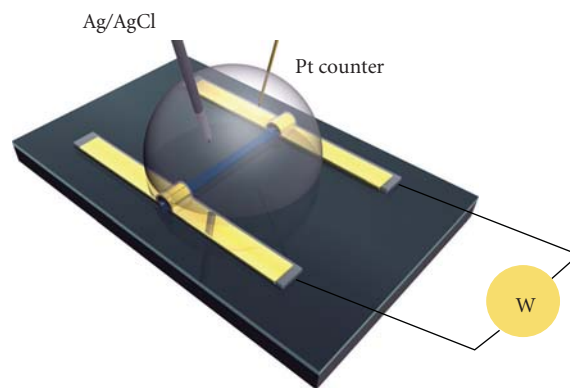
(a)



(b)

FIGURE 5: The effect of ionic concentration on target DNA hybridization when a single mismatch was present. (a) Atomic force micrograph of the Au-decorated device; (b)  $I$ - $V_g$  characteristics of the device at each functionalization and hybridization step.

in DI water resulted in a decrease in real-time conductance, and we confirmed that hybridization has indeed occurred on Au nanoparticles by measuring fluorescence signal from Cy-3-labeled target DNA. In contrast, introduction of SNP target yields negligible change of conductance in DI water. However, clear decrease of conductance observed when hybridization with SNP target is performed in hybridization buffer; SNP target is indiscernible from perfect match in high ionic conditions. Therefore, we may conclude that hybridization of mismatched DNA with PNA immobilized on nanoscale surfaces is difficult in low ionic conditions, at least in the timescale of 20 minutes.



SCHEME 1: Schematic diagram for Au decoration of SWNT-FETs.

### 3. Experiments

**3.1. Device Fabrication.** SWNTs were grown on a Si/SiO<sub>2</sub> substrate using a patterned chemical vapor deposition (CVD). Liquid catalyst consists of Fe(NO<sub>3</sub>)<sub>2</sub>·9H<sub>2</sub>O, and Mo(acac)<sub>2</sub> in methanol was dispersed on substrates with patterned poly(methyl metacrylate). After liftoff, SWNT growth was carried out in 900°C-heated furnace for 10 minutes with CH<sub>4</sub> or ethanol as a carbon source. To grow ultralong SWNTs, 0.5 M FeCl<sub>3</sub> in DI water was placed at the edge of the sample. Ethanol was used as a carbon source, and the growth was carried out at 970°C for 20~30 minutes. Patterns for electrical leads were formed by photolithography, followed by thermal evaporation of Ti and Au. For real-time characterization and metal decoration, all electrodes were insulated with SiO<sub>x</sub> or SU8-2000.5 negative photoresist.

**3.2. Au Decoration.** By cyclic voltammetry or chronoamperometry, it is possible to control both Au nanoparticle size and packing density. Scheme 1 shows a schematic diagram of our Au-decoration process. A droplet of 100 μM HAuCl<sub>4</sub> in 100 mM KCl (supporting electrolyte) was placed on the device, both source and drain electrodes were used as working electrodes, and a reduction potential was applied with respect to the Ag/AgCl reference electrode with current monitoring using a Pt counter electrode. We found that cyclic voltammetry afforded better decoration control than did chronoamperometry. Uniform 20- to 60-nm-sized Au nanoparticles were formed on SWNTs by sweeping the potential from -0.2 V to 0.6 V.

### Supporting Information Available

Optical microscope images and AFM images of Au-decorated CNT and electrical transport that show the effect of Au decoration, confocal micrographs showing Cy-3-labeled probe PNA immobilization condition, both a confocal micrograph and a scanning electron micrograph of Au-decorated ultralong nanotubes after Cy3-labeled DNA hybridization, Electronic transfer characteristics of 5 different devices upon hybridization of DNA, and statistic of SWNT-FETs with nonspecifically bound PNA after the hybridization of matching DNA.

## Acknowledgments

Financial support was obtained from the Korea Research Council for Industrial Science and Technology, and Ministry of Environment as “The Eco-technopia 21 project.” The authors thank Professor Hee Chul Choi and his group members for valuable discussion and assistance during this work and Professor Jing Kong’s group for their help in growing ultralong nanotubes.

## References

- [1] S. J. Welsh and G. Powis, “Toward personalized therapy for cancer,” in *Current Clinical Oncology: Targeted Cancer Therapy*, R. Kurzrock and M. Markman, Eds., pp. 411–412, Humana Press, Totowa, NJ, USA, 2008.
- [2] F. Patolsky, A. Lichtenstein, and I. Willner, “Detection of single-base DNA mutations by enzyme-amplified electronic transduction,” *Nature Biotechnology*, vol. 19, no. 3, pp. 253–257, 2001.
- [3] F. Pouthas, C. Gentil, D. Côte, and U. Bockelmann, “DNA detection on transistor arrays following mutation-specific enzymatic amplification,” *Applied Physics Letters*, vol. 84, no. 9, pp. 1594–1596, 2004.
- [4] Y. Xiao, X. Qu, K. W. Plaxco, and A. J. Heeger, “Label-free electrochemical detection of DNA in blood serum via target-induced resolution of an electrode-bound DNA pseudoknot,” *Journal of the American Chemical Society*, vol. 129, no. 39, pp. 11896–11897, 2007.
- [5] G. Liu, Y. Wan, V. Gau et al., “An enzyme-based E-DNA sensor for sequence-specific detection of femtomolar DNA targets,” *Journal of the American Chemical Society*, vol. 130, no. 21, pp. 6820–6825, 2008.
- [6] Z. Li, Y. Chen, X. Li, T. I. Kamins, K. Nauka, and R. S. Williams, “Sequence-specific label-free DNA sensors based on silicon nanowires,” *Nano Letters*, vol. 4, no. 2, pp. 245–247, 2004.
- [7] J.-I. Hahn and C. M. Lieber, “Direct ultrasensitive electrical detection of DNA and DNA sequence variations using nanowire nanosensors,” *Nano Letters*, vol. 4, no. 1, pp. 51–54, 2004.
- [8] A. Star, E. Tu, J. Niemann, J.-C. P. Gabriel, C. S. Joiner, and C. Valcke, “Label-free detection of DNA hybridization using carbon nanotube network field-effect transistors,” *Proceedings of the National Academy of Sciences of the United States of America*, vol. 103, no. 4, pp. 921–926, 2006.
- [9] K. Besteman, J.-O. Lee, F. G. M. Wiertz, H. A. Heering, and C. Dekker, “Enzyme-coated carbon nanotubes as single-molecule biosensors,” *Nano Letters*, vol. 3, no. 6, pp. 727–730, 2003.
- [10] H.-M. So, K. Won, Y. H. Kim et al., “Single-walled carbon nanotube biosensors using aptamers as molecular recognition elements,” *Journal of the American Chemical Society*, vol. 127, no. 34, pp. 11906–11907, 2005.
- [11] M. Zheng, A. Jagota, E. D. Semke et al., “DNA-assisted dispersion and separation of carbon nanotubes,” *Nature Materials*, vol. 2, no. 5, pp. 338–342, 2003.
- [12] W. Zhao, Y. Gao, M. A. Brook, and Y. Li, “Wrapping single-walled carbon nanotubes with long single-stranded DNA molecules produced by rolling circle amplification,” *Chemical Communications*, no. 34, pp. 3582–3584, 2006.
- [13] E. S. Jeng, A. E. Moll, A. C. Roy, J. B. Gastala, and M. S. Strano, “Detection of DNA hybridization using the near-infrared band-gap fluorescence of single-walled carbon nanotubes,” *Nano Letters*, vol. 6, no. 3, pp. 371–375, 2006.
- [14] B.-K. Kim, N. Park, P. S. Na et al., “The effect of metal cluster coatings on carbon nanotubes,” *Nanotechnology*, vol. 17, no. 2, pp. 496–500, 2006.
- [15] D. R. Kauffman and A. Star, “Chemically induced potential barriers at the carbon nanotube-metal nanoparticle interface,” *Nano Letters*, vol. 7, no. 7, pp. 1863–1868, 2007.
- [16] H. R. Byon and H. C. Choi, “Network single-walled carbon nanotube-field effect transistors (SWNT-FETs) with increased schottky contact area for highly sensitive biosensor applications,” *Journal of the American Chemical Society*, vol. 128, no. 7, pp. 2188–2189, 2006.
- [17] V. Georgakilas, D. Gournis, V. Tzitzios, L. Pasquato, D. M. Guldi, and M. Prato, “Decorating carbon nanotubes with metal or semiconductor nanoparticles,” *Journal of Materials Chemistry*, vol. 17, no. 26, pp. 2679–2694, 2007.
- [18] H. C. Choi, M. Shim, S. Bangsaruntip, and H. Dai, “Spontaneous reduction of metal ions on the sidewalls of carbon nanotubes,” *Journal of the American Chemical Society*, vol. 124, no. 31, pp. 9058–9059, 2002.
- [19] B. M. Quinn, C. Dekker, and S. G. Lemay, “Electrodeposition of noble metal nanoparticles on carbon nanotubes,” *Journal of the American Chemical Society*, vol. 127, no. 17, pp. 6146–6147, 2005.
- [20] B. M. Quinn and S. G. Lemay, “Single-walled carbon nanotubes as templates and interconnects for nanoelectrodes,” *Advanced Materials*, vol. 18, no. 7, pp. 855–859, 2006.
- [21] Y.-S. Lo, D. H. Nam, H.-M. So et al., “Oriented immobilization of antibody fragments on ni-decorated single-walled carbon nanotube devices,” *ACS Nano*, vol. 3, no. 11, pp. 3649–3655, 2009.
- [22] D. S. Kim, T. Lee, and K. E. Geckeler, “Hole-doped single-walled carbon nanotubes: ornamenting with gold nanoparticles in water,” *Angewandte Chemie*, vol. 45, no. 1, pp. 104–107, 2005.
- [23] S. Huang and Y. Chen, “Ultrasensitive fluorescence detection of single protein molecules manipulated electrically on Au nanowire,” *Nano Letters*, vol. 8, no. 9, pp. 2829–2833, 2008.
- [24] J. Zhang, Y. Fu, M. H. Chowdhury, and J. R. Lakowicz, “Metal-enhanced single-molecule fluorescence on silver particle monomer and dimer: coupling effect between metal particles,” *Nano Letters*, vol. 7, no. 7, pp. 2101–2107, 2007.
- [25] S. Shakeel, S. Karim, and A. Ali, “Peptide nucleic acid (PNA)—a review,” *Journal of Chemical Technology and Biotechnology*, vol. 81, no. 6, pp. 892–899, 2006.
- [26] J. Wang, “DNA biosensors based on peptide nucleic acid (PNA) recognition layers. A review,” *Biosensors and Bioelectronics*, vol. 13, no. 7–8, pp. 757–762, 1998.
- [27] I. Y. Wong and N. A. Melosh, “Directed hybridization and melting of DNA linkers using counterion-screened electric fields,” *Nano Letters*, vol. 9, no. 10, pp. 3521–3526, 2009.
- [28] P. C. Rusu and G. Brocks, “Surface dipoles and work functions of alkythiolates and fluorinated alkythiolates on Au(111),” *Journal of Physical Chemistry B*, vol. 110, no. 45, pp. 22628–22634, 2006.
- [29] B.-K. Kim, J.-J. Kim, H.-M. So et al., “Carbon nanotube diode fabricated by contact engineering with self-assembled molecules,” *Applied Physics Letters*, vol. 89, no. 24, Article ID 243115, 2006.

- [30] I. Heller, A. M. Janssens, J. Männik, E. D. Minot, S. G. Lemay, and C. Dekker, "Identifying the mechanism of biosensing with carbon nanotube transistors," *Nano Letters*, vol. 8, no. 2, pp. 591–595, 2008.
- [31] D. C. Hansen, K. M. Hansen, T. L. Ferrell, and T. Thundat, "Discerning biomolecular interactions using Kelvin probe technology," *Langmuir*, vol. 19, no. 18, pp. 7514–7520, 2003.
- [32] X. Tang, S. Bansaruntip, N. Nakayama, E. Yenilmez, Y.-I. Chang, and Q. Wang, "Carbon nanotube DNA sensor and sensing mechanism," *Nano Letters*, vol. 6, no. 8, pp. 1632–1636, 2006.
- [33] E. L. Gui, L.-J. Li, K. Zhang et al., "DNA sensing by field-effect transistors based on networks of carbon nanotubes," *Journal of the American Chemical Society*, vol. 129, no. 46, pp. 14427–14432, 2007.
- [34] A. Reina, M. Hofmann, D. Zhu, and J. Kong, "Growth mechanism of long and horizontally aligned carbon nanotubes by chemical vapor deposition," *Journal of Physical Chemistry C*, vol. 111, no. 20, pp. 7292–7297, 2007.
- [35] J. Mertens, C. Rogero, M. Calleja et al., "Label-free detection of DNA hybridization based on hydration-induced tension in nucleic acid films," *Nature Nanotechnology*, vol. 3, no. 5, pp. 301–307, 2008.
- [36] M. Cha, J. Shin, J.-H. Kim et al., "Biomolecular detection with a thin membrane transducer," *Lab on a Chip*, vol. 8, no. 6, pp. 932–937, 2008.
- [37] H. Park, A. Germini, S. Sforza, R. Corradini, R. Marchelli, and W. Knoll, "Effect of ionic strength on PNA-DNA hybridization on surfaces and in solution," *Biointerphases*, vol. 2, no. 2, pp. 80–88, 2007.

## Letter to the Editor

# Study of Mg Powder as Catalyst Carrier for the Carbon Nanotube Growth by CVD

Jianli Kang,<sup>1,2</sup> Jiajun Li,<sup>3</sup> Naiqin Zhao,<sup>3,4</sup> Philip Nash,<sup>5</sup> Chunsheng Shi,<sup>3</sup> and Ronglu Sun<sup>1,2</sup>

<sup>1</sup> School of Mechanical and Electronic Engineering, Tianjin Polytechnic University, Tianjin 300160, China

<sup>2</sup> Advanced Mechatronics Equipment Technology Tianjin Area Major Laboratory, Tianjin 300160, China

<sup>3</sup> School of Materials Science and Engineering, Tianjin University, Tianjin 300072, China

<sup>4</sup> State Key Laboratory of Metal Matrix Composites, Shanghai Jiaotong University, Shanghai 200240, China

<sup>5</sup> Thermal Processing Technology Center, Illinois Institute of Technology, Chicago, IL 60616, USA

Correspondence should be addressed to Jianli Kang, kangjianli@yahoo.com.cn

Received 26 May 2010; Accepted 3 September 2010

Copyright © 2011 Jianli Kang et al. This is an open access article distributed under the Creative Commons Attribution License, which permits unrestricted use, distribution, and reproduction in any medium, provided the original work is properly cited.

The possibility of using magnesium powder as catalyst carrier for carbon nanotube growth by chemical vapor deposition, which may pave a new way to in situ fabricate CNT/Mg composites with high CNT dispersion, was investigated for the first time. The fabrication process of the catalyst supported on Mg powder involves the preparation of colloid by a deposition-precipitation method, followed by calcination and reduction. The results show that the interaction between catalyst and support plays an important role for the catalytic property of the catalyst. Ni alloyed with Mg shows no activity for the decomposition of methane. The introduction of Y in Ni/Mg catalyst can promote the reaction temperature between Ni and Mg and thus enhance the activity of the catalyst. A large amount of carbon nanotubes (CNTs) with an average diameter of 20 nm was obtained using Ni/Y/Mg catalyst at 450°C, while only a few short CNTs were obtained using Ni/Mg catalyst due to the low activity of the catalyst at lower temperature.

## 1. Introduction

Since the first observation of carbon nanotubes (CNTs) [1], extensive experimental and theoretical researches have been performed to exploit their properties and applications [2, 3]. The experimental and theoretical studies on the mechanical properties of CNTs predict them to be amongst the strongest materials. The elastic modulus of CNTs is comparable to that of diamond, and their tensile strength is about 100 times than that of steel. Therefore, the CNT as reinforcement in the composites is an obvious choice. Although the CNT/polymer composites exhibit a tremendous strengthening effect for the composites [4, 5], the issues of CNT dispersion in metal matrix and nanotube/matrix interaction factors are still very complex and have not been solved for the moment [6, 7]. In order to solve these issues, the authors have attempted to use metal powders as catalyst carrier to in situ obtain CNT/metal composite powders and have successfully performed in Al and Cu composites [8–10], which exhibit a higher advantage

than traditional methods. The key issues for this novel process are to prepare effective catalyst supported on metal powders and synthesize CNTs with controllable conditions.

Mg and its alloys are increasingly used in engineering structures due to their high specific strength. Effort has been made to increase the specific strength further through use of suitable reinforcements such as carbon nanotubes (CNTs), and the CNTs were found to improve the properties of the alloy significantly [11, 12]. In the present work, the possibility of using magnesium powder as catalyst carrier for the carbon nanotube growth by chemical vapor deposition (CVD) was investigated for the first time, which may pave a new way to fabricate CNT/Mg composites. Although it has been reported that nano-intermetallic alloy, MgNi, can be used as catalyst for the CNT growth, a little amount of Mg element is simply used to prevent the catalyst thermal aggregation [13]. The effect of Mg and its interaction with the catalyst (Ni) on the carbon nanotube growth is still unclear. In this paper, the effect of the reaction between the

TABLE 1: The parameters of the CNT growth by CVD.

Catalyst	Reducing temperature (°C)	Reducing time (h)	Growth temperature (°C)	Growth time (h)
10%Ni/Mg	400	5	400	1
	450	2	450	1
	500	2	500	1
16%Ni4%Y/Mg	450	2	450	1
	500	2	500	1
	500	2	600	1

carrier (Mg) and catalyst (Ni or Ni/Y) on the CNT growth was investigated systematically.

## 2. Experimental

**2.1. Preparation of the Catalyst.** The magnesium-carried Ni/Y catalyst was prepared by deposition-precipitation. For a typical process, the right amounts of Mg powder (8 g) and NaOH (2.721 g, 98.0% purity) were mixed in 500 mL distilled water. Ni(NO<sub>3</sub>)<sub>2</sub>·6H<sub>2</sub>O (7.926 g, 98.0% purity) and Y(NO<sub>3</sub>)<sub>3</sub>·6H<sub>2</sub>O (1.723 g, 98.0% purity) were dissolved in 300 mL distilled water and added to the previous mixture dropwise with constant stirring. The coprecipitate was then aged, washed several times, and dried at 100°C in Ar (99.9% purity). Then, the ternary colloid was calcined in Ar atmosphere at 250°C and 400°C consecutively for 2 hours each time to form the Ni/Y/Mg catalyst precursor, which would be employed in the following catalytic synthesis experiments. For comparison, 10%Ni/Mg catalyst was prepared using the same process.

**2.2. Synthesis of Carbon Nanotubes.** The catalyst of 0.5 g was kept in a quartz boat and placed in a horizontal quartz tube reactor. The quartz tube, mounted in an electrical tube furnace, was heated to reduction temperature in an Ar atmosphere. Then the hydrogen (100 mL/min, 99.9% purity) was introduced to reduce the catalyst. Subsequently, the hydrogen flow was shut off, and the quartz tube was heated again to the reaction temperature in an Ar atmosphere. A mixture of CH<sub>4</sub>/Ar (100/300 mL/min, v/v) was introduced into the quartz tube for 60 minutes. The parameter details are listed in Table 1. Finally, the system was cooled to the room temperature under Ar.

**2.3. Characterization of the Catalyst and Carbon Nanotubes.** The catalysts and products by CVD were characterized by an X-ray diffractometer (XRD, Rigaku D/max 2500 V/pc), scanning electron microscope (SEM, JEOL JSM-T330 and JSM-6700F), and high-resolution transmission electron microscope (HRTEM, PHILIPS TECNAI G2 F20).

## 3. Results and Discussion

Figure 1 shows the XRD analysis of the 10%Ni/Mg catalyst and reaction products by CVD. It can be seen that there are several weak peaks, apart from that corresponding to Mg in

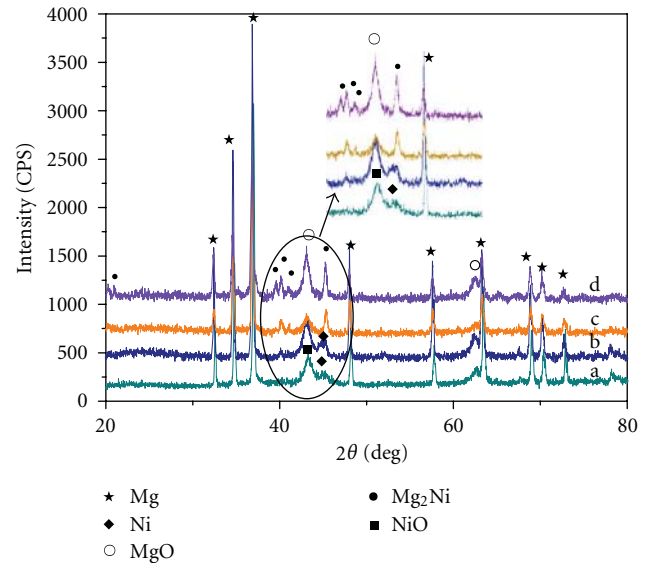
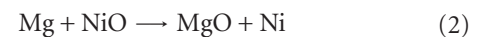
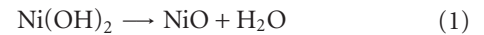


FIGURE 1: XRD analysis of the 10%Ni/Mg catalyst precursor after calcination (a) and reaction products by CVD at 400°C (b), 450°C (c), and 500°C (d).

the XRD pattern of the catalyst precursor after calcination (Figure 1(a)). The peak at 43.335° is very similar to that of Ni. However, there is no reductive gas during the calcination process. The possible reactions during this process are as follows:



Thus, the formation of Ni during calcination process simultaneously produces MgO. It is known that the peaks of NiO (43.095°) and MgO (42.916°) are very close. The broad peak near 43° may be indicated to the existence of MgO or NiO. In order to identify the peak near 43°, the samples were calcined for a longer time or reduced by H<sub>2</sub>. The XRD analysis shows that the peak near 43° had no obvious changes (not shown here), proving the existence of MgO, and the reaction equations of (1) and (2) were reasonable. After reduction and reaction at 400°C, the peaks of Ni phase still exist. However, the phases of the samples became more complex when the temperatures were above 450°C. From the binary phase diagram of Ni and Mg, it is known that Ni can react with Mg and result in Mg<sub>2</sub>Ni at 506°C. However,

when the sample was reduced and reacted at 450 °C, there were no obvious peaks related to Ni, and some other peaks appeared, which should be responsible to Mg<sub>2</sub>Ni, apart from that related to Mg and MgO. This may be due to the effect of nanosize level of Ni particles that promote the activity of Ni phase. The peaks between 37°–40° (indicated by black dots in Figure 1) proved the formation of Mg<sub>2</sub>Ni. The peak near 45° is corresponding to the (203) peak of Mg<sub>2</sub>Ni. In all the 10%Ni/Mg samples, there are almost no obvious C peaks observed.

Figure 2 shows the XRD analysis of the 16%Ni4%Y/Mg catalyst and reaction products by CVD. From the XRD pattern of the catalyst precursor after calcination (Figure 2(a)), we can see that there are no obvious peaks corresponding to Ni, inferring that yttria doped in NiO can stabilize the structure of NiO. Meanwhile, when the reduction and reaction temperatures were performed at 450 °C, carbon peaks were obviously observed and no Mg<sub>2</sub>Ni peaks appeared (Figure 2(b)). However, the peaks near 43° still existed. This may be due to either incompletely reduction of NiO or the existence of MgO. In order to distinguish this, the same catalyst was reduced at 400 °C for different times and reacted at 450 °C. As shown in Figure 3, the peak near 43° had almost no change and existed even in the sample that reduced for 5 hours, inferring that this peak was not related to NiO. The existence of MgO peaks indicated that the raw Mg was in some sort oxidized during the process due to the pure Mg with highly active chemical property. The peak intensity of MgO increased with the reaction temperature arose, further indicating that active Mg reacted with oxygen even in Ar at high temperature. When the sample was reduced and reacted at 450 °C, the peaks of Mg<sub>2</sub>Ni appeared (in Figure 2(c)). With the temperature increasing, there are no C and Ni peaks detected. At 600 °C, Mg reacted with Ni almost completely. Another alloy, Mg<sub>6</sub>Ni, was detected apart from Mg<sub>2</sub>Ni (Figure 2(d)).

The morphologies of the products obtained by CVD were characterized by SEM and TEM. From Figures 4(a) and 4(b), it can be seen that some very short CNTs are obtained by CVD at 400 °C using Ni/Mg catalyst, and all catalyst nanoparticles are located on the top of the CNTs (indicated by arrows in Figure 4(b)), inferring that “top-growth mode” is suitable for this experiment. However, the activity of the catalyst is very low due to the lower reaction temperatures (only about 1 wt.% of carbon deposit was obtained, which may be the cause why XRD could not detect the existence of carbon). With the reaction temperature increasing, there is almost no obvious carbon deposit observed by SEM and TEM. Furthermore, the catalyst particles become larger and joint together (Figures 4(c) and 4(d)), compared with the catalyst nanoparticles located on the top of CNTs in Figure 4(b)). Combined with the XRD results (Figure 1), it can be concluded that Ni nanoparticles begin to react with Mg and lose their catalytic activity at and above 450 °C.

Figure 5(a) shows the low-magnification SEM image of the product obtained at 450 °C using Ni/Y/Mg catalyst. Almost all the Mg particles were covered by a dense CNT coating. Figure 5(b) is the high-magnification SEM image of the CNTs at 450 °C. It can be seen that the CNTs with an

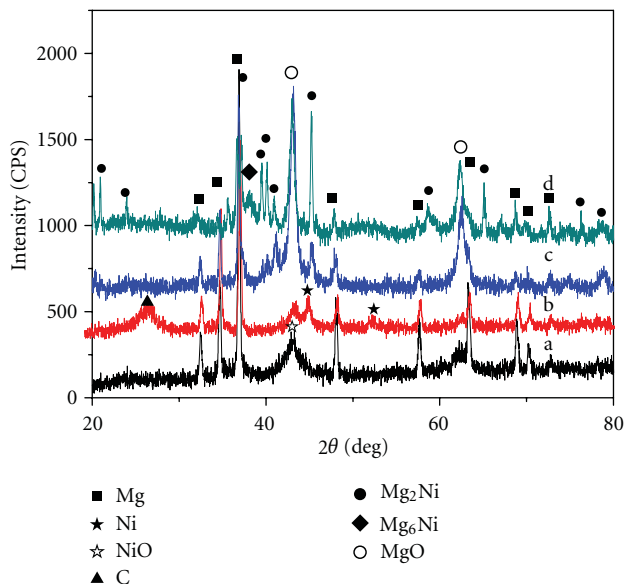


FIGURE 2: XRD images of the 16%Ni4%Y/Mg catalyst precursor after calcination (a) and reaction products by CVD at 450 °C (b), 500 °C (c), and 600 °C (d).

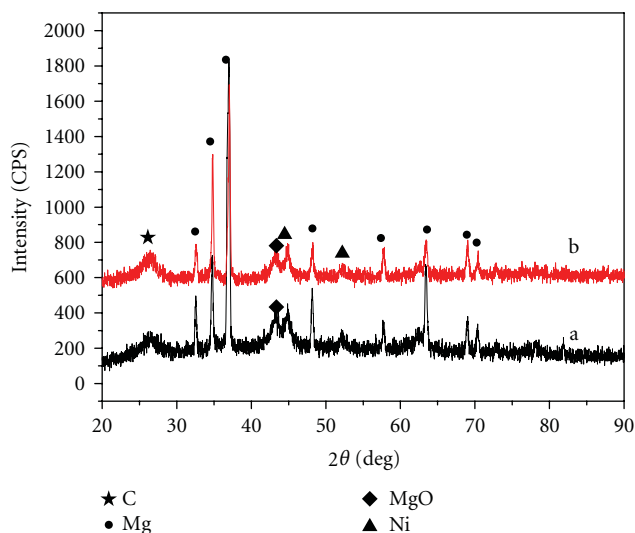


FIGURE 3: XRD images of and reaction products by CVD using the 16%Ni4%Y/Mg catalyst reduced for 3 hours (a), 5 hours (b).

average diameter of 20 nm were also grown based on “top-growth mode” (indicated by arrows). TEM images of the CNTs indicate that the structure of the CNT is herringbone or bamboo-shaped (Figures 5(c) and 5(d)). At 500 °C, there were no CNTs formed instead of big particles (Figure 5(e)), similar to that obtained at 450 °C using 10%Ni/Mg. When the reaction temperature increased to 600 °C, Ni reacted with Mg completely and formed two phases: Mg<sub>2</sub>Ni and Mg<sub>6</sub>Ni. SEM images of the products show that the surface morphologies of the product obtained become petaline nanosheets (Figure 5(f)).

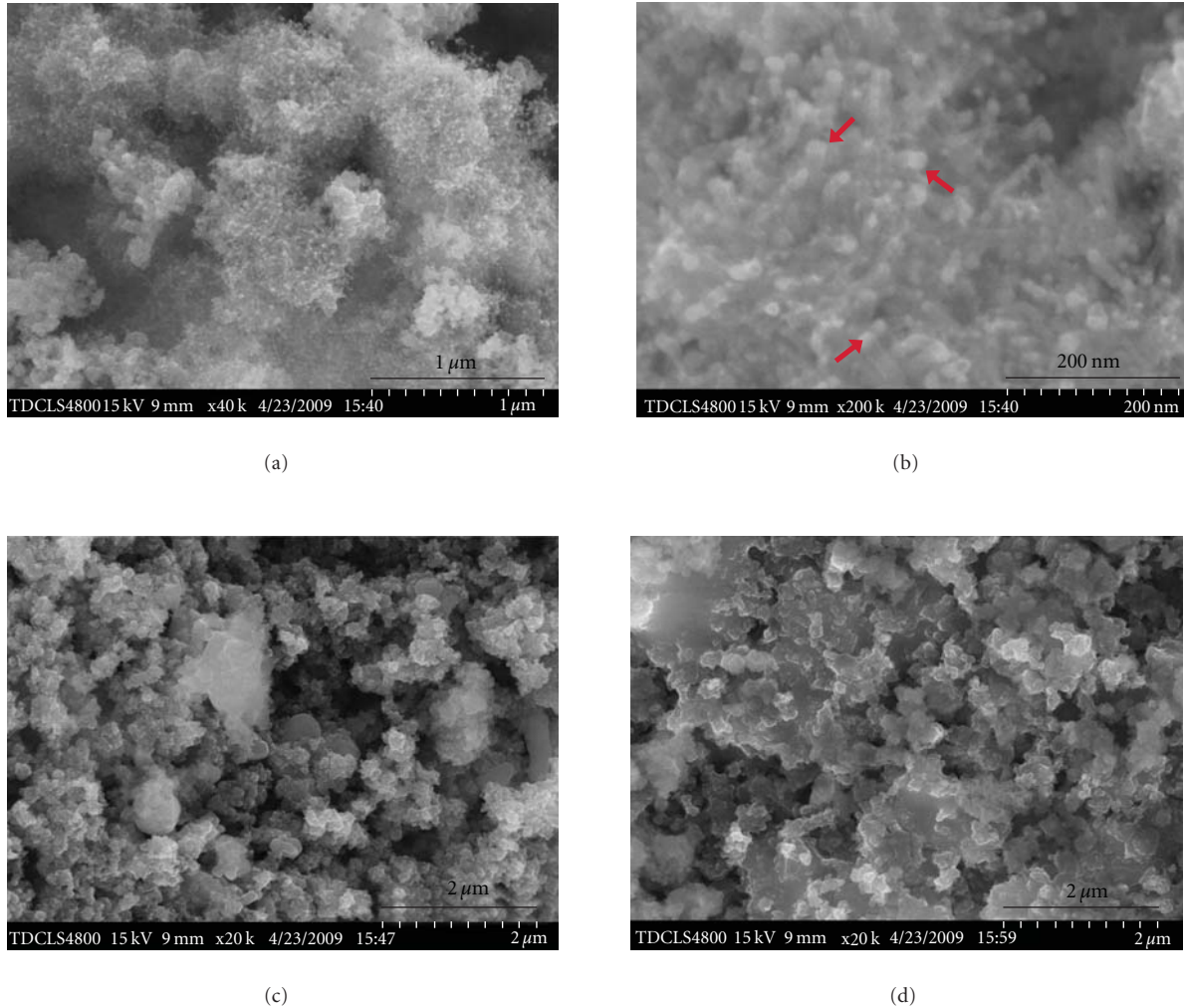


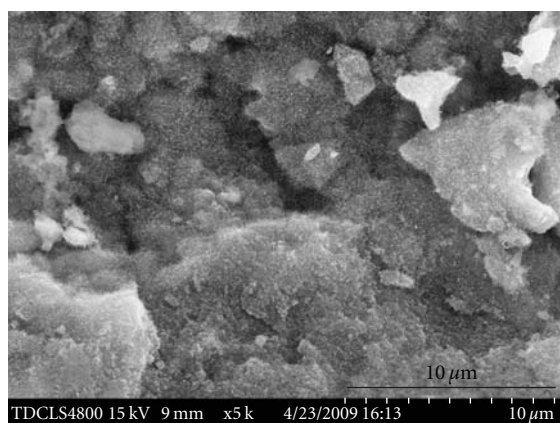
FIGURE 4: SEM images of the products obtained by CVD at different conditions using 10%Ni/Mg catalyst (a, b) at 400°C (c) at 450°C (d) at 500°C.

Based on the above analysis, it is obvious that the reaction between catalyst and support play an important role for the activity of the catalyst. Ni alloyed with Mg has no activity for the decomposition of methane. Thus, the key issue to use Mg as catalyst support is to prevent the reaction between Ni and Mg. Although Ni can be used as catalyst directly, the low activity of the catalyst will limit its further application in composite fabrication process. Preliminary results show that Y doped in Ni can elevate the reaction temperature between Ni and Mg0020 and promote the activity of the catalyst (52.3 wt.% carbon deposit obtained using Ni/Y catalyst compared to the mass of the raw catalyst, while only about 1 wt.% carbon deposit obtained using Ni catalyst). Thus, it is possible to obtain dispersed CNTs with higher quantity and quality using less Ni/Y catalyst supported on Mg powder by optimizing the process parameters. Mg oxidation can be reduced to a minimum content, which has little influence on the property of Mg composites, by using inert gas with higher purity and other solutions instead of water (to avoid the possible reaction between water and Mg). Thus, it is

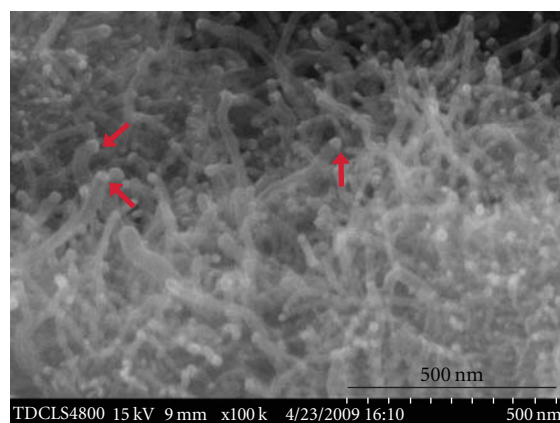
reasonable to prepare CNT/Mg composites with high CNT dispersion using the in situ synthesized CNT-Mg composite powders. Such work is in process.

#### 4. Conclusions

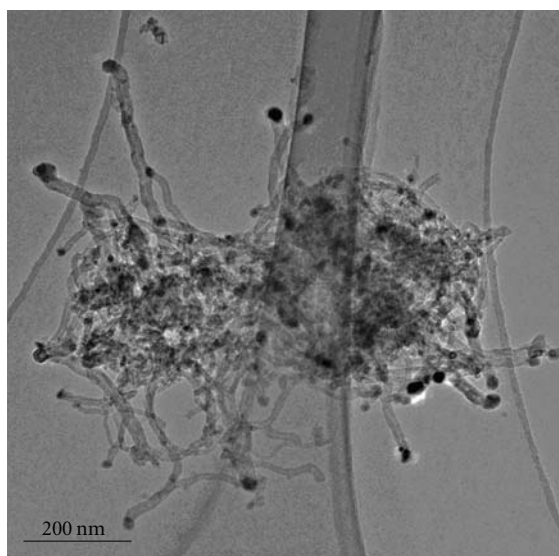
The present paper demonstrates that Mg powder can be used as a suitable catalyst carrier for the CNT growth by CVD. However, the chemical interactions between the catalyst and substrate should be avoided, because any Ni alloy with Mg demonstrates no activity for the decomposition of methane. The introduction of Y in Ni/Mg catalyst can promote the reaction temperature between Ni and Mg and thus enhance the activity of the catalyst. A large amount of CNTs with an average diameter of 20 nm was obtained by CVD using Ni/Y/Mg catalyst at 450°C, while only a few short CNTs were obtained using Ni/Mg catalyst due to the too low activity of the catalyst at lower temperature.



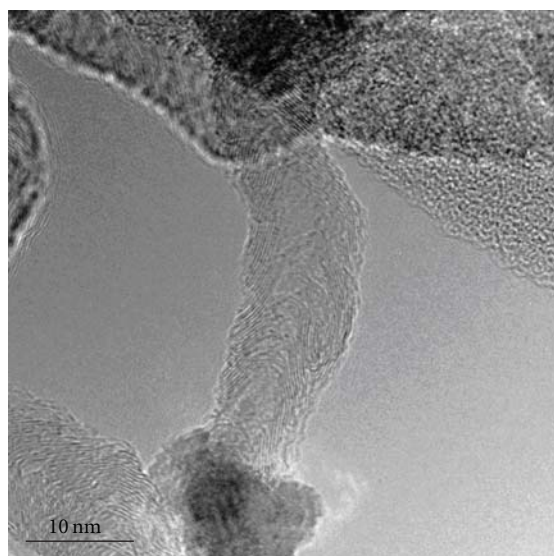
(a)



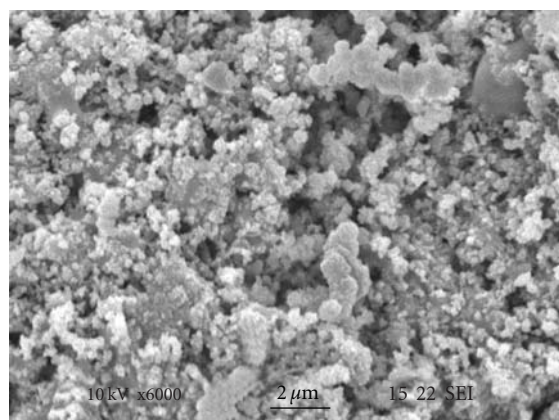
(b)



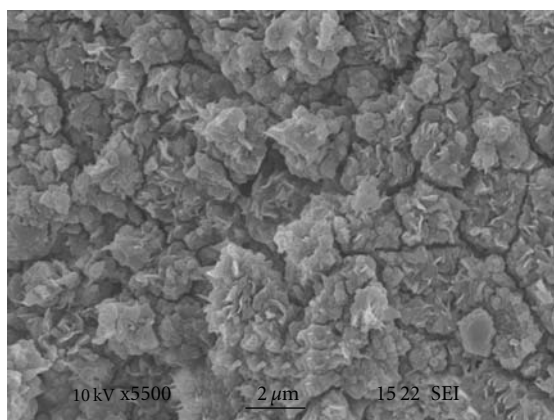
(c)



(d)



(e)



(f)

FIGURE 5: SEM and TEM images of the products obtained by CVD at different conditions using 16%Ni4%Y/Mg catalyst (a, b, c, d) at 450°C, (e) at 500°C, and (f) at 600°C.

## Acknowledgments

This paper was sponsored by the Young Scientists Fund of National Natural science Foundation of China (no. 51001080), the Education Ministry Doctorate Foundation (no. 20091201110002) of China, the Tianjin International Collaboration Foundation (no. 08ZCGHHZ00800) the open project of The State Key Laboratory of Metal Matrix Composites (no. mmc-kf09-03), and the Thermal Processing Technology Center, IIT, USA.

## References

- [1] S. Iijima, "Helical microtubules of graphitic carbon," *Nature*, vol. 354, no. 6348, pp. 56–58, 1991.
- [2] T. Fujita, Y. Hayashi, T. Tokunaga, and K. Yamamoto, "Cobalt nanorods fully encapsulated in carbon nanotube and magnetization measurements by off-axis electron holography," *Applied Physics Letters*, vol. 88, no. 24, Article ID 243118, 3 pages, 2006.
- [3] D. Vairavapandian, P. Vichchulada, and M. D. Lay, "Preparation and modification of carbon nanotubes: review of recent advances and applications in catalysis and sensing," *Analytica Chimica Acta*, vol. 626, no. 2, pp. 119–129, 2008.
- [4] W. Lin, K.-S. Moon, and C. P. Wong, "A combined process of in situ functionalization and microwave treatment to achieve ultrasmall thermal expansion of aligned carbon nanotube-polymer nanocomposites: toward applications as thermal interface materials," *Advanced Materials*, vol. 21, no. 23, pp. 2421–2424, 2009.
- [5] T.-W. Chou, L. Gao, E. T. Thostenson, Z. Zhang, and J.-H. Byun, "An assessment of the science and technology of carbon nanotube-based fibers and composites," *Composites Science and Technology*, vol. 70, no. 1, pp. 1–19, 2010.
- [6] K. T. Kim, S. I. Cha, T. Gemming, J. Eckert, and S. H. Hong, "The role of interfacial oxygen atoms in the enhanced mechanical properties of carbon-nanotube-reinforced metal matrix nanocomposites," *Small*, vol. 4, no. 11, pp. 1936–1940, 2008.
- [7] K. Chu, Q. Wu, C. Jia et al., "Fabrication and effective thermal conductivity of multi-walled carbon nanotubes reinforced Cu matrix composites for heat sink applications," *Composites Science and Technology*, vol. 70, pp. 298–304, 2010.
- [8] C. He, N. Zhao, C. Shi et al., "An approach to obtaining homogeneously dispersed carbon nanotubes in Al powders for preparing reinforced Al-matrix composites," *Advanced Materials*, vol. 19, no. 8, pp. 1128–1132, 2007.
- [9] J. Kang, P. Nash, J. Li, C. Shi, and N. Zhao, "Achieving highly dispersed nanofibres at high loading in carbon nanofibre-metal composites," *Nanotechnology*, vol. 20, no. 23, Article ID 235607, 2009.
- [10] J. Kang, P. Nash, J. Li, C. Shi, N. Zhao, and S. Gu, "The effect of heat treatment on mechanical properties of carbon nanofiber reinforced copper matrix composites," *Journal of Materials Science*, vol. 44, no. 20, pp. 5602–5608, 2009.
- [11] C. S. Goh, J. Wei, L. C. Lee, and M. Gupta, "Ductility improvement and fatigue studies in Mg-CNT nanocomposites," *Composites Science and Technology*, vol. 68, no. 6, pp. 1432–1439, 2008.
- [12] Q. Li, A. Viereckl, C. A. Rottmair, and R. F. Singer, "Improved processing of carbon nanotube/magnesium alloy composites," *Composites Science and Technology*, vol. 69, no. 7-8, pp. 1193–1199, 2009.
- [13] C.-M. Chen, Y.-M. Dai, J. G. Huang, and J.-M. Jehng, "Intermetallic catalyst for carbon nanotubes (CNTs) growth by thermal chemical vapor deposition method," *Carbon*, vol. 44, no. 9, pp. 1808–1820, 2006.

## Research Article

# The Microstructure of Ni Layer on Single-Walled Carbon Nanotubes Prepared by an Electroless Coating Process

Weixue Li,<sup>1,2</sup> Hui Jin,<sup>2</sup> Yuan Hao,<sup>1</sup> Tijun Chen,<sup>1</sup> Jianfeng Dai,<sup>1,2</sup> and Qing Wang<sup>1,2</sup>

<sup>1</sup> State Key Laboratory of Gansu Advanced Non-Ferrous Metal Materials, Lanzhou University of Technology, Lanzhou 730050, China

<sup>2</sup> Department of Physics, Lanzhou University of Technology, Lanzhou 730050, China

Correspondence should be addressed to Jianfeng Dai, daijf@lut.cn

Received 26 April 2010; Accepted 3 September 2010

Academic Editor: Sulin Zhang

Copyright © 2011 Weixue Li et al. This is an open access article distributed under the Creative Commons Attribution License, which permits unrestricted use, distribution, and reproduction in any medium, provided the original work is properly cited.

The single-walled carbon nanotubes (SWNTs, diameter: 2~3 nm), which were obtained in the suspension of purification solution, with Ni-P coating layers were obtained by an electroless deposition process. The SWNTs before and after coating were characterized by transmission electron microscopy (TEM) and energy dispersive spectrometry (EDS). An Ni-P layer on individual nanotube with thickness of 20 nm can be obtained after the deposition process. The X-ray diffraction (XRD) and selected area electron diffraction (SAED) analysis of Ni-P SWNTs before and after heat treatment show that the heat treatment caused the transformation of the amorphous Ni-P layer to the nanocrystalline Ni-P (crystalline Ni and Ni<sub>3</sub>P intermetallic compound) layer. The XRD pattern of SWNTs with Ni-P layers after heat treatment revealed that the crystal structures of Ni in plating layer contained: hexagonal close-packed (hcp) structure and face-centered cubic (fcc) structure. The lattice parameters of Ni (fcc) and Ni<sub>3</sub>P are larger than the bulk's, indicating that the lattice expansion has taken place. However, the lattice parameter of Ni (hcp) has no difference from the bulk's.

## 1. Introduction

Since the discovery of carbon nanotubes (CNTs) by Iijima in 1991 [1], much attention has been focused on one-dimensional nanomaterials for their outstanding properties, including high length/diameter ratio, low density, and mechanical properties [2, 3]. Significant interest has been recently focused on CNTs-metal composites. However, the bonding of interface between carbon nanotubes and metal is not strong enough. Metal-coated CNTs increase surface active sites to improve interfacial bonding between CNTs and metal matrix. Ni-P layers have been adopted for an increasing number of CNT applications in recent years.

Electroless deposition is an effective approach for the preparation of the CNTs with Ni-P layers. This means that CNTs can be used as reinforcing fibers for metal matrix composites with surface treatment. It will be essential to achieve good interfacial adhesion. The coated layers can serve as medium for adhesion and transferring loads. There have been studies on the morphology of metallic nanoparticles

as a function of deposition time in electroless deposition of metal on carbon nanotubes [4].

Multiwalled carbon nanotubes (MWNTs) subjected to electroless deposition are produced by CVD which appear to be curved, twisted together, and hard to disperse [5, 6]. Single-walled carbon nanotubes (SWNTs) adopted in this experiment are straight and easy to disperse. SWNTs with Ni-P coating layers could improve the interfacial bonding between SWNTs and metal matrix and the dispersion of SWNTs in metal matrix.

In order to understand the combining mechanism at the interface, it is necessary to investigate crystal structures under heat treatment. Better thermodynamical stability can be achieved through the nanocrystallization process of the metastable amorphous structure in Ni-P layers, leading to an improvement of the composite properties.

In this study, we prepared SWNTs, which were obtained in the suspension of purification solution, with Ni-P layers by electroless deposition processing. The Ni-P layers are thick and smooth. SWNTs with nanocrystalline Ni-P layers were

prepared by heat treatment at 400°C. The samples were characterized with TEM, EDS, SAED, and XRD.

## 2. Experimental

Single-walled carbon nanotubes were prepared by anodic arc discharging plasma. The purification of SWNTs was conducted by using mixed acid ( $\text{HNO}_3:\text{H}_2\text{SO}_4 = 1:3$ ) to take away amorphous carbon and catalytic nanoparticles. For the purification before further pretreatments for electroless plating, the SWNTs were obtained in the suspension of purification solution, then filtered and washed with deionized water and dried in air at 80°C. Next, the cleaned SWNTs were sensitized in the aqueous solution containing  $\text{SnCl}_2 + \text{HCl}$  and activated in the aqueous solution containing  $\text{PdCl}_2 + \text{HCl}$  (the so-called two-step process), followed by washing thoroughly with deionized water. Finally, the pre-treated SWNTs were immersed in the electroless plating bath, which contains  $\text{NiSO}_4$ ,  $\text{Na}_3\text{C}_6\text{H}_5\text{O}_7$ , and  $\text{NaH}_2\text{PO}_2$ . Ammonia solution was used as buffer to adjust and maintain pH value between 8.5 and 8.7. The sample was heat treated under argon atmosphere at 400°C for 3 h, where heating rate was 10°C/min. The SWNTs before and after coating were characterized with TEM (JEM-2010) and EDS. The Ni-P-SWNTs before and after heat treatment were studied using XRD (D8) and SAED.

## 3. Results and Discussions

**3.1. Morphological Features of Ni-Coated SWNTs.** Figure 1 shows the TEM image of SWNTs after purification, which shows that the CNTs are straight. The diameter of SWNTs is almost 2.6 nm. The purification processing has two effects: taking away the impurities and introducing functional groups on SWNTs surface, such as carboxyl ( $-\text{COOH}$ ) and hydroxyl ( $-\text{C}-\text{OH}$ ) [7]. These functional groups change the surface state of SWNTs, which plays an important role in electroless deposition [8, 9]. The SWNTs have to be oxidized to introduce high density and distributed homogeneously functional groups on their surface. This would subsequently lead to a sufficiently high density of adsorbed activator nuclei and a correspondingly distribution of growing Ni metal nuclei. The growth of Ni would be insufficient to cover the whole tube surface unless the initial density of catalytic sites is very high and homogenous.

Figure 2 shows the representative TEM image of SWNTs with Ni-P coating layers, which clearly indicates that the Ni-P layers coat the tube surface uniformly. The electrolessly deposited Ni-P layers are distributed on the individual tube homogeneously. The thickness of the coating layer is more than 20 nm and as ten times as the semidiameter of the nanotube. The coating thickness can be controlled via reaction time of plating. The layer is symmetric around the SWNTs. Compared to SWNTs produced by CVD, SWNTs adopted in this experiment are straighter, leading to the fewer defects exist on the surface of SWNT. The preparation of tubes with continuous and smooth coating layer has been influenced by two crucial factors: the curvatures of tube [10, 11] and the distance between catalytic centers [12].

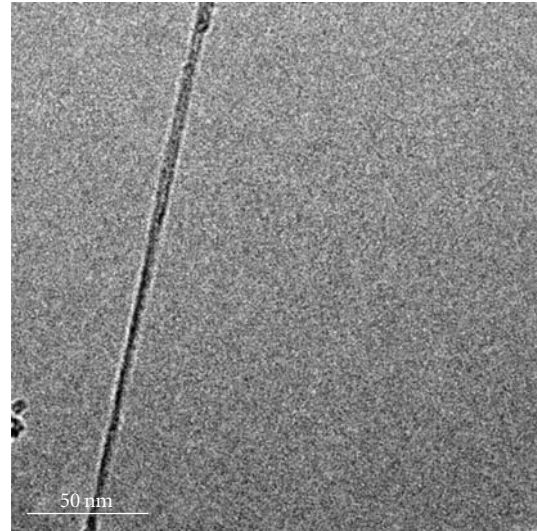


FIGURE 1: TEM image of purified SWNTs.

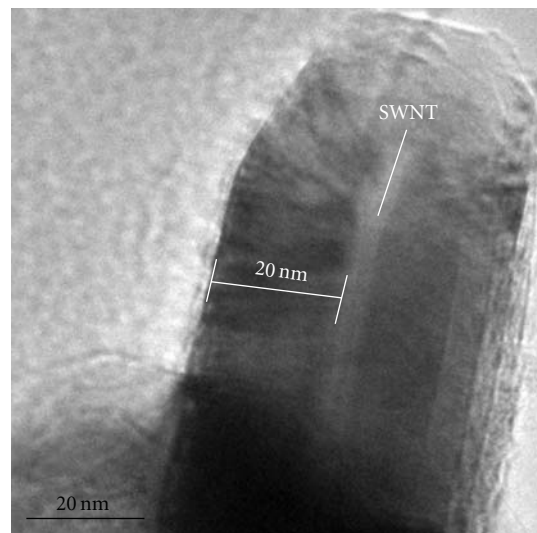


FIGURE 2: TEM image of the end of as-coated SWNTs.

Figure 3 shows the representative TEM, EDS image of SWNTs with Ni-P layers. The EDS shows the major component in deposited layer is Ni, with a little P and Pd. The peak of Cu is due to the grid used in TEM.

**3.2. The Transformation of Crystal Structures of Ni-P Layers.** The electroless deposition Ni is a metastable and supersaturated alloy consisting of P atoms between Ni atoms. The face-centered cubic (fcc) structure of Ni may be maintained within small grains. The structure is essentially amorphous in the regions where the fcc structure cannot be maintained at all [13]. The as-coated SWNTs have been confirmed to be the SWNTs with the amorphous Ni-P layers, and the SWNTs with nanocrystalline Ni-P layers can be prepared by the heat treatment at 400°C.

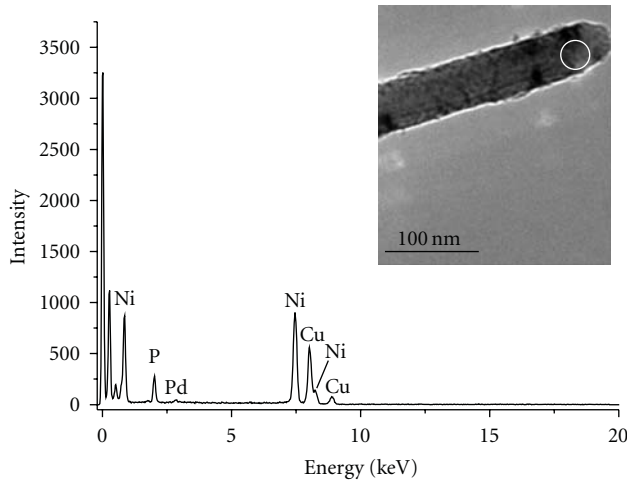


FIGURE 3: TEM image of as-coated SWNTs and EDS, which was selectively taken on the edge of SWNTs with Ni-P layers.

In order to observe the nanocrystallization structures, the SWNTs with Ni-P deposition layers were analyzed by XRD method. In addition to XRD, the SAED analysis was also performed to determine the phase transformation. Figure 4 shows the results.

The XRD pattern of as-coated SWNTs afforded only a broad peak showing the amorphous phase structure [14, 15]. And the SAED is a broad ring characteristic of an amorphous phase without any trace of crystalline phases. Under heat treatment, the Ni and Ni<sub>3</sub>P (intermetallic compound) peaks became sharp [16, 17]. The SAED shows a polycrystalline structural feature, which is in agreement with the results of the XRD analysis. These results have demonstrated that the SWNTs with nanocrystalline Ni-P layer can be prepared by heat treatment at 400°C using the SWNTs with amorphous Ni-P layers as the precursors.

### 3.3. Microstructure of Ni-P Layers under Heat-Treatment.

Figure 5 shows the part of XRD pattern of SWNTs with Ni-P layers under heat treatment.  $2\theta = (40^\circ, 56^\circ)$ . There is one sharp and intense peak of Ni<sub>3</sub>P at  $2\theta = 41.65^\circ$ , several weak peaks are observed, and these peaks correspond to the (231), (330), (112), (141), (222) and (132) planes of body-centered tetragonal structure of Ni<sub>3</sub>P. The XRD pattern clearly shows that Ni has two crystal structures in deposition layers after heat treatment: hexagonal close-packed (hcp) structure and face-centered cubic (fcc) structure. The peaks at  $2\theta = 45.07^\circ$  and at  $2\theta = 44.37^\circ$  correspond to the (011) plane of Ni (hcp) and (111) plane of Ni (bcc), respectively. As we know, there are three crystal structures of Ni: face-centered cubic (fcc), hexagonal close-packed (hcp) and body-centered cubic (bcc). The Ni (hcp) is metastable, but Ni (hcp) stably exists in the deposition layers under heat treatment.

As shown in Figure 6, there is an obvious phenomenon in XRD pattern. The crystal plane distance calculated from XRD spectrum is different with the bulk's value, which reflects the change of lattice parameter.

For example,  $d_{(111)}$  of Ni (fcc) is 2.04006 Å in Figure 6 and is larger than the bulk's value  $d_{(111)0} = 2.01000$  Å indicating

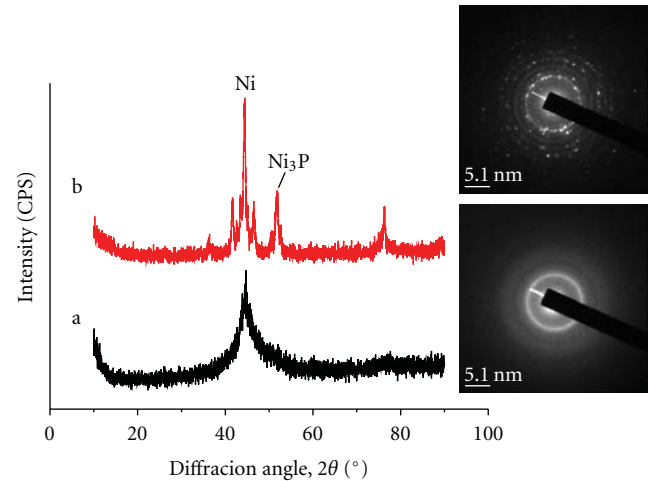


FIGURE 4: XRD and SAED image of SWNTs with Ni-P layers: a as-coated, b under heat treatment.

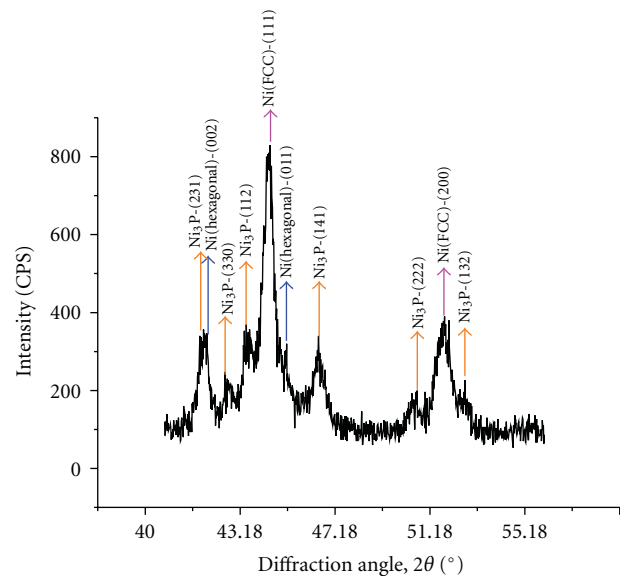


FIGURE 5: Partly of XRD pattern of SWNTs with Ni-P layers under heat treatment.

the emergence of lattice expansion. The rate of the change of crystal plane distance is  $(d_{(111)} - d_{(111)0})/d_{(111)0} = 1.5\%$ . And  $d_{(231)}$  of Ni<sub>3</sub>P (body-centered tetragonal) is 2.16654 Å, but the bulk's value  $d_{(231)0} = 2.16100$  Å. The rate of the change of crystal plane distance is  $(d_{(231)} - d_{(231)0})/d_{(231)0} = 0.26\%$ .

While the lattice of Ni (fcc) and Ni<sub>3</sub>P (bct) has expanded, the lattice of Ni (hcp) has no change nearly. The change of the lattice parameters of Ni (hcp) can be ignored.

The change of crystal plane distance shows that the lattice of Ni (fcc) and Ni<sub>3</sub>P (bct) has expanded. There is a reason as following: the relationship between the lattice parameter and the grain size has been studied by Wei Zhi-Qiang and Lu Ke using the experiment. These studies indicate that the lattice parameter increase significantly with the decrease of the grain size [18, 19]. So the lattice parameter of nanocrystalline

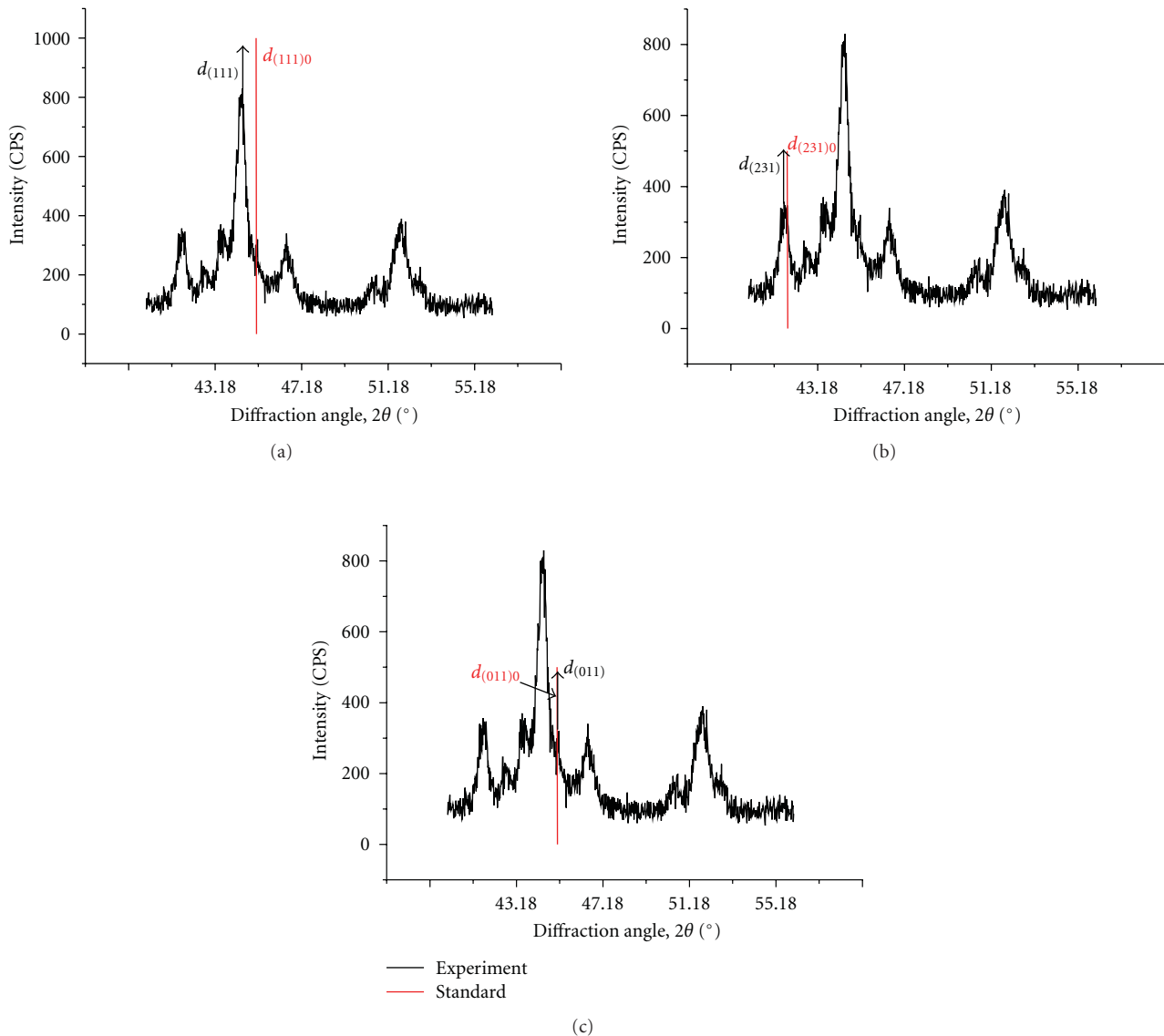


FIGURE 6: The change of crystal plane distance: a-Ni (fcc); b-Ni<sub>3</sub>P; c-Ni (hcp).

in Ni-P layers will increase when they are in nanometer scale due to the grain refinement of nanocrystalline.

#### 4. Conclusion

In this paper, the one-dimensional SWNTs with continuous and dense coating layer have been successfully synthesized by an electroless deposition process. The thickness of the coated layer is more than 20 nm. It has been found that the heat treatment can convert the amorphous Ni-P coating layers into the nanocrystalline Ni-P (Ni and Ni<sub>3</sub>P) layers. Our results show that the lattice of Ni (fcc) and Ni<sub>3</sub>P (bct) has expanded but the rates of expansionary not equal. At the same time, the lattice of Ni (hcp) has contracted and the the change could be ignored.

#### Acknowledgments

This work is financially supported by the Natural Science Foundation of China (no. 50873047) and the Natural Science Foundation of Gansu Province (no. 3ZS062-B25-020), China.

#### References

- [1] S. Iijima, "Helical microtubules of graphitic carbon," *Nature*, vol. 354, no. 6348, pp. 56–58, 1991.
- [2] Z. W. Pan, S. S. Xie, L. Lu et al., "Tensile tests of ropes of very long aligned multiwall carbon nanotubes," *Applied Physics Letters*, vol. 74, no. 21, pp. 3152–3154, 1999.
- [3] M. S. Dresselhaus, G. Dresselhaus, and P. C. Eklund, *Science of Fullerenes & Carbon Nanotubes*, Academic Press, San Diego, Calif, USA, 1996.

- [4] J. H. Byeon and J. Hwang, "Morphology of metallic nanoparticles as a function of deposition time in electroless deposition of metal on multi-walled carbon nanotubes," *Surface and Coatings Technology*, vol. 203, no. 1-2, pp. 357–363, 2008.
- [5] Z. P. Huang, J. W. Xu, Z. F. Ren, J. H. Wang, M. P. Siegal, and P. N. Provencio, "Growth of highly oriented carbon nanotubes by plasma-enhanced hot filament chemical vapor deposition," *Applied Physics Letters*, vol. 73, no. 26, pp. 3845–3847, 1998.
- [6] P. M. Ajayan and O. Z. Zhou, "Applications of carbon nanotubes," *Carbon Nanotubes*, vol. 80, pp. 391–425, 2001.
- [7] C.-S. Chen, X.-H. Chen, Z. , W.-H. Li, L.-S. Xu, and B. Yi, "Effect of multi-walled carbon nanotubes as reinforced fibres on tribological behaviour of Ni-P electroless coatings," *Diamond and Related Materials*, vol. 15, no. 1, pp. 151–156, 2006.
- [8] P. Serp, M. Corrias, and P. Kalck, "Carbon nanotubes and nanofibers in catalysis," *Applied Catalysis A*, vol. 253, no. 2, pp. 337–358, 2003.
- [9] M. A. Fraga, E. Jordão, M. J. Mendes, M. M. A. Freitas, J. L. Faria, and J. L. Figueiredo, "Properties of carbon-supported platinum catalysts: role of carbon surface sites," *Journal of Catalysis*, vol. 209, no. 2, pp. 355–364, 2002.
- [10] Q. Li, S. Fan, W. Han, C. Sun, and W. Liang, "Coating of carbon nanotube with nickel by electroless plating method," *Japanese Journal of Applied Physics, Part 2*, vol. 36, no. 4, pp. L501–L503, 1997.
- [11] X. Chen, J. Xia, J. Peng, W. Li, and S. Xie, "Carbon-nanotube metal-matrix composites prepared by electroless plating," *Composites Science and Technology*, vol. 60, no. 2, pp. 301–306, 2000.
- [12] F. Z. Kong, X. B. Zhang, W. Q. Xiong et al., "Continuous Ni-layer on multiwall carbon nanotubes by an electroless plating method," *Surface and Coatings Technology*, vol. 155, no. 1, pp. 33–36, 2002.
- [13] L. M. Ang, T. S. A. Hor, G. Q. Xu, C. H. Tung, S. P. Zhao, and J. L. S. Wang, "Decoration of activated carbon nanotubes with copper and nickel," *Carbon*, vol. 38, no. 3, pp. 363–372, 2000.
- [14] F. Wang, S. Arai, and M. Endo, "The preparation of multi-walled carbon nanotubes with a Ni-P coating by an electroless deposition process," *Carbon*, vol. 43, no. 8, pp. 1716–1721, 2005.
- [15] Á. Révész, J. Lendvai, J. Lóránth, J. Pádár, and I. Bakonyi, "Nanocrystallization Studies of an Electroless Plated Ni-P Amorphous Alloy," *Journal of the Electrochemical Society*, vol. 148, no. 11, pp. C715–C720, 2001.
- [16] K. G. Keong, W. Sha, and S. Malinov, "Crystallization and phase transformation behaviour of electroless nickel-phosphorus deposits with low and medium phosphorus contents under continuous heating," *Journal of Materials Science*, vol. 37, no. 20, pp. 4445–4450, 2002.
- [17] Á. Révész, J. Lendvai, Á. Cziráki, H. H. Liebermann, and I. Bakonyi, "Formation of nanocrystalline phases during decomposition of amorphous Ni-P alloys by continuous linear heating," *Zeitschrift für Metallkunde*, vol. 92, no. 5, pp. 483–488, 2001.
- [18] Z.-Q. Wei, T.-D. Xia, J. Wang, Z.-G. Wu, and P.-X. Yan, "Lattice expansion of Ni nanopowders," *Acta Physica Sinica*, vol. 56, no. 2, pp. 1004–1008, 2007.
- [19] L. Ke and X.-Z. Haoyue, "Lattice expansion in nanocrystalline pure Ni," *Acta Metallurgica Sinica*, vol. 431, no. 2, pp. A74–A78, 1995.

## Research Article

# Pore-Width-Dependent Preferential Interaction of $sp^2$ Carbon Atoms in Cyclohexene with Graphitic Slit Pores by GCMC Simulation

Natsuko Kojima,<sup>1</sup> Tomonori Ohba,<sup>1</sup> Yasuhiko Urabe,<sup>2</sup> Hirofumi Kanoh,<sup>1</sup>  
and Katsumi Kaneko<sup>1,3</sup>

<sup>1</sup>Graduate School of Science, Chiba University, 1-33 Yayoi, Inage, Chiba 263-8522, Japan

<sup>2</sup>Technology Development Division, TOKYO GAS Co., Ltd., 2-7, Suehirocho 1, Tsurumiku, Yokohama 230-0045, Japan

<sup>3</sup>Research Center for Exotic NanoCarbon Project, Shinshu University, 4-17-1, Wakasato, Nagano 380-8553, Japan

Correspondence should be addressed to Tomonori Ohba, ohba@pchem2.s.chiba-u.ac.jp

Received 2 June 2010; Accepted 1 November 2010

Academic Editor: Sulin Zhang

Copyright © 2011 Natsuko Kojima et al. This is an open access article distributed under the Creative Commons Attribution License, which permits unrestricted use, distribution, and reproduction in any medium, provided the original work is properly cited.

The adsorption of cyclohexene with two  $sp^2$  and four  $sp^3$  carbon atoms in graphitic slit pores was studied by performing grand canonical Monte Carlo simulation. The molecular arrangement of the cyclohexene on the graphitic carbon wall depends on the pore width. The distribution peak of the  $sp^2$  carbon is closer to the pore wall than that of the  $sp^3$  carbon except for the pore width of 0.7 nm, even though the Lennard-Jones size of the  $sp^2$  carbon is larger than that of the  $sp^3$  carbon. Thus, the difference in the interactions of the  $sp^2$  and  $sp^3$  carbon atoms of cyclohexene with the carbon pore walls is clearly observed in this study. The preferential interaction of  $sp^2$  carbon gives rise to a slight tilting of the cyclohexene molecule against the graphitic wall. This is suggestive of a  $\pi$ - $\pi$  interaction between the  $sp^2$  carbon in the cyclohexene molecule and graphitic carbon.

## 1. Introduction

There has been an increase in the use of activated carbons in the construction of environmentally friendly technologies with sufficient safety. Activated carbon has basically slit-shaped micropores, which provide much better accessibility for most molecules than the cylindrical pores of zeolites [1, 2]. Recent researches have succeeded in controlling the pore width in the range from subnanometers to several nanometers; this has resulted in improvements in a wide range of applications, such as air separation (or air purification), solvent recovery, and manufacture of automobile canisters [3–7]. Furthermore, activated carbons have high electronic conductivities, allowing them to be used in electrochemical applications such as supercapacitors [8–10]. Another striking advantage of activated carbons is the fact that their production from natural products that fix atmospheric  $CO_2$  can contribute to  $CO_2$  sequestration [5, 11, 12]. However, there are still many research issues that need to

be resolved to improve the performance of activated carbons. With the exception of the surface functional groups involved in the adsorption of polar molecules, the specific interaction involved in the gas adsorbability of activated carbons has not been studied sufficiently. Smith et al. [13] conducted the first study on the comparison between benzene and cyclohexane adsorptions on graphite; in this study, stronger cyclohexane adsorption was observed than benzene adsorption. On the other hand, the strong  $\pi$ -electron interaction of benzene with nanopore surfaces was observed by Dosseh et al. [14]. Moreover, comparison studies on adsorbed molecules of  $sp^2$  and  $sp^3$  carbons have been conducted for benzene and cyclohexane and for ethylene and ethane [15–17]. The adsorption isotherms of ethane and ethylene on activated carbons showed larger amounts of adsorbed ethylene than ethane [18], indicating stronger interaction of  $sp^2$  carbon with pore walls. Radovic and Bockrath used molecular orbital calculations to emphasise the essential importance of the conjugated  $\pi$ -electron nature of the basal plane of

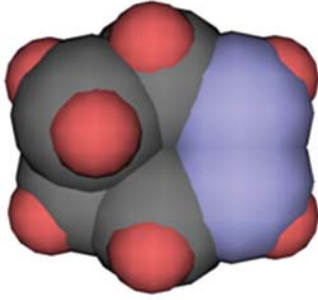


FIGURE 1: Space-filled model of cyclohexene. Blue, black, and red spheres represent  $sp^2$  carbon atoms,  $sp^3$  carbon atoms, and hydrogen atoms, respectively.

the graphite in the adsorption of organic molecules [19]. The characteristic interaction, the  $\pi$ - $\pi$  interaction of the  $sp^2$  carbons in an adsorbed molecule with graphite, is caused by the electron cloud delocalization between the  $sp^2$  carbons in the molecule and graphite. We still need to understand the difference between the adsorbed structures of the  $sp^2$  and  $sp^3$  carbon atoms of the adsorbate molecules upon adsorption on graphitic pores along with the dependence on pore width in order to obtain a better carbon adsorbent of high specificity for use in future technologies for the selective reaction and separation of unsaturated molecules. Vernov and Steele showed the orientation of adsorbed benzene on graphite using a 12-site model [20–22]. Do et al. studied the orientation structures of organic molecules on graphite and porous carbons using grand canonical Monte Carlo (GCMC) simulation, taking into account the molecular structures [23, 24]. Such molecular simulation studies can reveal the interactions between  $sp^2$  carbon and a graphitic carbon surface along with the molecular structures.

Cyclic hydrocarbons are important intermediates in many chemical reactions on transition metal surfaces [25, 26]. Cyclohexene is one of the critical intermediates in catalytic reforming. Many studies on the reforming process have been reported [25–27]. The cyclohexene molecule has two  $sp^2$  carbon atoms in addition to four  $sp^3$  carbon atoms, making it an appropriate probe molecule for research on the comparison of the adsorptions of  $sp^2$  and  $sp^3$  carbon atoms. To understand the difference between the adsorbed structures of the  $sp^2$  and  $sp^3$  carbon atoms, we adopted GCMC simulation for studying cyclohexene adsorption on activated carbon. In addition, this study could serve as a guide in the development of better adsorption media for separating cyclohexene from commercial natural gas [4, 6, 15].

## 2. Simulation Procedures

Figure 1 shows a space-filled model of cyclohexene; the structural parameters are given in the paper by Faller et al. [28]. The cyclohexene molecule has a distorted plane structure that consists of five single bonds (C–C) and one

double bond (C=C). The  $sp^3$  and  $sp^2$  carbon atoms must be distinguished by using interaction potential calculation and GCMC simulation. Faller et al. determine the parameters of cyclohexene for the flexible model [28]. As rigid and flexible models give no significant difference in structure [29, 30], a 16-centre model for the rigid cyclohexene structure in this study was adopted for the calculation ( $\epsilon/k_B = 31.9$  K for H and 35.6 K for  $sp^3$  and  $sp^2$  carbons;  $\sigma = 0.252$  nm for H, 0.311 nm for  $sp^3$  carbon, and 0.321 nm for  $sp^2$  carbon) [28, 31]. The availability is verified by the comparison between the rigid and flexible models before the calculation; the assembly structures of cyclohexene in the rigid and flexible models are almost agreeing with each other, although the structure distribution in the flexible model is slightly dispersed due to the flexibility. The intermolecular interactions were described by the Lennard-Jones potentials:

$$\phi_{AB} = 4 \sum_i \sum_j \epsilon_{ij} \left[ \left( \frac{\sigma_{ij}}{r_{ij}} \right)^{12} - \left( \frac{\sigma_{ij}}{r_{ij}} \right)^6 \right]. \quad (1)$$

Here,  $r_{ij}$  is the distance between the  $i$ th atom in molecule A and the  $j$ th atom in molecule B. The Lorentz-Berthelot mixing rules were applied to obtain the interaction energy and size parameters for the heteroatomic interaction:

$$\sigma_{ij} = \frac{\sigma_i + \sigma_j}{2} \quad \epsilon_{ij} = \sqrt{\epsilon_i \epsilon_j}. \quad (2)$$

Here, each component atom in the molecule was assumed to be electrically neutral; the stable molecular geometry of a single molecule in the flexible model was used for the calculation.

The slit-shaped pore was modelled using the interface between two semi-infinite graphite slabs; the molecule-carbon wall interaction was approximated by the 10-4-3 Steele potential [32]:

$$\phi_{sf} = \sum_i A \left[ \frac{2}{5} \left( \frac{\sigma_{sfi}}{z_i} \right)^{10} - \left( \frac{\sigma_{sfi}}{z_i} \right)^4 - \frac{\sigma_{sfi}^4}{1.005(z_i + 0.20435)^3} \right]. \quad (3)$$

Here,  $A$  is  $76.38 \pi \epsilon_{sfi} \sigma_{sfi}^2$ , and  $z$  is the vertical distance of the  $i$ th atom in a molecule from the centre of a carbon atom on one side of a carbon surface;  $\sigma_{sfi}$  and  $\epsilon_{sfi}$  were derived from the Lorentz-Berthelot mixing rules.  $\sigma_s$  and  $\epsilon_s$  are the Lennard-Jones parameters for the carbon atom in graphite ( $\sigma_s = 0.3416$  nm and  $\epsilon_s/k_B = 30.14$  K), and  $\sigma_{fi}$  and  $\epsilon_{fi}$  are the Lennard-Jones parameters for the  $i$ th atom in the molecule [33]. Strictly speaking, the molecule-graphite slab interaction was summed and smoothed by all of the interactions between the component atoms in the molecule and the graphite slab using the Steele potential. In the case of the graphite slit pore, the interaction of the cyclohexene molecule with the pore was expressed by the sum of the interaction potentials of the cyclohexene molecule with both graphite walls, as given by (4):

$$\phi_p = \phi_{sf}(z) + \phi_{sf}(H - z). \quad (4)$$

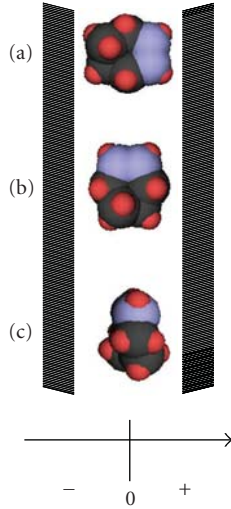


FIGURE 2: Molecular arrangements of adsorbed cyclohexene. Head-on (a), side-on (b), and in-plane (c) arrangements.

Here,  $H$  is the physical slit pore width, which is the internuclear distance between opposite graphite walls. The physical slit pore width was associated with the pore width,  $w$ , which can be experimentally measured as follows [34]:

$$w = H - 2z_0, \quad z_0 = 0.856 \sigma_{sf} - \frac{\sigma_{ff}}{2}. \quad (5)$$

Here,  $z_0$  is the closest contact distance between the  $sp^2$  carbon and the graphite pore wall.

The electrostatic interaction between a polar molecule and a graphitic slab must be taken into account for a detailed analysis of the adsorption of polar molecules, as reported in previous papers [20, 35]. The electrically neutral cyclohexene atoms assumed here nominally give no electrostatic contribution to the interaction between the cyclohexene and the pore wall. However, the electrostatic interaction is roughly included in the Lennard-Jones parameters obtained from the *ab initio* calculation by Faller et al. [28]. Grand canonical Monte Carlo simulations of the cyclohexene were performed using  $3 \times 10^6$  steps at 298 K, with three equivalent trials for the creation, deletion, and movement of the molecules. The pressure was calculated from the bulk molecular density in the unit cell of  $6 \times 6 \times 6 \text{ nm}^3$  by using the van der Waals equation after more than  $1 \times 10^8$  calculation steps and the accumulation of  $9 \times 10^7$  steps. A unit cell size of  $6 \times 6 \times H \text{ nm}^3$  and a 2-dimensional periodic boundary condition were used in this calculation.

### 3. Results and Discussion

The molecule-graphite pore interaction energy was calculated for three arrangements, as shown in Figure 2. The molecular plane is perpendicular to the graphite wall in arrangements (a) and (b). The double bond is head-on toward a plus-side wall for (a), whereas there is side-on adsorption on the wall for (b). Hence, (a) and (b) are called head-on and side-on arrangements, respectively. On the

other hand, because the molecular plane is parallel to the wall in (c), arrangement (c) is called an in-plane configuration. The molecule-pore interaction potentials were calculated as a function of the vertical distance of the molecular centre of gravity from the pore centre for the three arrangements.

Figure 3 shows the molecule-pore interaction potentials for the three arrangements shown in Figure 2. For the smallest pore ( $w = 0.6 \text{ nm}$ ), the in-plane arrangement gets a large stabilization energy of  $-8000 \text{ K}$ , suggesting the presence of adsorption from an extremely low pressure. The side-on arrangement provides the considerably large stabilization energy of  $-4000 \text{ K}$ , whereas the head-on arrangement leads only to repulsive interaction energy. The potential profiles for  $w = 0.7 \text{ nm}$  are remarkably different from those for  $w = 0.6 \text{ nm}$ . The most stable arrangement ( $-7000 \text{ K}$ ) is found to be the side-on type with  $w = 0.7 \text{ nm}$ . The in-plane arrangement gives double potential minima, and the head-on and side-on arrangements give a single minimum. All the potential minima are close to each other, within  $500 \text{ K}$ , for  $w = 0.8 \text{ nm}$ . The head-on arrangement leads to the single deepest potential minimum for  $w = 0.8 \text{ nm}$ , and the side-on and in-plane arrangements have double minima. In the case of  $w > 0.9 \text{ nm}$ , the in-plane arrangement gave the deepest potential double minima, which are situated near the pore wall. Then, cyclohexene molecules on the pore walls will be adsorbed on the pore walls with  $w > 0.9 \text{ nm}$  in the in-plane structure. Similar double potential minima were obtained for the side-on arrangement, and the depth was slightly shallower than that for the in-plane arrangement. It is worth noting that the head-on arrangement gave an asymmetrical potential profile for  $w > 0.9 \text{ nm}$ ;  $sp^2$  carbon leads to a stronger interaction than  $sp^3$  carbon. Even the single potential minima for  $w = 0.7$  and  $0.8 \text{ nm}$  shift slightly in the positive direction due to the contribution by the  $sp^2$  carbons (see Figures 3(b) and 3(c)). This interaction potential difference in the  $sp^2$  and  $sp^3$  carbon atoms is clearly observed in the adsorbed structure obtained from the GCMC simulation. The potential profiles for  $w = 1.0 \text{ nm}$  have features that are almost similar to those for  $w = 0.9 \text{ nm}$  (Figure 3(d)). Figure 4 shows the changes in the interaction potential minimum with the pore width for different adsorption structures. The interaction energy depends sensitively on the pore width and the molecular arrangement in the pore; the most favourable arrangement predicted from the interaction potential varies with the pore width. The deepest potential energy is obtained in the in-plane arrangement for  $w < 0.64 \text{ nm}$ . The side-on arrangement provides the deepest potential energy in the  $w$  range of  $0.64$  to  $0.75 \text{ nm}$ . The head-on arrangement gives the deepest interaction potential energy for  $w = 0.75$ – $0.84 \text{ nm}$ , indicating a contribution by the  $sp^2$  carbon atoms in the pores when  $w$  is approximately  $0.8 \text{ nm}$ , although the energy difference from the side-on arrangement is not marked compared with the difference for smaller pores.

Figure 5 shows the adsorption isotherms of cyclohexene in pores with  $w = 0.5$ – $2.0 \text{ nm}$  at  $298 \text{ K}$ . The ordinate represents the number of cyclohexene molecules adsorbed in the pore, with wider pores resulting in larger numbers of molecules above  $10^{-5} \text{ MPa}$ . As the pore with  $w = 0.5 \text{ nm}$  is

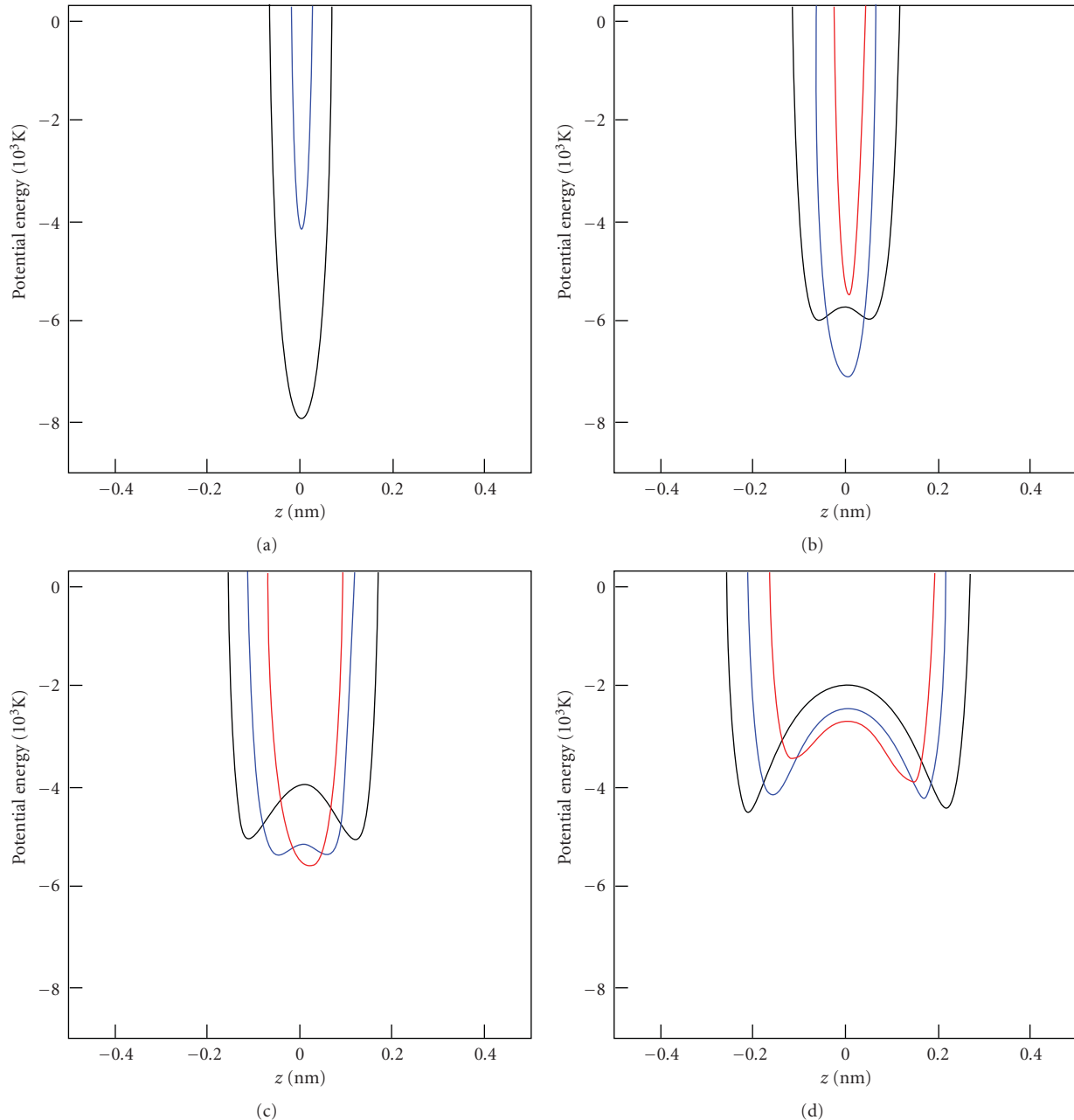


FIGURE 3: Potential profiles of a cyclohexene molecule in graphitic slit pores with  $w = 0.6$  (a),  $0.7$  (b),  $0.8$  (c), and  $1.0 \text{ nm}$  (d). Red curve: head-on arrangement, blue curve: side-on arrangement, and black curve: in-plane arrangements.

too narrow to accommodate cyclohexene molecules easily, adsorption begins above  $10^{-8} \text{ MPa}$ . On the other hand, the pore with  $w = 0.6 \text{ nm}$ , which has the deepest potential minimum ( $-8000 \text{ K}$ ) for the in-plane arrangement, exhibits a quite intensive adsorption for cyclohexene; this adsorption begins even below  $10^{-10} \text{ MPa}$ . As the pore with  $w = 1.0 \text{ nm}$  has double minima, which are in the range from  $-4000$  to  $-4500 \text{ K}$ , adsorption begins at  $5 \times 10^{-9} \text{ MPa}$ . The adsorption for  $w > 1.0 \text{ nm}$  begins above  $5 \times 10^{-9} \text{ MPa}$ . The cyclohexene molecule has a distorted ring structure, making

dense packing in a smaller slit pore space very difficult. This can be understood from the following snapshot analysis.

Figure 6 shows the snapshots at  $10^{-3} \text{ MPa}$  for  $w = 0.6, 0.7, 0.8,$  and  $1.0 \text{ nm}$ . Cyclohexene molecules form a single adsorbed layer that is inherent to the pore width for  $w = 0.6\text{--}0.8 \text{ nm}$ , as shown in Figure 4. In the pore with  $w = 0.6 \text{ nm}$ , the cyclohexene molecules basically exhibit the in-plane arrangement. Strictly speaking, the cyclohexene molecules are tilted against the pore wall due to the stronger  $\text{sp}^2$  carbon-pore wall interaction. The tilt angle will be shown

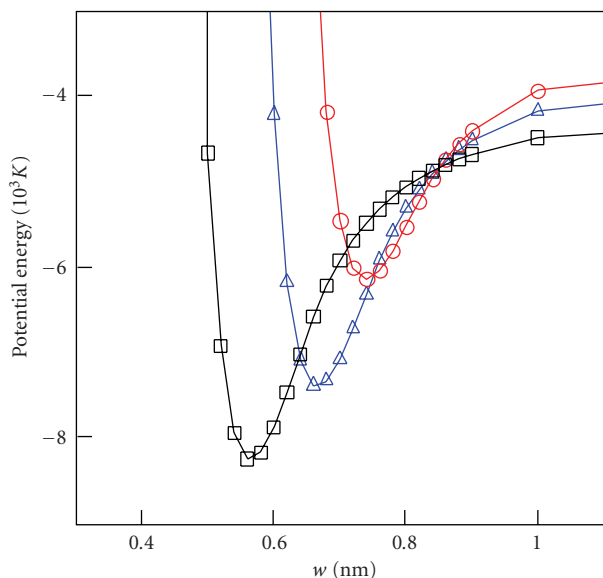


FIGURE 4: Potential minima as function of pore width.  $\circ$ : head-on arrangement,  $\Delta$ : side-on arrangement, and  $\square$ : in-plane arrangements.

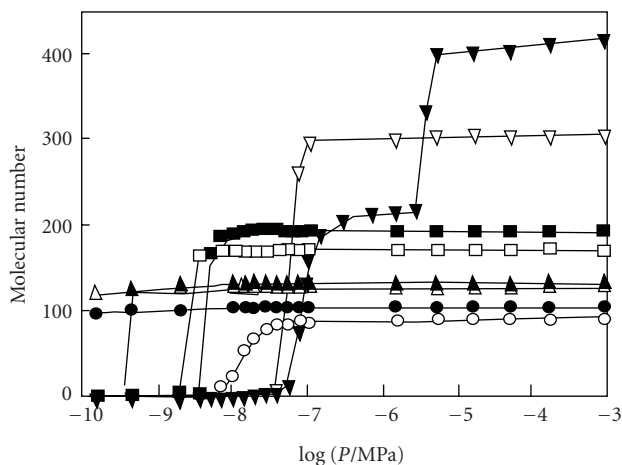


FIGURE 5: Adsorption isotherms of cyclohexene at 298 K.  $\circ$ :  $w = 0.5$  nm,  $\bullet$ :  $w = 0.6$  nm,  $\Delta$ :  $w = 0.7$  nm,  $\blacktriangle$ :  $w = 0.8$  nm,  $\square$ :  $w = 0.9$  nm,  $\blacksquare$ :  $w = 1.0$  nm,  $\nabla$ :  $w = 1.5$  nm, and  $\blacktriangledown$ :  $w = 2.0$  nm.

later. Single adsorbed layers having the side-on and head-on arrangements are observed in the pores with  $w = 0.7$  and  $0.8$  nm, respectively, which is expected from the results shown in Figure 4. Two adsorbed layers of cyclohexene molecules are formed in the pore with  $w = 1.0$  nm. Three layers and four layers are observed in the pores with  $w = 1.5$  and  $2.0$  nm, respectively, which are not shown in this paper. In the case of the pores with  $w = 1.5$  and  $2.0$  nm, molecules at the monolayer position orientate along the pore walls; molecules in the central space of the pore have almost a perpendicular configuration against the pore wall with less molecular orientation.

The tilting of the cyclohexene molecules toward the pore walls clearly shows the molecular orientation to a pore wall.

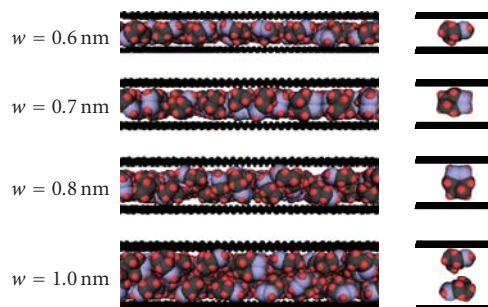


FIGURE 6: Snapshots of adsorbed cyclohexene in the nanopores with  $w = 0.6$ ,  $0.7$ ,  $0.8$ , and  $1.0$  nm at  $P = 10^{-3}$  MPa. Right side: schematic model of typical structure of adsorbed cyclohexene. Blue, grey, and red spheres depict  $sp^2$  carbon,  $sp^3$  carbon, and hydrogen, respectively. Graphitic carbon walls are represented by the loose lines composed of black spheres.

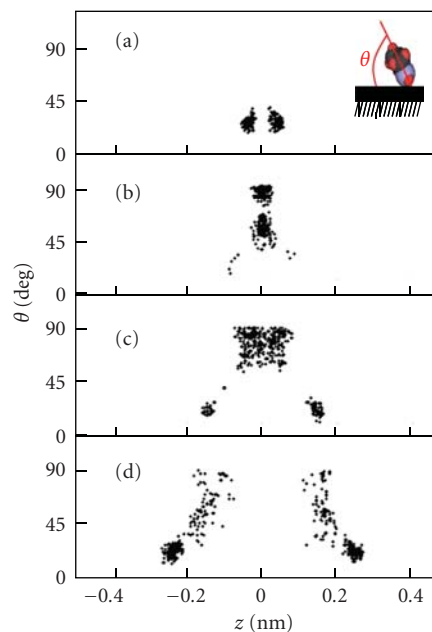


FIGURE 7: Angular distribution of cyclohexene against the plane of the pore wall of  $w = 0.6$  (a),  $0.7$  (b),  $0.8$  (c), and  $1.0$  nm (d).

Figure 7 shows the angular distribution between the normal vector of a cyclohexene molecule and the pore wall surface. Here, the normal vector is defined as a perpendicular vector to the plane of two  $sp^2$  carbons and two  $sp^3$  carbons next to the  $sp^2$  carbon; that is, the in-plane arrangement is at  $0^\circ$  and the head-on or side-on arrangement is at  $90^\circ$ . The probable angles for  $w = 0.6$  and  $0.7$  nm are  $20\text{--}30^\circ$  and  $50\text{--}90^\circ$ , respectively. Thus, the in-plane arrangement is expected for  $w = 0.6$  nm, while the head-on or side-on arrangement should be formed in the pore with  $w = 0.7$  nm. For  $w = 0.8$  and  $1.0$  nm, angles of  $20\text{--}30^\circ$  are observed in the contacts with the pore walls. Angle distributions above  $50^\circ$  are also observed at some pore-centred positions, suggesting the head-on or side-on arrangement. The head-on or side-on arrangement is mainly formed for  $w = 0.8$  nm. On the other

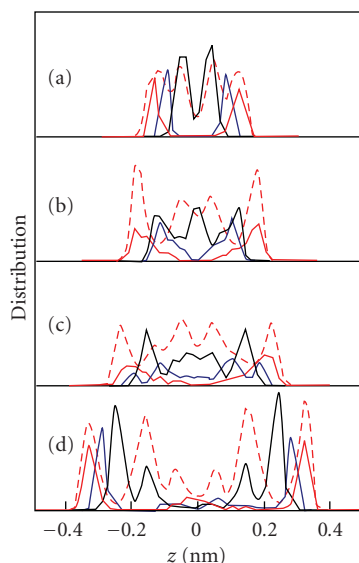


FIGURE 8: Distributions of cyclohexene in a direction perpendicular to the pore wall at  $10^{-3}$  MPa, for  $w = 0.6$  (a),  $0.7$  (b),  $0.8$  (c), and  $1.0$  nm (d). Black curve:  $sp^3$  carbon, blue curve:  $sp^2$  carbon, red solid curve: hydrogen bound to  $sp^2$  carbon, and red dashed curve: hydrogen bound to  $sp^3$  carbon.

hand, the in-plane arrangement is the most common for  $w = 1.0$  nm.

As the exact arrangement of the molecules facing the pore wall can provide useful information on the role of the  $sp^2$  carbon atoms in the molecule-pore wall interaction, distribution profiles were determined for the  $sp^2$  and  $sp^3$  carbons in the adsorbed cyclohexene against the perpendicular axis of the pore walls, as shown in Figure 8. The snapshots in Figure 6 and angular distribution in Figure 7 cannot provide a clear insight into the role of the  $sp^2$  carbon atoms in the cyclohexene-pore wall interaction. Cruz and Mota found a slight difference between the distances of the  $sp^2$  and  $sp^3$  carbons from pore walls [16]. In contrast, Figure 8 distinctly shows the difference in the positions of the  $sp^2$  and  $sp^3$  carbon atoms and the hydrogen atoms bonding to the  $sp^2$  and  $sp^3$  carbons. The  $sp^2$  carbon atoms are actually in contact with a pore wall for  $w = 0.6$  and  $1.0$  nm, although the remarkable difference between the  $sp^2$  and  $sp^3$  carbon atoms near the walls is not observed well for  $w = 0.7$  and  $0.8$  nm. The  $sp^2$  carbon has a considerably uniform distribution for  $w = 0.8$  nm, and a few  $sp^2$  carbons are closer to the wall than the  $sp^3$  carbon, whereas the  $sp^3$  carbon prefers the monolayer position. The distributions for  $w = 1.5$  and  $2.0$  nm had tendencies similar to that for  $w = 1.0$  nm; these distributions for  $w > 1.0$  nm have sharp peaks near the pore walls, and no clear peak exists at around the centre of the pore. The distribution peak of the  $sp^2$  carbon is closer to the pore walls than that of the  $sp^3$  carbon atoms for  $w = 0.6, 1.0, 1.5,$  and  $2.0$  nm, despite the fact that the Lennard-Jones diameter of the  $sp^2$  carbon is larger than that of the  $sp^3$  carbon by  $0.01$  nm. Therefore, the  $sp^2$  carbon atoms can interact preferentially with the graphite walls in comparison

with the interaction of the  $sp^3$  carbon atoms for the specific pore widths. The hydrogen atoms bound to the  $sp^2$  carbons are also distributed on the pore walls, whereas those bound to the  $sp^3$  carbons are orderly distributed in the pores. In comparison to the carbon atoms, there exist nearer hydrogen atoms to the pore walls.

## 4. Conclusion

The preferential interaction of  $sp^2$  carbon atoms with a graphite wall is explicitly observed in the adsorption of cyclohexene in graphite slit pores, with the exception of pores with  $w = 0.7$  and  $0.8$  nm, as cyclohexene has both  $sp^2$  and  $sp^3$  carbon atoms. The preferential interactions of the  $sp^2$  carbon atoms and the hydrogen atoms bound to the  $sp^2$  carbon atoms in cyclohexene are enhanced in a restricted nanoscale pore space; this results in cyclohexene having a slightly tilted conformation. The application of the preferential interaction nature of the  $sp^2$  carbon atoms to the design of a better adsorbent for aromatic compounds is expected to be quite useful, because the orientation of cyclohexene to the graphite walls depends on the pore width.

## Acknowledgments

The financial support provided by the Kurata Memorial Hitachi Science and Technology Foundation, Kurita Water and Environment Foundation, Nippon Sheet Glass Foundation, and Global COE program, MEXT, Japan, is gratefully acknowledged.

## References

- [1] K. Kaneko, C. Ishii, M. Ruike, and H. Kuwabara, "Origin of superhigh surface area and microcrystalline graphitic structures of activated carbons," *Carbon*, vol. 30, no. 7, pp. 1075–1088, 1992.
- [2] T. Ohba, D. Nicholson, and K. Kaneko, "Temperature dependence of micropore filling of N in slit-shaped carbon micropores: experiment and grand canonical Monte Carlo simulation," *Langmuir*, vol. 19, no. 14, pp. 5700–5707, 2003.
- [3] J. Laine and S. Yunes, "Effect of the preparation method on the pore size distribution of activated carbon from coconut shell," *Carbon*, vol. 30, no. 4, pp. 601–604, 1992.
- [4] M. M. A. Freitas and J. L. Figueiredo, "Preparation of carbon molecular sieves for gas separations by modification of the pore sizes of activated carbons," *Fuel*, vol. 80, no. 1, pp. 1–6, 2001.
- [5] K. Gergova and S. Eser, "Effects of activation method on the pore structure of activated carbons from apricot stones," *Carbon*, vol. 34, no. 7, pp. 879–888, 1996.
- [6] T. J. Bandoz, "Effect of pore structure and surface chemistry of virgin activated carbons on removal of hydrogen sulfide," *Carbon*, vol. 37, no. 3, pp. 483–491, 1999.
- [7] T. Kyotani, "Control of pore structure in carbon," *Carbon*, vol. 38, no. 2, pp. 269–286, 2000.
- [8] D. Qu and H. Shi, "Studies of activated carbons used in double-layer capacitors," *Journal of Power Sources*, vol. 74, no. 1, pp. 99–107, 1998.

- [9] E. Frackowiak and F. Béguin, "Electrochemical storage of energy in carbon nanotubes and nanostructured carbons," *Carbon*, vol. 40, no. 10, pp. 1775–1787, 2002.
- [10] P. Simon and Y. Gogotsi, "Materials for electrochemical capacitors," *Nature Materials*, vol. 7, no. 11, pp. 845–854, 2008.
- [11] F. Dreisbach, R. Staudt, and J. U. Keller, "High pressure adsorption data of methane, nitrogen, carbon dioxide and their binary and ternary mixtures on activated carbon," *Adsorption*, vol. 5, no. 3, pp. 215–227, 1999.
- [12] M. Sudibandriyo, Z. Pan, J. E. Fitzgerald, R. L. Robinson, and K. A. M. Gasem, "Adsorption of methane, nitrogen, carbon dioxide, and their binary mixtures on dry activated carbon at 318.2 K and pressures up to 13.6 MPa," *Langmuir*, vol. 19, no. 13, pp. 5323–5331, 2003.
- [13] R. N. Smith, C. Pierce, and H. Cordes, "Adsorption of benzene and cyclohexane by graphite," *Journal of the American Chemical Society*, vol. 72, no. 12, pp. 5595–5597, 1950.
- [14] G. Dosseh, Y. Xia, and C. Alba-Simionesco, "Cyclohexane and benzene confined in MCM-41 and SBA-15: confinement effects on freezing and melting," *Journal of Physical Chemistry B*, vol. 107, no. 26, pp. 6445–6453, 2003.
- [15] S. Curbelo and E. A. Müller, "Modelling of ethane/ethylene separation using microporous carbon," *Adsorption Science and Technology*, vol. 23, no. 10, pp. 855–865, 2005.
- [16] F. J. A. L. Cruz and J. P. B. Mota, "Thermodynamics of adsorption of light alkanes and alkenes in single-walled carbon nanotube bundles," *Physical Review B*, vol. 79, no. 16, Article ID 165426, 2009.
- [17] T. R. Rybolt, C. E. Wells, C. R. Sisson, C. B. Black, and K. A. Ziegler, "Evaluation of molecular mechanics calculated binding energies for isolated and monolayer organic molecules on graphite," *Journal of Colloid and Interface Science*, vol. 314, no. 2, pp. 434–445, 2007.
- [18] B. U. Choi, D. K. Choi, Y. W. Lee, B. K. Lee, and S. H. Kim, "Adsorption equilibria of methane, ethane, ethylene, nitrogen, and hydrogen onto activated carbon," *Journal of Chemical and Engineering Data*, vol. 48, no. 3, pp. 603–607, 2003.
- [19] L. R. Radovic and B. Bockrath, "On the chemical nature of graphene edges: origin of stability and potential for magnetism in carbon materials," *Journal of the American Chemical Society*, vol. 127, no. 16, pp. 5917–5927, 2005.
- [20] A. Vernov and W. A. Steele, "The electrostatic field at a graphite surface and its effect on molecule-solid interactions," *Langmuir*, vol. 8, no. 1, pp. 155–159, 1992.
- [21] A. Vernov and W. A. Steele, "Computer simulations of benzene adsorbed on graphite. 2. 298 k," *Langmuir*, vol. 7, no. 11, pp. 2817–2820, 1991.
- [22] A. Vernov and W. A. Steele, "Computer simulations of benzene adsorbed on graphite. 1. 85 K," *Langmuir*, vol. 7, no. 12, pp. 3110–3117, 1991.
- [23] D. D. Do and H. D. Do, "Adsorption of carbon tetrachloride on graphitized thermal carbon black and in slit graphitic pores: five-site versus one-site potential models," *Journal of Physical Chemistry B*, vol. 110, no. 19, pp. 9520–9528, 2006.
- [24] D. D. Do and H. D. Do, "Adsorption of ethylene on graphitized thermal carbon black and in slit pores: a computer simulation study," *Langmuir*, vol. 20, no. 17, pp. 7103–7116, 2004.
- [25] M. Saeys, M. F. Reyniers, M. Neurock, and G. B. Marin, "Adsorption of cyclohexadiene, cyclohexene and cyclohexane on Pt(1 1 1)," *Surface Science*, vol. 600, no. 16, pp. 3121–3134, 2006.
- [26] C. Papp, R. Denecke, and H. P. Steinrück, "Adsorption and reaction of cyclohexene on a Ni(111) surface," *Langmuir*, vol. 23, no. 10, pp. 5541–5547, 2007.
- [27] W. G. Xu, Z. F. Shang, and G. C. Wang, "Adsorption of cyclohexene on nAu/Pt(1 0 0) (n = 0, 1, 2): a DFT study," *Journal of Molecular Structure: THEOCHEM*, vol. 869, no. 1–3, pp. 47–52, 2008.
- [28] R. Faller, H. Schmitz, O. Biermann, and F. Müller-Plathe, "Automatic parameterization of force fields for liquids by simplex optimization," *Journal of Computational Chemistry*, vol. 20, no. 10, pp. 1009–1017, 1999.
- [29] G. Cardini, "A comparison between the rigid and flexible model of cyclohexane in the plastic phase by molecular dynamic simulations," *Chemical Physics*, vol. 193, no. 1–2, pp. 101–108, 1995.
- [30] I. G. Tironi, R. M. Brunne, and W. F. Van Gunsteren, "On the relative merits of flexible versus rigid models for use in computer simulations of molecular liquids," *Chemical Physics Letters*, vol. 250, no. 1, pp. 19–24, 1996.
- [31] H. Schmitz, R. Faller, and F. Müller-Plathe, "Molecular mobility in cyclic hydrocarbons: a simulation study," *Journal of Physical Chemistry B*, vol. 103, no. 44, pp. 9731–9737, 1999.
- [32] W. A. Steele, "The physical interaction of gases with crystalline solids. I: gas-solid energies and properties of isolated adsorbed atoms," *Surface Science*, vol. 36, no. 1, pp. 317–352, 1973.
- [33] Y. F. Yin, B. McEnaney, and T. J. Mays, "Dependence of GCEMC simulations of nitrogen adsorption on activated carbons on input parameters," *Carbon*, vol. 36, no. 10, pp. 1425–1432, 1998.
- [34] K. Kaneko, R. F. Cracknell, and D. Nicholson, "Nitrogen adsorption in slit pores at ambient temperatures: comparison of simulation and experiment," *Langmuir*, vol. 10, no. 12, pp. 4606–4609, 1994.
- [35] X. Zhao and J. K. Johnson, "An effective potential for adsorption of polar molecules on graphite," *Molecular Simulation*, vol. 31, no. 1, pp. 1–10, 2005.

## Research Article

# Synthesis of Fe<sub>3</sub>O<sub>4</sub>/Pt Nanoparticles Decorated Carbon Nanotubes and Their Use as Magnetically Recyclable Catalysts

Hongkun He and Chao Gao

MOE Key Laboratory of Macromolecular Synthesis and Functionalization, Department of Polymer Science and Engineering, Zhejiang University, 38 Zheda Road, Hangzhou 310027, China

Correspondence should be addressed to Chao Gao, cgao18@gmail.com

Received 26 July 2010; Accepted 12 October 2010

Academic Editor: Jianyu Huang

Copyright © 2011 H. He and C. Gao. This is an open access article distributed under the Creative Commons Attribution License, which permits unrestricted use, distribution, and reproduction in any medium, provided the original work is properly cited.

We report a facile approach to prepare Fe<sub>3</sub>O<sub>4</sub>/Pt nanoparticles decorated carbon nanotubes (CNTs). The superparamagnetic Fe<sub>3</sub>O<sub>4</sub> nanoparticles with average size of 4 ~ 5 nm were loaded on the surfaces of carboxyl groups functionalized CNTs via a high-temperature solution-phase hydrolysis method from the raw material of FeCl<sub>3</sub>. The synthesis process of magnetic CNTs is green and readily scalable. The loading amounts of Fe<sub>3</sub>O<sub>4</sub> nanoparticles and the magnetizations of the resulting magnetic CNTs show good tunability. The Pt nanoparticles with average size of 2.5 nm were deposited on the magnetic CNTs through a solution-based method. It is demonstrated that the Fe<sub>3</sub>O<sub>4</sub>/Pt nanoparticles decorated CNTs have high catalytic activity in the reduction reaction of 4-nitrophenol and can be readily recycled by a magnet and reused in the next reactions with high efficiencies for at least fifteen successive cycles. The novel CNTs-supported magnetically recyclable catalysts are promising in heterogeneous catalysis applications.

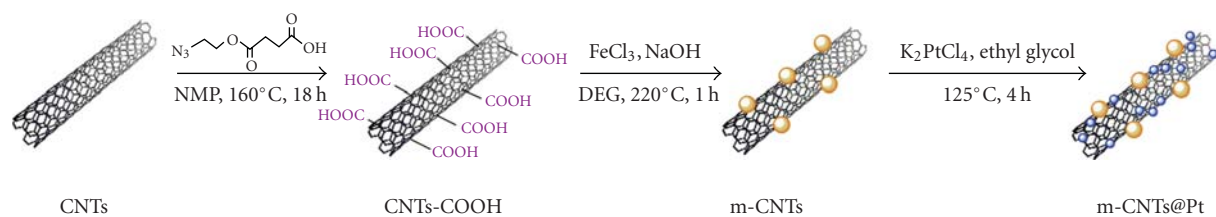
## 1. Introduction

The discovery of carbon nanotubes (CNTs) in the early 1990s has vitalized a flurry of research activities over the past decade [1]. Due to their fascinating structural, optoelectronic, physicochemical, and mechanical properties, CNTs serve as an excellent candidate for the model systems of nanoscale science and technology [2–7]. Among the applications of CNTs in various fields, magnetic CNTs (m-CNTs) produced by functionalizing CNTs with magnetic nanomaterials are one of the most useful nanocomposites, which incorporate the features of both magnetism and CNTs, and thus have great potential in biomanipulations [8, 9], alignment [10], contrast agents for magnetic resonance imaging [11], targeted drug delivery [12], and so forth.

Up to date, various kinds of m-CNTs have been synthesized by decorating CNTs with Ni [13], Co [14], CoO [15], Fe [16] nanoparticles, and so forth. Among them, magnetic iron oxide (e.g., maghemite  $\gamma$ -Fe<sub>2</sub>O<sub>3</sub> or magnetite Fe<sub>3</sub>O<sub>4</sub>) nanoparticles have attracted tremendous attentions due to their low toxicity, stability, and biocompatibility in the physiological environment [17–19].

In this regard, numerous reports related to functionalizing CNTs with iron oxide nanoparticles have progressively sprung up, which can be broadly categorized into three methodologies.

- (1) The first strategy can be termed as “simultaneous” methodology, in which the nanoparticles and CNTs are formed and combined together simultaneously. For example, CNTs containing magnetic iron oxide were obtained by chemical vapor deposition of coal gas with ferrocene as catalyst [20], by carbonization of iron-complex-doped polypyrrole nanotubes [21], and by a carbonization process using ferric chloride-embedded polyimide precursor [22].
- (2) The second strategy is “inside-filling”: iron oxide nanoparticles were encapsulated inside the hollow tubular structures of CNTs to produce magnetic nanotubes. There have been many studies on the fractionation of Fe<sub>2</sub>O<sub>3</sub>- or Fe<sub>3</sub>O<sub>4</sub>-filled carbon nanotubes [23–28].
- (3) The third and more commonly used strategy is “outside-decorating”: iron oxide nanoparticles were



SCHEME 1: Schematic description of the preparation of MWNTs-COOH, m-MWNTs, and m-MWNTs@Pt.

connected onto the outer convex surfaces of CNTs. This type of decorating can be generated, for instance, by in situ growth [17, 29], covalent [30], or noncovalent linkage [10] of functionalized magnetic nanoparticles.

On the other hand, CNTs are also suitable nanoparticle supports for heterogeneous catalysts due to their unique geometry and electronic properties [31]. The activities of CNTs-supported metal nanoparticles would be enhanced through metal-support interactions [32]. This phenomenon is presumably caused by the facts that CNTs are consisted of rolled graphene sheets with curved surface that changes the  $\pi$ -bonding in the graphene sheets, leading to different electronic structures. There have been plenty of reports about the decorating of CNTs with various noble metal nanoparticles such as Pt [33, 34], Pd [32], Ag [35, 36], and Au [37].

Recently, magnetic catalysts have received increasing attention because of the recycled use of the catalyst by an external magnetic field. However, the concept of magnetic catalyst made of magnetic CNTs and catalytic nanoparticles has never been presented and tried despite magnetic catalysts with other substrates such as silica spheres have been reported and demonstrated to be powerful in the reusable catalysts [38]. Based on their large surface area and the intrinsic electronic properties, CNTs would be a superior candidate for the magnetic catalyst support. But in the actual practice, there exist big challenges in the synthesis of CNT-supported magnetic catalysts, since (1) the loss of magnetism or noble nanoparticles is difficult to be avoided, and (2) it is difficult to load different nanoparticles independently on CNTs. So in the previous synthesis of magnetic nanocatalysts, the magnetic nanoparticles were usually stabilized by coating with a silica shell that could not only protect the magnetic particles from chemical attacking but also provide functional groups for subsequently loading the metal catalysts [38]. However, such a process would lead to complex experimental procedures and higher cost.

In this study, we present a facile and versatile approach to acquire CNT-supported magnetic catalysts. The synthesis method is simple and does not need any other stabilizing components. The carboxyl-functionalized CNTs were firstly decorated with  $\text{Fe}_3\text{O}_4$  nanoparticles in a controlled manner and subsequently deposited with Pt nanoparticles by taking advantage of the unoccupied carboxyl groups on CNTs. The resulting  $\text{Fe}_3\text{O}_4/\text{Pt}$  nanoparticles decorated CNTs still maintain strong magnetism and catalytic activities. The

superiorities of our approach are summarized as follows: (1) the superparamagnetic nanoparticles are highly crystalline, monodispersed, and evenly decorated on the convex surfaces of CNTs; (2) the fraction of magnetic nanoparticles deposited on CNTs and magnetic intensity of the resulting m-CNTs can be easily controlled to some extent by adjusting the feed ratio of the precursor to CNTs; (3) the synthesis process is simple, facile, and readily scalable, and the starting materials and other reagents are all commercially available, which will facilitate the large-scale and economically favorable production of m-CNTs catalysts; (4) this approach is in consonance with green chemistry principles. As the “green” concept has been highlighted by worldwide researchers nowadays, this approach is doomed to be promising with its environmentally harmonious features.

Moreover, we also studied the catalytic performance of the resulting catalysts in the reduction of 4-nitrophenol. Recycling the CNTs-supported catalytic nanoparticles can be easily accomplished by applying an external magnetic field, and the separated catalysts can be reused for many times. The novel  $\text{Fe}_3\text{O}_4/\text{Pt}$  nanoparticles decorated CNTs reported herein take advantage of both the unique properties of CNTs supports and the superparamagnetism of the  $\text{Fe}_3\text{O}_4$  nanoparticles, offering promising applications in the heterogeneous catalysis.

## 2. Experimental

**2.1. Materials.** The pristine multiwalled carbon nanotubes (p-MWNTs) were purchased from Tsinghua-Nafine Nano-Powder Commercialization Engineering Center in Beijing (purity >95%). Anhydrous iron (III) chloride ( $\text{FeCl}_3$ , 98%) and diethylene glycol (DEG, 99%) were purchased from Alfa Aesar and used as received. Sodium hydroxide (NaOH, 99%) and ethanol were obtained from Sinopharm Chemical Reagent Co., Ltd. and used as received. The carboxyl-functionalized MWNTs (MWNTs-COOH) were prepared in our lab previously [33], and the density of carboxyl group was calculated to be 0.52 mmol ( $-\text{COOH}$ )/g from the corresponding TGA data.

**2.2. Instrument.** Thermal gravimetric analysis (TGA) was carried out on a TA Instruments TGA-2050 Thermogravimetric Analyzer with a heating rate of  $20^\circ\text{C}/\text{min}$  under a nitrogen flow rate of 60 mL/min. Transmission electron microscopy (TEM) and energy-dispersive X-ray spectrometer (EDS) analyses were performed on a JEOL JEM2010 electron microscope at 200 kV. X-ray diffraction (XRD)

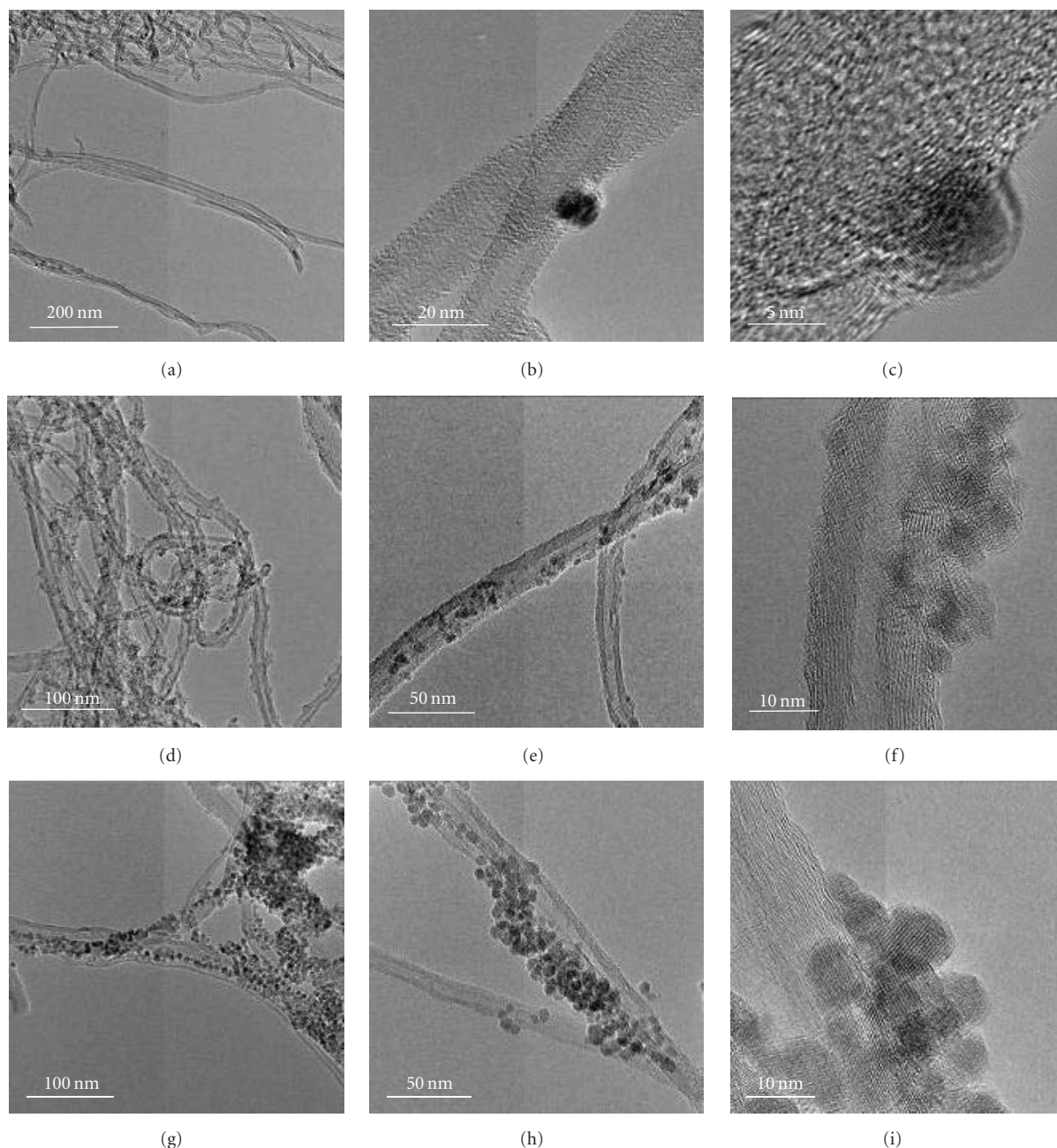


FIGURE 1: TEM images of p-MWNTs (a), m-MWNTs with feed ratios of 0.2/1 (b) and (c), 1/1 ((d)–(f)), and 5/1 ((g)–(i)).

patterns were recorded on a Rigaku X-ray diffractometer D/max-2200/PC equipped with Cu  $K\alpha$  radiation (40 kV, 20 mA) at the rate of 5.0 deg/min over the range of 10–70° ( $2\theta$ ). The magnetic properties were measured using a sample-vibrating magnetometer (VSM, Lake Shore 7410). Raman spectra were collected on a LabRam-1B Raman spectroscopy equipped with a 632.8 nm laser source. UV-visible spectra were recorded using a Varian Cary 300 Bio UV–vis spectrophotometer.

**2.3. Synthesis of Magnetic Multiwalled Carbon Nanotubes (*m*-MWNTs).** First, a solution of NaOH dissolved in DEG

(10 mg/mL) was prepared in advance. NaOH (100 mg, 2.5 mmol) was added into 10 mL of DEG under nitrogen and magnetic stirring, which was heated to 120°C for 1 hour, and then cooled down to 70°C and maintained for later use. In a typical synthesis of *m*-MWNTs (feed ratio = 1/1 (w/w)), MWNTs-COOH (30 mg) and DEG (10 mL) were placed in a three-neck round-bottom flask equipped with a condenser. The mixture was treated with an ultrasonic bath (40 kHz) for 1 minute and then placed on a magnetic stirrer with an oil bath. After  $FeCl_3$  (63 mg, 0.388 mmol, the iron content was equivalent to 30 mg of  $Fe_3O_4$ ) was added under nitrogen atmosphere and magnetic stirring, the mixture was

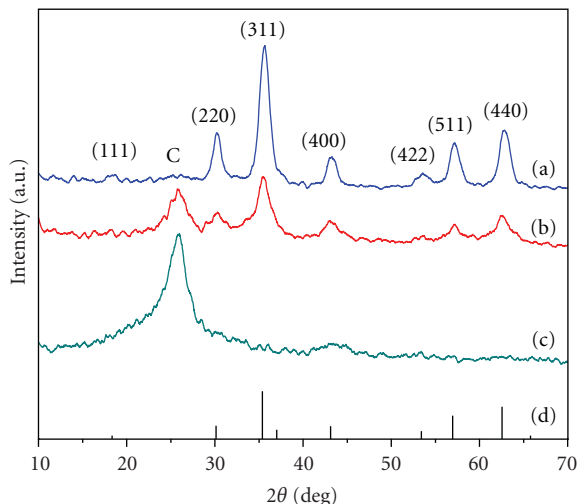


FIGURE 2: X-ray powder diffraction patterns for m-MWNTs with feed ratios of 5/1 (a), 1/1 (b), and 0.2/1 (c), and standard XRD peaks for magnetite (JCPDS card, file No. 19-0629).

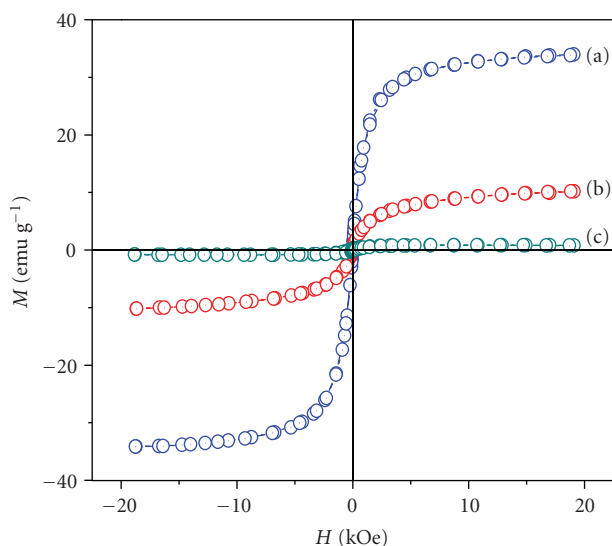


FIGURE 3: The curves of magnetic hysteresis loop at 300 K of m-MWNTs with feed ratios of 5/1 (a), 1/1 (b), and 0.2/1 (c).

then heated and maintained around 220°C for 30 minutes. A NaOH/DEG stock solution (5 mL) was injected quickly into the rapidly stirring mixture via a syringe. The resulting mixture was further heated at around 220°C for 1 hour. After cooling down to room temperature, the product was separated by centrifugation, redispersed in ethanol and collected by centrifugation several times, and then redispersed in water and collected by centrifugation several times. The black solid was dried under vacuum at 60°C overnight to give 48 mg of m-MWNTs. The same protocol was used to prepare m-MWNTs of different feed ratios, except that (1) for the synthesis of m-MWNTs (feed ratio = 1/5 (w/w)), FeCl<sub>3</sub> (0.325 g, 2 mmol) and NaOH/DEG solution (100 mg/mL, 2.5 mL) were used; and (2) for the synthesis of m-MWNTs

((feed ratio = 1/0.2 (w/w)), FeCl<sub>3</sub> (12.6 mg, 0.078 mmol) and NaOH/DEG solution (10 mg/mL, 1 mL) were used.

**2.4. Synthesis of Pt Nanoparticles Decorated m-MWNTs (m-MWNTs@Pt).** Typically, the as-prepared m-MWNTs (10 mg) and 10 mL of ethylene glycol-water solution (3 : 2 volume ratio) were placed into a 25 mL Schlenk flask, which was then treated with an ultrasonic bath (40 kHz) for 3 minute. K<sub>2</sub>PtCl<sub>4</sub> (6.4 mg) was added into the reaction mixture and then heated in a 125°C oil bath under nitrogen atmosphere for 4 hour. The product was centrifuged, rinsed several times with deionized water, and dried under vacuum at 60°C.

### 3. Results and Discussion

**3.1. Preparation and Characterization of m-MWNTs.** The synthesis protocol of magnetic multiwalled carbon nanotubes (m-MWNTs) is illustrated in Scheme 1. Firstly, we used an improved one-step nitrene chemistry to functionalize CNTs [33]. The pristine multiwalled carbon nanotubes (p-MWNTs) were mixed with 4-(2-azidoethoxy)-4-oxobutanoic acid in N-methyl-2-pyrrolidinone (NMP), and the carboxyl groups were covalently linked on the surfaces of nanotubes by nitrene addition at elevated temperature, affording carboxyl-functionalized multiwalled carbon nanotubes (MWNTs-COOH). To produce m-MWNTs, we used a high-temperature solution-phase hydrolysis method [19, 39]. The Fe precursor, FeCl<sub>3</sub>, was firstly coordinated to the carboxyl groups on the surfaces of MWNTs-COOH in diethylene glycol (DEG), then hydrolyzed upon the addition of NaOH at elevated temperature, and eventually dehydrated to in situ generate Fe<sub>3</sub>O<sub>4</sub> nanoparticles.

It is worth noting that instead of using the most commonly used acid oxidation method, the MWNTs-COOH were prepared by the nitrene addition method, which has several advantages: (1) the pollutive acid (concentrated H<sub>2</sub>SO<sub>4</sub>/HNO<sub>3</sub>) could be avoided, making the synthesis process cleaner and more convenient in practice; (2) the reaction is a weight increasing process and the reagents involved in the reaction are cheaply available in large quantity, making the synthesis economically favorable; (3) the severe erosion of CNTs by acid oxidation could be avoided, and thus the damages to the intrinsic morphology and properties of CNTs were significantly reduced. It is also worth mentioning that unlike some widely used iron sources including iron pentacarbonyl and iron acetylacetonate, the FeCl<sub>3</sub> (as well as the solvent DEG) used in the synthesis of m-CNTs is more environmentally friendly and inexpensive. Thus, the entire synthesis route (from the raw materials of CNTs to the final product of m-CNTs) is a totally clean, cheap, and green process.

In the synthesis of m-MWNTs, different feed ratios of FeCl<sub>3</sub> to MWNTs-COOH were used and the transmission electron microscopy (TEM) observation results are shown in Figure 1. The Fe<sub>3</sub>O<sub>4</sub> nanoparticles appear as spherical nanocrystals that spread on the sidewalls of MWNTs. With the feed ratios raise from 0.2/1 to 1/1 and then to 5/1,

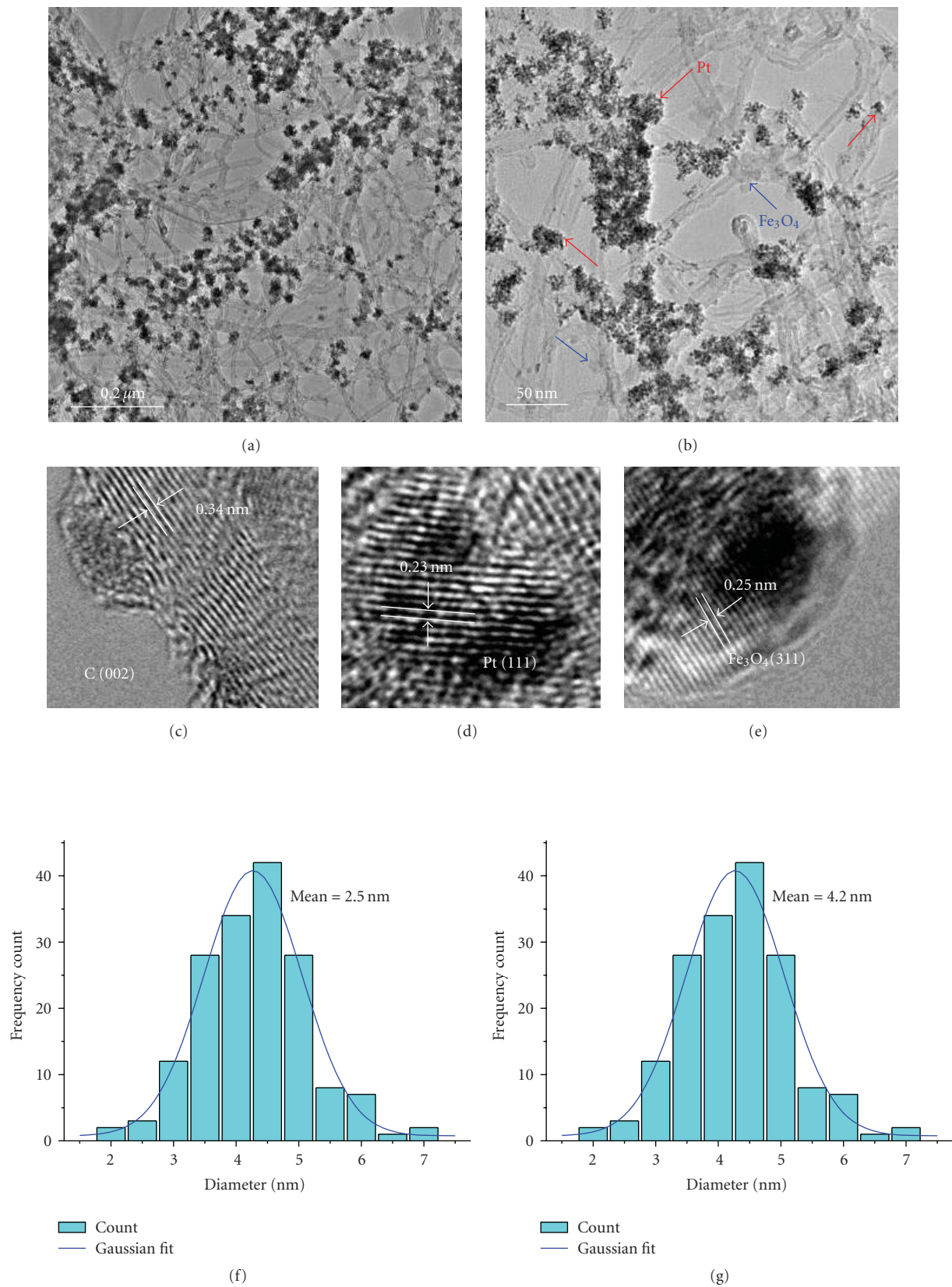


FIGURE 4: TEM images of m-MWNTs@Pt: low-resolution images ((a) and (b)), high-resolution images of the side walls of MWNTs (c), Pt nanoparticles (d), and  $\text{Fe}_3\text{O}_4$  nanoparticles (e). The size distribution analysis of Pt nanoparticles (f) and  $\text{Fe}_3\text{O}_4$  nanoparticles (g) of m-MWNTs@Pt.

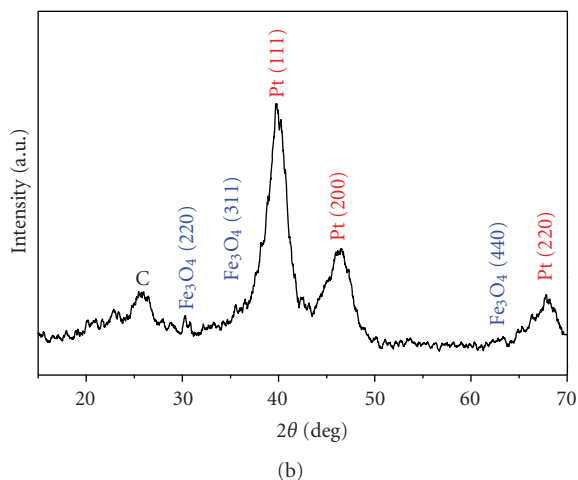
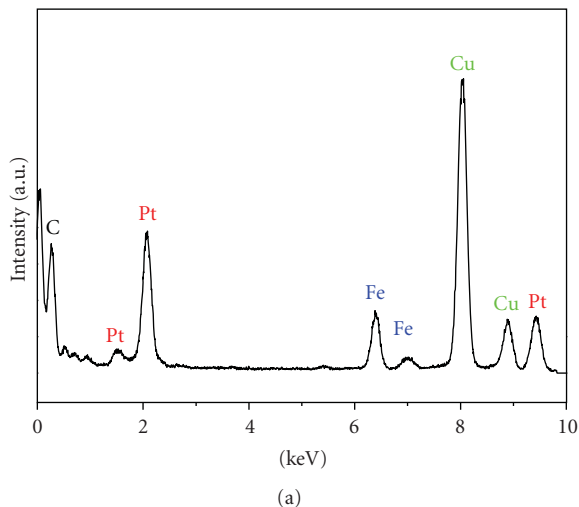


FIGURE 5: The EDS spectrum (a) and XRD pattern (b) of m-MWNTs@Pt.

the average sizes of  $\text{Fe}_3\text{O}_4$  nanoparticles are all in the range of 4 ~ 5 nm, but the amounts of  $\text{Fe}_3\text{O}_4$  nanoparticles on the nanotubes increase remarkably. It is concluded that there are plenty of carboxyl groups along the entire surfaces of MWNTs-COOH, and the relatively amounts of the carboxyl groups that are occupied and unoccupied by  $\text{Fe}_3\text{O}_4$  nanoparticles can be adjusted by varying the feed ratios. The unoccupied carboxyl groups, thereby, could be used to deposit metal nanoparticles in the succeeding reaction.

In addition, the saturated magnetizations of m-MWNTs are also increased from 0.8 to 10.2 and then to 34.1 emu/g with the feed ratios raise from 0.2/1 to 1/1 and then to 5/1. As seen in Figure 2, the magnetic hysteresis loops of all these samples have no remanence or coercivity and exhibit superparamagnetic characteristics at room temperature. All of the resulting samples of m-MWNTs can move toward a magnet placed nearby, and the magnetic response is more obvious for the sample with higher feed ratio (see Figures S3, S5 and S7 in Supplementary Material available online at doi: 10.1155/2011/193510).

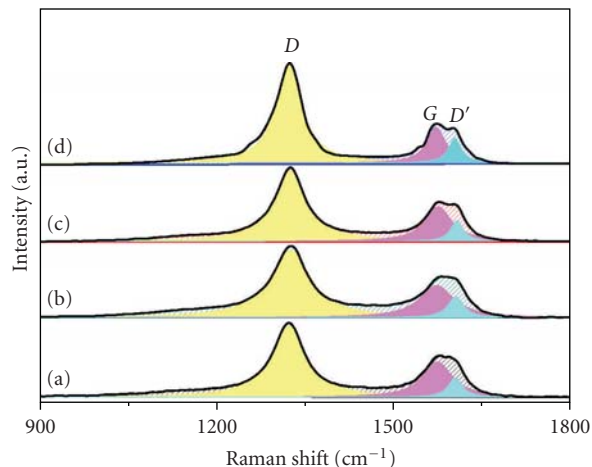


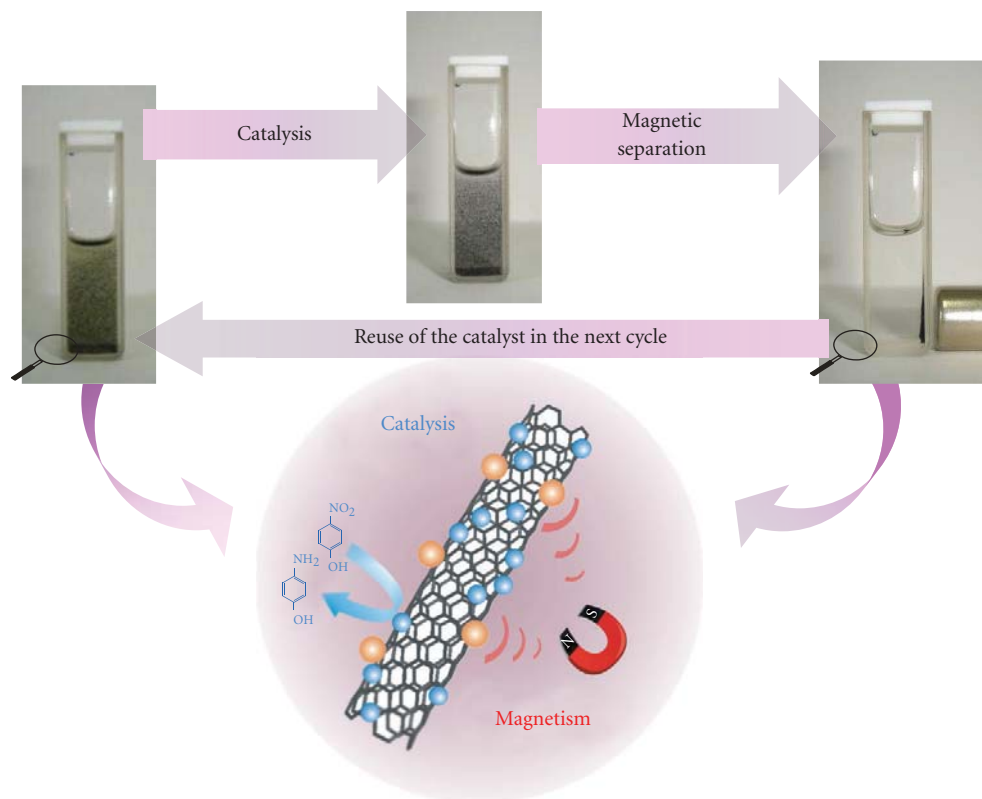
FIGURE 6: Raman spectra of p-MWNTs (a), MWNTs-COOH (b), m-MWNTs (c), and m-MWNTs@Pt (d).

The X-ray diffraction (XRD) analysis in Figure 3 further proved that the nanoparticles on m-MWNTs have good crystalline quality and the diffraction peak positions fit well with the standard XRD data for magnetite (JCPDS card, file No. 19-0629). The diffraction peak at  $2\theta$  25.9 is attributed to the graphite crystalline phase of CNTs, and the intensities of  $\text{Fe}_3\text{O}_4$  diffraction peaks become stronger than those of CNTs with the enlarging of feed ratios.

In comparison, m-MWNTs could not be obtained in the control experiment using p-MWNTs instead of MWNTs-COOH as the templates, as confirmed by the TEM images in Figure S3. This is due to there are no carboxyl groups on p-MWNTs, and the  $\text{Fe}^{3+}$  ions could not be coordinated onto the surfaces of p-MWNTs to form  $\text{Fe}_3\text{O}_4$  nanoparticles. Moreover, the oxidized MWNTs produced by a commonly used acid oxidation method [35] were also used in the control experiment and m-MWNTs could be successfully produced because of their abundant carboxyl groups (Figure S3).

### 3.2. Preparation and Characterization of m-MWNTs@Pt.

Here we select Pt nanoparticles as a typical example of noble metal nanoparticles in this study to prepare Pt nanoparticles decorated m-MWNTs (m-MWNTs@Pt) by using  $\text{K}_2\text{PtCl}_4$  as the Pt precursor and m-MWNTs as the templates via a solution-based method (Scheme 1). The m-MWNTs with feed ratio of 1/1 was chosen as the starting sample for the preparation of m-MWNTs@Pt since the decoration density of  $\text{Fe}_3\text{O}_4$  nanoparticles is moderate and the magnetization is strong enough to enable them to be separated by magnetic force quickly. The residual carboxyl groups on the surfaces of m-MWNTs that are not occupied by  $\text{Fe}_3\text{O}_4$  nanoparticles could serve as the nucleation centers for Pt nanoparticles. By mixing m-MWNTs and  $\text{K}_2\text{PtCl}_4$  in ethylene glycol and heating at elevated temperature, the Pt nanoparticles were generated under the reductive atmosphere. Besides, by replacing  $\text{K}_2\text{PtCl}_4$  with different metal precursors and



SCHEME 2: The schematic illustration of the recycling of m-MWNTs@Pt for the catalytic reduction of 4-nitrophenol into 4-aminophenol in a quartz cuvette.

optimizing the synthesis conditions if necessary, we could probably obtain other kinds of metal nanoparticles (e.g., Pd, Au, Ag, Ru) decorated m-MWNTs.

The typical TEM images of m-MWNTs@Pt are shown in Figure 4. The  $\text{Fe}_3\text{O}_4$  nanoparticles on MWNTs (marked by blue arrows) show the same scattered distribution pattern as those in Figures 1(d)–1(f), while the Pt nanoparticles mostly appear as nanoscale clusters that consist of many Pt nanoparticles (marked by red arrows). In the high-resolution TEM (HR-TEM) images of m-MWNTs@Pt (Figures 4(c)–4(e)), the lattice fringes of carbon walls (002), Pt(111), and  $\text{Fe}_3\text{O}_4$  (311) were clearly observed, which denote that the sidewall structures of MWNTs were not spoiled after being modified with surface carboxyl groups and deposited with nanoparticles, and the Pt and  $\text{Fe}_3\text{O}_4$  nanoparticles have good crystalline quality. The statistical sizes of Pt and  $\text{Fe}_3\text{O}_4$  nanoparticles are 2.5 and 4.2 nm, respectively, with narrow size distributions (Figures 4(f) and 4(g)).

Figure 5(a) shows the EDS spectrum of m-MWNTs@Pt, revealing the presence of Fe and Pt elements on the carbon supports (the Cu signs origin from the TEM copper grid loaded with the samples). From the EDS analysis results, it is also found that contents of Pt and Fe in m-MWNTs@Pt are 35.9 and 14.5 wt%, respectively. The crystalline structure of m-MWNTs@Pt was confirmed with powder XRD measurements (Figure 5(b)). The main reflection peaks of  $\text{Fe}_3\text{O}_4$

and Pt crystals were clearly presented and the assignments of their peaks are indexed in Figure 5(b).

The Raman spectra for p-MWNTs, MWNTs-COOH, m-MWNTs, and m-MWNTs@Pt are shown in Figure 6. The G and D bands located around  $1580$  and  $1320\text{ cm}^{-1}$  were clearly observed and are related to the vibration of  $\text{sp}^2$ -bonded carbon atoms in a 2D hexagonal lattice and the defects/disorder-induced modes, respectively [40]. The ratios of D- to G-band intensity ( $I_D/I_G$ ) for MWNTs-COOH (2.44), m-MWNTs (2.48), and m-MWNTs@Pt (3.81) are greater than those of p-MWNTs (2.38), which are resulted from the increase in the degree of disorder after functionalization of MWNTs. The  $D'$ -bands around  $1602\text{ cm}^{-1}$  are not very distinct for the p-MWNTs and MWNTs-COOH, but they become more obvious for m-MWNTs and m-MWNTs@Pt, indicating the defects and disorder of MWNTs increase after functionalization [41].

**3.3. Catalysis Applications.** The catalysis activity of the resulting sample of m-MWNTs@Pt is measured by using a model reaction of the catalytic reduction of 4-nitrophenol into 4-aminophenol with  $\text{NaBH}_4$ , which has been demonstrated to be an effective way to evaluate the catalytic capability of noble metal nanocatalysts [38, 42–44]. The ultraviolet-visible (UV-vis) spectroscopy was used to monitor the reduction process, and the results for the first reduction

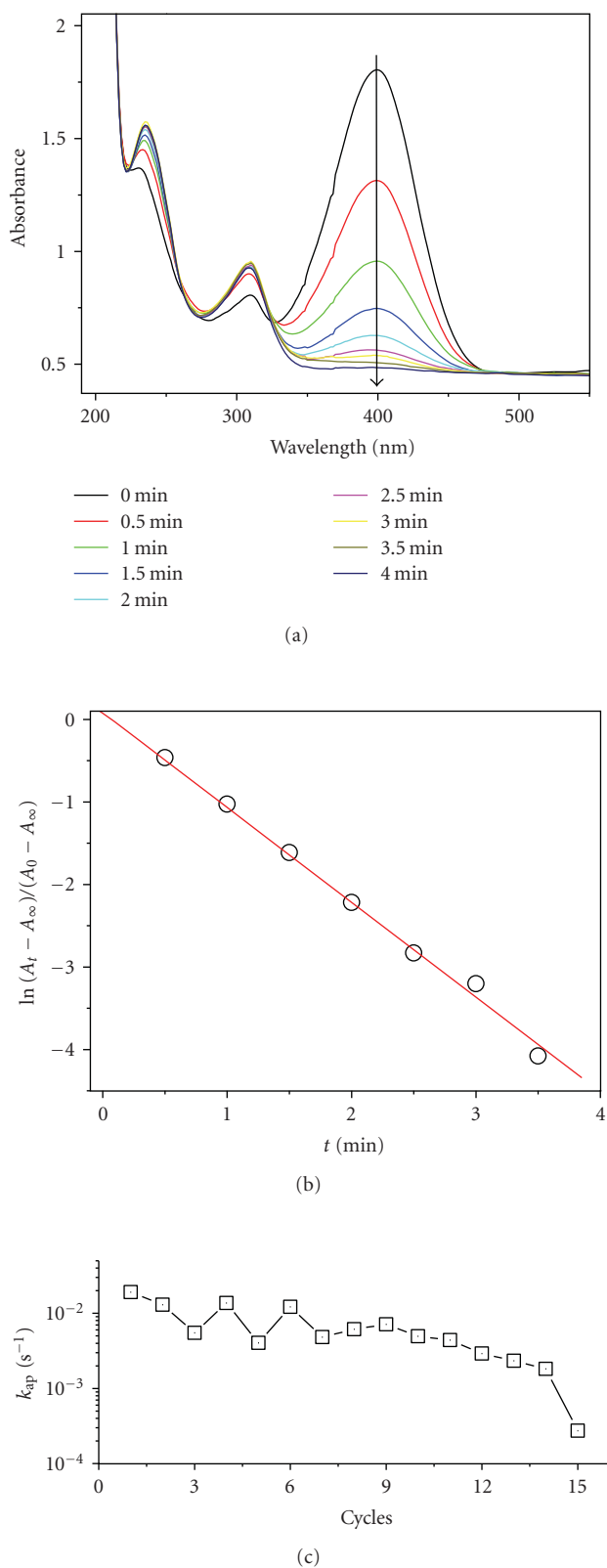


FIGURE 7: (a) Successive UV-vis spectra for the reduction of 4-nitrophenol into 4-aminophenol with the catalyst of m-MWNTs@Pt in the first cycle. (b) The linearized data for first-order analysis corresponding to (a). (c) The calculated values of  $k_{ap}$  in the fifteen successive cycles of reduction and magnetic separation with the catalyst of m-MWNTs@Pt.

cycle are shown in Figure 7(a). Before the catalysts were added, the characteristic absorption peak of 4-nitrophenol located at 400 nm remained constant, suggesting no reduction is occurred. Once the catalysts were added into the reaction mixture, the peak at 400 nm decreased quickly and completely disappeared within several minutes. Meanwhile, a new peak at 290 nm appeared that was attributed to 4-aminophenol. The reduction could also be clearly observed by naked eyes since the yellow color of 4-nitrophenol solution gradually faded out during the reduction process (Scheme 2).

The concentration of  $\text{NaBH}_4$  greatly exceeded those of 4-nitrophenol and the catalyst and remained essentially constant during the reduction. Therefore, the kinetics of this reduction is supposed to follow pseudo-first-order to the concentration of 4-nitrophenol, and the kinetic equation can be defined as follows:

$$\ln\left(\frac{A_t - A_\infty}{A_0 - A_\infty}\right) = -k_{ap}t, \quad (1)$$

where  $t$  is the reaction time,  $A_0$  is the initial absorbance at time zero,  $A_t$  is the absorbance at time  $t$ ,  $A_\infty$  is the absorbance when the reaction is completed, and  $k_{ap}$  is the apparent rate constant [45]. As seen in Figure 7(b), the linear-fit plot coincides with (1), indicating the pseudo-first-order kinetics of this reduction with m-MWNTs@Pt. When the reduction is completed, the m-MWNTs@Pt could be quickly separated from the reaction system by applying an external magnetic field. The magnetically separated m-MWNTs@Pt could be reused in the next run of the same catalytic reaction. It is found that the m-MWNTs@Pt still possess catalytic activity even after 15 consecutive cycles of catalytic reduction and magnetic separation. In each cycle of catalytic reduction, the data show good linear correlation with time as (1) (Figure S7). The calculated values of  $k_{ap}$  in the fifteen successive cycles of catalytic reduction are shown in Figure 7(c). The values of  $k_{ap}$  exhibit a general trend of decrease with the increase of the number of cycles (from  $1.92 \times 10^{-2} \text{ s}^{-1}$  for cycle 1 to  $2.74 \times 10^{-4} \text{ s}^{-1}$  for cycle 15). The changing range of  $k_{ap}$  is comparable with or higher than some other types of supported metal nanocatalysts, such as dendrimer-metal nanocomposites ( $10^{-5} \sim 10^{-1} \text{ s}^{-1}$ ) [42, 46] and  $\text{SiO}_2$ -Pt nanohybrids ( $\sim 10^{-3} \text{ s}^{-1}$ ) [38]. The large values of  $k_{ap}$  in the successive cycles of catalytic reduction (even after 15 cycles) demonstrated the high catalytic activity of m-MWNTs@Pt and the feasibility to use them as magnetically recyclable catalysts.

## 4. Conclusions

In summary, we developed a novel kind of  $\text{Fe}_3\text{O}_4/\text{Pt}$  nanoparticles decorated CNTs for use as the magnetically recyclable catalysts for the first time. The synthesis of magnetic CNTs is facile, well controllable, and readily scalable. The resulting catalysts show high catalytic activity in the reduction of 4-nitrophenol and can be reused for at least fifteen cycles. The superparamagnetic property of the catalysts enables them to be easily separated by an external

magnetic field, which greatly facilitates the recycle of the catalysts. This synthesis approach reported here is a general one that is expected to be applicable with (1) different types of CNTs: single-walled, double-walled, and multiwalled carbon nanotubes; (2) different types of magnetic nanoparticles:  $\text{Fe}_3\text{O}_4$ ,  $\gamma\text{-Fe}_2\text{O}_3$ , Co, CoO, Ni, and so forth; (3) different embedding types of magnetic nanoparticles to the CNTs: inside-filling, outside-decorating, and so forth; (4) different types of metals: Pt, Pd, Ag, Au, Ru, and so forth; and (5) different types of catalytic reactions: hydrogenation, oxidation of alcohols, Heck reaction, and so forth. It is believed that the novel CNTs-supported magnetically recyclable catalysts will find important applications in heterogeneous catalysis.

## Acknowledgments

This work was financially supported by the National Natural Science Foundation of China (nos. 50773038 and 20974093), National Basic Research Program of China (973 Program) (no. 2007CB936000), the Fundamental Research Funds for the Central Universities (2009QNA4040), Qianjiang Talent Foundation of Zhejiang Province (2010R10021), and the Foundation for the Author of National Excellent Doctoral Dissertation of China (no. 200527).

## References

- [1] S. Iijima, "Helical microtubules of graphitic carbon," *Nature*, vol. 354, no. 6348, pp. 56–58, 1991.
- [2] L. Dai and A. W. H. Mau, "Controlled synthesis and modification of carbon nanotubes and  $\text{C}_{60}$ : carbon nanostructures for advanced polymeric composite materials," *Advanced Materials*, vol. 13, no. 12–13, pp. 899–913, 2001.
- [3] S. Niyogi, M. A. Hamon, H. Hu et al., "Chemistry of single-walled carbon nanotubes," *Accounts of Chemical Research*, vol. 35, no. 12, pp. 1105–1113, 2002.
- [4] H. Dai, "Carbon nanotubes: synthesis, integration, and properties," *Accounts of Chemical Research*, vol. 35, no. 12, pp. 1035–1044, 2002.
- [5] R. H. Baughman, A. A. Zakhidov, and W. A. De Heer, "Carbon nanotubes—the route toward applications," *Science*, vol. 297, no. 5582, pp. 787–792, 2002.
- [6] V. Georgakilas, D. Gournis, V. Tzitzios, L. Pasquato, D. M. Guldi, and M. Prato, "Decorating carbon nanotubes with metal or semiconductor nanoparticles," *Journal of Materials Chemistry*, vol. 17, no. 26, pp. 2679–2694, 2007.
- [7] D. Eder, "Carbon nanotube-inorganic hybrids," *Chemical Reviews*, vol. 110, no. 3, pp. 1348–1385, 2010.
- [8] C. Gao, W. Li, H. Morimoto, Y. Nagaoka, and T. Maekawa, "Magnetic carbon nanotubes: synthesis by electrostatic self-assembly approach and application in biomanipulations," *Journal of Physical Chemistry B*, vol. 110, no. 14, pp. 7213–7220, 2006.
- [9] W. Li, C. Gao, H. Qian, J. Ren, and D. Yan, "Multiamino-functionalized carbon nanotubes and their applications in loading quantum dots and magnetic nanoparticles," *Journal of Materials Chemistry*, vol. 16, no. 19, pp. 1852–1859, 2006.
- [10] M. A. Correa-Duarte, M. Grzelczak, V. Salgueiriño-Maceira et al., "Alignment of carbon nanotubes under low magnetic fields through attachment of magnetic nanoparticles," *Journal of Physical Chemistry B*, vol. 109, no. 41, pp. 19060–19063, 2005.
- [11] C. Richard, B.-T. Doan, J.-C. Beloeil, M. Bessodes, É. Tóth, and D. Scherman, "Noncovalent functionalization of carbon nanotubes with amphiphilic  $\text{Cd}^{3+}$  chelates: toward powerful  $T_1$  and  $T_2$  MRI contrast agents," *Nano Letters*, vol. 8, no. 1, pp. 232–236, 2008.
- [12] Z. Liu, S. Tabakman, K. Welsher, and H. Dai, "Carbon nanotubes in biology and medicine: in vitro and in vivo detection, imaging and drug delivery," *Nano Research*, vol. 2, no. 2, pp. 85–120, 2009.
- [13] D. Gozzi, A. Latini, G. Capannelli et al., "Synthesis and magnetic characterization of Ni nanoparticles and Ni nanoparticles in multiwalled carbon nanotubes," *Journal of Alloys and Compounds*, vol. 419, no. 1–2, pp. 32–39, 2006.
- [14] R. Kozhuharova, M. Ritschel, D. Elefant et al., "Well-aligned Co-filled carbon nanotubes: preparation and magnetic properties," *Applied Surface Science*, vol. 238, no. 1–4, pp. 355–359, 2004.
- [15] H. Zhang, N. Du, P. Wu, B. Chen, and D. Yang, "Functionalization of carbon nanotubes with magnetic nanoparticles: general nonaqueous synthesis and magnetic properties," *Nanotechnology*, vol. 19, no. 31, Article ID 315604, 2008.
- [16] Y. Li, T. Kaneko, T. Ogawa, M. Takahashi, and R. Hatakeyama, "Magnetic characterization of Fe-nanoparticles encapsulated single-walled carbon nanotubes," *Chemical Communications*, no. 3, pp. 254–256, 2007.
- [17] J. Wan, W. Cai, J. Feng, X. Meng, and E. Liu, "In situ decoration of carbon nanotubes with nearly monodisperse magnetite nanoparticles in liquid polyols," *Journal of Materials Chemistry*, vol. 17, no. 12, pp. 1188–1192, 2007.
- [18] I. Brigger, C. Dubernet, and P. Couvreur, "Nanoparticles in cancer therapy and diagnosis," *Advanced Drug Delivery Reviews*, vol. 54, no. 5, pp. 631–651, 2002.
- [19] J. Ge, Y. Hu, M. Biasini, W. P. Beyermann, and Y. Yin, "Superparamagnetic magnetite colloidal nanocrystal clusters," *Angewandte Chemie International Edition*, vol. 46, no. 23, pp. 4342–4345, 2007.
- [20] J. Qiu, Q. Li, Z. Wang, Y. Sun, and H. Zhang, "CVD synthesis of coal-gas-derived carbon nanotubes and nanocapsules containing magnetic iron carbide and oxide," *Carbon*, vol. 44, no. 12, pp. 2565–2568, 2006.
- [21] J. Jang and H. Yoon, "Fabrication of magnetic carbon nanotubes using a metal-impregnated polymer precursor," *Advanced Materials*, vol. 15, no. 24, pp. 2088–2091, 2003.
- [22] J. Jang, K. J. Lee, and Y. Kim, "Fabrication of polyimide nanotubes and carbon nanotubes containing magnetic iron oxide in confinement," *Chemical Communications*, no. 30, pp. 3847–3849, 2005.
- [23] G. Korneva, H. Ye, Y. Gogotsi et al., "Carbon nanotubes loaded with magnetic particles," *Nano Letters*, vol. 5, no. 5, pp. 879–884, 2005.
- [24] W. Chen, X. Pan, M.-G. Willinger, D. S. Su, and X. Bao, "Facile autoreduction of iron oxide/carbon nanotube encapsulates," *Journal of the American Chemical Society*, vol. 128, no. 10, pp. 3136–3137, 2006.
- [25] W. Chen, X. Pan, and X. Bao, "Tuning of redox properties of iron and iron oxides via encapsulation within carbon nanotubes," *Journal of the American Chemical Society*, vol. 129, no. 23, pp. 7421–7426, 2007.
- [26] F. Cao, K. Zhong, A. Gao, C. Chen, Q. Li, and Q. Chen, "Reducing reaction of  $\text{Fe}_3\text{O}_4$  in nanoscopic reactors of a-CNTs," *Journal of Physical Chemistry B*, vol. 111, no. 7, pp. 1724–1728, 2007.

- [27] S. Qu, F. Huang, G. Chen, S. Yu, and J. Kong, "Magnetic assembled electrochemical platform using Fe<sub>2</sub>O<sub>3</sub> filled carbon nanotubes and enzyme," *Electrochemistry Communications*, vol. 9, no. 12, pp. 2812–2816, 2007.
- [28] B. T. Hang, H. Hayashi, S.-H. Yoon, S. Okada, and J.-I. Yamaki, "Fe<sub>2</sub>O<sub>3</sub>-filled carbon nanotubes as a negative electrode for an Fe-air battery," *Journal of Power Sources*, vol. 178, no. 1, pp. 393–401, 2008.
- [29] S. F. Chin, K. S. Iyer, and C. L. Raston, "Fabrication of carbon nano-tubes decorated with ultra fine superparamagnetic nano-particles under continuous flow conditions," *Lab on a Chip*, vol. 8, no. 3, pp. 439–442, 2008.
- [30] H. He, Y. Zhang, C. Gao, and J. Wu, "'Clicked' magnetic nanohybrids with a soft polymer interlayer," *Chemical Communications*, no. 13, pp. 1655–1657, 2009.
- [31] G. G. Wildgoose, C. E. Banks, and R. G. Compton, "Metal nanoparticles and related materials supported on Carbon nanotubes: methods and applications," *Small*, vol. 2, no. 2, pp. 182–193, 2006.
- [32] Y. S. Chun, J. Y. Shin, C. E. Song, and S.-G. Lee, "Palladium nanoparticles supported onto ionic carbon nanotubes as robust recyclable catalysts in an ionic liquid," *Chemical Communications*, no. 8, pp. 942–944, 2008.
- [33] C. Gao, H. He, L. Zhou, X. Zheng, and Y. Zhang, "Scalable functional group engineering of carbon nanotubes by improved one-step nitrene chemistry," *Chemistry of Materials*, vol. 21, no. 2, pp. 360–370, 2009.
- [34] A. Kaniyoor, R. I. Jafri, T. Arockiadoss, and S. Ramaprabhu, "Nanostructured Pt decorated graphene and multi walled carbon nanotube based room temperature hydrogen gas sensor," *Nanoscale*, vol. 1, no. 3, pp. 382–386, 2009.
- [35] C. Gao, C. D. Vo, Y. Z. Jin, W. Li, and S. P. Armes, "Multi-hydroxy polymer-functionalized carbon nanotubes: synthesis, derivatization, and metal loading," *Macromolecules*, vol. 38, no. 21, pp. 8634–8648, 2005.
- [36] C. Gao, W. Li, Y. Z. Jin, and H. Kong, "Facile and large-scale synthesis and characterization of carbon nanotube/silver nanocrystal nanohybrids," *Nanotechnology*, vol. 17, no. 12, article 010, pp. 2882–2890, 2006.
- [37] H. C. Choi, M. Shim, S. Bangsaruntip, and H. Dai, "Spontaneous reduction of metal ions on the sidewalls of carbon nanotubes," *Journal of the American Chemical Society*, vol. 124, no. 31, pp. 9058–9059, 2002.
- [38] L. Zhou, C. Gao, and W. Xu, "Robust Fe<sub>3</sub>O<sub>4</sub>/SiO<sub>2</sub>-Pt/Au/Pd magnetic nanocatalysts with multifunctional hyperbranched polyglycerol amplifiers," *Langmuir*, vol. 26, no. 13, pp. 11217–11225, 2010.
- [39] J. Ge, Y. Hu, M. Biasini et al., "One-step synthesis of highly water-soluble magnetite colloidal nanocrystals," *Chemistry*, vol. 13, no. 25, pp. 7153–7161, 2007.
- [40] Y. Zhang, H. K. He, and G. Chao, "Clickable macroinitiator strategy to build amphiphilic polymer brushes on carbon nanotubes," *Macromolecules*, vol. 41, no. 24, pp. 9581–9594, 2008.
- [41] Y. Zhang, H. He, C. Gao, and J. Wu, "Covalent layer-by-layer functionalization of multiwalled carbon nanotubes by click chemistry," *Langmuir*, vol. 25, no. 10, pp. 5814–5824, 2009.
- [42] K. Esumi, R. Isono, and T. Yoshimura, "Preparation of PAMAM- and PPI-Metal (Silver, Platinum, and Palladium) nanocomposites and their catalytic activities for reduction of 4-nitrophenol," *Langmuir*, vol. 20, no. 1, pp. 237–243, 2004.
- [43] J. Wu, H. He, and C. Gao, "β-Cyclodextrin-capped polyrotaxanes: one-pot facile synthesis via click chemistry and use as templates for platinum nanowires," *Macromolecules*, vol. 43, no. 5, pp. 2252–2260, 2010.
- [44] H. He and C. Gao, "A general strategy for the preparation of carbon nanotubes and graphene oxide decorated with PdO nanoparticles in water," *Molecules*, vol. 15, no. 7, pp. 4679–4694, 2010.
- [45] I. Pastoriza-Santos, J. Pérez-Juste, S. Carregal-Romero, P. Hervés, and L. M. Liz-Marzán, "Metallodielectric hollow shells: optical and catalytic properties," *Chemistry*, vol. 1, no. 5, pp. 730–736, 2006.
- [46] K. Esumi, K. Miyamoto, and T. Yoshimura, "Comparison of PAMAM-Au and PPI-Au nanocomposites and their catalytic activity for reduction of 4-nitrophenol," *Journal of Colloid and Interface Science*, vol. 254, no. 2, pp. 402–405, 2002.